Michael V. Sadovskii

Reviews on Condensed Matter Physics

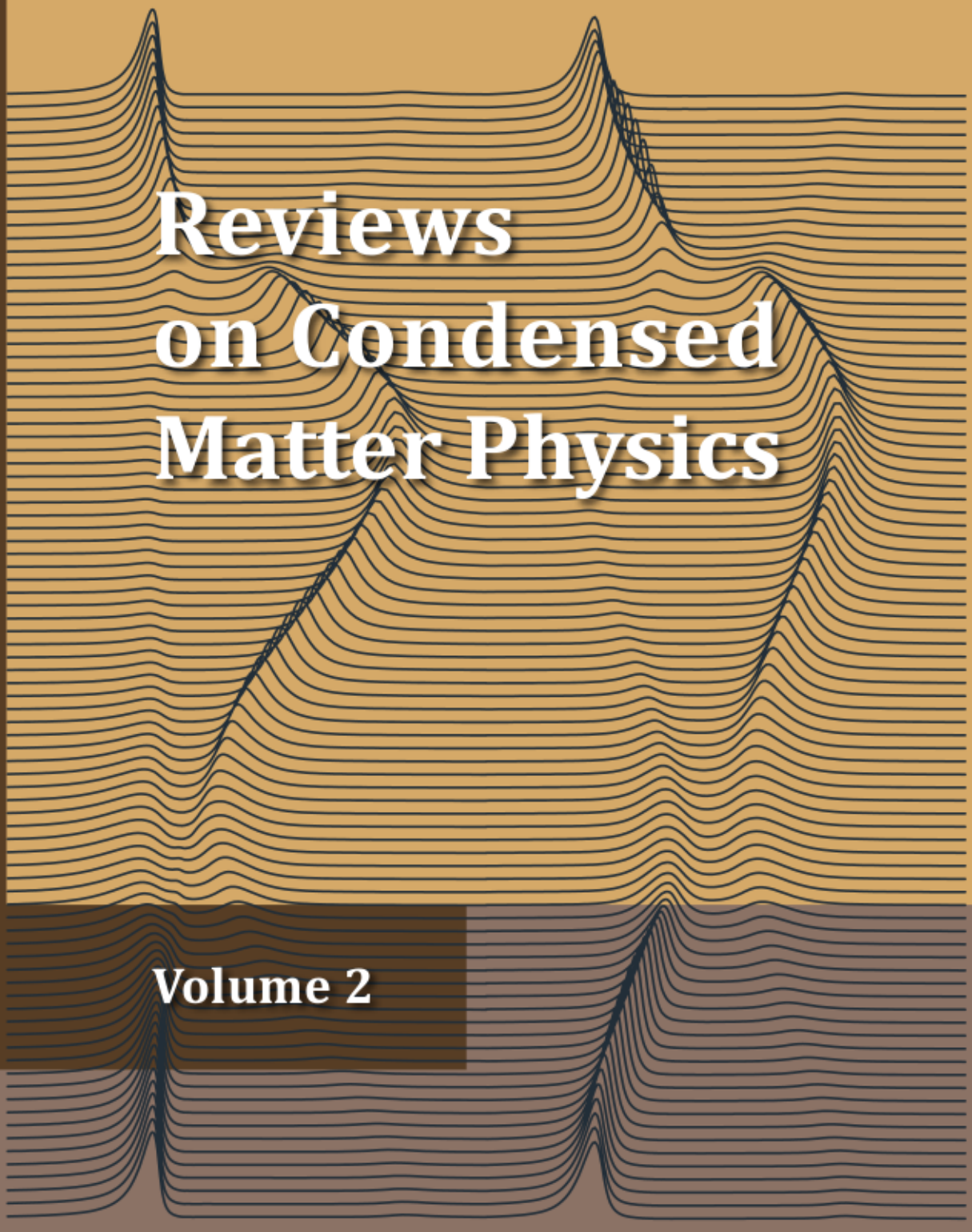

Volume 2

Reviews on Condensed Matter Physics

Michael V. Sadovskii

Institute of Electrophysics, Russian Academy of Sciences

Volume 2

УДК 538.9
S 12

Michael V. Sadovskii

Reviews on Condensed Matter Physics (in Two Volumes), Vol. 2.
Ekaterinburg, 2022. – 272 p.

ISBN 978-5-907502-81-9

В издании представлены избранные обзорные работы академика РАН М.В. Садовского.

I том охватывает обзоры, опубликованные в 1980–2000 гг. и посвященные физике сильно неупорядоченных систем: теории перехода полупроводник–металл в жидких полупроводниках, теории локализации и андерсоновского перехода металл–диэлектрик, а также анализу сверхпроводимости вблизи такого перехода.

Во II томе представлены обзоры, опубликованные в 2001–2022 гг. и, в основном, посвященные исследованию высокотемпературной сверхпроводимости. Эти работы охватывают достаточно широкий круг проблем (псевдощелевое состояние, сильные электронные корреляции), возникающих при описании сверхпроводимости и нормального состояния в высокотемпературных сверхпроводниках.

Издание может быть полезно специалистам в области физики неупорядоченных и сильнокоррелированных систем, физики высокотемпературной сверхпроводимости, студентам соответствующих специальностей, а также всем интересующимся физикой конденсированного состояния.

ISBN 978-5-907502-81-9
© M.V. Sadovskii, 2022

CONTENTS

M.V. Sadovskii
Pseudogap in High-Temperature Superconductors
Physics Uspekhi, v. 44, No. 5, 515–540 (2001) 5

M.V. Sadovskii
Models of the Pseudogap State in High-Temperature Superconductors
In "Strings, branes, lattices, networks, pseudogaps and specks of dust" (Proceedings of I.E. Tamm Seminar), 357–441, "Scientific World", Moscow, 2007 (in Russian); ArXiv:cond-mat/0408489 30

E.Z. Kuchinskii, I.A. Nekrasov, M.V. Sadovskii
Pseudogaps: Introducing the Length Scale into DMFT
Low Temp. Phys., v. 32, No. 4/5, 398–405 (2006) 108

M.V. Sadovskii
High-Temperature Superconductivity in Iron Based Layered Compounds
Physics Uspekhi, v. 51, No. 12, 1201–1227 (2008) 118

E.Z. Kuchinskii, I.A. Nekrasov, M.V. Sadovskii
Generalized Dynamical Mean Field Theory in the Physics of Strongly Correlated Systems
Physics Uspekhi, v. 55, No. 4, 325–355 (2012) 145

I.A. Nekrasov, M.V. Sadovskii
Electronic Structure of New Iron-Based Superconductors: from Pnictides to Chalcogenides and Other Similar Systems
JETP Letters, v. 99, No. 10, 598–612 (2014) 176

E.Z. Kuchinskii, M.V. Sadovskii
DMFT+Σ Approach to Disordered Hubbard Model
JETP, v. 122, No. 3, 510–525 (2016) 191

M.V. Sadovskii
High-Temperature Superconductivity in FeSe Monolayers
Physics Uspekhi, v. 59, No. 10, 947–967 (2016) 207

M.V. Sadovskii
Planckian Relaxation Delusion in Metals
Physics Uspekhi, v. 64, No. 2, 157–190 (2021) 228

M.V. Sadovskii
Limits of Eliashberg Theory and Bounds for Superconducting Transition Temperature
Physics Uspekhi, v. 65, No. 7 (2022) 244

List of scientific publications by M.V. Sadovskii 262

Physics – Uspekhi **44** (5) 515 – 539 (2001) © 2001 Uspekhi Fizicheskikh Nauk, Russian Academy of Sciences

REVIEWS OF TOPICAL PROBLEMS PACS numbers: 74.20.Mn, **74.72.–h**, **74.25.–q**, 74.25.Jb

Pseudogap in high-temperature superconductors

M V Sadovskiĭ

DOI: 10.1070/PU2001v044n05ABEH000902

Contents

1. **Introduction** **515**
2. **Basic experimental facts** **516**
   2.1 Specific heat and tunneling; 2.2 NMR and kinetic properties; 2.3 Optical conductivity; 2.4 Fermi surface and ARPES; 2.5 Other experiments
3. **Theoretical models of the pseudogap state** **522**
   3.1 Scattering on short-range-order fluctuations: Qualitative ideas; 3.2 Recurrent procedure for the Green functions; 3.3 Spectral density and the density of states; 3.4 Two-particle Green function and optical conductivity
4. **Superconductivity in the pseudogap state** **529**
   4.1 Gor'kov equations; 4.2 Transition temperature and the temperature dependence of the gap; 4.3 Cooper instability; 4.4 Ginzburg – Landau equations and the basic properties of superconductors with a pseudogap near T_c; 4.5 Effects of the non-self-averaging nature of the order parameter
5. **Conclusion. Problems and prospects** **536**
   References **538**

Abstract. The paper reviews the basic experimental facts and a number of theoretical models relevant to the understanding of the pseudogap state in high-temperature superconductors. The state is observed in the region of less-than-optimal current-carrier concentrations in the HTSC cuprate phase diagram and manifests itself as various anomalies in the electronic properties, presumably due to the antiferromagnetic short-range-order fluctuations that occur as the antiferromagnetic region of the phase diagram is approached. The interaction of current carriers with these fluctuations leads to an anisotropic transformation of the electron spectrum and causes the system to behave as a non-Fermi liquid in certain regions of the Fermi surface. Simple theoretical models for describing the basic properties of the pseudogap state, in particular renormalization-induced anomalies in the superconducting state, are discussed.

1. Introduction

The study of high-temperature (or high-T_c) superconductivity (HTSC) in copper oxides remains one of the central avenues of research in the physics of the condensed state. Despite enormous efforts of both experimenters and theoreticians, the nature of this phenomenon remains unclear. It is a well-known fact that the main difficulties here are related to the very unusual properties of these systems in the normal (nonsuperconducting) state, and without a clear understanding of the nature of these properties there is little hope for completely elucidating the microscopic mechanism of high-T_c superconductivity. In recent years one of the main aspects of high-T_c superconductor physics has been the study of the anomalies of what is known as the pseudogap state [1], which is observed in the region of the phase diagram corresponding to charge-carrier concentrations lower than optimal one (i.e. the concentration corresponding to the maximum temperature of the superconducting transition, T_c); it is usually called the 'underdoped' region. In this region there are many anomalies of the electronic properties in both the normal and the superconducting state, which are related to the drop in the single-particle density of states and to the anisotropic transformation of the charge-carrier spectral density. The understanding of the nature and properties of the pseudogap state is the central problem of any approach to the description of the complex phase diagram of HTSC systems. Hundreds of experimental and theoretical papers have been devoted to this problem [1].

The goal of the present review is to present the main experimental facts pertaining to the observations of the pseudogap state in underdoped high-T_c cuprates and to discuss a number of simple theoretical models of this state. The review is not exhaustive in either describing the experimental data or giving the full theoretical picture. The experimental data are presented fairly briefly, since the literature already has a number of good reviews [2 – 6]

M V Sadovskiĭ Institute of Electrophysics, Ural Branch of the Russian Academy of Sciences
ul. Amundsena 106, 620016 Ekaterinburg, Russian Federation
Tel. (7-3432) 67 87 86. Fax (7-3432) 67 87 94
E-mail: sadovski@iep.uran.ru

Received 27 November 2000, revised 8 February 2001
Uspekhi Fizicheskikh Nauk **171** (5) 539 –564 (2001)
Translated by E Yankovsky; edited by A V Getling

[1] Suffice it to say that the well-known E-archive of preprints, cond-mat, contains more than 600 papers devoted, in one way or another, to the physics of the pseudogap sate. At the major conference on superconductivity held in Houston, M^2S – HTSC-VI (February 2000), four section meetings were devoted to this problem — more than to any other problem of HTSC physics.

devoted to these problems in one way or another. The theoretical part is also fairly subjective and, to a large extent, reflects the author's viewpoint. There are two basic theoretical scenarios for explaining the pseudogap anomalies of HTSC systems. The first one is based on the model in which Cooper pairs are formed above the transition temperature [7–10], with the subsequent establishment of their phase coherence at $T < T_c$. The second scenario assumes that the pseudogap state emerges due to 'dielectric' type, short-range-order fluctuations, which are present in the region of underdoped compositions in the phase diagram. The most popular picture here is that of antiferromagnetic (AFM) fluctuations [11–15], although one cannot exclude that fluctuations of charge-density waves (CDW), structural distortions, or phase separation on a microscopic scale can play a similar role. I believe that many experiments conducted in recent years speak in favor (fairly persuasively) of the second scenario. Hence in our theoretical discussion we will limit ourselves to relevant models, giving a quite full description of the work of the present author and his collaborators, and also of the work of other researchers whose main ideas and approaches are in the same vein. Accordingly, in the most part of the review we will deal with the model of antiferromagnetic fluctuations, although its validity cannot be thought of as fully corroborated.

Neither can we claim that the list of references is complete and, the more so, that it reflects priorities in this field. It is assumed that the reader will find the necessary literature from the papers in the list of references. The author would like to apologize to the numerous authors of papers not cited here — the aim was to make the list not too long.

2. Basic experimental facts

Typical variants of the phase diagram of HTSC cuprates are depicted in Fig. 1. Depending on the concentration of charge carriers (mainly holes), several phases and regions with anomalous physical properties can be observed in the high-conductivity CuO_2 plane. In the region of low hole concentrations all known HTSC cuprates are antiferromagnetic insulators. As the current-carrier concentration increases, the Néel temperature T_N rapidly drops from values of several hundred kelvins and vanishes at hole concentrations p lower or of order 0.05, with the system becoming a (poor) metal. A further increase in the hole concentration transforms the system into a superconductor, with the transition temperature increasing with the carrier concentration and going through a characteristic maximum at $p_0 \sim 0.15-0.17$ (optimum doping) and then decreasing and vanishing at $p \sim 0.25-0.30$, although in this (overdoped) region the metallic behavior is still quite evident. Here, at $p > p_0$ the metallic properties are fairly traditional (Fermi-liquid behavior), while at $p < p_0$ the system becomes an anomalous metal, whose behavior (as most researchers believe) cannot be described by the Fermi-liquid theory [2].

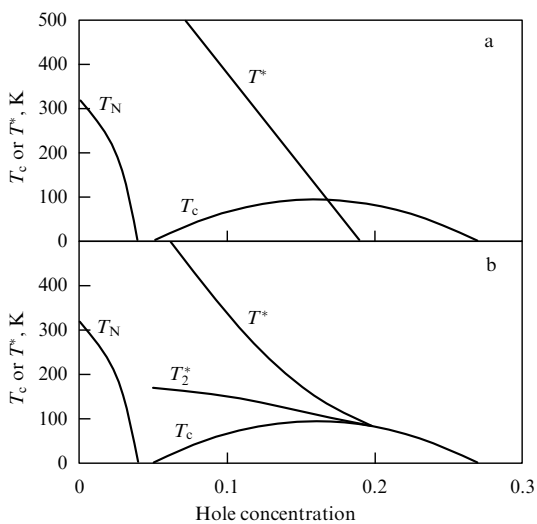

Figure 1. Variants of the phase diagram of high-T_c cuprates.

The anomalies of physical properties currently attributed to the formation of a pseudogap state are observed in the metallic phase at $p < p_0$ and at temperatures $T < T^*$, where T^* decreases from values of order T_N at $p \sim 0.05$ and vanish at a certain 'critical' carrier concentration p_c somewhat higher than p_0 (Fig. 1a). For instance, Tallon and Loram [6] stated that this happens at $p = p_c \approx 0.19$. According to some researchers (mostly adherents of the idea of the superconducting nature of the pseudogap), T^* merges with the line of the superconducting-transition temperature T_c near the optimum concentration p_0 (Fig. 1b). Below we will see that the majority of new experimental data most likely support the variant of the phase diagram depicted in Fig. 1a (for more details see Ref. [6]). Note that most researchers agree that T^* does not have the meaning of the temperature of a phase transition; rather, it simply defines a characteristic temperature scale below which pseudogap anomalies appear in the system. In this region of the phase diagram a system exhibits no features characteristic of phase transitions in the behavior of thermodynamic quantities [3]. The general idea is that all these anomalies, to put it simply, are related to the suppression (in the given region) of the density of states of single-particle excitations near the Fermi level, which is what the general concept of the pseudogap means [4]. Here T^* is simply proportional to the size of the pseudogap on the energy scale. Sometimes another characteristic temperature scale is specified, T_2^* (see Fig. 1b), which is related to the transition from a 'weak'- to a 'strong'-pseudogap regime [14]. The reasoning here is based on a change in the spin response of the system in the vicinity of this temperature. In the present review we almost never touch on the corresponding details.

Now let us turn to a detailed description of the most typical experimental manifestations of the corresponding anomalies in HTSC cuprates.

[2] Note that the problem of whether or not HTSC systems behave like Fermi liquids has become very involved due to the discussions of numerous researchers belonging to different schools and often using very different definitions of the idea of a Fermi liquid. In what follows we use the terminology adopted by the majority of researchers (although this majority is not cleary defined).

[3] However, it is only proper to note that recently Chakravarty et al. [16] proposed an opposite idea, namely, that the line of T^* in the phase diagram is directly linked to a 'hidden' symmetry breaking, strongly 'blurred' by the internal disorder.

[4] The idea of a pseudogap was first formulated by Mott in the qualitative theory of disordered (noncrystalline) semiconductors [17]. According to Mott, a pseudogap is a region of reduced electronic-state density within an energy interval corresponding to the forbidden band of an ideal crystal and is simply a 'recollection' about this band that is retained even under strong disordering (amorphization, melting, etc.).

2.1 Specific heat and tunneling

Let us consider data on the electronic contribution to the specific heat of HTSC cuprates. For metals this contribution is usually written as $C = \gamma(T)T$, so that in the normal state ($T > T_c$) we have $\gamma \sim N(0)$, where $N(0)$ is the density of states at the Fermi level. At $T = T_c$ there emerges a well-known anomaly related to a second-order phase transition, and the temperature dependence $\gamma(T)$ has a characteristic peak (discontinuity). As an example, Fig. 2 depicts typical experimental data for the $Y_{0.8}Ca_{0.2}Ba_2Cu_3O_{7-\delta}$ system at different values of δ [18]. In optimally doped and overdoped samples, the temperature dependence $\gamma(T)$ is practically a straight line parallel to the temperature axis over the entire region where $T > T_c$, while in underdoped samples there is a substantial lowering of $\gamma(T)$ in the temperature range $T < 150-200$ K. This fact directly indicates that the density of electronic states at the Fermi level drops and that a pseudogap forms when $T < T^*$.

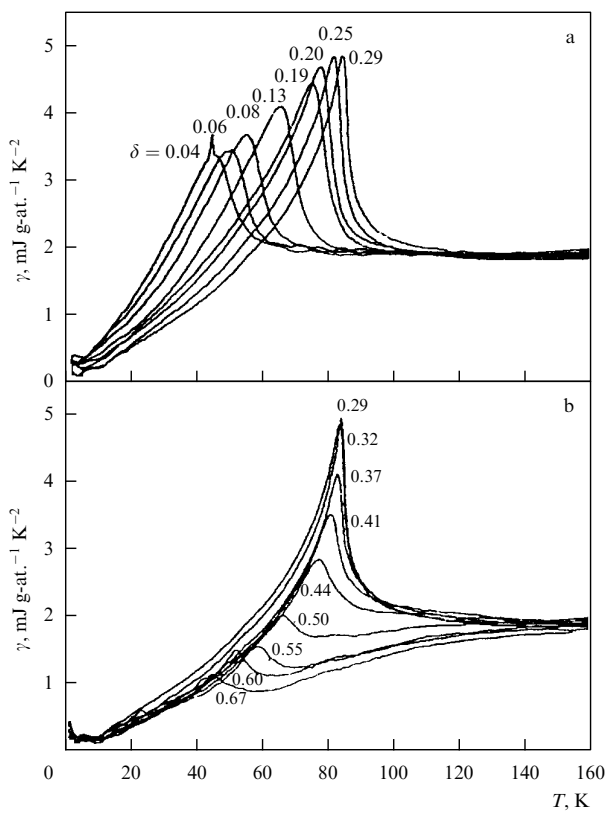

Figure 2. Electronic specific-heat coefficient γ in (a) overdoped and (b) underdoped $Y_{0.8}Ca_{0.2}Ba_2Cu_3O_{7-\delta}$ [18].

We also note that near the transition temperature T_c the size of the specific-heat discontinuity decreases substantially with the transition to the region of underdoped compositions. A more thorough analysis done by Tallon and Loram [6] shows that the corresponding discontinuity $\Delta\gamma_c$ begins to rapidly diminish starting with the 'critical' carrier concentration $p_c \approx 0.19$, which is considered the moment of emergence of a pseudogap in the electron spectrum.

Combining the data on the specific heat with the more or less standard ideas of the BCS theory, we can attempt to estimate the width of the energy gap in the electron spectrum and its temperature dependence. Figure 3 depicts the data on

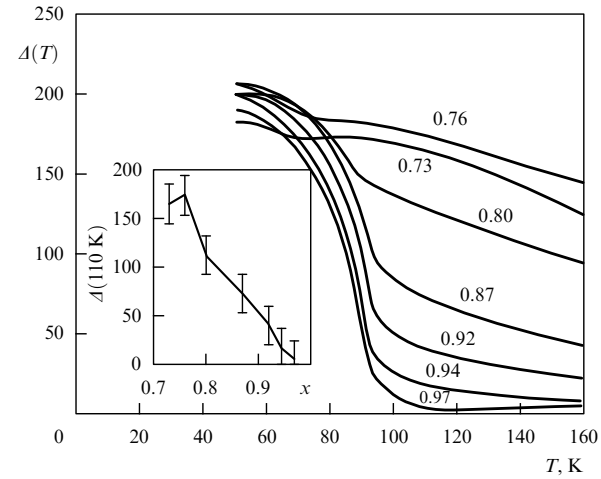

Figure 3. Temperature dependence of the energy gap for different compositions of $YBa_2Cu_3O_{6+x}$ determined from the specific-heat data of Loram et al. [19]. The numbers at the curves specify the corresponding values of x. The inset shows the data for the gap at $T = 110$ K.

the $YBa_2Cu_3O_{7-\delta}$ (YBCO) system gathered by Loram et al. [19]. Clearly, the energy gap in the spectrum estimated in this manner does not vanish at $T = T_c$ (as it should vanish in a standard superconductor) but instead extends itself into the region of higher temperatures, and the greater the underdoping the stronger the effect. Very often these data are naively interpreted as evidence for the existence of Cooper pairs at temperatures $T > T_c$.

The formation of a pseudogap in the density of states is clearly seen from experiments on single-particle tunneling. For instance, the frequently cited paper written by Renner et al. [20] describes tunneling experiments involving single crystals of $Bi_2Sr_2CaCu_2O_{8+\delta}$ (Bi-2212) with varying oxygen content. For underdoped samples the formation of a pseudogap in the density of states was clearly observed at temperatures much higher than T_c. Here the pseudogap smoothly evolved into a superconducting gap in the region $T < T_c$, which has also been frequently interpreted as direct evidence for the superconducting nature of the pseudogap. Traces of the existence of a pseudogap were also observed by the same researchers in slightly overdoped samples.

Usually, in discussing tunneling experiments involving HTSC cuprates, the question of the quality of the surfaces of the investigated samples is important. Hence of special interest are the recent investigations conducted by Krasnov et al. [21, 22]. They measured the intrinsic tunneling in mesa-structures [5] created on the surface of the same Bi-2212 system and were able to clearly demonstrate the existence of a superconducting gap, which vanishes at $T = T_c$, against the background of a smooth pseudogap, which exists even at higher temperatures. The relevant data are depicted in Fig. 4a. Clearly, typical features of the formation of a superconducting gap exist against the background of a smooth minimum of the density of states. What is especially important is that Krasnov et al. [22] have shown that the superconducting features of the tunnel characteristics are suppressed by an

[5] Mesa (Spanish 'table'), flat-topped tableland with one or more steep sides, common in the Colorado Plateau regions of the United States and Mexico (Mesa Central) (*Britannica CD97, 1997*).

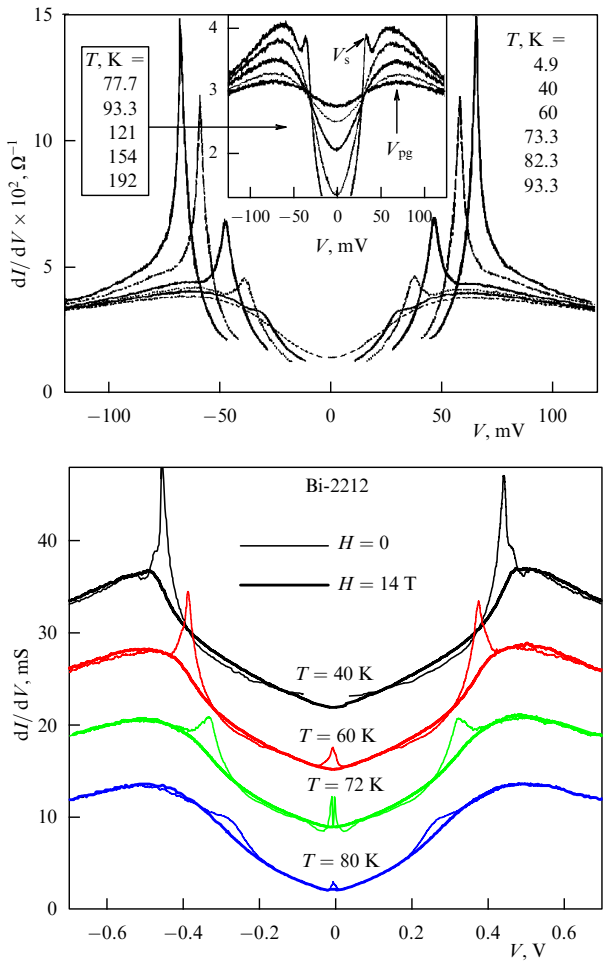

Figure 4. (a) Differential conductance of almost optimally doped Bi-2212 at different temperatures. The inset shows the results for high temperatures [21]. (b) Similar data in an external magnetic field $H = 0$ (light lines) and in a field $H = 14$ T (heavy lines) [22].

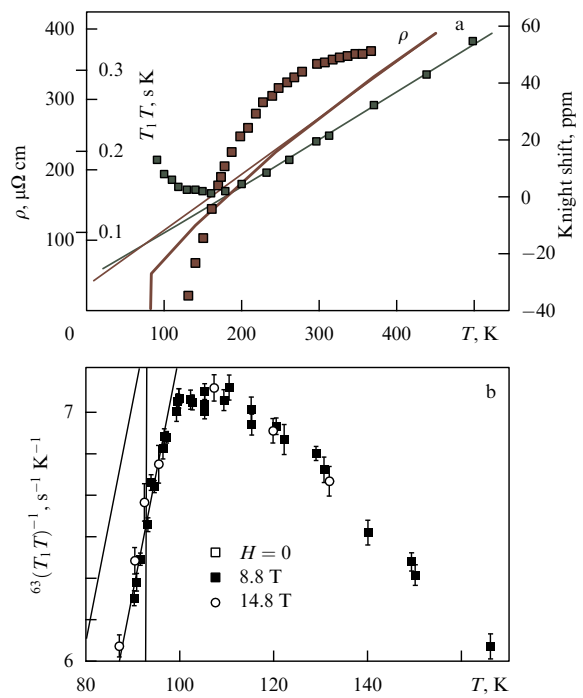

Figure 5. (a) Effect of pseudogap formation on the electrical resistivity, the Knight shift, and the NMR relaxation time in underdoped $YBa_2Cu_4O_8$. The changes in the temperature dependence in the region $T < 200-300$ K are attributed to pseudogap formation in the density of states [1]. (b) The NMR relaxation frequency $(TT_1)^{-1}$ of slightly underdoped $YBa_2Cu_3O_{7-\delta}$ in a strong magnetic field directed along the crystallographic c-axis [26]. The vertical line corresponds to T_c for zero field, and the slanted line gives an estimate for the shift in the data expected in the case of suppression of the pseudogap by a magnetic field; its position is determined by the observed shift in T_c.

external magnetic field, while the size of the pseudogap proves to be almost independent of the field strength, which points to its nonsuperconducting nature. The corresponding data are depicted in Fig. 4b.

2.2 NMR and kinetic properties

Pseudogap formation also manifests itself in the kinetic properties of HTSC systems in the normal state, the Knight shift, and the NMR relaxation time. In particular, a feature related to such formation is the change in the standard (for optimally doped compositions) linear temperature dependence of the electrical resistivity in the region $T < T^*$ for underdoped samples. The Knight shift in such samples proves to be temperature dependent: in the region $T < T^*$ there is a rapid drop in the value of this quantity. In underdoped samples the quantity $(TT_1)^{-1}$, where T_1 is the NMR spin–lattice relaxation time, behaves in a similar manner. The reader will recall that in common metals the Knight shift is proportional to $N(0)$, while $(TT_1)^{-1} \sim N^2(0)$ (Korringa behavior), and the electrical resistivity ρ is proportional to the scattering rate (the inverse of the mean free time) $\gamma \sim N(0)$. Hence it is natural that the significant decrease in all these quantities is related to the drop in the density of electronic states, $N(0)$, at the Fermi level [6]. Figure 5a, taken from Batlogg and Varma's paper [1], shows a summary of the relevant experimental data for underdoped samples of the $YBa_2Cu_4O_8$ system based on the papers of Bucher et al. [23], Yasuoka [24], and Alloul and Adrian [25]. Note that this interpretation is, of course, extremely simplified, especially when one is speaking of the temperature dependence of the corresponding quantities. For instance, in the case of electrical resistivity this dependence is largely determined by inelastic scattering, whose physics in HTSC systems still remains not completely understood. In particular, a decrease in the density of states (with the spectrum becoming partially dielectric) could lead to a corresponding increase in electrical resistivity.

Figure 5b depicts the experimental data of Gorny et al. [26], who measured $(TT_1)^{-1}$ on ^{63}Cu nuclei in slightly underdoped $YBa_2Cu_3O_{7-\delta}$ in a sufficiently strong magnetic field. Clearly, there is no magnetic-field dependence, which is a strong argument in favor of the nonsuperconducting nature of the pseudogap, since otherwise a magnetic field would substantially change the magnitude of the effect. Note that

[6] Historically speaking, the first data on the significant drop in the density of states in underdoped cuprates were gathered precisely in NMR experiments and in the magnetic scattering of neutrons. Hence the first term actively used was 'spin gap.' Later studies revealed similar effects related not only to the spin degrees of freedom, and so the term 'pseudogap' became generally accepted.

the strong influence of a magnetic field on the size of the Knight shift and the NMR relaxation frequency of ^{63}Cu was observed in slightly overdoped $TlSr_2CaCu_2O_{6.8}$, where it can be described fairly well in terms of the effect of suppression of superconducting fluctuations [27]. This fact is strong evidence in favor of the disappearance (at a certain lower carrier concentration) of the pseudogap of a nonsuperconducting nature (independent of the magnetic field) discussed above.

Note that in different experiments the temperature T^* below which anomalies associated with pseudogap formation emerge is somewhat different, depending on the quantity that is measured. However, in all cases there is a systematic dependence of T^* on the doping level, and this temperature vanishes when the carrier concentration is equal to or somewhat higher than the optimal doping level. This implies that T^* is not a clearly defined temperature (say, of a phase transition); it only determines the scale of the temperature (energy) below which these anomalies manifest themselves. One can attempt to determine the corresponding energy scale from experiments, say, by modeling the pseudogap by a V-like energy dependence (with a width E_g) of the density of states near the Fermi level (then $T^* = 0.4E_g$) [6]. Figure 6 depicts the consolidated data for the gap widths in YBCO found in this manner (from processing the results of different experiments) as a function of hole concentration [6]. Clearly, the pseudogap 'closes' at the critical value $p_c \approx 0.19$. We note once more that both the T^*-line in the phase diagram and the 'critical' concentration p_c have a fairly conventional meaning. Nevertheless, some researchers have attempted to interpret p_c as a 'quantum' critical point (QCP) of some sort [28].

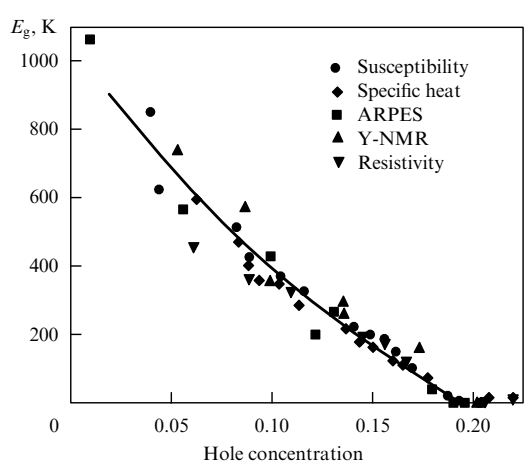

Figure 6. Dependence of the energy width E_g of the pseudogap in YBCO on the hole concentration p according to the data from different experiments [6].

2.3 Optical conductivity

Pseudogap formation in the region of underdoped compositions of HTSC cuprates also manifests itself very clearly in experiments measuring optical conductivity, both in the direction of the electric field vector along the high-conductivity CuO_2 plane and in the perpendicular direction along the tetragonal c-axis. The relevant data have been described fairly thoroughly by Timusk and Statt [2] and Puchkov et al. [29]. As a typical example, in Fig. 7a we depict the data of Startseva et al. [30] on optical conductivity in the CuO_2 plane of

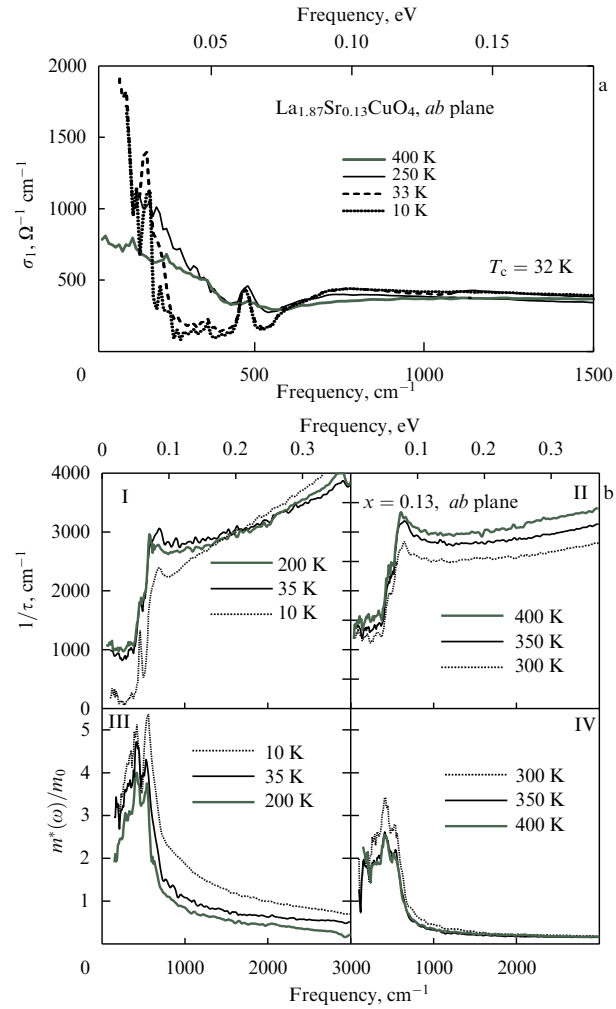

Figure 7. (a) Real part of the optical conductivity in the ab plane of $La_{1.87}Sr_{0.13}CuO_4$ at different temperatures T [30]. (b) Generalized scattering rate and effective mass as functions of the external-field frequency obtained through processing the optical data for the same system by the extended Drude formula [30]: I and III, for temperatures below 250 K, where a linear increase in $1/\tau$ with frequency is observed in the region $\omega > 700\ \text{cm}^{-1}$; II and IV, at higher temperatures, where a linear increase in $1/\tau$ is almost unnoticeable.\

underdoped $La_{1.87}Sr_{0.13}CuO_4$. Characteristic features of these data are the presence of a narrow Drude peak in the frequency range $\omega < 250\ \text{cm}^{-1}$ and the appearance of a 'pseudogap dip' in the interval from 250 to 700 cm^{-1} with a diffuse maximum in the vicinity of $\omega \sim 800\ \text{cm}^{-1}$. The pseudogap anomaly is especially pronounced when the optical data are processed by what is known as the extended Drude formula [2, 29], where effective (i.e. depending on the frequency of the external field) scattering rate and current-carrier mass are introduced:

$$\frac{1}{\tau(\omega)} = \frac{\omega_{\text{pl}}^2}{4\pi}\ \text{Re}\left[\frac{1}{\sigma(\omega)}\right], \tag{1}$$

$$\frac{m^*(\omega)}{m} = -\frac{1}{\omega}\,\frac{\omega_{\text{pl}}^2}{4\pi}\ \text{Im}\left[\frac{1}{\sigma(\omega)}\right], \tag{2}$$

with $\sigma(\omega)$ the observed complex-valued conductivity, ω_{pl} the plasma frequency, and m the free-electron mass. Strictly

speaking, the use of equations (1) and (2) implies only data processing, since one uses them for representation in the form $1/\tau(\omega)$ and $m^*(\omega)$ instead of two other characteristics, the real and imaginary parts of the conductivity. Accordingly, $\tau(\omega)$ and $m^*(\omega)$ have no deep physical meaning. Nevertheless, such a representation of experimental data is extremely popular among researchers.

Figure 7b depicts the results of such processing of the data presented in Fig. 7a [30]. Clearly, at temperatures below $T^* \sim 450$ K the effective scattering rate decreases dramatically in the range of external-field frequencies below 700 cm^{-1}, while at higher frequencies $1/\tau(\omega)$ increases linearly with ω, demonstrating anomalous non-Fermi liquid behavior. It is the presence of this dip in $1/\tau(\omega)$ that reflects, as it is commonly assumed, the presence of a pseudogap in optical data. At the same time, taking into account the above notes, it should be noted that the data on $m^*(\omega)$ depicted in Fig. 7b do not allow for any graphic interpretation.

Similar behavior of $1/\tau(\omega)$ is also observed in the data on the transverse optical conductivity $\sigma_c(\omega)$ in almost all studied HTSC cuprates in the region of underdoped compositions [2, 29].

2.4 Fermi surface and ARPES

The most dramatic effects related to pseudogap formation manifest themselves in angle-resolved photoemission spectroscopy (ARPES) experiments [4, 5]. Such experiments play the leading role in studies of the topology of the Fermi surface of HTSC cuprates [4, 31, 32] and are practically the only source of information in this area of research.

Figure 8 depicts the data, gathered by Ino et al. [33], on the Fermi surface of the $La_{2-x}Sr_xCuO_4$ system for two different compositions. In the overdoped state ($x = 0.3$) the Fermi surface is electronic with its center at point $\Gamma(0,0)$ of the Brillouin zone. As x decreases, the topology of the surface changes, so that for the optimal concentration of Sr and in the underdoped state ($x = 0.1$) it becomes a hole surface with its center at point $Y(\pi,\pi)$. It is this latter topology of the Fermi surface that is observed in almost all ARPES experiments for the majority of other HTSC cuprates.

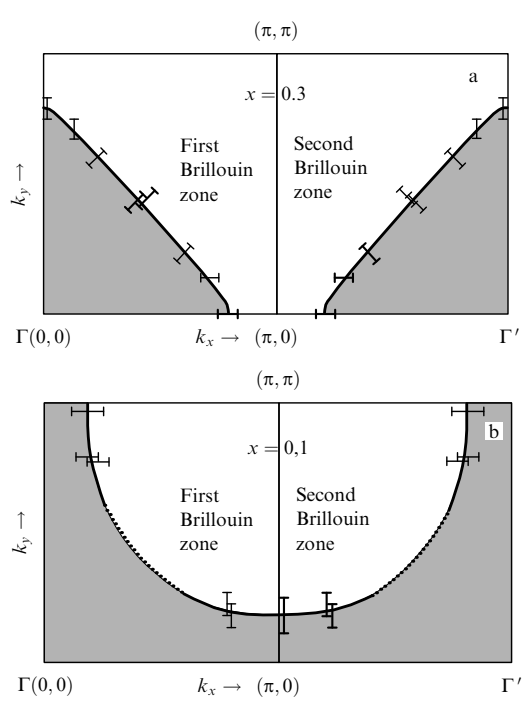

Figure 8. Fermi surfaces of $La_{2-x}Sr_xCuO_4$ for the overdoped (a) and underdoped (b) cases [33].

An interesting example is presented in Fig. 9, taken from the paper of Gatt et al. [34]. It depicts the hole Fermi surface of the Bi-2212 system in the overdoped state, a system that has been most thoroughly studied by the ARPES method. A distinctive feature here is the discovery in these experiments of large flat regions of the Fermi surface that are orthogonal to the symmetric directions YM. This result was corroborated independently by Feng et al. [35] for an optimally doped system. The presence of flat regions on the Fermi surface may be extremely important in developing microscopic theories of the electronic properties of HTSC systems.

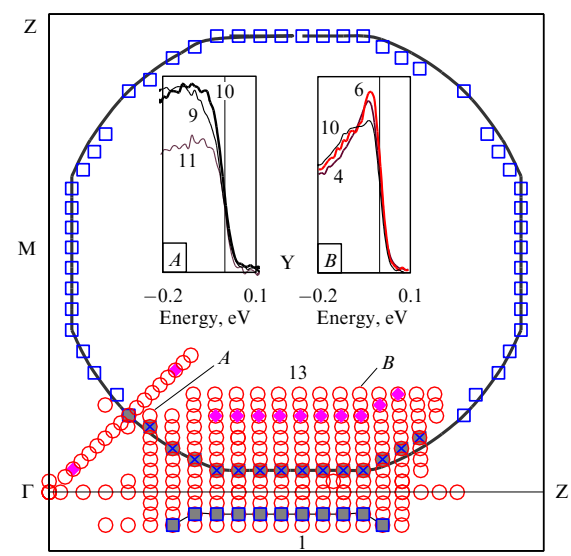

Figure 9. Fermi surface of overdoped Bi-2212 [34]. The small circles indicate the points at which the measurements were taken.

If we ignore these details, then, to a rather rough approximation, the topology of the Fermi surface and the spectrum of elementary excitations in the CuO_2 plane, which are observed in ARPES, can be described fairly well by the strong-coupling model:

$$\varepsilon_{\mathbf{k}} = -2t(\cos k_x a + \cos k_y a) - 4t' \cos k_x a \cos k_y a\,, \qquad (3)$$

where $t \approx 0.25$ eV is the transport integral between nearest neighbors; t' is the transport integral between next nearest neighbors, which can vary from $t' \approx -0.4t$ for $YBa_2Cu_3O_{7-\delta}$ to $t' \approx -0.25t$ for $La_{2-x}Sr_xCuO_4$; and a is the (square-) lattice constant.

Very recently the above simple picture was substantially revised by several researchers [35–38]. They used new ARPES data obtained with synchrotron radiation whose energy was higher than that used in previous experiments. The researchers claim that the Fermi surface of Bi-2212 is electronic with its center at point Γ. The main disagreement with the earlier data is related to the most interesting, from our viewpoint, neighborhood of the point $(0,\pi)$ in the reciprocal space. These results met with strong opposition

from other groups of ARPES experimenters [39–43]. The problem is being actively debated, but in the present review we will keep to the traditional interpretation.

Since there are several good reviews describing the observations of pseudogap anomalies in ARPES [3–5], we will only briefly describe the main qualitative statements. The ARPES intensity (the energy distribution of photoelectrons) is in fact defined as follows [4]:

$$I(\mathbf{k},\omega) = I_0(\mathbf{k}) f(\omega) A(\mathbf{k},\omega)\,, \tag{4}$$

where $\mathbf{k}$ is the momentum in the Brillouin zone, ω is the energy of the initial state measured from the Fermi level (the chemical potential)[7], and $I_0(\mathbf{k})$ incorporates kinematic factors and the square of the matrix element of the electron–photon interaction and, to a rough approximation, is kept constant. The quantity

$$A(\mathbf{k},\omega) = -\frac{1}{\pi}\,\mathrm{Im}\,G(\mathbf{k},\omega+\mathrm{i}\delta)\,, \tag{5}$$

with $G(\mathbf{k},\omega)$ the Green function, is the carrier spectral density. The Fermi distribution function $f(\omega) = [\exp(\omega/T)+1]^{-1}$ reflects the fact that electrons from occupied states participate in the photoemission process. Thus, to the rough approximation mentioned earlier, we can say that it is the product $f(\omega)A(\mathbf{k},\omega)$ that is directly measured in ARPES experiments; thus, we get direct information about the spectral properties of single-particle excitations of the system.

Figure 10 depicts typical ARPES data for the $Bi_2Sr_2CaCu_2O_8$ system [44] obtained for three different points on the Fermi surface at different temperatures. The presence of a gap (pseudogap) manifests itself in the shift (to the left) of the threshold (leading edge) of the energy distribution of photoelectrons from the sample, as compared to the reference spectrum of a good metal (Pt). Clearly, the gap closes at different temperatures for different values of $\mathbf{k}$, and the size (width) of the gap decreases with the departure from the $(0,0)-(0,\pi)$ direction. In the direction of the zone's diagonal $(0,0)-(\pi,\pi)$ there is no pseudogap. At low temperatures this agrees fairly well with the picture of d-pairing, well established in numerous experiments involving HTSC cuprates [45–47]. What is important, however, is that the 'gap' in ARPES data is also observed at temperatures much higher the superconducting transition temperature T_c.

Figure 11 depicts the angular behavior of the gap width in the Brillouin zone and the temperature dependence of the maximum size of the gap for a number of samples of Bi-2212 of different compositions, as obtained from ARPES data by Ding et al. [48]. Clearly, in the case of the general d-wave symmetry, the gap in the spectrum of an optimally doped system vanishes virtually at $T = T_c$, while in the spectrum of underdoped samples there appear 'tails' of the temperature dependence of the gap in the region $T > T_c$, which are quite similar to those shown in Fig. 3. Qualitatively we can say that the formation of a pseudogap anisotropic in the reciprocal space at $T > T_c$, which is continuously transformed into a superconducting gap at $T < T_c$, leads to the 'destruction' of the Fermi surface of underdoped samples even at $T < T^*$ in regions surrounding point $(0,\pi)$ (and symmetric with respect

[7] In a real experiment ω is measured with respect to the Fermi level of a good metal of the Pt or Ag type that is in electrical contact with the sample.

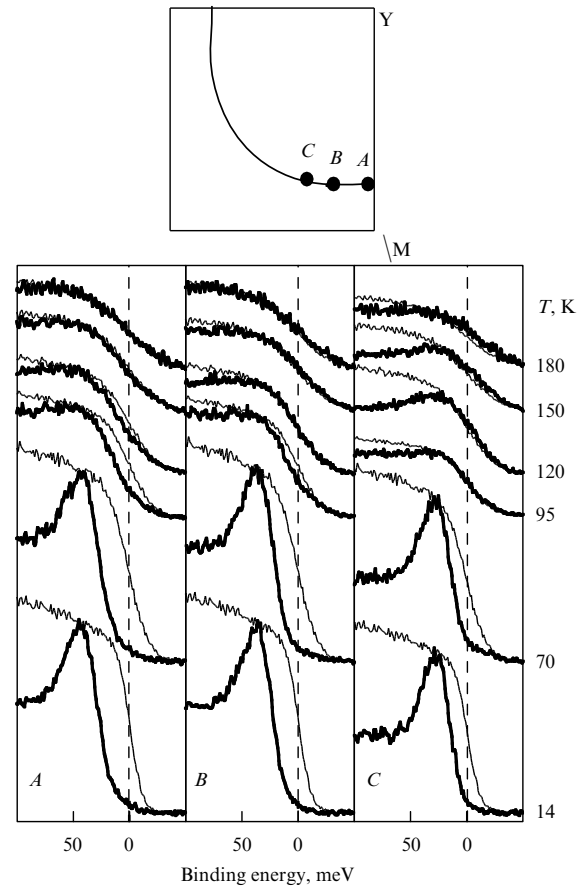

Figure 10. ARPES spectra at three different points A, B, and C on the Fermi surface of Bi-2212 for an underdoped sample with $T_c = 85$ K. The light lines represent the spectrum of a reference Pt sample (data of Norman et al. [44]).

to this point), with the width of these regions increasing as the temperature decreases [49].

Of course, the most interesting problem is here the evolution of the spectral density $A(\mathbf{k}_F,\omega)$ at the Fermi surface. Under fairly weak assumptions, this function can be extracted from ARPES data [49]. It there is electron–hole symmetry, we have $A(\mathbf{k}_F,\omega) = A(\mathbf{k}_F,-\omega)$ (which is always true near the Fermi surface and actually occurs when $|\omega|$ is smaller than several tenths of meV), so that combining $f(-\omega) = 1 - f(-\omega)$ and equation (4) with $\mathbf{k} = \mathbf{k}_F$ immediately yields $I(\omega) + I(-\omega) = A(\mathbf{k}_F,\omega)$. Hence the spectral density on the Fermi surface can be directly obtained from experiment by means of constructing a symmetrized spectrum $I(\omega) + I(-\omega)$. As an example, in Fig. 12 we depict the data of Norman et al. [50] for an underdoped sample of Bi-2212 with $T_c = 83$ K and an overdoped sample with $T_c = 82$ K at different temperatures. Clearly, a pseudogap manifests itself in the form of a characteristic 'double-humped' structure of the spectral density, which appears (for an undoped system) at temperatures much higher than T_c.

Note that well-defined quasiparticles correspond to a fairly narrow peak in the spectral density $A(\mathbf{k}_F,\omega)$ at $\omega = 0$. Such behavior is almost never encountered in HTSC cuprates, at least at temperatures higher than T_c. This fact, however, is not very surprising, since it is difficult to imagine well-defined quasiparticles in systems at $T > 100$ K, almost

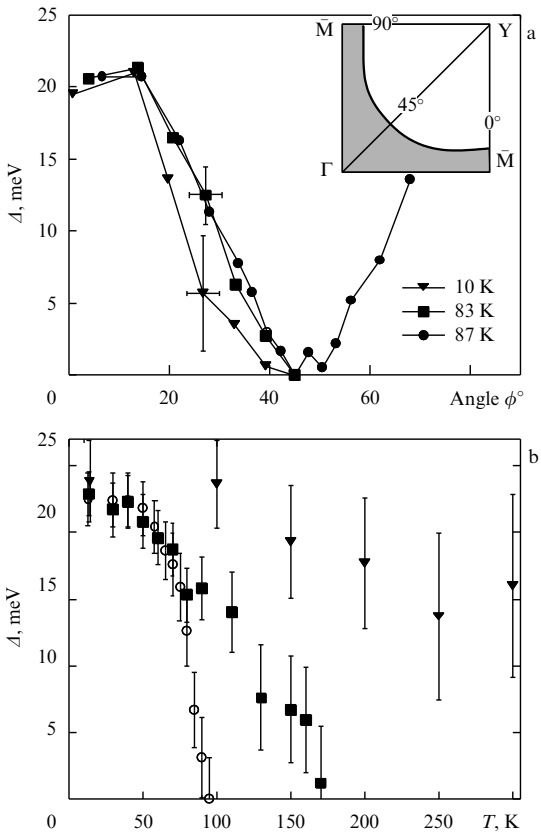

Figure 11. Angular and temperature dependences of the energy gap in Bi-2212 obtained from ARPES data [49] for samples with $T_c = 87$ K (almost optimally doped), $T_c = 83$ K, and $T_c = 10$ K (underdoped): (a) the size of the ARPES gap measured at different points of the Fermi surface (depicted in the inset) whose positions are determined by the polar angle ϕ measured from the direction $\Gamma\bar{M}$ (the d-symmetry of the gap is clearly visible); (b) the temperature dependence of the maximum gap measured near point $\bar{M}$.

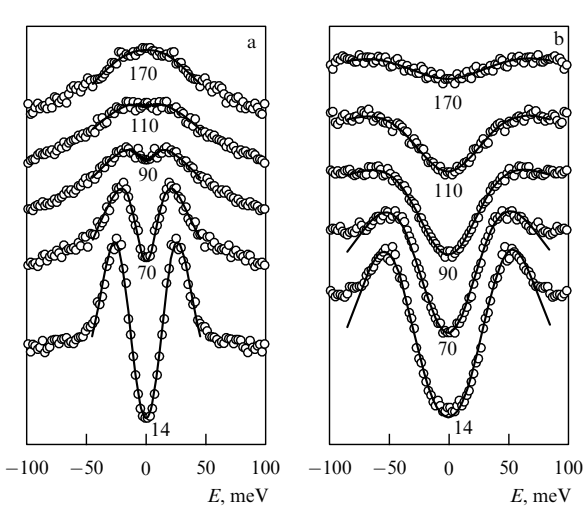

Figure 12. Symmetric ARPES spectra for (a) an overdoped sample of Bi-2212 with $T_c = 82$ K and (b) an underdoped sample with $T_c = 83$ K at the point of intersection of the Fermi surface and the zone boundary $(0, \pi) - (\pi, \pi)$ [50].

without exception. Nevertheless, the resolution of modern ARPES devices apparently provides reasons to state that the width of the corresponding peak is larger than the experimental resolution, so the problem is accessible to experiments [51]. It turns out that in the superconducting phase, at $T \ll T_c$, near the point of intersection of the Fermi surface and the diagonal of the Brillouin zone [the $(0, 0) - (\pi, \pi)$ direction] there appears a fairly sharp spectral-density peak corresponding to well-defined quasiparticles [51]. Near point $(0, \pi)$ the Fermi surface is 'destroyed' by a superconducting gap corresponding to d-type pairing, which results in a double-peaked structure of the spectral density.

The smooth evolution of an ARPES pseudogap at $T > T_c$ into a superconducting gap corresponding to d-pairing at $T < T_c$ is often considered an argument in favor of the superconducting nature of the pseudogap state. Most likely this is not the case, however. In this connection note the very interesting work of Ronning et al. [52], who carried out ARPES investigations of the dielectric oxide $Ca_2CuO_2Cl_2$, which is structurally similar to La_2CuO_4 and becomes a high-T_c superconductor when doped with sodium or potassium. ARPES measurements in this system also proved to be possible in the dielectric phase due to the good quality of the samples' surface. A remarkable feature of this paper [52] is that it apparently presents the first report of an observation of the 'residual' Fermi surface in this Mott insulator, which is, naturally, 'blocked' by a gap (probably of the Mott – Hubbard type). At the same time, Ronning et al. [52] observed a strong anisotropy of this gap in the reciprocal space with a d-type symmetry, closely resembling similar data on HTSC oxides in the metallic phase. It is quite natural to assume that this anisotropic gap is of the same nature as the pseudogap in the high-energy region, say, in Bi-2212 [52]. Clearly there is no Cooper pairing in the insulator.

2.5 Other experiments

The pseudogap behavior also manifests itself in other experiments, such as Raman scattering of light on electrons [53] or magnetic scattering of neutrons [54]. All these data point, in one way or another, to a substantial suppression of the density of states of single-particle excitations near the Fermi level of underdoped HTSC cuprates at temperatures below T^*, i.e. even in the normal phase. In view of the shortage of space, we will not discuss these data in greater detail, the more so that good reviews can be found in the above-cited papers and in Ref. [2].

3. Theoretical models of the pseudogap state

3.1 Scattering on short-range-order fluctuations: Qualitative ideas

As noted in the Introduction, there are two main theoretical scenarios for explaining the pseudogap anomalies in HTSC systems. The first one is based on the model of Cooper pair formation above the superconducting transition temperature (precursor pairing), while the second one assumes that the origin of the pseudogap state is related to short-range-order fluctuations of a 'dielectric' type (e.g. antiferromagnetic or of the charge-density-wave type), which exist in the underdoped-composition range and strongly scatter electrons, which leads to a pseudogap transformation of the electron spectrum. We believe the second scenario to be preferable, which follows

from both the experimental data[8] discussed in Section 2 and the simple fact that all pseudogap anomalies intensify as underdoping increases, i.e. as the system departs from the phase-diagram region optimal for superconductivity and approaches the region of the dielectric (antiferromagnetic) phase.

Let us examine a typical Fermi surface of carriers in the CuO_2 plane depicted in Fig. 13a. The phase transition to the antiferromagnetic state doubles the lattice spacing and leads to the emergence of a 'magnetic' Brillouin zone in the reciprocal space, depicted in Fig. 13a by dashed lines. If the carrier spectrum is given by equation (3) with $t' = 0$, then for a half-filled zone the Fermi surface is a square coinciding with the boundaries of the magnetic zone, so that there is complete nesting, i.e. translation by the antiferromagnetism vector $\mathbf{Q} = (\pm\pi/a, \pm\pi/a)$ results in the alignment of the flat regions of the Fermi surface. At $T = 0$ the electron spectrum is unstable: a gap opens everywhere on the Fermi surface and the system passes to a dielectric state caused by an antiferromagnetic spin-density wave (SDW)[9]. Such ideas form the basis for the popular explanation of antiferromagnetism in HTSC cuprates — see, for instance, Ref. [55]. A review of such models can be found in Ref. [56]. In the case of the Fermi surface depicted in Fig. 13a, as antiferromagnetic long-range order emerges, then, according to the general principles of band theory [57], at the points of intersection of constant-energy surfaces (the Fermi surface, for one thing) and the boundaries of the new (magnetic) Brillouin zone, these surfaces experience a discontinuity related to the opening of a gap in the spectrum at points connected by the vector $\mathbf{Q}$.

In the region of the phase diagram of HTSC cuprates of interest to us there is no antiferromagnetic long-range order, but there are convincing experimental indications that everywhere below the T^*-line there are well-developed fluctuations of antiferromagnetic short-range order. The model of a 'nearly antiferromagnetic' Fermi liquid [58, 59] introduces an effective interaction between electrons and spin fluctuations, which is described by the dynamic spin susceptibility $\chi_{\mathbf{q}}(\omega)$, whose shape is determined through matching to the data of NMR experiments [46, 60]:

$$V_{\text{eff}}(\mathbf{q}, \omega) = g^2 \chi_{\mathbf{q}}(\omega) \approx \frac{g^2 \xi^2}{1 + \xi^2 (\mathbf{q} - \mathbf{Q})^2 - \mathrm{i}\omega/\omega_{\text{sf}}}\,, \qquad (6)$$

where g is the coupling constant, ξ is the correlation length of the spin fluctuations, $\mathbf{Q} = (\pm\pi/a, \pm\pi/a)$ is the vector of antiferromagnetic ordering in the dielectric phase, and ω_{sf} is the characteristic spin – fluctuation frequency.

Since the dynamic spin susceptibility $\chi_{\mathbf{q}}(\omega)$ has peaks at wave vectors lying in the neighborhood of $(\pm\pi/a, \pm\pi/a)$, two types of quasiparticles appear in the system — 'hot' quasiparticles, whose momenta are in the neighborhood of 'hot' spots on the Fermi surface (Fig. 13a) and whose energies obey the inequality

$$|\varepsilon_{\mathbf{k}} - \varepsilon_{\mathbf{k}+\mathbf{Q}}| < \frac{v_{\text{F}}}{\xi} \qquad (7)$$

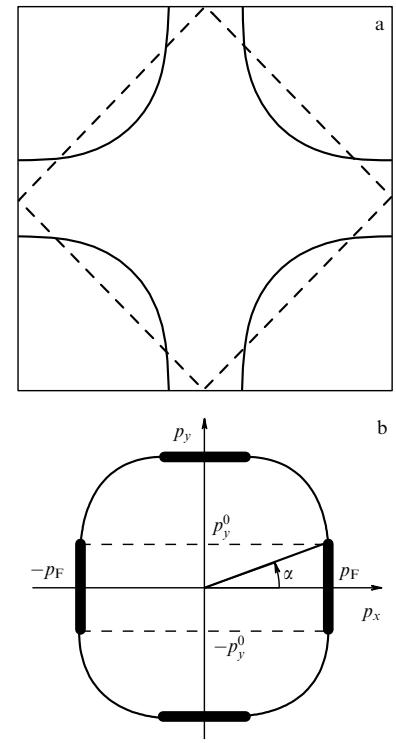

Figure 13. (a) Fermi surface in the Brillouin zone and the hot-point model. The dashed lines depict the boundaries of the magnetic Brillouin zone, which emerges as a result of lattice-spacing doubling related to the appearance of antiferromagnetism. The 'hot' spots are the points of intersection of the Fermi surface and the boundaries of the magnetic zone. (b) The Fermi surface in the hot-regions model (the hot spots, or hot regions, are depicted by heavy lines). The width of the hot spots is of order $\sim \xi^{-1}$. Angle α determines the size of a hot region [63], with $\alpha = \pi/4$ corresponding to a square Fermi surface.

(v_{F} is the velocity on the Fermi surface), and 'cold' quasiparticles, whose momenta are near the regions of the Fermi surface that surround the diagonals of the Brillouin zone, $|p_x| = |p_y|$, and do not satisfy the condition (7) [14]. This terminology reflects the fact that quasiparticles in the vicinity of 'hot' spots experience a strong scattering of order $\mathbf{Q}$ due to interactions with spin fluctuation [Eqn (6)], while for quasiparticles with momenta far from the 'hot' spots this interaction is fairly weak. In what follows we call such a model the 'hot'-spots model[10].

We will see that the correlation length ξ of antiferromagnetic short-range-order fluctuations, described by equation (6), plays an important role. Note that in real HTSC systems ξ is usually not very large and can vary from $2a$ to $8a$ [61, 62].

Depending on the type of the compound and doping level, the characteristic spin-fluctuation frequency ω_{sf} ranges from 10 to 100 K [61, 62], so that in the most part of the pseudogap region on the phase diagram the condition $\pi T \gg \omega_{\text{sf}}$ holds fairly well. This condition makes it possible to ignore the spin dynamics and restrict the analysis to the quasistatic approx-

[8] For instance, in my opinion, the tunneling experiments of Krasnov et al. [21, 22] bear out almost entirely the 'superconducting' scenario of pseudogap formation.

[9] A similar picture emerges in the case of dielectrization due to charge-density-wave formation.

[10] Note that the antiferromagnetic nature of the fluctuations is unimportant for further analysis, and the model is of a more general nature. What is important here is the strong scattering of electrons by vectors fairly close to the vector $\mathbf{Q}$, which 'moves' electrons from one side of the Fermi surface to the other. Both charge-density-wave (CDW) fluctuations and structural fluctuations may be responsible for such processes.

imation [11]:

$$V_{\text{eff}}(\mathbf{q}) = \widetilde{W}^2 \frac{\xi^2}{1+\xi^2(\mathbf{q}-\mathbf{Q})^2}\,, \tag{8}$$

where $\widetilde{W}$ is an effective parameter with dimensions of energy, which can be written in the model of antiferromagnetic fluctuations [14] as

$$\widetilde{W}^2 = g^2 T \sum_{m,\mathbf{q}} \chi_{\mathbf{q}}(\mathrm{i}\omega_m) = \frac{g^2\langle \mathbf{S}_i^2\rangle}{3}\,, \tag{9}$$

with $\mathbf{S}_i$ the spin at the lattice site (the Cu ion in the CuO_2 plane for HTSC cuprates).

In what follows both $\widetilde{W}$ and ξ are interpreted as phenomenological parameters of the theory. In particular, $\widetilde{W}$ defines the effective width of the pseudogap. Here we will not attempt to develop a complete microscopic theory of the pseudogap state. In what follows we will mainly model the corresponding transformation of the electron spectrum and its effect on the physical properties of the system (e.g. on superconductivity).

All calculations can be made much simpler if instead of (8) we use a model interaction of the form

$$V_{\text{eff}}(\mathbf{q}) = W^2 \frac{2\xi^{-1}}{\xi^{-2}+(q_x-Q_x)^2}\,\frac{2\xi^{-1}}{\xi^{-2}+(q_y-Q_y)^2}\,, \tag{10}$$

where $W^2 = \widetilde{W}^2/4$ (the first to use this approach were Kampf and Schrieffer [11]). Qualitatively, equation (10) closely resembles (8) and quantitatively differs very little in the most interesting region $|\mathbf{q}-\mathbf{Q}| < \xi^{-1}$. A similar (but somewhat different in form) effective interaction was used by Schmalian et al. [14]. Actually, such an approach effectively reduces the problem to a one-dimensional one.

The scattering on antiferromagnetic fluctuations in HTSC cuprates not always reaches its intensity maximum at the vector $\mathbf{Q} = (\pi/a, \pi/a)$ commensurate with the spacing of the original lattice; generally, the vector $\mathbf{Q}$ may correspond to incommensurate scattering. The observed topology of the Fermi surface with flat regions of the type depicted in Fig. 9 suggests another model of scattering on short-range-order fluctuations of the antiferromagnetic type [12], which we will call the hot-region model [63]. Let us assume that the Fermi surface of a two-dimensional electronic system has a shape as depicted in Fig. 13b. The size of the 'hot' regions is determined by the angular parameter α. It is well known that the presence of flat regions on the Fermi surface leads to the instability of the system against the formation of charge- or spin-density waves, with the onset of a corresponding long-range order and the formation of a (dielectric) energy gap in these regions. However, we are interested in situations characteristic of the fluctuation region of the corresponding phase diagram, when there is no long-range order [13]. Such a model of the Fermi surface has been applied to HTSC cuprates for a fairly long time by Virosztek and Ruvalds [65], Ruvalds et al. [66], and Zheleznyak et al. [67], who, in particular, analyze in detail the microscopic criteria for the existence of the antiferromagnetic and superconducting phases (the phase diagram).

We assume that short-range-order fluctuations are static and have a Gaussian form [14] and define the correlation function of these fluctuations as follows (in a manner similar to that assumed in Ref. [11]):

$$S(\mathbf{q}) = \frac{1}{\pi^2}\,\frac{\xi^{-1}}{(q_x-Q_x)^2+\xi^{-2}}\,\frac{\xi^{-1}}{(q_y-Q_y)^2+\xi^{-2}}\,. \tag{11}$$

Here ξ is again the correlation length of fluctuations, and the scattering vector is taken in the form $Q_x = \pm 2k_{\mathrm{F}}$, $Q_y = 0$ or $Q_y = \pm 2k_{\mathrm{F}}$, $Q_x = 0$. We also assume that only the electrons from the flat ('hot') regions of the Fermi surface, which are shown in Fig. 13b, interact with these fluctuations, and the scattering is actually one-dimensional. In particular, at $\alpha = \pi/4$ we simply have a square Fermi surface, and the problem becomes purely one-dimensional. When $\alpha < \pi/4$, the Fermi surface has 'cold' regions, where the scattering is either absent or very weak. The effective interaction of the electrons from the 'hot' regions with fluctuations will be described here by the quantity $(2\pi)^2 W^2 S(\mathbf{q})$, where the parameter W with dimensions of energy again determines the energy scale (width) of the pseudogap [15]. The choice of the scattering vector, $\mathbf{Q} = (\pm 2k_{\mathrm{F}}, 0)$ or $\mathbf{Q} = (0, \pm 2k_{\mathrm{F}})$, generally implies that there are incommensurate fluctuations, since the Fermi momentum $p_{\mathrm{F}} = \hbar k_{\mathrm{F}}$ is generally not related to the reciprocal lattice spacing. The commensurate case can also be considered with this model (see Ref. [63]).

As noted earlier, the main idea of the models under consideration consists in examining strong scattering on short-range-order fluctuations, which, in accordance with (6), (10), or (11), is effectively finite only within a limited region of the reciprocal space, of the size of order ξ^{-1}, surrounding 'hot' spots or regions, which leads to a pseudogap transformation of the electron spectrum in such regions [16].

Let us qualitatively examine the nature of the corresponding changes in the one-electron spectral density (5). In the standard Fermi-liquid theory [69], the one-electron Green function of a metal has the form

$$G(\omega, \mathbf{k}) = \frac{Z_{\mathbf{k}}}{\omega - \xi_{\mathbf{k}} - \mathrm{i}\gamma_{\mathbf{k}}} + G_{\text{incoh}}\,, \tag{12}$$

[11] According to the terminology used by Schmalian et al. [14], this corresponds to a 'weak' pseudogap.

[12] Since in what follows we ignore, for the sake of simplicity, the spin structure of the interaction, our reasoning is, strictly speaking, applicable to the case of interaction of electrons and short-range-order CDW-type fluctuations. This simplification, however, is unimportant from the viewpoint of the qualitative manifestations of the pseudogap transformation of the electron spectrum. Note that some researchers suggest using the interaction with CDW-type fluctuations to explain the anomalies of HTSC cuprates in the region of interest as an alternative to the spin fluctuation model [64].

[13] The assumption that there are flat regions on the Fermi surface is not really important in the model but substantially simplifies calculations, which can be done, at least in principle, for the more realistic 'hot'-spots model.

[14] Strictly speaking, this assumption is applicable only when the temperature is sufficiently high.

[15] We can say that we introduce an effective coupling constant of the electron-fluctuation interaction in the form $W_{\mathbf{p}} = W\big[\theta(p_x^0 - p_x)\times \theta(p_x^0 + p_x) + \theta(p_y^0 - p_y)\theta(p_y^0 + p_y)\big]$ (Fig. 13b).

[16] A similar situation is realized in molten metals and semiconductors, where the information about the lost crystalline structure is saved in the so-called structure factor and leads to a characteristic maximum in this factor in momentum space. This quantity plays a determinant role in the Ziman and Edwards theory of the electronic structure of liquid metals and semiconductors [68]. However, in 3D isotropic liquids averaging over angles usually leads to a significant weakening of pseudogap effects.

where $\xi_{\mathbf{k}} = \varepsilon_{\mathbf{k}} - \mu$ is the quasiparticle energy measured from the Fermi level (chemical potential) μ, and $\gamma_{\mathbf{k}}$ is the quasiparticle damping. For the residue at the pole, $0 < Z_{\mathbf{k}} < 1$, and G_{incoh} is the nonsingular (incoherent) contribution of many-particle excitations. Then the corresponding spectral density is given by the formula

$$A(\omega, \mathbf{k}) = \frac{1}{\pi} Z_{\mathbf{k}} \frac{\gamma_{\mathbf{k}}}{(\omega - \xi_{\mathbf{k}})^2 + \gamma_{\mathbf{k}}^2} + \ldots, \tag{13}$$

where the ellipsis stands for the more or less invariable contribution originating from G_{incoh}, and the quasiparticle spectrum manifests itself in a narrow (as $\gamma_{\mathbf{k}}$ is small) Lorentzian peak. The situation is illustrated in Fig. 14a.

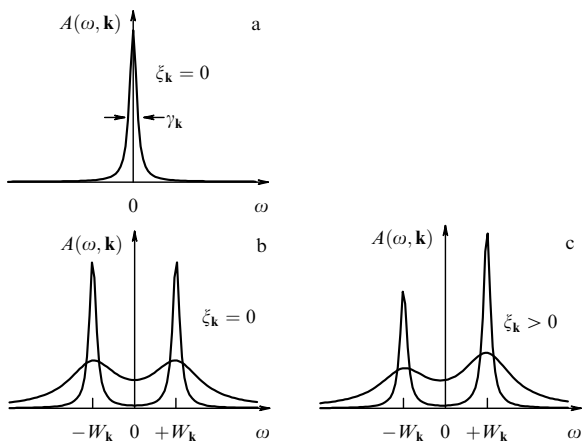

Figure 14. Qualitative picture of the evolution of the spectral density. (a) Normal metal (Fermi liquid) at $\xi_{\mathbf{k}} = 0$, i.e. at the Fermi surface. (b) Two narrow peaks corresponding to 'Bogolyubov' quasiparticles in a system with a dielectric gap $W_{\mathbf{k}}$ (in the presence of long-range CDW- or SDW-type order). The diffuse maxima represent a system without long-range order (pseudogap behavior), $\xi_{\mathbf{k}} = 0$ (at the Fermi surface). (c) The same as in (b) but with $\xi_{\mathbf{k}} > 0$, i.e. above the Fermi surface. In this case the spectral density acquires a characteristic asymmetry.

If long-range order (say, of SDW- or CDW-type) sets in in the system, a (dielectric) gap of width $W_{\mathbf{k}}$ opens in the spectrum of the elementary excitations of the system (the dependence on $\mathbf{k}$ emphasizes the possibility of the appearance of a finite gap only within a certain portion of the Fermi surface), and the one-electron Green function becomes the well-known Gor'kov function [55, 56] to which the decay $\Gamma_{\mathbf{k}}$ can be added:

$$G(\omega, \mathbf{k}) = \frac{u_{\mathbf{k}}^2}{\omega - E_{\mathbf{k}} + \mathrm{i}\Gamma_{\mathbf{k}}} + \frac{v_{\mathbf{k}}^2}{\omega + E_{\mathbf{k}} - \mathrm{i}\Gamma_{\mathbf{k}}}, \tag{14}$$

where the excitation spectrum is

$$E_{\mathbf{k}} = \sqrt{\xi_{\mathbf{k}}^2 + W_{\mathbf{k}}^2} \tag{15}$$

and where we have introduced the Bogolyubov coefficients

$$u_{\mathbf{k}}^2 = \frac{1}{2}\left(1 + \frac{\xi_{\mathbf{k}}}{E_{\mathbf{k}}}\right), \tag{16}$$

$$v_{\mathbf{k}}^2 = \frac{1}{2}\left(1 - \frac{\xi_{\mathbf{k}}}{E_{\mathbf{k}}}\right). \tag{17}$$

Then the spectral density is given by the formula

$$A(\omega, \mathbf{k}) = \frac{u_{\mathbf{k}}^2}{\pi} \frac{\Gamma_{\mathbf{k}}}{(\omega - E_{\mathbf{k}})^2 + \Gamma_{\mathbf{k}}^2} + \frac{v_{\mathbf{k}}^2}{\pi} \frac{\Gamma_{\mathbf{k}}}{(\omega + E_{\mathbf{k}})^2 + \Gamma_{\mathbf{k}}^2} + \ldots, \tag{18}$$

where we now have *two* peaks, narrow as $\Gamma_{\mathbf{k}}$ is small and corresponding to 'Bogolyubov' quasiparticles.

Now suppose that there is no CDW- or SDW-type long-range order but strong scattering on fluctuations with the corresponding wave vectors is present [cf. (6) and (10) or (11)]. Then it is easy to imagine that, in the region of momentum space where a dielectric gap opens in the presence of long-range order, the spectral density retains a 'recollection' (or 'premonition') of this gap in the form of a characteristic 'double-humped' structure, as shown qualitatively in Fig. 14[17]. Here the width of the peaks is naturally determined by a parameter like v_{F}/ξ, i.e. by the reciprocal time of transit of an electron through a region of size ξ in which the 'dielectric' order is effectively retained. Thus, the qualitative picture of the process agrees fairly well with the ARPES data displayed in Fig. 12. Below we will see that a systematic treatment of the problem leads to precisely these results. Our further discussion will be devoted to justifying this qualitative scheme and to deriving various corollaries.

3.2 Recurrent procedure for the Green functions

The model of the pseudogap state considered here is actually a two-dimensional generalization of the pseudogap model proposed many years ago by Lee et al. [70] and the present author [71–73] for the fluctuation region of the Peierls (CDW) structural transition in one-dimensional systems[18]. In particular, in Refs [71, 72] an exact solution of the problem was derived in the limit of very large correlation lengths of short-range-order fluctuations, $\xi \to \infty$, while in Ref. [73] a generalization to the case of finite ξ was carried out. What sets Refs [71–73] apart from the paper by Lee et al. [70] is the allowance for all diagrams of the Feynman series in the theory of perturbation in the interaction with fluctuations. A two-dimensional generalization of this approach was carried out by Schmalian et al. [14] and Kuchinskiĭ and Sadovskiĭ [15] in the 'hot'-spots model, while in the hot-region model such a generalization is trivial because the problem can be completely reduced to a one-dimensional one.

The contribution of an arbitrary diagram for the self-energy part of a one-electron Green function of the Nth order in the interaction (10) or (11) with fluctuations can be approximately written as follows [15]:

$$\Sigma^{(N)}(\varepsilon_n, \mathbf{p}) = W^{2N} \prod_{j=1}^{2N-1} \frac{1}{\mathrm{i}\varepsilon_n - \xi_j + \mathrm{i} n_j v_j \varkappa}, \tag{19}$$

where in the hot-point model $\xi_j = \xi_{\mathbf{p}+\mathbf{Q}}$ and $v_j = |v_{\mathbf{p}+\mathbf{Q}}^x| + |v_{\mathbf{p}+\mathbf{Q}}^y|$ for j odd and $\xi_j = \xi_{\mathbf{p}}$ and $v_j = |v_{\mathbf{p}}^x| + |v_{\mathbf{p}}^y|$ for j even, while in the hot-region model, $\xi_j = (-1)^j \xi_{\mathbf{p}}$ and $v_j = v_{\mathrm{F}}$. In equation (19) we have introduced the reciprocal correlation length $\varkappa = \xi^{-1}$, n_j is the number of interaction lines encompassing the jth Green function in the given

[17] In what follows, the term 'non-Fermi-liquid behavior' will be used only in this, fairly limited, sense.

[18] In Ref. [71] this model was used to explain the appearance of a pseudogap in liquid semiconductors.

diagram, $\varepsilon_n = (2n+1)\pi T$, and, for the sake of definiteness, $\varepsilon_n > 0$.

Actually, equation (19) is a fairly successful ansatz for calculating the contribution of a diagram of any order. In this case any diagram with the interaction lines crossed proves to be equal to a diagram of the same order but without interaction-line crossing. Hence we can actually consider only diagrams without interaction-line crossing and allow for the diagrams with line crossing by introducing additional combinatorial factors at the interaction vertices. Such an approach was first used (in another problem) by Elyutin [74] and was then employed in Ref. [73] for a one-dimensional model of the pseudogap state. Equation (19) is not exact [75] and can be justified in the two-dimensional case only for certain topologies of the Fermi surface, such that the projections of the electron velocities at 'hot' spots linked by the vector $\mathbf{Q}$ have the same sign and hence $v^x_{\mathbf{p}} v^x_{\mathbf{p}+\mathbf{Q}} > 0$ and $v^y_{\mathbf{p}} v^y_{\mathbf{p}+\mathbf{Q}} > 0$ [15]. This condition is obviously invalid in the one-dimensional case and for a topology of the Fermi surface typical of HTSC cuprates (see Fig. 13a). However, as shown in Ref. [15], in such cases the use of equation (19) also leads to a satisfactory description, reproducing the well-known exact results for the limits $\xi \to \infty$ and $\xi \to 0$ [19].

As a result we arrive at the following recurrent relation (represented in the form of a continued fraction [73]) for the one-electron Green function:

$$G^{-1}(\varepsilon_n, \xi_{\mathbf{p}}) = G_0^{-1}(\varepsilon_n, \xi_{\mathbf{p}}) - \Sigma_1(\varepsilon_n, \xi_{\mathbf{p}}) \,, \tag{20}$$

$$\Sigma_k(\varepsilon_n, \xi_{\mathbf{p}}) = W^2 \, \frac{v(k)}{\mathrm{i}\varepsilon_n - \xi_k + \mathrm{i}k v_k \varkappa - \Sigma_{k+1}(\varepsilon_n, \xi_{\mathbf{p}})} \,. \tag{21}$$

The combinatorial factor

$$v(k) = k \tag{22}$$

corresponds to the case of commensurate fluctuations with $\mathbf{Q} = (\pm\pi/a, \pm\pi/a)$ (considered here) [73]. It is really easy to examine also the case of incommensurate fluctuations, where $\mathbf{Q}$ is not related to the reciprocal lattice spacing. In this case the contribution of the diagrams in which the interaction lines encompass an odd number of vertices is much smaller than that of the diagrams in which the interaction lines encompass an even number of vertices. Hence only the latter type of diagram can be taken into account [71–73]. In this case the recurrent relation (21) is still valid, but the combinatorics of the diagrams changes and so do the factors $v(k)$ [73]:

$$v(k) = \begin{cases} \dfrac{k+1}{2} & \text{for odd } k \,, \\ \dfrac{k}{2} & \text{for even } k \,. \end{cases} \tag{23}$$

Schmalian et al. [14] allowed for the spin structure of the interaction in the model of an 'almost antiferromagnetic' Fermi liquid (the spin–fermion model). It proves that allowing for this structure leads to a more complex combinatorics of the diagrams in the commensurate case $\mathbf{Q} = (\pm\pi/a, \pm\pi/a)$. More precisely, scattering with spin conservation yields formally commensurate combinatorics, while scattering with a spin flip is described by diagrams for the incommensurate case (a 'charged' random field, in the terminology of Schmalian et al. [14]). As a result, the recurrent relation for the Green function is still of the form (21), but the combinatorial factor $v(k)$ becomes [14]

$$v(k) = \begin{cases} \dfrac{k+2}{3} & \text{for odd } k \,, \\ \dfrac{k}{3} & \text{for even } k \,. \end{cases} \tag{24}$$

3.3 Spectral density and the density of states

The recurrence relations (20) and (21) are very convenient for numerical calculations. Fairly detailed calculations of spectral densities, ARPES characteristics, and densities of states have been carried out for different variants of the 'hot'-spots model [14, 15]. As a typical example, Fig. 15a depicts the results of Ref. [15] for the spectral density of carriers in the incommensurate case. Clearly, the spectral density near a 'hot' spot has the expected non-Fermi-liquid shape, and the quasiparticle concept does not work here. Far from a 'hot' spot the spectral density has a sharp peak corresponding to well-defined quasiparticles (a Fermi liquid). In Fig. 15b (taken from Ref. [14]) we depict the product of the distribution function by the spectral density for different points on the 'renormalized' Fermi surface determined from the equation $\varepsilon_{\mathbf{k}} - \mathrm{Re}\,\Sigma(\omega = 0, \mathbf{k}) = 0$, where the 'bare' spectrum $\varepsilon_{\mathbf{k}}$ was taken in the form (3) with $t = -0.25$ eV, $t' = -0.35t$, hole concentration $n_{\mathrm{h}} = 0.16$, coupling constant in (6) $g = 0.8$ eV, and correlation length $\xi = 3a$ (the commensurate case and the spin–fermion model). There are clearly full qualitative agreement with the ARPES data discussed above and a qualitatively different behavior near the 'hot' spot and far from it. Finally, in Fig. 16 (taken from Ref. [14]) we depict the positions of the maximum of $A(\omega, \mathbf{k})$ calculated in the spin–fermion model with interaction (6) (the static limit) for two different hole concentrations, and the corresponding ARPES data of Marshall et al. [79] for the $Bi_2Sr_2Ca_{1-x}Dy_xCu_2O_{8+\delta}$ system. The point is that for an ideal system of a Fermi-liquid type the positions of the maximum of the spectral density in the $(\omega, \mathbf{k})$ plane found from ARPES data actually determine the dispersion law for the corresponding quasiparticles (Fig. 14a). For an overdoped system the values $n_{\mathrm{h}} = 0.22$ and $\xi = a$ were taken. The results demonstrate branches of the spectrum, defined fairly well, in both the direction of the diagonal of the Brillouin zone and the direction $(0,0)-(\pi,0)$. For an underdoped system the values $n_{\mathrm{h}} = 0.16$ and $\xi = 3a$ were assumed. Here in the direction of the diagonal one can clearly see the intersection of the spectrum with the Fermi level, while near 'hot' spots, in the neighborhood of $(\pi, 0)$, the diffuse maximum of the spectral density remains approximately 200 meV below the Fermi level (a pseudogap). On the whole, agreement between the theoretical model and the experimental data can be considered quite satisfactory.

Now let us turn to the one-electron density of states

$$N(E) = \sum_{\mathbf{p}} A(E, \mathbf{p}) = -\frac{1}{\pi} \sum_{\mathbf{p}} \mathrm{Im}\, G^{\mathrm{R}}(E, \mathbf{p}) \,, \tag{25}$$

[19] In the least favorable case of a one-dimensional model, ansatz (19) yields a very good quantitative approximation, e.g., for the density of states, which becomes evident from a direct comparison [76] of the results of Ref. [73] for an incommensurate case with the results of the exact numerical simulation of the problem in question done by Bartosh and Kopietz [77] and Millis and Monien [78]. In a commensurate case, (19) does not describe only a Dyson singularity in the density of states are the center of the pseudogap [77, 78], which is certainly absent in the 2D case.

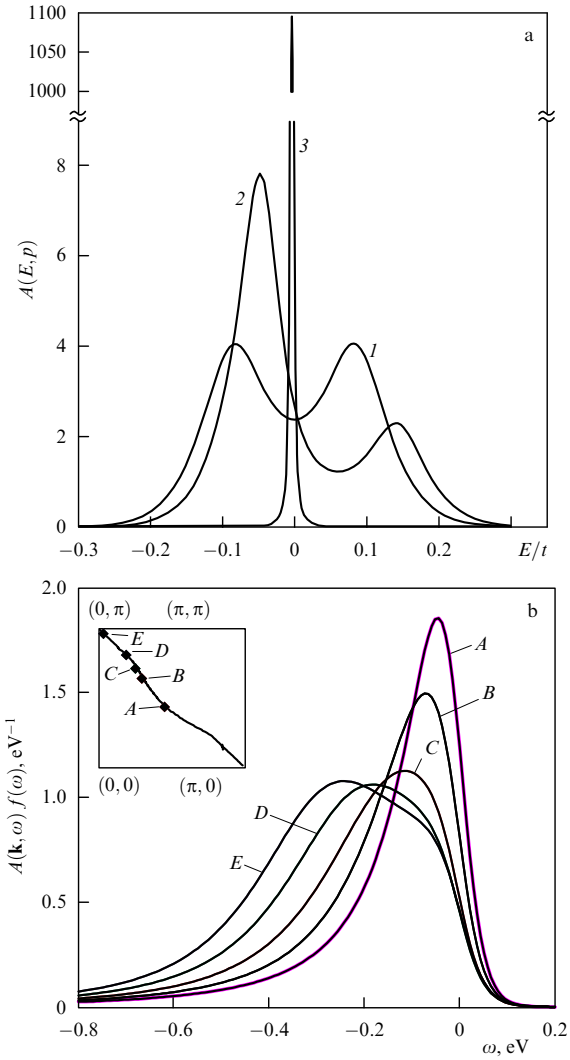

Figure 15. (a) Spectral density in the 'hot'-spots model, the case of incommensurate fluctuations, $\varkappa a = 0.01$ [15], at the 'hot' spot $p_x a/\pi = 0.142$, $p_y a/\pi = 0.587$ (curve *1*); near the 'hot' spot at $p_x a/\pi = 0.145$, $p_y a/\pi = 0.843$ (curve *2*); and far from the 'hot' spot at $p_x a/\pi = p_y a/\pi = 0.375$ (curve *3*). (b) The product of the spectral density by the Fermi distribution function at different points of the Fermi surface that are shown in the inset. The spin–fermion model, correlation length $\xi = 3a$ [14].

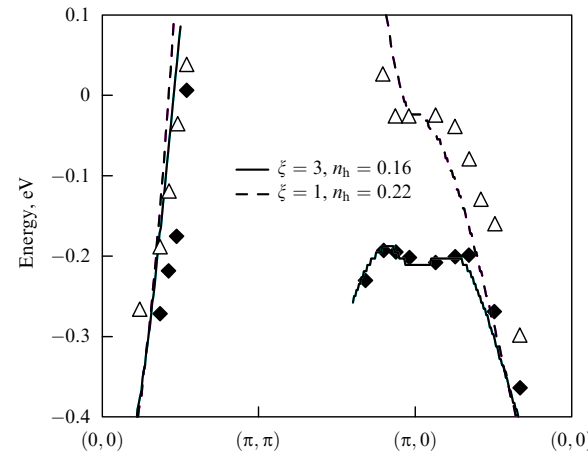

Figure 16. The position of the maximum in the spectral density as a function of the correlation length ξ and the hole concentration, calculated for the variant of the spin–fermion model under discussion [14], compared to the ARPES data of Ref. [79] for the $Bi_2Sr_2Ca_{1-x}Dy_xCu_2O_{8+\delta}$ system at $x = 1$ (triangles) and $x = 0.175$ (diamonds).

which is determined by an integral of $A(E,\mathbf{p})$ over the entire Brillouin zone. Detailed calculations of the density of states in the 'hot'-spots model were done in Ref. [15]. For a typical value $t'/t = -0.4$, a small dip (pseudogap) is observed in the density of states. The dip in the density of states only weakly depends on the correlation length ξ. At the same time, say at $t'/t = -0.6$ (which is not typical of HTSC cuprates), the Fermi surface does contain 'hot' spots, but a pseudogap in the density of states can hardly be identified. What is noticeable is the blurring of the Van Hove singularity, which exists in the absence of scattering on fluctuations.

In the hot-region model, the use of (20) and (21) leads to a spectral density quite similar in the 'hot' regions to that depicted in Fig. 15a [81, 82]. In the 'cold' regions of the Fermi surface the spectral density reduces to a Dirac delta function, which is typical of Fermi liquids (cf. Fig. 14a). The density of states is given by the formula

$$N(E) = -\frac{1}{\pi}\,N_0(0)\int_0^{2\pi}\frac{\mathrm{d}\phi}{2\pi}\int_{-\infty}^{\infty}\mathrm{d}\xi_{\mathbf{p}}\,\mathrm{Im}\,G^{\mathrm{R}}(E,\xi_{\mathbf{p}})$$
$$= \frac{4\alpha}{\pi}\,N_{\mathrm{W}}(E) + \left(1-\frac{4\alpha}{\pi}\right)N_0(0)\,, \qquad (26)$$

where $N_0(0)$ is the density of states of free electrons on the Fermi level, and $N_{\mathrm{W}}(E)$ is the density of states in the one-dimensional problem (a square Fermi surface), found earlier in Refs [71–73].

Let us present more detailed results for a rather artificial limit of very long fluctuation correlation lengths, $\xi \to \infty$. This limit allows easily summing the entire perturbation series for an electron scattered on such fluctuations [71, 72] and obtaining the exact analytical solution for the one-electron Green function in the form [63]

$$G(\varepsilon_n,p) = \int_0^{\infty}\mathrm{d}D\,\mathcal{P}(D)\,\frac{\mathrm{i}\varepsilon_n+\xi_p}{(\mathrm{i}\varepsilon_n)^2-\xi_p^2-D(\phi)^2}\,, \qquad (27)$$

where $D(\phi)$ is defined for $0 \leqslant \phi \leqslant \pi/2$ as

$$D(\phi) = \begin{cases} D\,, & 0 \leqslant \phi \leqslant \alpha\,, \quad \dfrac{\pi}{2}-\alpha \leqslant \phi \leqslant \dfrac{\pi}{2}\,, \\ 0\,, & \alpha \leqslant \phi \leqslant \dfrac{\pi}{2}-\alpha\,. \end{cases} \qquad (28)$$

For other values of ϕ the quantity $D(\phi)$ is obviously defined from symmetry considerations in a manner similar to (28).

The amplitude of the dielectric gap D is a random quantity distributed according to the Rayleigh law [73] [its phase is also random and is distributed uniformly over the interval $(0, 2\pi)$]:

$$\mathcal{P}(D) = \frac{2D}{W^2}\exp\left(-\frac{D^2}{W^2}\right). \qquad (29)$$

Thus, in the 'hot' regions, the Green function has the shape of a 'normal' Gor'kov function averaged over fluctuations of the

dielectric gap D [distributed according to (29)], which are spatially uniform. Here the 'anomalous' Gor'kov function is zero due to the randomness of the phases of the dielectric gap D, which corresponds to the absence of long-range order in the system [20].

For finite correlation lengths ξ the amplitude of our one-dimensional 'periodic' random field is approximately constant over a length of order ξ, and its values in different regions of size $\sim \xi$ are random. An electron is effectively scattered only when it passes from one such region to another, which takes a characteristic time $\sim \xi/v_{\mathrm{F}}$ and leads to decay $\sim v_{\mathrm{F}}/\xi$. Interesting data on simulation of a random field in which the motion of the electron is treated within the framework of the one-dimensional variant of the model at hand can be found in Ref. [75].

Outside the 'hot' regions [the second inequality in (28)] the Green function (27) is simply the Green function of free electrons.

The density of states corresponding to (27) has the form (26), where

$$\frac{N_{\mathrm{W}}(E)}{N_0(0)} = \left|\frac{E}{W}\right| \int_0^{E^2/W^2} \mathrm{d}\zeta\, \frac{\exp(-\zeta)}{\sqrt{E^2/W^2-\zeta}} = 2\left|\frac{E}{W}\right| \exp\left(-\frac{E^2}{W^2}\right) \mathrm{Erfi}\left(\frac{E}{W}\right). \tag{30}$$

Here $\mathrm{Erfi}(x)$ is the error function of imaginary argument.

Figure 17 depicts diagrams of the density of states in our model for different values of the parameter α, i.e. for 'hot' regions of different sizes. Clearly, the pseudogap in the density of states becomes 'blurred' rather rapidly with the decrease in the size of 'hot' regions and is in general not very distinct. In a certain sense the effect of decreasing α is similar to the effect of decreasing correlation length ξ of the fluctuations [73], so that the above approximation $\xi \to \infty$ is, possibly, not a very strong limitation on the applicability of the model. The finiteness of ξ can easily be taken into account using (20) and (21), which additionally suppresses of the pseudogap as ξ decreases. Note the general qualitative agreement between the shape of the pseudogap in the density of states in the hot-region model and the shape of the pseudogap observed in tunnel experiments, which becomes evident if we look at Fig. 4.

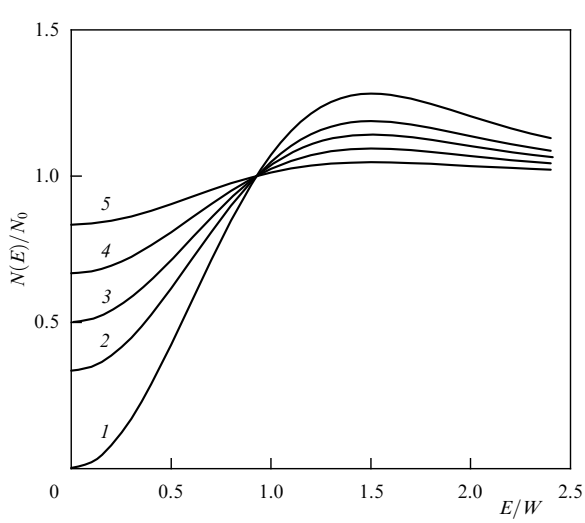

Figure 17. Density of electronic states for 'hot' regions of different sizes [63]: (*1*) $\alpha = \pi/4$, (*2*) $\alpha = \pi/6$, (*3*) $\alpha = \pi/8$, (*4*) $\alpha = \pi/12$, and (*5*) $\alpha = \pi/24$.

[20] Note that the pair averages of the anomalous functions are finite and contribute to the corresponding exact solution for the two-particle Green function [71, 72].

3.4 Two-particle Green function and optical conductivity

A remarkable feature of the models in question is the possibility of doing a fairly consistent calculation of the two-particle Green function of the electron in the field of random short-range-order fluctuations [80, 81] (see also Ref. [14]) that allows for *all* diagrams in the Feynman perturbation series. Since calculations in the hot-point model are fraught with serious difficulties related to the use of a 'realistic' current-carrier spectrum (3), we limit ourselves to a simplified analysis of the hot-region model [83].

We assume that in 'cold' regions of the Fermi surface there is weak static scattering of an arbitrary nature, whose rate we will describe by a phenomenological parameter γ assuming that always $\gamma \ll W$, so that in 'hot' regions this scattering can be ignored. Accordingly, in 'cold' regions the electron spectrum is described by the ordinary expressions for the Green functions in a system with weak scattering.

We begin with the limit $\xi \to \infty$, where the one-electron Green function has the form (27) and the two-particle Green function can also be found exactly by the methods described in Refs [71, 72].

The conductivity in the given model always consists of additive contributions from 'hot' and 'cold' regions, similar to (26). In particular, for the real part of the conductivity we have, as $\xi \to \infty$,

$$\mathrm{Re}\,\sigma(\omega) = \frac{4\alpha}{\pi}\,\mathrm{Re}\,\sigma_{\mathrm{W}}(\omega) + \left(1-\frac{4\alpha}{\pi}\right)\mathrm{Re}\,\sigma_{\mathrm{D}}(\omega), \tag{31}$$

where, with allowance for the results obtained in Refs [71, 72],

$$\mathrm{Re}\,\sigma_{\mathrm{W}}(\omega) = \frac{\omega_{\mathrm{pl}}^2}{4}\,\frac{W}{\omega^2}\int_0^{\omega^2/4W^2} \mathrm{d}\zeta\,\exp(-\zeta)\,\frac{\zeta}{\sqrt{\omega^2/4W^2-\zeta}}. \tag{32}$$

Here ω_{pl} is the plasma frequency, and

$$\mathrm{Re}\,\sigma_{\mathrm{D}}(\omega) = \frac{\omega_{\mathrm{pl}}^2}{4\pi}\,\frac{\gamma}{\omega^2+\gamma^2} \tag{33}$$

is the common Drude part of the conductivity due to 'cold' regions.

Even in this very simple approximation the ω-dependence of $\mathrm{Re}\,\sigma$ closely resembles the experimental data given in Refs [29, 30, 84, 85] and is characterized by a narrow Drude peak at low frequencies and a smooth maximum in the absorption through the pseudogap at $\omega \sim 2W$. As the rate γ of scattering on 'cold' regions increases, the characteristic Drude peak at low frequencies is more and more suppressed.

A more realistic case of a finite correlation length ξ of fluctuations of short-range 'antiferromagnetic' order in (11) can be analyzed using (20) and (21). The vertex part $J^{\mathrm{RA}}(\epsilon, \xi_{\mathbf{p}}; \epsilon+\omega, \xi_{\mathbf{p}+\mathbf{q}})$, which determines the density–density response function (the two-particle Green function) in 'hot' regions, can be found by the following recurrent procedure (for more details see Refs. [80, 81] and also

Ref. [14]), which allows for all diagrams in the interaction with fluctuations:

$$J_{k-1}^{\mathrm{RA}}(\epsilon,\xi_{\mathbf{p}};\epsilon+\omega,\xi_{\mathbf{p}+\mathbf{q}}) = e + W^2 v(k) G_k^{\mathrm{A}}(\epsilon,\xi_{\mathbf{p}}) \times G_k^{\mathrm{R}}(\epsilon+\omega,\xi_{\mathbf{p}+\mathbf{q}}) J_k^{\mathrm{RA}}(\epsilon,\xi_{\mathbf{p}};\epsilon+\omega,\xi_{\mathbf{p}+\mathbf{q}}) \times \left(1 + 2\mathrm{i}v_{\mathrm{F}}\varkappa k\left\{\omega - (-1)^k v_{\mathrm{F}} q + v(k+1)W^2 \times \left[G_{k+1}^{\mathrm{A}}(\epsilon,\xi_{\mathbf{p}}) - G_{k+1}^{\mathrm{R}}(\epsilon+\omega,\xi_{\mathbf{p}+\mathbf{q}})\right]\right\}^{-1}\right). \quad (34)$$

Here e is the electron charge, the superscript R(A) indicates the retarded (advanced) Green function, and the vertex of interest to us is determined by zero order, $k = 0$, in the given recurrent procedure. The contribution to the conductivity from 'hot' regions, $\mathrm{Re}\,\sigma_{\mathrm{W}}(\omega)$, in (31) can now be calculated as in Refs [80, 81], while $\mathrm{Re}\,\sigma_{\mathrm{D}}(\omega)$ is still given by (33).

The typical results of calculations are depicted in Fig. 18 for the case of incommensurate fluctuations. The allowance for the combinatorics of the spin–fermion model leads to only slight quantitative changes. The general qualitative picture for the commensurate case is the same [83]. Conductivity is always characterized by the presence of a fairly narrow Drude peak at low frequencies, $\omega < \gamma$, which emerges from the 'cold' regions on the Fermi surface, and a gently sloping maximum at frequencies $\omega \sim 2W$, which corresponds to absorption through the pseudogap that opens in the 'hot regions. The Drude peak rapidly becomes blurred as γ increases. The dependence on the fluctuation correlation length $\xi = \varkappa^{-1}$ in the most interesting region of parameters is fairly weak. This qualitative picture closely resembles the pattern of experimental data for a broad range of HTSC systems [29, 30, 84, 85], with a typical example of such data depicted in Fig. 7. In the model in question we can calculate not only the real but also the imaginary part of the conductivity and, accordingly, the parameters of the extended Drude model (1) and (2) [86]. The calculated behavior of $1/\tau(\omega)$ is shown in the inset in Fig. 18 and represents the pseudogap behavior at frequencies $\omega < W$, similar to that depicted in Fig. 7b [21]. Thus, the resulting dip in $1/\tau(\omega)$ in the frequency range $\omega < W$ is a direct reflection of the presence of a pseudogap in the electron spectrum. It is probably easy to fit our results to the experimental data using the well-known values $\omega_{\mathrm{pl}} \sim 1.5-2.5$ eV and $2W \sim 0.1$ eV, as well as the values of γ determined experimentally from the width of the Drude peak, and varying the adjustable parameters α (the size of 'hot' regions) and ξ (for the latter quantity we can use the well-known estimates from other experiments [14]).

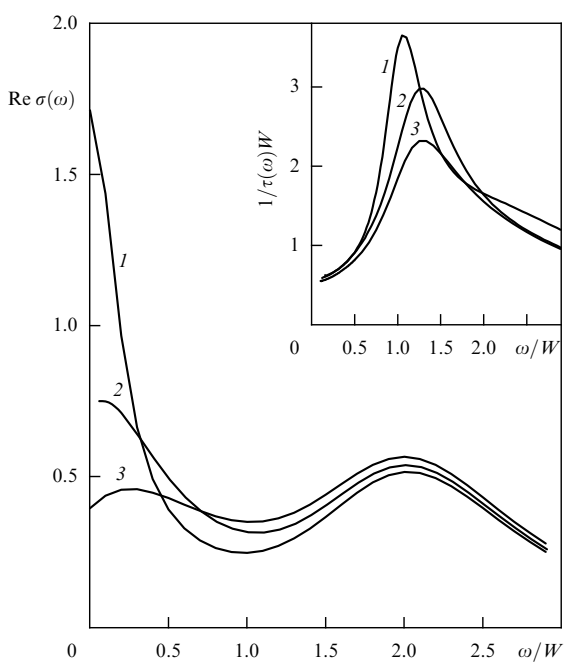

Figure 18. Real part of the conductivity as a function of the frequency of the external field at a fixed value of the correlation length $v_{\mathrm{F}}\varkappa = 0.5W$ for different values of γ (conductivity is in units of $\omega_{\mathrm{pl}}^2/4\pi W$): (*1*) $\gamma/W = 0.2$, (*2*) $\gamma/W = 0.5$, and (*3*) $\gamma/W = 1.0$. The size of the 'hot' regions is $\alpha = \pi/6$ [83]. The inset presents the calculated generalized scattering rate $1/\tau$ (in units of W) as a function of the frequency of the external field at a fixed $\gamma = 0.2W$ for different values of the correlation length: (*1*) $v_{\mathrm{F}}\varkappa = 0.1$, (*2*) $v_{\mathrm{F}}\varkappa = 0.5$, and (*3*) $v_{\mathrm{F}}\varkappa = 1.0$ [86].

4. Superconductivity in the pseudogap state

4.1 Gor'kov equations

At present there is no unified viewpoint on the mechanism of Cooper pairing in HTSC cuprates. What has been firmly established is only the fact of anisotropic pairing and d-wave symmetry of Cooper pairs [45–47], although even in this problem there are alternative viewpoints. Apparently, there is a tendency among most researchers to adhering to one or another variant of pairing caused by the exchange of spin (antiferromagnetic) fluctuations. A recent review of the attempts made in this direction can be found in Ref. [46]. A typical example of theories of this type is the model of a 'nearly antiferromagnetic' Fermi liquid (the spin–fermion model), which is being actively developed by Pines and his collaborators (see Refs [58, 59]). The model is based on the assumption that electrons interact with spin fluctuations, and the form of this interaction [Eqn (6)] is determined, as noted above, by means of fitting to NMR data [60]. This approach is being actively developed (the results of recent work in this area of research can be found in Refs [87–89]), and there are conclusive experimental facts in favor of this HTSC mechanism [46, 90]. At the same time, we have seen that the interaction (6) can also be responsible for the formation of a 'dielectric' pseudogap at sufficiently high temperatures. Unfortunately, so far there has been no studies that would consistently examine in conjunction the phenomenon of Cooper pairing and the formation of a pseudogap with the spin–fermion model.

On the other hand, rephrasing Landau's statement (quoted in Ref. [91]) that 'nobody has abrogated the Coulomb law for metals,' we can say that nobody has abrogated the electron–phonon interaction as well, and this interaction can serve as a possible microscopic pairing mechanism in HTSC. Reviews of the corresponding calculations with really impressive results can be found in Refs [91, 92] and in an earlier review by Ginzburg and Maksimov [93]. Perhaps the main difficulty of the pairing models based on the

[21] When $\omega > W$, the linear increase of $1/\tau(\omega)$ with frequency is not reproduced, but, to allow for such an increase, one can use a phenomenological substitution like $\gamma(\omega) = \gamma_0 + a\omega$, in the spirit of the theory of marginal Fermi liquids. The meaning of such a substitution is to 'allow' for inelastic scattering processes, completely ignored in our model.

electron – phonon interaction in HTSC cuprates is the d-wave symmetry of Cooper pairs (mentioned earlier). At the same time, interesting attempts have been made to explain anisotropic pairing based on the electron – phonon interaction [91, 92], and there are serious doubts on the efficiency of the spin-fluctuation mechanism [91].

I am not inclined to take sides in this discussion and believe that these (or similar [94]) fairly traditional mechanisms probably play a leading role in the microscopic theory of high-T_c superconductivity. In any case, in this review there will be no discussion of other, more radical, approaches like the Luttinger-liquid model [95], which has been developed for many years in different variants. The reason is that there are no well-established results and conclusions in these new approaches.

The above-discussed substantial transformation of the electron spectrum (pseudogap) has inevitably a strong effect on the properties of the system in the superconducting state. In the approach considered above, which is based on the scenario of pseudogap formation due to 'dielectric' (AFM, SDW, or CDW) type, short-range-order fluctuations, the discussion is about the effect of the pseudogap on superconductivity. In such an approach the investigation can be carried out without knowing the specifics of the pairing mechanisms, as is done, for instance, in analyzing the effects of such factors as structural disordering and the presence of impurities on superconductivity. From the physical viewpoint, the least justified in our further investigation is the above assumption that short-range-order fluctuations are static, since the dynamics of these fluctuations [say, within the model (6)] can play a leading role at low temperatures (in the superconducting phase), being possibly responsible for the very mechanism of Cooper pairing. We deliberately introduce appropriate simplifications, since for the time being it is impossible to get the full solution of the problem in a dynamical model. Moreover, our analysis will entirely be based on the simplified hot-region model[22] discussed in Section 3.1. For the sake of completeness, we consider s- and d-pairing in conjunction.

In view of what we have said, without concretizing the microscopic mechanism, we adopt the simple BCS-type model for the pairing interaction and assume that Cooper pairing occurs because of an attractive 'potential' of the following simple type:

$$V_{\rm sc}(\mathbf{p},\mathbf{p}') = V(\phi,\phi') = -Ve(\phi)e(\phi')\,, \tag{35}$$

where ϕ is the polar angle determining the direction of the electron momentum $\mathbf{p}$ in the plane, and $e(\phi)$ is specified by the simple model dependence

$$e(\phi) = \begin{cases} 1 & \text{(s-pairing)}\,, \\ \sqrt{2}\cos 2\phi & \text{(d-pairing)}\,. \end{cases} \tag{36}$$

As usual, the attraction constant V is assumed to be nonzero within a certain layer of width $2\omega_c$ near the Fermi level (ω_c is the characteristic frequency of the quanta ensuring the attraction of electrons). The model interaction of type (35) has been successfully used by Borkowski and Hirschfeld [96] and Fehrenbacher and Norman [97] to analyze the effect of impurities on anisotropic Cooper pairing.

[22] This simplification is not very important. A similar analysis can be done within the hot-point model, but the complexity of the calculations increases substantially.

In this case the superconducting gap has the form

$$\Delta(\mathbf{p}) \equiv \Delta(\phi) = \Delta e(\phi)\,. \tag{37}$$

To avoid dealing with cumbersome formulas, we will hereinafter assume that Δ stands precisely for $\Delta(\phi)$ and will indicate the angular dependence explicitly only where this is required.

In the superconducting state, a theory that uses the interaction with AFM fluctuations (11) as a perturbation must be based on the 'free' normal and anomalous Green functions of the superconductor,

$$G_{00}(\varepsilon_n,\mathbf{p}) = -\frac{\mathrm{i}\varepsilon_n + \xi_{\mathbf{p}}}{\varepsilon_n^2 + \xi_{\mathbf{p}}^2 + |\Delta|^2}\,,$$
$$F_{00}^{+}(\varepsilon_n,\mathbf{p}) = \frac{\Delta^*}{\varepsilon_n^2 + \xi_{\mathbf{p}}^2 + |\Delta|^2}\,. \tag{38}$$

In this case, we can formulate a direct analog of the approximation (19) in the superconducting state [98]. The contribution of an arbitrary diagram of the Nth order in the interaction (10) to the normal or anomalous Green function has the form of the product of $N+1$ 'free' normal (G_{0k_j}) and anomalous ($F_{0k_j}^{+}$) Green functions, with frequencies and gaps renormalized in a certain way. Here k_j is the number of interaction lines encompassing the given jth (as counted from the beginning of the diagram) electron line. As in the normal phase, the contribution of any diagram is determined by a set of integers k_j, and each diagram with intersecting interaction lines is equal to a diagram of the same order without intersections of these lines. Hence we can again focus solely on diagrams without intersections, taking into account the contribution of other diagrams by introducing the same combinatorial factors $v(k)$ assigned to the interaction lines as in the normal phase. As a result, we arrive at an analog of the Gor'kov equations [69]. Accordingly, there emerge two coupled recurrent equations for the normal and anomalous Green functions:

$$G_k = G_{0k} + G_{0k}\widetilde{G}G_k - G_{0k}\widetilde{F}F_k^{+} - F_{0k}\widetilde{G}^{*}F_k^{+} - F_{0k}\widetilde{F}^{+}G_k\,,$$
$$F_k^{+} = F_{0k}^{+} + F_{0k}^{+}\widetilde{G}G_k - F_{0k}^{+}\widetilde{F}F_k^{+} + G_{0k}^{*}\widetilde{G}^{*}F_k^{+} + G_{0k}^{*}\widetilde{F}^{+}G_k\,, \tag{39}$$

where

$$\widetilde{G} = W^2 v(k+1)G_{k+1}\,, \qquad \widetilde{F}^{+} = W^2 v(k+1)F_{k+1}^{+}\,, \tag{40}$$

$$G_{0k}(\varepsilon_n,\mathbf{p}) = -\frac{\mathrm{i}\varepsilon_n + (-1)^k\xi_{\mathbf{p}}}{\tilde{\varepsilon}_n^2 + \xi_{\mathbf{p}}^2 + |\tilde{\Delta}|^2}\,, \quad F_{0k}^{+}(\varepsilon_n,\mathbf{p}) = \frac{\tilde{\Delta}^*}{\tilde{\varepsilon}_n^2 + \xi_{\mathbf{p}}^2 + |\tilde{\Delta}|^2} \tag{41}$$

and we have introduced the above-mentioned renormalized frequency $\tilde{\varepsilon}$ and gap $\tilde{\Delta}$,

$$\tilde{\varepsilon}_n = \eta_k\varepsilon_n\,, \qquad \tilde{\Delta} = \eta_k\Delta\,, \qquad \eta_k = 1 + \frac{kv_{\rm F}\varkappa}{\sqrt{\varepsilon_n^2 + |\Delta|^2}}\,, \tag{42}$$

similar to those that appear when one considers superconductors with impurities [69].

The normal and anomalous Green functions of the superconductor, in which we are interested, are determined by (39) with $k=0$ and represent the completely summed series of perturbation theory in the interaction of an electron

in the superconductor with antiferromagnetic short-range-order fluctuations.

Actually we are examining the Gor'kov-type Green functions averaged over the ensemble of random (Gaussian) short-range-order fluctuations in a similar way as is done in the problem of the effects of impurities on superconductivity [69]. Here we assume that the superconductor order parameter (the energy gap) Δ is self-averaging over these fluctuations, which makes it possible to average it irrespective of the electronic Green functions in the diagrammatic series. The usual arguments in favor of the possibility of such independent averaging is as follows [99–101]: the value of Δ varies over characteristic lengths of order $\xi_0 \sim v_F/\Delta$ (the coherence length of the BCS theory), while the Green functions vary rapidly over much smaller lengths, of the order of interatomic distances. Naturally, the last assumption does not hold if a new characteristic length $\xi \to \infty$ appears in the electronic subsystem. At the same time, in conditions where the AFM correlation length ξ is much smaller than ξ_0 (i.e. when AFM fluctuations correlate over distances shorter than the characteristic size of Cooper pairs), the assumption that Δ is self-averaging is valid, breaking down only in the region $\xi > \xi_0$. As a result, we can use the standard approach of the theory of disordered superconductors (the mean-field approximation, in the terminology of Ref. [102]). A possible manifestation of the non-self-averaging nature of Δ [102] will be considered below. Note that in real HTSC cuprates ξ is probably always of order ξ_0, so that they both are in the region that presents most difficulties for the theory.

4.2 Transition temperature and the temperature dependence of the gap

The energy gap of a superconductor is specified by the equation

$$\Delta(\mathbf{p}) = -T \sum_{\mathbf{p}'} \sum_{\varepsilon_n} V_{sc}(\mathbf{p}, \mathbf{p}')\, F(\varepsilon_n, \mathbf{p}')\,. \tag{43}$$

On flat sections of the Fermi surface the anomalous Green function can be found by applying the recurrent procedure (39). In the remaining ('cold') part of the Fermi surface there is no scattering on AFM fluctuations in our model, and the anomalous Green function has the form (38). The results of calculations of the temperature dependences of the energy gap for different values of the correlation length ξ of short-range order fluctuations can be found in Ref. [98]. These dependences are of a fairly traditional shape.

An equation for the superconducting transition temperature T_c immediately follows for (43) if $\Delta \to 0$. The dependences of T_c on the gap width W and the correlation length (the parameter $\varkappa = \xi^{-1}$) that were calculated in Ref. [98] are depicted in Fig. 19, where T_{c0} is the transition temperature in the absence of a pseudogap. In these calculations the value of α was rather arbitrarily taken equal to $\pi/6$, which is close to the experimental data of Gatt et al. [34].

The general qualitative conclusion is that a pseudogap suppresses superconductivity due to partial 'dielectrization' of the electron spectrum in the 'hot' regions of the Fermi surface. The suppression effect is maximum at $\varkappa = 0$ (infinite correlation length of AFM fluctuations [63, 102]) and decreases with the decrease of the correlation length, which completely agrees with the experimental phase diagram of HTSC systems. As noted above, the parameters of this model

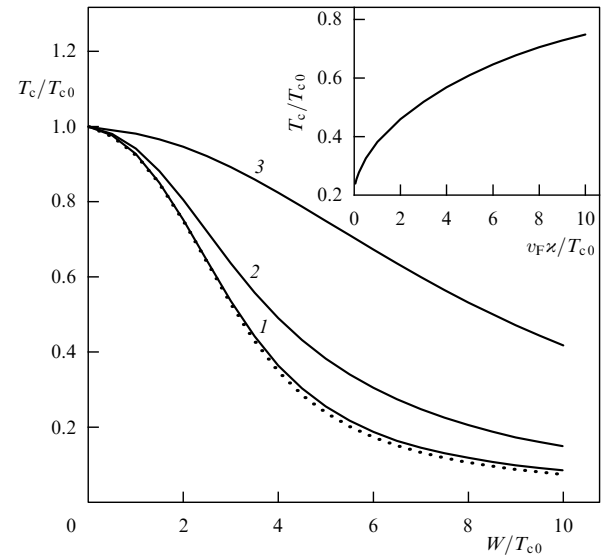

Figure 19. Dependence of the superconducting transition temperature on the pseudogap width W and the correlation length of antiferromagnetic fluctuations (the parameter $\varkappa = \xi^{-1}$): (*1*) $v_F\varkappa/W = 0.1$, (*2*) $v_F\varkappa/W = 1.0$, and (*3*) $v_F\varkappa/W = 10.0$. The dotted line corresponds to $\varkappa = 0$ [63]. The inset presents T_c as a function of $\varkappa$ at $W/T_{c0} = 5$ [98].

are phenomenological. For instance, the effective width of the pseudogap, $2W$, can probably be identified with the parameter E_g; experimental data on the magnitude of this parameter are depicted in Fig. 6 as a function of the doping level for the YBCO system. The data on the correlation length ξ and its temperature and concentration dependences are very incomplete. Indirectly the necessary information was extracted from data of NMR experiments [14, 60]. Direct data of neutron-scattering experiments are rather ambiguous. Nevertheless, as an example, we take the result of Balatsky and Bourges [103], who summarized the data on the width of the peak in neutron scattering by the vector $(\pi/a, \pi/a)$ in the YBCO system with varying oxygen content. It is only natural to identify the reciprocal of the peak width with ξ. These researchers found an interesting correlation between the superconducting transition temperature and the quantity ξ^{-1} defined in this manner (see Fig. 20). Obviously, this dependence is in direct correspondence to the dependence of T_c on $\varkappa = \xi^{-1}$ depicted in the inset in Fig. 19. A quantitative fitting of these data to the above-calculated dependences (which follow from the simple model of the pseudogap state considered here) is of course possible, but it requires taking into account rather ambiguous information about the concentration dependence of the parameter W. In particular, it is not quite clear whether there is any physical meaning in the vanishing of the quantity $E_g \sim W$ at a certain 'critical' carrier concentration, as shown in Fig. 6. The effect of the pseudogap can also disappear as a result of a proper decrease in the correlation length ξ, which leads to the 'filling' rather than 'collapse' of the pseudogap in the density of states. However, if we adopt the data [6] in Fig. 6 on the pseudogap width, then our parameter $2W$ changes from a value of order 700 K at a hole concentration of $p = 0.05$ to a value of order $T_c \sim 100$ K near the optimal concentration $p = 0.17$, vanishing at $p = 0.19$. If we use the microscopic expression (9) for the parameter W, which follows from the theory of a 'nearly

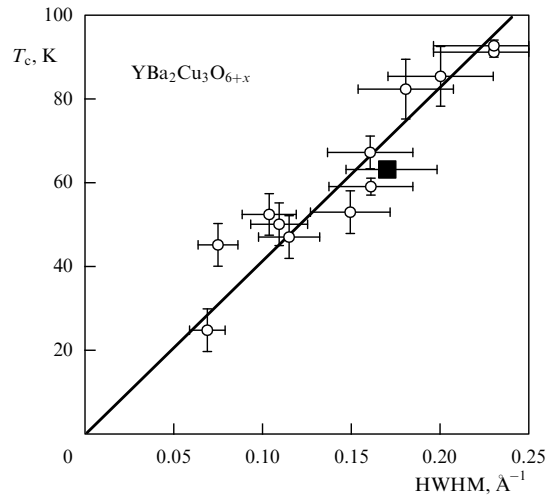

Figure 20. Superconducting transition temperature T_c as a function of the width of the peak in neutron scattering at $\mathbf{q} = (\pi/a, \pi/a)$, this width being identified with the reciprocal correlation length of short-range-order fluctuations [103].

antiferromagnetic' Fermi liquid, we can relate such a behavior of the concentration to the corresponding dependence for the local spin $\langle \mathbf{S}_i^2 \rangle$ on an ion of Cu. I am not aware any direct data of this kind, but it is worth mentioning a paper by Tallon [104], who demonstrated the vanishing of the effective interaction with antiferromagnetic spin fluctuations at $p = 0.19$ by means of processing the experimental data on NMR relaxation times.

We stress once more that the above theoretical results hold under the assumption that the superconducting order parameter (gap) is self-averaging over AFM fluctuations (the mean-field approximation, in the terminology of Ref. [102]), which is true if the correlation length is not too large, $\xi < \xi_0$, where ξ_0 is the coherence length of the superconductor (the size of the Cooper pairs at $T = 0$). We will see that, for $\xi \gg \xi_0$, non-self-averaging sets in, which results in the appearance of characteristic 'tails' in the temperature dependence of the averaged gap in the temperature range $T_c < T < T_{c0}$ [102].

4.3 Cooper instability

As is known, there is another way of finding the transition temperature, namely, from the equation for the Cooper instability of the normal phase,

$$1 - V\chi(0,0) = 0\,, \tag{44}$$

where $\chi(0,0)$ is the generalized Cooper susceptibility

$$\chi(\mathbf{q},0;T) = -T\sum_{\varepsilon_n}\sum_{\mathbf{p}} G(\varepsilon_n,\mathbf{p}+\mathbf{q})G(-\varepsilon_n,\mathbf{p}) \times e^2(\phi)\Gamma(\varepsilon_n,-\varepsilon_n,\mathbf{q})\,. \tag{45}$$

The problem is to calculate the 'triangular' vertex part $\Gamma(\varepsilon_n,-\varepsilon_n,\mathbf{q})$, which takes into account the interaction with AFM fluctuations. For a one-dimensional analog of our problem (and for real frequencies, $T = 0$), the corresponding recurrent procedure was formulated in Ref. [80]. For the two-dimensional model considered here, the optical conductivity was calculated on the basis of this procedure using the method discussed above [83]. The given procedure can be generalized fairly easily to the case of Matsubara frequencies [98]. For the sake of definiteness we will assume that $\varepsilon_n > 0$. Then we arrive at an expression similar to (34):

$$\begin{aligned}\Gamma_{k-1}(\varepsilon_n,-\varepsilon_n,\mathbf{q}) &= 1 + W^2 v(k) G_k \bar{G}_k \\ &\times \left[1 + \frac{2ikv_F\varkappa}{2i\varepsilon_n - (-1)^k v_F q - W^2 v(k+1)(G_{k+1} - \bar{G}_{k+1})}\right] \\ &\times \Gamma_k(\varepsilon_n,-\varepsilon_n,\mathbf{q})\,, \\ \Gamma(\varepsilon_n,-\varepsilon_n,\mathbf{q}) &\equiv \Gamma_0(\varepsilon_n,-\varepsilon_n,\mathbf{q})\,,\end{aligned} \tag{46}$$

where $G_k = G_k(\varepsilon_n, \mathbf{p}+\mathbf{q})$ and $\bar{G}_k = G_k(-\varepsilon_n, \mathbf{p})$ can be calculated using (21).

In calculating T_c we are interested in the vertex at $\mathbf{q} = 0$. Then $\bar{G}_k = G_k^*$, and the vertices Γ_k become real-valued, which substantially simplifies the procedure (46).

We have the following exact relation of the type of the Ward identity [98]:

$$G(\varepsilon_n,\mathbf{p})G(-\varepsilon_n,\mathbf{p})\Gamma(\varepsilon_n,-\varepsilon_n,0) = -\frac{\operatorname{Im} G(\varepsilon_n,\mathbf{p})}{\varepsilon_n}\,. \tag{47}$$

Numerical calculations completely corroborate this relation and demonstrate perfect consistency between the recurrent procedures for the single-particle Green function and the vertex part. Formula (47) leads to a situation in which the equation for T_c obtained from the condition for the Cooper instability is equivalent to the equation obtained through linearizing the equation for the gap, although seemingly different recurrent procedures of taking into account AFM fluctuations were used in deriving these equations.

4.4 Ginzburg – Landau equations and the basic properties of superconductors with a pseudogap near T_c

The Ginzburg – Landau expansion for the difference in the free-energy densities between the superconducting and normal states can be written in the following standard form:

$$F_s - F_n = A|\Delta_{\mathbf{q}}|^2 + q^2 C|\Delta_{\mathbf{q}}|^2 + \frac{B}{2}|\Delta_{\mathbf{q}}|^4\,, \tag{48}$$

where $\Delta_{\mathbf{q}}$ is the amplitude of the Fourier transform of the order parameter,

$$\Delta(\phi,\mathbf{q}) = \Delta_{\mathbf{q}} e(\phi)\,. \tag{49}$$

The expansion (48) is determined by the diagrams of the loop expansion for the free energy in the field of order-parameter fluctuations with a small wave vector $\mathbf{q}$ [63].

We write the Ginzburg – Landau coefficients in the form

$$A = A_0 K_A\,; \qquad C = C_0 K_C\,; \qquad B = B_0 K_B\,, \tag{50}$$

where A_0, B_0, and C_0 denote the standard expressions for these coefficients in the case of isotropic s-pairing:

$$A_0 = N_0(0)\,\frac{T - T_c}{T_c}\,, \qquad C_0 = N_0(0)\,\frac{7\zeta(3)}{32\pi^2}\,\frac{v_F^2}{T_c^2}\,,$$

$$B_0 = N_0(0)\,\frac{7\zeta(3)}{8\pi^2 T_c^2}\,. \tag{51}$$

All features of this model related to pseudogap formation are contained in the dimensionless coefficients K_A, K_C, and K_B. In

the absence of a pseudogap all these coefficients are equal to unity, and only in the case of d-pairing we have $K_B = 3/2$.

Now we go back to the generalized Cooper susceptibility (45). Using it allows us to easily write the coefficients K_A and K_C in the form [98]

$$K_A = \frac{\chi(0,0;T) - \chi(0,0;T_c)}{A_0}\,, \tag{52}$$

$$K_C = \lim_{q\to 0} \frac{\chi(\mathbf{q},0;T_c) - \chi(0,0;T_c)}{q^2 C_0}\,. \tag{53}$$

Then all calculations can be done via the recurrent procedure (46).

Generally, the situation with the coefficient B is complicated. Significant simplifications are possible if we limit ourselves to the case $q = 0$ in the order $|\Delta_{\mathbf{q}}|^4$, as is usually done. Then the coefficient B can be found directly from the anomalous Green function F, for which we already have the recurrent procedure (39) [98].

In the limit $\xi \to \infty$, all Ginzburg–Landau coefficients can be obtained in an analytic form [63] using the exact solution (discussed above) for the Green function of the pseudogap state.

The Ginzburg–Landau equations determine two characteristic lengths of a superconductor: the coherence length and the depth of magnetic-field penetration. The coherence length for a given temperature, $\xi(T)$, gives the characteristic scale of inhomogeneities in the order parameter Δ:

$$\xi^2(T) = -\frac{C}{A}\,. \tag{54}$$

In the absence of a pseudogap,

$$\xi^2_{\mathrm{BCS}}(T) = -\frac{C_0}{A_0}\,, \tag{55}$$

$$\xi_{\mathrm{BCS}}(T) \approx 0{,}74\,\frac{\xi_0}{\sqrt{1 - T/T_c}}\,, \tag{56}$$

where $\xi_0 = 0.18 v_{\mathrm{F}}/T_c$. For the model we consider here,

$$\frac{\xi^2(T)}{\xi^2_{\mathrm{BCS}}(T)} = \frac{K_C}{K_A}\,. \tag{57}$$

The corresponding dependences of $\xi^2(T)/\xi^2_{\mathrm{BCS}}(T)$ on the pseudogap width W and the fluctuation correlation length (the parameter $\varkappa$) for the case of d-pairing are given in Ref. [98]; they are fairly smooth, and the variations in the ratio (57) are relatively small.

For the depth of magnetic-field penetration for a superconductor without a pseudogap we have

$$\lambda_{\mathrm{BCS}}(T) = \frac{1}{\sqrt{2}}\,\frac{\lambda_0}{\sqrt{1 - T/T_c}}\,, \tag{58}$$

where $\lambda_0^2 = mc^2/(4\pi n e^2)$ is the penetration depth at $T = 0$. Generally,

$$\lambda^2(T) = -\frac{c^2}{32\pi e^2}\,\frac{B}{AC}\,. \tag{59}$$

Then we have from our model:

$$\frac{\lambda(T)}{\lambda_{\mathrm{BCS}}(T)} = \left(\frac{K_B}{K_A K_C}\right)^{1/2}. \tag{60}$$

The dependences of this quantity on the pseudogap width and the correlation length for the case of d-pairing can also be found in Refs. [98], and the corresponding variations of (60) are also fairly small.

Near T_c the upper critical field H_{c2} is determined in terms of the Ginzburg–Landau coefficients as follows:

$$H_{c2} = \frac{\phi_0}{2\pi\xi^2(T)} = -\frac{\phi_0}{2\pi}\,\frac{A}{C}\,, \tag{61}$$

where $\phi_0 = c\pi/e$ is the fluxoid. Then the slope of the curve of the upper critical field near T_c is

$$\left|\frac{\mathrm{d}H_{c2}}{\mathrm{d}T}\right|_{T_c} = \frac{24\pi\phi_0}{7\zeta(3)v_{\mathrm{F}}^2}\,T_c\,\frac{K_A}{K_C}\,. \tag{62}$$

The diagrams representing the dependence of the upper-critical-field slope $|\mathrm{d}H_{c2}/\mathrm{d}T|_{T_c}$ at the temperature T_{c0} on the effective width W of the pseudogap and the correlation-length parameter $\varkappa$ are given in Ref. [98]. At sufficiently large correlation lengths, the field slope rapidly decreases with the pseudogap width. However, at fairly short correlation lengths, this parameter may slowly increase at small pseudogap widths. At a fixed pseudogap width, the slope of H_{c2} increases appreciably as the fluctuation correlation length decreases.

Finally, let us examine the specific-heat discontinuity at the transition point:

$$\frac{C_s - C_n}{\Omega} = \frac{T_c}{B}\left(\frac{A}{T - T_c}\right)^2, \tag{63}$$

where C_s and C_n are, respectively, the specific heats of the superconducting and normal states, and Ω is the sample's volume. At T_{c0} (in the absence of a pseudogap, or $W = 0$) we have

$$\left(\frac{C_s - C_n}{\Omega}\right)_{T_{c0}} = N(0)\,\frac{8\pi^2 T_{c0}}{7\zeta(3)}\,. \tag{64}$$

Then the relative specific-heat discontinuity in this model can be written as

$$\frac{(C_s - C_n)_{T_c}}{(C_s - C_n)_{T_{c0}}} = \frac{T_c}{T_{c0}}\,\frac{K_A^2}{K_B}\,. \tag{65}$$

The corresponding dependences on the effective pseudogap width W and the correlation-length parameter $\varkappa$ for the case of d-pairing are depicted in Fig. 21. Clearly, the specific-heat discontinuity rapidly decreases with increasing pseudogap width and, on the other hand, increases as the correlation length of AFM fluctuations decreases.

For superconductors with s-pairing the dependences of the physical quantities considered here are similar, and the only difference is in a larger scale of W over which the changes take place, which corresponds to a greater stability of isotropic superconductors against partial 'dielectrization' of the electron spectrum caused by pseudogap formation in the 'hot' regions of the Fermi surface [63, 102].

These results are in full qualitative agreement with the data on the specific-heat discontinuity [6, 18, 19] discussed above. As seen from Fig. 2, the discontinuity rapidly decreases with the transition to the region of underdoped compositions, where the pseudogap grows according to the data depicted in Fig. 6.

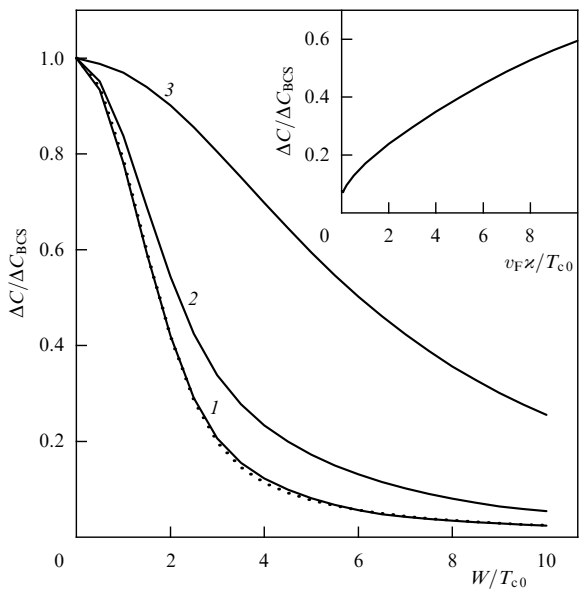

Figure 21. Specific-heat discontinuity as a function of the gap width W and the correlation length of AFM fluctuations (the parameter $\varkappa = \xi^{-1}$): (*1*) $v_F\varkappa/W = 0.1$, (*2*) $v_F\varkappa/W = 1.0$, and (*3*) $v_F\varkappa/W = 10.0$. The dotted curve corresponds to $\varkappa = 0$ [63]. The inset presents the specific-heat discontinuity as a function of $\varkappa$ at $W/T_{c0} = 5$.

4.5 Effects of the non-self-averaging nature of the order parameter

Our study of superconductivity was based on the assumption that the superconducting order parameter Δ is a self-averaging quantity. This assumption is justified only if the correlation length ξ of short-range-order (AFM) fluctuations is short compared to the characteristic size of the Cooper pairs, ξ_0 (the coherence length of the BCS theory). The opposite limit, $\xi \gg \xi_0$, can be treated within the scope of the exactly solvable model of the pseudogap state with $\xi \to \infty$, which has been described above in the variant of the hot-region model in equations (27) and (29) [102].

We begin with the problem of superconductivity in a system that has a *fixed* dielectric gap D in the 'hot' regions of the Fermi surface. The problem of superconductivity in a system with partial dielectrization of the spectrum in selected regions of the Fermi surface has been studied by many researchers (e.g. see Refs [105, 106]), and in a model closest to our case, by Bilbro and McMillan [107], whose results we can use here. We will employ the simplest model of pairing — equations (35) and (36) of the BCS theory.

If the value of the dielectric gap D in the 'hot' regions of the Fermi surface is fixed, the equation of our model for the superconducting gap Δ in the case of s-pairing assumes the form

$$1 = \lambda \int_0^{\omega_c} \mathrm{d}\xi \left\{ \tilde{\alpha}\, \frac{\tanh\left[\sqrt{\xi^2 + D^2 + \Delta^2(D)}/2T\right]}{\sqrt{\xi^2 + D^2 + \Delta^2(D)}} + (1-\tilde{\alpha})\, \frac{\tanh\left[\sqrt{\xi^2 + \Delta^2(D)}/2T\right]}{\sqrt{\xi^2 + \Delta^2(D)}} \right\}, \tag{66}$$

where $\lambda = VN_0(0)$ is the dimensionless coupling constant of the pairing interaction, and $\tilde{\alpha} = 4\alpha/\pi$. The first term on the right-hand side of equation (66) corresponds to the contribution of 'hot' (dielectric) regions in which the electron spectrum has the form [107] $E_p = (\xi_p^2 + D^2 + \Delta^2)^{1/2}$, while the second term represents the contribution of 'cold' (metallic) regions, where the spectrum is the same as in the BCS theory: $E_p = (\xi_p^2 + \Delta^2)^{1/2}$. Equation (66) yields the superconducting gap $\Delta(D)$ at a fixed value of the dielectric gap D, which is finite in 'hot' regions.

In the case of d-pairing a similar equation has the form

$$1 = \lambda \frac{4}{\pi} \int_0^{\omega_c} \mathrm{d}\xi \times \left\{ \int_0^{\alpha} \mathrm{d}\phi\, e^2(\phi)\, \frac{\tanh\left[\sqrt{\xi^2 + D^2 + \Delta^2(D) e^2(\phi)}/2T\right]}{\sqrt{\xi^2 + D^2 + \Delta^2(D) e^2(\phi)}} + \int_{\alpha}^{\pi/4} \mathrm{d}\phi\, e^2(\phi)\, \frac{\tanh\left[\sqrt{\xi^2 + \Delta^2(D) e^2(\phi)}/2T\right]}{\sqrt{\xi^2 + \Delta^2(D) e^2(\phi)}} \right\}. \tag{67}$$

These equations show that $\Delta(D)$ decreases with increasing D, and $\Delta(0)$ coincides with the ordinary gap Δ_0 in the absence of dielectrization in flat regions, i.e., the gap that appears at a temperature $T = T_{c0}$ specified by the equation

$$1 = \lambda \int_0^{\omega_c} \mathrm{d}\xi\, \frac{\tanh(\xi/2T_{c0})}{\xi}, \tag{68}$$

for both s- and for d-pairing.

As $D \to \infty$, the first terms on the right-hand sides of equations (66) and (67) vanish, so that the corresponding equations for $\Delta_\infty = \Delta(D \to \infty)$ are

$$1 = \lambda \int_0^{\omega_c} \mathrm{d}\xi\, (1-\tilde{\alpha})\, \frac{\tanh\left(\sqrt{\xi^2 + \Delta_\infty^2}/2T\right)}{\sqrt{\xi^2 + \Delta_\infty^2}} \quad \text{(s-pairing)}, \tag{69}$$

$$1 = \lambda \frac{4}{\pi} \int_0^{\omega_c} \mathrm{d}\xi \int_{\alpha}^{\pi/4} \mathrm{d}\phi \times e^2(\phi)\, \frac{\tanh\left[\sqrt{\xi^2 + \Delta_\infty^2 e^2(\phi)}/2T\right]}{\sqrt{\xi^2 + \Delta_\infty^2 e^2(\phi)}} \quad \text{(d-pairing)}. \tag{70}$$

Equation (69) coincides with the equation for a gap at $D = 0$ with the 'renormalized' coupling constant $\tilde{\lambda} = \lambda(1-\tilde{\alpha})$, so that for the case of s-pairing we have

$$\Delta_\infty = \Delta_0\left[\tilde{\lambda} = \lambda(1-\tilde{\alpha})\right], \tag{71}$$

and, accordingly, a nonzero gap with $D \to \infty$ emerges for $T < T_{c\infty}$:

$$T_{c\infty} = T_{c0}\left[\tilde{\lambda} = \lambda(1-\tilde{\alpha})\right]. \tag{72}$$

In the case of d-pairing, equation (70) yields

$$T_{c\infty} = T_{c0}\left[\tilde{\lambda} = \lambda(1-\alpha_d)\right], \tag{73}$$

where

$$\alpha_{\mathrm{d}} = \tilde{\alpha} + \frac{\sin \pi\tilde{\alpha}}{\pi} \tag{74}$$

is the 'effective' fraction of flat regions in the case of d-pairing. Thus, if $T < T_{\mathrm{c}\infty}$, the gap does not vanish for all values of D and decreases from Δ_0 to Δ_∞ as D increases. For $T_{\mathrm{c}\infty} < T < T_{\mathrm{c}0}$, the gap differs from zero only for $D < D_{\max}$. The corresponding dependences of Δ on D can easily be found by numerically solving equations (66) and (67).

In our model of the pseudogap state, the dielectric gap D is a random rather than fixed quantity distributed according to (29). The above equations must be averaged over these fluctuations. Here we can directly calculate the superconducting gap averaged over the fluctuations of D:

$$\langle \Delta \rangle = \int_0^\infty \mathrm{d}D\, \mathcal{P}(D)\Delta(D) = \frac{2}{W^2}\int_0^\infty \mathrm{d}D\, D \exp\left(-\frac{D^2}{W^2}\right)\Delta(D)\,. \tag{75}$$

In this case, the above-described behavior of $\Delta(D)$ leads to a situation in which the averaged gap (75) differs from zero until $T = T_{\mathrm{c}0}$, i.e. until the superconducting transition temperature in the absence of pseudogap anomalies. At the same time, the superconducting transition temperature T_{c} for a superconductor with a pseudogap is obviously lower than $T_{\mathrm{c}0}$ [63]. Such paradoxical behavior of $\langle \Delta \rangle$ apparently means the appearance of local regions with $\Delta \neq 0$ (superconducting 'drops') in the system, which are induced by fluctuations of D, over the entire temperature range $T_{\mathrm{c}} < T < T_{\mathrm{c}0}$, while a superconducting state coherent over the entire sample occurs only for temperatures below T_{c}. Obviously, analyzing a more realistic model with a finite correlation length ξ of antiferromagnetic short-ranger-order fluctuations is necessary to completely substantiate such a qualitative picture [23]. At the same time, the simplicity of our model with $\xi \to \infty$ makes it possible to immediately arrive at an exact solution for $\langle \Delta \rangle$.

To determine the superconducting transition temperature T_{c} in the sample as a whole we can employ the standard procedure of the mean-field approximation over random short-range-order fluctuations (cf., e.g., a similar approach in the problem of a superconductor with impurities [101]), which implies that the superconducting gap is self-averaging over fluctuations of D (i.e., actually, it is assumed that Δ is independent of fluctuations of D). Then the equations for the mean-field gap Δ_{mf} are

$$1 = \lambda \int_0^{\omega_{\mathrm{c}}} \mathrm{d}\xi \left[\tilde{\alpha}\, \frac{2}{W^2}\int_0^\infty \mathrm{d}D\, D \exp\left(-\frac{D^2}{W^2}\right) \times \frac{\tanh\left(\sqrt{\xi^2 + D^2 + \Delta_{\mathrm{mf}}^2}/2T\right)}{\sqrt{\xi^2 + D^2 + \Delta_{\mathrm{mf}}^2}} + (1-\tilde{\alpha})\, \frac{\tanh\left(\sqrt{\xi^2 + \Delta_{\mathrm{mf}}^2}/2T\right)}{\sqrt{\xi^2 + \Delta_{\mathrm{mf}}^2}}\right] \tag{76}$$

for the case of s-pairing and

$$1 = \lambda\, \frac{4}{\pi}\int_0^{\omega_{\mathrm{c}}} \mathrm{d}\xi \left\{\frac{2}{W^2}\int_0^\infty \mathrm{d}D\, D \exp\left(-\frac{D^2}{W^2}\right) \times \int_0^\alpha \mathrm{d}\phi\, e^2(\phi)\, \frac{\tanh\left[\sqrt{\xi^2 + D^2 + \Delta_{\mathrm{mf}}^2 e^2(\phi)}/2T\right]}{\sqrt{\xi^2 + D^2 + \Delta_{\mathrm{mf}}^2 e^2(\phi)}} + \int_\alpha^{\pi/4} \mathrm{d}\phi\, e^2(\phi)\, \frac{\tanh\left[\sqrt{\xi^2 + \Delta_{\mathrm{mf}}^2 e^2(\phi)}/2T\right]}{\sqrt{\xi^2 + \Delta_{\mathrm{mf}}^2 e^2(\phi)}}\right\} \tag{77}$$

for the case of d-pairing. These equations represent the limiting form (for $\xi \to \infty$) of the equations for the superconducting gap examined above [Eqn (43)] on the basis of the recurrent procedure (39).

From equations (76) and (77) we can easily obtain the corresponding equations for T_{c}, the temperature at which a gap homogeneous over the sample, Δ_{mf}, emerges. For instance, for the case of s-pairing we have

$$1 = \lambda\left[\tilde{\alpha}\, \frac{2}{W^2}\int_0^\infty \mathrm{d}D\, D \exp\left(-\frac{D^2}{W^2}\right) \times \int_0^{\omega_{\mathrm{c}}} \mathrm{d}\xi\, \frac{\tanh\left(\sqrt{\xi^2 + D^2}/2T_{\mathrm{c}}\right)}{\sqrt{\xi^2 + D^2}} + (1-\tilde{\alpha})\int_0^{\omega_{\mathrm{c}}} \mathrm{d}\xi\, \frac{\tanh(\xi/2T_{\mathrm{c}})}{\xi}\right]. \tag{78}$$

For the case of d-pairing, we must replace $\tilde{\alpha}$ in (78) with the 'effective' α_{d} from (74). These equations for T_{c} coincide with those obtained in the microscopic derivation of the Ginzburg–Landau expansion in Ref. [63] and with the limiting form (for $\xi \to \infty$) that emerges in an analysis based on (39) and (43). In general, we always have $T_{\mathrm{c}\infty} < T_{\mathrm{c}} < T_{\mathrm{c}0}$.

The temperature dependences of the averaged gap $\langle \Delta \rangle$ and the mean-field gap Δ_{mf} obtained through numerical solution of the equations of our model for the case of s-pairing are depicted in Fig. 22a [24]. The gap Δ_{mf} vanishes at $T = T_{\mathrm{c}} < T_{\mathrm{c}0}$, and $\langle \Delta \rangle$ is finite until $T = T_{\mathrm{c}0}$; we believe that the corresponding 'tails' in the temperature dependence of $\langle \Delta \rangle$ for $T_{\mathrm{c}} < T < T_{\mathrm{c}0}$ agree with to the above-mentioned idea of superconducting 'drops' in this temperature range present in the absence of superconductivity in the entire sample. Note that the temperature dependences $\langle \Delta(T) \rangle$ in Fig. 22a resemble the corresponding dependences of the gap in underdoped HTSC cuprates, which can be found from ARPES experiments [49] and specific-heat measurements [19] (see Figs 3 and 11), if we assume that the T_{c} observed in these samples corresponds to our mean-field T_{c}, while 'drops' with $\langle \Delta \rangle \neq 0$ exist even at temperatures higher than T_{c} up to $T_{\mathrm{c}0}$, which is much higher than T_{c}. The fact that the gap is not a self-averaging quantity also manifests itself in our model in that the variance $\langle \Delta^2 \rangle - \langle \Delta \rangle^2$ becomes nonzero over the entire temperature range $T < T_{\mathrm{c}0}$, which indirectly supports the proposed qualitative picture, a complete substantiation of which is possible only if one allows for the finiteness of ξ. Note that $T_{\mathrm{c}0}$ is defined rather poorly from the viewpoint of comparisons with experiment. In the above consideration of the transition temperature in the absence of a pseudogap, we assumed that $T_{\mathrm{c}0}$ is of order T_{c} for an optimal carrier

[23] Qualitatively, this situation resembles the onset of an inhomogeneous superconducting state induced by strong fluctuations in the local density of states near the Anderson metal–insulator transition [108, 101].

[24] Qualitatively, the temperature dependences of $\langle \Delta \rangle$ and Δ_{mf} in the case of d-pairing are similar to those in the case of s-pairing.

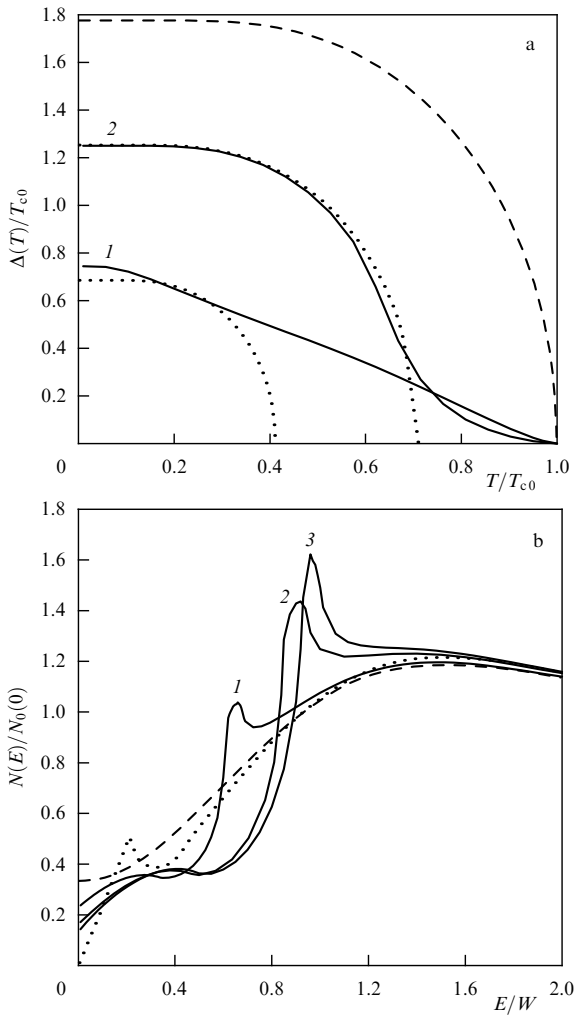

Figure 22. Temperature dependences of the superconducting gaps Δ_{mf} (dotted curves), $\langle\Delta\rangle$ (solid curves), and Δ_0 (dashed curve) in the case of s-pairing [102]: (*1*) $\lambda = 0.4$, $\tilde{\alpha} = 2/3$, and $\omega_c/W = 3$ ($T_c/T_{c0} = 0.42$); (*2*) $\lambda = 0.4$, $\tilde{\alpha} = 0.2$, $\omega_c/W = 1$ ($T_c/T_{c0} = 0.71$). (b) Density of states in the case of d-pairing [102] at $\lambda = 0.4$, $\tilde{\alpha} = 2/3$, and $\omega_c/W = 5$ ($T_c/T_{c0} = 0.48$, with $T_{c\infty}/T_{c0} \sim 10^{-18}$): (*1*) $T/T_{c0} = 0.8$, (*2*) $T/T_{c0} = 0.48$, and (*3*) $T/T_{c0} = 0.1$. The dotted curve represents the behavior of the mean-field density of states $N_{mf}(E)$ at $T/T_{c0} = 0.1$, and the dashed curve represents the pseudogap behavior of the density of states for $T > T_{c0}$.\

concentration. Here, for possible comparisons of the data of Fig. 22a with the data of Figs 3 and 11, the values of T_{c0} must be much higher than the optimal T_c. In this sense, the idea of superconducting 'drops' induced by 'dielectric' fluctuations is not radically different from the ideas used in the scenario of pseudogap formation (precursor pairing). Of course, the data like those presented in Figs 3 and 11 could be a direct implication of the existence of a dielectric pseudogap rather than of the effects of the non-self-averaging nature of the superconducting gap Δ. In particular, the superconducting gap extracted from tunneling data [21, 22] (which manifests itself against the background of a wider pseudogap) demonstrates a 'normal' temperature behavior and vanishes at $T = T_c$.

Although there is no superconductivity in the entire sample for $T_c < T < T_{c0}$, the presence in this temperature range of a nonzero averaged gap $\langle\Delta\rangle$ leads to the appearance of anomalies in the observed quantities, such as the tunneling density of states and the spectral density measured in ARPES experiments [102].

For instance, the tunneling density of states for the case of d-pairing has the form [102]

$$\frac{N(E)}{N_0(0)} = \frac{4}{\pi}\frac{2}{W^2}\int_0^\infty \mathrm{d}D\, D \exp\left(-\frac{D^2}{W^2}\right) \times \left\{\int_0^\alpha \mathrm{d}\phi \frac{|E|}{\sqrt{E^2 - D^2 - \Delta^2(D)e^2(\phi)}} \times \theta\left[E^2 - \Delta^2(D)e^2(\phi) - D^2\right] + \int_\alpha^{\pi/4} \mathrm{d}\phi \frac{|E|}{\sqrt{E^2 - \Delta^2(D)e^2(\phi)}}\,\theta\left[E^2 - \Delta^2(D)e^2(\phi)\right]\right\}. \tag{79}$$

Under the assumption of self-averaging, Δ equals Δ_{mf} and is independent of D. Then the width of the superconducting pseudogap in the density of states is of order Δ_{mf}, and as $T \to T_c$ the corresponding contribution vanishes, and only the pseudogap related to AFM fluctuations remains. Actually, Δ in (79) is $\Delta(D)$, which can be found from equation (67).

The behavior of the density of states in the d-case is depicted in Fig. 22b. Clearly, there is a substantial difference between the exact density of states and that obtained in the mean-field approximation, and this difference is related to fluctuations of the superconducting gap (superconducting 'drops') caused by antiferromagnetic short-range-order fluctuations. Actually, the exact density of states does not 'feel' the superconducting transition that occurs in the entire system at $T = T_c$; the characteristic width of the superconducting gap (pseudogap) in the density of states is of order Δ_0 rather than Δ_{mf} yielded by the approximation of the mean field over short-range-order fluctuations. The corresponding contributions become observable even at $T = T_{c0} > T_c$.

These results can, at least in principle, explain the unusually large values of the ratio $2\Delta/T_c$ observed in a number of tunnel experiments involving underdoped HTSC cuprates [20, 109] and in ARPES measurements [110]. The presence of superconducting 'drops' in the system can also explain the anomalous diamagnetism of these systems observed in many cases at temperatures higher than T_c [111].

5. Conclusion. Problems and prospects

In conclusion, we sum up the content of this article and examine remaining problems. The scenario of pseudogap formation based on the idea of AFM (SDW or CDW) type short-range-order fluctuations leads to a general qualitative agreement with the basic experimental facts. In our theoretical consideration, we deliberately employed a semi-phenomenological approach based on a simple model of the pseudogap transformation of the electron spectrum, described by two parameters — the effective pseudogap width W and the correlation length ξ, which can be determined (at least in principle) from experiments. The models of 'hot' spots or regions at the Fermi surface, considered here, admit an 'almost exact' solution [14, 15], which makes it possible to achieve a substantial progress in analyzing such problems as the effect of a pseudogap on

superconductivity. Actually, it is unimportant whether we are speaking about AFM fluctuations (as the most popular model) or about short-range-order fluctuations of a different nature that lead to a partial dielectrization of the spectrum, such as CDW or structural distortions.

The drawbacks of these models stem from the simplifying assumptions that are needed to obtained these 'almost exact' solutions. The most important assumptions are the static approximation and the hypothesis of the Gaussian nature of short-range-order fluctuations. Allowance for the dynamics of fluctuation is absolutely necessary in the low-temperature region, in particular, in the superconducting phase, where the pairing interaction itself may be controlled by the dynamics of these fluctuations [58, 59]. We believe, however, that the above simplified consideration can describe the most essential effects of changes in the electron spectrum (pseudogap formation in 'hot' regions of the Fermi surface) and the influence of these changes on superconductivity. To allow for the dynamics of spin fluctuations, we would have to go beyond the simple phenomenology of the BCS model. Also, the assumption of the Gaussian character of the statistics of fluctuations can be justified only at high temperatures and not very close to the line of antiferromagnetic instability. Nevertheless, even in this very simple variant of the model, one can qualitatively describe the basic features of pseudogap formation. The rejection of this very simple assumption also destroys the fairly simple structure of the equations of the theory, which actually makes it possible to analyze the superconducting phase.

We can step beyond the semi-phenomenological approach employed here by means of a complete microscopic analysis of the problem, say, using the Hubbard model. Such attempts have been made by some researchers, e.g., in Refs [11–13] cited above and in Refs [122, 113]. Although many qualitative conclusions of these studies coincide with those discussed here or are close to them, the treatment of the problem is usually limited to allowing for the first few diagrams in perturbation theory [114, 115] or to some variant of self-consistency based on these diagrams. Of course, in this way, one can take into account the dynamics of spin fluctuations. However, going beyond these simple qualitative estimates is fairly difficult.

What would be important is a microscopic justification of the existence of a broad region in the phase diagram with well-developed short-range-order AFM (SDW) fluctuations. Note that the region of such 'critical' fluctuations may be anomalously large simply because of the reduced dimensionality (quasi-two-dimensional structure) of the systems in question. For instance, the size of the region of superconducting fluctuations in HTSC systems is fairly large and can reach tens of kelvins [116]. Since AFM fluctuations are characterized by energies an order of magnitude higher, the presence of a 'critical' region with a width of hundreds of kelvins does not seem unlikely. Nevertheless, there is still no microscopic justification for such a picture.

Apparently, the main qualitative conclusion that can be drawn from the physical picture discussed above concerns the old discussion of whether the spectrum of electronic excitations in HTSC systems is of Fermi-liquid or non-Fermi-liquid nature. According to the simple models examined here, the electron spectrum (spectral density) is of Fermi-liquid nature only in the 'cold' regions of the Fermi surface (near the diagonals of the Brillouin zone), while in the 'hot' regions the spectrum undergoes a non-Fermi-liquid transformation (in the above-specified, narrow sense) due to the strong scattering on AFM fluctuations [14, 15]. The presence or absence of a Fermi-liquid behavior depends on the fluctuation correlation length ξ (cf. [81, 82]). In their recent paper, Abrahams and Varma [117] criticised such a picture on the basic of their fairly successful processing of experimental data [51, 118, 119] for ARPES in optimally doped Bi-2212, using ideas of the theory of marginal Fermi liquids. In particular, Abrahams and Varma [117] state that the decay of quasiparticles does not exhibit Fermi-liquid behavior anywhere on the Fermi surface and also declare that there is no evidence for a momentum dependence of this decay. Actually, however, they introduce a substantial dependence of the static decay on momentum, needed for the description of the data even in the case of optimal doping (under study), which they assign to the anisotropy of impurity scattering. On the other hand, the linear dependence of the decay on the quasiparticle energy, which is actually observed in HTSC systems (and postulated in the theory of marginal Fermi liquids), cannot serve as a refutation of the ordinary ideas of the Fermi-liquid theory, since a standard quadratic dependence can be observed only in a fairly narrow energy interval near the Fermi level that is beyond the limit of accuracy of ARPES experiments. An exhaustive discussion of these aspects can be found in reviews by Maksimov [91] and Ginzburg and Maksimov [93]. Generally, it should be noted that the presence of anomalous scattering on AFM fluctuations (with wave vectors of order of the antiferromagnetism vector) is beyond question [25].

Our theoretical consideration was based on the fairly traditional scheme of averaging over the mean field of AFM (SDW, CDW) fluctuations, which assumes the spatial homogeneity of the system on average. At the same time, some experimental data and theoretical ideas point to the possibility of phase separation in a number of HTSC systems (especially in the region of underdoped compositions) [121, 122]. Such separation occurs on a microscopic scale, so that the system separates into 'metallic' (superconducting) and 'dielectric' (antiferromagnetic) domains with characteristic sizes of order of several interatomic distances. Naturally, it is rather difficult to describe such a system using the above standard methods, while the very fact of phase separation may play, as many researchers believe, a crucial role in HTSC physics. In this context we only remark that the qualitative picture of the random field of AFM (SDW, CDW) short-range-order fluctuations, used above, also indirectly assumes the appearance of effective regions with AFM order in the system, of a characteristic size $\sim \xi$, that alternate with regions of the same size in which this order is destroyed. In this sense our picture does not strongly differ from the pattern of phase separation — the only difference is probably in that the boundaries of the corresponding regions are diffuse. Clearly the formalism of some models of phase separation based on the idea of proximity to a CDW-type instability [64, 123, 124] is fairly close to that used in this review and is based on the picture of scattering on fluctuations with some distinguished wave vectors.

[25] We would like to mention the interesting work done by Li Jian-Xin et al. [120], who managed to give a fairly good description of the kinetic properties of HTSC oxides on the basis of a simple consideration of Boltzmann scattering on spin fluctuations with a straightforward elimination of the contributions from 'hot' regions of the Fermi surface to the current-carrier kinetics.

Finally, it is worth noting that HTSC systems contain a large number of anomalies related to the behavior of such systems under sufficiently strong structural disordering [101]. The role of structural disordering in systems with a pseudogap is understood very poorly. There are only a few papers that examine the effect of substitutional impurities [125, 126]. They show that controlled disordering can serve as a fairly informative method of studying the pseudogap state. This problem has not yet been studied theoretically almost at all.

The study of anomalies in HTSC systems related to pseudogap formation is of considerable importance for applications. Since, as we have seen, the pseudogap suppresses, in a certain sense, superconductivity, such characteristics of a superconductor as the critical current and the critical magnetic fields prove to be maximum not at the 'optimal' carrier concentration $p_0 \sim 0.15-0.17$ corresponding to the maximum T_c but in the vicinity of the 'critical' concentration $p_c \approx 0.19$ [127]. This fact may be important for optimizing the compositions of commercial HTSC-type superconductors.

I am grateful to É Z Kuchinskiĭ, my coworker in a number of the most important studies, which were used in the theoretical section of this review.

The work was supported in part by the Russian Foundation for Basic Research (Grant No. 99-02-16285) and CRDF (Grant No. REC-005), the State Programs in Statistical Physics (Grant No. 108-11(00)-P) and High-T_c Superconductivity (Grant No. 96-051), and the Quantum Microphysics Program of Basic Research of the Presidium of the Russian Academy of Sciences.

References

1. Batlogg B, Varma C *Phys. World* **13** 33 (2000)
2. Timusk T, Statt B *Rep. Prog. Phys.* **62** 61 (1999)
3. Randeria M, in *Varenna Lectures 1997*; cond-mat/9710223
4. Randeria M, Campuzano J-C, in *Varenna Lectures 1997*; cond-mat/9709107
5. Tohyama T, Maekawa S *Supercond. Sci. Tech.* **13** R17 (2000); cond-mat/0002225
6. Tallon J L, Loram J W *Physica C* **349** 53 (2001); cond-mat/0005063
7. Geshkenbein V B, Ioffe L B, Larkin A I *Phys. Rev. B* **55** 3173 (1997)
8. Emery V, Kivelson S A, Zachar O *Phys. Rev. B* **56** 6120 (1997)
9. Maly J, Janko B, Levin K *Phys. Rev. B* **56** R11407 (1997); **59** 1354 (1999); cond-mat/9710187, 9805018
10. Gusynin V P, Loktev V M, Sharapov S G *Zh. Eksp. Teor. Fiz.* **115** 1243 (1999) [*JETP* **88** 685 (1999)]
11. Kampf A P, Schrieffer J R *Phys. Rev. B* **41** 6399 (1990); **42** 7967 (1990)
12. Langer M et al. *Phys. Rev. Lett.* **75** 4508 (1995)
13. Deisz J J, Hess D W, Serene J W *Phys. Rev. Lett.* **76** 1312 (1996)
14. Schmalian J, Pines D, Stojkovic B *Phys. Rev. Lett.* **80** 3839 (1998); *Phys. Rev. B* **60** 667 (1999)
15. Kuchinskiĭ É Z, Sadovskiĭ M V *Zh. Eksp. Teor. Fiz.* **115** 1765 (1999) [*JETP* **88** 968 (1999)]; cond-mat/9808321
16. Chakravarty S et al., cond-mat/0005443
17. Mott N F, Davis E A *Electronic Processes in Non-Crystalline Materials* (Oxford: Clarendon Press, 1971) [Translated into Russian (Moscow: Mir, 1974)]
18. Loram J W et al. *Physica C* **282–287** 1405 (1997)
19. Loram J W et al. *J. Supercond.* **7** 243 (1994)
20. Renner C et al. *Phys. Rev. Lett.* **80** 149 (1998)
21. Krasnov V M et al. *Phys. Rev. Lett.* **84** 5860 (2000)
22. Krasnov V M et al. *Phys. Rev. Lett.* **86** 2657 (2001); cond-mat/0006479
23. Bucher B et al. *Phys. Rev. Lett.* **70** 2021 (1993)
24. Yasuoka H *Hyperfine Interact.* **105** 27 (1997)
25. Alloul H, Adrian F J *Phys. Rev. Lett.* **63** 1700 (1989)
26. Gorny K et al. *Phys. Rev. Lett.* **82** 177 (1999); cond-mat/9812013
27. Zheng G-Q et al. *Phys. Rev. Lett.* **85** 405 (2000)
28. Tallon J L et al. *Phys. Status Solidi B* **215** 531 (1999); cond-mat/9911157
29. Puchkov A V, Basov D N, Timusk T *J. Phys.: Condens. Matter* **8** 10049 (1996)
30. Startseva T et al. *Phys. Rev. B* **59** 7184 (1999)
31. Dessau D S et al. *Phys. Rev. Lett.* **71** 2781 (1993)
32. Shen Z X, Dessau D S *Phys. Rep.* **253** 1 (1995)
33. Ino A et al. *J. Phys. Soc. Jpn.* **68** 1496 (1999); cond-mat/9809311
34. Gatt R et al., cond-mat/9906070
35. Feng D L et al., cond-mat/9908056
36. Chuang Y D et al. *Phys. Rev. Lett.* **83** 3717 (1999)
37. Gromko A D et al., cond-mat/0003017
38. Bogdanov P V et al., cond-mat/0005394
39. Fretwell H M et al. *Phys. Rev. Lett.* **84** 4449 (2000)
40. Mesot J et al., cond-mat/9910430
41. Bansil A et al. *Phys. Rev. Lett.* **83** 5154 (1999)
42. Borisenko S V et al. *Phys. Rev. Lett.* **84** 4453 (2000)
43. Legner S et al. *Phys. Rev. B* **62** 154 (2000); cond-mat/0002302
44. Norman M R et al., cond-mat/9710163
45. Annett J, Goldenfeld N, Leggett A, in *Physical Properties of High Temperature Superconductors* Vol. 5 (Ed. D M Ginsberg) (Singapore: World Scientific, 1996) p. 375; cond-mat/9601060
46. Izyumov Yu A *Usp. Fiz. Nauk* **169** 225 (1999) [*Phys. Usp.* **42** 215 (1999)]
47. Tsuei C C, Kirtley J R *Rev. Mod. Phys.* **72** 969 (2000)
48. Ding H et al. *Nature* **382** 51 (1996)
49. Norman M R et al. *Nature* **392** 157 (1998)
50. Norman M R et al. *Phys. Rev. B* **57** R11093 (1998)
51. Kaminski A et al. *Phys. Rev. Lett.* **84** 1788 (2000); cond-mat/9904390
52. Ronning F et al. *Science* **282** 2067 (1998); cond-mat/9903151
53. Hackl R, in *The Gap Symmetry and Fluctuations in High-T_c Superconductors* (Eds J Bok, G Deutscher, D Pavuna) (New York: Plenum Press, 1998) p. 249
54. Bourges P, in *The Gap Symmetry and Fluctuations in High-T_c Superconductors* (Eds J Bok, G Deutscher, D Pavuna) (New York: Plenum Press, 1998) p. 349
55. Schrieffer J R, Wen X G, Zhang S C *Phys. Rev. B* **39** 11663 (1989)
56. Izyumov Yu A *Usp. Fiz. Nauk* **161** (11) 1 (1991) [*Sov. Phys. Usp.* **34** 935 (1991)]
57. Ziman J M *Principles of the Theory of Solids* 2nd ed. (Cambridge: The Univ. Press, 1972) [Translated into Russian (Moscow: Mir, 1974)]
58. Monthoux P, Balatsky A V, Pines D *Phys. Rev. B* **46** 14803 (1992)
59. Monthoux P, Pines D *Phys. Rev. B* **47** 6069 (1993); **49** 4261 (1994)
60. Millis A J, Monien H, Pines D *Phys. Rev. B* **42** 167 (1990)
61. Barzykin V, Pines D *Phys. Rev. B* **52** 13585 (1995)
62. Pines D *Z. Phys. B* **103** 129 (1997)
63. Posazhennikova A I, Sadovskiĭ M V *Zh. Eksp. Teor. Fiz.* **115** 632 (1999) [*JETP* **88** 347 (1999)]
64. Benfatto L, Caprara S, Di Castro C *Eur. J. Phys. B* **71** 95 (2000)
65. Virosztek A, Ruvalds J *Phys. Rev. B* **42** 4064 (1990)
66. Ruvalds J et al. *Phys. Rev. B* **51** 3797 (1995)
67. Zheleznyak A T, Yakovenko V M, Dzyaloshinskii I E *Phys. Rev.* **55** 3200 (1997)
68. Ziman J M *Models of Disorder* (Cambridge: Cambridge Univ. Press, 1979) [Translated into Russian (Moscow: Mir, 1982)]
69. Abrikosov A A, Gor'kov L P, Dzyaloshinskiĭ I E *Metody Kvantovoĭ Teorii Polya v Statisticheskoĭ Fizike* (Quantum Field Theoretical Methods in Statistical Physics) (Moscow: Fizmatgiz, 1962) [Translated into English (Oxford: Pergamon Press, 1965)]
70. Lee P A, Rice T M, Anderson P W *Phys. Rev. Lett.* **31** 462 (1973)
71. Sadovskiĭ M V *Zh. Eksp. Teor. Fiz.* **66** 1720 (1974) [*Sov. Phys. JETP* **39** 845 (1974)]
72. Sadovskiĭ M V *Fiz. Tverd. Tela* (Leningrad) **16** 2504 (1974) [*Sov. Phys. Solid State* **16** 1632 (1974)]
73. Sadovskiĭ M V *Zh. Eksp. Teor. Fiz.* **77** 2070 (1979) [*Sov. Phys. JETP* **50** 989 (1979)]
74. Elyutin P V *Opt. Spektrosk.* **43** 542 (1977) [*Opt. Spectrosc.* **43** 318 (1977)]
75. Tchernyshyov O *Phys. Rev. B* **59** 1358 (1999)
76. Sadovskii M V *Physica C* **341–348** 811 (2000)

77. Bartosh L, Kopietz P *Phys. Rev. B* **60** 15488 (1999)
78. Millis A J, Monien H *Phys. Rev. B* **61** 12496 (2000)
79. Marshall D S et al. *Phys. Rev. Lett.* **76** 4841 (1996)
80. Sadovskiĭ M V, Timofeev A A *Sverkhprovodimost'*: *Fiz. Khim. Tekhnol.* **4** (1) 11 (1991) [*Superconductivity*: *Phys. Chem. Technol.* **4** 9 (1991)]; Sadovskii M V, Timofeev A A *Physica C* **185–189** 1431 (1991)
81. Sadovskii M V, Timofeev A A *J. Moscow Phys. Soc.* **1** 391 (1991)
82. McKenzie R H, Scarratt D *Phys. Rev. B* **54** R12709 (1996)
83. Sadovskiĭ M V *Pis'ma Zh. Eksp. Teor. Fiz.* **69** 447 (1999) [*JETP Lett.* **69** 483 (1999)]; *Physica C* **341–348** 939 (2000); cond-mat/9902192
84. Puchkov A V et al. *Phys. Rev. Lett.* **77** 3212 (1996)
85. Basov D N et al. *Phys. Rev. Lett.* **77** 4090 (1996)
86. Strigina N A, Diploma Thesis (Ekaterinburg: Ural State Univ., 2001)
87. Abanov Ar, Chubukov A V, Finkel'stein A M, cond-mat/9911445
88. Abanov Ar, Chubukov A V, cond-mat/0002122
89. Abanov Ar, Chubukov A V, Schmalian J, cond-mat/0005163
90. Abanov Ar, Chubukov A V, Schmalian J, cond-mat/0010403
91. Maksimov E G *Usp. Fiz. Nauk* **170** 1033 (2000) [*Phys. Usp.* **43** 965 (2000)]
92. Kuliĉ M *Phys. Rep.* **338** 1 (2000)
93. Ginzburg V L, Maksimov E G *Sverkhprovodimost'*: *Fiz. Khim. Tekhnol.* **5** 1543 (1992) [*Superconductivity*: *Phys. Chem. Technol.* **5** 1505 (1992)]
94. Friedel J, Kohmoto M, cond-mat/9901065
95. Anderson P W *The Theory of Superconductivity in the High-T_c Cuprates* (Princeton, N.J.: Princeton Univ. Press, 1997)
96. Borkowski L S, Hirschfeld P J *Phys. Rev. B* **49** 15404 (1994)
97. Fehrenbacher R, Norman M R *Phys. Rev. B* **50** 3495 (1994)
98. Kuchinskiĭ É Z, Sadovskiĭ M V *Zh. Eksp. Teor. Fiz.* **119** 553 (2001) [*JETP* **92** 480 (2001)]
99. Gor'kov L P *Zh. Eksp. Teor. Fiz.* **37** 1407 (1959) [*Sov. Phys. JETP* **10** 998 (1960)]
100. de Gennes P G *Superconductivity of Metals and Alloys* (New York: W A Benjamin, 1966) [Translated into Russian (Moscow: Mir, 1968)]
101. Sadovskii M V *Superconductivity and Localization* (Singapore: World Scientific, 2000); *Phys. Rep.* **282** 225 (1997); *Sverkhprovodimost'*: *Fiz. Khim. Tekhnol.* **8** 337 (1995)
102. Kuchinskiĭ É Z, Sadovskiĭ M V *Zh. Eksp. Teor. Fiz.* **117** 613 (2000) [*JETP* **90** 535 (2000)]; *Physica C* **341–348** 879 (2000)
103. Balatsky A V, Bourges P *Phys. Rev. Lett.* **82** 5337 (1999)
104. Tallon J L, cond-mat/9911422
105. Kopaev Yu V *Tr. Fiz. Inst. Akad. Nauk SSSR* **86** 3 (1975) [*Proc. Lebedev Phys. Inst.* Vol. 86 (New York: Plenum Press, 1977) p. 1]
106. Ginzburg V L, Kirzhnits D A (Eds) *Problema Vysokotemperaturnoĭ Sverkhprovodimosti* (The Problem of High-Temperature Superconductivity) Chap. 5 (Moscow: Nauka, 1977) p. 205 [Translated into English: *High-Temperature Superconductivity* (New York: Consultants Bureau, 1982)]
107. Bilbro G, McMillan W L *Phys. Rev. B* **14** 1887 (1976)
108. Bulaevskiĭ L N, Panyukov S V, Sadovskiĭ M V *Zh. Eksp. Teor. Fiz.* **92** 672 (1987) [*Sov. Phys. JETP* **65** 380 (1987)]
109. Miyakawa N et al. *Phys. Rev. Lett.* **80** 157 (1998)
110. Harris J M et al. *Phys. Rev. B* **54** R15665 (1996)
111. Carretta P et al., cond-mat/9911182
112. Schmalian J et al. *Phys. Rev. B* **54** 4336 (1996)
113. Vilk Y M, Tremblay A-M S *J. Phys. I* (Paris) **7** 1309 (1997)
114. Vilk Y M *Phys. Rev. B* **55** 3870 (1997)
115. Monthoux P *Phys. Rev. B* **55** 11111 (1997)
116. Junod A, Erb A, Renner C *Physica C* **317–318** 333 (1999)
117. Abrahams E, Varma C M, cond-mat/0003135; submitted to *Proc. Natl. Acad. Sci.*
118. Valla T et al. *Science* **285** 2110 (1999)
119. Valla T et al. *Phys. Rev. Lett.* **85** 828 (2000); cond-mat/0003407
120. Li Jian-Xin, Wu W C, Lee T K *Phys. Rev. B* **60** 3629 (1999); cond-mat/9901322
121. Nagaev É L *Usp. Fiz. Nauk* **165** 529 (1995) [*Phys. Usp.* **38** 497 (1995)]
122. Zaanen J *Physica C* **317–318** 217 (1999)
123. Castellani C, Di Castro C, Grilli M *Phys. Rev. Lett.* **75** 4650 (1995)
124. Caprara S et al. *Physica C* **317–318** 230 (1999)
125. Tallon J L et al. *Phys. Rev. Lett.* **79** 5294 (1997)
126. Tallon J L *Phys. Rev. B* **58** R5956 (1998)
127. Tallon J L, Williams G V M, Loram J W *Physica C* **338** 9 (2000)

Models of the Pseudogap State in High – Temperature Superconductors

M.V.Sadovskii
Institute for Electrophysics, Russian Academy of Sciences,
Ekaterinburg, 620016, Russia

Abstract

We present a short review of our basic understanding of the physics of copper – oxide superconductors and formulate the list of "solved" and "unsolved" problems. The main problem remains theoretical description of the properties of the normal state, requiring clarification of the nature of the so called pseudogap state.

We review simplified models of the pseudogap state, based on the scenario of strong electron scattering by (pseudogap) fluctuations of "dielectric" (AFM, CDW) short – range order and the concept of "hot" spots (patches) on the Fermi surface. Pseudogap fluctuations are described as appropriate static Gaussian random field scattering electrons.

We derive the system of recurrence equations for the one – particle Green's function and vertex parts, taking into account all Feynman diagrams for electron scattering by pseudogap fluctuations. Results of calculations of spectral density, density of states and optical conductivity are presented, demonstrating both pseudogap and localization effects.

We analyze the anomalies of superconducting state (both $s-$ and $d-$ wave pairing) forming on the "background" of these pseudogap fluctuations. Microscopic derivation of Ginzburg – Landau expansion allows calculations of critical temperature T_c and other basic characteristics of a superconductor, depending on the parameters of the pseudogap. We also analyze the role of "normal" (nonmagnetic) impurity scattering. It is shown that our simplified model allows semiquantitative modelling of the typical phase diagram of superconducting cuprates[1].

[1]Extended version of the talk given by the author on the seminar of I.E.Tamm Theoretical Department of P.N.Lebedev Physical Institute, Russian Academy of Sciences, Moscow, October 7, 2003.

Contents

1 Basic problems of the physics of high – temperature superconductors. 3
1.1 What is really KNOWN about copper oxides: 3
1.2 What is still UNKNOWN about copper oxides: 6

2 Basic experimental facts on the pseudogap behavior in high – temperature superconductors. 9

3 Theoretical considerations – variants of simplified model. 24

4 Elementary ("toy") model of the pseudogap. 29

5 "Hot spots" model. 36
5.1 "Nearly exact" solution for one – particle Green's function. 36
5.2 Recurrence relations for the vertex part and optical conductivity. 44
5.3 Interaction vertex for superconducting fluctuations. 54
5.4 Impurity scattering. 55
5.5 Superconducting transition temperature and Ginzburg – Landau expansion. 59
5.5.1 d – wave pairing. 64
5.5.2 s – wave pairing. 67

6 Modeling of the phase diagram of cuprates. 68

7 Conclusion. 72

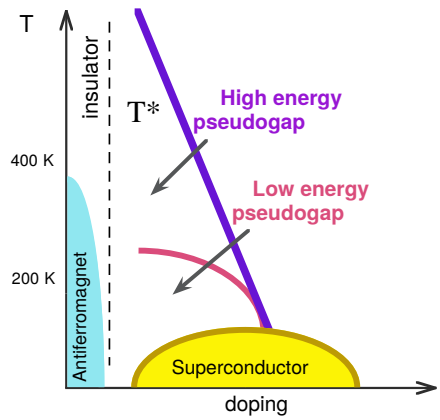

Figure 1: Typical phase diagram of copper oxide high – temperature superconductor. Different phases and anomalous regions are shown schematically. Carrier concentration, corresponding to a maximum of transition temperature T_c is called "optimal". Systems with lower concentrations are called "underdoped", those with larger — "overdoped".

1 Basic problems of the physics of high – temperature superconductors.

We shall start with brief review of the present day situation in the physics of high – temperature superconductors, which may be useful for the reader not involved in this field.

1.1 What is really KNOWN about copper oxides:

High – temperature superconducting (HTSC) copper oxides are intensively studied for more than 15 years now. In these years, considerable progress has been achieved in our understanding of the nature and basic physical properties of these systems, despite their complicated phase diagram, containing almost all the main phenomena studied by solid state physics (Fig. 1).

It is apparent that the number of facts are now well established and are not due to any revision in the future [2] If we talk about superconducting state, the list of "solved" problems may be formulated as follows:

- *Nature of superconductivity* $\rightleftharpoons$ *Cooper pairing.*

[2]Surely, any such list is subjective enough and is obviously based on some prejudices and "tastes" of the author. It is well known, that in HTSC physics quite opposite views are often "peacefully coexistent" with each other. However, such list may hopefully be of some interest.

It is definitely established that in these system we are dealing with

1. d – wave pairing,

   and in the spectrum of elementary excitations we observe

2. Energy gap $\Delta \cos 2\phi$,

   where the polar angle ϕ determines the direction of electronic momentum in two – dimensional inverse space, corresponding to CuO_2 plane. Thus, energy gap becomes zero and changes sign on the diagonals of two – dimensional Brillouin zone.

3. The size of pairs is relatively small: $\xi_0 \sim 5 - 10a$,

   where a is the lattice constant. This means that high – temperature superconductors belong to a crossover region between "large" pairs of BCS theory and "compact" Bosons picture of very strongly coupled electrons.

   Superconducting state always appears as

4. Second order phase transition

   with more or less usual thermodynamics.

All these facts were established during approximately first five years of studies of HTSC copper oxides. We do not give any references to original works here as the list will be to long, and quote only two review articles [1, 2].

Situation becomes much more complicated when we consider the properties of the normal state. Almost all anomalous properties of these unusual systems appear first of all in the normal state. However, here we also can list some definitely established facts:

- *Existence of the Fermi surface.*

  In this sense these systems are clearly *metals*, though rather unusual ("bad"). Most of the data on Fermi surfaces were obtained from ARPES [3, 4], and the progress here in recent years is quite spectacular due to the great increase (more than order of magnitude!) in resolution both in energy and momentum. As an illustration of these advances in Fig. 2 we show *experimentally* determined Fermi surface of $La_{2-x}Sr_xCuO_4$ with $x = 0.063$ [5]. Note the existence of characteristic "flat" parts of this Fermi surface. This form of the Fermi surface is rather typical for the majority of HTSC cuprates in superconducting region of the phase diagram.

- *Metal — Insulator transition,*

  which takes place with the change of chemical composition (as the number of carriers drops). Stochiometric La_2CuO_4 is an antiferromagnetic insulator (apparently of Mott type) with Neel temperature of the order of 400K. There exists well defined

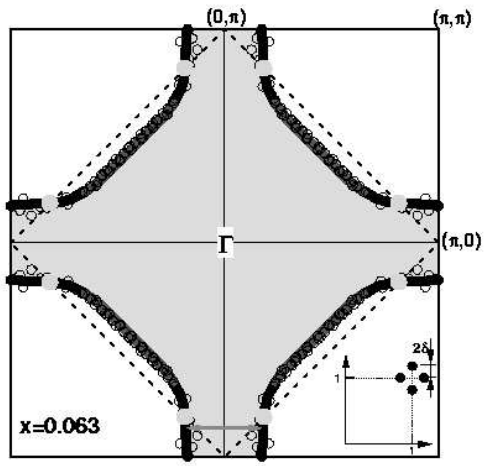

Figure 2: Experimentally determined Fermi surface of $La_{2-x}Sr_xCuO_4$ with $x = 0.063$. At the insert – schematic intensity of neutron scattering with four incommensurate peaks close to the scattering vector (π, π). Dashed lines show the borders of antiferromagnetic Brillouin zone, which appear after the establishment of antiferromagnetic long – range order (period doubling). Points, where these borders intersect the Fermi surface are called "hot" spots.

optical (energy) gap, and antiferromagnetism is due to the ordering of *localized* spins on Cu ions and is well described by two – dimensional Heisenberg model. This is more or less typical also for other HTSC oxides, which thus belong to a wide class of *strongly correlated* electronic systems. At the same time, this dielectric state is rapidly destroyed by introduction of few percents of doping impurities. Note that the Fermi surface shown in Fig. 2, is observed, in fact, in the system which is on the edge of metal – insulator transition, which takes place at $x \sim 0.05$.

- *Strong anisotropy of all properties (quasi – two – dimensional nature!).*

  Current carriers (in most cases — holes) are propagating more or less freely along CuO_2 planes (a and b directions in orthorombic crystal), while transverse motion in orthogonal direction (c axis) is strongly suppressed. Conductivity anisotropy is usually of the order of 10^2 — 10^5. This fact is seriously damaging from the point of view of practical applications. At the same time it is still unclear whether two – dimensionality is a necessary condition for realization of high – temperature supeconductivity.

1.2 What is still UNKNOWN about copper oxides:

Let us now list the main unsolved problems, remaining in the center of rather sharp discussions with participants sometimes not hearing each other. On the first place stays of course the

- *Mechanism of Cooper pairing.*

  Most researchers (not all!) do not have any doubt, that in HTSC – oxides we are dealing with Cooper pairing within more or less standard BCS "scenario". However, the question is — what kind of interaction leads to pair formation? A number of microscopic mechanisms are under consideration:

  1. Electron – phonon [6, 7]. The main unsolved problem here is an explanation of d – wave symmetry of Cooper pairing. Usually, electron – phonon coupling leads to s – wave pairing. Recently there was some progress in possible ways to solve this problem [8].
  2. Spin – fluctuation [9, 10, 11, 12].

     Historically, within this approach the d – wave nature of pairing in oxides was *predicted*. Further experimental confirmation, as well as the possibility of semiquantitative description of many properties of these systems made this approach probably most favorable (from my point of view!) among many other mechanisms.

3. Exchange – RVB, $SO(5)$, ...?

   These models [13, 14], as well as a number of more "exotic", were formulated in early days of HTSC research. Enormous intellectual resources of leading theorists were and are spent on their development. However (again it is only my personal view), the completeness and "stability" of results here is incomparably less than in more traditional approaches, while real connection with experiments is relatively slight, so that all these models still remain a kind of "brain gymnastics". Obviously, I do not deny usefulness of these models from purely theoretical point of view. For example, the discussion of symmetry connections of antiferromagnetism and superconductivity [14] is of great interest. At the same time, the most natural and useful among phenomenological approaches remains the description of superconductivity in oxides based on anisotropic version of the standard Ginzburg – Landau theory [3].

At this time it is unclear, which of these mechanisms is realized or is dominant in real HTSC – oxides. And the reason for this lies in the fact, that the properties of superconducting state are relatively independent of microscopic mechanism of pairing. It is rather difficult to propose some "crucial" experiment, which will definitely confirm one of these mechanisms. In some sense, situation here is somehow similar to those existing, actually for decades, in the theory of magnetism. Since the middle of the thirties, it is well known, that the nature of magnetism is connected with exchange interaction. There exist plenty microscopic mechanisms of exchange interaction between spins (e.g. direct exchange, superexchange, $s-d$ interaction, RKKY etc.). However, it is not always possible to tell, which of these mechanisms acts in some real magnetic system. Classical example here is the problem of magnetism of iron!

- *Nature of the normal state.*

  Here any consensus among researchers is almost absent. Usually, recognizing the metallic nature of these systems, theorist discuss several alternative possibilities:

  1. Fermi – liquid (Landau).
  2. "Marginal" or "bad" Fermi – liquid [15].
  3. Luttinger liquid [13].

     All the talking on the possible breaking of Fermi – liquid behavior (absence of "well defined" quasiparticles) originates, from theoretical point of view, from strong electronic correlations and quasi – two – dimensionality of electronic properties of these systems, while from experimental side this is mainly due

[3] This fact is of special significance as this seminar has taken place approximately an hour after the news came on the award of 2003 Nobel Prize in physics to V.L.Ginzburg.

to practical impossibility of performing studies of electronic properties of the *normal* state at low enough temperatures (when these properties are in fact "shunted" by superconductivity, which is impossible to suppress without significant changes of the system under study). One must remember, that Fermi – liquid behavior, by definition, appears only as limiting property at low enough temperature. Thus, it is not surprising at all that it is "absent" in experiments performed at temperatures of the order of 10^2K! At the same time, as we shall see below, recently there were an important experimental developments, possibly clarifying the whole problem.

4. Disorder and local inhomogeneities.

   Practically all high – temperature superconductors are internally disordered due to chemical composition (presence of doping impurity). Thus, any understanding of their nature is impossible without the detailed studies of the role of an internal disorder in the formation of electronic properties of strongly correlated systems with low dimensionality. In particular, localization effects are quite important in these systems, and studies of these has already a long history [16]. Situation with the role of internal disorder has complicated recently with the arrival of the new data, obtained in by scanning tunneling microscopy (STM), which clearly demonstrated inhomogeneous nature of the local density of states and superconducting energy gap on microscopic scale, even in practically ideal single – crystals of copper oxides. Of many recent papers devoted to these studies, we quote only two [17, 18], where further references can be found. These results significantly modify previous ideas on microscopic phase separation, "stripes" etc. On the other hand, the presence of such inhomogeneities makes these systems a kind of "nightmare" for theorists, though the picture of inhomogeneous superconductivity due to fluctuations in the local density of states was analyzed rather long time ago [16, 19].

5. Pseudogap.

   Now it is clear that most of the anomalies of the normal state of copper oxides is related to the formation of the so called pseudogap state. This state is realized in a wide region of the phase diagram as shown in Fig. 1, corresponding mainly to "underdoped" compositions and temperatures $T < T^*$. It is important to stress, that the line T^* on Fig. 1 is rather approximate and apparently do not correspond to any phase transition and signify only a kind of crossover to the region of well developed pseudogap anomalies[4]. In short, numerous experiments [20, 21] show that in the region of $T < T^*$ the systems, which are in the normal (non superconducting) state, do possess some kind of the gap –

[4]Sometimes the notion of "high energy pseudogap" is introduced and defined by T^*, while the "low energy pseudogap" is defined by another crossover line in the region of $T < T^*$ closer to superconducting "dome", as shown in Fig. 1.

like feature in the energy spectrum. However, this is not a real gap, but some kind of precursor of its appearance in the spectrum (which is the reason for the term "pseudogap", which appeared first in qualitative theory of amorphous and liquid semiconductors [22].). Some examples of the relevant experiments will be given below.

Crudely speaking, the gap in the spectrum can be either of superconducting or insulating nature. Accordingly, there exist two possible theoretical "scenarios" to explain pseudogap anomalies in copper oxides. The first one anticipates formation of Cooper pairs already at temperatures higher, than the temperature of superconducting transition, with phase coherence appearing only in superconducting state at $T < T_c$. The second assumes, that the origin of the pseudogap state is due to fluctuations of some kind of short range order of "dielectric" type, developing in the underdoped region. Most popular here is the picture of antiferromagnetic (AFM) fluctuations, though fluctuating charge density waves (CDW) cannot be excluded, as well as structural deformations or phase separation at microscopic scales. In my opinion, most of the recent experiments provide evidence for this second scenario. So, in further discussion we shall deal only with this type of models, mainly speaking about antiferromagnetic fluctuations.

It is common view, that the final understanding of the nature of high – temperature superconductivity is impossible without clarification of the nature of the normal state. Generally speaking, we have to explain all characteristic features of the phase diagram, shown in Fig. 1. This is the main task of the theory and it is still rather far from the complete solution. In the following we shall concentrate on the discussion of some simple models of the pseudogap state and attempts to illustrate possible ways to find a solution of this main problem.

2 Basic experimental facts on the pseudogap behavior in high – temperature superconductors.

Phase diagram of Fig. 1 shows that, depending on concentration of current carriers in highly conducting CuO_2 plane, a number of phases and regions with anomalous properties can be observed in copper oxides. For small concentrations, all the known HTSC – cuprates are antiferromagnetic insulators. With the growth of carrier concentration Neel temperature T_N rapidly drops from the values of the order of hundreds of K, vanishing at concentration of holes p less than or of the order of 0.05, and system becomes metallic. As concentration of holes is increasing further, the system becomes superconducting, and temperature of superconducting transition grows with the growth of carrier concentration, passing through characteristic maximum at $p_0 \approx 0.15 - 0.17$ (optimal doping), and

then drops and vanish at $p \approx 0.25 - 0.30$, though metallic behavior in this (overdoped) region remains. In the overdoped region with $p > p_0$ metallic properties are more or less traditional (Fermi – liquid), while for $p < p_0$ the system is a kind of anomalous metal, not described (in the opinion of majority of authors) by the usual theory of Fermi – liquid.

Anomalies of physical properties attributed to the pseudogap formation are observed in metallic phase for $p < p_x$ and temperatures $T < T^*$, where T^* drops from the values of the order of T_N at $p \sim 0.05$ vanishing at some "critical" concentration of carriers p_c, slightly greater than p_0, so that T^* – line in Fig.1 is actually continuing under the superconducting "dome". According to the data presented in Ref. [23] T^* vanishes at $p = p_c \approx 0.19$. In the opinion of some other authors (proponents of superconducting scenario for the pseudogap) T^* – line just passes to T_c – line of superconducting transition somewhere close to the optimal doping p_0. In my opinion, most recent data, apparently, confirm the first variant of the phase diagram (more details can be found in Ref. [23]).

Pseudogap anomalies, in general, are interpreted as due to suppression (in this region) of the density of single – particle excitations close to the Fermi level, which corresponds to the general concept of the pseudogap [22]. The value of T^* then determines characteristic scale of the observed anomalies and is proportional to effective energy width of the pseudogap. Let us now consider typical experimental manifestations of pseudogap behavior.

Consider first experimental data on electronic specific heat of cuprates. In metals this contribution is usually written as: $C = \gamma(T)T$, so that in the normal state ($T > T_c$) $\gamma \sim N(0)$, where $N(0)$ – is the density of states at the Fermi level. At $T = T_c$ we have the well known anomaly due to second order phase transition, so that $\gamma(T)$ demonstrates characteristic peak (discontinuity). As a typical example, in Fig. 3 we show experimental data for $Y_{0.8}Ca_{0.2}Ba_2Cu_3O_{7-\delta}$ for different values of δ [24]. We can see, that in optimally doped and overdoped samples $\gamma(T)$ is practically constant for all $T > T_c$, while for underdoped samples considerable drop of $\gamma(T)$ appears for $T < 150 - 200K$. This is a direct evidence of the appropriate drop of the density of states at the Fermi level due to pseudogap formation for $T < T^*$.

Note also that the value of specific heat discontinuity at superconducting T_c is significantly suppressed as we move to the underdoped region. More detailed analysis shows [23] that the drop of this discontinuity $\Delta\gamma_c$ actually starts at some "critical" carrier concentration $p_c \approx 0.19$, which is connected with the "opening" of the pseudogap.

Pseudogap formation in the density of states is clearly seen also in experiments on single particle tunneling. Thus, in highly cited Ref. [25] tunneling experiments were performed on single crystals of $Bi_2Sr_2CaCu_2O_{8+\delta}$ ($Bi-2212$) with different oxygen content. For underdoped samples pseudogap formation in the density of states was clearly observed at temperatures significantly higher than superconducting T_c. This pseudogap smoothly transformed into superconducting gap at $T < T_c$, which is often seen as an evidence of its superconducting nature. However, in Refs. [26, 27], where tunneling experiments were performed on the same system, it was directly shown, that superconducting gap exists

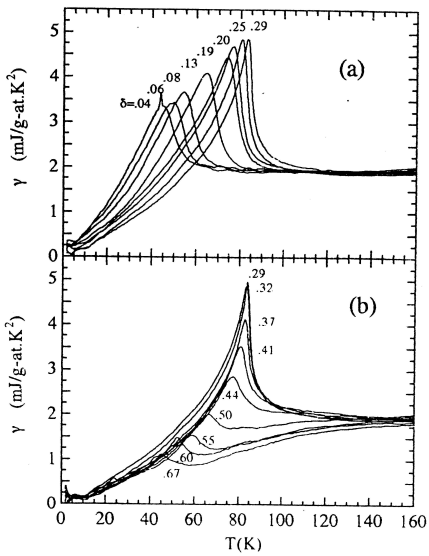

Figure 3: Coefficient γ of electronic specific heat in overdoped (a) and underdoped (b) $Y_{0.8}Ca_{0.2}Ba_2Cu_3O_{7-\delta}$.

on the "background" of the wider pseudogap and vanishes at $T = T_c$, while pseudogap persists at higher temperatures.

Pseudogap also shows itself in transport properties of HTSC – systems in normal state, Knight shift and NMR relaxation. In particular, changes from the usual for optimally doped linear temperature dependence of resistivity for underdoped samples and $T < T^*$ are often attributed to its formation. Also the value of Knight shift in such samples for $T < T^*$ becomes temperature dependent and drops as temperature lowers. Similar behavior is observed in underdoped samples for $(TT_1)^{-1}$, where T_1 – is NMR relaxation time. Let us remind, that in usual metals Knight shift is just proportional to the density of states at the Fermi level $N(0)$, while $(TT_1)^{-1} \sim N^2(0)$ (Korringa behavior), and resistivity ρ is proportional to the scattering rate (inverse mean free time) $\gamma \sim N(0)$. Thus, significant lowering of these characteristics is naturally attributed to the drop in the density of states $N(0)$ at the Fermi level. Note that these arguments are, of course, oversimplified, particularly when we are dealing with temperature dependences. E.g. in case of resistivity this dependence is determined by inelastic scattering and physics of these processes in HTSC is still unclear. Thus, the decrease in the density of states (due to partial dielectrization of the spectrum) can also lead, in fact, to the growth of resistivity.

Pseudogap in underdoped cuprates is also observed in experiments on optical conductivity, both for electric field polarization along highly – conducting CuO_2 plane and also along orthogonal direction (c – axis). These experiments are reviewed in detail in Ref. [20]. As a typical example in Fig. 4 we show the data of Ref. [28] on optical conductivity in the CuO_2 plane for different compositions of electronically conducting oxide

$Nd_{2-x}Ce_xCuO_4$. Characteristic feature here is the appearance (most clearly seen for underdoped samples with $x = 0.05$ and $x = 0.10$), of the shallow minimum at frequencies of the order of 0.25 eV and of smooth maximum due to absorption through unusually wide pseudogap around $\omega \sim 0.5$ eV. The nature of an additional absorption maximum seen at $\omega \sim 0.1$ eV can, apparently, bw attributed to localization (cf. below).

In underdoped cuprates with hole conductivity, optical conductivity is usually characterized by a narrow "Drude like" absorption peak at small frequencies, followed by a shallow minimum and smooth maximum due to pseudogap absorption through pseudogap of the order of $0.1eV$ [20, 21]. Additional peak due to localization is observed rarely, usually after the introduction of an additional disorder [29, 30, 31].

Most spectacular effects due to pseudogap formation are seen in experiments on angle resolved photoemission (ARPES). ARPES intensity (energy and momentum distribution of photoelectrons) is determined by [4]:

$$I(\mathbf{k}\omega) = I_0(\mathbf{k})f(\omega)A(\mathbf{k}\omega) \tag{1}$$

where $\mathbf{k}$ – is the momentum in the Brillouin zone, ω – energy of initial state, measured with respect to the Fermi level (chemical potential)[5], $I_0(\mathbf{k})$ includes some kinematic factors and the square of the matrix elements of electron – photon interaction and in crude approximation is considered to be some constant,

$$A(\mathbf{k},\omega) = -\frac{1}{\pi}ImG(\mathbf{k},\omega + i\delta) \tag{2}$$

where $G(\mathbf{k},\omega)$ – is Green's function of an electron, determines the spectral density. The presence of Fermi distribution $f(\omega) = [exp(\omega/T) + 1]^{-1}$ reflects the fact, that only occupied states can produce photoemission. Thus, in such a crude approximation it can be said, that ARPES experiments just measure the product $f(\omega)A(\mathbf{k}\omega)$, and we get direct information on the spectral properties of single – particle excitations.

Consider qualitative changes in single – electron spectral density (2) due to pseudogap formation. In the standard Fermi – liquid theory, single – electron Green' function can be written as:

$$G(\omega,\mathbf{k}) = \frac{Z_\mathbf{k}}{\omega - \xi_\mathbf{k} - i\gamma_\mathbf{k}} + G_{incoh} \tag{3}$$

where $\xi_\mathbf{k} = \varepsilon_\mathbf{k} - \mu$ – is quasiparticle energy with respect to the Fermi level (chemical potential) μ, $\gamma_\mathbf{k}$ – quasiparticle damping. The residue in the pole $0 < Z_\mathbf{k} < 1$, G_{incoh} – is some non singular contribution due to many particle excitations. Then the spectral density is:

$$A(\omega,\mathbf{k}) = \frac{1}{\pi}Z_\mathbf{k}\frac{\gamma_\mathbf{k}}{(\omega - \xi_\mathbf{k})^2 + \gamma_\mathbf{k}^2} + ... \tag{4}$$

[5]In real experiments ω is measured with respect to the Fermi level of some good metal, e.g. Pt or Ag, placed in electric contact with a sample.

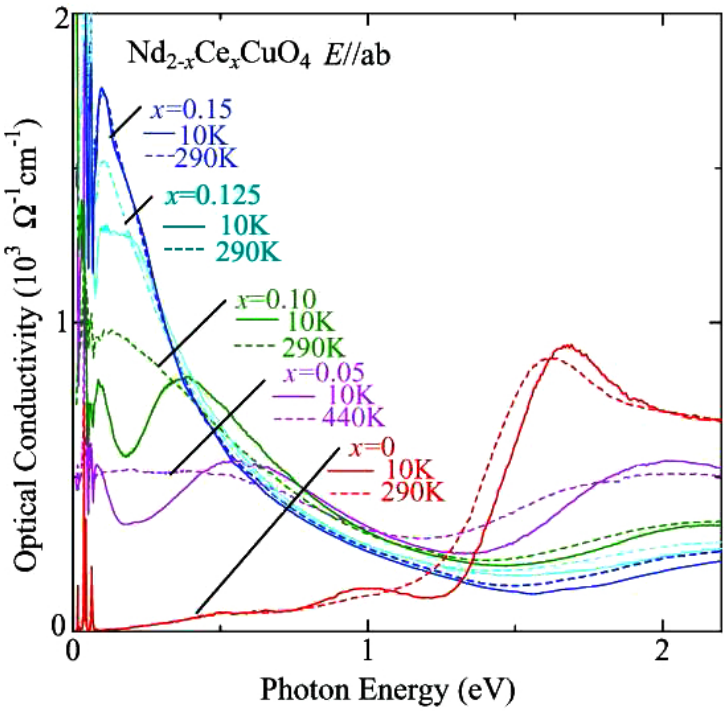

Figure 4: Real part of optical conductivity in the ab – plane of $Nd_{2-x}Ce_xCuO_4$ for different temperatures and compositions x.

where dots denote more or less smooth contribution from G_{incoh}, while quasiparticle spectrum determines a narrow (if damping $\gamma_{\mathbf{k}}$ is small in comparison to $\xi_{\mathbf{k}}$) Lorentzian peak. In the usual Fermi – liquid $\gamma \sim \omega^2 \sim |\mathbf{k} - \mathbf{k}_F|^2$ and quasiparticles are well defined in some (narrow enough) vicinity of the Fermi surface. In the model of "marginal" Fermi – liquid $\gamma \sim \omega \sim |\mathbf{k} - \mathbf{k}_F|$ and quasiparticles are "marginally" defined due to $\gamma \sim \xi_{\mathbf{k}}$. In the presence of static scattering (e.g. due to impurities) a constant (independent of ω) contribution γ_0 appears in damping.

Qualitative form of the spectral density in the Fermi – liquid picture is illustrated in Fig. 5(a).

If some long – range order (e.g. of SDW(AFM) or CDW type) appears in the system, an energy gap $W_{\mathbf{k}}$ (of dielectric nature) opens in the spectrum of elementary excitations ($\mathbf{k}$ – dependence stresses the possibility of gap opening only on the part of the Fermi surface), and single – particle Green's function acquires the form of Gorkov's function (where we also add some damping $\Gamma_{\mathbf{k}}$):

$$G(\omega, \mathbf{k}) = \frac{u_{\mathbf{k}}^2}{\omega - E_{\mathbf{k}} + i\Gamma_{\mathbf{k}}} + \frac{v_{\mathbf{k}}^2}{\omega + E_{\mathbf{k}} - i\Gamma_{\mathbf{k}}} \tag{5}$$

where the excitation spectrum is now:

$$E_{\mathbf{k}} = \sqrt{\xi_{\mathbf{k}}^2 + W_{\mathbf{k}}^2} \tag{6}$$

and we introduced Bogoliubov's coefficients:

$$u_{\mathbf{k}}^2 = \frac{1}{2}\left(1 + \frac{\xi_{\mathbf{k}}}{E_{\mathbf{k}}}\right) \tag{7}$$

$$v_{\mathbf{k}}^2 = \frac{1}{2}\left(1 - \frac{\xi_{\mathbf{k}}}{E_{\mathbf{k}}}\right) \tag{8}$$

Then the spectral density is:

$$A(\omega\mathbf{k}) = \frac{u_{\mathbf{k}}^2}{\pi}\frac{\Gamma_{\mathbf{k}}}{(\omega - E_{\mathbf{k}})^2 + \Gamma_{\mathbf{k}}^2} + \frac{v_{\mathbf{k}}^2}{\pi}\frac{\Gamma_{\mathbf{k}}}{(\omega + E_{\mathbf{k}})^2 + \Gamma_{\mathbf{k}}^2} + ... \tag{9}$$

where now appear *two* peaks, narrow if $\Gamma_{\mathbf{k}}$ is small enough, corresponding to "Bogoliubov's" quasiparticles.

If there is no long – range order, but only strong scattering by fluctuations of short – range order, characterized by some correlation length ξ, is present in our system, it is easy to imagine, that spectral density possesses (in the same region of momentum space and energy) some precursor structure, in the form of characteristic "double – hump" structure, as it is shown qualitatively in Fig. 5. The widths of these maxima are naturally determined by parameter v_F/ξ, i.e. inverse time of flight of an electron through the region of the size of ξ, where "dielectric" ordering is effectively conserved. Below we shall see that rigorous

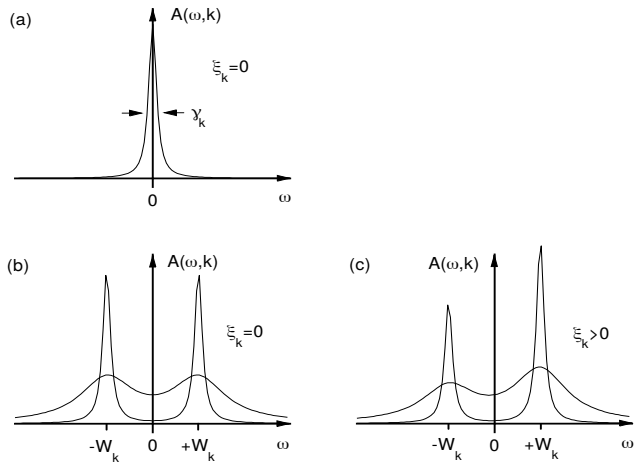

Figure 5: Qualitative evolution of spectral density. (a) – normal metal (Fermi – liquid), $\xi_{\mathbf{k}} = 0$ – at the Fermi surface. (b) – two narrow peaks, corresponding to "Bogoliubov's" quasiparticles in a system with dielectric gap $W_{\mathbf{k}}$ (in case of long – range order of CDW or SDW type). Smooth maxima – system without long – range order (pseudogap behavior), $\xi_{\mathbf{k}} = 0$ – at the Fermi surface. (c) – same as (b), but for $\xi_{\mathbf{k}} > 0$, i.e. above the Fermi surface. Note characteristic asymmetry of maxima in this case.

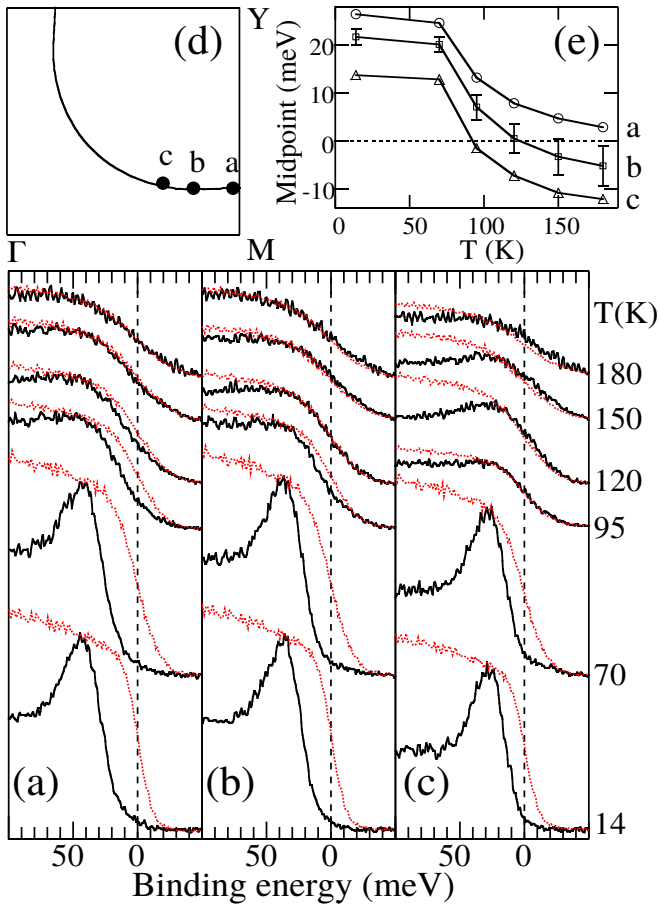

Figure 6: ARPES spectra in three different points a, b, c on the Fermi surface of $Bi-2212$ for underdoped sample with $T_c = 85K$. Thin curves — spectrum of the reference sample of Pt.

analysis leads just to these results. In this sense, the further theoretical discussion will be devoted to justification of this qualitative picture.

In Fig. 6 we show ARPES data for $Bi_2Sr_2CaCu_2O_8$ [32], obtained in three different points on the Fermi surface for different temperatures. The presence of the gap (pseudogap) manifests itself by the shift (to the left) of the leading edge of energy distribution of photoelectrons in comparison to the reference spectrum of a good metal (Pt). It is seen that this gap is closed at different temperatures for different values of $\mathbf{k}$, and the gap width diminishes as we move from $(0,0)-(0,\pi)$ direction in the Brillouin zone. Pseudogap is completely absent in the direction of zone diagonal $(0,0)-(\pi,\pi)$. At low temperatures this is in complete accordance with the picture of $d-$ wave pairing, which is confirmed in cuprates by many experiments [1, 2]. Important thing, however, is that this "gap" in ARPES data is observed also at temperatures significantly higher than the temperature

of superconducting transition T_c.

In Fig. 7 we show angular dependence of the gap in the Brillouin zone and temperature dependence of its maximal value, obtained from ARPES [33] for several samples of $Bi-2212$ with different compositions. It is seen that the general d – wave like symmetry is conserved and the gap in optimally doped sample vanishes practically at $T = T_c$, while for underdoped samples we observe typical "tails" in the temperature dependence of the gap for $T > T_c$. Qualitatively we may say that the formation of an anisotropic pseudogap at $T > T_c$, which smoothly transforms into superconducting gap for $T < T_c$, leads to "destruction" parts of the Fermi surface of underdoped samples, close to the point $(0, \pi)$ (and symmetrical to it), already for $T < T^*$, and the sizes of these parts grow as temperature lowers [32].

Of central interest is, of course, the evolution of the spectral density $A(\mathbf{k}_F, \omega)$ at the Fermi surface. Under rather weak assumptions it can be directly determined from ARPES data [32]. Assuming electron – hole symmetry (always valid close enough to the Fermi surface, in reality for $|\omega|$ less than some tenths of meV) we have $A(\mathbf{k}_F, \omega) = A(\mathbf{k}_F, -\omega)$, so that taking into account $f(-\omega) = 1 - f(-\omega)$, from (1) and for $\mathbf{k} = \mathbf{k}_F$ we obtain $I(\omega) + I(-\omega) = A(\mathbf{k}_F, \omega)$. Thus, the spectral density at the Fermi surface can be directly determined using symmetrized experimental data $I(\omega) + I(-\omega)$. As an example of such analysis, in Fig. 8 we show the dtat of Ref. [34] for underdoped sample of $Bi-2212$ with $T_c = 83K$ and overdoped with $T_c = 82K$ at different temperatures. It is seen that pseudogap existence clearly manifests itself in characteristic "double – humps" structure of spectral density, which appears (in an underdoped system) for temperatures significantly higher than T_c. We see that these data completely correspond to the expected qualitative form of spectral density in the pseudogap state.

Let us stress once again, that well defined quasiparticles correspond to narrow enough peak in the spectral density $A(\mathbf{k}_F, \omega)$ at $\omega = 0$. Such behavior, until recently, was in practically never observed in copper oxides. However, it was discovered some time ago that in superconducting phase, at $T \ll T_c$, there exists sharp enough peak of the spectral density, corresponding to well defined quasiparticles, in the vicinity of an intersection of the Fermi surface with diagonal of the Brillouin zone (direction $(0,0) - (\pi, \pi)$), where superconducting gap vanishes [35]. At the same time, close to the point $(0, \pi)$ the Fermi surface remains "destroyed" by both superconducting gap and the pseudogap. The studies of these "nodal" quasiparticles id of great importance and lead to some clarification of the problem of Fermi – liquid behavior. Most recent data show, that quasiparticle peak in diagonal direction persists also at temperatures much higher than T_c. This is clearly seen from the data of Ref. [36], shown in Fig. 9, where we can see the evolution of this peak as we move along the Fermi surface. It is seen that quasiparticle behavior is valid everywhere for overdoped samples and only in the vicinity of diagonal for underdoped (and optimal). Quasiparticle peak in diagonal direction persists even for strongly underdoped samples, which are on the edge of metal – insulator transition [5]. From data shown in Fig. 10 [36], we can also see significant anisotropy of static (or more precisely quasistatic within limits

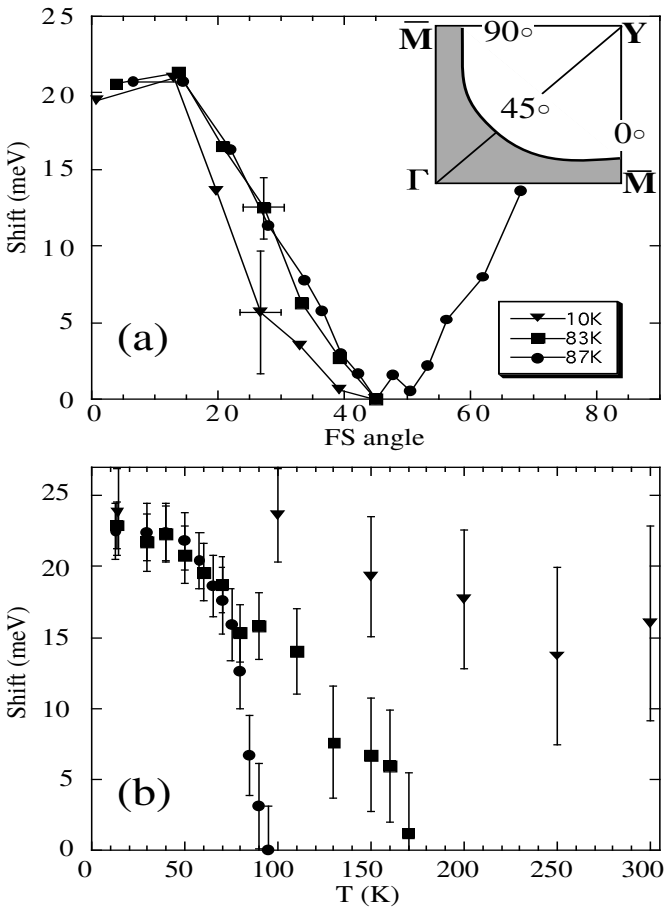

Figure 7: Angular and temperature dependences of energy gap in $Bi-2212$, obtained from ARPES data for samples with $T_c = 87K$ (nearly optimally doped), $T_c = 83K$ and $T_c = 10K$ (underdoped): (a) – the value of ARPES gap, measured at different points of the Fermi surface (shown at the insert), with positions determined by polar angle, measured from the direction $\Gamma\bar{M}$, d – wave symmetry of the gap is obvious. (b) – temperature dependence of the maximal gap, measured close to point $\bar{M}$.

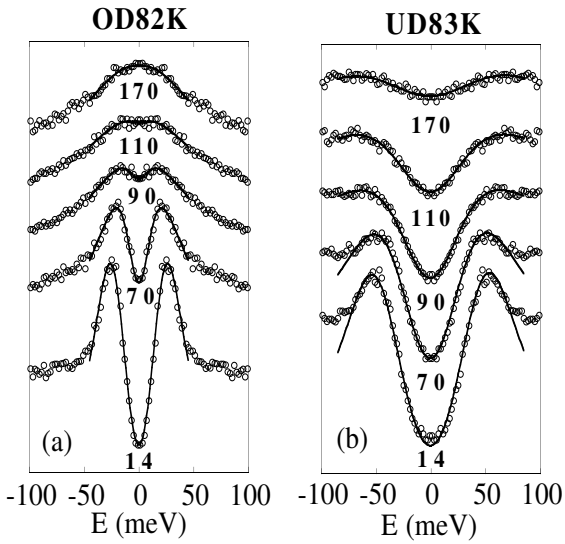

Figure 8: Symmetrized ARPES spectra for overdoped sample of $Bi-2212$ with $T_c = 82K$ (a) and underdoped sample with $T_c = 83K$ (b) at the point of intersection of the Fermi surface with the border of Brillouin zone $(0,\pi)-(\pi,\pi)$.

of ARPES resolution) scattering, growing as we move to the vicinity of $(0,\pi)$, which can obviously be related to pseudogap formation.

Finally, in Fig. 11 we show spectacular results of Ref. [37], obtained from ARPES measurements with significantly improved resolution, from which, even by the "naked eye", we can see that effective damping of "nodal" quasiparticles is in general (except possibly underdoped samples) more or less quadratic in energy, as we can expect for a standard Fermi – liquid. Only close to optimal doping and well into underdoped region we can see some additional contribution to scattering, most probably of magnetic nature. These newest results provide quite new information on much discussed problem of Fermi – liquid behavior in HTSC – oxides. Apparently we observe typical Fermi – liquid behavior in overdoped samples, but it is "destroyed" as we move to optimal doping and into underdoped region, though only in parts of the momentum space (in the vicinity of the points like $(0,\pi)$), where pseudogap appears, leading to additional strong scattering (damping).

The growth of pseudogap anomalies as we move to the region around $(0,\pi)$, where also becomes maximal the amplitude of superconducting d – wave gap, is often interpreted as an evidence of d – wave symmetry of the pseudogap and of its superconducting nature, smoothly transforming into the real gap for $T < T_c$. However, there is lot of evidence that pseudogap actually competes with superconductivity and is, most probably, of dielectric nature. Detailed discussion of this evidence can be found e.g. in Refs. [21, 23]. Here we only limit ourselves to the most general argument — pseudogap anomalies in HTSC grow as we move deep into underdoped region, where superconductivity just vanish. It is

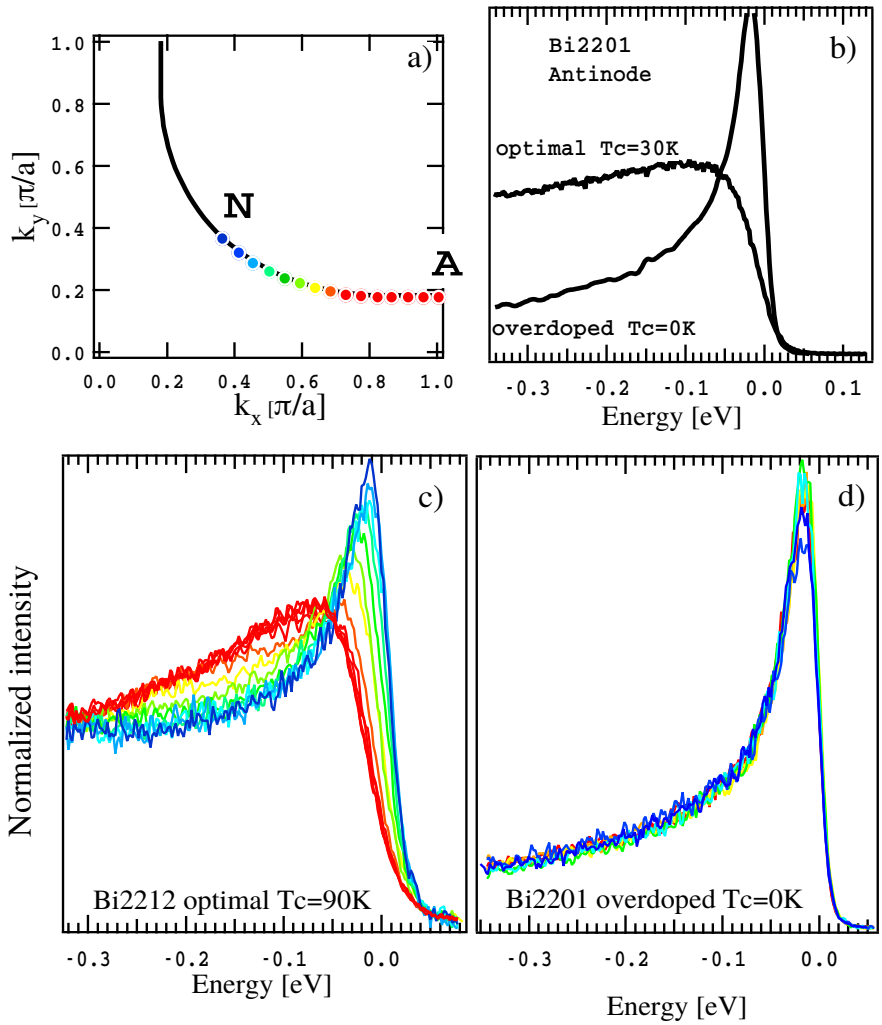

Figure 9: ARPES spectra, measured at different point at the Fermi surface, moving from the diagonal direction in Brillouin zone to $(\pi, 0)$: (a) – points, where data were taken; (b) – comparison of data in в "antinodal" point A (vicinity of $(\pi, 0)$) in optimally doped and overdoped $Bi2201$; (c) – data for optimally doped $Bi2212$ with $T_c = 90K$, obtained at $T = 140K$; (d) – similar data for overdoped $Bi2201$ with $T_c = 0$, obtained at $T = 140K$.

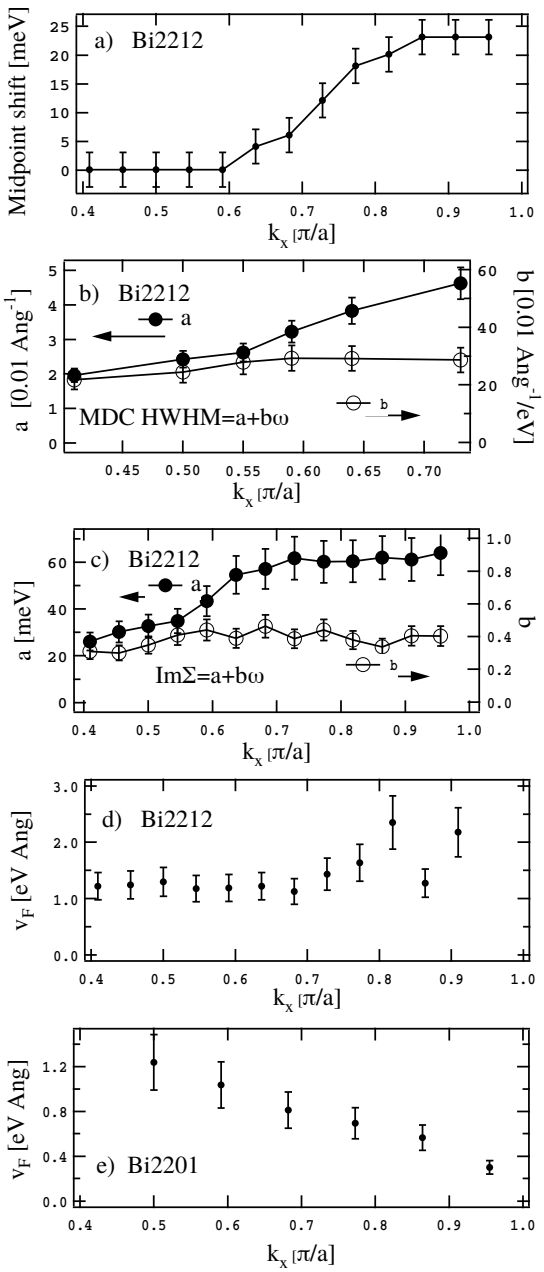

Figure 10: The fit of data on ARPES spectrum width to "marginal" dependence of the imaginary part of self – energy: $Im\Sigma = a + b\omega$. Clearly seen is anisotropy of static (quasistatic) scattering in optimally doped $Bi2212$, while dynamic (inelastic) scattering remains isotropic (c). Behavior of the velocity on the Fermi surface as shown on (d) and (e) (overdoped $Bi2201$).

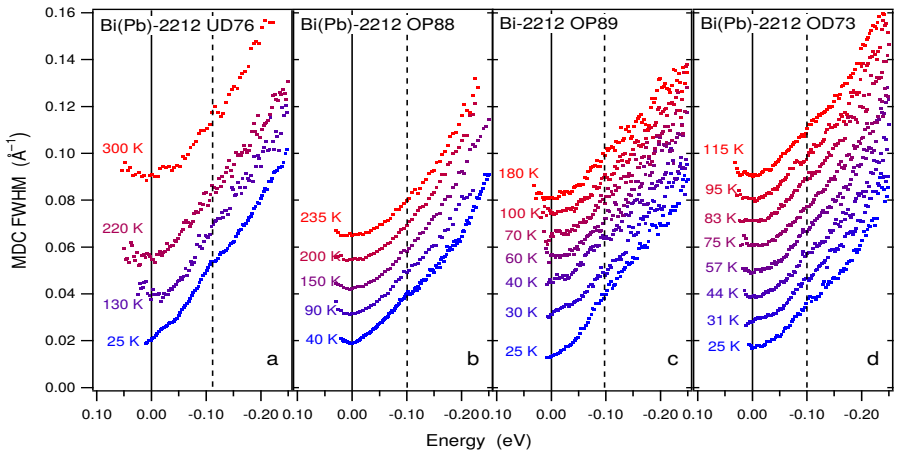

Figure 11: Experimental data on the width of ARPES peaks in $Bi(Pb)2212$ and $Bi2212$ for different temperatures, as doping level changes from underdoped sample with $T_c = 76K$ (a) to overdoped with c $T_c = 73K$ (d).

difficult to imagine, how this type of behavior can be due to precursor Cooper pairing at $T > T_c$.

Of course, there are experimental data, giving direct evidence for "dielectric" nature of the pseudogap. In Fig. 12 we present ARPES data on the Fermi surface of electronic superconductor $Nd_{1.85}Ce_{0.15}CuO_4$ [38], which clearly show, that the "destruction" of the Fermi surface due to pseudogap formation takes place in the region around "hot spots", appearing at intersections of the Fermi surface with borders of the "future" antiferromagnetic Brillouin zone, which would have appeared after the establishment of antiferromagnetic long – range order. Real gap in this case is obviously of the usual "band" or "insulating" nature, nothing to do with Cooper pairing of d – wave symmetry. Most ARPES experiments in HTSC – oxides are performed on systems with hole – like conductivity, where the distance (in momentum space) between sides of the Fermi surface in the vicinity of $(0, \pi)$ is just smaller, than in $NdCeCuO$. Also smaller in these systems is characteristic energy scale (width) of the pseudogap, as was mentioned previously during the discussion of optical data shown in Fig. 4. Accordingly, the resolution of ARPES is apparently insufficient to resolve separate "hot spots", which are too close to each other in the vicinity of $(0, \pi)$. In my opinion, the results of Ref. [38] practically solve the problem in favor of "dielectric" scenario of pseudogap formation in cuprates.

In conclusion, we must stress that in different experiments discussed above, characteristic temperature T^*, defining crossover into the pseudogap state can somehow change, depending on the property which is being studied. However, in all cases there is some systematic dependence of T^* on the doping level and this temperature vanishes at some concentration of carriers slightly higher than optimal. In Fig. 13 we show a compendium of data (derived from a number of different experiments) on the energy width of the

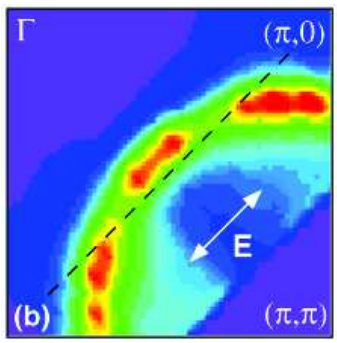

Figure 12: Fermi surface of electronic superconductor $Nd_{1.85}Ce_{0.15}CuO_4$ in one quadrant of the Brillouin zone, obtained by direct integration of ARPES spectra. Dashed line denotes the border of antiferromagnetic Brillouin zone.

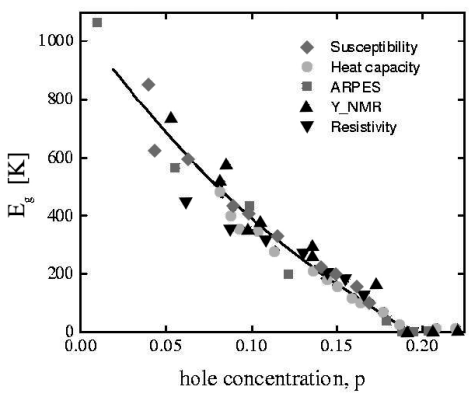

Figure 13: Dependence of the energy width of the pseudogap E_g in $YBCO$ on hole concentration determined from different experiments.

pseudogap E_g for $YBCO$ as a function of hole concentration [23] (in this reference it was assumed, rather arbitrarily, that $E_g = 2.5T^*$). It is seen that pseudogap vanishes at the critical concentration $p_c \approx 0.19$, slightly higher than optimal concentration of carriers, which, by the way, is an additional argument in favor of non superconducting nature of the pseudogap in cuprates.

More detailed review of miscellaneous experiments on the pseudogap formation in high temperature superconductors can be found in Refs. [20, 23].

3 Theoretical considerations – variants of simplified model.

As we mentioned above, there are two alternative scenarios to explain pseudogap anomalies in HTSC – systems. The first one is based on the model of Cooper pair formation already above the temperature of superconducting transition (precursor pairing), while the second assumes, that the origin of the pseudogap state is due to scattering by fluctuations of short – range order of "insulating" type (e.g. antiferromagnetic (SDW) or charge density wave (CDW)), existing in underdoped region of copper oxides. This second scenario seems to be more attractive, both due to a number of experimental evidences and due to a simple fact, that all pseudogap anomalies become stronger, as carrier concentration drops and the system moves farther away from optimal concentration for superconductivity towards dielectric (antiferromagnetic) phase.

Consider typical Fermi surface of electrons moving in the CuO_2 plane, shown in Fig. 2. If we neglect fine details, the observed (e.g. in ARPES) Fermi surface topology (and also the spectrum of elementary excitations) in CuO_2 plane, in the first approximation are well enough described by the usual tight – binding model:

$$\varepsilon_{\mathbf{k}} = -2t(\cos k_x a + \cos k_y a) - 4t' \cos k_x a \cos k_y a \tag{10}$$

where $t \approx 0.25eV$ is the nearest neighbor transfer integral, while t' is the transfer integral between second – nearest neighbors, which can change between $t' \approx -0.45t$ for $YBa_2Cu_3O_{7-\delta}$ and $t' \approx -0.25t$ for $La_{2-x}Sr_xCuO_4$, a is the square lattice constant.

Phase transition to antiferromagnetic state induces lattice period doubling and leads to the appearance of "antiferromagnetic" Brillouin zone in inverse space as shown in Fig. 14. If the spectrum of carriers is given by (10) with $t' = 0$ and we consider the half – filled case, Fermi surface becomes just a square conciding with the borders of antiferromagnetic zone and we have a complete "nesting" — flat parts of the Fermi surface match each other after the translation by vector of antiferromagnetic ordering $\mathbf{Q} = (\pm\pi/a, \pm\pi/a)$. In this case and for $T = 0$ the electronic spectrum is unstable, energy gap appears everywhere on the Fermi surface and the system becomes insulator, due to the formation

of antiferromagnetic spin density wave (SDW)[6]. This picture corresponds to one of the popular schemes to explain antiferromagnetism in cuprates, see e.g. Ref. [39] and a review paper [40], though, as was noted above, experimental situation is well described by simple Heisenberg model with localized spins. In the case of the Fermi surface shown in Fig.14 the appearance of antiferromagnetic long - range order, in accordance with general rules of the band theory, leads to the appearance of discontinuities of isoenergetic surfaces (e.g. Fermi surface) at crossing points with borders of new (magnetic) Brillouin zone due to gap opening at points connected by vector $\mathbf{Q}$. Note similarity of this picture with experimental data shown in Fig. 12.

In the region of cuprate phase diagram of interest to us antiferromagnetic long – range order is absent, however, a number of experiments support the existence (everywhere below the T^* – line) of well developed fluctuations of antiferromagnetic short – range order which scatter electrons with characteristic momentum transfer of the order of $\mathbf{Q}$. In principle, it is not very important to consider AFM(SDW) fluctuations, similar effects may be due CDW fluctuations. There is no doubt, that such scattering processes exist (and dominate!) in cuprates in the whole pseudogap region. To convince yourself, just look at the data shown in Fig. 9!

For concreteness consider, however, the model of "nearly antiferromagnetic" Fermi – liquid [41, 42], where the effective interaction of electrons with spin fluctuations is described by dynamic spin susceptibility $\chi_{\mathbf{q}}(\omega)$, the form of which was determined by fitting to NMR experiments [43, 44]:

$$V_{eff}(\mathbf{q},\omega) = g^2\chi_{\mathbf{q}}(\omega) \approx \frac{g^2\xi^2}{1+\xi^2(\mathbf{q}-\mathbf{Q})^2 - i\frac{\omega}{\omega_{sf}}} \tag{11}$$

where g is coupling constant, ξ – correlation length of spin fluctuations, $\mathbf{Q} = (\pm\pi/a, \pm\pi/a)$ is vector of antiferromagnetic ordering in dielectric phase, ω_{sf} – characteristic frequency of spin fluctuations.

Dynamical spin susceptibility $\chi_{\mathbf{q}}(\omega)$ is peaked around wave vectors $(\pm\pi/a, \pm\pi/a)$, and this leads to appearance of "two types" of quasiparticles — "hot" one, with momenta in the vicinity of "hot spots" on the Fermi surface (Fig.14) and energies satisfying the inequality (v_F – velocity at the Fermi surface):

$$|\varepsilon_{\mathbf{k}} - \varepsilon_{\mathbf{k+Q}}| < v_F/\xi, \tag{12}$$

and "cold" one with momenta close to the parts of the Fermi surface surrounding diagonals of Brillouin zone $|p_x| = |p_y|$ and not satisfying (12). This terminology is connected with strong scattering of quasiparticles in the vicinity of "hot spots" with momentum transfer of the order of $\mathbf{Q}$ due to interaction with spin fluctuations (11), while for quasiparticles with momenta far from "hot spots" this interaction is weak enough. In the following

[6] Analogous dielectrization is realized also in the case of the formation of the similar charge density wave (CDW).

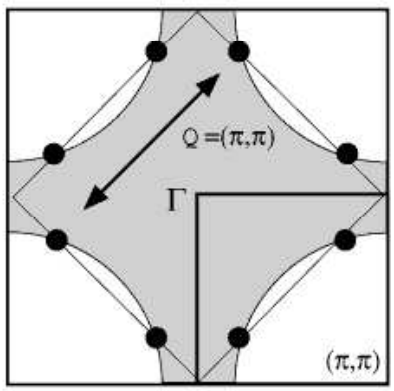

Figure 14: Fermi surface in the Brillouin zone and "hot spots" model. Magnetic zone appears in the presence of antiferromagnetic long – range order. "Hot spots" correspond to intersections of its borders with Fermi surface and are connected by the scattering vector of the order of $\mathbf{Q} = (\frac{\pi}{a}, \frac{\pi}{a})$.

we shall call this "hot spots" model. Correlation length of fluctuations of short – range antiferromagnetic order ξ, described by (11), is an important parameter of this theory. Note that in real HTSC – systems this length is not very large, usually $2a < \xi < 8a$ [45, 46].

Characteristic frequency of spin fluctuations ω_{sf}, depending on the compound and doping level, is usually in the limits of $10 - 100K$ [45, 46], so that in most part of the pseudogap region on the phase diagram we have $2\pi T \gg \omega_{sf}$ and actually can neglect spin dynamics, limiting ourselves to quasistatic approximation:

$$V_{eff}(\mathbf{q}) = W^2 \frac{\xi^2}{1 + \xi^2(\mathbf{q} - \mathbf{Q})^2} \tag{13}$$

where W is an effective parameter with dimensions of energy, which in the model of AFM fluctuations can be written as [47]:

$$W^2 = g^2 \frac{< \mathbf{S}_i^2 >}{3} = g^2 < (n_{i\uparrow} - n_{i\downarrow})^2 > \tag{14}$$

where g is interaction constant of electrons and spin fluctuations, $< \mathbf{S}_i^2 >$ is the average square of spin on a lattice site, $n_{i\uparrow}$, $n_{i\downarrow}$ – operators of a number of electrons on a given site with appropriate spin direction. In this approximation, dynamic field of spin fluctuations is just replaced by the static Gaussian random field of "quenched"[7] spins, antiferromagnetically correlated on lengths of the order of ξ.

It is clear that in the framework of our semiphenomenological approach, both correlation length ξ and parameter W are to be considered as some functions of carrier concentration (and temperature) to be determined from the experiment. In particular, W determines the effective width of the pseudogap. Full microscopic theory of the pseudogap state is not our aim here, and in the following we shall deal only with simple modelling of appropriate transformation of electronic spectrum and its influence on different physical properties, e.g. on superconductivity.

Considerable simplification of calculations can be achieved if we substitute (13) by model interaction of the following form [48] (similar simplification was first used in Ref. [49]):

$$V_{eff}(\mathbf{q}) = W^2 \frac{\xi^{-1}}{\xi^{-2} + (q_x - Q_x)^2} \frac{\xi^{-1}}{\xi^{-2} + (q_y - Q_y)^2} \tag{15}$$

In fact (15) is qualitatively quite similar to (13) and almost do not differ from it quantitatively in most interesting region of $|\mathbf{q} - \mathbf{Q}| < \xi^{-1}$. This introduces effective one – dimensionality into our problem.

[7] In this case all "loop" insertions into interaction lines of perturbation theory and corresponding to quantum corrections of higher orders to spin (or charge) fluctuations, and inevitably present in full dynamical problem, just vanish.

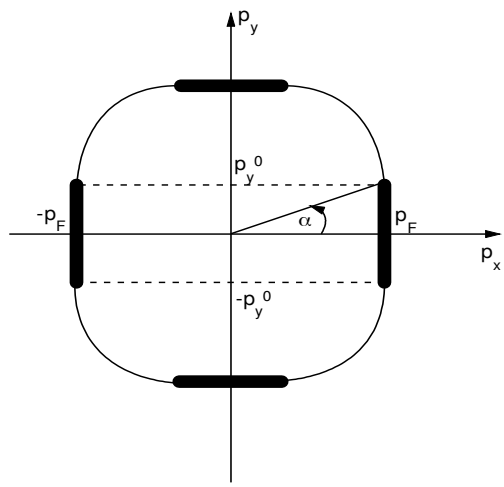

Figure 15: Fermi surface with "hot patches", which are shown by thick lines of the width $\sim \xi^{-1}$. The angle α determines the size of a "hot patch", $\alpha = \pi/4$ corresponds to the square Fermi surface.

Scattering by antiferromagnetic fluctuations in HTSC – oxides is not always most intensive at commensurate vector $\mathbf{Q} = (\pi/a, \pi/a)$, in general case $\mathbf{Q}$ may correspond to incommensurate scattering (see e.g. insert at Fig. 2). Taking into account the observed topology of the Fermi surface with flat parts, as shown in Fig. 2, we can introduce another model of scattering by fluctuations of short – range order, which we call the "hot patches" model [50]. In this model we assume the Fermi surface of two – dimensional electronic system as shown in Fig. 15. The size of "hot patches" is determined by the angular parameter α. It is well known that flat parts of the Fermi surface usually lead to instabilities towards formation of charge (CDW) or spin (SDW) density wave and formation of the appropriate long – range order and (dielectric) energy gap at these flat parts. We are interested in fluctuation region, when long – range order is not yet established. Fluctuations of the short – range order are again assumed to be static and Gaussian, and effective interaction is determined by (15), with scattering vectors $Q_x = \pm 2p_F$, $Q_y = 0$ or $Q_y = \pm 2p_F$, $Q_x = 0$. It is also assumed that fluctuations interact only with electrons from these flat ("hot") parts of the Fermi surface, shown in Fig. 15, so that this scattering is in fact one – dimensional. In the case of $\alpha = \pi/4$ we have just a square Fermi surface and purely one – dimensional problem. For $\alpha < \pi/4$ there are also "cold" parts of the Fermi surface, where scattering is either absent or small. The choice

of scattering vector $\mathbf{Q} = (\pm 2k_F, 0)$ or $\mathbf{Q} = (0, \pm 2p_F)$ corresponds, in general, to the case of incommensurate fluctuations, as the Fermi momentum p_F has no direct relation to the period of inverse lattice. Commensurate case can also be analyzed within this model [50].

Thus, the main idea of models under discussion reduces to the assumption of strong scattering by fluctuations of short – range order, which, according to (11), (15), is effective in a limited part of momentum space with characteristic size of the order of ξ^{-1} around "hot" spots or patches, which leads to pseudogap transformation of the spectrum in these regions. It will be seen in the following, that within our assumptions these models can be solved "nearly exactly", and much of the remaining discussion will be devoted to a description of this solution. Mostly we shall pay our attention to the discussion of the "hot spots" model as more "realistic" and not described in detail in previous reviews. As to "hot patches" model – detailed discussion and further references can be found in Ref. [21].

4 Elementary ("toy") model of the pseudogap.

Before we go to the analysis of "realistic hot spots model" it may be useful to consider an elementary one – dimensional model of the pseudogap, which allows an exact solution in analytic form [51]. Consider an electron moving in one dimension in a random field of Gaussian fluctuations with correlation function (in momentum representation and identified with an interaction line in appropriate diagram technique) of the following form:

$$V_{eff}(Q) = 2W^2 \left\{ \frac{\kappa}{(Q-2p_F)^2+\kappa^2} + \frac{\kappa}{(Q+2p_F)^2+\kappa^2} \right\} \tag{16}$$

where $\kappa = \xi^{-1}(T)$. The choice of scattering vector $Q \sim \pm 2p_F$, corresponds to the case of incommensurate fluctuations. An exact solution can be obtained in the asymptotic limit of $\xi \to \infty$ ($\kappa \to 0$), i.e. for very large correlation length of fluctuations of short range order[8]. Now we can sum *all* Feynman diagrams of perturbation theory for an "interaction" of the form of (16), which in this limit reduces to:

$$V_{eff}(Q) = 2\pi W^2 \{\delta(Q-2p_F) + \delta(Q+2p_F)\} \tag{17}$$

Consider the simplest contribution to self – energy of an electron, described by diagram shown in Fig. 16, which we write in Matsubara representation:

$$\Sigma(\varepsilon_n p) = \int \frac{dQ}{2\pi} V_{eff}(Q) \frac{1}{i\varepsilon_n - \xi_{p-Q}} \approx 2W^2 \int_{-\infty}^{\infty} \frac{dx}{2\pi} \frac{\kappa}{x^2+\kappa^2} \frac{1}{i\varepsilon_n + \xi_p - v_F x} =$$
$$= 2W^2 \int_{-\infty}^{\infty} \frac{dx}{2\pi} \frac{\kappa}{(x-i\kappa)(x+i\kappa)} \frac{1}{i\varepsilon_n + \xi_p - v_F x} =$$

[8] Let stress, that this limit here does not mean the establishment of any long – range order. Electron moves in the Gaussian random field with special pair correlator, not in periodic system.

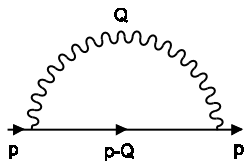

Figure 16: Simplest diagram for self – energy part of an electron. Wavy line denotes interaction $V_{eff}(Q)$.

$$= \frac{W^2}{i\varepsilon_n + \xi_p + iv_F\kappa} \qquad (18)$$

where, for definiteness, we assumed $p \sim +p_F$, $\varepsilon_n > 0$ and defined a new integration variable x as $Q = 2p_F + x$. We also used here "nesting" property of the spectrum $\xi_{p-2p_F} = -\xi_p$, which is always valid in one dimension for the standard $\xi_p = v_F(|p| - p_F)$.

The limit of $\xi(T) \to \infty$ ($\kappa \to 0$) should be understood as:

$$v_F\kappa = v_F\xi^{-1} \ll Max\{2\pi T, \xi_p\} \qquad (19)$$

or

$$v_F\kappa = v_F\xi^{-1} \ll 2\pi T, \qquad \xi(T) \gg |p - p_F|^{-1} \qquad (20)$$

Then (18) reduces to:

$$\Sigma(\varepsilon_n p) \approx \frac{W^2}{i\varepsilon_n + \xi_p} \qquad (21)$$

Now, for an "interaction" of the form of (17), there is no problem to write down the contribution of an arbitrary diagram of the type shown in Fig. 17. In such diagram, in the n – th order in $V_{eff}(Q)$ we have $2n$ vertices, connected, in all possible ways, by interaction lines. These lines alternatively[9] either "take away" or "bring" the momenta

[9] This alternation is important to guarantee that an electron remains close to the Fermi surface (points $\pm p_F$), or large denominators will appear in terms of perturbation theory. This is not important in the case of commensurate fluctuations, like period doubling, when we are dealing with tight – binding spectrum and "bringing" or "taking away" of any number of momenta $Q = (\pi/a, \pi/a)$ does not take electron far from the Fermi surface. In this case combinatorics of diagrams is different [52].

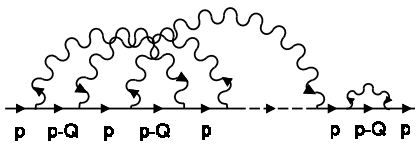

Figure 17: Diagram of an arbitrary order for the single – electron Green's function.

$Q = 2p_F$. As a result, the appropriate analytic expression for our diagram contains alternating Green's functions $\frac{1}{i\varepsilon_n - \xi_p}$ (entering n times) and $\frac{1}{i\varepsilon_n + \xi_p}$ (also entering n times) plus an extra (initial) $\frac{1}{i\varepsilon_n - \xi_p}$[10]. Also we have to take an account of the factor W^{2n}. Finally, we can see, that contributions of all diagrams in a given order just coincide and their sum can be determined from pure combinatorics and is determined just by their number, which is equal to $n!$. It is obvious — there are $2n$ points (vertices) with "ingoing" or "outgoing" interaction lines. Out of these, n points are connected with "outgoing" lines, which can "enter" the remaining "free" n vertices in any of $n!$ ways. Use now the identity[11]:

$$\sum_{n=0}^{\infty} n! z^n = \sum_{n=0}^{\infty} \int_0^{\infty} d\zeta e^{-\zeta} (\zeta z)^n = \int_0^{\infty} d\zeta e^{-\zeta} \frac{1}{1 - \zeta z} \tag{22}$$

Then we can easily sum the *whole* series for the Green's function and obtain the following exact solution:

$$G(\varepsilon_l p) = \sum_{n=0}^{\infty} \frac{W^{2n} n!}{(i\varepsilon_l - \xi_p)^n (i\varepsilon_l + \xi_p)^n (i\varepsilon_l - \xi_p)} \equiv \sum_{n=0}^{\infty} n! z^n (\varepsilon_l, \xi_p) G_0(\varepsilon_l \xi_p) =$$
$$= \int_0^{\infty} d\zeta e^{-\zeta} \frac{i\varepsilon_l + \xi_p}{(i\varepsilon_l)^2 - \xi_p^2 - \zeta W^2} \equiv < G_{\zeta W^2}(\varepsilon_l \xi_p) >_{\zeta}, \qquad \varepsilon_l = (2l+1)\pi T \tag{23}$$

[10]Of course, similar analysis applies to the problem with an arbitrary scattering vextor Q, when we have alternating $\frac{1}{i\varepsilon_n - \xi_p}$ and $\frac{1}{i\varepsilon_n - \xi_{p-Q}}$. We have taken $Q = 2p_F$ only to make formula more compact and to put the pseudogap precisely at the Fermi level.

[11]In mathematics this is called Borel summation.

where we have used the notation:

$$z(\varepsilon_l, \xi_p) = W^2 G_0(\varepsilon_l, \xi_p) G_0(\varepsilon_l, -\xi_p) \tag{24}$$

Now, what has appeared is just the "normal" Green's function of an insulator (of Peierls type):

$$G_{W^2}(\varepsilon_l p) = \frac{i\varepsilon_l + \xi_p}{(i\varepsilon_l)^2 - \xi_p^2 - W^2} \tag{25}$$

under the "averaging" procedure of the form:

$$< ... >_\zeta = \int_0^\infty d\zeta e^{-\zeta} ... \tag{26}$$

It is easy to convince yourself (formal proof, as well as many other details on this model can be found in Ref. [53]) that (23) is just the Green's function of an electron moving in an external field of the form $2V\cos(2p_F x + \phi)$, with amplitude "fluctuating" according to the so called Rayleigh distribution[12]:

$$\mathcal{P}(V) = \frac{2V}{W^2} e^{-\frac{V^2}{W^2}} \tag{27}$$

while the phase ϕ is distributed homogeneously on the interval from 0 to 2π.

Performing analytical continuation $i\varepsilon_l \to \varepsilon \pm i\delta$ from (23) we obtain (for $\varepsilon > 0$):

$$\begin{aligned} ImG^{R,A}(\varepsilon\xi_p) &= \mp\pi(\varepsilon + \xi_p) \int_0^\infty d\zeta e^{-\zeta} \delta(\varepsilon^2 - \xi_p^2 - \zeta W^2) = \\ &= \mp \frac{\pi}{W^2} (\varepsilon + \xi_p) \theta(\varepsilon^2 - \xi_p^2) e^{-\frac{\varepsilon^2 - \xi_p^2}{W^2}} \end{aligned} \tag{28}$$

so that the spectral density

$$A(\varepsilon\xi_p) = -\frac{1}{\pi} ImG^R(\varepsilon\xi_p) \tag{29}$$

has "non Fermi – liquid like " form, shown in Fig. 18. Let us stress, that our Green's function does not have any poles on the real axis of ε, which may correspond to quasi-particle energies as required in Fermi – liquid theory.

Electronic density of states has the following form:

$$\begin{aligned} \frac{N(\varepsilon)}{N_0(E_F)} &= \left|\frac{\varepsilon}{W}\right| \int_0^{\frac{\varepsilon^2}{W^2}} d\zeta \frac{e^{-\zeta}}{\sqrt{\frac{\varepsilon^2}{W^2} - \zeta}} = 2\left|\frac{\varepsilon}{W}\right| \exp\left(-\frac{\varepsilon^2}{W^2}\right) Erfi\left(\frac{\varepsilon}{W}\right) = \\ &= \begin{cases} 1 & \text{при} \quad |\varepsilon| \to \infty \\ \frac{2\varepsilon^2}{W^2} & \text{при} \quad |\varepsilon| \to 0 \end{cases} \end{aligned} \tag{30}$$

[12]This distribution is well known in statistical radiophysics, see e.g.: S.M.Rytov. Introduction to Statistical Radiophysics. Part I. "Nauka", Moscow, 1976.

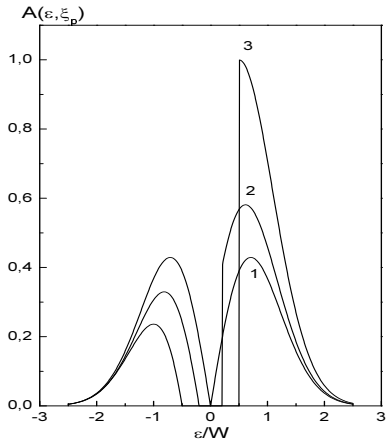

Figure 18: Spectral density in the model of pseudogap state: (1)—$\xi_p = 0$; (2)—$\xi_p = 0.1W$; (3)—$\xi_p = 0.5W$.

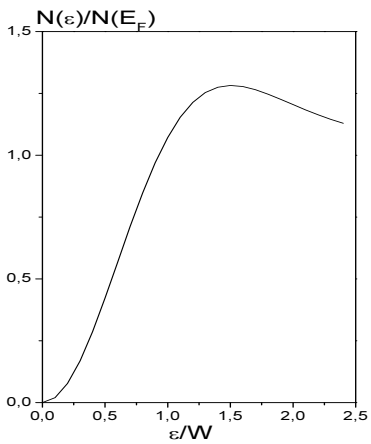

Figure 19: Density of states with pseudogap.

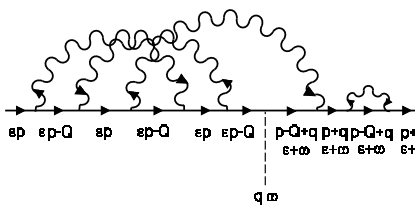

Figure 20: Diagram of an arbitrary order for the vertex part of an interaction with an external electromagnetic field.

where $N_0(E_F)$ is the density of states of free electrons at the Fermi level, and $Erfi(x) = \int_0^x dx e^{x^2}$ is error function of imaginary argument. Characteristic form of this density of states is shown in Fig. 19 and demonstrate the presence of a "soft" pseudogap around the Fermi level. Obviously, this is just the density of states of one – dimensional insulator with the energy gap $2V$, averaged over fluctuations of this gap with probability distribution (27).

Remarkable property of this model is the possibility of obtaining an exact solution (sum *all* diagrams) also for the response function to an external electromagnetic field [51, 53]. The arbitrary diagram for the vertex part, describing the response to an external field, can be obtained from an arbitrary diagram for the Green's function (of the type shown in Fig. 17) by an "insertion" of an external field line into any of electronic lines, as shown in Fig. 20. Making such "insertions" into all diagrams of the series (23) it is possible (after some long, but direct calculations) to sum the whole series for the vertwx part and obtain closed expression for response functions, e.g. for polarization operator. Details can be found in Refs. [51, 53]). However, the structure of an answer is clear without any calculations — you must just calculate the response of an insulator with fixed gap $2V$ and afterwards average the result over gap fluctuations with distribution function (27). In particular, for polarization operator we obtain the following elegant expression ($\omega_m = 2\pi m T$):

$$\Pi(\mathbf{q}\omega_m) = \int_0^\infty d\zeta e^{-\zeta} 2T \sum_n \int_{-\infty}^{\infty} \frac{dp}{2\pi} \{G_{\zeta W^2}(\varepsilon_n \mathbf{p}) G_{\zeta W^2}(\varepsilon_n + \omega_m \mathbf{p} + \mathbf{q}) +$$

$$+F_{\zeta W^2}(\varepsilon_n \mathbf{p}) F^+_{\zeta W^2}(\varepsilon_n + \omega_m \mathbf{p} + \mathbf{q})\Big\} =< \Pi_{\zeta W^2}(\mathbf{q}\omega_m) >_\zeta \tag{31}$$

where automatically appears the product of two "anomalous" Green's functions:

$$F(\varepsilon_n p) = \frac{W^*}{(i\varepsilon_n)^2 - \xi_p^2 - |W|^2}, \quad F^+(\varepsilon_n + \omega_m p) = \frac{W}{(i\varepsilon_n + i\omega_m)^2 - \xi_p^2 - |W|^2} \tag{32}$$

describing Umklapp processes in a system with long – range order [53]. Due to the absence of any long – range order in our model, the value of (32) vanishes after averaging over phase, while the average of pair of these functions in two – particle response (31) is non zero. Finally, under the averaging procedure over the gap fluctuations we have simply the polarization operator of an insulator (of Peierls type).

The real part of conductivity for such one – dimensional insulator with fixed gap $2W$ has the following form [53]:

$$Re\sigma_{W^2}(\omega) = \begin{cases} \frac{ne^2}{m\omega} \frac{\pi}{\sqrt{\frac{\omega^2}{4W^2}-1}} \frac{W}{\omega} & \text{при} \quad |\omega| > 2W \\ 0 \quad \text{при} \quad |\omega| < 2W \end{cases} \tag{33}$$

It is seen, that absorption of electromagnetic energy is going through quasiparticle excitation via the energy gap and is non zero for $\omega > 2W$. In the pseudogap state this expression must be averaged over fluctuations of W, described by distribution function (26) or (27). So finally, from (33) we get:

$$Re\sigma(\omega) = \frac{\omega_p^2}{4} \frac{W}{\omega^2} \int_0^{\frac{\omega^2}{4W^2}} d\zeta e^{-\zeta} \frac{\zeta}{\sqrt{\frac{\omega^2}{4W^2} - \zeta}} \tag{34}$$

Appropriate frequency dependence id shown in Fig. 21. We can see characteristic smooth maximum of absorption through the pseudogap.

This elementary model of the pseudogap state is very useful for an analysis of a number of problems. It is easily generalized to two – dimensional case for the "hot patches" model [50]. This allows the analysis of the problem of formation of superconducting state on the "background" of this (dielectric) pseudogap [50, 54, 55, 59, 56]. In particular, due to the possibility of obtaining an exact solution in closed analytic form, it is possible to study rather fine problems of the absence of self – averaging property of superconducting order parameter in the random field of pseudogap fluctuations [54], showing the possible mechanism of formation of local inhomogeneities ("superconducting drops") at temperatures higher than the mean – field critical temperature of superconducting transition. This may help to explain e.g. experimentally observed manifestations of superconductivity at these high temperatures (like anomalous Nernst effect), which are usually interpreted in the spirit of superconducting scenario of pseudogap formation. Possible direct connection with the picture of inhomogeneous superconductivity, observed in STM experiments [17, 18], is also obvious.

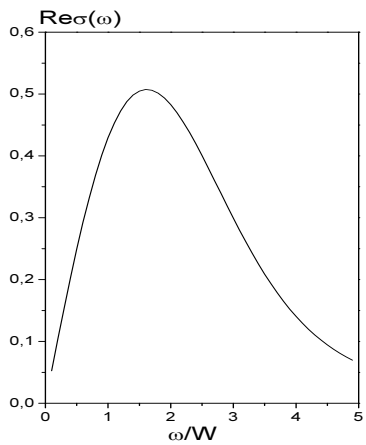

Figure 21: Frequency dependence of the real part of conductivity in the pseudogap state. Conductivity is given in units of $\frac{\omega_p^2}{4\pi W}$.

However, advantages of the model determine also its deficiencies. In particular, absolutely unrealistic is asymptotics of infinite correlation length of pseudogap fluctuations. In real systems, as was noted above, this correlation length is usually not larger than few interatomic spacings. Besides that, the growth of correlation length inevitably leads to the breaking of our assumption of the Gaussian nature of pseudogap fluctuations. Analysis of effects of finiteness of correlation length is actually a complicated problem. For one – dimensional model such generalization of the model under discussion was proposed in Ref. [57]. It was shown, that as correlation length ξ becomes smaller, it leads to smooth "filling" of the pseudogap, due to the growth of the scattering parameter v_F/ξ, i.e. of the inverse time of flight of an electron through the region of the size of $\sim \xi$, where effectively we have "dielectric" ordering. The method used in Ref. [57] forms the basis of appropriate generalization to two dimensions [48, 47], which will be discussed below during our analysis of "hot spots" model. Let us also mention the simplified version of one – dimensional model with finite correlation length, similar in spirit to the model of Ref. [51, 57], proposed in Ref. [58] and used in Ref. [59] to analyze the problems of self – averaging properties of superconducting order parameter in the "hot patches" model.

5 "Hot spots" model.

5.1 "Nearly exact" solution for one – particle Green's function.

Let us now describe our "nearly exact" solution for "hot spots" model. Consider first – order (in V_{eff} (15)) contribution to electron self – energy, corresponding to simplest

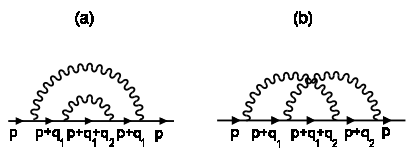

Figure 22: Diagrams of second order in effective interaction with pseudogap fluctuations.

diagram, shown in Fig. 16:

$$\Sigma(\varepsilon_n \mathbf{p}) = \sum_{\mathbf{q}} V_{eff}(\mathbf{q}) \frac{1}{i\varepsilon_n - \xi_{\mathbf{p}+\mathbf{q}}} \tag{35}$$

For large enough correlation lengths ξ, the main contribution to the sum over $\mathbf{q}$ comes from the vicinity of $\mathbf{Q} = (\pi/a, \pi/a)$. Then we can write:

$$\xi_{\mathbf{p}+\mathbf{q}} = \xi_{\mathbf{p}+\mathbf{Q}+\mathbf{k}} \approx \xi_{\mathbf{p}+\mathbf{Q}} + \mathbf{v}_{\mathbf{p}+\mathbf{Q}}\mathbf{k} \tag{36}$$

where $\mathbf{v}_{\mathbf{p}+\mathbf{Q}} = \frac{\partial \xi_{\mathbf{p}+\mathbf{Q}}}{\partial \mathbf{p}}$ is the appropriate velocity of a quasiparticle on the Fermi surface. Then (35) is easily calculated and we get:

$$\Sigma(\varepsilon_n \mathbf{p}) = \frac{W^2}{i\varepsilon_n - \xi_{\mathbf{p}+\mathbf{Q}} + i(|v^x_{\mathbf{p}+\mathbf{Q}}| + |v^y_{\mathbf{p}+\mathbf{Q}}|)\kappa sign \varepsilon_n} \tag{37}$$

where $\kappa = \xi^{-1}$. Let us stress that both here and below "linearization" of the quasiparticle spectrum (36) under the integral (35) is performed only over small, due to large enough ξ, correction (of the order of $v_F \xi^{-1}$) to the spectrum close to the Fermi surface, while the forms of the spectrum itself $\xi_{\mathbf{p}}$ and $\xi_{\mathbf{p}+\mathbf{Q}}$ are given by the general expression (10) with $\xi_{\mathbf{p}} = \varepsilon_{\mathbf{p}} - \mu$.

Consider now correction of the second order, shown in Fig. 22. Using (15) we obtain:

$$\Sigma(a) = W^4 \int \frac{d\mathbf{k_1}}{\pi^2} \int \frac{d\mathbf{k_2}}{\pi^2} \frac{\kappa}{\kappa^2 + k_{1x}^2} \frac{\kappa}{\kappa^2 + k_{1y}^2} \frac{\kappa}{\kappa^2 + k_{2x}^2} \frac{\kappa}{\kappa^2 + k_{2y}^2}$$
$$\frac{1}{i\varepsilon_n - \xi_{\mathbf{p+Q}} - v^x_{\mathbf{p+Q}} k_{1x} - v^y_{\mathbf{p+Q}} k_{1y}} \frac{1}{i\varepsilon_n - \xi_{\mathbf{p}} - v^x_{\mathbf{p}}(k_{1x} + k_{2x}) - v^y_{\mathbf{p}}(k_{1y} + k_{2y})}$$
$$\frac{1}{i\varepsilon_n - \xi_{\mathbf{p+Q}} - v^x_{\mathbf{p+Q}} k_{1x} - v^y_{\mathbf{p+Q}} k_{1y}} \tag{38}$$

$$\Sigma(b) = W^4 \int \frac{d\mathbf{k_1}}{\pi^2} \int \frac{d\mathbf{k_2}}{\pi^2} \frac{\kappa}{\kappa^2 + k_{1x}^2} \frac{\kappa}{\kappa^2 + k_{1y}^2} \frac{\kappa}{\kappa^2 + k_{2x}^2} \frac{\kappa}{\kappa^2 + k_{2y}^2}$$
$$\frac{1}{i\varepsilon_n - \xi_{\mathbf{p+Q}} - v^x_{\mathbf{p+Q}} k_{1x} - v^y_{\mathbf{p+Q}} k_{1y}} \frac{1}{i\varepsilon_n - \xi_{\mathbf{p}} - v^x_{\mathbf{p}}(k_{1x} + k_{2x}) - v^y_{\mathbf{p}}(k_{1y} + k_{2y})}$$
$$\frac{1}{i\varepsilon_n - \xi_{\mathbf{p+Q}} - v^x_{\mathbf{p+Q}} k_{2x} - v^y_{\mathbf{p+Q}} k_{2y}} \tag{39}$$

where we have used the explicit form of the spectrum (10), from which it follows, in particular, that $\xi_{\mathbf{p+2Q}} = \xi_{\mathbf{p}}$, $\mathbf{v_{p+2Q}} = \mathbf{v_p}$ for $\mathbf{Q} = (\pi/a, \pi/a)$. If the signs of $v^x_{\mathbf{p}}$ and $v^x_{\mathbf{p+Q}}$, as well as of $v^y_{\mathbf{p}}$ and $v^y_{\mathbf{p+Q}}$ coincide, the integrals in (38) and (39) are completely determined by contributions from the poles of Lorentzians, which describe interaction with fluctuations of short – range order, so that after elementary contour integration we get:

$$\Sigma(a) = \Sigma(b) = \frac{W^4}{[i\varepsilon_n - \xi_{\mathbf{p+Q}} + i(|v^x_{\mathbf{p+Q}}| + |v^y_{\mathbf{p+Q}}|)\kappa]^2} \frac{1}{i\varepsilon_n - \xi_{\mathbf{p}} + i2(|v^x_{\mathbf{p}}| + |v^y_{\mathbf{p}}|)\kappa} \tag{40}$$

Here and in the following, for definiteness, we assume $\varepsilon_n > 0$.

It is not difficult to convince yourself, that in case of coinciding signs of velocity projections at "hot spots", similar calculation is valid for an arbitrary diagram of higher order.

Thus, in case of coinciding signs of velocity projections at the Fermi surface $v^x_{\mathbf{p}}$ and $v^x_{\mathbf{p+Q}}$, and those of $v^y_{\mathbf{p}}$ and $v^y_{\mathbf{p+Q}}$, Feynman integrals in any diagram of arbitrary order are determined only by contributions form the poles of Lorentzians in (15) and are easily calculated. Similar situation holds also in the case of velocities at "hot spots", connected by vector $\mathbf{Q}$, are perpendicular to each other. In this case the contribution of an arbitrary diagram of N – th order in (15) for electron self – energy has the following form:

$$\Sigma^{(N)}(\varepsilon_n \mathbf{p}) = W^{2N} \prod_{j=1}^{2N-1} \frac{1}{i\varepsilon_n - \xi_j(\mathbf{p}) + i n_j v_j \kappa} \tag{41}$$

where $\xi_j(\mathbf{p}) = \xi_{\mathbf{p+Q}}$ and $v_j = |v^x_{\mathbf{p+Q}}| + |v^y_{\mathbf{p+Q}}|$ for odd j and $\xi_j(\mathbf{p}) = \xi_{\mathbf{p}}$ and $v_j = |v^x_{\mathbf{p}}| + |v^y_{\mathbf{p}}|$ for even j. Here n_j is the number of interaction lines, surrounding j – th Green's function (counting from the first one in diagram) and we again take $\varepsilon_n > 0$.

In Ref. [48] we have studied in detail when these conditions on velocity projections are satisfied in the points of the Fermi surface connected by vector $\mathbf{Q}$ ("hot spots") and have presented explicit examples of appropriate geometries of the fermi surface, which can be realized for specific relations between parameters t and t' in (10). In these cases expression (41) is exact, with only limitation being related to our use of "linearization" (36). In all other cases (for other relations between t and t') we use (41) as rather successful *Ansatz*

for the contribution of an arbitrary order, obtained by simple continuation of spectrum parameters t and t' to the region of interest to us. Even in most inappropriate one – dimensional case [57], corresponding to square Fermi surface, appearing for (10) if $t' = 0$ and $\mu = 0$, the use of this *Ansatz* produces results (e.g. for the density of state) which are very close quantitatively [60] to the results of an exact numerical simulation of this problem [61].

Generally speaking, note that in standard diagrammatic approaches we usually perform summation some *subseries* of diagrams, which are considered as dominant over some smallness parameter. Here we are dealing with much more rare situation — we can sum the *whole* diagram series, though contribution of each diagram is calculated probably approximately. It is in this sense that we use the term "nearly exact" solution.

Using *Ansatz* (41) we can see, that *the contribution of an arbitrary diagram with intersecting interaction lines is actually equal to the contribution of some diagram of the same order without intersections of these lines* [57]. Thus, in fact we can limit ourselves to consideration of only diagrams without intersecting interaction lines, taking the contribution of diagrams with intersections into account with the help of additional combinatorial factors, which are attributed to "initial" vertices or just interaction lines [57]. As a result we obtain the following recursion relation (continuous fraction representation [57]), which gives an effective algorithm for numerical computations [48]:

$$G_k(\varepsilon_n \xi_{\mathbf{p}}) = \frac{1}{i\varepsilon_n - \xi_k(\mathbf{p}) + ikv_k\kappa - \Sigma_{k+1}(\varepsilon_n \xi_{\mathbf{p}})} \equiv$$
$$\equiv \left\{ G_{0k}^{-1}(\varepsilon_n \xi_{\mathbf{p}}) - \Sigma_{k+1}(\varepsilon_n \xi_{\mathbf{p}}) \right\}^{-1} \tag{42}$$

$$\Sigma_k(\varepsilon_n \xi_{\mathbf{p}}) = W^2 \frac{v(k)}{i\varepsilon_n - \xi_k(\mathbf{p}) + ikv_k\kappa - \Sigma_{k+1}(\varepsilon_n \xi_{\mathbf{p}})} \tag{43}$$

Graphically this recursion relation for the Green's function is shown in Fig. 23. The "physical" Green's function is obtained as: $G(\varepsilon_n \xi_{\mathbf{p}}) = G_{k=0}(\varepsilon_n \xi_{\mathbf{p}})$. In (42) we also defined:

$$G_{0k}(\varepsilon_n \xi_{\mathbf{p}}) = \frac{1}{i\varepsilon_n - \xi_k(\mathbf{p}) + ikv_k\kappa} \tag{44}$$

Combinatorial factor:

$$v(k) = k \tag{45}$$

for the case of commensurate fluctuations with $\mathbf{Q} = (\pi/a, \pi/a)$ [57], if we don not take into spin structure od interaction (CDW – type fluctuations). For incommensurate CDW fluctuations [57]:

$$v(k) = \begin{cases} \frac{k+1}{2} & \text{for odd } k \\ \frac{k}{2} & \text{for even } k \end{cases} \tag{46}$$

If we take into account (Heisenberg) spin structure of interaction with pseudogap fluctuations in "nearly antiferromagnetic Fermi – liquid" (spin – fermion model [47]),

Figure 23: Graphical representation of recursion relation for the single – particle Green's function.

combinatorics of diagrams becomes more complicated. Thus, spin – conserving scattering processes obey commensurate combinatorics, while spin – flip scattering is described by diagrams of incommensurate case ("charged" random field in terms of Ref. [47]). In this model recursion relation for the Green's function again is given by (43), but combinatorial factor $v(k)$ takes now the following form [47]:

$$v(k) = \begin{cases} \frac{k+2}{3} & \text{for odd } k \\ \frac{k}{3} & \text{for even } k \end{cases} \tag{47}$$

The obtained solution for the single – particle Green's function is asymptotically exact in the limit of $\xi \to \infty$, when solution can be found also in analytical form [51, 47]. It is also exact in trivial limit of $\xi \to 0$, when for fixed values of W interaction (15) just vanishes. For all intermediate values of ξ our solution gives, as already noted, very good interpolation, being practically exact for certain geometries of the Fermi surface, appearing for certain relations between parameters of the spectrum (10) [48]. Note also that our formalism can be easily used also to describe pseudogap within superconducting scenario [48, 62]. Our preference for "dielectric" scenario is based mainly on physical considerations.

Using (42) we can easily perform numerical calculations of single – electron spectral density:

$$A(E\mathbf{p}) = -\frac{1}{\pi} Im G^R(E\mathbf{p}) \tag{48}$$

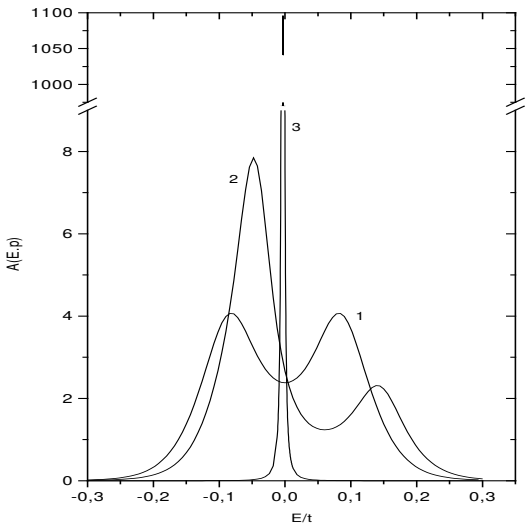

Figure 24: Spectral density in the "hot spots" model, the case of incommensurate fluctuations, $\kappa a = 0.01$: (1) – at the "hot spot" $p_x a/\pi = 0.142, p_y a/\pi = 0.587$, (2) – close to "hot spot" at $p_x a/\pi = 0.145, p_y a/\pi = 0.843$, (3) – far from "hot spot" at $p_x a/\pi = p_y/\pi = 0.375$.

which can also be determined from ARPES experiments [21]. In (48) $G^R(E\mathbf{p})$ represents retarded Green's function obtained by the usual analytic continuation of (42) from Matsubara frequencies to the real axis of E. Analogously we cam compute single – particle density of states as:

$$N(E) = \sum_{\mathbf{p}} A(E\mathbf{p}) = -\frac{1}{\pi} \sum_{\mathbf{p}} ImG^R(E\mathbf{p}) \tag{49}$$

Details of these calculations and discussion of the results for our two – dimensional model can be found in Refs. [47, 48]. Here we shall demonstrate only few most important results.

As a typical example in Fig. 24 we show the results [48] for spectral density of electrons for the incommensurate (CDW) case. We can see that spectral density close to the "hot spot" has an expected non Fermi – liquid like form and there are no well defined quasiparticle peaks. Far from the "hot spot" spectral density is characterized by a narrow peak, corresponding to well defined quasiparticles (Fermi – liquid). In Fig. 25 from Ref. [47] we show the product of the Fermi distribution and spectral density at different points of the "renormalized" Fermi surface, defined by the equation $\varepsilon_{\mathbf{p}} - Re\Sigma(E = 0\mathbf{p}) = 0$, where the "bare" spectrum $\varepsilon_{\mathbf{p}}$ is given by (10) with $t = -0.25eV, t' = -0.35t$ and for hole concentration $n_h = 0.16$, with coupling constant in (11) $g = 0.8eV$ and correlation length $\xi = 3a$ (commensurate case, spin – fermion model). We can clearly see complete qualitative agreement with ARPES data discussed above with quite different behavior close and far from the "hot spot". Finally, in Fig. 26 taken from Ref. [47] we show calculated (for spin fermion – model) positions of the maximum of $A(\omega\mathbf{k})$ for two different

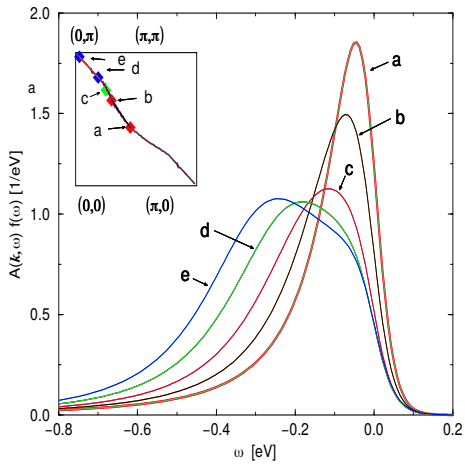

Figure 25: The product of spectral density and Fermi distribution function at different points on the Fermi surface, shown at the insert. Spin – fermion model, correlation length $\xi = 3a$.

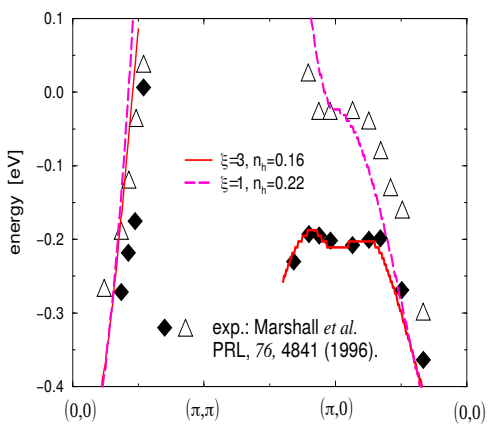

Figure 26: Positions of the maximum of the spectral density for different values of correlation length ξ and hole concentrations, calculated for spin – fermion model and compared with ARPES data for $Bi_2Sr_2Ca_{1-x}Dy_xCu_2O_{8+\delta}$ with $x = 1$ (triangles) and $x = 0.175$ (diamonds).

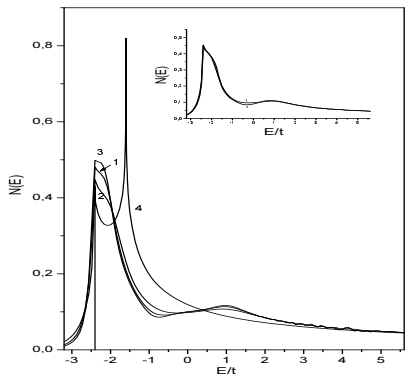

Figure 27: Single – electron density of states (in units of $1/ta^2$) for for different combinatorics of diagrams and $t'/t = -0.4$, $\mu/t = -1.3$, which is typical for HTSC – cuprates: (1) — incommensurate case, (2) — commensurate case, (3) — combinatorics of spin – fermion model, (4) — in the absence of pdeudogap fluctuations. We assume $W/t = 1$ and correlation length $\kappa a = 0.1$. At the insert: Density of states for commensurate combinatorics and: (1)—$\kappa a = 0.1$; (2)—$\kappa a = 0.01$

concentrations of holes compared with appropriate experimental ARPES data of Ref. [63] for $Bi_2Sr_2Ca_{1-x}Dy_xCu_2O_{8+\delta}$. The point is, that positions of the maxima of spectral density in the plane of $(\omega, \mathbf{k})$, determined from ARPES, in an ideal system of the Fermi – liquid type define dispersion (spectrum) of quasiparticles (cf. Fig. 5(a)). For overdoped system the values of $n_h = 0.22$ and $\xi = a$ were assumed during these calculations. The results obtained demonstrate rather well defined dispersion curves both along the diagonal of Brillouin zone, and in the direction $(0,0) - (\pi, 0)$. For underdoped system it was assumed that $n_h = 0.16$ and $\xi = 3a$. In this case, in diagonal direction we again see spectral curve crossing the Fermi level, while close to "hot spots" (in the vicinity of $(\pi, 0)$) there is seen only a smeared maximum of spectral density remaining approximately 200 meV below the Fermi level (pseudogap). In general, agreement between theory and experiment is rather satisfactory.

Ley us now consider the single – electron density of states, defined by the integral of the spectral density $A(E\mathbf{p})$ over the whole Brillouin zone. Detailed calculations of the density of states in "hot spots" model were performed in Ref. [48]. As an example, in Fig. 27 we show appropriate data for the Fermi surface topology typical for HTSC – systems. We can see, that for typical value $t'/t = -0.4$ there is a shallow minimum in the density of states (pseudogap), which is only slightly dependent on the value of correlation length ξ. At the same time, e.g. for $t'/t = -0.6$ (which is untypical for HTSC – cuprates) there are "hot spots" on the Fermi surface, but pseudogap in the density of states is practically unobservable [48]. We can see only smearing of Van Hove singularity, which is present for an ideal case in the absence of pseudogap scattering. In this sense most clear manifestations of the pseudogap behavior are not in the density of states, but in spectral

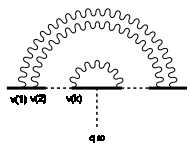

Figure 28: General form of higher order correction to the vertex part.

density, which is in general accordance with experiments.

5.2 Recurrence relations for the vertex part and optical conductivity.

To calculate optical conductivity we need to know the vertex part, describing electromagnetic response of our system. This vertex part can be found using the method, proposed for similar one – dimensional model in Refs. [64, 65]. Below we are following Ref. [66]. Above we have seen, that any diagram for irreducible vertex part can be obtained by the insertion of an external field line in appropriate diagram for electron self – energy [51]. As in our model it is sufficient to take account only of self – energy diagrams without intersecting interaction lines with additional combinatorial factors $v(k)$ in "initial" vertices, to calculate vertex corrections it is possible to limit ourselves only to diagrams of the type shown in Fig. 28. Diagrams with intersecting interaction lines are also accounted for automatically. Now we immediately obtain the system of recursion equations for the vertex parts, shown graphically in Fig. 29. To obtain appropriate analytic expressions, consider the simplest vertex correction, shown in Fig. 30 (a). Performing calculations for $T = 0$ in RA – channel, we can easily obtain its contribution as:

$$\mathcal{J}_1^{(1)RA}(\varepsilon\mathbf{p};\varepsilon+\omega\mathbf{p}+\mathbf{q}) = \sum_{\mathbf{K}} V_{eff}(\mathbf{K}) G_{00}^{A}(\varepsilon\xi_{\mathbf{p}-\mathbf{K}}) G_{00}^{R}(\varepsilon+\omega\xi_{\mathbf{p}-\mathbf{K}+\mathbf{q}}) =$$

$$= W^2 \left\{ G_{00}^{A}(\varepsilon,\xi_1(\mathbf{p})+iv_1\kappa) - G_{00}^{R}(\varepsilon+\omega,\xi_1(\mathbf{p}+\mathbf{q})-iv_1\kappa) \right\} \frac{1}{\omega+\xi_1(\mathbf{p})-\xi_1(\mathbf{p}+\mathbf{q})} =$$

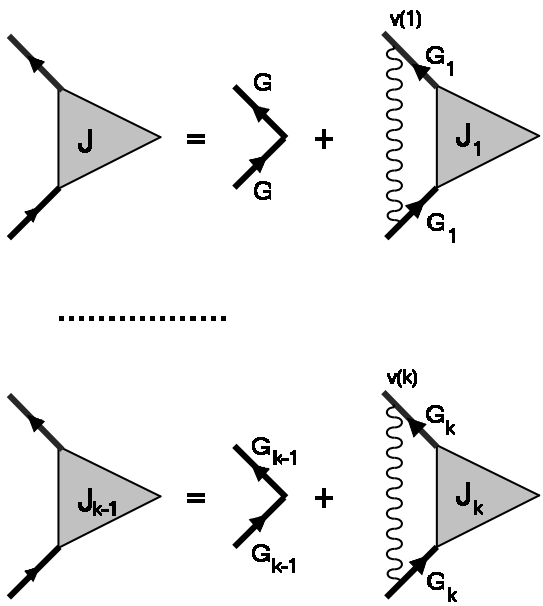

Figure 29: Recursion relations for the vertex part.

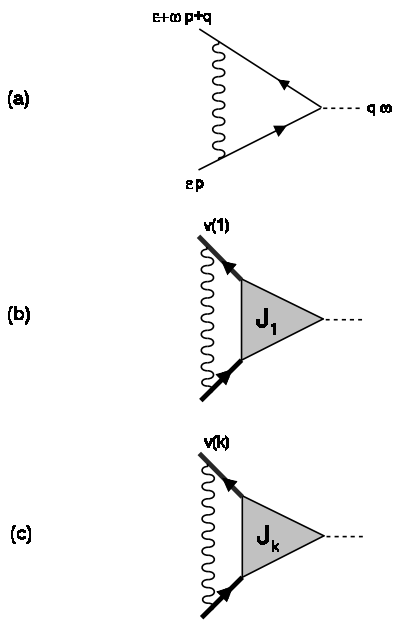

Figure 30: Simplest corrections to the vertex parts.

$$= W^2 G^A_{00}(\varepsilon, \xi_1(\mathbf{p}) + iv_1\kappa) G^R_{00}(\varepsilon+\omega, \xi_1(\mathbf{p}+\mathbf{q}) - iv_1\kappa) \left\{ 1 + \frac{2iv_1\kappa}{\omega + \xi_1(\mathbf{p}) - \xi_1(\mathbf{p}+\mathbf{q})} \right\} \equiv$$

$$\equiv W^2 G^A_{01}(\varepsilon, \xi_{\mathbf{p}}) G^R_{01}(\varepsilon+\omega, \xi_{\mathbf{p}+\mathbf{q}}) \left\{ 1 + \frac{2iv_1\kappa}{\omega + \xi_1(\mathbf{p}) - \xi_1(\mathbf{p}+\mathbf{q})} \right\} \tag{50}$$

where, during calculations of integrals, we have used the following identity, valid for free – particle Green's functions:

$$G^A_{00}(\varepsilon\xi_{\mathbf{p}}) G^R_{00}(\varepsilon+\omega\xi_{\mathbf{p}+\mathbf{q}}) = \left\{ G^A_{00}(\varepsilon\xi_{\mathbf{p}}) - G^R_{00}(\varepsilon+\omega\xi_{\mathbf{p}+\mathbf{q}}) \right\} \frac{1}{\omega - \xi_{\mathbf{p}+\mathbf{q}} + \xi_{\mathbf{p}}} \tag{51}$$

"Dressing" internal electronic lines we obtain diagram, shown in Fig. 30 (b), and using the identity:

$$G^A(\varepsilon\xi_{\mathbf{p}}) G^R(\varepsilon+\omega\xi_{\mathbf{p}+\mathbf{q}}) = \left\{ G^A(\varepsilon\xi_{\mathbf{p}}) - G^R(\varepsilon+\omega\xi_{\mathbf{p}+\mathbf{q}}) \right\} \times$$

$$\times \frac{1}{\omega - \xi_{\mathbf{p}+\mathbf{q}} + \xi_{\mathbf{p}} - \Sigma^R_1(\varepsilon+\omega\xi_{\mathbf{p}+\mathbf{q}}) + \Sigma^A_1(\varepsilon\xi_{\mathbf{p}})} \tag{52}$$

valid for full Green's functions, we can write down the contribution of this diagram as:

$$\mathcal{J}^{RA}_1(\varepsilon\mathbf{p}; \varepsilon+\omega\mathbf{p}+\mathbf{q}) = W^2 v(1) G^A_1(\varepsilon, \xi_{\mathbf{p}}) G^R_1(\varepsilon+\omega, \xi_{\mathbf{p}+\mathbf{q}}) \Bigg\{ 1 +$$

$$+ \frac{2iv_1\kappa}{\omega - \xi_1(\mathbf{p}+\mathbf{q}) + \xi_1(\mathbf{p}) - \Sigma^R_2(\varepsilon+\omega\xi_{\mathbf{p}+\mathbf{q}}) + \Sigma^A_2(\varepsilon\xi_{\mathbf{p}})} \Bigg\} J^{RA}_1(\varepsilon\mathbf{p}; \varepsilon+\omega\mathbf{p}+\mathbf{q}) \tag{53}$$

Here we assumed, that interaction line in the vertex correction diagram of Fig. 30 (b) "transforms" self – energies $\Sigma^{R,A}_1$ of internal electronic lines into $\Sigma^{R,A}_2$, in accordance with our main approximation for self – energies used above (cf. Fig. 23)[13].

Now it is not difficult to write down similar expression for the diagram of general form, shown in Fig. 30 (c):

$$\mathcal{J}^{RA}_k(\varepsilon\mathbf{p}; \varepsilon+\omega\mathbf{p}+\mathbf{q}) = W^2 v(k) G^A_k(\varepsilon, \xi_{\mathbf{p}}) G^R_k(\varepsilon+\omega, \xi_{\mathbf{p}+\mathbf{q}}) \Bigg\{ 1 +$$

$$+ \frac{2iv_k\kappa k}{\omega - \xi_k(\mathbf{p}+\mathbf{q}) + \xi_k(\mathbf{p}) - \Sigma^R_{k+1}(\varepsilon+\omega\xi_{\mathbf{p}+\mathbf{q}}) + \Sigma^A_{k+1}(\varepsilon\xi_{\mathbf{p}})} \Bigg\} J^{RA}_k(\varepsilon\mathbf{p}; \varepsilon+\omega\mathbf{p}+\mathbf{q}) \tag{54}$$

Accordingly, we can write dowm the following fundamental recursion relation for the vertex part, shown in Fig. 23:

$$J^{RA}_{k-1}(\varepsilon\mathbf{p}; \varepsilon+\omega\mathbf{p}+\mathbf{q}) = 1 + W^2 v(k) G^A_k(\varepsilon, \xi_{\mathbf{p}}) G^R_k(\varepsilon+\omega, \xi_{\mathbf{p}+\mathbf{q}}) \Bigg\{ 1 +$$

[13] This assumption is justified by the fact, that it guarantees validity of certain exact relation, following from the Ward identity (see below) [64].

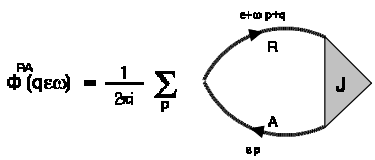

Figure 31: Diagrammatic representation for two – particle function $\Phi^{RA}(q\omega)$.

$$+\frac{2iv_k\kappa k}{\omega-\xi_k(\mathbf{p}+\mathbf{q})+\xi_k(\mathbf{p})-\Sigma^R_{k+1}(\varepsilon+\omega\xi_{\mathbf{p}+\mathbf{q}})+\Sigma^A_{k+1}(\varepsilon\xi_{\mathbf{p}})}\Bigg\}\, J^{RA}_k(\varepsilon\mathbf{p};\varepsilon+\omega\mathbf{p}+\mathbf{q}) \tag{55}$$

"Physical" vertex $J^{RA}(\varepsilon\mathbf{p};\varepsilon+\omega\mathbf{p}+\mathbf{q})$ is defined as $J^{RA}_{k=0}(\varepsilon\mathbf{p};\varepsilon+\omega\mathbf{p}+\mathbf{q})$. Recursion procedure (55) takes into account all diagrams of perturbation theory for the vertex part. For $\kappa\to 0$ $(\xi\to\infty)$ (55) redoces to the series. studied in Refs. [51] (see also Ref. [47]), which can be summed exactly in analytic form. Standard "ladder" approximation is obtained from our scheme putting all combinatorial factors $v(k)$ in (55) to unity [65].

Conductivity is expressed via retarded density – density response function $\chi^R(q\omega)$ [67]:

$$\sigma(\omega)=e^2\lim_{q\to 0}\left(-\frac{i\omega}{q^2}\right)\chi^R(q\omega) \tag{56}$$

where e is electronic charge,

$$\chi^R(q\omega)=\omega\left\{\Phi^{RA}(0q\omega)-\Phi^{RA}(00\omega)\right\} \tag{57}$$

where two – particle Green's function $\Phi^{RA}(\varepsilon q\omega)$ is defined by loop diagram shown in Fig. 31.

Direct numerical computations confirm, that the recurrence procedure (55) satisfies an exact relation, which directly follows (for $\omega\to 0$) from the Ward identity [67]:

$$\Phi^{RA}(00\omega)=-\frac{N(E_F)}{\omega} \tag{58}$$

where $N(E_F)$ is the density of states at the Fermi level $E_F = \mu$. Actually, this is our main motivation for the *Ansatz*, used during the derivation of (53), (54) and (55).

Finally, conductivity is written in the following symmetrized form, convenient for numerical computations:

$$\sigma(\omega) = \frac{e^2\omega^2}{\pi} \lim_{q\to 0} \frac{1}{q^2} \sum_{\mathbf{p}} \Big\{ G^R\left(\frac{\omega}{2}, \mathbf{p}+\frac{\mathbf{q}}{2}\right) J^{RA}\left(\frac{\omega}{2}, \mathbf{p}+\frac{\mathbf{q}}{2}; -\frac{\omega}{2}, \mathbf{p}-\frac{\mathbf{q}}{2}\right) G^A\left(-\frac{\omega}{2}, \mathbf{p}-\frac{\mathbf{q}}{2}\right) - \\ -G^R\left(\frac{\omega}{2}, \mathbf{p}\right) J^{RA}\left(\frac{\omega}{2}, \mathbf{p}; -\frac{\omega}{2}, \mathbf{p}\right) G^A\left(-\frac{\omega}{2}, \mathbf{p}\right) \Big\} \tag{59}$$

where we also accounted for an extra factor of 2, due to summation over spin.

Direct numerical calculations [66] were performed, for different values of parameters of the "bare" spectrum (10), using (59), (55), (42), with recursion procedure starting at some high value of k, where all Σ_k and J_k were assumed to be zero. Integration in (59) was made over the Brillouin zone. Integration momenta are naturally made dimensionless with the help of lattice constant a, all energies below are given in units of transfer integral t. Conductivity is measured in units of universal conductivity of two – dimensional system: $\sigma_0 = \frac{e^2}{\hbar} = 2.5\ 10^{-4}$ Ohm^{-1}, and density of states — in units of $1/ta^2$. For definiteness, below we always take $W = t$.

First let us consider Fermi surfaces close to the case of half – filled band $\mu = 0$ and $t' = 0$, shown (in the first quadrant of Brillouin zone) in Fig. 32 (a). We know that for $\mu = 0$ and $t' = 0$ Fermi surface is simply square (complete "nesting"), so that we practically are dealing with one – dimensional case, analyzed long ago in Refs. [51, 64, 65]. Results of our calculations for real part of optical conductivity in our two – dimensional model, for the case of spin – fermion diagram combinatorics and different values of correlation length of AFM short – range order (parameter $\kappa = \xi^{-1}$, where ξ is measured in units of lattice constant a) are shown in Fig. 33. Qualitative behavior of conductivity is quite similar to those found for one – dimensional model (for the case of incommensurate fluctuations of CDW – type) in Refs. [64, 65]. It is characterized by the presence of large pseudogap absorption maximum (appropriate densities of states with pseudogap close to the Fermi level are shown at the insert in Fig. 33) at $\omega \sim 2W$ and also by a maximum at small frequencies, connected with carrier localization in static (in our approximation) random field of AFM fluctuations. Localization nature of this maximum is confirmed by its transformation into characteristic "Drude – like" peak (with maximum at $\omega = 0$) if we perform calculations in "ladder" approximation, when combinatorial factors $v(k) = 1$, which corresponds to "switching off" the contribution from diagrams with intersecting interaction lines, leading to two – dimensional Anderson localization [67, 68]. Qualitative form of conductivity in this case is also quite similar to those found in Ref. [65]. Narrowing of localization peak with diminishing correlation length of fluctuations can be explained, as was noted in Ref. [65], by suppression of effective interaction (15) for small ξ (with fixed value of W), leading to general suppression of scattering, also on the "cold" part of the Fermi surface. Note that general behavior of the density of states and optical

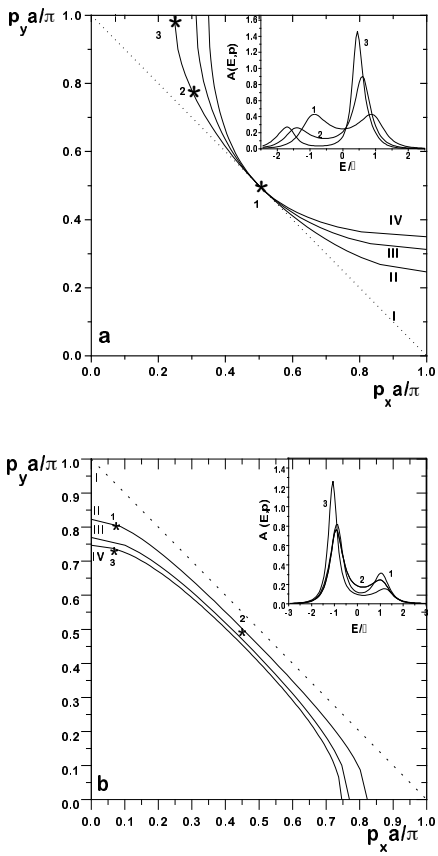

Figure 32: Fermi surfaces for different values of t' and chemical potential μ. (a) corresponds to $\mu = 0$ and the following values of t'/t: 0 – I; -0.2 – II; -0.4 – III; -0.6 – IV. (b) corresponds to $t' = 0$ and the following values of μ/t: 0 – I; -0.3 – II; -0.5 – III; -0.6 – IV. At the inserts we show energy dependences of spectral densities for spin – fermion model for $\kappa a = 0.1$ at points of the momentum space denotes by stars.

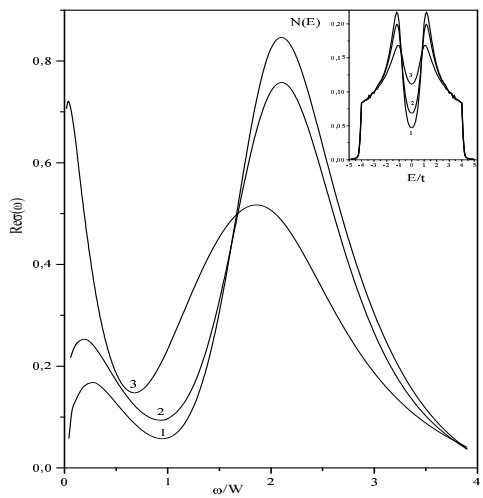

Figure 33: Real part of optical conductivity in spin – fermion model for the case of square Fermi surface ($\mu = 0$, $t' = 0$) for different values of inverse correlation length κa: 0.1 – 1; 0.2 – 2; 0.5 – 3. At the insert we show appropriate densities of states.

conductivity obtained here is in complete qualitative agreement with the results, obtained for the similar two – dimensional model of Peierls transition by quantum Monte – Carlo calculations in Ref. [69].

Now, if we keep $\mu = 0$ and "switch on" the transfer integral t' between second nearest neighbors in (10), we shall obtain Fermi surfaces different from square one, as shown in Fig. 32 (a). At the insert on this figure we also show the energy dependence of spectral density (48) at several typical points on these Fermi surfaces. It is seen that spectral density demonstrates characteristic "non Fermi – liquid" behavior, of the type studied in Refs. [47, 48], practically everywhere on the Fermi surface, until this surface is not very different from the square, despite the fact that the "hot spot" in this case lies precisely at the intersection of the Fermi surface with diagonal of the Brillouin zone. Appropriate dependences of the real part of optical conductivity are shown in Fig. 34. At the insert in this figure we show appropriate densities of states. It is seen that as we move away from the complete "nesting", pseudogap absorption maximum becomes more shallow, while localization peak (in accordance with the general sum rule for conductivity) grows. Note, however, that pseudogap absorption remains noticeable even when pseudogap in the density of states is practically invisible (curves 4 in Fig. 34).

Let us return now to the case of $t' = 0$ and change the value of μ, so that Fermi surfaces are close to the square, as shown in Fig. 32 (b). Strictly speaking, "hot spots" on these surfaces are absent, but spectral density shown at the insert on Fig. 32 (b), is still typically pseudogap like. Appropriate dependences of the real part of optical conductivity are shown in Fig. 35.

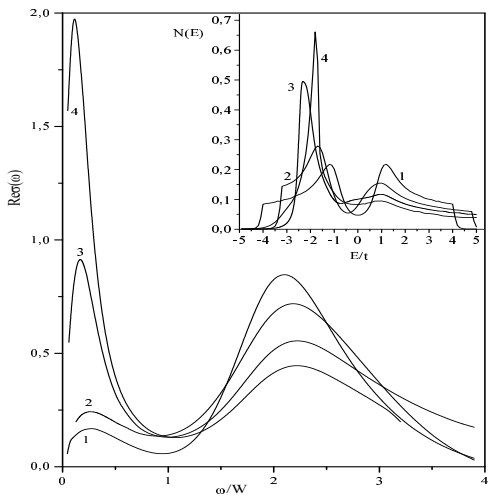

Figure 34: Real part of optical conductivity in spin – fermion model for $\mu = 0$ and $\kappa a = 0.1$ and for different Fermi surfaces, obtained from the square after "switching on" the transfer integral t'/t: 0 – 1; -0.2 – 2; -0.4 – 3; -0.6 – 4. At the insert — appropriate densities of states.

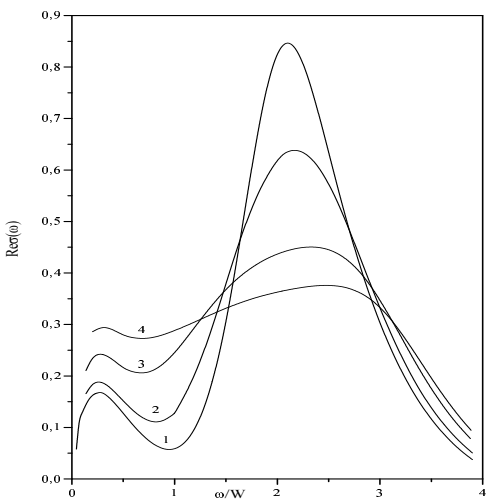

Figure 35: Real part of optical conductivity in spin – fermion model for $t' = 0$ and $\kappa a = 0.1$ and for different Fermi surfaces, obtained from square as we move from the case of half – filled band. Chemical potential μ/t: 0 – 1; -0.3 – 2; -0.5 – 3; -0.6 – 4.

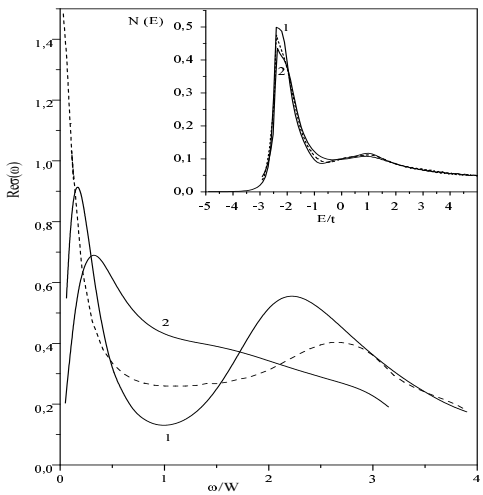

Figure 36: Real part of optical conductivity for $t'/t = -0.4$ and $\mu = 0$ for $\kappa a = 0.1$ and for different combinatorics of diagrams: 1 – spin – fermion combinatorics; 2 – commensurate case. Dashed curve — "ladder" approximation. At the insert — appropriate densities of states.

Consider now geometry of the Fermi surface with "hor spots" typical for most of HTSC – oxides, like that shown in Fig. 14. First, in Fig. 36 we show the real part of optical conductivity, calculated (for different combinatorics of diagrams) for characteristic value of $t' = -0.4t$ and for chemical potential $\mu = 0$, when "hot spots" are on the diagonals of the Brillouin zone. It is seen that pseudogap behavior of conductivity is conserved even in the case of practically absent pseudogap in the density of states (shown at the insert in Fig. 36). Dashed curve in Fig. 36 shows the result of "ladder" approximation, demonstrating disappearance of two – dimensional localization. In general, as correlation length of the short – range order diminishes, we observe "smearing" of the pseudogap maximum in conductivity.

For most copper oxide superconductors characteristic geometry of the Fermi surface can be described by $t' = -0.4t$ and $\mu = -1.3t$ [47]. In this case, results of our calculations of optical conductivity for different values of inverse correlation length κ are shown in Fig. 37 (for the case of spin – fermion combinatorics). here we introduced additional weak scattering due to inelastic processes via standard replacement $\omega \to \omega + i\gamma$ [70], which leads to the appearance of a narrow "Drude – like" peak for $\omega < \gamma$ (destruction of two – dimensional localization due to phase decoherence). It is easy to see that with the growth of inelastic scattering rate γ, localization peak is completely "smeared" and transformed to the "usual" Drude – like peak at small frequencies. Pseudogap absorption maximum becomes more pronounced with the growth of correlation length ξ (diminishing κ). Similar results for the "hot patches" model were obtained in Ref. [71]

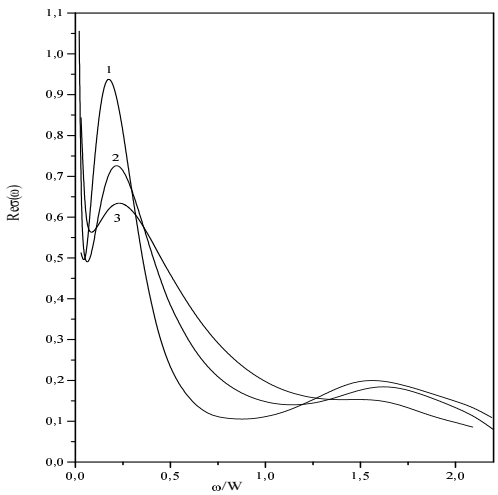

Figure 37: Real part of optical conductivity in spin – fermion model for $t'/t = -0,4$ and $\mu/t = -1.3$ and for different values of correlation length κa: 0.05 – 1; 0.1 – 2; 0.2 – 3. Damping factor $\gamma/t = 0.005$.

Direct correspondence of these results with experimental data shown in Fig. 4 [28] is obvious. Simple estimates show that characteristic values of conductivity in theory and experiment are also of the same order of magnitude. In principle, it is quite possible to make quantitative fit to the experiment, varying parameters of our model.

5.3 Interaction vertex for superconducting fluctuations.

Now we are going to discuss superconductivity formation on the "background" of pseudogap fluctuations. To take into account pseudogap fluctuations during the analysis of Cooper instability and derivation of Ginzburg – Landau expansion we need knowledge of the vertex part, describing electron interaction with an arbitrary fluctuation of superconducting order parameter (gap) of a given symmetry [72]:

$$\Delta(\mathbf{p}, \mathbf{q}) = \Delta_{\mathbf{q}} e(\mathbf{p}) \tag{60}$$

where the symmetry factor determining the type (symmetry) of pairing is:

$$e(\mathbf{p}) = \begin{cases} 1 & (\ s - \text{wave pairing}) \\ \cos p_x a - \cos p_y a & (\ d_{x^2-y^2} - \text{pairing}) \end{cases} . \tag{61}$$

and we always assume singlet pairing.

Almost immediately we can write down recursion relations [72, 73] for "triangular" vertices in Cooper channel, similar to those introduced above during the analysis of response to electromagnetic field [66]. The vertex part of interest to us can be defined

as:

$$\Gamma(\varepsilon_n, -\varepsilon_n, \mathbf{p}, -\mathbf{p}+\mathbf{q}) \equiv \Gamma_{\mathbf{p}}(\varepsilon_n, -\varepsilon_n, \mathbf{q}) e(\mathbf{p}) \tag{62}$$

Then $\Gamma_{\mathbf{p}}(\varepsilon_n, -\varepsilon_n, \mathbf{q})$ is determined by the recursion procedure of the following form:

$$\Gamma_{\mathbf{p}k-1}(\varepsilon_n, -\varepsilon_n, \mathbf{q}) = 1 \pm W^2 r(k) G_k(\varepsilon_n, \mathbf{p}+\mathbf{q}) G_k(-\varepsilon_n, \mathbf{p}) \Bigg\{ 1 + \\ + \frac{2ik\kappa v_k}{G_k^{-1}(\varepsilon_n, \mathbf{p}+\mathbf{q}) - G_k^{-1}(-\varepsilon_n, \mathbf{p}) - 2ik\kappa v_k} \Bigg\} \Gamma_{\mathbf{p}k}(\varepsilon_n, -\varepsilon_n, \mathbf{q}) \tag{63}$$

which is represented by diagrams shown in Fig. 38. "Physical" vertex corresponds to $\Gamma_{\mathbf{p}k=0}(\varepsilon_n, -\varepsilon_n, \mathbf{q})$. Additional combinatorial factor $r(k) = v(k)$ for the simplest case of charge (or Ising like spin) pseudogap fluctuations analyzed in Ref. [72]. For the most interesting case of Heisenberg spin (SDW) fluctuations, which are mainly considered below, this factor is given by [47, 73]:

$$r(k) = \begin{cases} k & \text{for even } k \\ \frac{k+2}{9} & \text{for odd } k \end{cases} \tag{64}$$

The choice of the sign before W^2 in the r. h. s. of (63) depends on the symmetry of superconducting order parameter and the type of pseudogap fluctuations [72, 73]. Summary of all variants is given in Table I.

Table I. The choice of sign in recursion procedure for the vertex part.

Pairing	CDW	SDW (Ising)	SDW (Heisenberg)
s	$+$	$-$	$+$
d	$-$	$+$	$-$

From this table we can see, that in most interesting case of d – wave pairing and Heisenberg pseudogap fluctuations this sign is "$-$", so that we have recursion procedure with alternating signs. At the same time, for the case of s – wave pairing and the same type of fluctuations we have to take this sign "$+$" and signs in recursion procedure are always the same. In Ref. [72] it was shown that this difference in types of recursion procedure leads to two different variants of qualitatively different behavior of all the main characteristics of superconductors.

5.4 Impurity scattering.

Scattering by normal (nonmagnetic) impurities is easily taken into account in self – consistent Born approximation, writing down "Dyson's equation" shown diagrammatically in Fig. 39 (a), where in addition to Fig. 38, we have added impurity scattering contribution to electron self – energy.

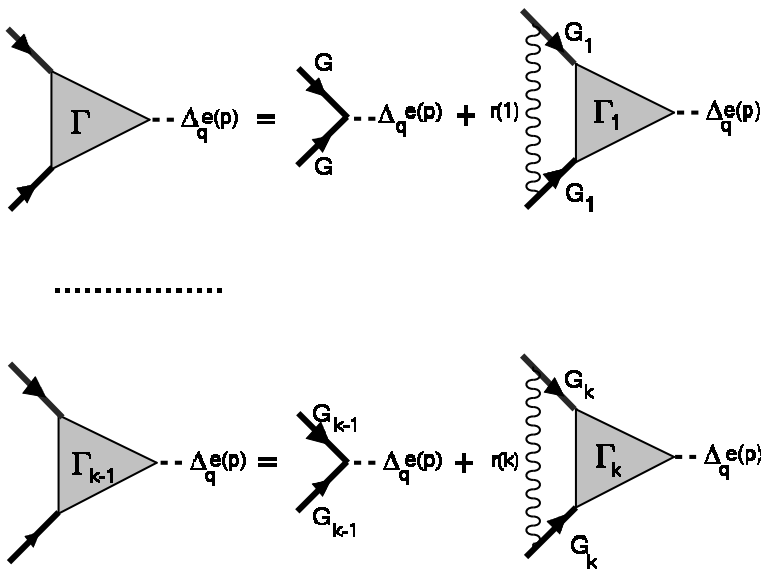

Figure 38: Recursion equations for "triangular" vertex in Cooper channel.

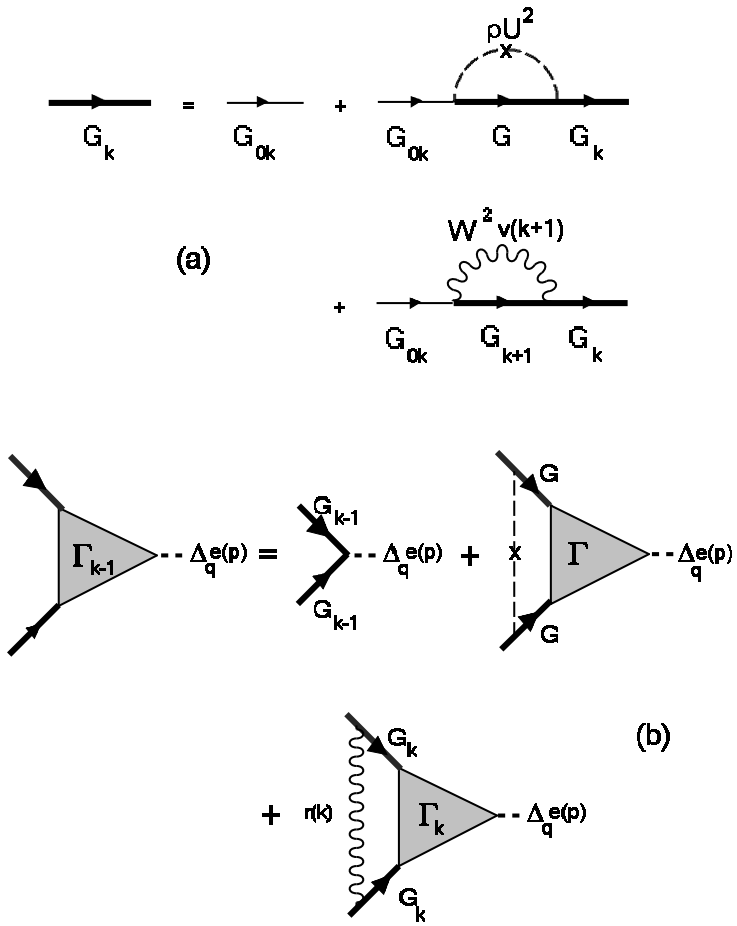

Figure 39: Recursion equations for the Green's function (a) and "triangular" vertex (b) with the account of scattering by impurities.

As a result, recursion equation for the Green's function is written as:

$$G_k(\varepsilon_n \mathbf{p}) = \frac{1}{G_{0k}^{-1}(\varepsilon_n \mathbf{p}) - \rho U^2 \sum_{\mathbf{p}} G(\varepsilon_n \mathbf{p}) - W^2 v(k+1) G_{k+1}(\varepsilon_n \mathbf{p})} \tag{65}$$

where ρ is the concentration of impurities with point – like potential U, and impurity scattering self – energy contains full Green's function $G(\varepsilon_n \mathbf{p}) = G_{k=0}(\varepsilon_n \mathbf{p})$, which is to be determined self – consistently by our recursion procedure. A contribution to impurity scattering self – energy form the real part of Green's function reduces, as usual, to irrelevant renormalization of the chemical potential, so that (65) reduces to:

$$G_k(\varepsilon_n \mathbf{p}) = \frac{1}{i(\varepsilon_n - \rho U^2 \sum_{\mathbf{p}} ImG(\varepsilon_n \mathbf{p}) + k v_k \kappa) - \xi_k(\mathbf{p}) - W^2 v(k+1) G_{k+1}(\varepsilon_n \mathbf{p})} \tag{66}$$

Thus, in comparison with impurity free case, we have just a substitution (renormalization):

$$\varepsilon_n \to \varepsilon_n - \rho U^2 \sum_{\mathbf{p}} ImG(\varepsilon_n \mathbf{p}) \equiv \varepsilon_n \eta_\epsilon \tag{67}$$

$$\eta_\epsilon = 1 - \frac{\rho U^2}{\varepsilon_n} \sum_{\mathbf{p}} ImG(\varepsilon_n \mathbf{p}) \tag{68}$$

If we do not perform fully self – consistent calculations of impurity self – energy, in the simplest approximation we simply have:

$$\varepsilon_n \to \varepsilon_n - \rho U^2 \sum_{\mathbf{p}} ImG_{00}(\varepsilon_n \mathbf{p}) \equiv \varepsilon_n \eta_\epsilon = \varepsilon_n + \gamma_0 sign \varepsilon_n \tag{69}$$

$$\eta_\epsilon = 1 + \frac{\gamma_0}{|\varepsilon_n|} \tag{70}$$

where $\gamma_0 = \pi \rho U^2 N_0(0)$ is the standard Born impurity scattering rate ($N_0(0)$ is the density of states of free electrons at the Fermi level).

For "triangular" vertices of interest to us, recursion equations with the account of impurity scattering is shown diagrammatically in Fig. 39 (b). For the vertex, describing electron interacting with superconducting order parameter fluctuation (60) with d – wave symmetry (61), this equation is considerably simplified, as the contribution of the second diagram in the r. h. s. of Fig. 39 (b) in fact vanishes due to $\sum_{\mathbf{p}} \epsilon(\mathbf{p}) = 0$ (cf. discussion of similar situation in Ref. [50]). Then the recursion equation for the vertex takes the form (63), where $G_k(\pm\varepsilon_n \mathbf{p})$ are given by (65), (66), i.e. are just Green's functions "dressed" by impurity scattering, determined gy diagrams of Fig. 39 (a). For the vertex describing interaction with order parameter fluctuations with s – wave symmetry, we have the following equation:

$$\Gamma_{\mathbf{p}k-1}(\varepsilon_n, -\varepsilon_n, \mathbf{q}) = 1 + \rho U^2 \sum_{\mathbf{p}} G(\varepsilon_n, \mathbf{p}+\mathbf{q}) G(-\varepsilon_n, \mathbf{p}) \Gamma_{\mathbf{p}}(\varepsilon, -\varepsilon_n, \mathbf{q}) \pm$$

$$\pm W^2 r(k) G_k(\varepsilon_n, \mathbf{p}+\mathbf{q}) G_k(-\varepsilon_n, \mathbf{p}) \Big\{ 1 + \tag{71}$$

$$+ \frac{2ik\kappa v_k}{G_k^{-1}(\varepsilon_n, \mathbf{p}+\mathbf{q}) - G_k^{-1}(-\varepsilon_n, \mathbf{p}) - 2ik\kappa v_k} \Big\} \Gamma_{\mathbf{p}k}(\varepsilon_n, -\varepsilon_n, \mathbf{q})$$

where $G_k(\pm\varepsilon_n \mathbf{p})$ is again given by (65), (66), and the sign before W^2 is determined according to the rules formulated above. The difference with the case of the vertex, describing interaction with d – wave fluctuations, is in the appearance of the second term in the r. h. s. of (71), so that we have to substitute:

$$1 \to \eta_\Gamma = 1 + \rho U^2 \sum_{\mathbf{p}} G(\varepsilon_n, \mathbf{p}+\mathbf{q}) G(-\varepsilon_n, \mathbf{p}) \Gamma_{\mathbf{p}}(\varepsilon, -\varepsilon_n, \mathbf{q}) \tag{72}$$

Now the self – consistent procedure look as follows. We start from "zeroth" approximation $G = G_{00}$, $\Gamma_{\mathbf{p}} = 1$, then in Eqs. (66), (71) we just have $\eta_\varepsilon = \eta_\Gamma = 1 - \rho U^2/\varepsilon_n \sum_{\mathbf{p}} Im G_{00}(\varepsilon_n \mathbf{p})$. Then perform recursions (starting from some big enough value of k) and determine new values of $G = G_{k=0}$ and $\Gamma_{\mathbf{p}} = \Gamma_{k=0}$. Again calculate η_ε and η_Γ using (68) and (72), put these into (66), (71) etc., until convergence.

While analyzing vertices with d – wave symmetry, we have simply to put $\eta_\Gamma = 1$ at all stages of calculation. In fact, in these case there is no serious need to perform fully self – consistent calculation, because it leads only to insignificant corrections to the results of non self – consistent calculation, using only simplest substitution (69) [75].

As an illustration, in Fig. 40 we show comparison of ARPES data of Ref. [36] for momentum dependence of $a = Im\Sigma(E = 0, \mathbf{p})$, taken from Fig. 10 (c), with the results of non self – consistent calculation using (66), (69), (70). Assumed values of parameters, typical for HTSC, are shown on the figure, for the parameters of the spectrum (10) we have taken $t = 0.25eV$, $t' = -0.4t$, while chemical potential was calculated for two limiting doping levels. It can be seen that we obtain correct order of magnitude estimate of anisotropy in momentum space, but the general form of this dependence is only qualitatively similar to that observed in the experiment, which lies in between two calculated curves. More or less similar results are obtained also in the case of spin – fermion combinatorics. In principle, rather approximate agreement of calculated results with experiment is not very surprising. Our model is certainly oversimplified, and experimental data are also not very precise. Besides, we practically know nothing about the values of parameters of the model, appropriate for the system, studied in these experiments.

5.5 Superconducting transition temperature and Ginzburg – Landau expansion.

Critical temperature of superconducting transition is determined by the equation for Cooper instability of the normal phase:

$$1 - V\chi(0; T) = 0 \tag{73}$$

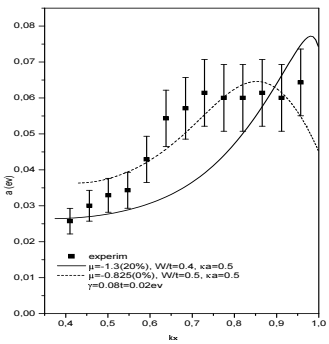

Figure 40: Comparison of ARPES data for the static contribution to the imaginary part of electron self – energy $a = Im\Sigma(E = 0, \mathbf{p})$ with calculated results for the "hot spots" model with impurity scattering, for typical set of model parameters, shown in the figure. Shown are the results for commensurate combinatorics and two values of doping: 0% and 20%. Momentum k_x is given in units of $\frac{\pi}{a}$, and its change between 0 and 1 corresponds to measurement point moving along the Fermi surface from the diagonal of the Brillouin zone towards the vicinity of the point $(0, \pi)$.

where generalized Cooper susceptibility is defined by diagram shown in Fig. 41 and is equal to:

$$\chi(\mathbf{q}; T) = -T \sum_{\varepsilon_n} \sum_{\mathbf{p}} G(\varepsilon_n \mathbf{p} + \mathbf{q}) G(-\varepsilon_n, -\mathbf{p}) e^2(\mathbf{p}) \Gamma_{\mathbf{p}}(\varepsilon_n, -\varepsilon_n, \mathbf{q}) \tag{74}$$

Pairing coupling constant V is assumed to be nonzero in some layer of the width of $2\omega_c$ around the Fermi level and determines the "bare" transition temperature T_{c0} in the absence of the pseudogap fluctuations via standard BCS equation[14]:

$$1 = \frac{2VT}{\pi^2} \sum_{n=0}^{\bar{m}} \int_0^{\pi/a} dp_x \int_0^{\pi/a} dp_y \frac{e^2(\mathbf{p})}{\xi_{\mathbf{p}}^2 + \varepsilon_n^2} \tag{75}$$

where $\bar{m} = [\frac{\omega_c}{2\pi T_{c0}}]$ is dimensionless cut – off parameter of the sum over Matsubara frequencies. All calculations [72, 73] were performed for the typical spectrum of quasiparticles (10), for different relations between t, t' and μ. Choosing, rather arbitrarily, $\omega_c = 0.4t$ and $T_{c0} = 0.01t$, we can easily find the appropriate value of pairing interaction V in (75), leading to this given value of T_{c0} for different types of pairing. In particular, for $t'/t = -0.4$, $\mu/t = -1.3$ and for s – wave pairing we get $\frac{V}{ta^2} = 1$, while for $d_{x^2-y^2}$ – pairing we obtain $\frac{V}{ta^2} = 0.55$.

To determine T_c we need only the knowledge of Cooper susceptibility for $q = 0$ which considerably simplifies all calculations [72]. In general case, e.g. to derive coefficients of Ginzburg – Landau expansion we need to know $\chi(q; T)$ for arbitrary (small) q.

[14] We do not discuss the microscopic nature of this interaction – it can be due to an exchange by AFM spin fluctuations, phonons, or combination of both.

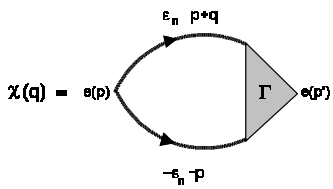

Figure 41: Diagrammatic representation for generalized susceptibility $\chi(\mathbf{q})$ in Cooper channel.

Ginzburg – Landau expansion for the difference of free energies of superconducting and normal states is written in the following standard form:

$$F_s - F_n = A|\Delta_{\mathbf{q}}|^2 + q^2 C|\Delta_{\mathbf{q}}|^2 + \frac{B}{2}|\Delta_{\mathbf{q}}|^4 \tag{76}$$

and is determined by the loop expansion of free energy of an electron in the field of fluctuations of suoerconducting order parameter (60), shown in Fig. 42.

It is convenient to normalize Ginzburg – Landau coefficients A, B, C by their values in the absence of pseudogap fluctuations, writing the following representation [72]:

$$A = A_0 K_A; \qquad C = C_0 K_C; \qquad B = B_0 K_B, \tag{77}$$

$$A_0 = N_0(0)\frac{T - T_c}{T_c} < e^2(\mathbf{p}) >; \quad C_0 = N_0(0)\frac{7\zeta(3)}{32\pi^2 T_c^2} < |\mathbf{v}(\mathbf{p})|^2 e^2(\mathbf{p}) >;$$
$$B_0 = N_0(0)\frac{7\zeta(3)}{8\pi^2 T_c^2} < e^4(\mathbf{p}) >, \tag{78}$$

where the angular brackets denote the usual averaging over the Fermi surface: $< \ldots >= \frac{1}{N_0(0)}\sum_p \delta(\xi_{\mathbf{p}})\ldots$, where $N_0(0)$ – density of states on the Fermi level for free electrons.

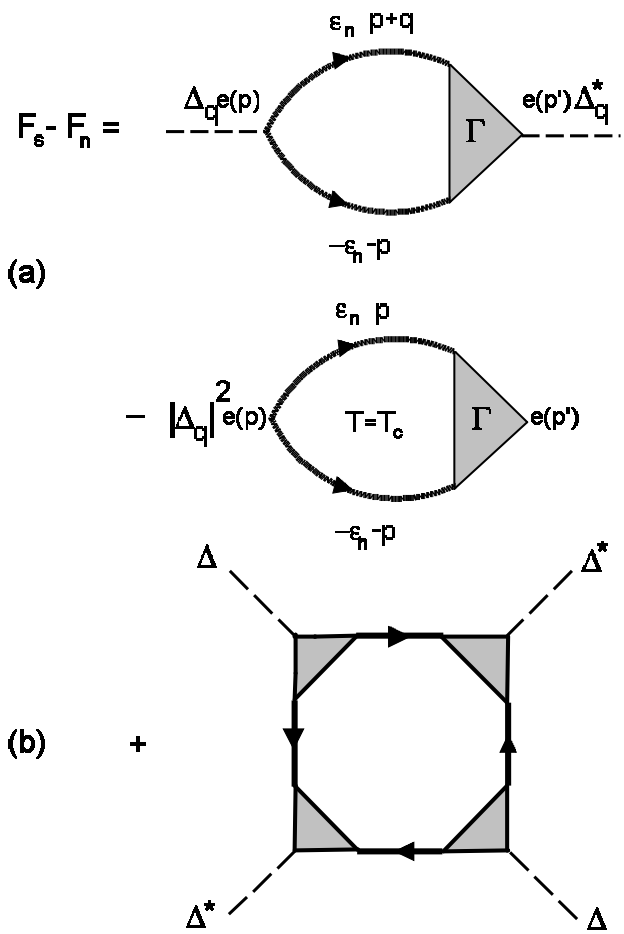

Figure 42: Diagrammatic representation of Ginzburg – Landau expansion.

Then we obtain the following general expressions [72]:

$$K_A = \frac{\chi(0;T) - \chi(0;T_c)}{A_0} \tag{79}$$

$$K_C = \lim_{q\to 0} \frac{\chi(\mathbf{q};T_c) - \chi(0;T_c)}{q^2 C_0} \tag{80}$$

$$K_B = \frac{T_c}{B_0} \sum_{\varepsilon_n} \sum_{\mathbf{p}} e^4(\mathbf{p}) (G(\varepsilon_n \mathbf{p}) G(-\varepsilon_n, -\mathbf{p}))^2 (\Gamma_{\mathbf{p}}(\varepsilon_n, -\varepsilon_n, 0))^4 \tag{81}$$

which were used for direct numerical calculations. In the presence of impurities all Green's functions and vertices, entering these expressions, should be calculated using Eqs. (66) and (71), derived above.

The knowledge of the coefficients of Ginzburg – Landau expansion allows to determination of all major characteristics of a superconductor close to the transition temperature T_c. Coherence length is defined as:

$$\frac{\xi^2(T)}{\xi^2_{BCS}(T)} = \frac{K_C}{K_A}, \tag{82}$$

where $\xi_{BCS}(T)$ is the value of this length in the absence of the pseudogap. Penetration depth is:

$$\frac{\lambda(T)}{\lambda_{BCS}(T)} = \left(\frac{K_B}{K_A K_C}\right)^{1/2}, \tag{83}$$

where we again normalized to the value of $\lambda_{BCS}(T)$ in the absence of pseudogap fluctuations. Analogously, normalized slope of the upper critical field close to T_c is:

$$\frac{\left|\frac{dH_{c2}}{dT}\right|_{T_c}}{\left|\frac{dH_{c2}}{dT}\right|_{T_{c0}}} = \frac{T_c}{T_{c0}} \frac{K_A}{K_C}. \tag{84}$$

Specific heat discontinuity at the transition:

$$\Delta C = \frac{(C_s - C_n)_{T_c}}{(C_s - C_n)_{T_{c0}}} = \frac{T_c}{T_{c0}} \frac{K_A^2}{K_B}. \tag{85}$$

Results of these calculations for the cases of charge (CDW) and Ising like spin (SDW) fluctuations of short range order can be found in Ref. [72]. Here we shall concentrate mainly on the analysis of most important and interesting case of Heisenberg spin (SDW) fluctuations and also on the discussion of the role of impurity scattering (disordering) [73, 74]. Due to particular importance of the case of d – wave pairing in the physics of copper oxide high – temperature superconductors, more attention will be given to this case.

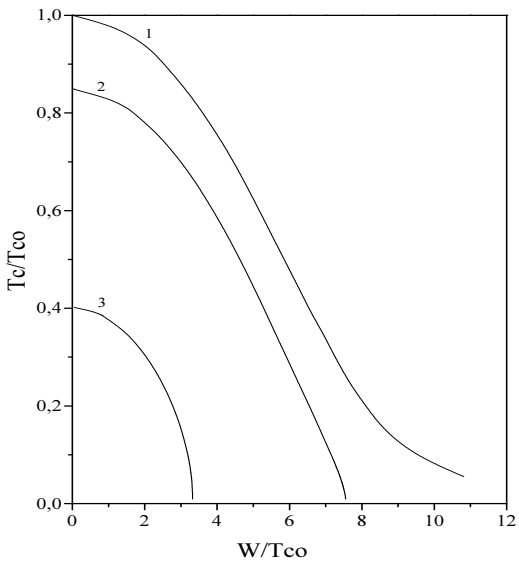

Figure 43: Dependence of T_c on the effective width of the pseudogap W in the case of d – wave pairing, for several values of impurity scattering rate γ_0/T_{c0}: 0 – 1; 0.18 – 2; 0.64 – 3. Inverse correlation length κa=0.2

In the following we give the results of calculations made for typical values of spectrum parameters $t'/t = -0.4$, $\mu/t = -1.3$, while for correlation length we assume $\kappa a = 0.2$. To spare space we do not show the results for dimensionless GL – coefficients K_A, K_B, K_C, but restrict ourselves to demonstration of more important dependences of all major physical characteristics.

When we are dealing with dependences on the effective width of the pseudogap, all characteristics are normalized to their values at $T = T_{c0}$, while in case of dependences on the impurity scattering rate γ_0 we normalize to the values at $T = T_{c0}(W)$, i.e. at the value of the "bare" transition temperature at a given value of W, but in the absence of impurity scattering ($\gamma_0 = 0$).

5.5.1 d – wave pairing.

In Fig. 43 we show the dependence of superconducting transition temperature T_c on the effective pseudogap width W for several values of impurity scattering rate. It is seen that pseudogap fluctuations lead to significant suppression of superconductivity, and in the presence of finite disorder we always obtain some "critical" value of W, where the value of T_c vanishes. This suppression of T_c is naturally due to a partial "dielectrization" of electronic spectrum in the vicinity of "hot spots". [47, 48].

Similar dependences for the slope of the upper critical field and specific heat discon-

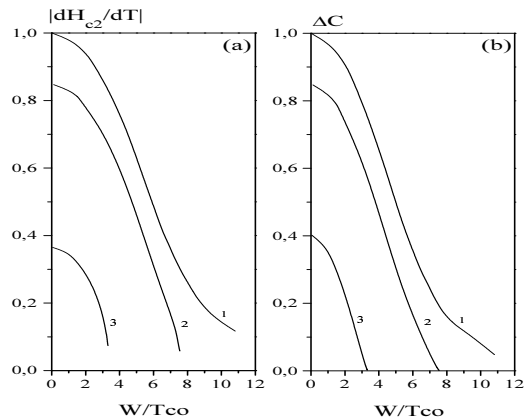

Figure 44: Dependence of the slope of the upper critical field and specific heat discontinuity at the transition on the effective width of the pseudogap W in case of d – wave pairing, for several values of impurity scattering rate γ_0/T_{c0}: 0 – 1; 0.18 – 2; 0.64 – 3.

tinuity at the transition point are shown in Fig. 44. Typically we see fast suppression of these characteristics by pseudogap fluctuations.

Dependence on the value of correlation length of pseudogap fluctuations is more slow — in all cases the growth of ξ (drop of κ) enhances the effect of pseudogap fluctuations. We drop appropriate results to spare space.

In Fig. 45 we show the dependences of superconducting transition temperature T_c on impurity scattering rate γ_0 for several values of the effective pseudogap width. We note that in the presence of pseudogap fluctuations, suppression of T_c by disorder is significantly faster, than in their absence ($W = 0$), when T_c dependence on γ_0 in case of d – wave pairing is described by the standard Abrikosov – Gorkov curve (first obtained for s – wave pairing and scattering by magnetic impurities) [76, 77]. Similar dependences for the slope of $H_{c2}(T)$ and specific heat discontinuity are shown in Fig. 46. Again we see, that impurity scattering (disorder) leads to the fast drop of these two characteristics, i.e. enhances similar effect of pseudogap fluctuations.

Similar dependences were obtained in Ref. [72] for the case of pseudogap fluctuations of CDW type, when we also obtain recursion procedure for the vertex part wit alternating signs. At the same time, in this case we observe some quantitative difference in the behavior of all characteristics due to another combinatorics of diagrams.

Dependences obtained in our model are in qualitative agreement with most of the experimental data on superconductivity in the pseudogap region (underdoped region of the phase diagram of cuprates). Below we shall show that these results may be used for direct modelling of a typical phase diagram of a high – temperature superconductor.

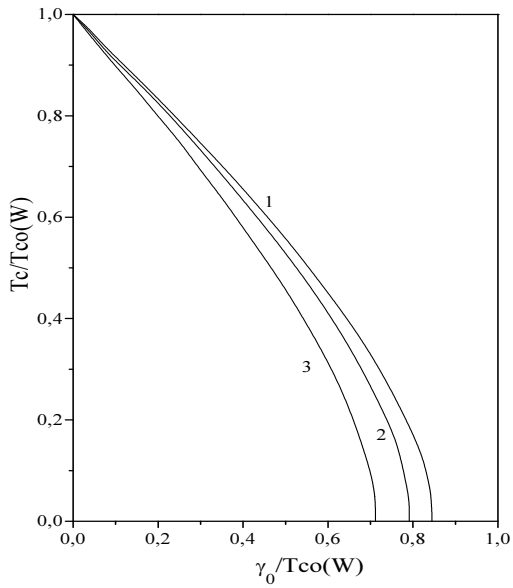

Figure 45: Dependence of T_c on impurity scattering rate (disorder) γ_0 for the case of d – wave pairing, for several values of the effective pseudogap width: W/T_{c0}: 0 – 1; 2.8 – 2; 5.5 – 3.

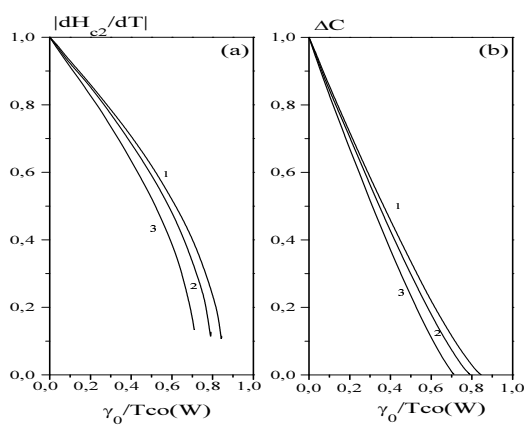

Figure 46: Dependence of the slope of the upper critical field and specific heat discontinuity at the transition on impurity scattering rate (disorder) γ_0 in case of d – wave pairing, for several values of effective pseudogap width W/T_{c0}: 0 – 1; 2.8 – 2; 5.5 – 3.

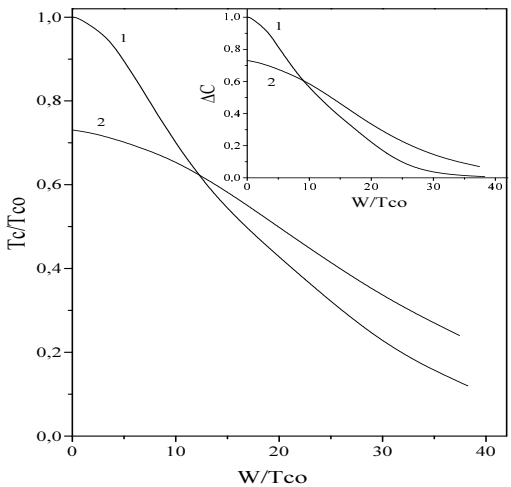

Figure 47: Dependence of T_c on effective width of the pseudogap W for the case of s – wave pairing, for two values of impurity scattering rate: γ_0/T_{c0}: $0-1$; $20-2$. Inverse correlation length κa=0.2. At the insert – characteristic behavior of specific heat discontinuity for the same parameters.

5.5.2 s – wave pairing.

The case of s – wave pairing is interesting to us mainly with the aim of demonstration of major differences from the case of d – wave case. There are no experimental evidence for s – wave superconductivity in systems with pseudogap, though such systems may well be discovered in some future.

Our calculation show that pseudogap fluctuations suppress superconducting transition temperature also in this case (Fig. 47), though characteristic scale of these fluctuations, necessary for significant suppression of superconductivity here is much larger, than in the case of d – wave pairing. This result was obtained in Ref. [72], but we must note the absence (in the case of Heisenberg (SDW) pseudogap fluctuations) of characteristic "plateau" in the dependence of T_c on W, which was obtained for the case of scattering by pseudogap fluctuations of CDW type in Ref. [72]. On the same scale of W we also observe here the suppression of specific heat discontinuity at the transition, which is shown at the insert in Fig. 47.

As to dependence of T_c on impurity scattering rate (disorder), we can see that besides relatively small effect of T_c suppression due to [75] disorder "smearing" of the density of states at the Fermi level, even some weak effect of T_c enhancement with the growth of γ_0 can be also observed, apparently due to the "filling" the pseudogap in the density of states induced by impurity scattering [73].

In Fig. 48 we show the influence of impurity scattering (disorder) on the slope of the

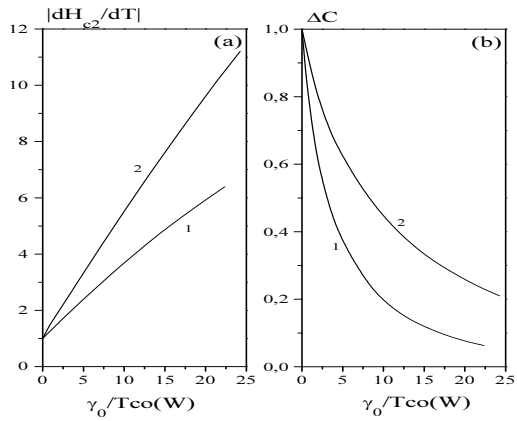

Figure 48: Dependence of the slope of the upper critical field and specific heat discontinuity at the transition on impurity scattering rate (disorder) γ_0 in case of s – wave pairing, for two values of pseudogap width: W/T_{c0}: 0 – 1; 15 – 2.

upper critical field and specific heat discontinuity. Specific heat discontinuity is significantly suppressed by disorder, while the slope of $H_{c2}(T)$ behaves qualitatively different from the case of d – wave pairing: the growth of disorder leads to the growth of this characteristic, as in the case of standard theory of "dirty" superconductors [16], and pseudogap fluctuations enhance the slope of $H_{c2}(T)$. In the absence of pseudogap fluctuations, similar differences between s – wave and d – wave superconductors in behavior of the slope of $H_{c2}(T)$ under disordering were discussed in Ref. [76].

6 Modeling of the phase diagram of cuprates.

This model for the influence of pseudogap fluctuations on superconductivity allows to perform a simple modeling of typical phase diagram of HTSC cuprates [73, 74][15] First attempt of such modeling in quite simplified version of our model was undertaken in Ref. [56]. Basic idea is to identify our parameter W with experimentally observable effective width of the pseudogap (temperature of crossover into pseudogap region on the phase diagram) $E_g \approx T^*$, determined from numerous experiments [24, 21]. This characteristic, as was already noted above, drops almost linearly with the growth of the concentration of doping impurity (concentration of carriers), starting from the values of the order of 10^3K and vanishing at some critical concentration $x_c \approx 0.19..0.22$, slightly higher than "optimal" value $x_o \approx 0.15..0.17$ [24, 78]. Accordingly, we can assume similar concentration

[15] Here we neglect the existence of a narrow region of antiferromagnetism in Mott insulator state, at low concentrations of doping impurity, limiting ourselves to a wide region of "bad" metallic state.

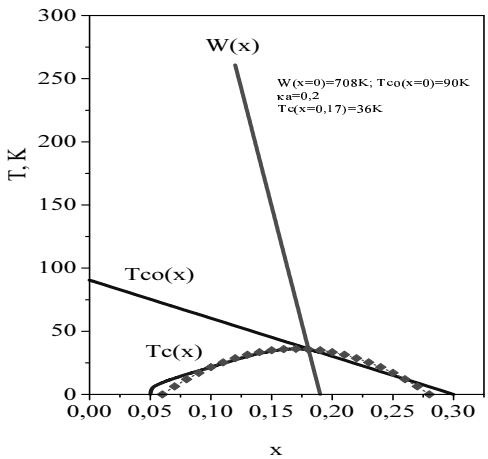

Figure 49: Model phase diagram for the case of scattering by pseudogap fluctuations of CDW – type (d – wave pairing) and "bare" superconducting transition temperature T_{c0} linear in carrier concentration.

dependence of our pseudogap width $W(x)$[16]. In this sense we can say that $W(x)$ is determined directly from the experiment. Then, the only parameter we need remains concentration dependence of the "bare" temperature of superconducting transition $T_{c0}(x)$, which would have been existing in the absence of pseudogap fluctuations. Its knowledge would allow us to determine the concentration dependence of the observable transition temperature $T_c(x)$, solving the equations of our model. Unfortunately, concentration dependence $T_{c0}(x)$ is, generally, unknown and is not determined by any known experiment, remaining just free fitting parameter of our theory.

Following Ref. [56] we can assume, that $T_{c0}(x)$ can also be described by linear function of x, going to zero at $x = 0.3$, and choosing the value of $T_{c0}(x = 0)$, which give us experimentally observed $T_c(x = x_o)$. Then we can calculate the whole "observed" dependence $T_c(x)$. Results of such calculation for the case of d – wave pairing and scattering by charge (CDW) pseudogap fluctuations [72], using typical $W(x)$ dependence, are shown in Fig. 49. We see that even with such arbitrary assumptions the "hot spots" model allows to obtain $T_c(x)$ dependence, which is rather close to experimentally observable. Similar calculations for Ising like model of spin fluctuations (leading to the absence of sign alternation in the recursion procedure for the vertex part [72]) show, that reasonable values for $T_c(x)$ can be obtained only for unrealistic values of $W(x)$, at least an order of magnitude larger than observed in the experiments.

In the framework of our BCS – like model for the "bare" T_{c0}, an assumption of its

[16] Naturally, such identification can be done up to an unknown proportionality coefficient ~ 1.

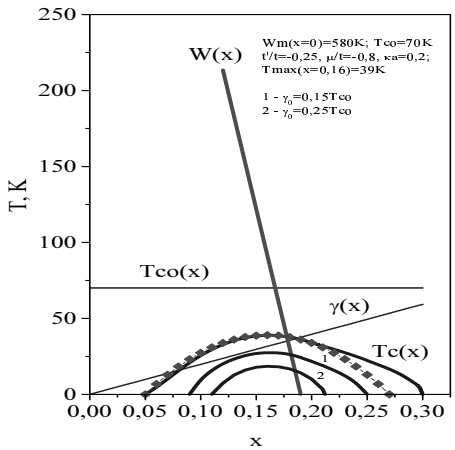

Figure 50: Model phase diagram for the case of scattering by Heisenberg (SDW) pseudogap fluctuations (d – wave pairing) and "bare" temperature of superconducting transition T_{c0} independent of carrier concentration, with the account of internal disorder linear in concentration of doping impurity $\gamma(x)$.

strong concentration dependence seems rather unrealistic[17]. Thus, let us assume that the value of T_{c0} does not depend on carrier concentration x at all, but take into account the fact that introduction of doping impurity inevitably leads to appearance random impurity scattering (internal disorder), which can be described by appropriate linear dependence of $\gamma(x)$. Let us assume that it is this growth of disorder, which leads to complete suppression of d – wave pairing at $x = 0.3$, in accordance with Abrikosov – Gorkov dependence [76, 77]. Results of our modeling of the phase diagram for the system of the type of $La_{2-x}Sr_xCuO_4$, for the case of Heisenberg pseudogap fluctuations, with the account of the abovementioned role of internal disorder, are shown in Fig. 50. The values of different parameters used in this calculation are also shown at the same figure. "Experimental" values of $T_c(x)$, shown at this figure (as well as at Fig. 49) by "diamonds", were obtained from empirical relation [78, 79]:

$$\frac{T_c(x)}{T_c(x = x_o)} = 1 - 82.6(x - x_o)^2 \tag{86}$$

which gives rather good fit to experimental data on concentration dependence of T_c for a number of HTSC cuprates. It is seen, that in the whole underdoped region our model gives practically ideal description of "experimental" data with very reasonable values of $W(x)$. At the end of overdoped region agreement is less good, but you must take into account,

[17] In this approach any dependence of T_{c0} on x can be only due to relatively weak changes of density of states at the Fermi level, as chemical potential moves with x.

that Eq. (86) also usually does not give very good fit here, and the obvious crudeness of our assumptions for underdoped region. Also note, that we have not undertaken any special attempts to improve agreement in this region.

It is interesting to analyze the behavior of superconducting transition temperature T_c under additional disordering of our system at different compositions (carrier concentrations). There are many experimental studies [16], where such an additional disordering was introduced by chemical substitutions (impurities) [81, 82] or by irradiation with fast neutrons [80] or electrons [83, 84]. However, special discussion of the role of this additional disordering in the context of the studies of the pseudogap state was made only in Ref. [82].

In our model, such disordering may be simulated by introduction of additional "impurity" scattering parameter γ_0, which is just added to the parameter of internal disorder $\gamma(x)$. Results of our calculations of superconducting critical temperature for two values of this parameter are also shown in Fig. 50. We see, that in complete agreement with experiments [82], introduction of "impurities" (disorder) leads to fast narrowing of the superconducting region on the phase diagram. Also in complete accordance with our conclusions made above with respect to Fig. 45, and also with experiments [80, 82], superconductivity suppression by disorder in the underdoped region (pseudogap state) is significantly faster, than at optimal composition. We could have expected that introduction of "normal" disorder. obviously leading to some suppression of the pseudogap in the density of states, could also lead to certain "slowing" down of T_c suppression. However, in case of d – wave pairing, this effect is apparently absent.

The problem, however, is that in all cases our suppression of T_c by disorder is faster than that described by the standard Abrikosov – Gorkov dependence for the case of d – wave pairing [77]. At the same time, attempts to fit the results of majority of experiments on disordering in HTSC cuprates to this dependence show [81, 83, 84], that such suppression actually is significantly slower, than predicted by Abrikosov – Gorkov dependence. This, still unsolved, problem remains one of the major problems of the theory of high – temperature superconductors [16]. One possible solution may be connected with consistent description of the role of disorder in superconductors, which belong to the crossover region from "large" pairs of BCS theory to "compact" Bosons, appearing in the limit of very strong coupling [85]. Another interesting possibility to explain such "slowing down" of T_c suppression is connected with the role of anisotropy of elastic scattering by impurities analyzed in Refs. [76, 86]. This last effect can be rather easily included in our calculational scheme. It is of particular interest in connection with established fact of rather strong anisotropy of elastic scattering (with d – wave symmetry), which was observed in ARPES experiments on $Bi_2Sr_2CaCu_2O_{8+\delta}$ [36]. Appropriate scattering rate in these experiments changed in the interval of $20-60\ meV$ (cf. Fig. 10 (c)) [36], which is nearly an order of magnitude larger than maximal value of $\gamma(x)$, used in our calculations. This is an additional evidence of unusual stability of d – wave pairing in cuprates towards static disorder. Note that our model for electron self – energy in fact describes similar

anisotropy of elastic scattering, corresponding to its growth in the vicinity of "hot spots", yet the effect of "slowing down" of T_c suppression under disordering is not observed.

Our results show that despite the obvious crudeness of our assumptions, the "hot spots" model rather easily leads to a reasonable (sometimes even semiquantitative) description of superconductivity region on the phase diagram of HTSC cuprates[18]. The main shortcoming this approach remains considerable arbitrariness of our "scenario" of the origin of concentration dependence of the "bare" superconducting transition temperature.

7 Conclusion.

Our discussion demonstrates the variety of results, which can be obtained in this class of models of the pseudogap state. We must stress once again quite simplified nature of our approximations, though allowing to obtain what was called "nearly exact" solution. This solution is interesting, first of all, from purely theoretical point of view, as rare enough example of the problem, when it is possible to sum the complete Feynman perturbation theory series (though, in general, certain classes of higher order diagrams are calculated approximately). Probably the main theoretical "lesson" to learn is, that the results of such complete summation are rather radically different from the results, obtained by one or other "partial" summation (e.g. of simple geometrical progression).

Probably the main shortcoming of our approach is the neglect of dynamics of fluctuations of short – range order. This is justified, as was shown above, only for high enough temperatures, which is bad, e.g. from the point of view of description of superconducting state for $T \ll T_c$ [19]

Another shortcoming, as was mentioned many times [57, 48], is our limitation to Gaussian fluctuations, which is also justified only for high enough temperatures. In some sense it is only technical limitation, though it is quite important for the formal structure of our solution.

We already mentioned that in this class of models we can demonstrate the breaking of the fundamental property of self – averaging of superconducting order parameter [54, 59]. Unfortunately, this can be done only in rather unrealistic case of infinite correlation length of pseudogap fluctuations [54], or in very special model with finite correlation length [58, 59], and in an oversimplified model with "hot patches" on the fermi surface. Qualitative picture emerging from this analysis demonstrates the possibility of formation of "superconducting drops" at temperatures higher than mean – field T_c [19, 54, 59],

[18] Above we always assumed that we are dealing with hole doped systems, where concentration dependence of $T^*(x)$ is well established [24, 78]. For electronically doped cuprates similar data are practically absent.

[19] Thus, and also to spare space, we have dropped discussion of Gorkov's equations, which can also be derived and analyzed [55, 75], taking into account all higher orders of perturbation theory over pseudogap fluctuations.

which may have direct relation to the existence of the "low energy" pseudogap (signatures of superconducting response at $T > T_c$) and experimentally observed inhomogeneous superconductivity in cuprates [17, 18]. In the "hot spots" model this kind of analysis is still to be done.

At the same time, we have seen that in some cases we can make even direct comparison of predictions of these simplified models with the experiments, and the results of such comparison are rather promising. In this sense the "hot spots" model can pretend to give quasi realistic description of the properties of the pseudogap state in high – temperature superconductors.

The author is grateful to E.Z.Kuchinskii and N.A.Kuleeva (Strigina) for their collaboration during our work on the "hot spots" model. This work was supported in part by RFBR grant 02-02-16031 and programs of the Presidium of the Russian Academy of Sciences (RAS) "Quantum macrophysics" and of the Division of Physical Sciences of the RAS "Strongly correlated electrons in semiconductors, metals, superconductors and magnetic materials".

References

[1] J.Annett, N.Goldenfeld, A.J.Leggett. Physical Properties of High Temperature Superconductors. Vol. 5, p. 375 (Ed. by D.M.Ginsberg), World Scientific, Singapore, 1996. ArXiv: cond-mat/9601060

[2] C.C.Tsui, J.R.Kirtley. Rev. Mod. Phys. **72**, 969 (2000)

[3] Z.-X.Shen, D.S.Dessau. Phys. Reports **253**, 1 (1995)

[4] A.Damasceli, Z.Hussain, Z.-X.Shen. Rev. Mod. Phys. **75**, 475 (2003)

[5] X.J.Zhou, T.Yoshida, D.-H.Lee, W.L.Yang, V.Brouet, F.Zhou, W.X.Ti, J.W.Xiong, Z.X.Zhao, T.Sasagawa, T.Kakeshita, H.Eisaki, S.Uchida, A.Fujimori, Z.Hussain, Z.-X.Shen. Phys. Rev. Lett. **92**, 187001 (2004).

[6] E.G.Maksimov. Physics – Uspekhi **43**, 965 (2000)

[7] M.Kuliĉ. Phys. Reports **338**, 1 (2000)

[8] M.Kuliĉ. ArXiv: cond-mat/0404287

[9] D.J.Scalapino. Phys. Reports **250**, 329 (1995)

[10] T.Moriya, K.Ueda. Adv. Phys. **49**, 555 (2000)

[11] A.V.Chubukov, D.Pines, J.Schmalian. The Physics of Superconductors. (Ed. K.-H.Bennemann and J.B.Ketterson), Springer 2002. ArXiv: cond-mat/0201140

[12] Y.Yanase, T.Jugo, T.Nomura, H.Ikeda, T.Hotta, K.Yamada. Phys. Reports **387**, 1 (2004). ArXiv: cond-mat/0309094

[13] P.W.Anderson. The Theory of Superconductivity in the High – T_c Cuprates. Princeton University Press, Princeton, 1997

[14] E.Demler, W.Hanke, Shou-Cheng Zhang. ArXiv: cond-mat/0405038

[15] C.M.Varma, Z.Nussinov, Wim van Saarlos. Phys. Reports **361**, 267 (2002)

[16] M.V.Sadovskii. Superconductivity and Localization. World Scientific, Singapore 2000.

[17] S.H.Pan, J.P.O'Neil, R.L.Badzey, C.Chamon, H.Ding, J.R.Engelbrecht, Z.Wang, H.Eisaki, S.Uchida, A.K.Gupta. Nature **413**, 282 (2001)

[18] K.McElroy, D.-H.Lee, J.E.Hoffman, K.M.Lang, E.W.Hudson, H.Eisaki, S.Uchida, J.Lee, J.C.Davis. ArXiv: cond-mat/0404005

[19] L.N.Bulaevskii, S.V.Panyukov, M.V.Sadovskii. JETP **65**, 380 (1987)

[20] T.Timusk, B.Statt. Rep.Progr.Phys. **62**, 61 (1999)

[21] M.V.Sadovskii. Physics – Uspekhi **44**, 5i5 (2001)

[22] N.F.Mott, E.A.Davis. Electronic Pocesses in Non – Crystalline materials. Clarendon Press, Oxford. 1971

[23] J.L.Tallon, J.W.Loram, Physica **C349**, 53 (2001), ArXiv: cond-mat/0005063

[24] J.W.Loram, K.A.Mirza, J.R.Cooper, J.L.Tallon. Physica **C 282-287**, 1405 (1997)

[25] C.Renner, B.Revaz, J.Y.Genoud, K.Kadowaki, Ø.Fisher. Phys.Rev.Lett. **80**, 149 (1998)

[26] V.M.Krasnov, A.Yurgens, D.Winkler, P.Delsing, T.Claeson. Phys.Rev.Lett. **84**, 5860 (2000)

[27] V.M.Krasnov, A.E.Kovalev, A.Yurgens, D.Winkler, Phys. Rev. Lett. **86**, 2657 (2001)

[28] Y.Onose, Y.Taguchi, K.Ishizaka, Y,Tokura. Phys. Rev. Lett. **87**, 217001 (2001); Preprint (2003)

[29] D.N.Basov, A.V.Puchkov, R.A.Hughes, T.Strach, J.Preston, T.Timusk. Phys.Rev. **B49**, 12165 (1994)

[30] D.N.Basov, B.Dabrowski, T.Timusk. Phys.Rev.Lett. **81**, 2132 (1998)

[31] E.J.Singley, D.N.Basov, K.Kurahashi, T.Uefuji, K.Yamada. Phys. Rev. **B64**, 224503 (2001)

[32] M.R.Norman, H.Ding, M.Randeria, J.C.Campuzano, T.Yokoya, T.Takeuchi, T.Takahashi, T.Mochiku, K.Kadowaki, P.Guptasarma, D.G.Hinks. Nature **392**, 157 (1998)

[33] H.Ding T.Yokoya, J.C.Campuzano, T.Takahashi, M.Randeria, M.R.Norman, T.Mochiku, K.Kadowaki, J.Giapintzakis. Nature **382**, 51 (1996)

[34] M.R.Norman, M.Randeria, H.Ding, J.C.Campuzano. Phys.Rev. **B57**, R11093 (1998)

[35] A.Kaminski, J.Mesot, H.Fretwell, J.C.Campuzano, M.R.Norman, M.Randeria, H.Ding, T.Sato, T.Takahashi, T.Mochiku, K.Kadowaki, H.Hoechst. Phys. Rev. Lett. **84**, 1788 (2000)

[36] A.Kaminski, H.M.Fretwell, M.R.Norman, M.Randeria, S.Rosenkranz, J.C.Campuzano, J.Mesot, T.Sato, T.Takahashi, T.Terashima, M.Takano, K.Kadowaki, Z.Z.Li, H.Raffy. ArXiv: cond-mat/0404385

[37] A.A.Kordyuk, S.V.Borisenko, A.Koitzsch, J.Fink, M.Knupfer, B.Büchner, H.Berger, G.Margaritondo, C.T.Lin, B.Keimer, S.Ono, Y.Ando. Phys. Rev. Lett. **92**, 257006 (2004)

[38] N.P.Armitage, D.H.Lu, C.Kim, A.Damascelli, K.M.Shen, F.Ronning, D.L.Feng, P.Bogdanov, Z.-X.Shen. Phys.Rev.Lett. **87**, 147003 (2001)

[39] J.R.Schrieffer, X.G.Wen, S.C.Zhang. Phys.Rev. **B39**, 11663 (1989)

[40] Yu.A.Izyumov. Physics – Uspekhi **34**, 935 (1991)

[41] P.Monthoux, A.Balatsky, D.Pines. Phys.Rev. **B46**, 14803 (1992)

[42] P.Monthoux, D.Pines. Phys.Rev. **B47**, 6069 (1993); Phys.Rev. **B48**, 4261 (1994)

[43] A.Millis, H.Monien, D.Pines. Phys.Rev. **B42**, 1671 (1990)

[44] Yu.A.Izyumov. Physics – Uspekhi **42**, 215 (1999)

[45] V.Barzykin, D.Pines. Phys.Rev. **B52**, 13565 (1995)

[46] D.Pines. Z.Phys. **B103**, 129 (1997)

[47] J.Schmalian, D.Pines, B.Stojkovič. Phys.Rev.Lett. **80**, 3839(1998); Phys.Rev. **B60**, 667 (1999)

[48] E.Z.Kuchinskii, M.V.Sadovskii. JETP **88**, 968 (1999)

[49] A.P.Kampf, J.R.Schrieffer. Phys.Rev. **B41**,6399(1990), **B42**,7967(1990)

[50] A.I.Posazhennikova, M.V.Sadovskii. JETP **88**, 347 (1999)

[51] M.V.Sadovskii. JETP **39**, 845 (1974); Sov. Phys. - Solid State **16**, 743 (1974)

[52] W.Wonneberger, R.Lautensschlager. J.Phys. C **9**, 2865 (1976)

[53] M.V.Sadovskii. Diagrammatics (Lectures on selected problems of condensed matter theory). Moscow – Izhevsk, 2004; http://sadovski.iep.uran.ru/ENGLISH/Diagramm.ps (pdf) – in Russian

[54] E.Z.Kuchinskii, M.V.Sadovskii. JETP **90**, 535 (2000)

[55] E.Z.Kuchinskii, M.V.Sadovskii. JETP **92**, 480 (2001)

[56] A.Posazhennikova, P.Coleman. Phys.Rev. **B67**, 165109 (2003)

[57] M.V.Sadovskii. JETP **50**, 989 (1979)

[58] L.Bartosch, P.Kopietz. Eur. Phys. J. **B17**, 555 (2000)

[59] E.Z.Kuchinskii, M.V.Sadovskii. JETP **94**, 654 (2002)

[60] M.V.Sadovskii. Physica **C341-348**, 811 (2000)

[61] L.Bartosch, P.Kopietz. Phys.Rev. **B60**, 15488 (1999)

[62] Y.Yanase. J. Phys. Soc. Jpn. **73**, 1000 (2004)

[63] D.S.Marshall, D.S.Dessau, A.G.Loeser, C-H.Park, A.Y.Matsuura, J.N.Eckstein, I.Bozovic, D.Fournier, A.Kapitulnik, W.E.Spicer, Z.-X.Shen. Phys.Rev.Lett. **76**, 4841 (1996)

[64] M.V.Sadovskii, A.A.Timofeev. Superconductivity – Phys. Chem. Technol. **4**, 9 (1991)

[65] M.V.Sadovskii, A.A.Timofeev. J.Moscow Phys.Soc. **1**, 391 (1991)

[66] M.V.Sadovskii, N.A.Strigina. JETP **95**, 526 (2002)

[67] D.Vollhardt, P.Wolfle. Phys.Rev. **B22**, 4666 (1980)

[68] L.P.Gorkov, A.I.Larkin, D.E.Khmelnitskii. JETP Lett. **30**, 228 (1979)

[69] P.Monthoux, D.J.Scalapino. Phys. Rev. **B65**, 235104 (2002)

[70] A.A.Gogolin, G.T.Zimanyi. Sol.St.Comm. **46**, 469 (1983)

[71] M.V.Sadovskii. JETP Lett. **69**, 483 (1999); Physica **C341-348**, 939 (2000)

[72] E.Z.Kuchinskii, M.V.Sadovskii, N.A.Strigina. JETP **98**, 748 (2004)

[73] N.A.Kuleeva, E.Z.Kuchinskii, M.V.Sadovskii. JETP (to be published); ArXiv: cond-mat/0406156

[74] E.Z.Kuchinskii, N.A.Kuleeva, M.V.Sadovskii. J. Phys. Chem. Solids (to be published); ArXiv: cond-mat/0405691

[75] N.A.Kuleeva, E.Z.Kuchinskii. Fiz. Tverd. Tela **46**, 1557 (2004)

[76] A.I.Posazhennikova, M.V.Sadovskii. JETP Lett. **63**, 358 (1996); JETP **85**, 1162 (1997)

[77] R.J.Radtke, K.Levin, H.-B.Schüttler, M.R.Norman. Phys.Rev. B **48**, 653 (1993)

[78] S.H.Naqib, J.R.Cooper, J.L.Tallon, R.S.Islam, R.A.Chakalov. ArXiv:cond-mat/0312443

[79] M.R.Presland, J.L.Tallon, R.G.Buckley, R.S.Liu, N.E.Flower. Physica C **176**, 95 (1991)

[80] A.E.Karkin, S.A.Davydov, B.N.Goshchitskii, S.V.Moshkin, M.Yu.Vlasov. Fiz. Met. Metallogr. **76**, 103 (1993)

[81] Y.Fukuzumi, K.Mizuhashi, K.Takenaka, S.Uchida. Phys.Rev.Lett. **76**, 684 (1996)

[82] J.L.Tallon, C.Bernhard, G.V.M.Williams, J.W.Loram. Phys.Rev.Lett. **79**, 5294 (1997)

[83] S.K.Tolpygo, J.-Y.Lin, M.Gurvitch, S.Y.Hou, J.M.Phillips. Phys.Rev. B **53**, 12454, 12462 (1996)

[84] F.Rullier-Albenque, H.Alloul, R.Tourbot. Phys.Rev.Lett. **91**, 047001 (2003)

[85] A.I.Posazhennikova, M.V.Sadovskii. JETP Lett. **65**, 270 (1997)

[86] G.Haran, A.D.S.Nagy. Phys.Rev. **54**, 15463 (1996)

Fizika Nizkikh Temperatur, 2006, v. 32, Nos. 4/5, p. 528–537

Pseudogaps: introducing the length scale into dynamical mean-field theory

E.Z. Kuchinskii, I.A. Nekrasov, and M.V. Sadovskii

Institute for Electrophysics, Russian Academy of Sciences, Ekaterinburg, 620016, Russia
E-mail: sadovski@iep.uran.ru

Received June 10, 2005

Pseudogap physics in strongly correlated systems is essentially scale dependent. We generalize the dynamical mean-field theory (DMFT) by introducing into the DMFT equations dependence on the correlation length of pseudogap fluctuations via an additional (momentum-dependent) self-energy $\Sigma_{\mathbf{k}}$. This self-energy describes nonlocal dynamical correlations induced by short-ranged collective SDW-like antiferromagnetic spin (or CDW-like charge) fluctuations. At high enough temperatures these fluctuations can be viewed as a quenched Gaussian random field with finite correlation length. This generalized DMFT + $\Sigma_{\mathbf{k}}$ approach is used for the numerical solution of the weakly doped one-band Hubbard model with repulsive Coulomb interaction on a square lattice with nearest and next nearest neighbor hopping. The effective single impurity problem is solved by the numerical renormalization group (NRG). Both types of strongly correlated metals, namely (i) the doped Mott insulator and (ii) the case of bandwidth $W \lesssim U$ (U is the value of local Coulomb interaction) are considered. Densities of states, spectral functions and ARPES spectra calculated within DMFT + $\Sigma_{\mathbf{k}}$ show a pseudogap formation near the Fermi level of the quasiparticle band. We also briefly discuss effects of random impurity scattering. Finally we demonstrate the qualitative picture of Fermi surface «destruction» due to pseudogap fluctuations and formation of «Fermi arcs» which agrees well with ARPES observations.

PACS: 71.10.Fd, 71.10.Hf, **71.27.+a**, **71.30.+h**, **74.72.−h**

Keywords: pseudogap, strongly correlated systems, spin fluctuations.

1. Introduction

Pseudogap formation in the electronic spectrum of underdoped copper oxides [1,2] is an especially striking anomaly of the normal state of high-temperature superconductors. Despite continuing discussions on the nature of the pseudogap, we believe that the preferable «scenario» for its formation is most likely based on the model of strong scattering of the charge carriers by short-ranged antiferromagnetic (AFM, SDW) spin fluctuations [2,3]. In the momentum representation this scattering transfers momenta of the order of $\mathbf{Q} = (\pi/a, \pi/a)$ (a is the lattice constant of the two dimensional lattice). This leads to the formation of structures in the one-particle spectrum, which are precursors of the changes in the spectra due to long-range AFM order (period doubling). As a result we obtain non-Fermi liquid like behavior (dielectrization) of the spectral density in the vicinity of the so-called «hot spots» on the Fermi surface, appearing at intersections of the Fermi surface with the antiferromagnetic Brillouin zone boundary [2].

Within this spin-fluctuation scenario a simplified model of the pseudogap state was studied [2,4,5] under the assumption that the scattering by dynamic spin fluctuations can be reduced for high enough temperatures to static Gaussian random field (quenched disorder) of pseudogap fluctuations. These fluctuations are defined by a characteristic scattering vector from the vicinity of $\mathbf{Q}$, with a width determined by the inverse correlation length of short-range order $\kappa = \xi^{-1}$.

Undoped cuprates are antiferromagnetic Mott insulators with $U >> W$ (U is the value of local Coulomb interaction, W is the bandwidth of noninteracting band), so that correlation effects are actually very important. It is thus clear that the electronic properties

© E.Z. Kuchinskii, I.A. Nekrasov, and M.V. Sadovskii, 2006

of underdoped (and probably also optimally doped) cuprates are governed by strong electronic correlations too, so that these systems are typical strongly correlated metals. Two types of correlated metals can be distinguished: (i) the doped Mott insulator and (ii) the bandwidth-controlled correlated metal $W \approx U$.

A state-of-the-art tool to describe such correlated systems is the dynamical mean-field theory (DMFT) [6–10]. The characteristic features of correlated systems within the DMFT are the formation of incoherent structures, the so-called Hubbard bands, split by the Coulomb interaction U, and a quasiparticle (conduction) band near the Fermi level dynamically generated by the local correlations [6–10].

Unfortunately, the DMFT is not useful to the study the «antiferromagnetic» scenario of pseudogap formation in strongly correlated metals. This is due to the basic approximation of the DMFT, which amounts to the complete neglect of nonlocal dynamical correlation effects. The aim of the present paper is to describe the main results of a semiphenomenological approach, formulated by us recently to overcome this difficulty [11].

The paper is organized as follows. In Sec. 2 we present a formulation of the self-consistent generalization we call DMFT + $\Sigma_{\mathbf{k}}$ which includes short-ranged (nonlocal) correlations. Section 3 describes the construction of the **k**-dependent self-energy, and some computational details are presented in Sec. 4.1. Results and a discussion are given in the Secs. 4 and 5.

2. Introducing length scale into DMFT: DMFT + $\Sigma_{\mathbf{k}}$ approach

A basic shortcoming of traditional DMFT approach [6–10] is the neglect of momentum dependence of electron self-energy. This approximation in principle allows for an exact solution of correlated electron systems (in infinite dimensions) fully preserving the local part of the dynamics introduced by electronic correlations. To include nonlocal effects, while remaining within the usual «impurity analogy» of DMFT, we propose the following procedure. To be definite, let us consider a standard one-band Hubbard model. The extension to multi-orbital or multi-band models is straightforward. The major assumption of our approach is that the lattice and Matsubara «time» Fourier transform of the single-particle Green function can be written as:

$$G_{\mathbf{k}}(i\omega) = \frac{1}{i\omega + \mu - \varepsilon(\mathbf{k}) - \Sigma(i\omega) - \Sigma_{\mathbf{k}}(i\omega)}, \qquad \omega = \pi T(2n+1), \tag{1}$$

where $\Sigma(i\omega)$ is the *local* contribution to the self-energy, surviving in the DMFT, while $\Sigma_{\mathbf{k}}(i\omega)$ is some momentum-dependent part. We suppose that this last contribution is due to either electron interactions with some «additional» collective modes or order parameter fluctuations, or may be due to similar nonlocal contributions within the Hubbard model itself. To avoid possible confusion we must stress that $\Sigma_{\mathbf{k}}(i\omega)$ can also contain local (momentum-independent) contribution which obviously *vanishes* in the limit of infinite dimensionality $d \to \infty$ and is not taken into account within the standard DMFT. Due to this fact there is no double counting of diagrams problem within our approach for the Hubbard model. This question does not arise at all if we consider $\Sigma_{\mathbf{k}}(i\omega)$ appearing due to some «additional» interaction. More important is that the assumed additive form of self-energy $\Sigma(i\omega) + \Sigma_{\mathbf{k}}(i\omega)$ implicitly corresponds to neglect of possible interference of these local (DMFT) and nonlocal contributions.

The self-consistency equations of our generalized DMFT + $\Sigma_{\mathbf{k}}$ approach are formulated as follows [11]:

1. Start with some initial guess of *local* self-energy $\Sigma(i\omega)$, e.g., $\Sigma(i\omega) = 0$.
2. Construct $\Sigma_{\mathbf{k}}(i\omega)$ within some (approximate) scheme, taking into account interactions with collective modes or order parameter fluctuations which in general can depend on $\Sigma(i\omega)$ and μ.
3. Calculate the local Green function

$$G_{ii}(i\omega) = \frac{1}{N}\sum_{\mathbf{k}} \frac{1}{i\omega + \mu - \varepsilon(\mathbf{k}) - \Sigma(i\omega) - \Sigma_{\mathbf{k}}(i\omega)}. \tag{2}$$

4. Define the «Weiss field»

$$\mathcal{G}_0^{-1}(i\omega) = \Sigma(i\omega) + G_{ii}^{-1}(i\omega). \tag{3}$$

5. Using some «impurity solver» to calculate the single-particle Green function for the effective Anderson impurity problem, defined by Grassmanian integral

$$G_d(\tau - \tau') = \frac{1}{Z_{\text{eff}}}\int Dc_{i\sigma}^{+} Dc_{i\sigma} c_{i\sigma}(\tau) c_{i\sigma}^{+}(\tau') \exp(-S_{\text{eff}}) \tag{4}$$

with effective action for a fixed site («impurity») i

$$S_{\text{eff}} = -\int_0^{\beta} d\tau_1 \int_0^{\beta} d\tau_2\, c_{i\sigma}(\tau_1)\mathcal{G}_0^{-1}(\tau_1 - \tau_2) c_{i\sigma}^{+}(\tau_2) + \int_0^{\beta} d\tau\, U n_{i\uparrow}(\tau) n_{i\downarrow}(\tau), \tag{5}$$

$Z_{\text{eff}} = \int Dc_{i\sigma}^{+} Dc_{i\sigma} \exp(-S_{\text{eff}})$, and $\beta = T^{-1}$. This step produces a *new* set of values $G_d^{-1}(i\omega)$.

6. Define a *new* local self-energy

$$\Sigma(i\omega) = \mathcal{G}_0^{-1}(i\omega) - G_0^{-1}(i\omega) . \quad (6)$$

7. Using this self-energy as «initial» one in step 1, continue the procedure until (and if) convergency is reached to obtain

$$G_{ii}(i\omega) = G_d(i\omega) . \quad (7)$$

Eventually, we get the desired Green function in the form of (1), where $\Sigma(i\omega)$ and $\Sigma_{\mathbf{k}}(i\omega)$ are those appearing at the end of our iteration procedure.

3. Construction of k-dependent self-energy

For the momentum-dependent part of the single-particle self-energy we concentrate on the effects of scattering of electrons from collective short-range SDW-like antiferromagnetic spin (or CDW-like charge) fluctuations. To calculate $\Sigma_{\mathbf{k}}(i\omega)$ for an electron moving in the quenched random field of (static) Gaussian spin (or charge) fluctuations with dominant scattering momentum transfers from the vicinity of some characteristic vector $\mathbf{Q}$ («hot spots» model [2]), we use a slightly generalized version of the recursion procedure proposed in Refs. 4, 5, 12 which takes into account *all* Feynman diagrams describing the scattering of electrons by this random field. This becomes possible due to a remarkable property of our simplified version of «hot spots» model that *the contribution of an arbitrary diagram with intersecting interaction lines is actually equal to the contribution of some diagram of the same order without intersections of these lines* [5,12]. Thus, in fact we can limit ourselves to consideration of only diagrams without intersecting interaction lines, taking the contribution of diagrams with intersections into account with the help of additional combinatorial factors, which are attributed to «initial» vertices or just interaction lines [12]. As a result we obtain the following recursion relation (continuous fraction representation [12]) for the desired self-energy:

$$\Sigma_{\mathbf{k}}(i\omega) = \Sigma_{n=1}(i\omega\mathbf{k}) \quad (8)$$

with

$$\Sigma_n(i\omega\mathbf{k}) = \frac{\Delta^2 s(n)}{i\omega + \mu - \Sigma(i\omega) - \varepsilon_n(\mathbf{k}) + inv_n\kappa - \Sigma_{n+1}(i\omega\mathbf{k})} . \quad (9)$$

The quantity Δ characterizes the energy scale and $\kappa = \xi^{-1}$ is the inverse correlation length of short range SDW (CDW) fluctuations, $\varepsilon_n(\mathbf{k}) = \varepsilon(\mathbf{k}+\mathbf{Q})$ and $v_n = |v^x_{\mathbf{k}+\mathbf{Q}}| + |v^y_{\mathbf{k}+\mathbf{Q}}|$ for odd n while $\varepsilon_n(\mathbf{k}) = \varepsilon(\mathbf{k})$ and $v_n = |v^x_{\mathbf{k}}| + |v^y_{\mathbf{k}}|$ for even n. The velocity projections $v^x_{\mathbf{k}}$ and $v^y_{\mathbf{k}}$ are determined by usual momentum derivatives of the «bare» electronic energy dispersion $\varepsilon(\mathbf{k})$. Finally, $s(n)$ represents a combinatorial factor with

$$s(n) = n \quad (10)$$

for the case of commensurate charge (CDW type) fluctuations with $\mathbf{Q} = (\pi/a, \pi/a)$ [12]. For incommensurate CDW fluctuations [12] one finds

$$s(n) = \begin{cases} \dfrac{n+1}{2} & \text{for odd } n , \\ \dfrac{n}{2} & \text{for even } n . \end{cases} \quad (11)$$

If we take into account the (Heisenberg) spin structure of interaction with spin fluctuations in «nearly antiferromagnetic Fermi liquid» (spin-fermion (SF) model Ref. 4), the combinatorics of diagrams becomes more complicated. Spin-conserving scattering processes obeys commensurate combinatorics, while spin-flip scattering is described by diagrams of incommensurate type («charged» random field in terms of Ref. 4). In this model the recursion relation for the single-particle Green function is again given by (9), but the combinatorial factor $s(n)$ now acquires the following form [4]:

$$s(n) = \begin{cases} \dfrac{n+2}{3} & \text{for odd } n , \\ \dfrac{n}{3} & \text{for even } n . \end{cases} \quad (12)$$

Obviously, with this procedure we introduce an important length scale ξ not present in standard DMFT. Physically this scale mimics the effect of short-range (SDW or CDW) correlations within fermionic «bath» surrounding the effective Anderson impurity. We expect that such a length-scale dependence will lead to a competition between local and nonlocal physics.

An important aspect of the theory is that both parameters Δ and ξ can in principle be calculated from the microscopic model at hand. For example, using the two-particle self-consistent approach of Ref. 13 with the approximations introduced in Refs. 4, 5, one can derive [11] within the standard Hubbard model the following microscopic expression for Δ:

$$\Delta^2 = \frac{1}{4}U^2 \frac{\langle n_{i\uparrow} n_{i\downarrow}\rangle}{\langle n_{i\uparrow}\rangle\langle n_{i\downarrow}\rangle} [\langle n_{i\uparrow}\rangle + \langle n_{i\downarrow}\rangle - 2\langle n_{i\uparrow} n_{i\downarrow}\rangle] =$$
$$= U^2 \frac{\langle n_{i\uparrow} n_{i\downarrow}\rangle}{n^2} \langle (n_{i\uparrow} - n_{i\downarrow})^2\rangle =$$
$$= U^2 \frac{\langle n_{i\uparrow} n_{i\downarrow}\rangle}{n^2} \frac{1}{3} \langle \mathbf{S}_i^2\rangle , \quad (13)$$

where we consider only scattering from antiferromagnetic spin fluctuations. Different local quantities here — spin fluctuation $\langle \mathbf{S}_i^2 \rangle$, density n and double occupancy $\langle n_{i\uparrow} n_{i\downarrow} \rangle$ — can easily be calculated within the standard DMFT [9]. We performed such calculations [11] for wide range of U and filling factors n using quantum Monte Carlo (QMC) [15]. From these calculations we can see that the values of Δ lie in the interval of $\Delta = (0.5–2.0)t$ and change rather smoothly with n and U.

Microscopic expressions for the correlation length $\xi = \kappa^{-1}$ can also be derived within the two-particle self-consistent approach [13]. However, we expect those results for ξ to be less reliable, because this approach is valid only for relatively small (or medium) values of U/t and for purely two-dimensional case (while real systems are quasi-two-dimensional).

Thus, in the following we will consider both Δ and especially ξ as some phenomenological parameters to be determined from experiments. This makes our approach somehow similar in the spirit to Landau approach to Fermi liquids.

Our construction can be further generalized to include other types of interactions. Thus scattering by random impurities with pointlike potential V is easily taken into account in self-consistent Born approximation [14]. Then, in comparison with impurity-free case, we have just a substitution (renormalization):

$$\varepsilon_n \to \varepsilon_n - \rho V^2 \sum_{\mathbf{p}} \operatorname{Im} G(\varepsilon_n \mathbf{p}) \equiv \varepsilon_n \eta_\varepsilon , \quad (14)$$

$$\eta_\varepsilon = 1 - \frac{\rho V^2}{\varepsilon_n} \sum_{\mathbf{p}} \operatorname{Im} G(\varepsilon_n \mathbf{p}) . \quad (15)$$

If we do not perform fully self-consistent calculations of impurity self-energy, in the simplest approximation we just have:

$$\varepsilon_n \to \varepsilon_n \eta_\varepsilon = \varepsilon_n + \gamma \operatorname{sign} \varepsilon_n , \quad (16)$$

$$\eta_\varepsilon = 1 + \frac{\gamma}{|\varepsilon_n|} , \quad (17)$$

where $\gamma = \pi\rho V^2 N_0(0)$ is the standard Born impurity scattering rate ($N_0(0)$ is the density of states of «free» electrons at the Fermi level).

4. Results and discussion

4.1. Computation details

In the following, we discuss results for a standard one-band Hubbard model on a square lattice. With nearest (t) and next nearest (t') neighbor hopping integrals the dispersion reads

$$\varepsilon(\mathbf{k}) = -2t(\cos k_x a + \cos k_y a) - 4t' \cos k_x a \cos k_y a , \quad (18)$$

where a is the lattice constant. The correlations are introduced by a repulsive local two-particle interaction U. We choose as energy scale the nearest neighbor hopping integral t and as length scale the lattice constant a.

For a square lattice the «bare» bandwidth is $W = 8t$. To study a strongly correlated metallic state obtained as doped Mott insulator we use $U = 40t$ as value for the Coulomb interaction and a filling $n = 0.8$ (hole doping). The correlated metal in the case of $W \gtrsim U$ is considered for the case of $U = 4t$ and filling factor $n = 0.8$ (hole doping). For Δ we have choosen rather typical values between $\Delta = 0.1t$ and $\Delta = 2t$ (actually as approximate limiting values obtained from (13) via QMC calculations in Ref. 11) and for the correlation length we considered mainly $\xi = 2a$ and $\xi = 10a$ (being motivated mainly by experimental data for cuprates [2,4]).

The DMFT maps the lattice problem onto an effective, self-consistent impurity defined by Eqs. (4), (5). In our work we employed as «impurity solvers» two reliable numerically exact methods — quantum Monte Carlo [15] and numerical renormalization group (NRG) [17,18]. Calculations were done both for $t' = 0$ and $t'/t = -0.4$ (more or less typical for cuprates) at two different temperatures $T = 0.088t$ and $T = 0.356t$ (for NRG computations). QMC computations of double occupancies as functions of filling were done at temperatures $T = 0.1t$ and $T = 0.4t$.

Below we present results only for most typical dependences and parameters, more details can be found in Ref. 11.

4.2. Generalized DMFT + $\Sigma_{\mathbf{k}}$ approach: densities of states

Let us start the discussion of results obtained within our generalized DMFT + $\Sigma_{\mathbf{k}}$ approach with the densities of states (DOSs) for the case of small (relative to bandwidth) Coulomb interaction $U = 4t$ with and without pseudogap fluctuations. As already discussed in the Introduction, the characteristic feature of the strongly correlated metallic state is the coexistence of lower and upper Hubbard bands split by the value of U with a quasiparticle peak at the Fermi level. Since at half-filling the bare DOS of the square lattice has a Van Hove singularity at the Fermi level ($t' = 0$) or close to it (in case of $t'/t = -0.4$) one cannot treat a peak on the Fermi level simply as a quasiparticle peak. In fact, there are two contributions to this peak from (i) the quasiparticle peak appearing in strongly correlated metals due to many-body effects

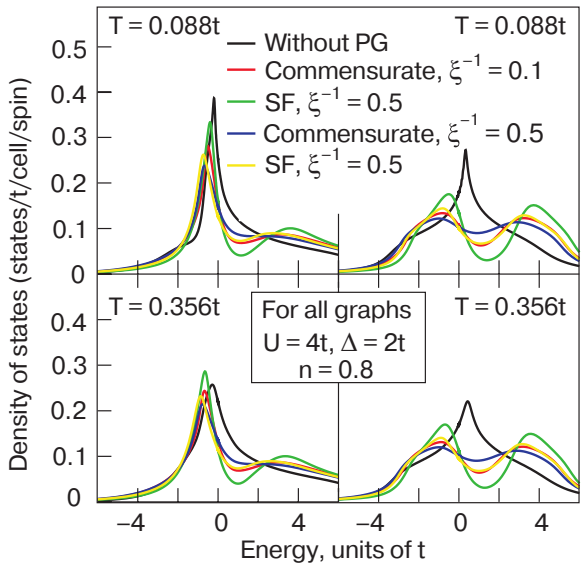

Fig. 1. Comparison of DOSs obtained from DMFT(NRG) + $\Sigma_{\mathbf{k}}$ calculations for different combinatorical factors (SF — spin-fermion model, commensurate), inverse correlation lengths (ξ^{-1}) in units of the lattice constant, temperatures (T) and pseudogap potential $\Delta = 2t$. Left column corresponds to $t'/t = -0.4$, right column to $t' = 0$. In all graphs the Coulomb interaction is $U = 4t$ and $n = 0.8$. The Fermi level corresponds to zero.

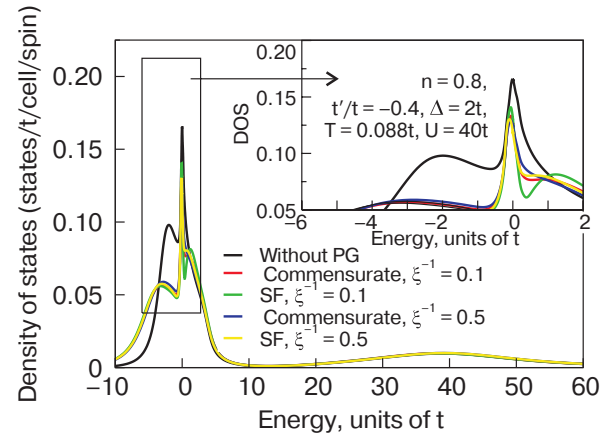

Fig. 2. Comparison of DOSs obtained from DMFT(NRG) + $\Sigma_{\mathbf{k}}$ calculations for $t'/t = -0.4$, $T = 0.088t$, $U = 40t$ and filling $n = 0.8$.

and (ii) the smoothed Van Hove singularity from the bare DOS. In Fig. 1 we show the corresponding DMFT(NRG) DOSs without pseudogap fluctuations as black lines for $n = 0.8$ for both bare dispersions $t'/t = -0.4$ (left panels) and for $t' = 0$ (right panels) for two different temperatures $T = 0.356t$ (middle panels) and $T = 0.088t$ (upper and lower panels). The remaining curves in Fig. 1 represent results for the DOSs with nonlocal fluctuations switched on. For all sets of parameters one can see that the introduction of nonlocal fluctuations into the calculation leads to the formation of pseudogap within the quasiparticle peak.

For $n = 0.8$ (Fig. 1) the picture of DOS is slightly asymmetric. The width of the pseudogap (the distance between peaks closest to Fermi level) appears to be of the order of $\sim 2\Delta$. We have checked that decreasing the value of Δ from $2t$ to t leads to a pseudogap that is correspondingly twice smaller and in addition more shallow. When one uses the combinatorial factors corresponding to the spin-fermion model (Eq. (12)), the pseudogap becomes more pronounced than in the case of commensurate charge fluctuations (combinatorial factors of Eq. (11)). The influence of the correlation length ξ is also as expected. Changing ξ^{-1} from $\xi^{-1} = 0.1$ to $\xi^{-1} = 0.5$, i.e., decreasing the range of the nonlocal fluctuations, slightly washes out the pseudogap. Also, increasing the temperature from $T = 0.088t$ to $T = 0.356t$ leads to a general broadening of the structures in the DOSs. Noteworthy is the fact that for $t'/t = -0.4$ and $\xi^{-1} = 0.5$ the pseudogap has almost disappeared for the temperatures studied here. Also very remarkable point is the similarity of the results obtained with the generalized DMFT + $\Sigma_{\mathbf{k}}$ approach with $U = 4t$ (smaller than the bandwidth W) to those obtained earlier without Hubbard-like Coulomb interactions [4,5].

Let us now consider the case of a doped Mott insulator (Fig. 2). The model parameters are again taken as $t'/t = -0.4$ with filling factor of $n = 0.8$, but the Coulomb interaction strength is set to $U = 40t$. Characteristic features of the DOS for such a strongly correlated metal are a strong separation of lower and upper Hubbard bands and a Fermi level crossing by the lower Hubbard band (for non-half-filled case). Without nonlocal fluctuations the quasiparticle peak is again formed at the Fermi level, but now the upper Hubbard band is far to the right and does not touch the quasiparticle peak (as it was for the case of small Coulomb interactions).

Pseudogap appears close to the middle of quasiparticle peak. In addition we observe that the lower Hubbard band is slightly broadened by fluctuation effects. Qualitative behavior of the pseudogap anomalies is similar to those described above for the case of $U = 4t$, e.g., a decrease of ξ makes the pseudogap less pronounced, while reducing Δ from $\Delta = 2t$ to $\Delta = t$ narrows of the pseudogap and also makes it more shallow. Note that for the doped Mott-insulator the pseudogap is remarkably more pronounced for the SDW-like fluctuations than for CDW-like fluctuations.

There are, however, quite clear differences to the case of $U = 4t$. For example, the width of the pseudo-

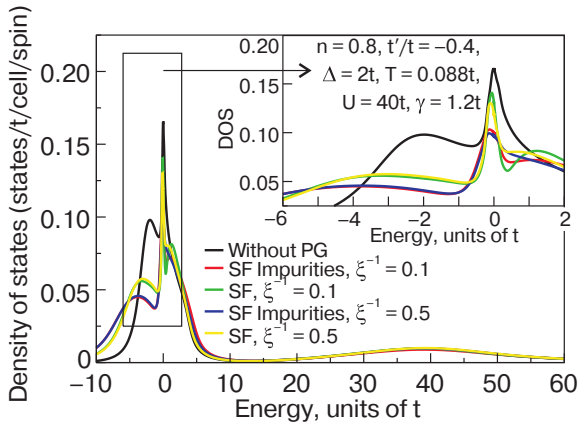

Fig. 3. Comparison of DOSs obtained from DMFT(NRG) + $\Sigma_{\mathbf{k}}$ calculations for $t'/t = -0.4$, $T = 0.088t$, $U = 40t$, $n = 0.8$ and for impurity scattering rate $\gamma = 1.2t$.

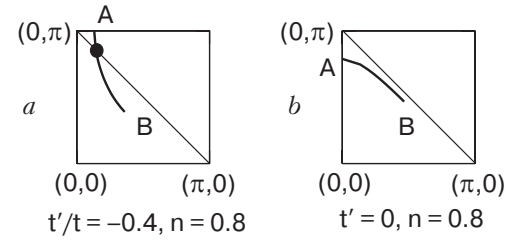

Fig. 4. 1/8-th of the bare Fermi surfaces for the different occupancies n and combinations (t,t') used for the calculation of spectral functions $A(\mathbf{k},\omega)$. The diagonal line corresponds to the antiferromagnetic Brillouin zone boundary at half-filling for a square lattice with nearest-neighbors hopping only. The full circle marks the so-called «hot spot».

gap appears to be much smaller than 2Δ, which we attribute to the fact that the quasiparticle peak itself is actually rather narrow in the case of doped Mott insulator.

Random impurity scattering, in general case leads to the filling of the pseudogap with the growth of impurity scattering rate both for correlated metal and doped Mott insulator. As a typical example, in Fig. 3 we show results of our calculations for the case of doped Mott insulator. These were obtained via non-self-consistent procedure (using (16), (17), as full self-consistent procedure leads only to rather insignificant quantitative changes.

4.3. Generalized DMFT + $\Sigma_{\mathbf{k}}$ approach: spectral functions $A(\omega,\mathbf{k})$

In the previous subsection we discussed the densities of states obtained self-consistently by the DMFT + $\Sigma_{\mathbf{k}}$ approach. Once we get a self-consistent solution of the DMFT + $\Sigma_{\mathbf{k}}$ equations with nonlocal fluctuations we can, of course, also compute the spectral functions $A(\omega,\mathbf{k})$

$$A(\omega,\mathbf{k}) = -\frac{1}{\pi}\,\mathrm{Im}\,\frac{1}{\omega + \mu - \varepsilon(\mathbf{k}) - \Sigma(\omega) - \Sigma_{\mathbf{k}}(\omega)}\,, \quad (19)$$

where self-energy $\Sigma(\omega)$ and chemical potential μ are calculated self-consistently as described in Sec. 2. To plot $A(\omega,\mathbf{k})$ we choose $\mathbf{k}$-points along the «bare» Fermi surfaces for different types of lattice spectra and fillings. In Fig. 4 one can see corresponding shapes of these «bare» Fermi surfaces (presented are only 1/8-th parts of the Fermi surfaces within the first quadrant of the Brillouin zone).

In the following we concentrate mainly on the case $U = 4t$ and filling $n = 0.8$ (Fermi surface of Fig. 4,*a*). The corresponding spectral functions $A(\omega,\mathbf{k})$ are depicted in Fig. 5. When $t'/t = -0.4$ (upper row), the spectral function close to the Brillouin zone diagonal (point B) has the typical Fermi-liquid behavior, consisting of a rather sharp peak close to the Fermi level. In the case of SDW-like fluctuations this peak is shifted down in energy by about $-0.5t$ (left upper corner). In the vicinity of the «hot spot» the shape of $A(\omega,\mathbf{k})$ is completely modified. Now $A(\omega,\mathbf{k})$ becomes double-peaked and non-Fermi-liquid-like. Directly at the «hot spot», $A(\omega,\mathbf{k})$ for SDW-like fluctuations has two equally intensive peaks situated symmetrically around the Fermi level and split from each other by $\sim 1.5\Delta$ Refs. 4, 5. For commensurate CDW-like fluctuations the spectral function in the «hot-spot» region has one broad peak centered at the Fermi level with width $\sim \Delta$. Such a merging of the two peaks at the «hot spot» for commensurate fluctuations was previously observed in Ref. 5. However close to point A this type of fluctuations also produces a double-peak structure in the spectral function.

In the lower panel of Fig. 5 we show spectral functions hole doping ($n = 0.8$) and the case of $t' = 0$ (Fermi surface from Fig. 4,*b*). Since the Fermi surface now is everywhere close to the antiferromagnetic zone boundary, the pseudogap anomalies are rather strong and almost nondispersive along the Fermi surface.

For the case of a doped Mott insulator ($U = 40t$, $n = 0.8$), the spectral functions obtained by the DMFT + $\Sigma_{\mathbf{k}}$ approach are presented in Fig. 6. Qualitatively, the shapes of these spectral functions are similar to those shown on Fig. 5. As was pointed out above, the strong Coulomb correlations lead to a narrowing of the quasiparticle peak and a corresponding decrease of the pseudogap width. One should also note that in contrast to $U = 4t$ the spectral functions are now less intensive, because part of the spectral weight is transferred to the upper Hubbard band.

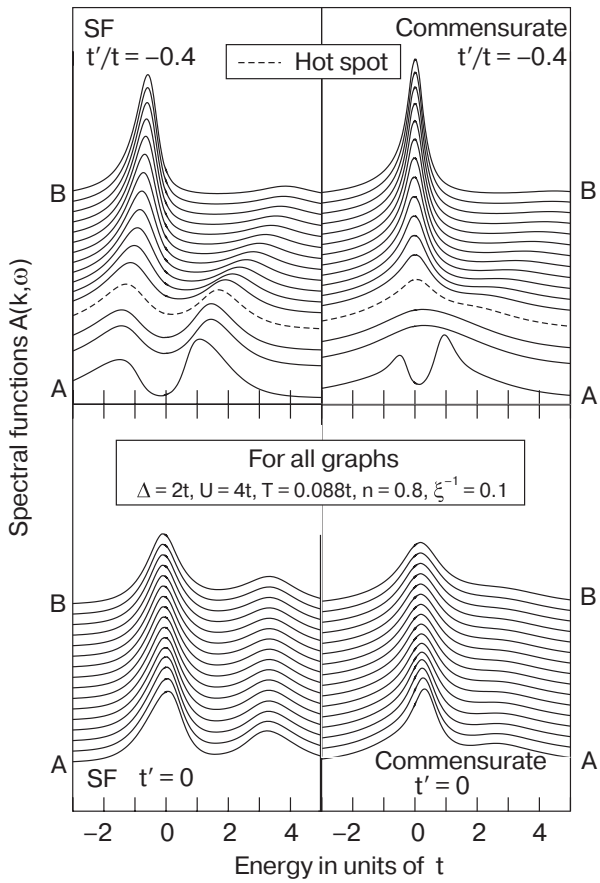

Fig. 5. Spectral functions $A(\mathbf{k},\omega)$ obtained from the DMFT(NRG) + $\Sigma_{\mathbf{k}}$ calculations along the directions shown in Fig. 4. Model parameters were chosen as $U = 4t$, $n = 0.8$, $\Delta = 2t$, $\xi^{-1} = 0.1$ and temperature $T = 0.088t$. The «hot spot» **k**-point is marked as fat dashed line. The Fermi level corresponds to zero.

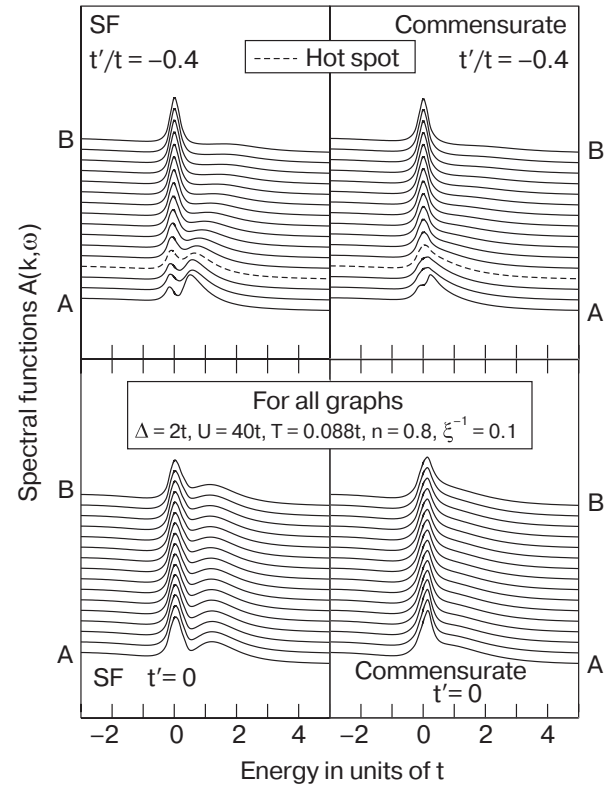

Fig. 6. Spectral functions $A(\mathbf{k},\omega)$ obtained from the DMFT(NRG) + $\Sigma_{\mathbf{k}}$ calculations for $U = 40t$, other parameters as in Fig. 5.

Using another quite common choice of **k**-points we can compute $A(\omega,\mathbf{k})$ along high-symmetry directions in the first Brillouin zone: $\Gamma(0,0)$–$X(\pi,0)$–$M(\pi,\pi)$–$\Gamma(0,0)$. The spectral functions for these **k**-points are shown in Fig. 7 for the case of SDW-like fluctuations and $U = 4t$. For all sets of parameters one can see a characteristic double-peak pseudogap structure close to the X point. In the middle of M–Γ direction (so-called «nodal» point) one can see the reminiscence of AFM gap which has its biggest value here in case of perfect antiferromagnetic ordering. Also in the nodal point «kink»-like behavior is observed caused by interactions between correlated electrons with pseudogap fluctuations. A change of the filling leads mainly to a rigid shift of spectral functions with respect to the Fermi level. For the case of $U = 40t$ spectral densities demonstrate rather similar behavior [11].

With the spectral functions we are now in a position to calculate angle resolved photoemission spectra (ARPES), which is the most direct experimental way to observe pseudogap in real compounds. For that purpose, we only need to multiply our results for the spectral functions with the Fermi function at appropriate temperature. Typical example of the resulting DMFT + $\Sigma_{\mathbf{k}}$ ARPES spectra are presented in Fig. 8. One should note that for $t'/t = -0.4$ (upper panel of Fig. 8) as **k** goes from point «A» to point «B» the peak situated slightly below the Fermi level changes its position and moves down in energy. Simultaneously it becomes more broad and less intensive. The dotted line guides the motion of the peak maximum. Such behavior of the peak in the ARPES is rather reminiscent of those observed experimentally in underdoped cuprates [2,4,19].

4.4. «Destruction» of the Fermi surface

Within the standard DMFT approach Fermi surface is not renormalized by interactions and just coincides with that of the «bare» quasiparticles [7]. However, in the case of nontrivial momentum dependence of electron self-energy, important renormalization of the Fermi surface appears due to pseudogap formation [4]. There are a number of ways to define Fermi surface in strongly correlated system with pseudogap fluctuations. In the following we are using intensity

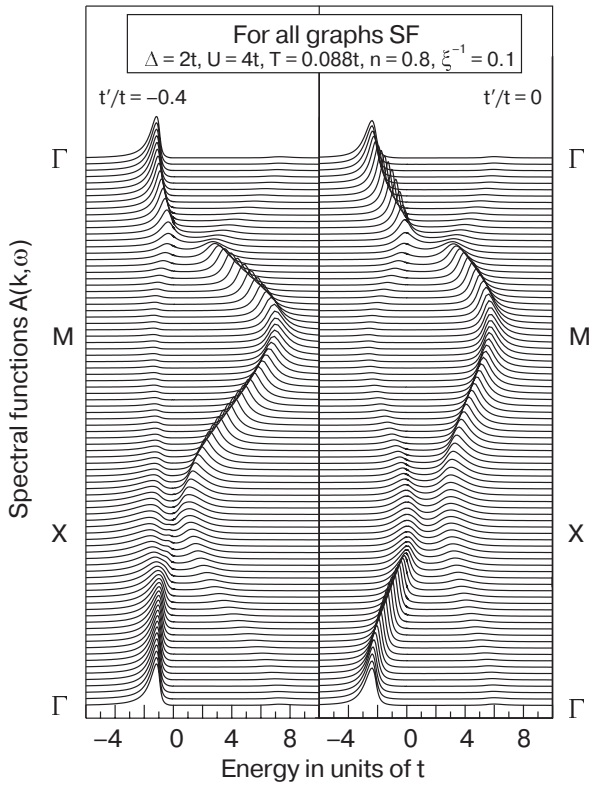

Fig. 7. Spectral functions $A(\mathbf{k},\omega)$ obtained from the DMFT(NRG) + $\Sigma_{\mathbf{k}}$ calculations along high-symmetry directions of first Brilloin zone $\Gamma(0,0) - X(\pi,0) - M(\pi,\pi) - \Gamma(0,0)$, $t'/t = -0.4$ (left column) and $t'/t = 0$ (right column). Other parameters are $U = 4t$, $n = 0.8$, $\Delta = 2t$, $\xi^{-1} = 0.1$ and temperature $T = 0.088t$. The Fermi level corresponds to zero.

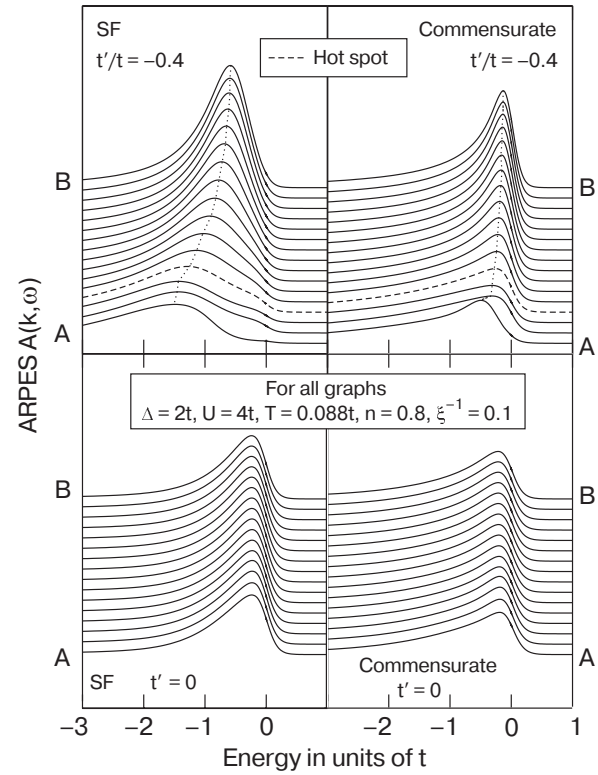

Fig. 8. ARPES spectra obtained from the DMFT(NRG) + + $\Sigma_{\mathbf{k}}$ calculations for $U = 4t$ and $n = 0.8$ along the lines in the first BZ as depicted by Fig. 4, all other parameters as in Fig. 5.

plots (within the Brillouin zone) of the spectral density (19) taken at $\omega = 0$. These are readily measured by ARPES and appropriate peak positions define the Fermi surface in the usual Fermi liquid case.

Our results [20] are shown in Fig. 9 for the case of correlated metal with $U = 4t$ and in Fig. 10 for the doped Mott insulator ($U = 40t$) (in both cases we assume spin-fermion combinatorics). The qualitative behavior observed in Fig. 9 clearly demonstrates the «destruction» of the well defined Fermi surface in the strongly correlated metal with the growth of the pseudogap amplitude Δ. Quite similar behavior was first observed in pioneering paper by Norman et al. [21] and in numerous later ARPES experiments. It is seen, that «destruction» of the Fermi surface starts in the vicinity of «hot spots» for small values of Δ, but almost immediately it disappears in the whole antinodal region of the Brillouin zone, while only «Fermi arcs» remain in the nodal region very close to the «bare» Fermi surface. These results give a natural explanation of the observed behavior and also of the fact that the existence of «hot spots» regions was observed only in some rare cases [22].

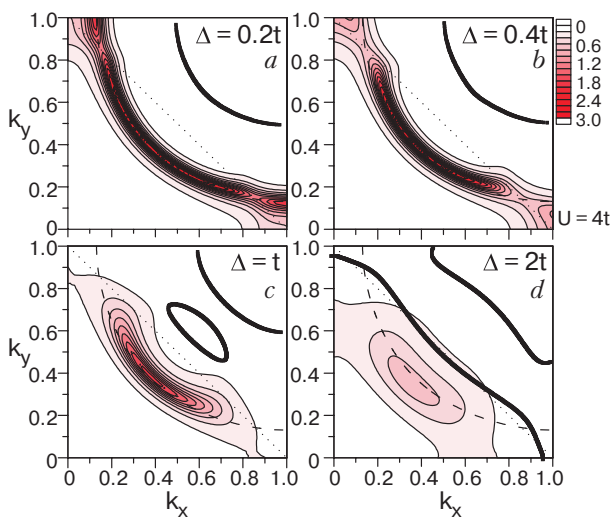

Fig. 9. Fermi surfaces obtained from the DMFT(NRG) + $\Sigma_{\mathbf{k}}$ calculations for $U = 4t$ and $n = 0.8$. Shown are intensity plots of spectral density (19) for $\omega = 0$ and $\xi = 10a$. $\Delta = 0.2t$ (*a*); $\Delta = 0.4t$ (*b*); $\Delta = t$ (*c*); $\Delta = 2t$ (*d*). Dashed line denotes «bare» Fermi surface. Thick black lines show the solution of Eq. (20).

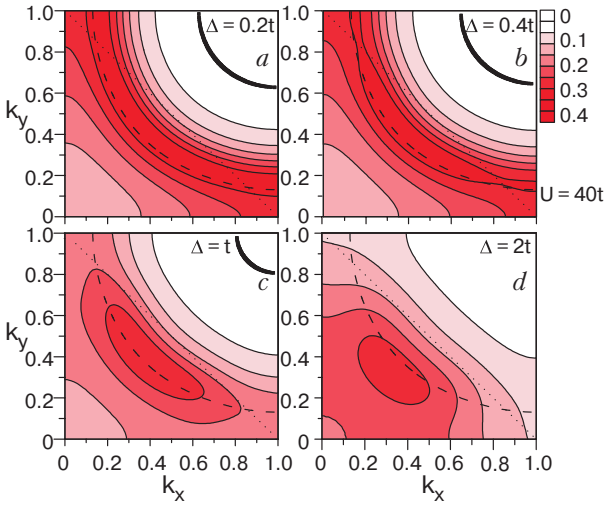

Fig. 10. «Destruction» of the Fermi surface obtained from the DMFT(NRG) + $\Sigma_{\mathbf{k}}$ calculations for $U = 40t$ and $n = 0.8$. Other parameters and notations are the same as in Fig. 9.

For the case of doped Mott insulator shown in Fig. 10 we see that the Fermi surface is rather poorly defined for all values of Δ, as the spectral density profiles are much more «blurred» than in the case of smaller values of U, reflecting important role of correlations.

It is interesting to note that from Figs. 9, 10 it is clearly seen that rather natural definition of the Fermi surface as defined by the solution of the equation

$$\omega - \varepsilon(\mathbf{k}) + \mu - \mathrm{Re}\,\Sigma(\omega) - \mathrm{Re}\,\Sigma_{\mathbf{k}}(\omega) = 0 \qquad (20)$$

for $\omega = 0$, used, e.g., in Ref. 4 is inadequate for strongly correlated systems with finite U and nonlocal interactions (pseudogap fluctuations).

5. Conclusion

To summarize, we propose a generalized DMFT + + $\Sigma_{\mathbf{k}}$ approach, which is meant to take into account the important effects due to nonlocal correlations in a systematic, but to some extent phenomenological fashion. The main idea of this extension is to stay within a usual effective Anderson impurity analogy, and introduce length scale dependence due to nonlocal correlation via the effective medium («bath») appearing in the standard DMFT. This becomes possible by incorporating scattering processes of fermions in the «bath» from nonlocal collective SDW-like antiferromagnetic spin (or CDW-like charge) fluctuations. Such a generalization of the DMFT allows one to overcome the well-known shortcoming of **k**-independence of self-energy of the standard DMFT. It in turn opens the possibility to access the physics of low-dimensional strongly correlated systems, where different types of spatial fluctuations (e.g., of some order parameter), become important. However, we must stress that our procedure in no way introduces any kind of systematic $1/d$-expansion, being only a qualitative method to include length scale into DMFT.

In our present study we addressed the problem of pseudogap formation in the strongly correlated metallic state. We showed evidence that the pseudogap appears at the Fermi level within the quasiparticle peak, introducing a new small energy scale of the order of Δ in the DOSs and spectral functions $A(\omega, \mathbf{k})$ and significant renormalization of the Fermi surface.

Let us stress, that our generalization of DMFT leads to nontrivial and in our opinion physically sensible **k**-dependence of spectral functions. Similar results were obtained in recent years using the cluster mean-field theories [23]. The major advantage of our approach over these theories is, that we stay in an effective single-impurity picture. This means that our approach is computationally much less expensive and therefore also easily generalizable for the account of additional interactions .

6. Acknowledgments

We are grateful to Th. Pruschke for providing us with his NRG code and helpful discussions. This work was supported in part by RFBR grants 05-02-16301, 05-02-17244, and programs of the Presidium of the Russian Academy of Sciences (RAS) «Quantum macrophysics» and of the Division of Physical Sciences of the RAS «Strongly correlated electrons in semiconductors, metals, superconductors and magnetic materials». I.N. acknowledges support from the Dynasty Foundation and International Centre for Fundamental Physics in Moscow program for young scientists 2005 and Russian Science Support Foundation program for young PhD of the Russian Academy of Sciences 2005.

1. T. Timusk and B. Statt, *Rep. Progr. Phys.* **62**, 61 (1999).
2. M.V. Sadovskii, *Usp. Fiz. Nauk* **171**, 539 (2001) [*Physics-Uspekhi* **44**, 515 (2001)].
3. D. Pines, *ArXiv: cond-mat/0404151*.
4. J. Schmalian, D. Pines, and B. Stojkovic, *Phys. Rev.* **B60**, 667 (1999).
5. E.Z. Kuchinskii and M.V. Sadovskii, *Zh. Eksp. Teor. Fiz.* **115**, 1765 (1999) [*JETP* **88**, 347 (1999)].
6. W. Metzner and D. Vollhardt, *Phys. Rev. Lett.* **62**, 324 (1989).
7. D. Vollhardt, in: *Correlated Electron Systems*, V.J. Emery (ed.), World Scientific, Singapore (1993), p. 57.

8. Th. Pruschke, M. Jarrell, and J.K. Freericks, *Adv. Phys.* **44**, 187 (1995).
9. A. Georges, G. Kotliar, W. Krauth, and M.J. Rozenberg, *Rev. Mod. Phys.* **68**, 13 (1996).
10. G. Kotliar and D. Vollhardt, *Physics Today* **57**, No. 3, 53 (2004).
11. M.V. Sadovskii, I.A. Nekrasov, E.Z. Kuchinskii, Th. Prushke, and V.I. Anisimov, *Phys. Rev.* **B72**, 155105 (2005)
12. M.V. Sadovskii, *Zh. Eksp. Teor. Fiz.* **77**, 2070 (1979) [*Sov. Phys. JETP* **50**, 989 (1979)].
13. Y.M. Vilk and A.-M.S. Tremblay, *J. Phys. I France* **7**, 1309 (1997).
14. N.A. Kuleeva, E.Z. Kuchinskii, and M.V. Sadovskii, *Zh. Eksp. Teor. Fiz.* **126**, 1446 (2004) [*JETP* **99**, 1264 (2004)].
15. J.E. Hirsch and R.M. Fye, *Phys. Rev. Lett.* **56**, 2521 (1986); M. Jarrell, *Phys. Rev. Lett.* **69**, 168 (1992); M. Rozenberg, X.Y. Zhang, and G. Kotliar, *Phys. Rev. Lett.* **69**, 1236 (1992); A. Georges and W. Krauth, *Phys. Rev. Lett.* **69**, 1240 (1992); M. Jarrell in: *Numerical Methods for Lattice Quantum Many-Body Problems*, D. Scalapino (ed.), Addison Wesley (1997). For review of QMC for DMFT see Ref. [16].
16. K. Held, I.A. Nekrasov, N. Blümer, V.I. Anisimov, and D. Vollhardt, *Int. J. Mod. Phys.* **B15**, 2611 (2001); K. Held, I.A. Nekrasov, G. Keller, V. Eyert, N. Blümer, A.K. McMahan, R.T. Scalettar, T. Pruschke, V.I. Anisimov, and D. Vollhardt, *cond-mat/0112079* (Published in: *Quantum Simulations of Complex Many-Body Systems: From Theory to Algorithms*, J. Grotendorst, D. Marks, and A. Muramatsu (eds.), NIC Series Volume 10, NIC Directors, Forschunszentrum Jülich (2002), p. 175.
17. K.G. Wilson, *Rev. Mod. Phys.* **47**, 773 (1975); H.R. Krishna-murthy, J.W. Wilkins, and K.G. Wilson, *Phys. Rev.* **B21**, 1003 (1980); *ibid.* **21**, 1044 (1980); for a comprehensive introduction to the NRG see, e.g., A.C. Hewson, *The Kondo Problem to Heavy Fermions,* Cambridge University Press (1993).
18. R. Bulla, A.C. Hewson, and Th. Pruschke, *J. Phys.: Condens. Matter* **10**, 8365 (1998); R. Bulla, *Phys. Rev. Lett.* **83**, 136 (1999).
19. A. Kaminski, H.M. Fretwell, M.R. Norman, M. Randeria, S. Rosenkranz, U. Chatterjee, J.C. Campuzano, J. Mesot, T. Sato, T. Takahashi, T. Terashima, M. Takano, K. Kadowaki, Z.Z. Li, and H. Raffy, *Phys. Rev.* **B71**, 014517 (2005).
20. E.Z. Kuchinskii, I.A. Nekrasov, and M.V. Sadovskii. *JETP Lett.* **82**, 198 (2005).
21. M.R. Norman, M. Randeria, J.C. Campuzano, T. Yokoya, T. Takeuchi, T. Takahashi, T. Mochiku, K. Kadowaki, P. Guptasarma, and D.G. Hinks, *Nature* **382**, 51 (1996).
22. N.P. Armitage, D.H. Lu, C. Kim, A. Damascelli, K.M. Shen, F. Ronning, D.L. Feng, P. Bogdanov, and Z.-X. Shen, *Phys. Rev. Lett.* **87**, 147003 (2001).
23. Th. Maier, M. Jarrell, Th. Pruschke, and M. Hettler, *Rev. Mod. Phys.* **77**, 1027 (2005); *ArXiv: cond-mat/0404055*.

Physics – Uspekhi **51** (12) 1201 – 1227 (2008) © 2008 Uspekhi Fizicheskikh Nauk, Russian Academy of Sciences

REVIEWS OF TOPICAL PROBLEMS PACS numbers: **74.20.–z**, **74.25.–q**, **74.62.–c**, **74.70.–b**

High-temperature superconductivity in iron-based layered compounds*

M V Sadovskii

DOI: 10.1070/PU2008v051n12ABEH006820

Contents

1. **Introduction** **1201**
   1.1 Peculiarities of high-temperature superconductivity in copper oxides; 1.2 Other superconductors with unusual properties
2. **Basic experimental data on new superconductors** **1203**
   2.1 Electrical properties and superconductivity; 2.2 Crystal structure and anisotropy; 2.3 Magnetic structure and phase diagram; 2.4 Specific heat; 2.5 NMR (NQR) and tunneling spectroscopy; 2.6 Optical properties; 2.7 Phonons and spin excitations: neutron spectroscopy; 2.8 Other experiments
3. **Electronic spectrum and magnetism** **1214**
   3.1 Band structure (LDA); 3.2 'Minimal' model; 3.3 Angle-resolved photoemission spectroscopy (ARPES); 3.4 Correlations (LDA + DMFT); 3.5 Spin ordering: localized or itinerant spins?
4. **Mechanisms and types of pairing** **1222**
   4.1 Multiband superconductivity; 4.2 Electron – phonon mechanism; 4.3 Magnetic fluctuations
5. **Conclusion: end of cuprate monopoly** **1224**

References **1225**

From the Editorial Board. An outstanding scientific discovery was made in early 2008 and extremely active research is now in progress. I am talking about a new class of superconductors. With this in mind, the Editorial Board requested one of its members (M V Sadovskii) to write a review article devoted to these new superconductors. During its preparation, however, two more reviews (one written by A L Ivanovskii, and the other by Yu A Izyumov and E Z Kurmaev) arrived in the editorial office. Encountering such a display of scientific activity in this field, and due to its obvious great significance, the Editorial Board took the exceptional decision to publish all three reviews in one and the same issue of the *Physics – Uspekhi* journal. The decision is all the more remarkable as the authors hold somewhat different viewpoints relative to the physics of the superconductors discovered. It is believed that such a decision will help our readers look deeply into this new area of research. At the same time, we recognize that our decision on the above matter is extraordinary and it is justified only by the topicality of the research in the field.

V L Ginzburg

M V Sadovskii Institute of Electrophysics, Ural Branch of the Russian Academy of Sciences,
ul. Amundsena 106, 620016 Ekaterinburg, Russian Federation
Tel. (7-343) 267 87 86. Fax (7-343) 267 87 94
E-mail: sadovski@iep.uran.ru

Requested by the Editorial Board on 31 May 2008, received 31 October 2008
Uspekhi Fizicheskikh Nauk **178** (12) 1243 – 1271 (2008)
DOI: 10.3367/UFNr.0178.200812b.1243
Translated by M V Sadovskii; edited by A Radzig

Abstract. Basic experimental data are presented for a new class of high-temperature superconductors — iron-based layered compounds of the types *RE*OFeAs (*RE* = La, Ce, Nd, Pr, Sm, ...), AFe$_2$As$_2$ (A = Ba, Sr, ...), AFeAs (A = Li, ...), and FeSe(Te). The structure of electronic spectra in these compounds is discussed, including the correlation effects, as is the spectrum and role of collective excitations (phonons and spin waves). Basic models for describing various types of magnetic ordering and Cooper pairing are reviewed.

1. Introduction

The discovery of high-temperature superconductivity (HTSC) in copper oxides more than 20 years ago [1] stirred up profound interest and has led to the publication of thousands of experimental and theoretical papers. During this time, a number of reviews have been published in *Physics – Uspekhi*, which have been devoted to different aspects of superconductivity in cuprates and prospects for further progress in the growth of the critical temperature T_c of superconducting transition and appeared both immediately after this discovery [2 – 4] and much later [5 – 10]. The physics of HTSC and of a variety of new and unusual superconductors was discussed in a number of individual and collective monographs [11 – 14].

* This review represents an expanded report under the same name delivered to the special meeting of the Editorial Board of the *Physics – Uspekhi* journal held on November 19, 2008 at the P N Lebedev Physical Institute, RAS in Moscow. This verbal issue of *Physics – Uspekhi* was timed to commemorate the 90th anniversary of the journal's first publication in Russian and the 50th anniversary of the first issue translated into English. (*Editor's note.*)

Unfortunately, despite these unprecedented efforts by researchers all over the world, the physical nature of high-temperature superconductivity in cuprates is still not completely understood. Basic difficulties here are attributed to the significant role of electronic correlations — in the opinion of the majority of authors cuprates make up strongly correlated systems, which leads to anomalies of their normal state (inapplicability of Fermi-liquid theory) and a wide spectrum of possible explanations for the microscopic mechanism of superconductivity — from relatively traditional [6, 9] to more or less exotic [12].

In this respect, the discovery in early 2008 of a new class of high-temperature superconductors, i.e., iron-based layered superconducting compounds [15], has attracted tremendous interest. This discovery has broken the cuprate 'monopoly' in the physics of HTSC compounds and revived hopes both of further progress in this field, related to the synthesis of new potential high-temperature superconductors, and of a deeper theoretical understanding of the mechanisms revealing themselves in HTSC. Naturally, a direct comparison between superconductivity in cuprates and new iron-based superconductors holds out the promise of identifying common peculiarities of these systems, which are relevant for high values of T_c, as well as important differences and properties not directly related to the phenomenon of high-temperature superconductivity and, in fact, complicating its theoretical interpretation.

The aim of the present review is to give a short introduction to the physics of new iron-based layered superconductors and to compare their properties with well-established facts concerning HTSC in copper oxides. Progress in this field has been rather spectacular and rapid, so that this review is in no sense exhaustive.[1] Nevertheless, the author hopes that it will serve as an elementary introduction to this new field of research and may help promote deeper studies of original papers.

1.1 Peculiarities of high-temperature superconductivity in copper oxides

At present, dozens of HTSC compounds based on copper oxides are known to have superconducting transition temperature T_c exceeding 24 K [16]. In Table 1 we present critical temperatures for a number of the most 'popular' cuprates.

Table 1. Superconducting transition temperatures in copper oxides.

Compound*	T_c, K
$HgBa_2Ca_2Cu_3O_{8+\delta}$	134
$Tl_2Ca_2Ba_2Cu_3O_{10}$	127
$YBa_2Cu_3O_7$	92
$Bi_2Sr_2CaCu_2O_8$	89
$La_{1.83}Sr_{0.17}CuO_4$	37
$Nd_{1.85}Ce_{0.15}CuO_4$	24

* T_c of $HgBa_2Ca_2Cu_3O_{8+\delta}$ reaches ~ 150 K under pressure.

[1] Suffice it to say that during the first six months of the studies of new superconductors about 600 original papers (preprints) were published. Obviously, in this review it is not even possible just to cite all these works, and our choice of citations is rather subjective. The author apologizes in advance to those authors of important papers which remained outside our reference list, as this is attributed to an obvious limitation on the size of the review and the author's own ignorance.

More than 20 years of experience has led to a quite deep understanding of the nature of superconductivity in these systems. It is clear, for example, that HTSC in cuprates is not connected with some 'essentially new' physics, which is different in comparison with other superconductors, superfluid Fermi liquids like He^3, nucleons in atomic nuclei or nuclear matter in neutron stars, dilute Fermi gases with Cooper pairing actively studied at present, or even the hypothetical 'color' superconductivity of quarks.

In this respect, let us list below

What we definitely know about cuprates:

• *The nature of superconductivity in cuprates* $\rightleftharpoons$ *Cooper pairing*.

(1) This pairing is anisotropic and of the d-type, so that the energy gap acquires zeroes at the Fermi surface: $\Delta \cos 2\phi$, where ϕ is the polar angle determining momentum direction in the two-dimensional Brillouin zone.

(2) The size of Cooper pairs (coherence length at zero temperature $T = 0$) is relatively small: $\xi_0 \sim (5-10)a$, where a is the lattice constant in the CuO_2 plane.

• *There exists a relatively well-defined* (*at least in part of the Brillouin zone*) *Fermi surface*; *in this sense these systems are metals*.

• *However, appropriate stoichiometric compounds constitute antiferromagnetic insulators — their superconductivity is realized close to the Mott metal – insulator phase transition* (*controlled by composition*) *induced by strong electronic correlations*.

• *Strong anisotropy of all electronic properties is observed — conductivity* (*and superconductivity*) *is realized mainly within* CuO_2 *layers* (*quasi-two-dimensionality*!).

At the same time, many things are still not understood. Accordingly, we may list

What we do not really know about cuprates:

• *Mechanism of Cooper pairing* (*a* '*glue*' *ensuring a formation of Cooper pairs*).

Possible variants:

(1) Electron – phonon mechanism.

(2) Spin fluctuations.

(3) Exchange – RVB, SO(5), or something more 'exotic'.

The difficulties of choice here are mainly due to the unclear

• *Nature of the normal state*.

(1) Is Fermi-liquid theory (Landau) valid here?

(2) Or is some more complicated scenario realized, like a 'marginal' or 'bad' Fermi liquid?

(3) Possible also is some variant of a Luttinger liquid, essentially different from a Fermi liquid.

(4) Still mysterious is the nature of the pseudogap state.

(5) Not completely clear is the role of internal disorder and local inhomogeneities.

Of course, we observe here continuous, though slow, progress. For example, most researchers are now leaning towards the spin-fluctuation (nonphonon) mechanism of pairing. The pseudogap state is most likely connected with fluctuations of some competing (with superconductivity) order parameter (antiferromagnetic or charged) [7, 17, 18]. The Fermi-liquid description is apparently applicable in most parts of the Brillouin zone, where the Fermi surface remains not 'destroyed' by pseudogap fluctuations, etc. However, a consensus in the HTSC community is still absent, which is obviously related to the complicated nature of these systems, attributed first and foremost to strong electronic correlations which control this nature and impede theoretical under-

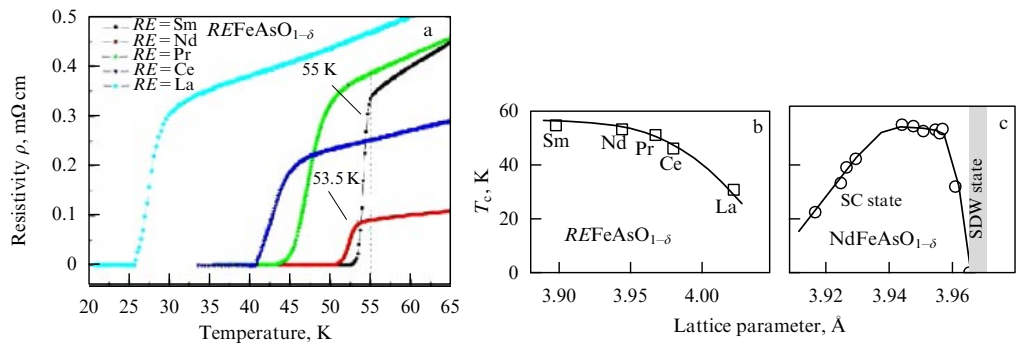

Figure 1. (a) Resistivity behavior in *RE*OFeAs (*RE* = La, Ce, Pr, Nd, Sm) close to the superconducting (SC) transition. (b, c) Dependence of T_c (the onset of transition) on the value of the lattice constant [33].

standing. Just because of that, the discovery of a new class of HTSC compounds holds out definite hope, as new possibilities of HTSC studies in completely different systems appear, and where some of these difficulties may just be absent.

1.2 Other superconductors with unusual properties

Obviously, during all the years since the discovery of HTSC in cuprates active efforts have continued in the search for new compounds with potentially high superconducting transition temperatures. A number of systems discovered during this search are listed in Table 2.

Table 2. Superconducting transition temperatures in some 'unusual' superconductors.

Compound	T_c, K
MgB_2	39
$RbCs_2C_{60}$	33
K_3C_{60}	19
Sr_2RuO_4	1.5

Despite the obvious interest from the viewpoint of physics and the unusual properties of some of these systems, there has been no significant progress in this area. This is mainly due to the fact that all the systems listed in Table 2 are, in some sense, 'exceptional' — none is representative of a wide class of compounds with the possibility of changing system properties (parameters) in a wide range, as in cuprates. All these systems have been studied in detail, and summaries of these studies can be found in the relevant reviews [19–23]. In fact, these studies have added very little to our understanding of the superconductivity of cuprates. Up to now, there has been a kind of 'cuprate monopoly' in the physics of 'real' HTSC materials with a great potential for further studies and the search for compounds with even higher values of T_c and practical applications.[2]

2. Basic experimental data on new superconductors

2.1 Electrical properties and superconductivity

2.1.1 *RE*OFeAs (*RE* = La, Ce, Pr, Nd, Sm, ...) system. The discovery of superconductivity with $T_c = 26$ K in $LaO_{1-x}F_xFeAs$ ($x = 0.05-0.12$) [15] was preceded by studies of the electrical properties of a number of oxypnictides like LaO*MPn* (M = Mn, Fe, Co, Ni, and Pn = P, As) gone with the discovery of superconductivity in LaOFeP with $T_c \sim 5$ K [24] and LaONiP with $T_c \sim 3$ K [25], which has not attracted much attention from the HTSC community. This situation has changed sharply since Ref. [15] appeared, and shortly afterwards many papers followed (see, e.g., Refs [26–35]), where this discovery was confirmed, and the substitution of lanthanum by a number of other rare earths, according to the simple chemical formula $(RE)^{+3}O^{-2}Fe^{+2}As^{-3}$, has led to more than a doubling of T_c up to values on the order of 55 K in systems based upon NdOFeAs and SmOFeAs, with electron doping effected through the addition of fluorine or creation of an oxygen deficit, or hole doping implemented by partial substitution of the rare earth (e.g., La by Sr) [36]. Note also work [37] where the record values of $T_c \sim 55$ K were achieved by partial substitution of Gd in GdOFeAs by Th, which, according to the authors, also corresponded to electron doping. In these early works, different measurements of electrical and thermodynamic properties of superconductors were performed on polycrystalline samples.

Figure 1a taken from Ref. [33] demonstrate typical temperature dependences of electric resistivity in different *RE*OFeAs compounds. It can be seen that for most of these compounds T_c lies within the interval 40–50 K, while the LaOFeAs system slightly drops out of this series, with its significantly lower transition temperature of ~ 25 K. In this respect, we can mention Ref. [34] in which a synthesis of this system under high pressure was reported, producing samples with T_c (the onset of the superconducting transition) on the order of 41 K. In Ref. [38], an analogous increase in T_c in such a system was achieved under an external pressure of ~ 4 GPa. Probably, this last result is characteristic only of the La system, as a further increase in pressure leads to a drop in T_c, while in other systems (e.g., Ce-based systems) T_c lowers with an increase in external pressure from the very beginning (see, e.g., Ref. [39, 40]).

In many papers, the growth in T_c induced by La replacement with other rare earths (with a smaller ion radius) is often attributed to 'chemical' pressure, which is illustrated, for instance, by the qualitative dependence of T_c on lattice spacing, depicted in Fig. 1b [33]. At the same time, Fig. 1c taken from the same work shows that lattice compression leads to a growth in T_c only up to a certain limit, and after that T_c drops (compare this evidence with

[2] Surely, when we speak about practical applications we should not underestimate the prospects of the MgB_2 compound.

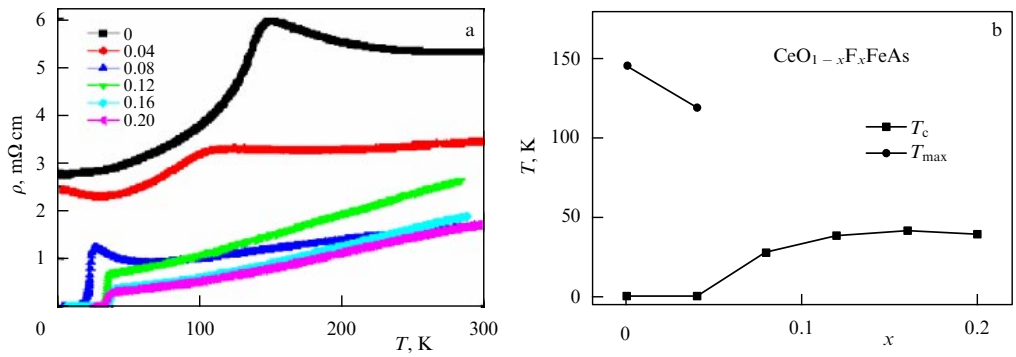

Figure 2. (a) Temperature dependence of resistivity in $CeO_{1-x}F_xFeAs$ for different compositions x given on the graph. (b) Phase diagram showing the superconducting region and concentration dependence of high-temperature anomaly T_{max} of resistivity, associated with the SDW transition [30].

the results of the high-pressure experiments mentioned above).

In a wider temperature interval, the typical temperature behavior of resistivity is illustrated by the data for $CeO_{1-x}F_xFeAs$ shown in Fig. 2a (taken from Ref. [30]). It can be seen that the prototype system CeOFeAs is characterized by a *metallic* behavior of resistivity up to the lowest temperatures achieved, with the characteristic anomaly in the vicinity of $T \sim 145$ K and a sharp drop in resistivity at lower temperatures. The metallic nature of prototype *RE*OFeAs systems contrasts with the insulating nature of stoichiometric cuprates. After doping, for example, by fluorine, the value of resistivity drops, and its anomaly becomes less pronounced and disappears at higher dopings, where superconductivity appears. The highest value of $T_c = 41$ K is achieved for $x = 0.16$, and the resulting F-concentration phase diagram is displayed in Fig. 2b. The high-temperature anomaly of resistivity in prototype and slightly doped systems in most of the works was attributed to a structural phase transition and (or) subsequent spin density wave (SDW) transition, while the degradation of the SDW state under doping is usually connected with the breaking of 'nesting' of the Fermi surfaces (cf. below). This behavior of resistivity is rather typical and is observed in all *RE*OFeAs systems (see, e.g., Ref. [32]), which are for the sake of brevity now called 1111-systems.

In fact, the recently synthesized compound Sr(Ca)FFeAs belongs to the same class [41, 42]. Here, the typical SDW anomaly of resistivity is also observed in the vicinity of 175 K. Further doping of this system with Co leads to the appearance of superconductivity with $T_c \sim 5$ K [43], while in $Sr_{1-x}La_xFFeAs$, a superconducting transition with $T_c = 36$ K [44] was obtained.

2.1.2 AFe_2As_2 (A = Ba, Sr, ...) system. A simpler (structurally and chemically) class of iron-based superconductors was discovered in Ref. [45] by the synthesis of the $Ba_{1-x}K_xFe_2As_2$ compound, where superconductivity with $T_c = 38$ K was observed for $x = 0.4$. The relevant data on the temperature dependence of resistivity are given in Fig. 3 [45].

In the prototype $BaFe_2As_2$ compound, temperature dependence of resistivity demonstrates typically metallic behavior with a characteristic anomaly in the vicinity of $T \sim 140$ K, which is connected to a spin density wave (SDW) and structural phase transitions (cf. below). According to the simple chemical formula $Ba^{+2}(Fe^{+2})_2(As^{-3})_2$, the partial substitution of K^{+1} for Ba^{+2} leads to hole doping which suppresses SDW transition and gives rise to superconductivity in a certain concentration interval. Obviously, these results are quite similar to those quoted above for *RE*OFeAs (1111) systems.

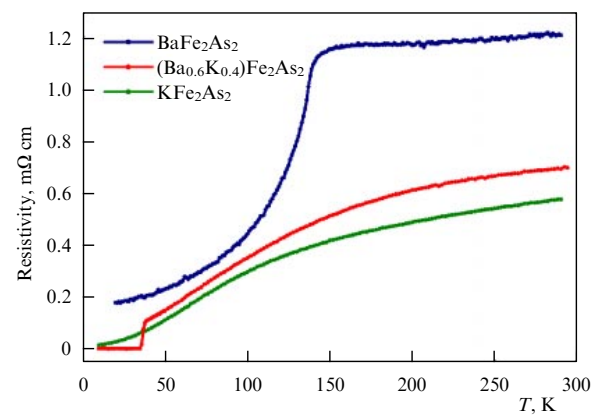

Figure 3. Temperature dependence of resistivity in $Ba_{1-x}K_xFe_2As_2$ for different compositions x shown on the graph [45].

In Ref. [46], a similar behavior was observed in $Sr_{1-x}K_xFe_2As_2$ with maximal $T_c \sim 38$ K, while in Ref. [47] systems like AFe_2As_2 with $A = K, Ca, K/Sr, Ca/Sr$ were studied, and electron doping by Sr of compounds with $A = K$ and $A = Cs$ produced values of $T_c \sim 37$ K followed by SDW transition. This new class of Fe-based HTSCs is sometimes denoted for brevity as 122-systems.

Notice also the interesting paper [48] where superconductivity with T_c up to 29 K was obtained in the prototype (undoped) $BaFe_2As_2$ and $SrFe_2As_2$ compounds under external pressure, but only in a limited interval of pressures. Superconductivity also appears under electron doping of these systems by Co [49].

2.1.3 AFeAs (A = Li, ...) system. One more type of Fe-based superconductors is represented by the $Li_{1-x}FeAs$ (111) system, where superconductivity appears at $T_c \sim 18$ K [50, 51]. Up to now there have been few works on this system; however, it is clear that it is quite similar to 1111- and 122-systems and is rather promising in the sense of comparing its properties with those of the other systems discussed above.

2.1.4 FeSe(Te) system. Finally, rather unexpectedly, superconductivity was discovered in the very 'simple' α-$FeSe_x$ ($x < 1$) system [52] with $T_c = 8$ K, reaching 27 K under a pressure of 1.48 GPa [53]. Later on, the system $Fe(Se_{1-x}Te_x)_{0.82}$ was also studied, and the maximum value of $T_c = 14$ K was achieved for $0.3 < x < 1$ [54]. Here, there are still very few detailed studies, though it is quite clear that the electronic structures of these systems are again similar to those discussed above, so that in the nearest future we can expect many papers devoted to the comprehensive studies of their electronic properties.

2.1.5 Search for new systems. Naturally, at present an active search for other similar systems is underway with the hope of obtaining even higher values of T_c. Up to now, excepting the domain of FeAs-based systems, successes have been rather modest. We shall mention only a few works where new superconductors were synthesized.

We have already mentioned compounds like LaOFeP with $T_c \sim 5$ K [24] and LaONiP with $T_c \sim 3$ K [25], which are representatives of the same class of superconducting oxypnictides (1111) as the whole series of *RE*OFeAs. Superconductivity with $T_c \sim 4$ K was discovered in the $LaO_{1-\delta}NiBi$ compounds [55], while in GdONiBi and $Gd_{0.9}Sr_{0.1}ONiBi$, the value of $T_c \sim 0.7$ K was found in Ref. [56]. Transition temperature $T_c \sim 2.75$ K was obtained in $LaO_{1-x}F_xNiAs$ [57].

In the class of 122-systems, the value of $T_c \sim 0.7$ K was revealed in $BaNi_2As_2$ [58].

An interesting new system, $La_3Ni_4P_4O_2$, with a different crystal structure demonstrated superconductivity close to $T_c \sim 2.2$ K [59]. In this work, a number of promising systems of the same type were also discussed.

Certainly, none of these results is very exciting. However, there are a rather large number of systems somehow similar to already known FeAs-based compounds where we can also expect the manifestation of superconductivity at fairly high temperatures. A wide set of promising compounds was considered in Ref. [60].

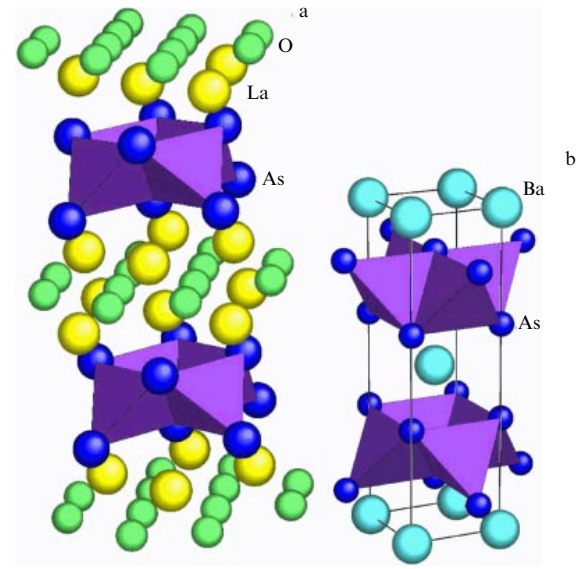

Figure 4. Crystal structures of LaOFeAs (a) and $BaFe_2As_2$ (b). FeAs tetrahedra form two-dimensional layers surrounded by layers of LaO or Ba. Iron ions inside the tetrahedra form a square lattice.

Table 3. Structural data for $BaFe_2As_2$ and LaOFeAs.

Parameters	$BaFe_2As_2$ [45]	LaOFeAs [15]
Group	$I4/mmm$	$P4/nmm$
a, Å	3.9090(1)	4.03533(4)
c, Å	13.2122(4)	8.74090(9)
z_{La}	—	0.14154(5)
z_{As}	0.3538(1)	0.6512(2)
Ba – As, Å	3.372(1) × 8	—
La – As, Å	—	3.380 × 4
Fe – As, Å	2.388(1) × 4	2.412 × 4
Fe – Fe, Å	2.764(1) × 4	2.853 × 4
As – Fe – As, deg.	109.9(1)°	113.6°
	109.3(1)°	107.5°

2.2 Crystal structure and anisotropy

The crystal structure of $BaFe_2As_2$ and LaOFeAs compounds and their analogs corresponds to tetragonal symmetry and space groups $I4/mmm$ and $P4/nmm$, respectively. Both compounds are formed by layers of $(FeAs)^-$ with covalent bonding, interlaced by layers of $Ba^{2+}_{0.5}$ or $(LaO)^+$, while interlayer bonding is ionic. Fe^{2+} ions are surrounded by four ions of As, which form tetrahedra. The general view of crystal structures of LaOFeAs and $BaFe_2As_2$ is illustrated in Fig. 4. The layered (quasi-two-dimensional) nature of these compounds is similar to that of HTSC cuprates. At 140 K, $BaFe_2As_2$ undergoes a structural phase transition from a tetragonal ($I4/mmm$) to an orthorhombic ($Fmmm$) structure [61]. An analogous transition also takes place in LaOFeAs at 150 K: $P4/nmm$ (tetragonal) $\rightarrow$ $Cmma$ (orthorhombic) [62]. Experimental atomic positions in $BaFe_2As_2$ are as follows: Ba $(0, 0, 0)$, Fe $(0.5, 0, 0.25)$, and As $(0, 0, z)$. For LaOFeAs, these are: La $(0.25, 0.25, z)$, Fe $(0.75, 0.25, 0.5)$, As $(0.25, 0.25, z)$, and O $(0.75, 0.25, 0)$. The rest of crystallographic data for both compounds in tetragonal phase are given in Table 3. It is seen that in $BaFe_2As_2$ the Fe – As distance is smaller than in LaOFeAs. Thus, in $BaFe_2As_2$ we can expect stronger Fe-d – As-p hybridization in comparison with LaOFeAs and, correspondingly, a larger d-band width for Fe. Similarly, the distance between adjacent Fe atoms within the FeAs layers in $BaFe_2As_2$ is also significantly smaller than in LaOFeAs (and related compounds). After the phase transition of $BaFe_2As_2$ into an orthorhombic structure, the four (initially equal) Fe – Fe distances are broken up into two pairs of bonds with lengths of 2.808 and 2.877 Å. Moreover, two As – Fe – As angles are significantly different in the LaOFeAs system (113.6° and 107.5°) and very close in $BaFe_2As_2$ ($\sim 109°$). Such differences in the nearest neighborhood of Fe ions should lead to appropriate distinctions in their electronic structure.

Doping of prototype *RE*OFeAs compounds by fluorine (or by the creation of an oxygen deficit) or $BaFe_2As_2$ by substitution of K for Ba(Sr), etc., leads to the suppression of transition from the tetragonal to orthorhombic structure and the appearance of superconductivity in the tetragonal phase.

Recently, the crystal structure of the LiFeAs compound was also refined [51]. LiFeAs forms a tetragonal structure with space group $P4/nmm$ and lattice parameters $a = 3.7914(7)$ Å, $c = 6.364(2)$ Å. The experimentally determined atomic positions are as follows: Fe(2b) $(0.75, 0.25, 0.5)$, Li(2c) $(0.25, 0.25, z_{Li})$, As(2c) $(0.25, 0.25, z_{As})$, $z_{As} = 0.26351$, and $z_{Li} = 0.845915$ [51]. The crystal structure of LiFeAs is

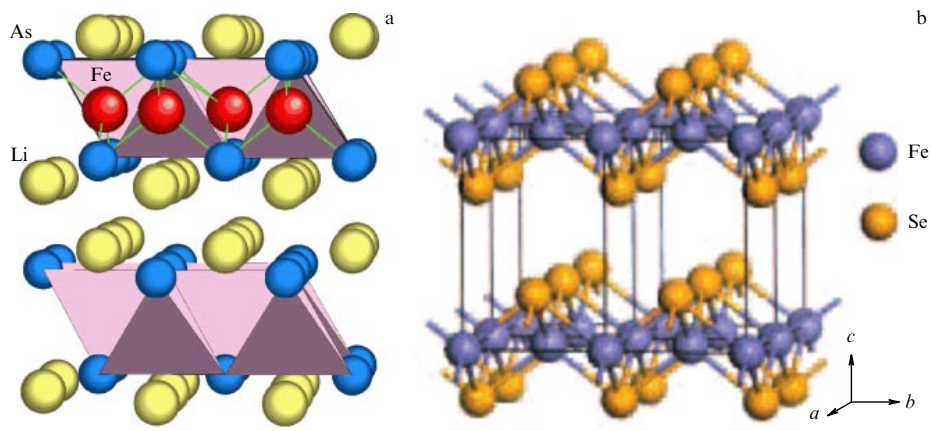

Figure 5. (a) Crystal structure of LiFeAs. FeAs tetrahedra form two-dimensional layers separated by layers of Li ions. (b) Crystal structure of α-FeSe.

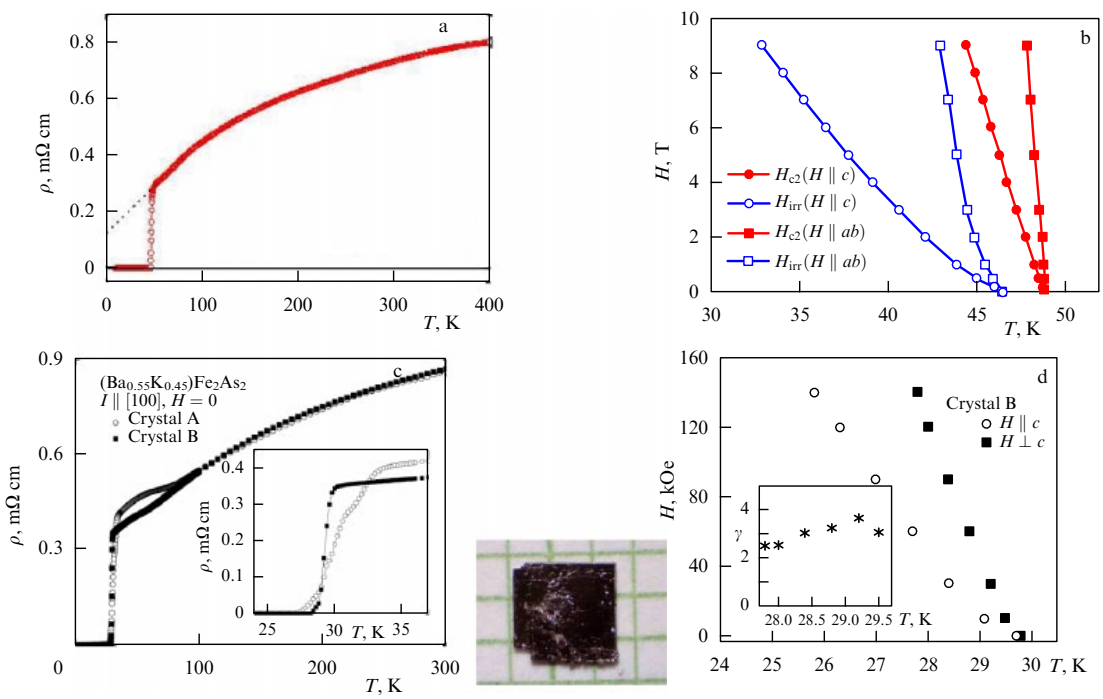

Figure 6. (a) Superconducting transition and (b) anisotropic behavior of the upper critical field H_{c2} (and irreversibility field H_{irr}) in a single crystal of $NdO_{0.82}F_{0.18}FeAs$ [64]. (c) Superconducting transition and (d) anisotropic behavior of the upper critical field H_{c2} in single crystals of $Ba_{1-x}K_xFeAs$ [65], where in the insets we also show a weak temperature dependence of the anisotropy of H_{c2}. Shown in the photo is a typical single crystal of $Ba_{1-x}K_xFe_2As_2$.

illustrated in Fig. 5a and is again characterized by clearly defined layering, which suggests quasi-two-dimensional electronic properties and is clearly analogous to the structure of LaOFeAs [15] and $BaFe_2As_2$ [61]. Most important Fe–Fe and Fe–As distances are 2.68 and 2.42 Å, respectively. At present, this structure is most spatially compact among similar compounds. As–Fe–As angles in LiFeAs have the values of $\sim 103.1°$ and $\sim 112.7°$, which can also lead to some fine differences in electronic structure of LiFeAs in comparison with LaOFeAs and $BaFe_2As_2$.

The crystal structure of α-FeSe is especially simple — it forms the layered tetragonal phase (like PbO) with a square sublattice of Fe and space group $P4/nmm$. The α-FeSe crystal consists of layers of $FeSe_4$ edge-sharing tetrahedra, as shown in Fig. 5b. Experimentally determined lattice constants are as follows [52]: $a = 3.7693(1)$ Å, $c = 5.4861(2)$ Å for $FeSe_{0.82}$, and $a = 3.7676(2)$ Å, $c = 5.4847(1)$ Å for $FeSe_{0.88}$. An analogy with oxypnictides like *RE*OFeAs and systems like $BaFe_2As_2$ is obvious. At $T \sim 105$ K, this system undergoes a structural phase transition from a tetragonal to a triclinic phase (group P-1) [52].

Up to now, only very small single crystals of 1111-compounds have been successfully synthesized ($\sim 100 \times 100$ μm^2) (see, e.g., Refs [63, 64]). The situation with 122-systems is much better, where almost immediately single crystals of millimeter sizes were obtained (see Fig. 6) [65]. Thus, most of the measurements in what follows were made on single crystals of this system

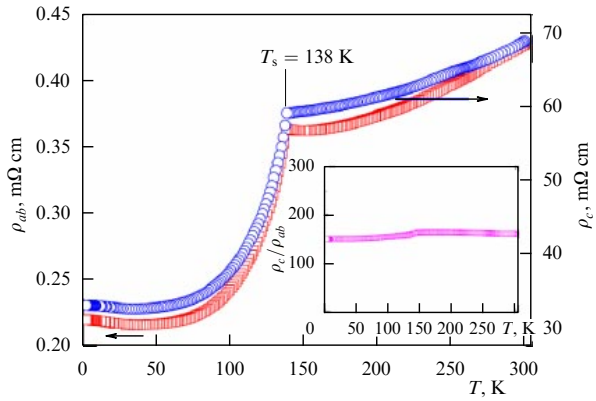

Figure 7. Temperature dependences of resistivity ρ_{ab} in the *ab* plane and of transverse resistivity ρ_c in the orthogonal direction in a single crystal of $BaFe_2As_2$ [67]. Shown in the inset is the temperature dependence of the resistivity anisotropy.

(though for 1111-systems a number of interesting studies on single crystals were also performed). Recently, rather small single crystals ($\sim 200 \times 200$ μm^2) of α-FeSe with $T_c \sim 10$ K have also been obtained [66], but detailed physical measurements on this system have yet to be done.

Typical results of measurements on single crystals of 1111 [64] and 122 [65] systems are given in Fig. 6. In particular, the anisotropy of the upper critical field H_{c2} testifies to the quasi-two-dimensional nature of the electronic subsystem in these superconductors, which is already evident from their crystal structure. At the same time, we can see that this anisotropy of critical fields is not too large.

In Fig. 7 taken from Ref. [67] we depicted the temperature dependences of resistivity ρ_{ab} in the *ab* plane and of transverse resistivity ρ_c in the orthogonal direction for a single crystal of a prototype (undoped) $BaFe_2As_2$ system [67]. It can be seen that the resistivity anisotropy exceeds 10^2, which confirms the quasi-two-dimensional nature of the electronic properties of this system. This anisotropy is significantly larger than the value which can be expected from simple estimates[3] based on the above-mentioned anisotropy of H_{c2}. However, we must stress that data on the anisotropy of the resistivity of superconducting samples in Refs [65, 67] are absent. In the data given in Fig. 7 we can also clearly see an anomaly in the temperature dependence of resistivity at $T_s = 138$ K, which is connected with the antiferromagnetic (SDW) transition.

The question concerning the anisotropy of electronic properties has become more acute after measurements in Ref. [68] of H_{c2} in single crystals of $Ba_{1-x}K_xFe_2As_2$ were performed in a much wider temperature interval than in Ref. [65], up to the field values on the order of ~ 60 T. According to Ref. [68], the anisotropy of H_{c2} is observed only in the relatively narrow temperature interval close to T_c, changing to almost isotropic behavior as the temperature lowers.

2.3 Magnetic structure and phase diagram

As mentioned above, with lowering temperature the prototype (undoped) 1111 and 122 compounds undergo a structural transition accompanied by a simultaneous or later antiferromagnetic transition (probably of the SDW type). Direct confirmation of this picture was obtained in neutron scattering experiments. The first results for an LaOFeAs system were given in Ref. [69]. It was discovered that the structural transition in this compound (according to Ref. [69], from the orthorhombic $P4/nmm$ to the monoclinic $P112/n$ structure, which differs from the evidence of other authors [62]) takes place at $T \sim 150$ K (where an anomaly in the temperature dependence of resistivity is observed), and afterwards antiferromagnetic ordering appears at $T \sim 134$ K.

Shown in Fig. 8a are the antiferromagnetic structure obtained in these experiments, as well as the temperature dependence of the square of the magnetic moment at the Fe site. The value of this moment is not larger than $0.36(5)\,\mu_B$. We see that spin ordering in the *ab* plane takes the form of characteristic chains of ferromagnetically oriented spins with opposite spin orientations in neighboring chains (stripes). Along the *c*-axis there occurs typical period doubling.

In Fig. 8b we compare the magnetic structures in the CuO_2 plane of cuprates and in the FeAs plane of new FeAs-based superconductors. Analogies and significant distinctions alike can clearly be seen. Both structural and antiferromagnetic transitions in FeAs planes are suppressed by doping, similarly to the situation in cuprates. At the same time, it should be stressed that the antiferromagnetic phase of cuprates is an insulator, while it remains metallic in FeAs-based superconductors, as is clearly seen from the data on resistivity quoted above.

The phase diagram of new superconductors (with a changing concentration of the doping element) is also significantly different from that of cuprates. Shown in Fig. 9 is the phase diagram for the $LaO_{1-x}F_xFeAs$ system, obtained in Ref. [70] from μSR experiments. It can be seen that the temperatures of structural and magnetic transitions are clearly separated, while the superconducting region does not overlap with the antiferromagnetic region.

An analogous phase diagram for the $CeO_{1-x}F_xFeAs$ compound, obtained in Ref. [71] from neutron scattering data, is drawn in Fig. 9b. According to this work, a structural tetra–ortho transition ($P4/nmm \to Cmma$) is also well resolved from the antiferromagnetic transition, which takes place at lower temperatures, while the superconducting region does not overlap with the region of antiferromagnetic ordering on Fe. At the same time, the magnetic structure of $CeO_{1-x}F_xFeAs$, demonstrated in Fig. 10, is somewhat different from that of $LaO_{1-x}F_xFeAs$ (obtained by the same team [69]). In the FeAs plane we again have a stripe structure similar to that in LaOFeAs, but spins on the adjacent planes are parallel and in consequence there occurs no period doubling along the *c*-axis. The value of the magnetic moment on Fe is as high as $0.8(1)\,\mu_B$ at 40 K, which is roughly twice as large as in LaOFeAs. Also in Ref. [71], a magnetic structure due to Ce spin ordering was determined at $T = 1.7$ K. According to this work, a strong correlation between the spins of Fe and Ce appears already at temperatures below 20 K. It should be noted that spin ordering on rare-earth ions in an *RE*OFeAs series typically takes place at temperatures on the order of a few K, which are nearly an order of magnitude higher than similar temperatures in cuprates like $REBa_2Cu_3O_{7-\delta}$ [72], giving evidence of a significantly stronger interaction between these spins. The general picture of spin ordering in $CeO_{1-x}F_xFeAs$ is portrayed in Fig. 10.

Notice that data obtained by neutron scattering are still sometimes contradictory. For example, in Ref. [73], where the

[3] The anisotropy of H_{c2} is usually on the order of the square root of the resistivity anisotropy.

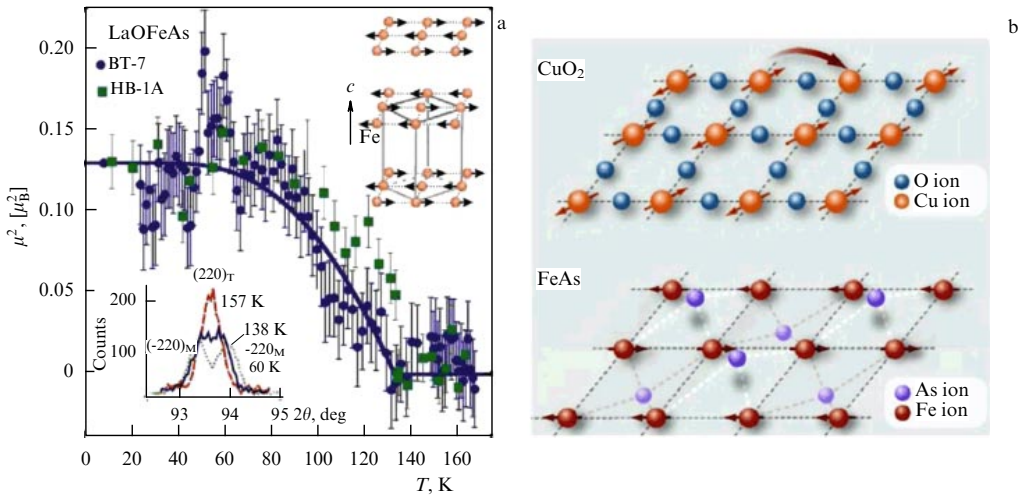

Figure 8. (a) Temperature dependence of the square of the magnetic moment at the Fe site in LaOFeAs obtained by neutron scattering (data from two spectrometers denoted as BT-7 and HB-1A) [69]. Shown in the inset in the upper right corner is the experimentally determined antiferromagnetic structure in the $\sqrt{2}a \times \sqrt{2}b \times 2c$ lattice cell. Distortion of the nuclear scattering peak shown in the inset in the lower left corner suggests that structural transition precedes magnetic transition. (b) Comparison of antiferromagnetic ordering in the CuO_2 plane of cuprates and in the FeAs plane of new superconductors.

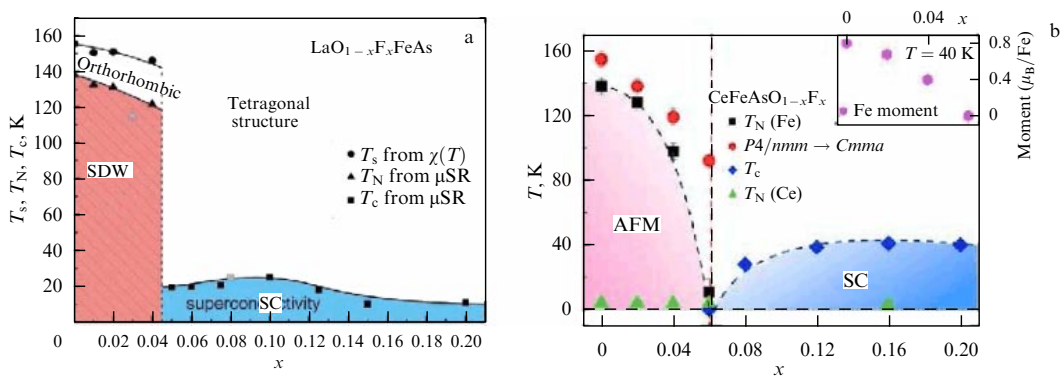

Figure 9. (a) Phase diagram of $LaO_{1-x}F_xFeAs$ obtained from μSR experiments [70]. It portrays the concentration dependences of critical temperatures of superconducting (T_c), magnetic (T_N), and structural (T_s) transitions (determined from resistivity measurements). (b) Phase diagram of the $CeO_{1-x}F_xFeAs$ system obtained from neutron scattering data in Ref. [71]. Shown in the inset is the concentration dependence of the Fe magnetic moment.

$NdO_{1-x}F_xFeAs$ system was studied, it was claimed that spin ordering on Fe does not appear up to temperatures of about 2 K, where ordering of Fe and Nd spins takes place simultaneously, with the general picture of ordering similar to that shown in Fig. 10 for Fe and Ce. However, it was revealed in Ref. [74] that antiferromagnetic ordering on Fe, similar to that discussed above, in fact occurs in NdOFeAs at $T \sim 140$ K, while difficulties with its observability are due, apparently, to the rather small value of the magnetic moment on Fe, which was found to be only $0.25\,\mu_B$.

As to the phase diagram of 1111-systems, here some questions also remain. It was claimed in Ref. [75] that μSR data on $SmO_{1-x}F_xFeAs$ suggest the existence of some narrow coexistence region of superconductivity and antiferromagnetism at doping levels in the range $0.1 < x < 0.15$. Naturally, a complete understanding of this situation will appear only in the course of further studies.

Neutronographic studies were also performed on different 122-compounds. Polycrystalline samples of $BaFe_2As_2$ were studied in Ref. [76]. It was shown that a tetra – ortho structural transition ($I4/mmm \to Fmmm$) takes place practically at the same temperature $T_s \approx 142$ K as the antiferromagnetic transition, and spin ordering on Fe is the same as in 1111-systems, as illustrated in Fig. 11a. The magnetic moment on Fe at $T = 5$ K is equal to $0.87(3)\,\mu_B$. Similar data were also obtained on the $SrFe_2As_2$ single crystal [77], where structural transition at $T_s = 220 \pm 1$ K is very sharp, indicating, in the authors' opinion, a first-order transition. At the same temperature, antiferromagnetic ordering of spins on Fe appears, which is of the same type as in $BaFe_2As_2$ (Fig. 11a), and this transition is continuous. The magnetic moment on Fe at $T = 10$ K is equal to $0.94(4)\,\mu_B$. These results unambiguously point to the same nature of antiferromagnetic ordering of Fe spins in two-dimensional FeAs planes in 1111- and 122-systems.

A series of single crystals of $Ba_{1-x}K_xFe_2As_2$ with a different x content were studied in Ref. [78] by X-ray, neutron scattering, and electrical measurement methods. As a result, the authors have produced the phase diagram shown in Fig. 11b, where a coexistence region of superconductivity

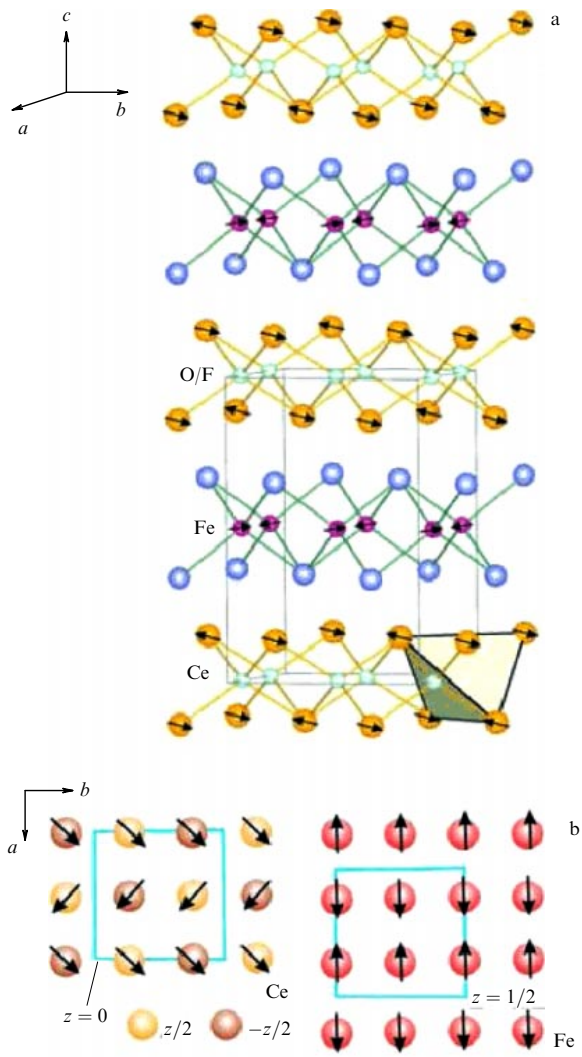

Figure 10. Magnetic structure of CeOFeAs: (a) general picture of spin ordering at low temperatures, and (b) magnetic elementary cells of Fe and Ce.

and antiferromagnetism is clearly seen for the interval $0.2 < x < 0.4$.

Concluding this section, let us highlight the recent work [79], where a neutron scattering study was performed on a α-Fe($Te_{1-x}Se_x$) system for the first time. It was found that in the prototype α-FeTe system (with an excess of Fe), antiferromagnetic ordering of Fe spins takes place at temperatures lower than $T_s \approx 75$ K (for $Fe_{1.076}Te$) and $T_s \approx 63$ K (for $Fe_{1.141}Te$) and has the form of an incommensurate spin density wave accompanied by structural transition from the tetragonal to the orthorhombic phase ($P4/nmm \rightarrow Pmmm$). The qualitative picture of spin ordering compared with the FeAs plane is displayed in Fig. 12. At the same temperature T_s, a rather sharp anomaly is also observed in the temperature dependence of electrical resistivity. For the superconducting $Fe_{1.080(2)}Te_{0.67(2)}Se_{0.33(2)}$ compound with $T_c \approx 14$ K, spin ordering and a structural transition are absent, though well-developed fluctuations of incommensurate SDW short-range order were observed.

2.4 Specific heat

Specific heat measurements in new superconductors have been performed starting from the earliest works [30, 80]. As a typical example of specific heat behavior in 1111-systems, let us consider $SmO_{1-x}F_xFeAs$ data from Ref. [80]. Shown in Fig. 13a is the temperature behavior of specific heat in this system at $x = 0$ and $x = 0.15$ (superconducting sample). A pronounced anomaly of specific heat is observed at $T_s \approx 130$ K, which is obviously attributed to antiferromagnetic (SDW) (or structural tetra–ortho) transition. In the superconducting sample ($x = 0.15$), this anomaly is absent. Besides this, in both samples there is a clear anomaly at $T \approx 5$ K, which is connected with (antiferromagnetic) ordering of Sm spins. As to specific heat discontinuity at the superconducting transition, it is rather hard to resolve, and is observed, according to Ref. [80], at temperatures significantly lower than superconducting transition temperature T_c determined by zero-resistivity measurements. Apparently, this is due to the rather poor quality of samples (inhomogeneous content?).

In 122-systems, the studies of specific heat were done on single-crystal samples [81, 82]. We illustrate in Fig. 14a the

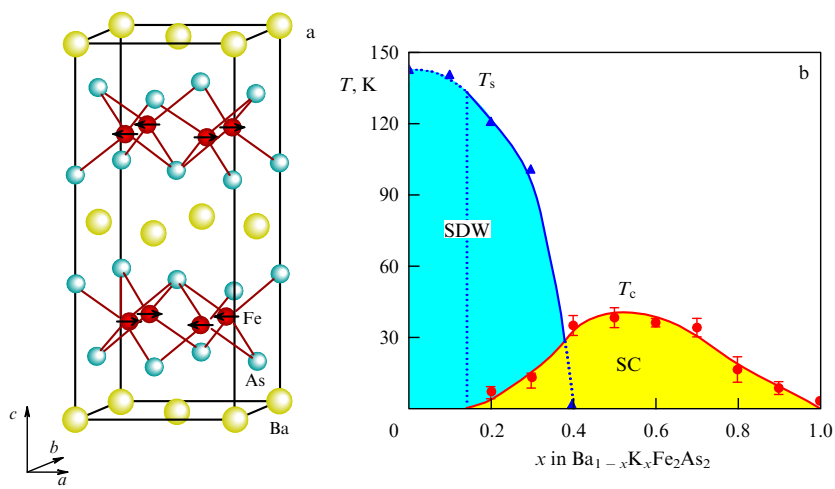

Figure 11. (a) Magnetic and crystal structures of $BaFe_2As_2$ in an orthorhombic ($Fmmm$) cell [76]. (b) Phase diagram of $Ba_{1-x}K_xFe_2As_2$ according to Ref. [78]. T_s is the temperature of antiferromagnetic ordering (and structural transition), and T_c is the superconducting transition temperature.

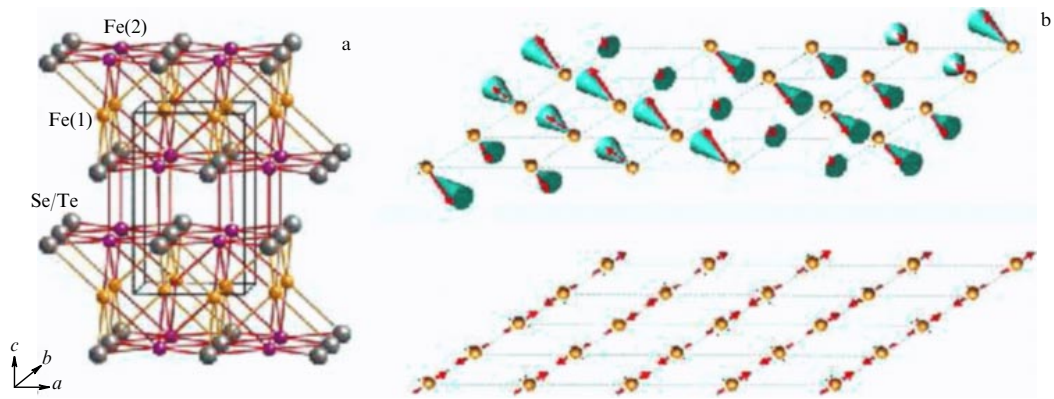

Figure 12. (a) Crystal structure of α-FeTe/Se, with excessive iron occupying Fe(2) positions. (b) Spin ordering in α-FeTe according to the data of Ref. [79], compared with antiferromagnetic ordering in the FeAs plane.

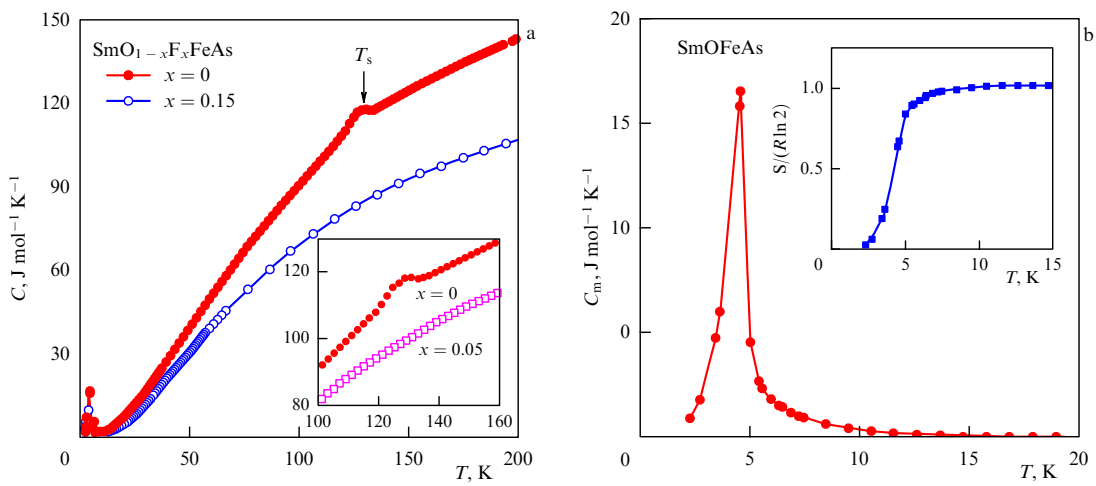

Figure 13. (a) Specific heat of $SmO_{1-x}F_xFeAs$ for $x = 0$ and $x = 0.15$ (superconducting sample) [80]. Shown in the inset is the region around $T_s = 130$ K, where (at $x = 0$) an anomaly is observed, usually attributed to antiferromagnetic transition of spins on Fe and absent in the superconducting sample. (b) Magnetic contribution to specific heat of SmOFeAs in the vicinity of the Sm spin ordering temperature [80]. Shown in the inset is an entropy change due to this ordering.

temperature behavior of specific heat in a superconducting single crystal of $Ba_{0.6}K_{0.4}Fe_2As_2$ with $T_c = 35.8$ K [82]. Detailed analysis allowed the authors to single out and study electronic specific heat coefficient γ_n in the normal phase, induced by a magnetic field, and in the superconducting phase. The observed dependence of γ_n on the magnitude of the magnetic field allowed coming to the conclusion that pairing in this system follows the s type, with a nonzero energy gap everywhere at the Fermi surface (absence of gap zeroes characteristic, e.g., of d-wave pairing in cuprates).

In Fig. 14b, a comparison is made of accurately resolved electronic specific heat discontinuity ΔC_e at the superconducting transition with predictions of the BCS theory (weak coupling!). Agreement is quite impressive — the use of the thus determined value of $\gamma_n \approx 63.3$ mJ mol^{-1} K^{-2} gives the value of $\Delta C_e/\gamma_n T|_{T=T_c} \approx 1.55$, compared with the BCS theory prediction of 1.43. The fit to the BCS theoretical dependences allowed the authors to determine also the value of the energy gap at low temperatures, which was found to be $\Delta_0 \approx 6$ meV. In Section 3.3 we shall see that this value is in good agreement with other (ARPES) available data.

2.5 NMR (NQR) and tunneling spectroscopy

There are already a couple of studies of peculiarities in NMR (NQR) spectra of new superconductors, pointing to certain conclusions about the possible types of superconducting pairing in these systems. In Ref. [83], ^{75}As and ^{139}La NMR were studied in $LaO_{1-x}F_xFeAs$ for $x = 0$, 0.04, 0.11. In undoped LaOFeAs, a characteristic peak (divergence) of NMR relaxation time $1/T_1$ on ^{139}La was observed at the antiferromagnetic transition temperature $T_s \sim 142$ K, while below the NMR spectrum was too broadened, which is attributed to antiferromagnetic ordering. In a superconducting sample with $x = 0.4$ ($T_c = 17.5$ K), the value of $1/TT_1$ increases as temperature lowers down to ~ 30 K, following the Curie–Weiss law: $1/TT_1 \sim C/(T+\theta)$, where $\theta \sim 10$ K, without appearing divergence at finite temperatures, so that the occurrence of superconductivity is accompanied by the suppression of magnetic ordering. The overall picture of nuclear spin relaxation for the sample with $x = 0.11$ ($T_c = 22.7$ K) is qualitatively different. The value of $1/TT_1$ both on ^{139}La and ^{75}As nuclei decreases with lowering temperature, which is similar to the NMR picture of pseudogap behavior in underdoped cuprates, approaching a

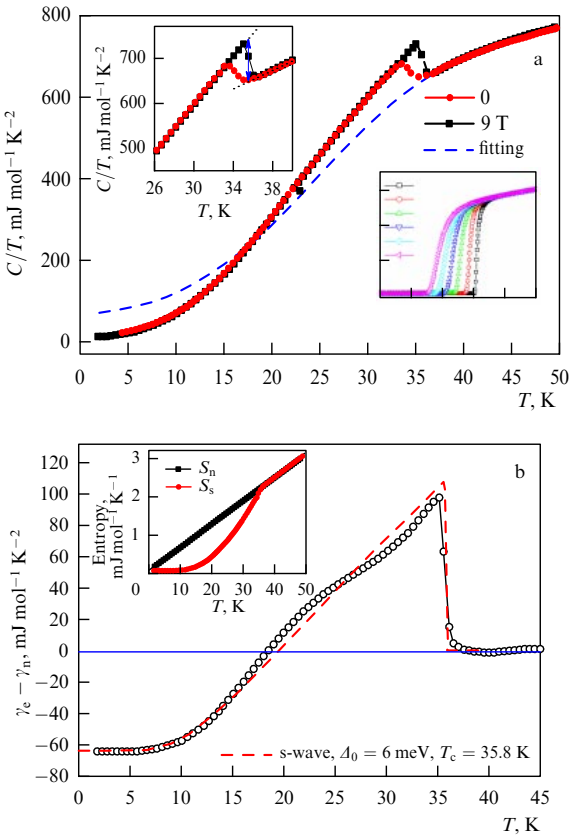

Figure 14. (a) Initial data on the specific heat of $Ba_{0.6}K_{0.4}Fe_2As_2$ [82]. Shown in the insets are detailed behavior of specific heat in the vicinity of T_c and resistivity behavior in the neighborhood of the superconducting transition in different magnetic fields. (b) Electronic specific heat discontinuity and its comparison with predictions of BCS theory. Shown in the inset is the temperature behavior of entropy in the normal and superconducting states [82].

constant in the vicinity of T_c, and is well fitted by activation temperature dependence with the pseudogap value of $\Delta_{PG} = 172 \pm 17$ K [83].

In Fig. 15a we portray the temperature dependence $1/T_1$ on ^{75}As in the $LaO_{1-x}F_xFeAs$ system in the superconducting state ($x = 0.04$ and $x = 0.11$) and in an undoped LaOFeAs sample (on ^{139}La nucleus, normalized according to $^{139}(1/T_1)/^{75}(1/T_1) \sim 0.135$) [83]. It should be noted the absence of the Gebel–Slichter peak of $1/T_1$ in the vicinity of T_c, and T^3 type dependence of $1/T_1$ in the superconducting region, characteristic of anomalous (non-s-wave!) pairing with an energy gap with zeroes at the Fermi surface, for instance, as in d-wave pairing. In fact, these dependences are well fitted using $\Delta(\phi) = \Delta_0 \sin(2\phi)$, where ϕ is the polar angle determining the direction of the momentum in two-dimensional inverse space corresponding to the FeAs plane, with the value of $2\Delta_0/T_c = 4.0$ [83].

Quite similar results were obtained in work [85] during the studies of NMR and NQR spectra of ^{75}As nuclei in $LaO_{1-\delta}FeAs$ ($\delta = 0, 0.25, 0.4$), with T_c up to 28 K, and in $NdO_{0.6}FeAs$ with $T_c = 53$ K. In particular, these authors come to the conclusion that their NQR relaxation rate data for $LaO_{0.6}FeAs$ in the superconducting phase correspond to an energy gap of the form $\Delta = \Delta_0 \cos(2\phi)$ with $2\Delta_0/T_c \approx 5$, which corresponds to d-wave pairing with gap zeroes at the Fermi surface, i.e., the same pairing symmetry as in cuprates. The temperature behavior of $1/T_1$ for $T > T_c$, found in this work, also gives evidence of pseudogap occurrence with the gap width $\Delta_{PG} \approx 196$ K.

In Ref. [86], ^{75}As Knight shift measurements were done in $PrO_{0.89}F_{0.11}FeAs$. The sharp drop in the Knight shift for $T < T_c$ unambiguously points to the singlet nature of pairing. Details of the temperature dependence of the Knight shift were well fitted into the model with two d-wave superconducting gaps: $\Delta = \Delta_0 \cos(2\phi)$, $\Delta_0 = \alpha\Delta_1 + (1-\alpha)\Delta_2$ with $2\Delta_1/T_c \approx 7$ and $2\Delta_2/T_c \approx 2.2$, $\alpha = 0.4$. In the same

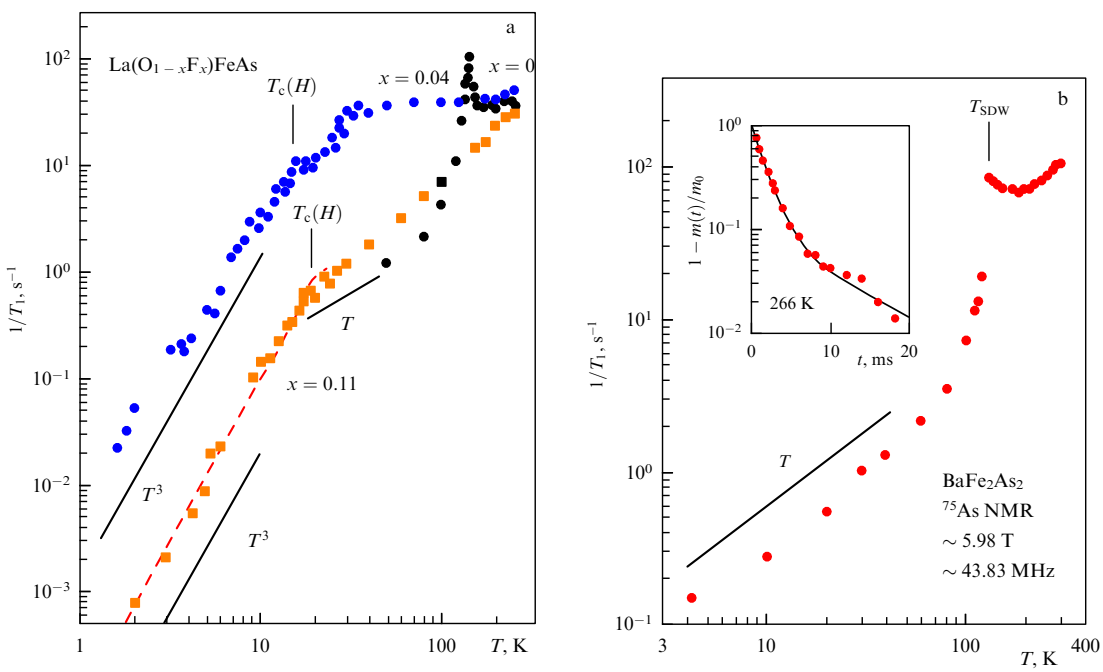

Figure 15. (a) Temperature dependence of NMR relaxation rate $1/T_1$ in $LaO_{1-x}F_xFeAs$ for $x = 0, 0.04, 0.11$ in the low-temperature region on the order of T_c and below [83]. (b) Temperature dependence of $1/T_1$ on ^{75}As nuclei in undoped $BaFe_2As_2$ [84].

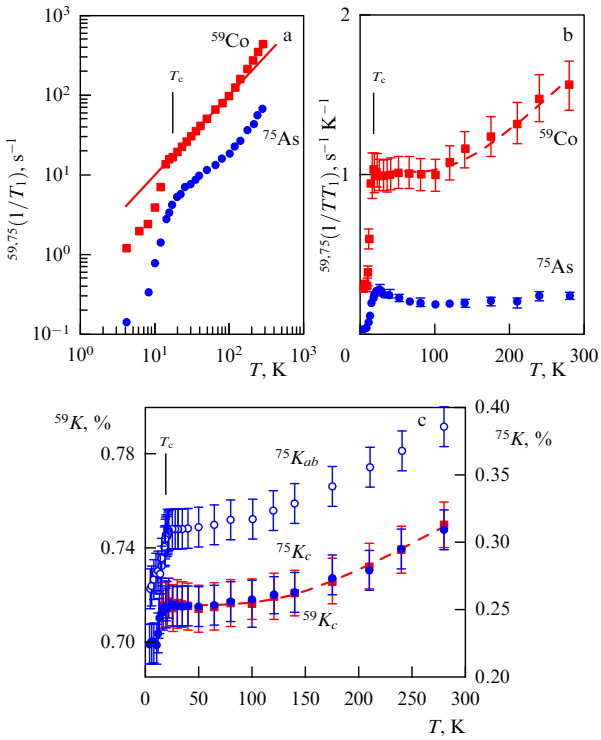

Figure 16. (a) Temperature dependence of $1/T_1$ on ^{59}Co and ^{75}As nuclei in $BaFe_{1.8}Co_{0.2}As_2$, and (b) similar dependence of $1/TT_1$, where the dashed curve corresponds to activation dependence with pseudogap width $\Delta_{PG} = 560 \pm 150$ K [87]. (c) Temperature dependence of the Knight shift on ^{59}Co and ^{75}As in the same system, where the dashed curve is described by activation dependence with the same pseudogap width.

model, the authors of Ref. [86] have successfully described the temperature dependence of $1/T_1$ on ^{19}F nuclei for $T < T_c$.

An NMR study of undoped $BaFe_2As_2$ was performed in Ref. [84]. The temperature dependence of $1/T_1$ is depicted in Fig. 15b. A clear anomaly is observed at $T = 131$ K, which was connected by the authors to an antiferromagnetic (SDW) transition. The sharp drop in $1/T_1$ is attributed to SDW-gap opening on part of the Fermi surface. The linear-over-T behavior of the relaxation rate for $T < 100$ K can be assigned to the relaxation of nuclear spins on conduction electrons, remaining on the 'open' parts of the Fermi surface. On the whole, the situation here is reminiscent of similar behavior in LaOFeAs, though there are some significant quantitative differences [84].

An NMR study of the superconducting phase in the 122-system was done on $BaFe_{1.8}Co_{0.2}As_2$ with $T_c = 22$ K in Ref. [87]. In Fig. 16, results on the nuclear spin relaxation rate and Knight shift are given. For temperatures below 280 K, a drop in $1/TT_1$ is observed, which is approximated by activation dependence with (pseudo)gap width $\Delta_{PG} \approx 560$ K (Fig. 16b). The last result is significantly larger than the pseudogap width estimates for $LaO_{0.9}F_{0.1}FeAs$, obtained in Ref. [83] and quoted above. Data on the Knight shift (Fig. 16c), similarly to the 1111 case, give evidence of singlet pairing. Moreover, the temperature dependence of the Knight shift above T_c also reveals pseudogap behavior with the same pseudogap width as obtained from fitting the data on the relaxation rate.

Thus, NMR data on 1111 and 122 systems are in many respects similar. Singlet pairing follows unambiguously, as does evidence for the anomalous nature of symmetry of superconducting order parameter with probable gap zeroes at the Fermi surface (and probably the presence of two superconducting gaps). However, below we shall see that the inference about gap zeroes contradicts some other experiments and interpretations of NMR data may be quite different.

As for the α-FeSe system, up to now there is only one NMR study on $FeSe_{0.92}$ with $T_c = 8$ K [88] (NMR on ^{77}Se nuclei), demonstrating the absence of the Gebel–Slichter peak in the temperature dependence of $1/T_1$ in the vicinity of T_c and the absence of any anomaly which can be attributed to any kind of magnetic ordering at higher temperatures, as well as the absence there of any kind of 'pseudogap' behavior (validity of the Korringa relation). At the same time, $\sim T^3$-behavior of $1/T_1$ was observed in the $T < T_c$ region, probably giving evidence of zeroes of the superconducting gap on the Fermi surface.

Among a number of studies using different kinds of tunneling spectroscopy, let us mention Refs [89–91]. Up to now, these experiments have been carried out on polycrystalline samples and their results are somewhat contradictory.

In Ref. [89], the method of Andreev spectroscopy was applied to $SmO_{0.85}F_{0.15}FeAs$ with $T_c = 42$ K. Only one superconducting gap was observed with $2\Delta = 13.34 \pm 0.3$ meV (nearby $T = 0$), which corresponds to $2\Delta/T_c = 3.68$, i.e., quite close to a standard BCS value of 3.52. The temperature dependence of the gap, determined in Ref. [89], also closely followed BCS theory. In the authors' opinion, these results give evidence of the usual (s-wave) order parameter with no zeroes at the Fermi surface, in obvious contradiction to NMR findings quoted above.

A similar system, $SmO_{0.85}FeAs$ with $T_c = 52$ K, was studied in Ref. [90] by scanning tunneling spectroscopy at $T = 4.2$ K. Good quality tunneling characteristics were obtained only from some parts of the sample surface, and these were fitted to the tunneling characteristics of a d-wave superconductor with $\Delta = 8-8.5$ meV, which corresponds to $2\Delta/T_c \sim 3.55-3.8$.

The same method of scanning tunneling spectroscopy (microscopy) was also applied in Ref. [91] to the $NdO_{0.86}F_{0.14}FeAs$ compound with $T_c = 48$ K, and measurements were done at different temperatures. At temperatures significantly lower than T_c, two gaps were observed on different parts of the sample surface: the bigger one with $\Delta \sim 18$ meV, and the smaller one with $\Delta \sim 9$ meV. Both gaps closed at the transition point $T = T_c$, with the smaller gap more or less following the BCS temperature dependence. On the same parts of the surface, where the smaller gap was observed below T_c, a jumplike opening pseudogap appeared slightly above T_c, closing only at $T = 120$ K. At present there is no reasonable interpretation of this unexpected behavior.

Notice also Ref. [92] where $SmO_{0.9}F_{0.1}FeAs$ with $T_c = 51.5$ K was studied by point contact spectroscopy. The authors also observed two superconducting gaps — the larger one with $\Delta = 10.5 \pm 0.5$ meV, and the smaller one with $\Delta = 3.7 \pm 0.4$ meV, with both gaps following BCS-like temperature dependence.

Up to now there has been no systematic tunneling data for 122-systems.

The contradictory nature of existing data measured by tunneling spectroscopy is more or less obvious. It seems likely that we have to wait for the results of experiments on single crystals.

2.6 Optical properties

Measurements of the optical properties of new superconductors have been done in a number of works, both on polycrystalline samples of 1111-systems [93, 94] and on single crystals of 122-systems [95, 96].

Thus, ellipsometry measurements of the dielectric permeability of the $RE O_{0.82}F_{0.18}FeAs$ ($RE = $ Nd, Sm) samples were made in the far infrared (IR) region [93]. It was shown that the electronic properties of these systems are strongly anisotropic (quasi-two-dimensional) and, in this sense, are analogous to those of cuprates. A noticeable suppression of optical conductivity in the superconducting state was also discovered, which was attributed by the authors to the opening of superconducting gap with $2\Delta \approx 300$ cm^{-1} (37 meV), which corresponds to $2\Delta/T_c \sim 8$, i.e., to the strong coupling limit.

In Ref. [94], the same method was applied to studies of the dielectric permeability of $LaO_{0.9}F_{0.1}FeAs$ with $T_c = 27$ K in a wide frequency interval of 0.01 – 6.5 eV at temperatures ranging $10 \leqslant T \leqslant 350$ K. An unusually narrow region of Drude behavior was observed, corresponding to the density of free carriers as low as 0.040 ± 0.005 per unit cell, as well as signatures of pseudogap behavior at 0.65 eV. Besides that, the authors also observed a significant transfer of spectral weight to the frequency region above 4 eV. These results allowed concluding that electronic correlations [and (or) electron – phonon coupling] are very important in these systems.

Studies of reflectance and the real part of the optical conductivity in a single crystal of $Ba_{0.55}K_{0.45}Fe_2As_2$ [95] have shown that the absorption spectrum of this system in the IR region consists of a noticeable Drude peak at low frequencies and a wide absorption band with a maximum at 0.7 eV, which the authors attributed to carrier scattering by collective (bosonic) excitations (e.g., spin fluctuations) with energies on the order of 25 meV and a strongly temperature-dependent coupling constant (with carriers).

The most convincing and interesting optical data were obtained in Ref. [96], where detailed measurements of reflectance were performed on a single crystal of $Ba_{0.6}K_{0.4}Fe_2As_2$ with $T_c = 37$ K in the infrared region and in a wide temperature interval of 10 – 300 K.

Figure 17 presents the data on the real part of optical conductivity $\sigma_1(\omega)$ obtained in Ref. [96]. It is seen that close to and below T_c (curves, corresponding to 27 K and 10 K), a rapid drop in $\sigma_1(\omega)$ takes place at frequencies below 300 cm^{-1}, so that conductivity is practically zero below 150 cm^{-1}, which gives evidence of a superconducting s-wave gap opening. The gap width determined by the absorption edge is $2\Delta \simeq 150$ cm^{-1}, which correlates well with the ARPES data to be discussed in Section 3.3.

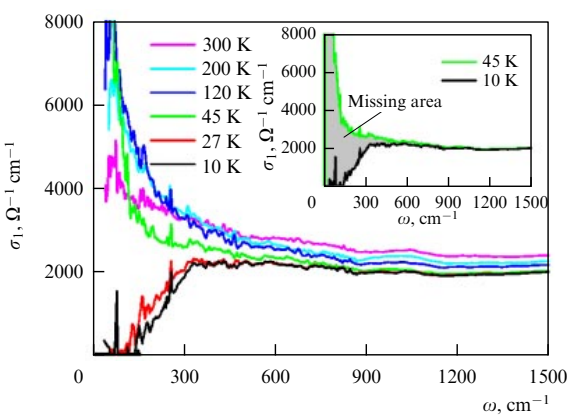

Figure 17. Real part of optical conductivity in $Ba_{0.6}K_{0.4}Fe_2As_2$ at different temperatures [96]. Inset to the figure draws a comparison of the data at 10 and 45 K, where the 'missing area', connected with the superconducting gap opening and the formation of a condensate of Cooper pairs, is clearly seen.

Thus, a considerable suppression of low-frequency conductivity is observed at temperatures significantly lower than T_c, which is connected with the formation of condensate of Cooper pairs. According to the well-known Ferrell – Glover – Tinkham sum rule [97, 98], the difference in conductivities at $T \simeq T_c$ and for $T \ll T_c$ (i.e., the so-called 'missing area' between appropriate curves, shown in the inset to Fig. 17) directly determines the value of condensate density:

$$\omega_{ps}^2 = 8 \int_{0^+}^{\omega_c} \left[\sigma_1(\omega, T \simeq T_c) - \sigma_1(\omega, T \ll T_c)\right] d\omega \,, \qquad (1)$$

where $\omega_{ps}^2 = 4\pi n_s e^2/m^*$ is the square of the plasma frequency of superconducting carriers, n_s is their density, and ω_c is a cut-off frequency which is chosen to guarantee the convergence of ω_{ps}^2. Then we can determine the penetration depth defined as $\lambda = c/\omega_{ps}$. Equation (1) yields (via the general optical sum rule) the fraction of electron (carrier) density, which is transferred to the $\delta(\omega)$ singularity of $\sigma_1(\omega)$, corresponding to the superconducting response of the condensate. A direct estimate of the missing area gives for the penetration depth λ the value equal to 2080 Å, which agrees well with other data [96].

2.7 Phonons and spin excitations: neutron spectroscopy

Up to now, a number of experiments have already been carried out to study collective excitations, i.e., phonons and spin waves, in new superconductors, which is of principal importance for the clarification of the nature of Cooper pairing in these systems. Below we shall mainly deal with experiments on inelastic neutron scattering.

In Ref. [99], inelastic neutron scattering was studied in the $LaO_{0.87}F_{0.13}FeAs$ compound with $T_c \approx 26$ K. Characteristic maxima of phonon density of states were observed at 12 and 17 meV.

The phonon density of states in $LaO_{1-x}F_xFeAs$ (for $x = 0$ and $x \sim 0.1$) was studied in more detail in Ref. [100], where it was also compared with the results of phonon spectrum calculations done in Ref. [101]. The main findings of this work are given in Fig. 18a – c, where we can see both the general structure of the phonon density of states and satisfactory agreement with the available calculations [101]. It is also evident that the phonon spectrum of a prototype 1111-system differs very little from that observed in a doped (superconducting) sample. The origin of the peaks in the phonon density of states is well explained on the basis of theoretical calculations.

The phonon density of states in 1111-systems was also studied by nuclear resonance inelastic synchrotron radiation scattering [103] (in La-based systems) and by inelastic X-ray scattering [104] (in La- and Pr-based systems). In all cases, the results are quite similar to those obtained by inelastic neutron scattering and are in satisfactory agreement with theoretical calculations.

As for 122-systems, up to now there has been work on inelastic neutron scattering in the prototype $BaFe_2As_2$ system

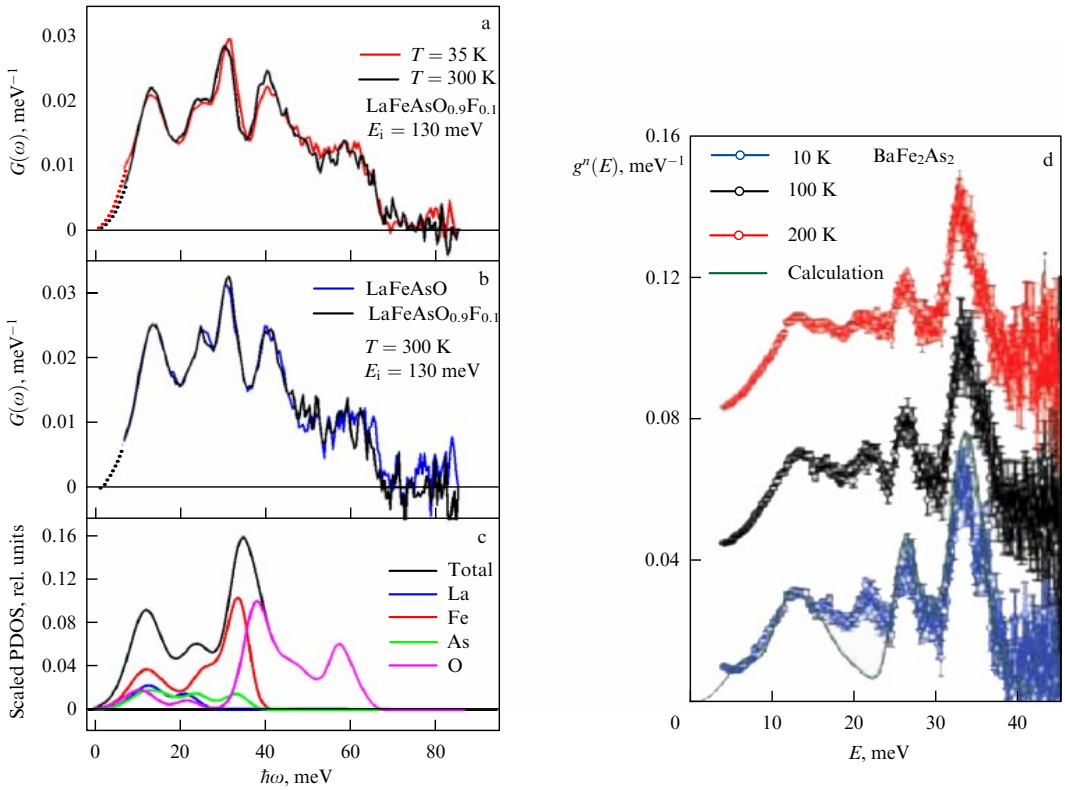

Figure 18. Phonon density of states in $LaO_{1-x}F_xFeAs$, obtained from inelastic neutron scattering (a, b) [100] and compared with calculations (c) in Ref. [101]. (d) Comparison of experimental and calculated phonon density of states in $BaFe_2As_2$ [102].

[102, 105], where consistent results have been obtained, which are also in agreement with the calculated results for the phonon spectrum, obtained in these works. As an example, we compare in Fig. 18d calculated and experimental phonon densities of states for this system, which were found in Ref. [102]. From this figure we see quite satisfactory agreement, except for an additional peak at a frequency on the order of 21.5 meV, observed in the experiments.

The dynamics of spin excitations in new superconductors were studied by neutronography in $SrFe_2As_2$ [106] and $BaFe_2As_2$ [107], i.e., in undoped samples, where antiferromagnetic ordering takes place at low temperatures.

In particular, it was shown in Ref. [106] that the spectrum of magnetic excitations is characterized by a gap of width $\Delta \leqslant 6.5$ meV, while above this gap well-defined spin waves are observed, and the measurement of their velocity allowed estimating exchange integrals (in the localized spin model). In the vicinity of the temperature of antiferromagnetic transition, no signs of critical scattering were observed, which in the opinion of the authors implies that the magnetic transition here is of the first order [106].

Qualitatively similar results (though without detailed measurements of spin wave dispersion) were obtained in Ref. [107], where it was shown that the magnon spectrum continues up to energies which are significantly higher than typical phonon frequencies (~ 40 meV) and ends at energies of about 170 meV.

2.8 Other experiments

In our rather concise review of experiments on studying new superconductors we could not pay attention to a number of important investigations; a more detailed discussion of experiments on critical magnetic fields (in particular, measurements of H_{c1}), direct measurements of penetration depth, and experiments on X-ray photoemission remained outside our presentation. We have practically paid no attention to experiments on traditional transport properties in the normal state (such as the Hall effect and thermoelectricity). This is connected mainly with the limited size of this review, as well as with the personal preferences of the author. In Section 3.3 comprising the theoretical part of this review, we shall return to the discussion of a number of extra experiments. In particular, we shall pay great attention to experiments with angle-resolved photoemission (ARPES), which are more appropriately considered in parallel with discussions of the electronic spectrum of these systems. The same applies to some other experiments on the determination of Fermi surfaces (quantum oscillation effects in strong magnetic fields).

3. Electronic spectrum and magnetism

3.1 Band structure (LDA)

Clarification of the structure of the electronic spectrum of new superconductors is crucial for explaining their physical properties. Accordingly, since the first days, different teams have started detailed band-structure calculations for all classes of these compounds, based primarily on different realizations of the general local density approximation (LDA) approach.

The first calculations of the electronic spectrum of iron oxypnictide LaOFeP were performed in Ref. [108], yet before the discovery of high-temperature superconductivity in FeAs-based systems. For LaOFeAs, such calculations were done almost simultaneously in Refs [101, 109–111]. In the following, similar calculations were also performed for other 1111-systems, as well as for 122-systems [112, 113], 111-systems [113–115], and α-FeSe [116]. As the results obtained in all these works were more or less similar, we shall concentrate below in more detail on our group works [117–120], referring to publications of other authors where necessary. We shall also limit ourselves mainly to the results obtained for the nonmagnetic tetragonal phase of 1111 and 122 systems (as well as 111), as superconductivity is realized just in this phase.

In Ref. [117] we have performed *ab initio* calculations of the electronic structure for a number of oxypnictides from the series $RE\mathrm{O}_{1-x}\mathrm{F}_x\mathrm{FeAs}$ [where RE = La, Ce, Nd, Pr, Sm, and also for the hypothetical (at that time) case of RE = Y] in the framework of the standard LDA–LMTO approach [121].

In Fig. 19a we made a comparison of electronic spectra of the LaOFeAs and PrOFeAs compounds [117] in the main symmetry directions in the Brillouin zone. It can be seen that differences in the spectra related to the replacement of the rare-earth ion (as well as a small change in lattice constants) are rather small. In a narrow enough energy interval (on the order of ± 0.2 eV) close to the Fermi energy, which is relevant to superconductivity, these spectra practically coincide.

This is also clearly seen from a comparison of the densities of states shown in Fig. 19b. In fact, the densities of states of both compounds close to the Fermi level are just the same (up to a few percent). This is typical also for other compounds from the rare-earth series $RE\mathrm{O}_{1-x}\mathrm{F}_x\mathrm{FeAs}$ [117].

The only noticeable difference in the spectra of these systems with different rare-earth ions manifests itself in the growth of tetrahedral splitting due to lattice compression, which appears at energies on the order of -1.5 eV for d-states of Fe, and -3 eV for p-states of As.

From a comparison of partial densities of states we can also see that the value of the density of states close to the Fermi level is determined almost entirely by d-states of Fe (with a very insignificant contribution from p-states of As). In this sense, we can say that all phenomena related to superconductivity in these compounds take place in the square lattice of Fe within the FeAs layer.

Naturally, most of these peculiarities of electronic spectra may be attributed to the quasi-two-dimensional character of the compounds under study. For example, the insensitivity of electronic spectra to the type of a rare-earth ion is simply due to the fact that electronic states of REO layers are far from the Fermi level, and p-states of O only weakly overlap with the d-states of Fe and p-states of As in FeAs layers. Accordingly, hybridization of the d-states of Fe and p-states of As is more significant, but still not very strong, as demonstrated by band structure calculations.

Thus, the situation with rare-earth substitutions in the REOFeAs series seems to be largely analogous to the similar one in cuprates like $RE\mathrm{Ba}_2\mathrm{Cu}_3\mathrm{O}_{7-x}$, which were studied in the early days of HTSC research [72, 122]. In these compounds, the electronic states of rare-earth ions do not overlap with the electronic states in conducting CuO_2 planes either, which leads to the well-known fact of the almost complete independence of superconducting $T_c \sim 92$ K on the type of rare earth in the series RE = Y, Nd, Sm, Eu, Gd, Ho, Er, Tm, Yb, Lu, Dy [124], with only two exceptions relating to a much lower $T_c \sim 60$ K in the case of La and the complete absence of superconductivity in the case of a Pr-based compound [72].

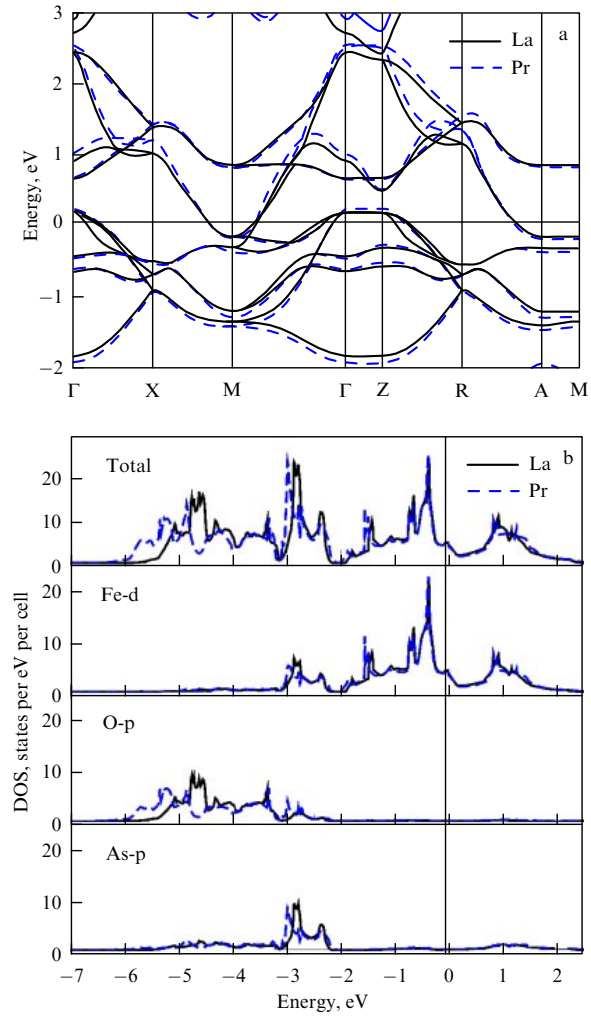

Figure 19. (a) Electronic spectra of LaOFeAs and PrOFeAs in high-symmetry directions in the Brillouin zone of a tetragonal lattice, obtained within the LDA approach [117]. (b) Comparison of the total and partial densities of states in LaOFeAs and PrOFeAs [117].

Similarly, the almost identical electronic structure of iron oxypnictides like REOFeAs with different RE in a wide enough energy interval around the Fermi level seems to lead inevitably to approximately the same values of superconducting transition temperature T_c (for any BCS-like microscopic mechanism of pairing). Different rare-earth ions just do not influence electronic structure, at least in this energy interval around the Fermi level, and, accordingly, do not change the value of the pairing coupling constant. Also, there is no special reasons to believe that the replacement of rare-earth ion will change the phonon spectrum of these systems much, or the spectrum of magnetic excitations in the FeAs layer.

Thus, it would seem that we have a kind of rare-earth puzzle — in contrast to cuprate series $RE\mathrm{Ba}_2\mathrm{Cu}_3\mathrm{O}_{7-x}$, different rare-earth substitutions in the REOFeAs series lead to a rather wide scatter in T_c values, from ~ 26 K in the case of La-based system to ~ 55 K in the case of Nd and Sm. At the

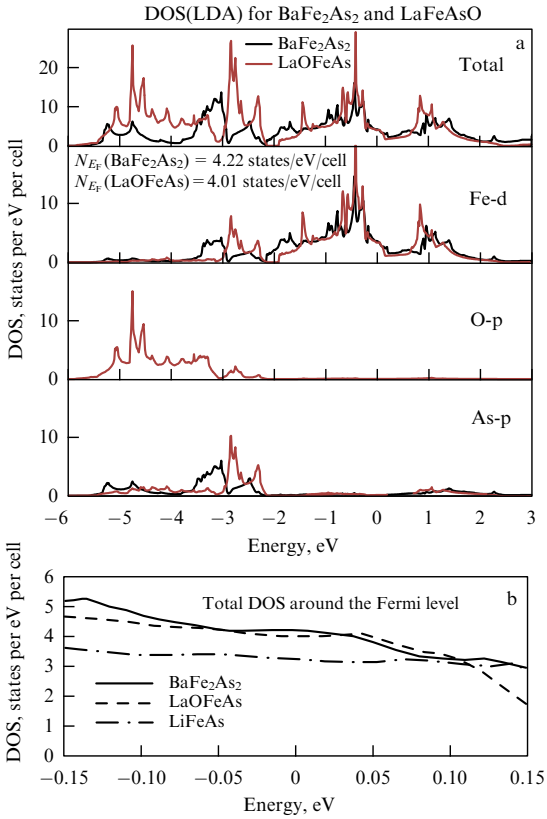

Figure 20. (a) Comparison of the total electronic density of states and partial densities of states in LaOFeAs and $BaFe_2As_2$ [118]. (b) Comparison of densities of states in a narrow energy interval around the Fermi level in LaOFeAs, $BaFe_2As_2$, and LiFeAs [119].

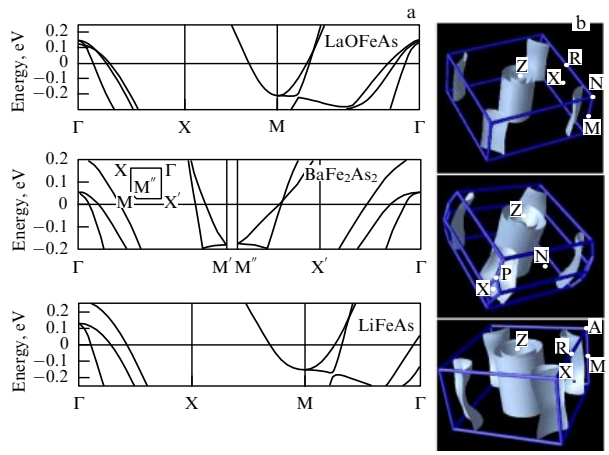

Figure 21. (a) Electronic spectra of $LaO_{1-x}F_xFeAs$, $BaFe_2As_2$, and LiFeAs in a narrow interval of energies close to the Fermi level, relevant to the formation of the superconducting state. (b) Fermi surfaces of these compounds [117, 119].

moment, we can propose two possible explanations of this puzzle:

(1) Different qualities of samples (disorder effects) can lead to a rather wide scatter in T_c values, because internal disorder can strongly influence the value of critical temperature, especially for anomalous pairings (anisotropic s-wave, even more so p- or d-wave pairing, triplet pairing, etc.), which are widely being discussed at present for FeAs superconductors [110, 123]. This possibility is qualitatively analogous to the case of copper oxides, where d-wave pairing is realized, which is strongly suppressed by disorder. This argumentation was used, for example, to explain typically lower values of T_c in $LaBa_2Cu_3O_{7-x}$, which were attributed to disorder in the positions of La and Ba ions, as well as to oxygen vacancies [72]. In fact, this point of view is confirmed by reports on the synthesis of $LaO_{1-x}FeAs$ with $T_c \sim 41$ K [34], as well as by the synthesis of the initially hypothetical [117] $YO_{1-x}FeAs$ system, first with $T_c \sim 10$ K [124] and later (synthesis under high pressure) with $T_c \sim 46$ K [125]. In this last paper, 1111-compounds based on Ho, Dy, and Tb were also synthesized, leading to T_c values on the order of 50, 52, and 48 K, respectively. It seems quite probable that the best prepared samples of the 1111 series may achieve values of $T_c \sim 55$ K, as obtained in the most 'favorable' cases of Sm and Nd. This stresses the necessity of systematic studies of disorder effects in new superconductors.

(2) However, we cannot exclude also the other physical reasons for T_c variability in the *RE*OFeAs series, connected, for instance, with spin ordering on rare-earth ions (like Ce, Pr, Nd, Sm, Gd, which possess magnetic moments). Above, we have already mentioned the unusually high coupling of these moments with moments on Fe. Moreover, the temperature of rare-earth moments ordering is known experimentally to be an order of magnitude higher than in the $REBa_2Cu_3O_{7-x}$ systems [72], which also points to rather strong magnetic couplings. The latter may significantly influence, for example, the spin fluctuation spectrum in FeAs layers (and T_c values in the case of the magnetic mechanisms of pairing [110, 123]).

In Fig. 20a we made a comparison of the total electronic density of states and partial densities of states in the LaOFeAs and $BaFe_2As_2$ samples [118]. It is seen that again we have almost the same values of DOSs in an energy interval around the Fermi level, relevant to superconductivity. We can see it in more detail in Fig. 20b, where densities of states are compared in a narrow (± 0.15 eV) energy interval close to the Fermi level in LaOFeAs, $BaFe_2As_2$, and LiFeAs [119]. The densities of states in this energy interval are almost energy independent (quasi-two-dimensionality!) and only slightly different (though, in principle, one can notice some correlation of these values of DOS at the Fermi level and the values of T_c in these compounds).

The bandwidth of d-states of Fe in $BaFe_2As_2$ is approximately 0.3 eV larger than in LaOFeAs, which may be connected with shorter Fe–As bonds, i.e., with larger Fe-d–As-p hybridization. In both compounds, bands crossing the Fermi level are formed mainly from three d-orbitals of Fe with t_{2g} symmetry, namely *xz*, *yz*, *xy*. A similar situation is also realized for LiFeAs.

In Fig. 21a we exhibit electronic dispersions in high-symmetry directions in all three main classes (1111, 122, and 111) of new superconductors in a narrow (± 0.2 eV) energy interval around the Fermi level, where the superconducting state is formed [118, 119]. It can be seen that electronic spectra of all systems in this energy interval are very close to each other. In the general case, the Fermi level is crossed by five bands formed by d-states of Fe. Of these, three form hole-like Fermi surface pockets close to the Γ point, and the others form two-electron-like pockets at the corners of the Brillouin zone (note that the Brillouin zones of 1111, 111, and 122 systems are slightly different due to existing differences in lattice symmetry).

It is not difficult to understand that this kind of a band structure leads to similar Fermi surfaces of these compounds — appropriate calculated results are given on the right-hand side of Fig. 21b: there are three hole-like cylinders at the center of the Brillouin zone and two electron-like ones at the corners. The almost cylindrical form of the Fermi surfaces reflects the quasi-two-dimensional nature of the electronic spectra in new superconductors. The smallest of the hole-like cylinders is usually neglected in the analysis of superconducting pairings, as its contribution to electronic properties is rather small (the smallness of its phase space volume). At the same time, from the general picture of the electronic spectrum it is clear that superconductivity is formed in a multiple band system with several Fermi surfaces of different (electron or hole-like) natures, which is drastically different from the simple one-band situation in HTSC cuprates. In Section 3.3 we shall see that the results of LDA calculations of an electronic structure correlate rather well with ARPES experiments.

LDA calculations of the band structure of α-FeSe were performed in a recent paper [116]. Dropping the details, it should be noted that the results are qualitatively quite similar to those described above for 1111, 122, and 111 systems. In particular, the form of Fermi surfaces is qualitatively the same, while conduction bands near the Fermi level are formed from d-states of Fe.

The first calculations of the band structure of the Sa(Ca)FFeAs compounds were done in Refs [120, 126]. Naturally enough, the band structure and Fermi surfaces in these compounds are also very similar to those obtained earlier for *RE*OFeAs systems. The only disparity lies in a slightly more pronounced quasi-two-dimensional nature of the electronic spectra in these compounds.

3.2 'Minimal' model

The relative simplicity of the electronic spectrum of FeAs superconductors in the neighborhood of the Fermi level (see Fig. 21) suggests a possibility to formulate a kind of 'minimal' analytic or semianalytic model of the spectrum (e.g., in the tight-binding approximation), which will provide a semi-quantitative description of electrons in the vicinity of the Fermi level, being sufficient for a theoretical description of the superconducting state and magnetic properties of FeAs planes. Up to now, several variants of such a model have already been proposed [127–130]. Below, we shall limit ourselves to a brief description of the simplest (and crudest) variant of this model, proposed by Scalapino and coworkers (see Ref. [127]).

The schematic structure of a single FeAs layer is displayed in Fig. 22a. Fe ions form a square lattice surrounded by layers of As ions which also form a square lattice and reside at the centers of squares of Fe ions and are displaced upwards or downwards with respect to the Fe lattice in a checkerboard manner, as illustrated in Fig. 22a. This leads to two inequivalent positions of Fe, so that there are two ions of Fe and two As ions in an elementary cell. The LDA calculations described in Section 3.1 imply that the main contribution to the electronic density of states in a wide enough energy interval around the Fermi level is due to the d-states of Fe. Thus, we can consider the simplified model which primarily takes into account three orbitals of Fe, namely d_{xz}, d_{yz}, and d_{xy} (or $d_{x^2-y^2}$, which is just the same). As a further simplification, the role of d_{xy} (or $d_{x^2-y^2}$) orbitals can be effectively taken into account by introducing transfer integrals between d_{xz}, d_{zy} orbitals on the second nearest neighbors. Accordingly, we may consider a square lattice with two degenerate 'd_{xz}, d_{yz}' orbitals at each site, with the transfer integrals shown in Fig. 22b. As we shall see below, such a model produces a picture of two-dimensional Fermi surfaces in the FeAs layer, which is in qualitative agreement with LDA results.

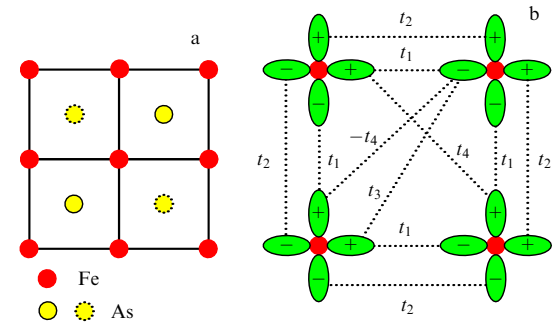

Figure 22. (a) Fe ions in an FeAs layer form a quadratic lattice containing two Fe ions and two As ions in an elementary cell. As ions are placed above (solid dots) or under (dashed circles) centers of the squares formed by Fe. (b) Transfer integrals taken into account in the two-orbital (d_{xz}, d_{yz}) model on the square lattice of Fe. Here, t_1 is the transfer integral between nearest σ-orbitals, and t_2 is the transfer integral between nearest π-orbitals. Also taken into account are transfer integrals t_4 between different orbitals, and t_3 between identical orbitals on the second nearest neighbors. Also shown are projections of d_{xz}, d_{yz} orbitals onto the xy plane [127].

For an analytical description of this model it is convenient to introduce a two-component spinor

$$\psi_{\mathbf{k}s} = \begin{pmatrix} d_{xs}(\mathbf{k}) \\ d_{ys}(\mathbf{k}) \end{pmatrix}, \tag{2}$$

where $d_{xs}(\mathbf{k})$ ($d_{ys}(\mathbf{k})$) annihilates the d_{xz} (d_{yz}) electron with spin s and wave vector $\mathbf{k}$. A tight-binding Hamiltonian can be written out as

$$H_0 = \sum_{\mathbf{k}s} \psi^+_{\mathbf{k}s}\big[\big(\varepsilon_+(\mathbf{k}) - \mu\big)\hat{1} + \varepsilon_-(\mathbf{k})\hat{\tau}_3 + \varepsilon_{xy}(\mathbf{k})\hat{\tau}_1\big]\psi_{\mathbf{k}s}\,, \tag{3}$$

where $\hat{\tau}_i$ are the Pauli matrices, and

$$\varepsilon_\pm(\mathbf{k}) = \frac{\varepsilon_x(\mathbf{k}) \pm \varepsilon_y(\mathbf{k})}{2}\,,$$
$$\varepsilon_x(\mathbf{k}) = -2t_1\cos k_x a - 2t_2\cos k_y a - 4t_3\cos k_x a\cos k_y a\,,$$
$$\varepsilon_y(\mathbf{k}) = -2t_2\cos k_x a - 2t_1\cos k_y a - 4t_3\cos k_x a\cos k_y a\,,$$
$$\varepsilon_{xy}(\mathbf{k}) = -4t_4\sin k_x a\sin k_y a\,.$$

Finally, the single-particle Green's function in the Matsubara representation takes the following form

$$\hat{G}_s(\mathbf{k}, \mathrm{i}\omega_n) = \frac{\big(\mathrm{i}\omega_n - \varepsilon_+(\mathbf{k})\big)\hat{1} - \varepsilon_-(\mathbf{k})\hat{\tau}_3 - \varepsilon_{xy}(\mathbf{k})\hat{\tau}_1}{\big(\mathrm{i}\omega_n - E_+(\mathbf{k})\big)\big(\mathrm{i}\omega_n - E_-(\mathbf{k})\big)}\,, \tag{4}$$

where

$$E_\pm(\mathbf{k}) = \varepsilon_+(\mathbf{k}) \pm \sqrt{\varepsilon_-^2(\mathbf{k}) + \varepsilon_{xy}^2(\mathbf{k})} - \mu\,. \tag{5}$$

In Fig. 23a we displayed the appropriate electronic spectrum for the following values of transfer integrals: $t_1 = -1$, $t_2 = 1.3$, and $t_3 = t_4 = -0.85$ (in units of $|t_1|$).

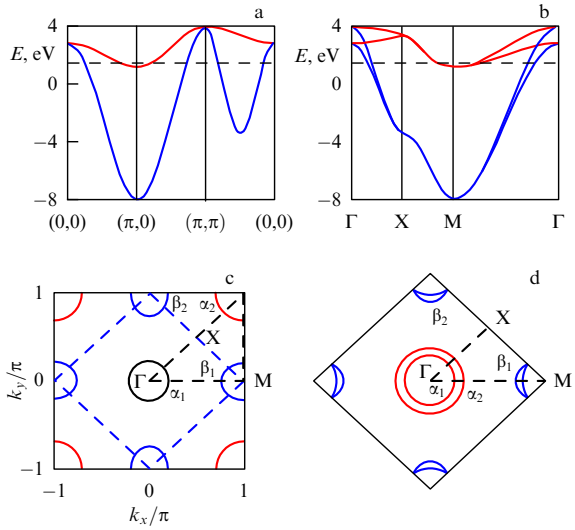

Figure 23. (a) Electronic spectrum in the two-orbital model with transfer integrals $t_1 = -1$, $t_2 = 1.3$, $t_3 = t_4 = -0.85$ (in units of $|t_1|$) and chemical potential $\mu = 1.45$, taken along directions $(0,0) \to (\pi/a, 0) \to (\pi/a, \pi/a) \to (0,0)$. (b) The same spectrum in a twice downfolded Brillouin zone, with an appropriate redefinition of the Γ, X, M points. (c) The Fermi surface in the two-orbital model in the Brillouin zone corresponding to one Fe ion per elementary cell; $\alpha_{1,2}$ — hole-like Fermi surfaces defined by $E_-(k_F) = 0$, and $\beta_{1,2}$ — electron-like Fermi surfaces defined by $E_+(k_F) = 0$. Dashed lines show the Brillouin zone for two Fe ions in an elementary cell. (d) Fermi surfaces in the downfolded Brillouin zone corresponding to two Fe ions in an elementary cell [127].

Let us now take into account the fact, mentioned above, that in a real FeAs layer there are two Fe ions per elementary cell. Accordingly, the Brillouin zone is twice as small and the spectrum must be folded down into this new zone, as shown in Fig. 23b. In Fig. 23c, d we depicted Fermi surfaces which are obtained in this simplified model of the electronic spectrum. In the large Brillouin zone corresponding to the lattice with one Fe ion per elementary cell there are two hole-like pockets, denoted as α_1 and α_2, which are defined by the equation $E_-(k_F) = 0$, and two electron-like pockets β_1 and β_2, defined by $E_+(k_F) = 0$. To compare them with the results of band structure calculations (LDA), these Fermi surfaces should be folded down into a Brillouin zone that is half as big, corresponding to two Fe ions in an elementary cell of the crystal and being shown by dashed lines in Fig. 23c. The result of such downfolding is given in Fig. 23d. It is evident that the Fermi surfaces obtained in this way are in qualitative agreement with the results of LDA calculations (only the third, less relevant, small hole-like pocket at the zone center is absent). Despite its crudeness, this model of the spectrum, proposed in Ref. [127], is quite appropriate for qualitative analysis of the electronic properties of FeAs-based superconductors.

3.3 Angle-resolved photoemission spectroscopy (ARPES)

At the moment there are already a number of papers where the electronic spectrum and Fermi surfaces in new superconductors were studied using angle-resolved photoemission spectroscopy [131 – 141], a reliable method which proved its effectiveness in HTSC cuprates [13, 142] due, by the way, to the quasi-two-dimensional nature of the electronic spectrum in these systems. In fact, ARPES studies for FeAs-based superconductors immediately provided valuable information clarifying the general form of their spectrum, Fermi surfaces, and widths and peculiarities of superconducting gaps. It should be noted that for 1111-systems there has so far been only one ARPES work [131], which is due to the absence of good single crystals, so that all the remaining studies were performed on single crystals of 122-systems. Below we shall discuss the results of some of these papers in more details.

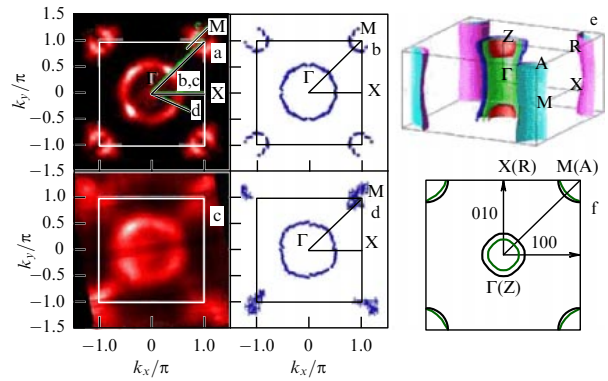

Figure 24. (a) ARPES intensity map, and (b) Fermi surfaces determined for $NdO_{0.9}F_{0.1}FeAs$ at a photon energy of 22 eV and $T = 70$ K. (c, d) The same as in figures a, b, but for a photon energy of 77 eV [131]. (e, f) Three-dimensional and two-dimensional pictures of Fermi surfaces in NdOFeAs, obtained from LDA calculations [131].

ARPES measurements in Ref. [131] were performed on micron-sized single crystals (on the order of $200 \times 200 \times 30$ μm, with $T_c \sim 53$ K). In Fig. 24 we exhibited ARPES intensity maps (which are proportional to spectral density) in the $NdO_{0.9}F_{0.1}FeAs$ system, allowing us to determine the form of Fermi surfaces in the two-dimensional Brillouin zone corresponding to FeAs planes. It can be seen that the general qualitative picture is in reasonable agreement with the results of LDA calculations of the band structure, though only one hole-like cylinder is resolved around the Γ point, and electron-like cylinders at the corners (point M) are resolved rather poorly. The width of the superconducting gap on the hole-like cylinder, estimated from ARPES spectra, was determined to be on the order of 20 meV [132], corresponding to $2\Delta/T_c \sim 8$.

In Ref. [134], ARPES measurements were carried out for a single crystal of superconducting $(Sr, K)Fe_2As_2$ with $T_c = 21$ K. The ARPES map of the Fermi surfaces obtained is displayed in Fig. 25. In contrast to other works, here the authors succeeded in resolving all three hole-like cylinders around the point Γ, in complete agreement with the majority of LDA calculations of the spectrum. Resolution at the corners of the Brillouin zone (point M) turned out to be much poorer, so that the topology of the electronic sheets of the Fermi surface remained unclear.

Shown in Fig. 26 are the energy bands in high-symmetry directions of the Brillouin zone, obtained from ARPES measurements [134]. On the one hand, these data correlate well with the results of the band structure calculations in work [118], taking into account the Fermi level shift in energy downwards by ~ 0.2 eV (in complete accordance with the hole doping of the superconducting sample). On the other hand, rather significant band narrowing in comparison with LDA results is also observed, which can be attributed to strong electronic correlations (cf. below).

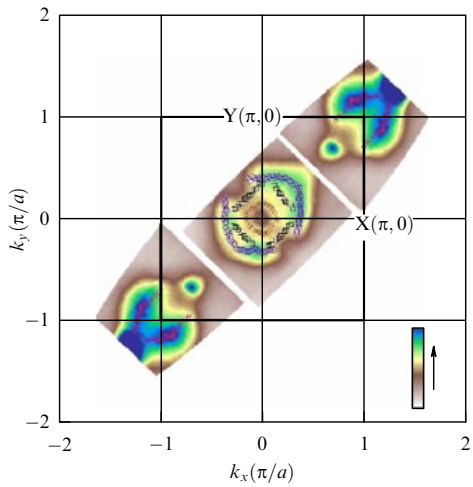

Figure 25. ARPES map of the Fermi surfaces in $(Sr, K)Fe_2As_2$ [134].

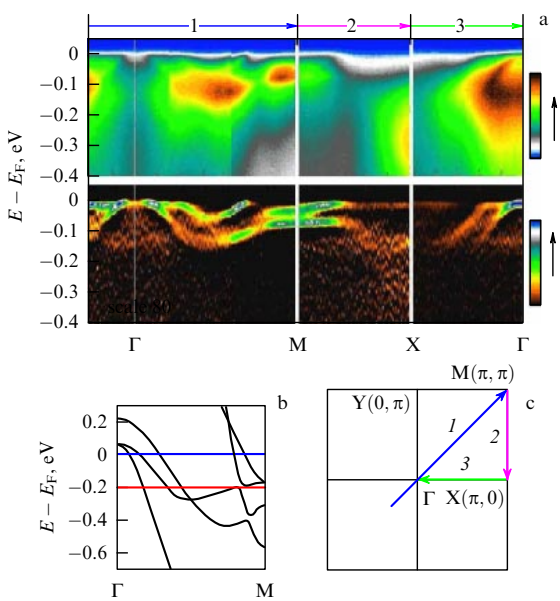

Figure 26. (a) Energy bands determined from ARPES data on $(Sr, K)Fe_2As_2$ [134]; in the upper part of the figure — initial ARPES intensity data, below — their second derivative, allowing following dispersion curves. (b) Band spectrum obtained in Ref. [118]. (c) Directions in the Brillouin zone, along which measurements have been made.

In Ref. [136] for the first time Fermi surfaces of $Ba_{0.6}K_{0.4}Fe_2As_2$ ($T_c = 37$ K) were studied in detail,[4] while ARPES measurements of superconducting gaps (and their temperature dependence) on different sheets of the Fermi surface were made. Schematically, the results of these measurements are given in Fig. 27. Two superconducting gaps were discovered — a large one ($\Delta \sim 12$ meV) on a small hole-like cylinder around point Γ and on the electron-like cylinders around point M, and a small one ($\Delta \sim 6$ meV) on a big hole-like cylinder around point Γ. Both gaps close at the same temperature coinciding with T_c, have no zeroes, and are

[4] A small third hole-like cylinder around point Γ was not observed, probably due to insufficient resolution of ARPES spectra.

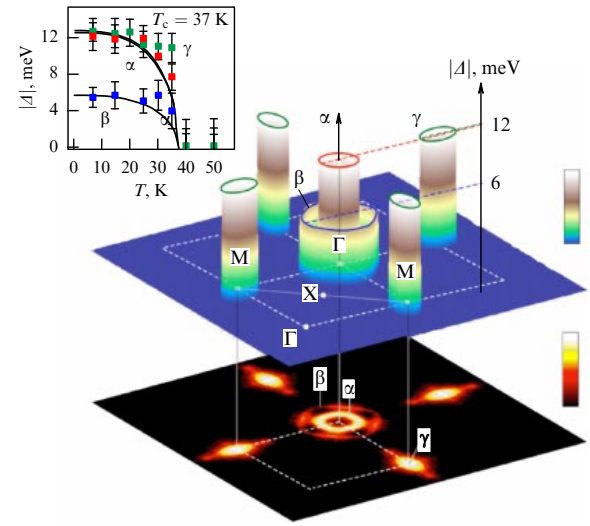

Figure 27. Schematic three-dimensional picture of the superconducting gap in $Ba_{0.6}K_{0.4}Fe_2As_2$ according to ARPES measurements [136]. Shown below are Fermi surfaces (ARPES intensity); temperature dependences of gaps on different sheets of the Fermi surface are plotted in the inset above.

practically isotropic on appropriate sheets of the Fermi surface. Accordingly, the $2\Delta/T_c$ ratio is different on different sheets (cylinders) and formally is consistent with both strong (large gap, the ratio is 7.5) and weak (small gap, the ratio is 3.7) coupling. These results correspond to the picture of generalized s-wave pairing, which will be discussed below.

Quite similar results for gap widths on different sheets of the Fermi surface were also obtained in Ref. [137] through ARPES measurements on single crystals of $(Sr/Ba)_{1-x}K_xFe_2As_2$. Also in this work, the electron dispersion was measured by ARPES in a rather wide energy interval, which demonstrated the presence of characteristic 'kinks' attributed to conduction electron interaction with collective oscillations (phonons or spin excitations), allowing determination of electron velocity in the neighborhood of the Fermi level: $v_F \sim 0.7 \pm 0.1$ eV Å, so that using the width of the 'large' gap, $\Delta \sim 12 \pm 2$ meV, gives an estimate of coherence length (the size of the Cooper pairs) $\xi_0 = \hbar v_F/\Delta < 20$ Å, i.e., a relatively small value (compact pairs).

Rather unexpected results for the topology of Fermi surfaces were obtained in Refs [139, 140] for $Ba_{1-x}K_xFe_2As_2$, where Fermi surface sheets close to the M point were discovered to have a characteristic 'propeller'-like form which does not agree with any LDA band calculations. Measurements of the superconducting gap width in Ref. [140] for the 'large' gap on an 'internal' hole-like cylinder around point Γ have given the value of $\Delta \sim 9$ meV, and the same value on propeller blades close to the M points, which corresponds to the ratio $2\Delta/T_c = 6.8$. On an 'external' hole-like cylinder around point Γ, the value of $\Delta < 4$ meV was obtained, corresponding to $2\Delta/T_c < 3$.

Notice also Ref. [142] where ARPES measurements were performed on the 'maximally doped' variant of the $Ba_{1-x}K_xFe_2As_2$ system with $x = 1$, i.e., on superconducting KFe_2As_2 compound ($T_c = 3$ K). It was revealed that the form of hole-like Fermi surfaces (sheets) surrounding the Γ point is qualitatively the same as in $Ba_{1-x}K_xFe_2As_2$ with $x = 0.4$

($T_c = 37$ K), while electron-like cylinders surrounding the M points are simply absent. This is a natural consequence of the downward shift of the Fermi level due to hole doping (cf. Fig. 21, where it is clearly seen that electronic branches of the spectrum are above the Fermi level, where it has a big enough downward energy shift). Furthermore, similarly to Ref. [134], the observed bands turned out to be significantly (2 – 4 times) narrower than those obtained in all LDA type calculations. This fact, as already noted above, most probably points to sufficiently strong electronic correlations (see Section 3.4). The absence of electronic pockets on the Fermi surface leads to the disappearance of interband mechanisms of pairing (see below) and a corresponding significant lowering of T_c.

Summing up, it should be emphasized that the results of ARPES studies of Fermi surfaces and the electronic spectrum of FeAs-based superconductors are in quite satisfactory agreement with LDA calculations of band structure. Remaining inconsistencies are most probably due to the unaccounted role of electronic correlations and, sometimes, due to insufficient resolution in the ARPES experiments.

Unfortunately, thus far there have been almost no experiments on determining the Fermi surfaces from low-temperature quantum oscillations (like de Haas – van Alphen effect). We can only mark Ref. [143] where the nonsuperconducting phase of $SrFe_2As_2$ was studied and the oscillation periods discovered corresponded to small Fermi surface pockets, which apparently can be attributed to hole-like cylinders close to the Γ point, almost completely 'closed' by the antiferromagnetic gap. In Ref. [144], quantum oscillations were studied in the LaOFeP compound and found to be in agreement with the Fermi surface predicted by LDA calculations, with due regard for an effective mass enhancement by approximately two times.

3.4 Correlations (LDA + DMFT)

LDA calculations of electronic spectrum neglect the potentially strong effects of local electron correlations (Hubbard – like repulsion of electrons), which can be naturally expected in bands formed mainly from d-states of Fe in FeAs layers. At present, the most consistent approach to the analysis of such correlations is considered to be the dynamical mean field theory (DMFT) [145 – 149], including its variant (LDA + DMFT) taking into account the LDA band structure of real systems [150 – 152].

The LDA + DMFT approach was employed in calculating the electronic structure of FeAs-based compounds in Refs [153 – 157]. In all of these, except for Ref. [156], only the LaOFeAs system was studied, while in Ref. [156] the authors analyzed the *RE*OFeAs (*RE* = La, Ce, Pr, Nd) series.

In Ref. [153], LDA + DMFT was utilized to calculate the spectral density and optical conductivity of $LaO_{1-x}F_xFeAs$. The magnitude of Hubbard repulsion was taken to be $U = 4$ eV, while the Hund (exchange) coupling was assumed to be equal to $J = 0.7$ eV [5]. In Fig. 28 we gave the results for the momentum dependence of the spectral density in high-symmetry directions in the Brillouin zone. The positions of the maxima of spectral density describe the effective dispersion of (damped) quasiparticles, which may be compared with the results of LDA calculations (infinite lifetime quasiparticles), which are also presented. Doping was described in the virtual crystal approximation. It can be ascertained that

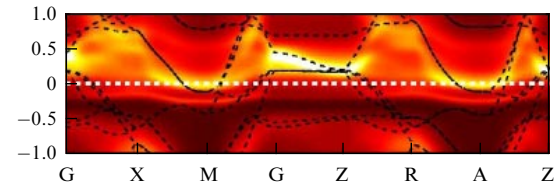

Figure 28. Momentum dependence of spectral density (with positions of the maxima defining the effective dispersion of quasiparticles) in the LDA + DMFT approximation for LaOFeAs with 10% doping. Dashed lines fit the results of the LDA approach [154].

electron correlations lead to a significant (3 – 5 times) enhancement of effective masses and strong damping of quasiparticles. The system remains metallic, though a kind of 'bad' metal with a strongly renormalized quasiparticle amplitude (residue at the Green's function pole) $Z \sim 0.2 - 0.3$.

The general picture of the spectrum displayed in Fig. 28 can be qualitatively compared with ARPES data given in the lower part of Fig. 26b. Though the experiment was carried out on another system, a certain similarity is obvious — conduction bands are significantly narrowed (in comparison with LDA results), while in the energy region around −0.5 eV the bands are simply 'destroyed' and a kind of energy gap reveals itself there.

According to Ref. [153], even a rather small enhancement of the Hubbard repulsion up to $U = 4.5$ eV transforms this system into a kind of Mott insulator with an energy gap at the Fermi level. Thus, it was concluded that the systems under consideration are characterized by intermediate correlations and are close to the Mott insulator, making them partly similar to HTSC cuprates. At the same time, contrary to cuprates, prototype (undoped) compounds constitute metals, not Mott insulators.

A quite different conclusion was reached by the authors of Ref. [154], who performed formally the same type of calculations (by the same methods and with the same choice of parameters). It was claimed in this work that even the use of U values up to 5 eV does not transform a system into a Mott insulator, and changes in spectral density (electron dispersion) and the density of states due to electron correlations are rather insignificant.

At present, the reasons for such drastic differences in the results obtained by two leading groups making LDA + DMFT calculations are unclear.

In general, it should be noted that the *ab initio* nature of LDA + DMFT approach is rather conditional, as, for example, the magnitude of Hubbard interaction U is, in fact, a kind of (semi)phenomenological parameter. There exist a number of *ab initio* approaches to calculating its magnitude, of which the most consistent is assumed to be the so-called method of constrained random phase approximation (constrained RPA) [158, 159]. Within this approach the magnitude of local Hubbard repulsion is calculated from the 'bare' Coulomb repulsion V using the RPA expression

$$U = \frac{V}{1 - V\Pi_r}\,, \tag{6}$$

where Π_r is the polarization operator taking into account screening by electrons from the outside of the (correlated)

[5] The DMFT impurity problem was solved by the quantum Monte Carlo (QMC) method with the temperature taken to be 116 K.

Table 4. 'Bare' and partly screened Coulomb interactions V and U, and Hund coupling J for LaOFeAs, obtained in Ref. [156] by excluding different groups of states (listed in the first column) from screening.

	V, eV	U, eV	J, eV
d	15.99	2.92	0.43
dpp	20.31	4.83	0.61
d-dpp	20.31	3.69	0.58

bands of interest. For example, if we limit ourselves only to the analysis of bands formed by d-states of Fe, we have to use the relation $\Pi_{\rm r} = \Pi - \Pi_{\rm d}$, where $\Pi_{\rm d}$ is the polarization operator calculated only on d-states. It is clear that the magnitude of U defined in this way depends essentially on the adopted scheme of calculations (accounting for the contribution from different groups of electrons to screening).

For FeAs-based compounds, this problem was studied in Ref. [156]. The values of different interaction parameters entering the LDA + DMFT calculation scheme, obtained by the exclusion of different groups of states from the screening of the bare Coulomb interaction, are given in Table 4.

It is readily seen that the magnitudes of interaction parameters entering LDA + DMFT calculation scheme can change within rather wide ranges.

The same questions were discussed in Refs [155, 157] (within the constrained DFT approach [160]), with the authors coming to the conclusion that the effective parameters of Coulomb (Hubbard) repulsion are relatively small if we limit ourselves to the framework of d-states of Fe. Accordingly, the LDA + DMFT calculations performed in these works produced an electronic structure which is only slightly different from LDA results.

In the opinion of the authors of Refs [154, 155, 157], their conclusion about the smallness of electron correlations in FeAs-based systems is confirmed by experiments on X-ray absorption and emission spectroscopy in Ref. [161]; however, this is in sharp contrast to available ARPES data [134, 141] which definitely indicate rather strong renormalization of the electronic spectrum due to correlations. It should be stressed that data on the topology of Fermi surfaces are, in fact, insufficient for making any judgments on the role of correlations: Fermi surfaces in the LDA + DMFT approach are just the same as in the LDA approximation. It is important to study in detail electronic dispersion, bandwidths, and quasiparticle damping far enough from the Fermi level, as well as quasiparticle residue Z. In our opinion, ARPES measurements have many advantages here and can help in solving this important problem.

Summarizing, the question of the role of electron correlations in new superconductors is still under discussion. It is most probable that correlations in these systems are of intermediate strength between typical metals and systems like Mott insulators, so that we are dealing here with the state of a *correlated* metal [147, 149].

3.5 Spin ordering: localized or itinerant spins?

In this section we shall briefly consider theoretical ideas on the nature of antiferromagnetic ordering in undoped FeAs-based compounds and the closely related problem of the structural transition from the tetragonal to orthorhombic phase. Broadly speaking, these questions are slightly outside the scope of our review (superconductivity in FeAs-based compounds), so our presentation will be very short.

The possibility of antiferromagnetic ordering in the systems under consideration had been noted even before the direct neutronographic observations discussed in Section 2.3 were made. Already in one of the earliest papers on the electronic structure of iron oxypnictides [110], as well as during the analysis of the 'minimal' two-band model [127], it was stressed that there is an approximate 'nesting' of hole-like Fermi surfaces around point Γ and electron-like Fermi surfaces around M points. It is most easily seen, for instance, in Fig. 23c — the shift of the hole-like cylinder by vector $(\pi, 0)$ or $(0, \pi)$ leads to its approximate coincidence with the electron-like cylinder. Direct calculations [110, 127] revealed that this fact leads to the formation of a rather wide, but still quite noticeable, peak in static magnetic susceptibility $\chi_0(\mathbf{q})$ (determined by the appropriate loop diagram) at $\mathbf{q} = (\pi, 0)$ and $\mathbf{q} = (0, \pi)$. In turn, this may lead to antiferromagnetic instability accompanied by the formation of a spin density wave (SDW) with the appropriate wave vector, at least in the case of a sufficiently strong exchange interaction. We have seen above that precisely this type of spin ordering was established experimentally in FeAs layers [69, 71, 74, 76–78]. Also, the observed, rather small values of magnetic moments on Fe provide evidence of the itinerant nature of magnetism (SDW). It is also natural to assume that well-developed spin fluctuations of the SDW type persist in doped (superconducting) compounds, which can provide the pairing interaction of electrons.

At the same time, magnetic ordering in FeAs layers can also be analyzed within a more traditional approach based on the qualitative picture of localized spins on Fe ions, interacting via the usual Heisenberg exchange between nearest and second nearest neighbors. Such an analysis was performed, for instance, in Ref. [162] for LaOFeAs, as well as *ab initio* calculations of appropriate exchange integrals and values of magnetic moments. For us here, the qualitative aspects of this analysis, which are illustrated in Fig. 29, are more important [162].

In this figure we displayed two possible antiferromagnetic configurations of spins in the FeAs layer. In the experiments [69], the AF2 (see Fig. 29) type spin structure is observed, which is realized when inequality $J_1 < 2J_2$ holds, where J_1 is an exchange integral between nearest neighbors, and J_2 between second nearest neighbors, with both integrals assumed positive (antiferromagnetism). Direct (FP-LAPW) calculations of the total ground state energy of LaOFeAs, performed in Ref. [162], confirmed the greater stability of precisely this state. AF2 configuration can be considered as two interpenetrating antiferromagnetic square sublattices shown by different colors in Fig. 29. In this case, each Fe ion

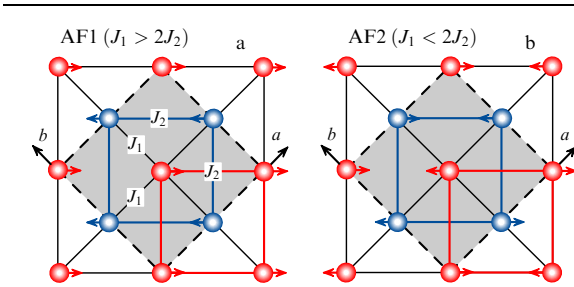

Figure 29. Two alternative spin configurations in the antiferromagnetic FeAs layer: (a) antiparallel spins on nearest neighbors, and (b) antiparallel spins on second nearest neighbors [162].

is placed at the center of an antiferromagnetically ordered cell, so that the mean molecular field acting on its spin is just zero. Therefore, each sublattice may freely (with no expenditure of energy) rotate with respect to the other. This is a situation of complete frustration. It is well known that such a state is usually unstable with respect to structural distortions. Thus, it can be expected that a structural distortion will appear in our system, making the spins of a pair of Fe ions closer to each other, while the pair on the other side of the square slightly farther apart. This is just the type of distortion (tetra – ortho transition) observed in the experiment [69]. Direct calculations of total energy confirm this assumption [162].

However, the general situation with the nature of magnetic ordering and structural transition in FeAs layers is rather far from being completely clear. *Ab initio* calculations as a rule produce highly overestimated values of magnetic moments on Fe, while the relative stability of magnetic structures strongly depends on the details of the methods used. Apparently, this is due to the itinerant nature of magnetism in these systems. Detailed discussions of these problems can be found in interesting papers [163, 164] where an original qualitative picture of strong magnetic fluctuations was proposed, allowing, in the authors' opinion, the explanation of all the anomalies of magnetic properties.

4. Mechanisms and types of pairing

After the discovery of high-temperature superconductivity in iron-based layered compounds, dozens of theoretical papers appeared with different proposals for the possible microscopic mechanisms and types of Cooper pairing in these systems. A review of all these papers here is impossible and below we shall deal only with a very few of, in our opinion, the most important works.

4.1 Multiband superconductivity

The main distinction of new superconductors is their multiple band nature. An electronic structure in a narrow enough energy interval around the Fermi level is formed practically only from the d-states of Fe. The Fermi surface consists of several hole-like and electron-like cylinders and on each its 'own' energy gap can be formed. Broadly speaking, this situation is not new and has already been analyzed in the scientific literature [165]. For the specific band structure typical of FeAs layers, however, we need an additional analysis.

In general, a sufficient formulation of this problem was considered in a paper by Barzykin and Gor'kov [166], and some of their results will be presented below. A typical electronic spectrum of FeAs-layered systems in the relevant (for superconductivity) energy interval was displayed in Fig. 21. A similar, in principle, spectrum was also obtained in the minimal model of Ref. [127]. An oversimplified view of this spectrum is represented in Fig. 30 [166].

This form of Fermi surfaces corresponds to the stoichiometric (undoped) composition of these compounds, with electrons and holes occupying the same volumes (compensated semimetal). [6] Electronic doping shrinks hole-like pockets, while hole doping shrinks electron-like pockets.

[6] In fact, this very form of the spectrum was assumed in numerous papers on excitonic instability and the excitonic insulator [167 – 171]. This instability may be considered as an alternative explanation of antiferromagnetic ordering and structural transition in these systems [166].

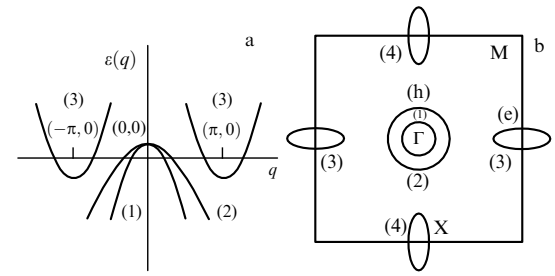

Figure 30. Schematic views of electronic spectrum (a) and Fermi surfaces (b) for LaOFeAs in the extended band picture. Around point Γ there are two hole-like sheets, while electron-like sheets are around X points [166].

In Ref. [166], a symmetry analysis of possible types of superconducting order parameter was performed along the lines of Refs [172, 173], and also the explicit solutions of BCS equations were found for a system with the electronic spectrum shown in Fig. 30.

Let $\Delta_i(\mathbf{p})$ be a superconducting order parameter (gap) on the ith sheet of the Fermi surface. The value of $\Delta_i(\mathbf{p})$ is determined by the self-consistency equation for the anomalous Gor'kov's function $F_i(\omega_n, \mathbf{p})$:

$$\Delta_i(\mathbf{p}) = T \sum_{j;\,\omega_n} \int \mathrm{d}\mathbf{p}' V^{i,j}(\mathbf{p} - \mathbf{p}')\, F_j(\omega_n, \mathbf{p}')\,, \tag{7}$$

where $V^{i,j}(\mathbf{p} - \mathbf{p}')$ is the pairing interaction. If Fermi surface pockets are sufficiently small (as they seem to be in FeAs-based systems), transferred momentum $\mathbf{p} - \mathbf{p}'$ is also small within each pocket and we can replace $V^{i,j}(\mathbf{p} - \mathbf{p}')$ by $V^{i,j}(0)$, which is favorable for the formation of momentum-independent gaps.

Pairing BCS interaction in this model can be represented by the following matrix

$$V = \begin{pmatrix} u & u & t & t \\ u & u & t & t \\ t & t & \lambda & \mu \\ t & t & \mu & \lambda \end{pmatrix}, \tag{8}$$

where $\lambda = V^{\mathrm{eX,eX}} = V^{\mathrm{eY,eY}}$ defines interaction in an electron-like pocket at point X, $\mu = V^{\mathrm{eX,eY}}$ connects electrons from different pockets at points $(\pi, 0)$ and $(0, \pi)$, $u = V^{\mathrm{h1,h1}} = V^{\mathrm{h2,h2}} = V^{\mathrm{h1,h2}}$ characterizes BCS interaction in two hole-like pockets [7] surrounding the point Γ, and $t = V^{\mathrm{h,eX}} = V^{\mathrm{h,eY}}$ connects electrons from points X and Γ.

The critical temperature T_{c} of superconducting transition is determined by the solution of the system of linearized gap equations:

$$\Delta_i = \sum_j \bar{V}^{i,j} \Delta_j \ln \frac{2\gamma\bar{\omega}}{\pi T_{\mathrm{c}}}\,, \tag{9}$$

where $\bar{\omega}$ is the usual cut-off frequency of logarithmic divergence in the Cooper channel, and

$$\bar{V}^{i,j} \equiv -\frac{1}{2} V^{i,j} \nu_j\,, \tag{10}$$

where ν_j is the density of states on the jth sheet (pocket) of the Fermi surface.

[7] An assumption that these couplings are the same seems to us to be too rigid.

Introducing an effective coupling constant g and writing down T_c as

$$T_c = \frac{2\gamma\bar{\omega}}{\pi}\exp\left(-\frac{2}{g}\right), \tag{11}$$

we arrive at the solutions of three types:

(1) solution corresponding to $d_{x^2-y^2}$ symmetry, when gaps on different pockets at points X differ in signs, while gaps on hole-like pockets are zero:

$$\Delta_1 = \Delta_2 = 0, \quad \Delta_3 = -\Delta_4 = \Delta, \tag{12}$$

$$g = (\mu - \lambda)\, v_3 . \tag{13}$$

The possibility of such a solution follows also from the general symmetry analysis [166];

(2) two solutions corresponding to the so-called $s^{\pm}$-pairing, when gaps at points X have the same sign, while gaps on the Fermi surfaces surrounding point Γ may have opposite signs, namely [8]

$$\begin{aligned} 2g_{+,-} &= -u(v_1+v_2) - (\lambda+\mu)\, v_3 \\ &\pm \sqrt{\left(u(v_1+v_2) - (\lambda+\mu)\, v_3\right)^2 + 8t^2 v_3 (v_1+v_2)} \end{aligned} \tag{14}$$

and

$$\Delta_1 = \Delta_2 = \kappa\Delta, \quad \Delta_3 = \Delta_4 = \Delta, \tag{15}$$

where $\kappa^{-1} = -\left(g_{+,-} + u(v_1+v_2)\right)/(tv_3)$.

The possibility of $s^{\pm}$-pairing in FeAs-based compounds was first noted in Ref. [110]. This solution is in qualitative agreement with available ARPES data [136, 137, 140], except for the results $\Delta_1 = \Delta_2$ from Eqn (15), which contradict the established fact that the gap on a small hole-like cylinder is approximately twice as large as on a big cylinder. In our opinion, this drawback is due to the unnecessary limitation of $u = V^{\mathrm{h1,h1}} = V^{\mathrm{h2,h2}} = V^{\mathrm{h1,h2}}$, used in Ref. [166]. For different BCS constants on hole-like cylinders we can easily obtain different values of the gap width, in agreement with experiments.

The presence of practically isotropic gaps (possibly of different signs) on hole-like and electron-like pockets of the Fermi surface, corresponding to $s^{\pm}$-pairing, seems at first to contradict the numerous NMR (NQR) data discussed in Section 2.5, which indicate possible d-wave gap symmetry. This contradiction was studied in Ref. [174], where it was shown rather convincingly that the absence of a Gebel–Slichter peak and power-like temperature dependence of NMR relaxation may also be easily explained in the case of $s^{\pm}$-pairing, taking into account impurity scattering.

4.2 Electron–phonon mechanism

The general discussion in the previous section tells us nothing about the origin of pairing coupling constants entering into the matrix (8), i.e., about the microscopic mechanism of Cooper pairing in new superconductors.

As a first candidate for such a mechanism we have to consider the conventional electron–phonon interaction. Such an analysis for LaOFeAs was performed in Ref. [109] using *ab initio* calculations of electron and phonon spectra and the Eliashberg function $\alpha^2 F(\omega)$ determining the electron–phonon pairing constant as

$$\lambda(\omega) = 2\int_0^{\omega} \mathrm{d}\,\Omega\, \frac{\alpha^2 F(\Omega)}{\Omega} . \tag{16}$$

The total electron–phonon pairing constant λ was obtained by numerical integration in formula (16) up to $\omega = \infty$ and was found to be 0.21. To estimate superconducting critical temperature T_c we can use a popular Allen–Dynes interpolation formula [175]:

$$T_c = \frac{f_1 f_2 \omega_{\ln}}{1.20}\exp\left(-\frac{1.04(1+\lambda)}{\lambda - \mu^* - 0.62\lambda\mu^*}\right), \tag{17}$$

where

$$f_1 = \left[1 + \left(\frac{\lambda}{\Lambda_1}\right)^{3/2}\right]^{1/3}, \quad \Lambda_1 = 2.46(1+3.8\mu^*),$$

$$f_2 = 1 + \frac{(\bar{\omega}_2/\omega_{\ln} - 1)\,\lambda^2}{\lambda^2 + \Lambda_2^2}, \quad \Lambda_2 = 1.82(1+6.3\mu^*)\,\frac{\bar{\omega}_2}{\omega_{\ln}},$$

$$\bar{\omega}_2 = \langle\omega^2\rangle^{1/2},$$

and $\langle\omega^2\rangle$ is the average square of the phonon frequency. Taking into account the value of the average logarithmic frequency of phonons, $\omega_{\ln} = 205$ K (and assuming $\omega_{\ln} \approx \bar{\omega}_2$), found in Ref. [109], and with the optimistic choice of Coulomb pseudopotential $\mu^* = 0$, formula (17) gives the value of $T_c = 0.5$ K. Numerical solution of Eliashberg equations with the calculated function $\alpha^2 F(\omega)$ gave the value of $T_c = 0.8$ K [109]. Actually, to reproduce the experimental value of $T_c = 26$ K, coupling constant λ should be approximately five times larger, even if we set $\mu^* = 0$. In the opinion of the authors of Ref. [109], such a strong discrepancy clearly indicates that the usual picture of Cooper pairing, based on electron–phonon coupling, is invalid.

Despite the quite convincing estimates of Ref. [109], it should be noted that these are based on the standard approach of the Eliashberg theory, which does not take into account, in particular, the important role of the multiband nature of superconductivity in these compounds, and possibly the importance of interband pairing interactions. Moreover, the estimates of the value of the electron–phonon coupling constant has also met with objections. Thus, it was argued in Ref. [176] that sufficiently strong coupling exists between electrons and a certain mode of Fe oscillations in the FeAs plane.

However, probably the most convincing objections to the claims of irrelevance of electron–phonon coupling can be based on experiments. In particular, we can estimate the electron–phonon coupling constant from the temperature dependence of resistivity. The measurements of resistivity of $PrFeAsO_{1-x}F_x$ were done in Ref. [177] in a satisfactorily wide temperature interval. Linear growth in resistivity with temperature for $T > 170$ K was saturated, which by itself suggests strong enough electron–phonon coupling. As a simple estimate, we can write down resistivity as

$$\rho(T) = \frac{4\pi}{\omega_p^2 \tau}, \tag{18}$$

where ω_p is the plasma frequency, and τ is the carrier relaxation time. In the region of sufficiently high tempera-

[8] Here, we have corrected small misprints in Ref. [166].

tures, where resistivity grows linearly with temperature, the relaxation frequency of carriers on phonons is given by [178]

$$\frac{\hbar}{\tau_{\rm ep}} = 2\pi\lambda_{\rm tr} k_{\rm B} T\,, \tag{19}$$

where 'transport' constant $\lambda_{\rm tr}$ of electron – phonon coupling is naturally on the order of λ of interest to us, usually differing from it by no more than 10%. From formulas (18) and (19) we have

$$\lambda_{\rm tr} = \frac{\hbar\omega_{\rm p}^2}{8\pi^2 k_{\rm B}}\,\frac{{\rm d}\rho}{{\rm d}T}\,. \tag{20}$$

Using the slope of the temperature dependence of resistivity determined in Ref. [177], ${\rm d}\rho/{\rm d}T \sim 8.6\ \mu\Omega\ {\rm K}^{-1}$, and the estimate of plasma frequency $\omega_{\rm p} \sim 0.8$ eV (which follows from measurements of penetration depth), we get $\lambda \sim 1.3$, which, according to formula (17), is quite sufficient for getting the observable values of transition temperatures in new superconductors.

Decisive evidence for the electron – phonon mechanism of Cooper pairing was always considered to be the observation of the isotope effect. Appropriate measurements were performed recently in Ref. [179] on $SmFeAsO_{1-x}F_x$, where ^{16}O was replaced by ^{18}O, and on $Ba_{1-x}K_xFe_2As_2$, where ^{54}Fe was substituted for ^{56}Fe. A finite shift in superconducting transition temperature was observed, which can be characterized in a standard way by the isotope effect exponent $\alpha = -{\rm d}\ln T_{\rm c}/{\rm d}\ln M$. For $SmFeAsO_{1-x}F_x$, the isotope effect turned out to be small enough, with $\alpha \sim 0.08$, which is quite natural as O ions reside exterior to the conducting FeAs layer. At the same time, the replacement of Fe ions in FeAs layers in $Ba_{1-x}K_xFe_2As_2$ has led to a large isotope effect with $\alpha \approx 0.4$, which is close to the 'ideal' value of $\alpha = 0.5$.

Thus, the rather wide pessimism in the literature on the role of electron – phonon interactions in new superconductors seems to be rather premature.

4.3 Magnetic fluctuations

The above-mentioned pessimism with respect to the role of electron – phonon interactions, as well as the closeness of the superconducting phase to the antiferromagnetic phase in the phase diagram of new superconductors, has led to the growth of popularity of pairing models based on the decisive role of magnetic (spin) fluctuations, being in many respects similar to those already considered for HTSC cuprates [4, 5].

Apparently, one of the first papers where the possible role of magnetic fluctuations in the formation of Cooper pairs of the $s^{\pm}$ type was stressed at the qualitative level was Ref. [110]. Similar conclusions were reached by the authors of Ref. [123], where the possibility of $d_{x^2-y^2}$-pairing was also noticed.

A rather detailed analysis of possible electronic mechanisms of pairing within the generalized Hubbard Hamiltonian applied to the minimal model of Ref. [127] was performed in Ref. [180]. In fact, this analysis was done in the framework of the generalized RPA approximation which takes into account an exchange by spin (and orbital) fluctuations in the particle – hole channel (cf. the review of similar one-band models utilized for cuprates [4]). It was shown that the pairing interaction due to these fluctuations leads to effective attraction in the case of singlet d-wave pairing and triplet p-wave pairing, with the tendency to d-wave pairing instability becoming stronger as the system moves towards magnetic (SDW) instability. In a rather general formulation, using the general renormalization group approach, a similar model was analyzed in Ref. [181].

Unfortunately, in most of the papers devoted to the pairing mechanism due to the exchange of magnetic fluctuations there are no direct calculations of $T_{\rm c}$ allowing comparison with experiments. Thus, we shall limit ourselves to these short comments.

5. Conclusion: end of cuprate monopoly

Let us briefly summarize. During the first six months of studies of new superconductors we have observed rather impressive progress in learning about their basic physical properties. Very few problems remain noninvestigated, though many results obtained require further clarification.[9] The main result of all these studies is certainly the end of the cuprate monopoly in the physics of high-temperature superconductivity. A new wide class of iron-based systems was discovered with high enough values of $T_{\rm c}$ and a variety of physical properties, which brings to mind copper oxides that for more than 20 years were the center of interest of the superconductor community. There are rather well-founded expectations that in some near future new systems will also be discovered, though there is now a certain impression that in the subclass of layered FeAs systems we have already reached the maximum values of $T_{\rm c} \sim 50$ K, so that for further enhancement of $T_{\rm c}$ we need some kind of a new approaches. Doubtless, the work already done has significantly deepened our understanding of the nature of high-temperature superconductivity, though we are still far from formulation of definite 'recipes' in the search for new superconductors with higher values of $T_{\rm c}$.

Let us formulate

What do iron-based and cuprate superconductors have in common?

- Both classes are represented by quasi-two-dimensional (layered) systems from the point of view of their electronic properties, which leads to more or less strong anisotropy.
- In both classes, the superconducting region in the phase diagram is close to the region of antiferromagnetic ordering. The prototype phase for both classes of superconductors is antiferromagnetic.
- Cooper pairing in both classes is of the singlet type, but 'anomalous', i.e., different from the simple s-wave pairing characteristic of traditional (low-temperature) superconductors.
- The basic properties of the superconducting state is more or less the same as in typical type II superconductors.

From the point of view of our understanding of the basic nature of high-temperature superconductivity, the meaning of these common properties remains rather unclear. Why do we need (and do we need?) two-dimensionality? Historically, the importance of two-dimensionality was first stressed in connection with the proposed high-temperature superconductivity based on the excitonic mechanism of Ginzburg and Little [182], but does it play any significant role for superconductivity in HTSC cuprates and new iron-based superconductors? Do we need 'closeness' to antiferromagnetism? Is antiferromagnetism just a competing phase, or is it helpful for

[9] In this respect, we want to stress the absence of any systematic studies on the disordering effects which may be unusual due to the anomalous nature of $s^{\pm}$-pairing.

HTSC, for example, via the replacement of electron – phonon pairing by a mechanism based on spin (antiferromagnetic) fluctuations? The answers to these questions are still unclear, though the presence of such coincidences in rather different classes of physical systems seem rather significant.

Let us now look

What is the difference between iron-based and cuprate superconductors?

- Prototype phases of HTSC cuprates are antiferromagnetic (strongly correlated, Mott type) insulators, while for new superconductors these are antiferromagnetic (intermediately correlated?) metals.
- Cuprates in the superconducting state are one-band metals with a single Fermi surface (hole-like or electron-like), while new superconductors are multiple band metals with several hole-like and electron-like Fermi surfaces.
- In cuprates, we have anisotropic d-wave pairing, while in new superconductors, almost surely, we have (almost?) isotropic $s^{\pm}$-pairing.
- It is quite possible that the microscopic mechanism of pairing in both classes of superconductors is different: in cuprates it is almost certainly an electronic mechanism (spin fluctuations), while in iron-based superconductors the role of electron – phonon coupling can be quite important (the isotope effect!).

It is evident that the differences between cuprates and new superconductors are probably more pronounced than are their common properties. In this sense, one of the main conclusions which can already be made is that HTSC is not a unique property of cuprates, i.e., strongly correlated systems close to the insulating state. In some respects, new superconductors are simpler and easier to understand — their normal state is not so mysterious as in the case of cuprates,[10] though their multiple band structure complicates situation.

To conclude, it is believed that high-temperature superconductivity is much more common than has been assumed during the last 20 years, so that the high-temperature superconductor community may look into the future with certain optimism.

The author is grateful to L P Gor'kov and I I Mazin for numerous discussions on the physics of new superconductors. He is also grateful to I A Nekrasov and Z V Pchelkina, who co-authored papers on calculations of electronic spectra of FeAs-based systems. This work was partly supported by the Russian Foundation for Basic Research, grant No. 08-02-00021, and by the programs of fundamental research of the Russian Academy of Sciences, titled 'Quantum Macrophysics' and 'Strongly Correlated Electrons in Semiconductors, Metals, Superconductors, and Magnetic Materials'.

References

1. Bednorz J G, Müller K A *Z. Phys. B* **64** 189 (1986)
2. Gor'kov L P, Kopnin N B *Usp. Fiz. Nauk* **156** 117 (1988) [*Sov. Phys. Usp.* **31** 850 (1988)]
3. Izyumov Yu A, Plakida N M, Skryabin Yu N *Usp. Fiz. Nauk* **159** 621 (1989) [*Sov. Phys. Usp.* **32** 1060 (1989)]
4. Izyumov Yu A *Usp. Fiz. Nauk* **161** (11) 63 (1991) [*Sov. Phys. Usp.* **34** 935 (1991)]
5. Izyumov Yu A *Usp. Fiz. Nauk* **169** 225 (1999) [*Phys. Usp.* **42** 215 (1999)]
6. Maksimov E G *Usp. Fiz. Nauk* **170** 1033 (2000) [*Phys. Usp.* **43** 965 (2000)]
7. Sadovskii M V *Usp. Fiz. Nauk* **171** 539 (2001) [*Phys. Usp.* **44** 515 (2001)]
8. Belyavskii V I, Kopaev Yu V *Usp. Fiz. Nauk* **176** 457 (2006) [*Phys. Usp.* **49** 441 (2006)]
9. Maksimov E G *Usp. Fiz. Nauk* **178** 175 (2008) [*Phys. Usp.* **51** 167 (2008)]
10. Kopaev Yu V, Belyavskii V I, Kapaev V V *Usp. Fiz. Nauk* **178** 202 (2008) [*Phys. Usp.* **51** 191 (2008)]
11. Plakida N M *Vysokotemperaturnye Sverkhprovodniki* (High-Temperature Superconductivity) (Moscow: Mezhdunarodnaya Programma Obrazovaniya, 1996) [Translated into English (Berlin: Springer-Verlag, 1995)]
12. Anderson P W *The Theory of Superconductivity in the High-T_c Cuprates* (Princeton, NJ: Princeton Univ. Press, 1997)
13. Schrieffer J R (Ed.) *Handbook of High-Temperature Superconductivity* (New York: Springer, 2007)
14. Bennemann K, Ketterson J B (Eds) *Superconductivity* Vols 1, 2 (Berlin: Springer-Verlag, 2008)
15. Kamihara Y et al. *J. Am. Chem. Soc.* **130** 3296 (2008)
16. Shaked H et al. *Crystal Structures of the High-T_c Superconducting Copper-Oxides* (Amsterdam: Elsevier Science B.V., 1994)
17. Sadovskii M V "Modeli psevdoshchelevogo sostoyaniya v vysokotemperaturnykh sverkhprovodnikov" ("Models of the pseudogap state in high-temperature superconductors"), in *Struny, Brany, Reshetki, Setki, Psevdoshcheli i Pylinki: Trudy Seminara im. I.E. Tamma* (Strings, Branes, Lattices, Nets, Pseudogaps and Dust. Proc. I E Tamm Seminar) (Moscow: Nauchnyi Mir, 2007) pp. 357 – 441; Sadovskii M V, cond-mat/0408489
18. Hüfner S et al. *Rep. Prog. Phys.* **71** 062501 (2008)
19. Pennington C H, Stenger V A *Rev. Mod. Phys.* **68** 855 (1996)
20. Mackenzie A P, Maeno Y *Rev. Mod. Phys.* **75** 657 (2003)
21. Ovchinnikov S G *Usp. Fiz. Nauk* **173** 27 (2003) [*Phys. Usp.* **46** 21 (2003)]
22. Vinod K, Varghese N, Syamaprasad U *Supercond. Sci. Technol.* **20** R31 (2007)
23. Putti M, Vaglio R, Rowell J M *Supercond. Sci. Technol.* **21** 043001 (2008)
24. Kamihara Y et al. *J. Am. Chem. Soc.* **128** 10012 (2006)
25. Watanabe T et al. *Inorg. Chem.* **46** 7719 (2006)
26. Chen G F et al. *Phys. Rev. Lett.* **101** 057007 (2008); arXiv:0803.0128
27. Zhu X et al. *Supercond. Sci. Technol.* **21** 105001 (2008)
28. Sefat A S et al. *Phys. Rev. B* **77** 174503 (2008); arXiv:0803.2528
29. Chen X H et al. *Nature* **453** 761 (2008); arXiv:0803.3603
30. Chen G F et al. *Phys. Rev. Lett.* **100** 247002 (2008); arXiv:0803.3790
31. Ren Z-A et al. *Europhys. Lett.* **82** 57002 (2008); arXiv:0803.4234
32. Chen G F et al. *Chinese Phys. Lett.* **25** 2235 (2008); arXiv:0803.4384
33. Ren Z-A et al. *Europhys. Lett.* **83** 17002 (2008); arXiv:0804.2582
34. Lu W et al. *Solid State Commun.* **148** 168 (2008); arXiv:0804.3725
35. Yang J et al. *Supercond. Sci. Technol.* **21** 082001 (2008); arXiv:0804.3727
36. Wen H-H et al. *Europhys. Lett.* **82** 17009 (2008); arXiv:0803.3021
37. Wang C et al. *Europhys. Lett.* **83** 67006 (2008); arXiv:0804.4290
38. Takahashi H et al. *Nature* **453** 376 (2008)
39. Zocco D A et al. *Physica C* **468** 2229 (2008); arXiv:0805.4372
40. Garbarino G et al., arXiv:0808.1132
41. Tegel M et al., arXiv:0810.2120
42. Han F et al., arXiv:0810.2475
43. Matsuishi S et al. *J. Phys. Soc. Jpn.* **77** 113709 (2008); arXiv:0810.2351
44. Zhu X et al., arXiv:0810.2531
45. Rotter M, Tegel M, Johrendt D *Phys. Rev. Lett.* **101** 107006 (2008); arXiv:0805.4630
46. Chen G F et al. *Chinese Phys. Lett.* **25** 3403 (2008); arXiv:0806.1209
47. Sasmal K et al. *Phys. Rev. Lett.* **101** 107007 (2008); arXiv:0806.1301
48. Alireza P L et al. *J. Phys. Condens. Matter* **21** 012208 (2009); arXiv:0807.1896
49. Sefat A S et al. *Phys. Rev. Lett.* **101** 117004 (2008); arXiv:0807.2237
50. Wang X C et al., arXiv:0806.4688
51. Tapp J H et al. *Phys. Rev. B* **78** 060505(R) (2008); arXiv:0807.2274
52. Hsu F-C et al., arXiv:0807.2369

[10] Some evidence for the pseudogap state was observed only in NMR data and it is unclear whether in new superconductors we have an additional pseudogap region in the phase diagram as in cuprates, with appropriate renormalization of the electronic spectrum, like, formation of 'Fermi arcs', etc.

53. Mizuguchi Y et al. *Appl. Phys. Lett.* **93** 152505 (2008); arXiv:0807.4315
54. Fang M H et al., arXiv:0807.4775
55. Kozhevnikov V L et al. *Pis'ma Zh. Eksp. Teor. Fiz.* **87** 747 (2008) [*JETP Lett.* **87** 649 (2008)]; arXiv:0804.4546
56. Ge J, Cao S, Zhang J, arXiv:0807.5045
57. Li Z et al. *Phys. Rev. B* **78** 060504(R) (2008); arXiv:0803.2572
58. Ronning F et al. *J. Phys. Condens. Matter* **20** 342203 (2008); arXiv:0807.3788
59. Klimczuk T et al., arXiv:0808.1557
60. Ozawa T C, Kauzlarich S M *Sci. Technol. Adv. Mater.* **9** 033003 (2008); arXiv:0808.1158
61. Rotter M et al. *Phys. Rev. B* **78** 020503(R) (2008); arXiv:0805.4021
62. Nomura T et al. *Supercond. Sci. Technol.* **21** 125028 (2008); arXiv:0804.3569
63. Zhigadlo N D et al. *J. Phys. Condens. Matter* **20** 342202 (2008); arXiv:0806.0337
64. Jia Y et al. *Appl. Phys. Lett.* **93** 032503 (2008); arXiv:0806.0532
65. Ni N et al. *Phys. Rev. B* **78** 014507 (2008); arXiv:0806.1874
66. Zhang S B et al., arXiv:0809.1905
67. Wang X F et al., arXiv:0806.2452
68. Yuan H Q et al., arXiv:0807.3137
69. de la Cruz C et al. *Nature* **453** 899 (2008); arXiv:0804.0795
70. Luetkens H et al., arXiv:0806.3533
71. Zhao J et al. *Nature Mater.* **7** 953 (2008); arXiv:0806.2528
72. Markert J T, Dalichaouch Y, Maple M B, in *Physical Properties of High Temperature Superconductors I* (Ed. D M Ginsberg) (Singapore: World Scientific, 1989) [Translated into Russian Vol. 1 (Moscow: Mir, 1990) p. 265]
73. Qiu Y et al., arXiv:0806.2195
74. Chen Y et al. *Phys. Rev. B* **78** 064515 (2008); arXiv:0807.0662
75. Drew A J et al., arXiv:0807.4876
76. Huang Q et al., arXiv:0806.2776
77. Zhao J et al. *Phys. Rev. B* **78** 140504(R) (2008); arXiv:0807.1077
78. Chen H et al., arXiv:0807.3950
79. Bao W et al., arXiv:0809.2058
80. Ding L et al. *Phys. Rev. B* **77** 180510(R) (2008); arXiv:0804.3642
81. Dong J K et al., arXiv:0806.3573
82. Mu G et al., arXiv:0808.2941
83. Nakai Y et al. *J. Phys. Soc. Jpn.* **77** 073701 (2008); arXiv:0804.4765
84. Fukuzawa H et al. *J. Phys. Soc. Jpn.* **77** 093706 (2008); arXiv:0806.4514
85. Mukuda H et al. *J. Phys. Soc. Jpn.* **77** 093704 (2008); arXiv:0806.3238
86. Matano K et al. *Europhys. Lett.* **83** 57001 (2008); arXiv:0806.0249
87. Ning F L et al. *J. Phys. Soc. Jpn.* **77** 103705 (2008); arXiv:0808.1420
88. Kotegawa H et al. *J. Phys. Soc. Jpn.* **77** 113703 (2008); arXiv:0808.0040
89. Chen T Y et al. *Nature* **453** 1224 (2008); arXiv:0805.4616
90. Millo O et al. *Phys. Rev. B* **78** 092505 (2008); arXiv:0807.0359
91. Pan M H et al., arXiv:0808.0895
92. Wang Y et al., arXiv:0806.1986
93. Dubroka A et al. *Phys. Rev. Lett.* **101** 097011 (2008); arXiv:0805.2415
94. Boris A V et al., arXiv:0806.1732
95. Yang J et al., arXiv:0807.1040
96. Li G et al. *Phys. Rev. Lett.* **101** 107004 (2008); arXiv:0807.1094
97. Ferrell R A, Glover R E (III) *Phys. Rev.* **109** 1398 (1958)
98. Tinkham M, Ferrell R A *Phys. Rev. Lett.* **2** 331 (1959)
99. Qiu Y et al. *Phys. Rev. B* **78** 052508 (2008); arXiv:0805.1062
100. Christianson A D et al. *Phys. Rev. Lett.* **101** 157001 (2008); arXiv:0807.3370
101. Singh D J, Du M-H *Phys. Rev. Lett.* **100** 237003 (2008); arXiv:0803.0429
102. Mittal R et al. *Phys. Rev. B* **78** 104514 (2008); arXiv:0807.3172
103. Higashitaniguchi S et al., arXiv:0807.3968
104. Fukuda T et al. *J. Phys. Soc. Jpn.* **77** 103715 (2008); arXiv:0808.0838
105. Zbiri M et al., arXiv:0807.4429
106. Zhao J et al. *Phys. Rev. Lett.* **101** 167203 (2008); arXiv:0808.2455
107. Ewings R A et al., arXiv:0808.2836
108. Lebègue S *Phys. Rev. B* **75** 035110 (2007)
109. Boeri L, Dolgov O V, Golubov A A *Phys. Rev. Lett.* **101** 026403 (2008); arXiv:0803.2703
110. Mazin I I et al. *Phys. Rev. Lett.* **101** 057003 (2008); arXiv:0803.2740
111. Xu G et al. *Europhys. Lett.* **82** 67002 (2008)
112. Shein I R, Ivanovskii A L *Pis'ma Zh. Eksp. Teor. Fiz.* **88** 115 (2008); [*JETP Lett.* **88** 107 (2008)]; arXiv:0806.0750
113. Singh D J *Phys. Rev. B* **78** 094511 (2008); arXiv:0807.2643
114. Ma F, Lu Z-Y, Xiang T, arXiv:0806.3526
115. Shein I R, Ivanovskii A L *Pis'ma Zh. Eksp. Teor. Fiz.* **88** 377 (2008) [*JETP Lett.* **88** (5) (2008)]
116. Subedi A et al. *Phys. Rev. B* **78** 134514 (2008); arXiv:0807.4312
117. Nekrasov I A, Pchelkina Z V, Sadovskii M V *Pis'ma Zh. Eksp. Teor. Fiz.* **87** 647 (2008) [*JETP Lett.* **87** 560 (2008)]; arXiv:0804.1239
118. Nekrasov I A, Pchelkina Z V, Sadovskii M V *Pis'ma Zh. Eksp. Teor. Fiz.* **88** 155 (2008) [*JETP Lett.* **88** 144 (2008)]; arXiv:0806.2630
119. Nekrasov I A, Pchelkina Z V, Sadovskii M V *Pis'ma Zh. Eksp. Teor. Fiz.* **88** 621 (2008) [*JETP Lett.* **88** 543 (2008)]; arXiv:0807.1010
120. Nekrasov I A, Pchelkina Z V, Sadovskii M V *Pis'ma Zh. Eksp. Teor. Fiz.* **88** 777 (2008) [*JETP* **88** (10) (2008)]; arXiv:0810.3377
121. Andersen O K *Phys. Rev. B* **12** 3060 (1975); Gunnarsson O, Jepsen O, Andersen O K *Phys. Rev. B* **27** 7144 (1983); Andersen O K, Jepsen O *Phys. Rev. Lett.* **53** 2571 (1984)
122. Goshchitskii B N, Kozhevnikov V L, Sadovskii M V *Int. J. Mod. Phys. B* **2** 1331 (1988)
123. Kuroki K et al. *Phys. Rev. Lett.* **101** 087004 (2008)
124. Chong S V, Mochiji T, Kadowaki K, arXiv:0808.0288
125. Yang J et al., arXiv:0809.3582
126. Shein I R, Ivanovskii A L, arXiv:0810.3498
127. Raghu S et al. *Phys. Rev. B* **77** 220503(R) (2008); arXiv:0804.1113
128. Cao C, Hirschfeld P J, Cheng H-P *Phys. Rev. B* **77** 220506(R) (2008); arXiv:0803.3236
129. Kuroki K et al., arXiv:0803.3325
130. Korshunov M M, Eremin I *Phys. Rev. B* **78** 140509(R) (2008); arXiv:0804.1793
131. Liu C et al., arXiv:0806.2147
132. Yang L X et al., arXiv:0806.2627
133. Liu C et al., arXiv:0806.3453
134. Liu H et al., arXiv:0806.4806
135. Zhao L et al. *Chinese Phys. Lett.* **25** 4402 (2008); arXiv:0807.0398
136. Ding H et al. *Europhys. Lett.* **83** 47001 (2008); arXiv:0807.0419
137. Wray L et al., arXiv:0808.2185
138. Zhang Y et al., arXiv:0808.2738
139. Zabolotnyy V B et al., arXiv:0808.2454
140. Evtushinsky D V et al., arXiv:0809.4455
141. Sato T et al., arXiv:0810.3047
142. Damascelli A, Hussain Z, Shen Z-X *Rev. Mod. Phys.* **75**, 473 (2003)
143. Sebastian S E et al. *J. Phys. Condens. Matter* **20** 422203 (2008); arXiv:0806.4726
144. Coldea A I et al., arXiv:0807.4890
145. Metzner W, Vollhardt D *Phys. Rev. Lett.* **62** 324 (1989)
146. Vollhardt D, in *Correlated Electron Systems* (Ed. V J Emery) (Singapore: World Scientific, 1993) p. 57
147. Pruschke Th, Jarrell M, Freericks J K *Adv. Phys.* **44** 187 (1995)
148. Izyumov Yu A *Usp. Fiz. Nauk* **165** 403 (1995) [*Phys. Usp.* **38** 385 (1995)]
149. Georges A et al. *Rev. Mod. Phys.* **68** 13 (1996)
150. Kotliar G, Vollhardt D *Phys. Today* **57** (3) 53 (2004)
151. Kotliar G et al. *Rev. Mod. Phys.* **78** 865 (2006)
152. Held K *Adv. Phys.* **56** 829 (2007)
153. Haule K, Singh J H, Kotliar G *Phys. Rev. Lett.* **100** 226402 (2008); arXiv:0803.1279
154. Shorikov A O et al., arXiv:0804.3283
155. Anisimov V I et al., arXiv:0807.0547
156. Miyake T et al., arXiv:0808.2442
157. Anisimov V I et al., arXiv:0810.2629
158. Aryasetiawan F et al. *Phys. Rev. B* **70** 195104 (2004)
159. Miyake T, Aryasetiawan F *Phys. Rev. B* **77** 085122 (2008)
160. Anisimov V I, Gunnarsson O *Phys. Rev. B* **43** 7570 (1991)
161. Kurmaev E Z et al., arXiv:0805.0668
162. Yildirim T *Phys. Rev. Lett.* **101** 057010 (2008); arXiv:0804.2252
163. Mazin I I et al. *Phys. Rev. B* **78** 085104 (2008); arXiv:0806.1869
164. Mazin I I, Johannes N D *Nature Phys.* **5** 141 (2009); arXiv:0807.3737
165. Moskalenko V A, Palistrant M E, Vakalyuk V M *Usp. Fiz. Nauk* **161** (8) 155 (1991) [*Sov. Phys. Usp.* **34** 717 (1991)]

166. Barzykin V, Gor'kov L P *Pis'ma Zh. Eksp. Teor. Fiz.* **88** 142 (2008) [*JETP Lett.* **88** 131 (2008)]; arXiv:0806.1933
167. Keldysh L V, Kopaev Yu V *Fiz. Tverd. Tela* **6** 2791 (1964) [*Sov. Phys. Solid State* **6** 2219 (1965)]
168. Kozlov A N, Maksimov L A *Zh. Eksp. Teor. Fiz.* **49** 1284 (1965) [*Sov. Phys. JETP* **22** 889 (1966)]
169. Halperin B I, Rice T M, in *Solid State Physics* (Eds F Seitz, D Turnball, H Ehrenreich) Vol. 21 (New York: Academic Press, 1968) p. 115
170. Kopaev Yu V *Trudy Fiz. Inst. Akad. Nauk SSSR* **86** 3 (1975)
171. Volkov B A *Trudy Fiz. Inst. Akad. Nauk SSSR* **104** 3 (1978)
172. Volovik G E, Gor'kov L P *Pis'ma Zh. Eksp. Teor. Fiz.* **39** 550 (1984) [*JETP Lett.* **39** 674 (1984)]
173. Volovik G E, Gor'kov L P *Zh. Eksp. Teor. Fiz.* **88** 1412 (1985) [*Sov. Phys. JETP* **61** 843 (1985)]
174. Parker D et al. *Phys. Rev. B* **78** 134524 (2008); arXiv:0807.3729
175. Allen P B, Dynes R C *Phys. Rev. B* **12** 905 (1975)
176. Eschrig H, arXiv:0804.0186
177. Bhoi D, Mandal P, Choudhury P *Supercond. Sci. Technol.* **21** 125021 (2008); arXiv:0808.2695
178. Allen P B, Pickett W E, Krakauer H *Phys. Rev. B* **37** 7482 (1988)
179. Liu R H et al., arXiv:0810.2694
180. Qi X-L et al., arXiv:0804.4332
181. Chubukov A V, Efremov D, Eremin I *Phys. Rev. B* **78** 134512 (2008); arXiv:0807.3735
182. Ginzburg V L, Kirzhnits D A (Eds) *Problema Vysokotemperaturnoi Sverkhprovodimosti* (High-Temperature Superconductivity) (Moscow: Nauka, 1977) [Translated into English (New York: Consultants Bureau, 1982)]

Physics – Uspekhi **55** (4) 325 – 355 (2012) ©2012 Uspekhi Fizicheskikh Nauk, Russian Academy of Sciences

REVIEWS OF TOPICAL PROBLEMS PACS numbers: 71.10.Fd, 71.10.Hf, **71.20.–b**, **71.27.+a**, **71.30.+h**, 72.15.Rn, **74.72.–h**

Generalized dynamical mean-field theory in the physics of strongly correlated systems

E Z Kuchinskii, I A Nekrasov, M V Sadovskii

DOI: 10.3367/UFNe.0182.201204a.0345

Contents

1. **Introduction** **325**
2. **Strongly correlated systems and dynamical mean-field theory (DMFT)** **326**
   2.1 The Hubbard model and the basics of DMFT; 2.2 Generalized DMFT + Σ approach; 2.3 Some other generalizations of DMFT
3. **Application of generalized DMFT + Σ approach to model problems** **330**
   3.1 Strongly correlated systems in the pseudogap state; 3.2 Mott–Anderson transition in disordered systems; 3.3 Singularities of electron dispersion in strongly correlated systems in DMFT and DMFT + Σ approaches
4. **Electronic structure of real strongly correlated systems: LDA + DMFT and LDA + DMFT + Σ** **345**
   4.1 Density functional theory (DFT). Local density approximation (LDA); 4.2 LDA + DMFT computational scheme; 4.3 Examples of LDA + DMFT calculations; 4.4 Electronic structure of copper oxides in the pseudogap state: LDA + DMFT + Σ
5. **Conclusions** **353**
   References **353**

Abstract. This review discusses the generalization of dynamical mean-field theory (DMFT) for strongly correlated electronic systems to include additional interactions necessary for the correct description of physical effects in such systems. Specifically, the additional interactions include: (1) the interaction of electrons with antiferromagnetic (or charge) order-parameter fluctuations in high-temperature superconductors leading to the formation of a pseudogap state; (2) scattering on static disorder and its role in the general picture of the Anderson–Hubbard metal–insulator transition, and (3) electron–phonon interaction and the features of electronic spectra in strongly correlated systems. The proposed DMFT + Σ approach incorporates the above interactions by introducing into the general DMFT model an additional (generally momentum-dependent) self-energy Σ which is calculated in a self-consistent way without violating the general structure of the DMFT iteration cycle. The paper formulates a general calculational scheme for both one-particle (spectral functions and densities of states) and two-particle (optical conductivity) properties. The problem of pseudogap formation is examined, including Fermi arc formation and partial destruction of the Fermi surface, as are the metal–insulator transition in the disordered Anderson–Hubbard model, and the general picture of kink formation in the electronic spectra of strongly correlated systems. A generalization of the DMFT + Σ approach to realistic materials with strong electron–electron correlations is presented based on the LDA + DMFT method. The general model of the LDA + DMFT method is reviewed, as are some of its applications to real systems. The generalized LDA + DMFT + Σ approach is employed to calculate pseudogap states in electron- and hole-doped HTSC cuprates. Comparisons with angle-resolved photoemission spectroscopy (ARPES) results are presented.

E Z Kuchinskii, I A Nekrasov Institute for Electrophysics, Ural Branch of the Russian Academy of Sciences,
ul. Amundsena 106, 620016 Ekaterinburg, Russian Federation
E-mail: kuchinsk@iep.uran.ru, nekrasov@iep.uran.ru
M V Sadovskii Institute for Electrophysics,
Ural Branch of the Russian Academy of Sciences,
ul. Amundsena 106, 620016 Ekaterinburg, Russian Federation
E-mail: sadovski@iep.uran.ru
Institute for Metal Physics,
Ural Branch of the Russian Academy of Sciences,
ul. S Kovalevskoi 18, 620219 Ekaterinburg, Russian Federation

Received 20 June 2011
Uspekhi Fizicheskikh Nauk **182** (4) 345 – 378 (2012)
DOI: 10.3367/UFNr.0182.201204a.0345
Translated by M V Sadovskii and I A Nekrasov; edited by A Radzig

1. Introduction

Strongly correlated electronic systems (SCSs), which are mainly realized in a number of compounds of transition or rare-earth elements with partially filled 3d, 4f, and 5f shells, have for more than half a century been attracting great interest of scientists because of their unusual physical properties and difficulties in their theoretical description. The question of metal–insulator phase transition observed in many transition metal oxides, heavy fermions systems with a great variety of different phase transitions and related phenomena, manganites with giant magnetoresistance — all these systems have become the focus for both experimentalists and theorists. Perhaps the most significant development in this area was the discovery of high-temperature superconductivity in copper oxides, which provoked a new wave of interest in the synthesis and description of such systems.

As already stressed above, the diversity of physical phenomena in all these compounds is due to partially filled 3d, 4f, and 5f electron shells. The strong interaction of electrons emerged from narrow bands belonging to these orbitals with each other or with itinerant electrons of outer shells is basically responsible for the unique properties of these systems. The early qualitative ideas formulated by Mott [1] have been further developed in many theoretical studies to follow, forming a new area of the modern theory of condensed matter. There are now thousands of such papers and many new reviews and monographs are regularly published [2].

Of course, nowadays, a single review cannot cover all this area of research and the aim of the authors is rather modest. The subject of this work concerns a description of a number of theoretical approaches formulated during recent years to account for some additional interactions which are important for the consistent description of strongly correlated systems. Here, we are speaking not only about 'external' perturbations due to the interaction of correlated electrons with bosonic excitations, such as phonons, spin fluctuations, or scattering of electrons by disorder, but also about attempts to improve the most developed and widely used theoretical approaches, such as dynamical mean-field theory (DMFT) [3–6].

These tasks are closely related to a variety of topical problems under active study at present, such as the nature of the pseudogap state of high-T_c cuprates, the evolution of their Fermi surfaces upon doping, with the formation of so-called 'Fermi arcs' observed in ARPES experiments, the problem of the formation of kinks in the electronic spectrum, and the general problem of metal–insulator transition in disordered systems due to the mutual interference of strong correlations and Anderson localization. In this review, we deal to some extent with all of these problems.

During recent years, the general theory of strongly correlated systems based on DMFT has practically merged with the so-called *ab initio* approaches to calculating electronic spectra of real solids (LDA + DMFT approach), with a significant success already achieved [2, 7]. To this end, we devote some attention in our review to the first attempts to generalize these approaches in an effort of accounting for the above-mentioned physical effects.

2. Strongly correlated systems and dynamical mean-field theory (DMFT)

2.1 The Hubbard model and the basics of DMFT

Starting with the pioneering works of Hubbard [8–13] in the early 1960s, the simplest model permitting the description of strongly correlated systems is the so-called Hubbard model. The one-band Hubbard model Hamiltonian is written down as

$$H = -t \sum_{\langle ij \rangle \sigma} c^{\dagger}_{i\sigma} c_{j\sigma} + U \sum_i n_{i\uparrow} n_{i\downarrow} \,, \tag{1}$$

where $t > 0$ is the nearest neighbors hopping amplitude, U is the single-site repulsion, $n_{i\sigma} = c^{\dagger}_{i\sigma} c_{i\sigma}$ is the particle number operator at the site, and $c_{i\sigma}$ ($c^{\dagger}_{i\sigma}$) is the annihilation (creation) electron operator for spin σ. The model has only two competing energy parameters: parameter t defines the kinetic energy of an electron and facilitates intersite hoppings (delocalization), while parameter U defines potential energy and favors electron localization at a lattice site. Energy bands formed by 3d, 4f, and 5f orbitals are rather narrow; thus, quite often kinetic and potential energy are of the same order of magnitude ($t \sim U$). In this case, there is no small parameter in the model and it is impossible to build any kind of perturbation theory. This fact alone leads to all the difficulties in describing SCSs, even for such an oversimplified model.

Almost for 30 years there were no satisfactory approaches to analyzing SCSs. It seemed that the theory of these systems would forever remain fragmentary and semiquantitative. The breakthrough came in 1989 in the work by Metzner and Vollhardt [14], who suggested formal consideration of the system of interacting electrons in the space of large dimension $d \to \infty$ (or in a lattice with large coordination number $z \to \infty$).[1]

Employing this limit, it is possible to neglect spatial fluctuations in the systems, while the full local dynamics are preserved. In Ref. [14], it was shown that in the limit of infinite spatial dimensions (or more precisely of infinite coordination number) the main role is played only by local contributions to the self-energy part of the full interacting Green function. All nonlocal contributions are proportional to $1/\sqrt{z} \sim 1/\sqrt{d}$ and can be dropped. In this limit, therefore, electron self-energy does not depend on momentum $\mathbf{k}$, and is a function of frequency only [real (ω) or Matsubara (ω_n, $n = 0, \pm 1, \ldots$)]:[2]

$$\Sigma_\sigma(\mathbf{k}, \omega) = \Sigma_\sigma(\omega) \,. \tag{2}$$

This statement represents the main simplification appearing in the limit of $d \to \infty$ [3, 5–7].

In Fig. 1, we show the 'skeleton' diagrams of DMFT self-energy Σ. Wavy lines indicate local (Hubbard) Coulomb interaction U, whereas full lines fit local Green functions G_{ii}. Strictly speaking, not only is the self-energy local in the limit of $d \to \infty$, but also in each vertex of the 'skeleton' diagram only one particular site enters, e.g. the i-th one, as shown in Fig. 1. Thus, this self-energy is a functional of interacting local Green function $G_{ii,\sigma}$: $\Sigma_{ii,\sigma} = F[G_{ii,\sigma}]$. Generally, it is not yet sufficient for our problem to become fully local, since interacting Green function $G_{ij,\sigma}$ is still nonlocal. A question then arises of whether it is possible to choose a purely local noninteracting ($U = 0$) problem (even with complex dynamics) yielding completely equivalent self-energy. Surely, it can be done! Let $\mathcal{G}_\sigma(\omega)$ be the 'bare' dynamical Green function of such a local problem without Coulomb interaction U, while $G_{d\sigma}(\omega)$ and $\Sigma_{d\sigma}(\omega)$ are corresponding interacting Green function and self-energy. If one can ensure

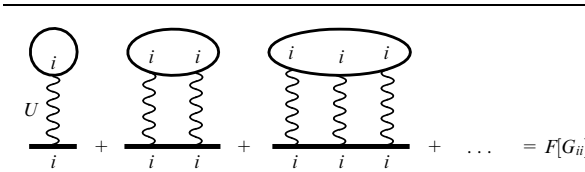

Figure 1. 'Skeleton' diagrams of local self-energy Σ in DMFT.

[1] For a hypercubic lattice $z = 2d$, and these two limits practically coincide. However, z could be quite large even for three-dimensional lattices, for example, in a body-centered lattice with $z = 8$, and for a face-centered lattice with $z = 12$. To this end, it is more correct to speak about the limit of large z.

[2] Large coordination numbers allow one to apply this approximation rather successfully even for rather small d.

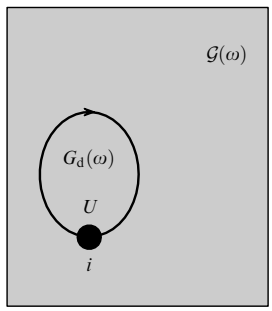

Figure 2. Within the DMFT, the Hubbard lattice model maps onto interacting electrons at a single site ('impurity') surrounded by the fermionic bath, which defines, in turn, dynamical (Weiss) mean field $\mathcal{G}(\omega)$.

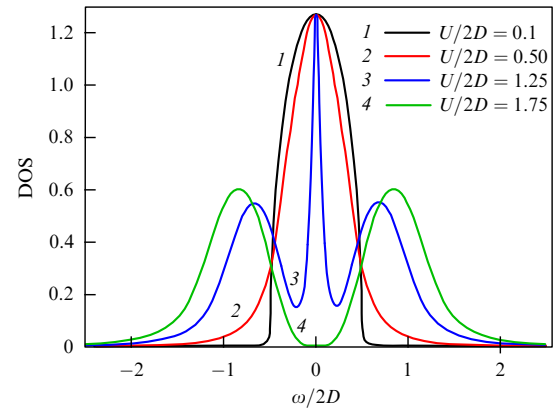

Figure 3. DMFT (NRG) densities of states at half-filling obtained for a semielliptic 'bare' density of states for different values of U.

the equality $G_{d\sigma}(\omega) = G_{ii,\sigma}(\omega)$, then corresponding self-energies are also equivalent, because the structure of diagrams for the weak-coupling (low U) perturbation theory is totally preserved, which means that the self-energy of the local problem is defined by the same functional $\Sigma_{d\sigma} = F[G_{d\sigma}]$. But $\mathcal{G}_\sigma$, $G_{d\sigma}$, and $\Sigma_{d\sigma}$ are connected through the Dyson equation which immediately gives us the bare dynamical Green function of the local problem:

$$\mathcal{G}_\sigma^{-1}(\omega) = \Sigma_\sigma(\omega) + G_{ii,\sigma}^{-1}(\omega)\,. \tag{3}$$

Thus, the lattice Hubbard model in the limit of $d \to \infty$ exactly maps onto the purely local dynamical problem. Physically, it corresponds (as shown in Fig. 2) to the problem of interacting electrons on a single 'Anderson impurity' in a 'bath', and interaction with the bath is contained in dynamical mean-field $\mathcal{G}(\omega)$. Quite often, in analogy with the internal magnetic field of molecular field theory in magnetism, this field is called the 'Weiss field'. This explains the name of such an approach — dynamical mean-field theory

Such a purely dynamical problem is still quite complicated. However, the problem is equivalent to a single-impurity Anderson model (SIAM) [15]. The latter model can be studied in detail by a number of different methods, and its physical nature is now well understood. For this model there are well-developed approximate analytical methods such as the iterative perturbation theory (IPT) [5] and noncrossing approximation (NCA) [16, 17], but most remarkable is the possibility of solving this model by exact numerical methods like quantum Monte Carlo (QMC) [18–22] or numerical renormalization group (NRG) [23, 24]. The solution to an effective SIAM employing any of these methods, usually called an 'impurity solver' (IS), completes the general outline of the DMFT approach.

Apparently, today DMFT is the most elaborate and reliable theoretical method for describing SCSs. In its framework, the so-called three-peak structure of the density of states (DOS) in SCSs was obtained for the first time [5], consisting of the narrow central (quasiparticle) peak on the Fermi level, and two wide maxima corresponding to upper and lower Hubbard bands. Also, the reliable theoretical description of Mott–Hubbard metal–insulator transition was obtained. In Fig. 3, we display DMFT (NRG) densities of states for the half-filled Hubbard model with a semielliptic bare density of states with bandwidth $2D$. As correlation strength U grows, the density of states demonstrates the formation of a characteristic three-peak structure, and a further increase in U leads to a collapse of the quasiparticle peak at $U/2D \approx 1.5$, leading to metal–insulator transition.

It turned out that within DMFT it is also possible to investigate some two-particle properties. In particular, it is quite easy to obtain dynamic optical conductivity [4, 5]. During recent years, the DMFT approach has been generalized to describe realistic SCSs by merging it with *ab initio* one-electron density functional theory in a local density approximation (DFT/LDA), leading to the combined computational LDA + DMFT scheme [25–31], which will be described later.

Despite all the obvious advantages of LDA + DMFT, this approach has a number of shortcomings. Namely, as we stressed above, all nonlocal correlations are completely neglected. A number of cluster generalizations of DMFT [32, 33] were proposed recently to overcome this drawback. However, all these methods require significant computing resources and are rather restricted in cluster size and with respect to their generalization to the multiorbital case. Also, in these approaches it is quite difficult to investigate two-particle properties. To overcome these difficulties, we have proposed recently [35–37] a new generalization of the conventional DMFT, allowing the consideration of nonlocal correlations or additional (with respect to the Hubbard) interactions (in principle, of any kind), remaining within a single-impurity DMFT picture and preserving a self-consistent set of DMFT equations.

2.2 Generalized DMFT + Σ approach

The main idea of the new approach consists in using the DMFT solution exact in the limit of $d \to \infty$ as a 'high-energy' zeroth order approximation describing electronic spectra on a sufficiently large energy scale on the order of the bandwidth or U value, while low-energy scale details caused by nonlocal effects or by effects of interaction of correlated electrons with different collective modes (e.g. phonons or spin fluctuations) are to be taken into account within some kind of perturbation theory, conserving, as far as possible, the general structure of DMFT equations. Actually, such a scenario can be realized in a rather simple way [35–37].

To be more specific, we shall consider in the following the standard one-band Hubbard model. Its generalizations for the multiorbital or multiband case are also possible. The main assumption of our approach is that the Matsubara lattice

one-particle Green function is chosen as

$$G_{\mathbf{k}}(\mathrm{i}\omega) = \frac{1}{\mathrm{i}\omega + \mu - \varepsilon(\mathbf{k}) - \Sigma(\mathrm{i}\omega) - \Sigma_{\mathbf{k}}(\mathrm{i}\omega)}\,, \qquad \omega = \pi T(2n+1)\,, \tag{4}$$

where μ is the chemical potential, $\Sigma(\mathrm{i}\omega)$ is the *local* DMFT type self-energy due to Hubbard interaction, $\Sigma_{\mathbf{k}}(\mathrm{i}\omega)$ is some 'external' (generally nonlocal, momentum-dependent) self-energy, T is the temperature, and $n = 0, \pm 1, \ldots$. This last contribution can arise from the interaction of correlated electrons with some 'additional' collective modes or order parameter fluctuations appearing in the Hubbard model itself, or from any other interactions (fluctuations) external with respect to the standard Hubbard model. For example, these can be phonons or scattering by impurities, when it is actually local (momentum-independent).

In should be emphasized that $\Sigma_{\mathbf{k}}(\mathrm{i}\omega)$ can contain a local (momentum-independent) contribution, even if the self-energy is considered in the framework of the Hubbard model itself. However, this contribution *disappears* in the limit of infinite spatial dimensions $d \to \infty$ and is not accounted for within the conventional DMFT, so that within our approach we do not encounter any double counting problem, even in this case. This question does not arise at all for self-energy $\Sigma_{\mathbf{k}}(\mathrm{i}\omega)$ caused by external interactions.

More important is that our assumption about the additive form of self-energy $\Sigma(\mathrm{i}\omega) + \Sigma_{\mathbf{k}}(\mathrm{i}\omega)$ implicitly corresponds to the neglect of interference between the local (DMFT) and nonlocal contributions. In Fig. 4, typical skeleton diagrams for the self-energy of the DMFT + Σ approach are given. The first two terms (*1*, *2*) are local DMFT self-energy diagrams; the two diagrams (*3*, *4*) in the middle stand for contributions to the nonlocal part of self-energy from additional interactions with collective modes or order parameter fluctuations, and the last diagram (*5*) is an example with the interference between the local and nonlocal parts neglected. Indeed, once we neglect such interference (i.e., diagram *5*), the total self-energy is defined as a simple sum of these two contributions (*1–4*) shown in Fig. 4. Two diagrams (*3*, *4*) in Fig. 4 provide an example of skeleton diagrams for nonlocal self-energy, where the solid line is the Green function $G_{\mathbf{k}}$ (4), and the dashed lines correspond to an additional interaction with collective modes or order parameter fluctuations.

As a consequence, the diagrammatic structure of the local self-energy remains identical to that of the standard DMFT, and we arrive at the following self-consistent set of equations of the generalized DMFT + Σ approach [35–37], which is solved applying the following iterative procedure:

(1) Start from some initial guess for the local self-energy $\Sigma(\mathrm{i}\omega)$, for instance, $\Sigma(\mathrm{i}\omega) = 0$.

(2) Calculate nonlocal self-energy $\Sigma_{\mathbf{k}}(\mathrm{i}\omega)$ in the framework of some (approximate) scheme taking into account the interaction of correlated electrons with collective modes or order parameter fluctuations, which, in general, can depend on $\Sigma(\mathrm{i}\omega)$ and μ.

(3) Calculate the local Green function

$$G_{ii}(\mathrm{i}\omega) = \frac{1}{N}\sum_{\mathbf{k}} \frac{1}{\mathrm{i}\omega + \mu - \varepsilon(\mathbf{k}) - \Sigma(\mathrm{i}\omega) - \Sigma_{\mathbf{k}}(\mathrm{i}\omega)}\,. \tag{5}$$

(4) Define the 'Weiss field' as

$$\mathcal{G}_0^{-1}(\mathrm{i}\omega) = \Sigma(\mathrm{i}\omega) + G_{ii}^{-1}(\mathrm{i}\omega)\,. \tag{6}$$

(5) Using some 'impurity solver', calculate the single-particle Green function of an effective single-impurity Anderson model, i.e. compute the following integral over Grassmann variables $c_{i\sigma}^{\dagger}$ and $c_{i\sigma}$:

$$G_d(\tau - \tau') = \frac{1}{Z_{\mathrm{eff}}} \int Dc_{i\sigma}^{\dagger} Dc_{i\sigma} c_{i\sigma}(\tau)\, c_{i\sigma}^{\dagger}(\tau')\, \exp(-S_{\mathrm{eff}}), \tag{7}$$

where an effective action for the fixed site ('Anderson impurity') i has the form

$$S_{\mathrm{eff}} = -\int_0^{\beta} \mathrm{d}\tau_1 \int_0^{\beta} \mathrm{d}\tau_2\, c_{i\sigma}(\tau_1)\, \mathcal{G}_0^{-1}(\tau_1 - \tau_2)\, c_{i\sigma}^{\dagger}(\tau_2) + \int_0^{\beta} \mathrm{d}\tau\, U n_{i\uparrow}(\tau)\, n_{i\downarrow}(\tau)\,, \tag{8}$$

with the 'partition function' $Z_{\mathrm{eff}} = \int Dc_{i\sigma}^{\dagger} Dc_{i\sigma} \times \exp(-S_{\mathrm{eff}})$, and the upper limit of integration $\beta = T^{-1}$.

(6) Define *new* local self-energy as

$$\Sigma(\mathrm{i}\omega) = \mathcal{G}_0^{-1}(\mathrm{i}\omega) - G_d^{-1}(\mathrm{i}\omega)\,. \tag{9}$$

(7) Using last self-energy as an initial one in step 1, continue the loop procedure until it converges to

$$G_{ii}(\mathrm{i}\omega) = G_d(\mathrm{i}\omega) \tag{10}$$

with a given accuracy.

At the end, we obtain the final Green function in the form of Eqn (4), where $\Sigma(\mathrm{i}\omega)$ and $\Sigma_{\mathbf{k}}(\mathrm{i}\omega)$ are self-energies coming out of our iterative procedure.

The success of such an approach (as well as its main drawback) is connected with an additive form of total self-energy (neglect of the interference between different contributions) in Eqn (4). This allows one to preserve the self-consistent set of equations derived in the standard DMFT. However, there are two significant distinctions from the conventional DMFT. First of all, the local Green function of an effective single-impurity problem takes the form of Eqn (5) at each step of the DMFT procedure. Second, during each DMFT iteration, external self-energy $\Sigma_{\mathbf{k}}(\mathrm{i}\omega)$ is recalculated within some (approximate) framework, taking into account, for instance, the interaction with collective modes (phonons, magnons, etc.) or with fluctuations of some order

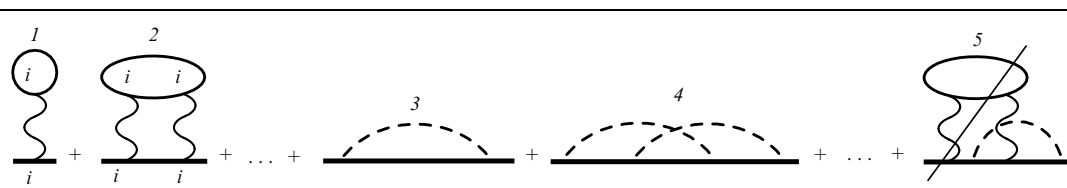

Figure 4. Typical skeleton self-energy diagrams of the DMFT + Σ approach.

parameter. To define nonlocal contribution $\Sigma_{\mathbf{k}}(\mathrm{i}\omega)$, it is convenient to introduce the function

$$\mathcal{G}_{0\mathbf{k}}(\mathrm{i}\omega) = \frac{1}{G_{\mathbf{k}}^{-1}(\mathrm{i}\omega) + \Sigma_{\mathbf{k}}(\mathrm{i}\omega)} = \frac{1}{\mathrm{i}\omega + \mu - \varepsilon(\mathbf{k}) - \Sigma(\mathrm{i}\omega)} \quad (11)$$

which plays the role of the bare Green function in building the perturbation theory with an external interaction as an expansion parameter. The choice of the bare Green function in the form of Eqn (11) guarantees that Green function 'dressed' by such an interaction, $G_{\mathbf{k}}^{-1}(\mathrm{i}\omega) = \mathcal{G}_{0\mathbf{k}}^{-1}(\mathrm{i}\omega) - \Sigma_{\mathbf{k}}(\mathrm{i}\omega)$, entering the skeleton diagrams for $\Sigma_{\mathbf{k}}(i\omega)$, coincides exactly with the full Green function $G_{\mathbf{k}}(\mathrm{i}\omega)$.

A remarkable feature of our approach is the possibility of its generalization to evaluate some two-particle properties, e.g. optical conductivity [38, 39]. The conductivity of a system is expressed via retarded density–density response function $\chi^{\mathrm{R}}(\omega, \mathbf{q})$ [40–42]:

$$\sigma(\omega) = -\lim_{q\to 0} \frac{\mathrm{i}e^2\omega}{q^2}\, \chi^{\mathrm{R}}(\omega, \mathbf{q})\,, \quad (12)$$

where e is electron charge. This response function is defined by analytical continuation to real frequencies of the full polarization loop in Matsubara representation [40, 41]. Note that conductivity is completely defined by the first derivative of this response function with respect to q^2 in the limit of $q \to 0$. This circumstance, as well as the neglect of interference between the local Hubbard and external interactions in the DMFT + Σ approach and the locality of irreducible vertices of the Hubbard interaction, allow one to perform a partial resummation of diagrams relevant for finding conductivity, making use of an exact (in the limit of $q \to 0$) Ward identity. In the end, the real part of optical conductivity in the DMFT + Σ approach has the form [38, 39]

$$\begin{aligned}\mathrm{Re}\,\sigma(\omega) = \frac{e^2\omega}{2\pi}\int_{-\infty}^{\infty} \mathrm{d}\varepsilon\big[f(\varepsilon_-) - f(\varepsilon_+)\big] \\ \times \mathrm{Re}\left\{\phi_\varepsilon^{0\mathrm{RA}}(\omega)\left[1 - \frac{\Sigma^{\mathrm{R}}(\varepsilon_+) - \Sigma^{\mathrm{A}}(\varepsilon_-)}{\omega}\right]^2 \right. \\ \left. - \phi_\varepsilon^{0\mathrm{RR}}(\omega)\left[1 - \frac{\Sigma^{\mathrm{R}}(\varepsilon_+) - \Sigma^{\mathrm{R}}(\varepsilon_-)}{\omega}\right]^2\right\}, \quad (13)\end{aligned}$$

where

$$\phi_\varepsilon^{0\mathrm{RR(RA)}}(\omega) = \lim_{q\to 0} \frac{\Phi_\varepsilon^{0\mathrm{RR(RA)}}(\omega, \mathbf{q}) - \Phi_\varepsilon^{0\mathrm{RR(RA)}}(\omega, 0)}{q^2} \quad (14)$$

and we introduced two-particle Green functions in the following form

$$\begin{aligned}\Phi_\varepsilon^{0\mathrm{RR(RA)}}(\omega, \mathbf{q}) = \sum_{\mathbf{k}} G^{\mathrm{R}}(\varepsilon_+, \mathbf{k}_+)\, G^{\mathrm{R(A)}}(\varepsilon_-, \mathbf{k}_-) \\ \times \Gamma^{\mathrm{RR(RA)}}(\varepsilon_-, \mathbf{k}_-; \varepsilon_+, \mathbf{k}_+)\,, \quad (15)\end{aligned}$$

which are diagrammatically represented in Fig. 5 ($\mathbf{k}_\pm = \mathbf{k} \pm \mathbf{q}/2$, and $\varepsilon_\pm = \varepsilon \pm \omega/2$). Vertices $\Gamma^{\mathrm{RR(RA)}}(\varepsilon_-, \mathbf{k}_-; \varepsilon_+, \mathbf{k}_+)$ contain all vertex corrections from external interactions (order parameter fluctuations, impurities, phonons, etc.) but *do not contain* vertex corrections from the Hubbard interaction.

Thus, one achieves a significant simplification of the problem. To calculate optical conductivity within the DMFT + Σ approach, we have only to solve the single-particle problem of obtaining the local self-energy $\Sigma(\varepsilon_\pm)$ with the help of the DMFT + Σ procedure described above,

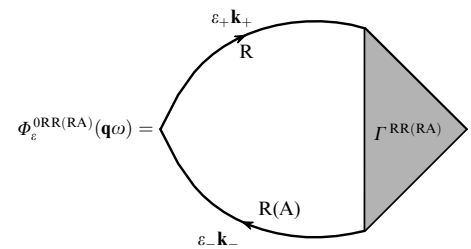

Figure 5. Diagrammatic representation of $\Phi_\varepsilon^{0\mathrm{RA}}(\omega, \mathbf{q})$ and $\Phi_\varepsilon^{0\mathrm{RR}}(\omega, \mathbf{q})$.

while a nontrivial contribution from nonlocal correlations or external perturbations enters via 'blocks' (14) which can be calculated in a suitable approximation accounting only for external interaction, with bare Green functions (11) containing the local self-energy from the DMFT + Σ procedure. In fact, Eqn (13) also provides an effective algorithm to compute optical conductivity in the framework of the conventional DMFT (neglecting all external nonlocal correlations). In this case, functions (14) could be easily found from the simple loop diagram defined by two Green functions and free *scalar* vertices. To get optical conductivity, there is actually no need to calculate vertex corrections in the framework of DMFT itself, as was first demonstrated for the loop with *vector* vertices in Refs [4, 5].

In what follows (see Sections 3 and 4), we shall discuss in detail some applications of the generalized DMFT + Σ approach to the solution of concrete physical problems.

2.3 Some other generalizations of DMFT

To date, a number of different theoretical approaches have been suggested to account for nonlocal effects within generalizations of DMFT. Here, we restrict ourselves to a brief review of some of these approaches.

First of all, we shall refer to the cluster methods already mentioned in Section 2.1. Instead of an isolated Anderson impurity, one can consider some cluster containing several such impurities, treating single-site correlations within DMFT, while considering intersite correlations with the aid of some other methods. This is the basic idea of the so-called cluster DMFT methods [5, 43–45].

A drawback of such approaches lies in the various treatment of nonlocal correlations inside a cluster and between clusters, though from the physical point of view (for example, because of translational invariance) they should be identical. To overcome this difficulty, it was proposed to average self-consistent 'cluster' self-energy over pairs of sites connected by translation vectors [43, 44]. Unfortunately, such an averaging procedure does not work well within the self-consistent DMFT cycle, since it breaks down the analytical properties of the Green function.

In some sense, the alternative approach referred to as the dynamical cluster approximation (DCA) was proposed in Refs [45–50]. This approach conserves translational invariance and ensures the physical behavior of the Green function. Within DCA, the Brillouin zone is divided into several cells with their centers defined by appropriate $\mathbf{K}$ vectors. At the same time, self-energy is assumed to be constant in each cell, $\Sigma_{\mathbf{k}}(\omega) = \Sigma_{\mathbf{K}}(\omega)$, but these constants differ for different $\mathbf{K}$. On going over to a direct space, a difference between DCA and cluster DMFT lies in the fact that a DMFT-cluster in DCA satisfies periodic boundary

conditions, instead of open boundary conditions, as in the cluster DMFT.

The choice of a particular cluster method is dictated by the physical problem under consideration. Naturally, the common drawback of cluster approaches deals with essentially more computational resources than in the standard DMFT, which is connected with the solution of the appropriate cluster problem. Nevertheless, a number of successes have been achieved in this path. Cluster DMFT generalizations were applied to different models, as well as to studies of some realistic systems. A detailed review of this work can be found in Ref. [32].

Recently, a number of diagrammatic DMFT generalizations have been proposed, shooting for a more or less consistent construction of the perturbation theory with the inverse powers of spatial dimensionality as an expansion parameter, and with the standard DMFT used as the zero-order approximation. We mention in this connection Ref. [51] and the so-called dynamical vertex approximation (DΓA) developed in Ref. [52]. Most promising in this respect seems to be the dual fermion approach formulated in Refs [53, 54], which puts in a claim on a consistent realization of such perturbation theory. Unfortunately, thus far only some simple model problems have been solved by applying these methods, while realistic systems have not yet been considered at all.

3. Application of generalized DMFT + Σ approach to model problems

3.1 Strongly correlated systems in the pseudogap state

3.1.1 Pseudogap fluctuations. A striking example of strongly correlated systems is provided by high-T_c cuprates. Parent stoichiometric cuprate compounds are antiferromagnetic (AFM) insulators with a well-developed optical gap and antiferromagnetism due to spin ordering on copper ions with a Néel temperature on the order of hundreds of kelvins. This insulating state is rapidly destroyed by the introduction of rather few doping impurities. Thus, these systems can be classified as doped Mott insulators with strong electronic correlations.

Among the many anomalies of the normal phase of high-temperature superconductors, observations of a pseudogap in the electronic spectra of underdoped cuprates are especially noteworthy [55, 56]. Despite continuing discussions about the physical nature of the pseudogap, the most preferable scenario of pseudogap formation from our point of view is that due to strong scattering of charge carriers on antiferromagnetic spin density wave (SDW) short-range order fluctuations [56, 57]. In the momentum representation, this scattering is characterized by momentum transfer on the order of $\mathbf{Q} = (\pi/a, \pi/a)$ (a is the two-dimensional lattice constant). This leads to the formation of certain features in the single-particle spectrum, which are precursors of changes in the spectra due to the appearance of AFM long-range order (period doubling). As a result, we end up with a non-Fermi liquid behavior (dielectrization) of the spectral density in the vicinity of so-called 'hot-spots' on the Fermi surface, appearing at intersections of the Fermi surface with the borders of the AFM Brillouin zone [56].

In the framework of this spin-fluctuation scenario, a simplified model of the pseudogap state was studied in Refs [56, 58–60]. This model is based on the assumption that, for high enough temperatures, the dynamics of spin fluctuations can be neglected, and one can consider instead the scattering of charge carriers by a static Gaussian random field (quenched disorder) of pseudogap fluctuations (AFM short-range order fluctuations). Scattering intensity on fluctuations is characterized by a narrow peak near scattering vectors on the order of $\mathbf{Q}$ with a width defined by inverse correlation length $\kappa = \xi^{-1}$ and corresponding energy scale Δ (on the order of pseudogap crossover temperature T^*).

For momentum-dependent self-energy, therefore, we shall concentrate on the case of electron scattering by such (SDW-like) antiferromagnetic spin fluctuations [a similar consideration also works fine for charge density wave (CDW-like) fluctuations] with short-range order. To calculate $\Sigma_{\mathbf{k}}(\mathrm{i}\omega)$ for the case of electrons propagating in a quenched random field of Gaussian spin (or charge) fluctuations with a dominating scattering momentum in proximity to characteristic vector $\mathbf{Q}$ ('hot-spot' model [56]), we shall apply the generalized version of the recurrent procedure proposed in Refs [58–61], allowing us to take into account *all* Feynman diagrams describing the scattering of electrons by this random field. This becomes possible because of a remarkable property of the simplified hot-spot model: *the contribution from an arbitrary diagram with crossing interaction lines is equal to the contribution of some diagram of the same order without crossing those lines* [61]. Thereby, we can restrict ourselves to the consideration of noncrossing diagrams only and take into account other diagrams by combinatorial prefactors attributed to interaction lines [60, 61]. Eventually, we arrive at the following recurrent relation for the self-energy (continuous fraction representation [60, 61]):

$$\Sigma_n(\mathrm{i}\omega, \mathbf{k}) = \Delta^2 \frac{s(n)}{\mathrm{i}\omega + \mu - \Sigma(\mathrm{i}\omega) - \varepsilon_n(\mathbf{k}) + \mathrm{i}n v_n \kappa - \Sigma_{n+1}(\mathrm{i}\omega, \mathbf{k})} \,. \tag{16}$$

Here, the term $\Sigma_n(\mathrm{i}\omega, \mathbf{k})$ of the recurrent procedure contains all diagrammatic contributions with the number of interaction lines $\geqslant n$. The recurrent procedure for $\Sigma_n(i\omega, \mathbf{k})$ converges rather fast: we can put $\Sigma_n(\mathrm{i}\omega, \mathbf{k})$ equal to zero for large enough n and, performing straightforward computations, obtain the desired physical self-energy at $n = 1$ [60], which can be subsequently used in the DMFT + Σ computational scheme:

$$\Sigma_{\mathbf{k}}(\mathrm{i}\omega) = \Sigma_{n=1}(\mathrm{i}\omega, \mathbf{k}) \,. \tag{17}$$

Parameter Δ entering formula (16) characterizes the energy scale (width) of the pseudogap, $\kappa = \xi^{-1}$ is the inverse correlation length of SDW (CDW) fluctuations, $\varepsilon_n(\mathbf{k}) = \varepsilon(\mathbf{k} + \mathbf{Q})$ and $v_n = |v^x_{\mathbf{k}+\mathbf{Q}}| + |v^y_{\mathbf{k}+\mathbf{Q}}|$ for odd n, and $\varepsilon_n(\mathbf{k}) = \varepsilon(\mathbf{k})$ and $v_n = |v^x_{\mathbf{k}}| + |v^y_{\mathbf{k}}|$ for even n, where velocity projections $v^x_{\mathbf{k}}$ and $v^y_{\mathbf{k}}$ are defined by the usual derivatives of the bare electron dispersion $\varepsilon(\mathbf{k})$ with respect to corresponding momentum components. Finally, $s(n)$ are combinatorial prefactors defining the number of coinciding diagrams:

$$s(n) = n \,, \tag{18}$$

for the case of commensurate charge (CDW type) fluctuations with $\mathbf{Q} = (\pi/a, \pi/a)$ [61]. For incommensurate CDW fluctuations [61] (when $\mathbf{Q}$ is not related to the lattice period), we get

$$s(n) = \begin{cases} \dfrac{n+1}{2} & \text{for odd } n \,, \\ \dfrac{n}{2} & \text{for even } n \,. \end{cases} \tag{19}$$

If we want to take into account the spin (Heisenberg) structure of interaction with spin fluctuations for a nearly antiferromagnetic Fermi liquid (spin–fermion model [58, 59]), the diagram combinatorics become more complicated. Scattering processes preserving spin projection are controlled by commensurate combinatorics, while spin flip scattering is described by incommensurate diagrams ('charged' random field, according to Refs [58, 59]). In this model, the recurrent procedure (16) for a single-particle Green function remains the same, but with other combinatorial prefactors $s(n)$ [58, 59]:

$$s(n) = \begin{cases} \dfrac{n+2}{3} & \text{for odd } n\,, \\ \dfrac{n}{3} & \text{for even } n\,. \end{cases} \tag{20}$$

Obviously, this procedure introduces an important length scale ξ, missed in standard DMFT. Physically, this length scale reflects the influence of short-range order fluctuations (SDW or CDW) on an electronic bath surrounding the effective Anderson impurity in DMFT.

After obtaining the self-consistent solution of DMFT + Σ set of equations (5)–(10) allowing also for nonlocal fluctuations, one can calculate the spectral density $A(\omega, \mathbf{k})$:

$$A(\omega, \mathbf{k}) = -\frac{1}{\pi}\,\mathrm{Im}\,\frac{1}{\omega + \mu - \varepsilon(\mathbf{k}) - \Sigma(\omega) - \Sigma_{\mathbf{k}}(\omega)}\,, \tag{21}$$

where $\Sigma(\omega)$, $\Sigma_{\mathbf{k}}(\omega)$, and chemical potential μ have already been computed in a self-consistent way. The density of states can be found by integration of formula (21) over the Brillouin zone.

An analogous approach can also be developed to determine two-particle vertices. The basic idea employed here is the possibility of obtaining an arbitrary vertex diagram by introducing the 'external field' line into the corresponding self-energy diagram [62–64]. In the model under consideration, we can again restrict ourselves to noncrossing diagrams, while the contribution from all other diagrams can be accounted for by combinatorial prefactors $s(n)$ attributed to interaction lines [58–61]. Thus, all vertex diagrams are generated by the simple ladder diagrams with additional $s(n)$ prefactors linked to corresponding interaction lines [63, 64] (see also monograph [42]). Then, we obtain the following system of recurrent relations for the vertex $\Gamma^{\mathrm{RA}}(\varepsilon_-, \mathbf{k}_-; \varepsilon_+, \mathbf{k}_+)$ [64], where the contribution of local DMFT self-energy (obtained within the DMFT + Σ procedure) is already included:

$$\begin{aligned} \Gamma^{\mathrm{RA}}_{n-1}(\varepsilon_-, \mathbf{k}_-; \varepsilon_+, \mathbf{k}_+) = 1 + \Delta^2 s(n)\, G^{\mathrm{A}}_n(\varepsilon_-, \mathbf{k}_-)\, G^{\mathrm{R}}_n(\varepsilon_+, \mathbf{k}_+) \\ \times \Big\{ 1 + 2\mathrm{i} v_n \kappa k \big[\omega - \varepsilon_n(\mathbf{k}_+) + \varepsilon_n(\mathbf{k}_-) - \Sigma^{\mathrm{R}}(\varepsilon_+) \\ + \Sigma^{\mathrm{A}}(\varepsilon_-) - \Sigma^{\mathrm{R}}_{n+1}(\varepsilon_+, \mathbf{k}_+) + \Sigma^{\mathrm{A}}_{n+1}(\varepsilon_-, \mathbf{k}_-)\big]^{-1} \Big\} \\ \times \Gamma^{\mathrm{RA}}_n(\varepsilon_-, \mathbf{k}_-; \varepsilon_+, \mathbf{k}_+)\,, \end{aligned} \tag{22}$$

where

$$G^{\mathrm{R,A}}_n(\varepsilon_\pm, \mathbf{k}_\pm) = \frac{1}{\varepsilon_\pm - \varepsilon_n(\mathbf{k}_\pm) \pm \mathrm{i} n v_n \kappa - \Sigma^{\mathrm{R,A}}(\varepsilon_\pm) - \Sigma^{\mathrm{R,A}}_{n+1}(\varepsilon_\pm, \mathbf{k}_\pm)}\,. \tag{23}$$

'Physical' vertex $\Gamma^{\mathrm{RA}}(\varepsilon_-, \mathbf{k}_-; \varepsilon_+, \mathbf{k}_+)$ is defined as $\Gamma^{\mathrm{RA}}_{n=0}(\varepsilon_-, \mathbf{k}_-; \varepsilon_+, \mathbf{k}_+)$. Recurrent procedure (22) accounts for *all* diagrams of perturbation theory for the vertex part. In the limit of $\kappa \to 0$ $(\xi \to \infty)$, formula (22) can be reduced to a series investigated in Ref. [62] (see also Refs [58, 59]), which can be exactly summed in analytical form. The standard ladder approximation is reproduced if all combinatorial factors $s(n)$ in formula (22) are made equal to unity for all n [63]. The recurrent procedure for $\Gamma^{\mathrm{RR}}(\varepsilon_-, \mathbf{k}_-; \varepsilon_+, \mathbf{k}_+)$ differs from that in formula (22) by the evident change of $A \to R$ and by replacing the whole expression in curly brackets on the r.h.s. of Eqn (22) by unity.

Equations (4), (16), and (22), along with (13) and (14), describe the complete self-consistent procedure of calculating optical conductivity in our model within the framework of the DMFT + Σ approach.

An important aspect of our theory is the possibility of the microscopic calculation of both effective parameters Δ and ξ. For example, applying the two-particle self-consistent theory of Ref. [65], together with approximations introduced in Refs [58–60] for the two-dimensional Hubbard model, we derived a microscopic expression for Δ [35], which can be calculated within the standard DMFT. It can be shown, in particular, that for a wide range of hole doping the pseudogap amplitude Δ varies in the interval from t to $2t$ (t is the nearest neighbor hopping integral).

3.1.2 Basic electronic properties in the pseudogap state. Let us discuss results for the standard single-band Hubbard model on a square lattice with electron dispersion

$$\varepsilon(\mathbf{k}) = -2t(\cos k_x a + \cos k_y a) - 4t' \cos k_x a \cos k_y a\,, \tag{24}$$

where t and t' stand for the nearest and next-to-nearest hopping integrals.

The energy scale in the following is defined by the nearest neighbor hopping integral t, and the length scale by the lattice constant a. The numerical renormalization group (NRG) was used as the impurity solver [23, 24]. Detailed computational results on the single-particle properties demonstrating pseudogap anomalies can be found in Refs [35–37], and on optical conductivity in Ref. [38]. Here, we only discuss the most typical results corresponding mostly to the case of $t'/t = -0.4$ (characteristic for cuprates) and band filling $n = 0.8$ (hole doping).

Density of states and spectral function. Let us start with results obtained within the generalized DMFT + Σ approach for the densities of states (DOSs) corresponding to rather weak (compared with bandwidth) Coulomb interaction $U = 4t$. A characteristic feature of the strongly correlated metallic state is the coexistence of lower and upper Hubbard subbands split by Coulomb interaction U with the quasiparticle peak at the Fermi level [4, 5]. Because the unperturbed DOS for the square lattice has Van Hove singularity near the Fermi level, in general the peak on the Fermi level cannot be treated simply as a quasiparticle one. Actually, there are two contributions to this peak: (i) from a quasiparticle peak appearing in strongly correlated metals due to many-body effects, and (ii) from the smoothed Van Hove singularity of unperturbed DOS.[3]

[3] With an increase in Coulomb repulsion, the Van Hove singularity gradually transforms into a quasiparticle peak at $U = (6-8)t$.

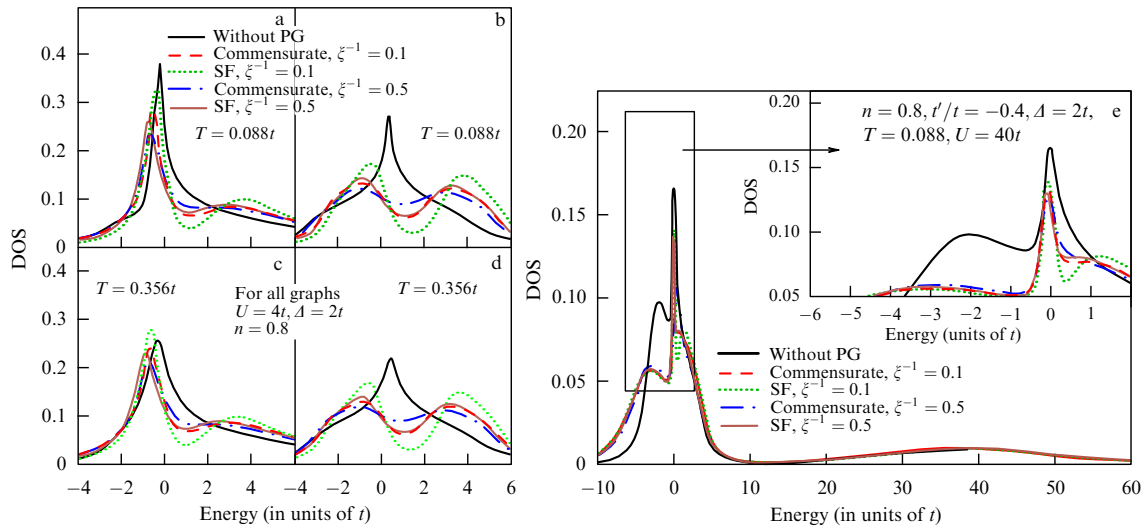

Figure 6. Comparison of DMFT(NRG) + Σ DOSs calculated in Ref. [35] for different combinatorial prefactors (SF — spin-fermion model, commensurate fluctuations), inverse correlation lengths ξ^{-1} (in units of the lattice constant), pseudogap amplitude $\Delta = 2t$, and band filling $n = 0.8$: (a–d) $U = 4t$, at $t'/t = -0.4$ (figures a, c) and $t' = 0$ (figures b, d), two temperatures $T = 0.088t$ (upper part) and $T = 0.356t$ (lower part); (e) $U = 40t$, $T = 0.088t$. The Fermi level corresponds to zero energy.

On the left side of Fig. 6, we show DMFT + Σ DOSs with $n = 0.8$ for the case of $t'/t = -0.4$ (left panel) and $t' = 0$ (right panel) for two different temperatures $T = 0.356t$ (lower panel) and $T = 0.088t$ (upper panel). Black solid curves were obtained in the absence of fluctuations. The other curves in Fig. 6 present results for DOSs with nonlocal fluctuations with amplitude $\Delta = 2t$. For all parameter sets, we see that the introduction of nonlocal fluctuations leads to pseudogap formation on a quasiparticle peak. The width of the pseudogap (energy interval between corresponding peaks in the DOSs) is on the order of 2Δ. A decrease in the value of Δ from $2t$ to t gives a pseudogap width that is half the size and makes it less deep. A more pronounced pseudogap is found for spin-fermion-model combinatorial prefactors [see formula (20)], as compared with the case of commensurate charge fluctuations [combinatorial prefactors (19)]. The influence of the correlation length value corresponds to general expectations. A decrease in correlation length, or an increase from $\xi^{-1} = 0.1$ to $\xi^{-1} = 0.5$ for inverse correlation length, slightly smears the pseudogap. The rise in temperature from $T = 0.088t$ to $T = 0.356t$ leads to general broadening of DOS structures. One should note that DMFT + Σ results at $U = 4t$ (which is less than the bandwidth W) are qualitatively similar to the results obtained earlier in the absence of the Hubbard interaction [58–60].

Let us consider now the case of a doped Mott insulator with a Hubbard interaction value of $U = 40t$, $t'/t = -0.4$ and band filling $n = 0.8$ (right side of Fig. 6e). A characteristic feature of the DOSs for such strongly correlated metals is the strong splitting of the lower and upper Hubbard bands, with the Fermi level falling within the lower Hubbard band (the case of hole doping). In the absence of nonlocal fluctuations, the quasiparticle peak is again formed on the Fermi level. However, the upper Hubbard band resides now quite far away to the right and does not touch the quasiparticle peak (as it does for weak Coulomb interaction).

For strong enough nonlocal fluctuations with $\Delta = 2t$, the pseudogap appears in the middle of the quasiparticle peak, and the lower Hubbard band is slightly broadened by fluctuation effects. Qualitatively, pseudogap anomaly behavior reminds us of that described above for the case of $U = 4t$ — a decrease in ξ smears the pseudogap and makes it less pronounced, and a decrease in Δ from $\Delta = 2t$ to $\Delta = t$ narrows the pseudogap and makes it more shallow (see Ref. [35]). Let us also notice that, for the doped Mott insulator, pseudogap is more evident for spin SDW-like fluctuations than for charge CDW-like ones.

Nevertheless, there are quite appreciable distinctions in contrast to the $U = 4t$ case. For example, the width of the pseudogap in the DOS is found to be essentially smaller than 2Δ, which is connected, in our opinion, with noticeable narrowing of the quasiparticle peak itself caused by local correlations.

In Fig. 7, we show spectral densities $A(\omega, \mathbf{k})$, calculated within the DMFT + Σ approach, along high-symmetry directions of the first Brillouin zone: $\Gamma(0,0)-\mathrm{X}(\pi,0)-\mathrm{M}(\pi,\pi)-\Gamma(0,0)$. In fact, this figure displays the quasiparticle band of a many-body system — positions of maxima of spectral densities specify quasiparticle dispersion, while their width defines quasiparticle damping. Also, we clearly observe the partial reconstruction ('destruction') of this band by pseudogap fluctuations. One can see a characteristic double-peak pseudogap structure in proximity to the X-point of the Brillouin zone. In the middle of the $\mathrm{M}-\Gamma$ direction (the so-called 'nodal' point), one can observe the emergence of the pseudogap, i.e. the presence of 'memory' of the AFM gap, which has a maximum here in the case of AFM long-range order. Generally speaking, changing the filling leads to a common shift of spectral functions with respect to the Fermi level.

Fermi surface 'destruction'. Within conventional DMFT, the Fermi surface is not renormalized by interaction, i.e. it remains the same as for bare quasiparticles [3]. However, in the case of nontrivial momentum dependence of self-energy, substantial renormalization of the Fermi surface may occur due to pseudogap formation [58, 59]. There are several ways

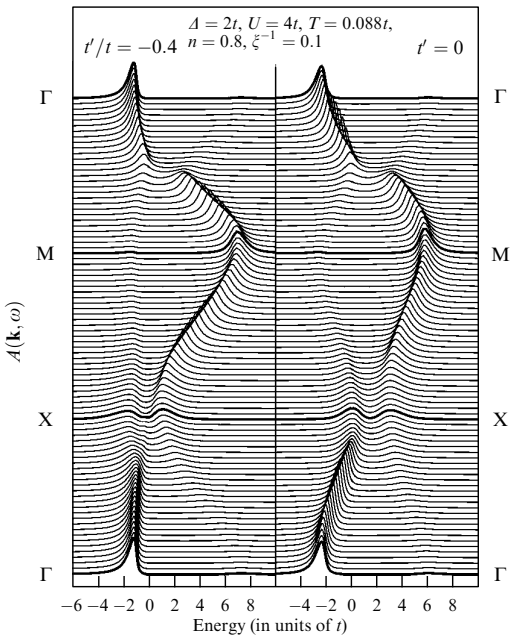

Figure 7. DMFT(NRG) + Σ spectral densities $A(\mathbf{k}, \omega)$ [35] along high-symmetry directions of the first Brillouin zone $\Gamma(0,0)$–$X(\pi,0)$–$M(\pi,\pi)$–$\Gamma(0,0)$, for spin-fermion diagram combinatorics (SF). The Fermi level is at zero energy.

to define the Fermi surface for strongly correlated systems. Below, we shall exploit the intensity map of the spectral function (spectral density) (21) at $\omega = 0$, which is often called the Fermi surface map. Such a map is directly measured in ARPES experiments, and positions of its intensity maxima specify the Fermi surface in the sense of the usual Fermi-liquid theory, where quasiparticle damping becomes negligibly small.

On the left side of Fig. 8, these maps are displayed for strongly correlated metal with $U = 4t$. This contour plot of the spectral function clearly demonstrates the 'destruction' of the Fermi surface in the 'hot-spots', attended with the formation of the 'Fermi arcs' upon Δ growth, similar to that observed in the pioneer work of Ding et al. [66], which was later confirmed in a large number of other studies. One should note that qualitatively analogous behavior is also evidenced in the absence of local electron correlations ($U = 0$) [36, 67]. The role of finite U values adds up to a decrease in spectral function intensity when compared with the case of $U = 0$ and leads to additional 'smearing', making hot-spots less visible. Destruction of the Fermi surface starts in the vicinity of hot spots for small Δ, but practically simultaneously it disappears in the whole antinodal region [near points X(π,0), Y(0,π)] of the Brillouin zone, while only 'Fermi arcs' in the nodal region remain, with the shape close to the bare Fermi surface. Those results naturally explain why in ARPES experiments the clear hot spots behavior is rather rarely observed [68]. The question of the possibility of observing hot spots will be elucidated in more detail in Section 4.4 below, devoted to the LDA + DMFT + Σ description of realistic cuprates.

In the case of a doped Mott insulator with $U = 40t$, shown in Fig. 8b, we see that the Fermi surface is rather ill-defined for all values of Δ. The profile of the spectral function is significantly more smeared for the smaller values of U, reflecting the important role of local correlations.

For comparison, we also show in Fig. 8 the renormalized Fermi surfaces obtained in this model by formal solution of equation (25) [4]

$$\omega - \varepsilon(\mathbf{k}) + \mu - \mathrm{Re}\,\Sigma(\omega) - \mathrm{Re}\,\Sigma_{\mathbf{k}}(\omega) = 0 \qquad (25)$$

at $\omega = 0$, used, for example, in the studies [58, 59]. Obviously, this definition gives a Fermi surface close to the one obtained from the intensity map for small Δ, but does not account for its significant damping essential for large Δ. For large

[4] This definition is used in the standard Fermi-liquid theory. In fact, in our particular case the influence of nonlocal pseudogap fluctuations leads to qualitative changes in the simple Fermi-liquid picture. Herewith, we leave aside the question of whether the Fermi-liquid theory is applicable on such a defined Fermi surface or not, as well in the limit $T \to 0$, since the static approximation used is by construction the high-temperature one — short-range order AFM fluctuations can be considered as quasistatic only if $T \gg \omega_{\mathrm{SF}}$, where ω_{SF} is the characteristic frequency of spin fluctuations [58–60].

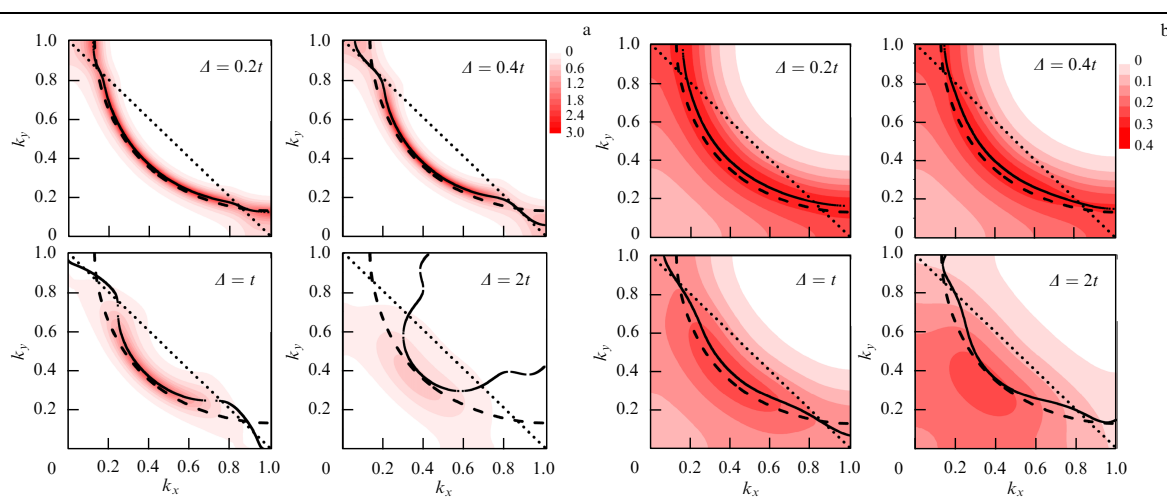

Figure 8. DMFT(NRG) + Σ picture of Fermi surface 'destruction' taken from Ref. [36]. On the left for $U = 4t$, and on the right for $U = 40t$ at various values of Δ specified in the figures. Band filling is $n = 0.8$. Dashed lines — 'bare' Fermi surface, dotted lines — boundaries of a Brillouin magnetic zone, and solid lines — solutions of equation (25).

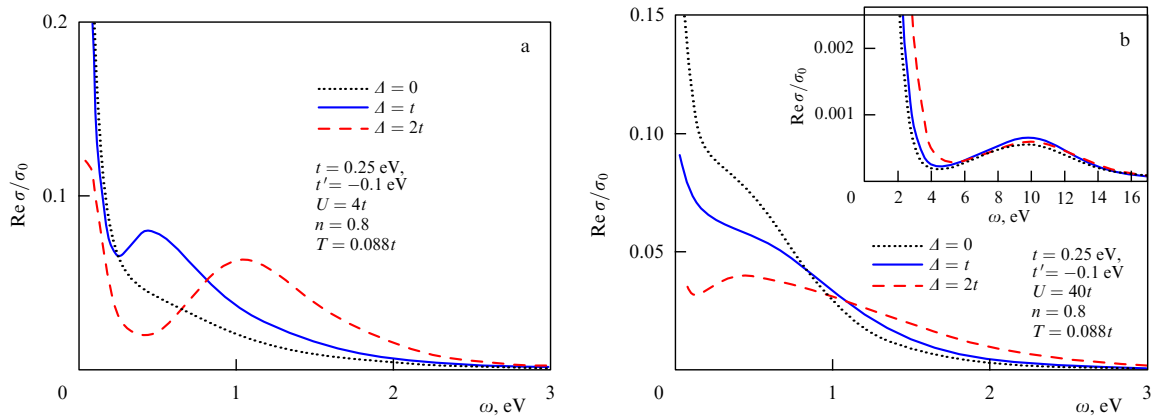

Figure 9. Real part of DMFT + Σ optical conductivity ($t' = -0.4t$, $t = 0.25$ eV) evaluated in Ref. [38] for various values of the pseudogap amplitude: $\Delta = 0, \Delta = t, \Delta = 2t$. Temperature is $T = 0.088t$, band filling $n = 0.8$ and correlation length $\xi = 10a$. (a) Strongly correlated metal with $U = 4t$. (b) Doped Mott insulator with $U = 40t$. Inset displays conductivity in a wide frequency range which includes transitions to the upper Hubbard band.

pseudogap amplitudes, this definition of the Fermi surface is qualitatively adequate for the true behavior, resulting from spectral function analysis, only in the nodal region. It is the contour plot of the spectral function (at $\omega = 0$) that gives the most complete and natural representation of the Fermi surface for systems with strong correlations and nonlocal fluctuations of some order parameter, which are present in a wide region of the phase diagram of high-T_c cuprate type systems because of their lessened dimensionality. Results obtained in a such an approach directly correspond to ARPES experiments, where exactly this definition of the Fermi surface is most conventional.

Optical conductivity. Let us set about discussing DMFT + Σ results for optical conductivity in the pseudogap state. In the left panel of Fig. 9, we give DMFT + Σ results for the real part of optical conductivity in the case of strongly correlated metal ($U = 4t$) for different pseudogap amplitudes. We clearly observe the formation of a typical pseudogap anomaly on the 'shoulder' of the Drude peak, and, as would be expected, it grows as Δ increases. This behavior is rather similar to the 'mid-infrared feature' which is evidenced in the optical conductivity of cuprate superconductors [69, 70]. The rise in temperature and decrease in fluctuation correlation length smear the pseudogap, making this anomaly less pronounced [38].

The right panel of Fig. 9 demonstrates DMFT + Σ optical conductivity of a doped Mott insulator ($U = 40t$) for several values of the pseudogap amplitude. We see that the frequency range, where the pseudogap anomaly manifests itself, gets narrower with the growth in local correlation strength, and for large U values pseudogap anomalies are strongly suppressed. Pseudogap fluctuations lead to noticeable changes in optical conductivity only for relatively low frequencies of order Δ. For higher frequencies (e.g. on the order of U, where transitions to the upper Hubbard band take place), pseudogap effects do not show themselves (see also inset to the right panel of Fig. 9). For low frequencies, we observe suppression of the Drude peak with a rather weak anomaly near $\omega \sim \Delta$, which disappears for small Δ or for short correlation lengths.

3.2 Mott–Anderson transition in disordered systems

The importance of accounting for both electron interactions and disorder effects in condensed matter research is well known [71, 7]. Coulomb interactions and disorder are two driving forces leading to metal–insulator transitions, connected with localization and delocalization of charge carriers. In particular, the Mott–Hubbard transition is caused by electron repulsion [1, 73], while the Anderson metal–insulator transition is related to the scattering of noninteracting particles by impurities [74]. It is well known that a subtle competition between disorder and interaction effects has many manifestations [71, 72, 75, 76]. This problem is most relevant in the case of strong disorder and strong electron correlations, determining the physical mechanisms of the Mott–Anderson metal–insulator transition [71, 72].

One of the main models allowing for the account of both electronic correlations (leading to the Mott metal–insulator transition [1, 73]) and strong disorder effects (leading to the Anderson metal–insulator transition) is the Anderson–Hubbard model [39, 77–82].

In Refs [77–79], the three-dimensional Anderson–Hubbard model was investigated in the framework of dynamical mean-field theory [3–5, 14]. The influence of local disorder was taken into account through averaged densities of states [83, 84] within the well-known coherent potential approximation (CPA) which does not describe Anderson localization. To overcome this difficulty, Dobrosavljević and Kotliar [77] have proposed a version of DMFT where the self-consistent solution of stochastic DMFT equations for an ensemble of systems with given realizations of disorder was used to calculate the averaged logarithmic (geometric mean) density of states, which gives information on critical disorder for the Anderson transition. This approach was further developed in Refs [78, 89], where a highly nontrivial phase diagram of the three-dimensional paramagnetic Anderson–Hubbard model [79] was obtained, containing a correlated metal phase, a Mott insulating phase, and a correlated Anderson insulator phase. The main problem of the approach worked out in Refs [77–79] is the impossibility of direct computation of measurable physical properties, such as conductivity which actually defines the metal–insulator transition.

At the same time, there exists the well-developed self-consistent theory of Anderson localization, based on the solution of equations for the generalized diffusion coefficient. The efficiency of this approach in the absence of interactions has been known for a long time [40–42, 56, 85–87]; certain attempts to include interaction effects in this

approach were undertaken with some promising results in Refs [86, 88, 89]. However, up to now this approach has not been extended to the modern theory of strongly correlated systems. Such an investigation was performed for the first time in Ref. [39] for three-dimensional systems, and later for the two-dimensional case [90].

Let us consider the disordered paramagnetic Anderson–Hubbard model at (mostly) half-filling for arbitrary interaction strength and disorder. Obviously, this model contains both Mott–Hubbard and Anderson metal–insulator transitions. The Hamiltonian of the model is given by

$$H = -t \sum_{\langle ij \rangle \sigma} a^{\dagger}_{i\sigma} a_{j\sigma} + \sum_{i\sigma} \epsilon_i n_{i\sigma} + U \sum_i n_{i\uparrow} n_{i\downarrow} , \tag{26}$$

where $t > 0$ is the nearest neighbor hopping amplitude, while U is on-site Hubbard repulsion, $n_{i\sigma} = a^{\dagger}_{i\sigma} a_{i\sigma}$ is the particle number operator on site, and $a_{i\sigma}$ ($a^{\dagger}_{i\sigma}$) is the annihilation (creation) operator of electrons on site i with spin σ. Local energies ϵ_i are assumed to be random and independent on different lattice sites. To simplify the diagram technique hereinafter, we assume the Gaussian distribution for ϵ_i:

$$\mathcal{P}(\epsilon_i) = \frac{1}{\sqrt{2\pi}\Delta} \exp\left(-\frac{\epsilon_i^2}{2\Delta^2} \right) . \tag{27}$$

Parameter Δ here is the measure of disorder. Such a Gaussian random field ('white noise') of energy levels ϵ_i at different lattice sites is equivalent to impurity scattering and can be described by the standard diagram technique for the averaged Green functions [42].

Self-energy $\Sigma_{\mathbf{p}}(\mathrm{i}\varepsilon)$ brought about by scattering on disorder may be evaluated in the simple one-loop approximation neglecting 'crossing' diagrams (i.e. in the self-consistent Born approximation) [42], which gives for Gaussian disorder (27) the following result

$$\Sigma_{\mathbf{p}}(\mathrm{i}\varepsilon) = \Delta^2 \sum_{\mathbf{p}} G(\mathrm{i}\varepsilon, \mathbf{p}) \equiv \Sigma_{\mathrm{imp}}(\mathrm{i}\varepsilon) , \tag{28}$$

so that our 'external' self-energy turns out to be independent of $\mathbf{p}$ momentum (i.e., local).

To analyze optical conductivity, we shall apply the general DMFT + Σ expression (13). The most important block $\Phi_{\varepsilon}^{0\mathrm{RA}}(\omega, \mathbf{q})$ can be evaluated using the ideology of self-consistent theory of localization [40–42, 56, 85–87], with some generalizations accounting for the role of Hubbard interaction via the DMFT + Σ approach [39, 90]. The main distinction from the standard derivation of the equations of self-consistent theory of localization is the use of Green functions (4) containing a local contribution to self-energy from the Hubbard interaction.

Following the standard derivation [40–42, 56, 85–87], we obtain a diffusion-like (for small ω and q) contribution to $\Phi_{\varepsilon}^{0RA}(\omega, \mathbf{q})$, which takes the form

$$\Phi_{\varepsilon}^{0\mathrm{RA}}(\tilde{\omega}, \mathbf{q}) = \frac{2\pi \mathrm{i} N(\varepsilon)}{\tilde{\omega} + \mathrm{i} D(\omega)\, q^2} , \tag{29}$$

where $D(\omega)$ is the generalized diffusion coefficient, and an important difference from the single-particle case is contained in the term

$$\begin{aligned} \tilde{\omega} &= \varepsilon_+ - \varepsilon_- - \Sigma^{\mathrm{R}}(\varepsilon_+) + \Sigma^{\mathrm{A}}(\varepsilon_-) \\ &= \omega - \Sigma^{\mathrm{R}}(\varepsilon_+) + \Sigma^{\mathrm{A}}(\varepsilon_-) \equiv \omega - \Delta\Sigma^{\mathrm{RA}}(\omega) , \end{aligned} \tag{30}$$

which substitutes for the usual ω term in the denominator of the standard expression for $\Phi_{\varepsilon}^{0\mathrm{RA}}(\omega, \mathbf{q})$. From general considerations, it is clear that in the metallic phase as $\omega \to 0$ we have $\Delta\Sigma^{\mathrm{RA}}(\omega = 0) = 2\mathrm{i}\,\mathrm{Im}\Sigma(\varepsilon) \sim \max\{T^2, \varepsilon^2\}$, which reflects the Fermi-liquid behavior in DMFT (which is not violated by elastic impurity scattering). For finite T, it leads to the usual phase decoherence caused by (inelastic) electron–electron scattering [71, 72, 75, 76].

Equation (13) then takes the form

$$\begin{aligned} \mathrm{Re}\,\sigma(\omega) &= \frac{e^2\omega}{2\pi} \int_{-\infty}^{\infty} \mathrm{d}\varepsilon \left(f(\varepsilon_-) - f(\varepsilon_+) \right) \\ &\times \mathrm{Re}\left[\frac{2\pi N(\varepsilon)\, D(\omega)}{\omega^2} - \phi_{\varepsilon}^{0\mathrm{RR}}(\omega) \left(1 - \frac{\Delta\Sigma^{\mathrm{RR}}(\omega)}{\omega} \right)^2 \right], \end{aligned} \tag{31}$$

where the second term in square brackets can, in fact, be neglected for small ω, while, if needed to describe a wide frequency range, it can be calculated using formula (14) with $\Phi_{\varepsilon}^{0\mathrm{RR}}(\omega, \mathbf{q})$ taken in the usual ladder approximation.

Next, following the standard framework of the self-consistent theory of localization [40–42, 56, 85–87], we get the closed self-consistent equation for the generalized diffusion coefficient

$$\begin{aligned} D(\omega) = \mathrm{i}\, \frac{\langle v \rangle^2}{d} \Bigg(&\tilde{\omega} - \Delta\Sigma_{\mathrm{imp}}^{\mathrm{RA}}(\omega) \\ &+ \Delta^4 \sum_{\mathbf{p}} (\Delta G_{\mathbf{p}})^2 \sum_{\mathbf{q}} \frac{1}{\tilde{\omega} + \mathrm{i} D(\omega)\, q^2} \Bigg)^{-1} , \end{aligned} \tag{32}$$

where d is the spatial dimensionality, $\Delta G_{\mathbf{p}} = G^{\mathrm{R}}(\varepsilon_+, \mathbf{p}) - G^{\mathrm{A}}(\varepsilon_-, \mathbf{p})$, $\Delta\Sigma_{\mathrm{imp}}^{\mathrm{RA}}(\omega) = \Sigma_{\mathrm{imp}}^{\mathrm{R}}(\varepsilon_+) - \Sigma_{\mathrm{imp}}^{\mathrm{A}}(\varepsilon_-)$, and average velocity $\langle v \rangle$, which can be well approximated just by the Fermi velocity, is given by the following expression

$$\langle v \rangle = \frac{\sum_{\mathbf{p}} |\mathbf{v}_{\mathbf{p}}|\, \Delta G_{\mathbf{p}}}{\sum_{\mathbf{p}} \Delta G_{\mathbf{p}}} , \tag{33}$$

where $\mathbf{v}_{\mathbf{p}} = \partial\epsilon(\mathbf{p})/\partial\mathbf{p}$. Equation (32) should be solved jointly with following the self-consistent DMFT + Σ procedure (5)–(10), (28). In fact, this equation is a transcendental one and can be easily solved by iterations for each $\tilde{\omega}$ value.

In accordance with the usual applicability limit of the diffusion approximation, summation over q in Eqn (32) should be restricted to [42, 86]

$$q < k_0 = \min\{l^{-1}, p_{\mathrm{F}}\} , \tag{34}$$

where $l = \langle v \rangle / 2\gamma$ is an elastic mean free path, γ is the Born scattering frequency by impurities, and p_{F} is the Fermi momentum. It is well known that in the two-dimensional case Anderson localization occurs at any infinitely weak disorder. However, the localization radius in this case is exponentially large, and the sample size begins to play a significant part. Sample size L can be introduced into the self-consistent theory of localization by cutting off the integration of the diffusion pole at small q [40, 41, 85], i.e. at

$$q \sim k_L = \frac{1}{L} . \tag{35}$$

When $\omega \to 0$ [and obviously $\tilde{\omega} \to 0$ on the Fermi surface ($\varepsilon = 0$)], in the Anderson insulator phase one gets a localization behavior of the generalized diffusion coeffi-

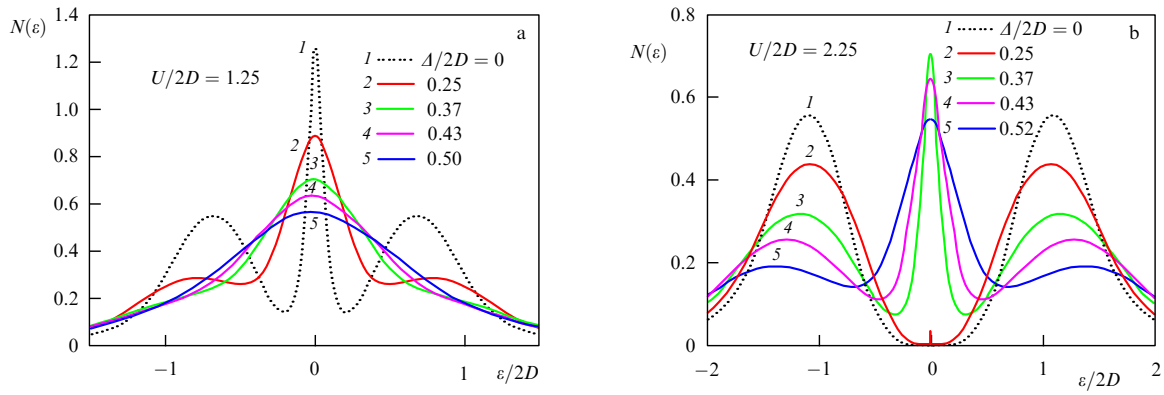

Figure 10. Anderson–Hubbard model density of states at half-filling for various disorder levels Δ [39]: (a) correlated metal with $U = 2.5D$, and (b) Mott insulator with $U = 4.5D$.

cient [40–42, 85]:

$$D(\omega) = -\mathrm{i}\tilde{\omega} R_{\mathrm{loc}}^2 \,. \tag{36}$$

After substituting formula (36) into equation (32), one obtains an equation defining localization radius R_{loc}:

$$R_{\mathrm{loc}}^2 = -\frac{\langle v\rangle^2}{d\Delta^4}\left\{\sum_{\mathbf{p}}(\Delta G_{\mathbf{p}})^2 \sum_{\mathbf{q}} \frac{1}{1 + R_{\mathrm{loc}}^2 q^2}\right\}^{-1}. \tag{37}$$

3.2.1 Three-dimensional systems. Below, we present the most interesting results for the three-dimensional Anderson–Hubbard model at half-filling on a cubic lattice with a model semielliptic bare density of states with the bandwidth $W = 2D$:

$$N_0(\varepsilon) = \frac{2}{\pi D^2}\sqrt{D^2 - \varepsilon^2}\,. \tag{38}$$

The density of states is always given in units of the number of states per energy interval for a unit cell of the volume a^3 (a is the lattice constant) and for one spin projection. Conductivities are given in natural units of $e^2/\hbar a$. For more detailed numerical results (also accounting for deviations from half-filling), we refer the reader to paper [39].

Evolution of the density of states. Within the standard DMFT approach, the Hubbard model density of states at half-filling has a typical three-peak structure [4, 5, 91, 92] with a narrow quasiparticle band (central peak) at the Fermi level and wide upper and lower Hubbard bands situated at energies $\varepsilon \sim \pm U/2$. As U grows, the quasiparticle band narrows within the metallic phase and disappears at the Mott–Hubbard metal–insulator transition at critical interaction $U_{c2} \approx 1.5W$. With a further increase in U, the insulating gap opens at the Fermi level.

We present in Fig. 10 our results for DMFT + Σ densities of states for a typical strongly correlated metal with $U = 2.5D = 1.25W$, in the absence of disorder and for different values of disorder Δ, including strong enough disorder transforming a correlated metal into a correlated Anderson insulator (see also below the discussion concerning optical conductivity). As one would expect, disorder leads to typical broadening and suppression of the density of states.

More unexpected is the result obtained for $U = 4.5D = 2.25W$, typical for Mott insulators and shown in the right panel of Fig. 10. Here we observe restoration of the central peak (quasiparticle band) in the DOS with an increase in disorder, transforming the Mott insulator into a correlated metal or into a correlated Anderson insulator. Similar DOS behavior was also reported in Ref. [79].

The physical origin of such quite unexpected central peak restoration is pretty clear. The control parameter of metal–insulator transition in DMFT is the ratio of Hubbard interaction U to bare bandwidth $W = 2D$. With disorder coming into play (in the absence of Hubbard interaction), new effective bandwidth W_{eff} appears and grows with increasing disorder. A semielliptic form of the DOS with well-defined band edges in the self-consistent Born approximation (28) is preserved. This all leads to diminishing the ratio U/W_{eff}, which in turn causes restoration of the quasiparticle band. This issue is discussed in more detail below, when considering the phase diagram of the Anderson–Hubbard model.

In the absence of disorder, a characteristic feature of the Mott–Hubbard metal–insulator transition is hysteresis DOS behavior appearing with a decrease in U starting from the insulating phase [5, 91, 92]. The Mott insulating phase is conserved (metastable) down to rather small U values 'wedging' deep in the correlated metal phase. The metallic phase is restored only at about $U_{c1} \approx 1.0W$. Corresponding interval $U_{c1} < U < U_{c2}$ is typically considered a coexistence region of the metallic and Mott insulating phases, where, from a thermodynamic point of view, the metallic phase is more stable [5, 91–93]. Such hysteresis DOS behavior (see Ref. [39]) is also observed in the presence of disorder and will be described below during the discussion of the phase diagram of the Anderson–Hubbard model.

Optical conductivity: Mott–Hubbard and Anderson transitions. Without disorder, our calculations reproduce conventional DMFT results [4, 5], where optical conductivity is characterized by the usual Drude peak at low frequencies and a wide maximum at about $\omega \sim U$, which corresponds to optical transitions to the upper Hubbard band. As U grows, the Drude peak diminishes and disappears at the Mott transition, when only the contribution from transitions through the Mott–Hubbard gap remains valid. The introduction of disorder leads to a qualitative change in the frequency dependence of optical conductivity.

In the left panel of Fig. 11, we depict the real part of optical conductivity of the Anderson–Hubbard model at half-filling for different disorder levels Δ and $U = 2.5D$ typical for correlated metal. Then, transitions to the upper Hubbard

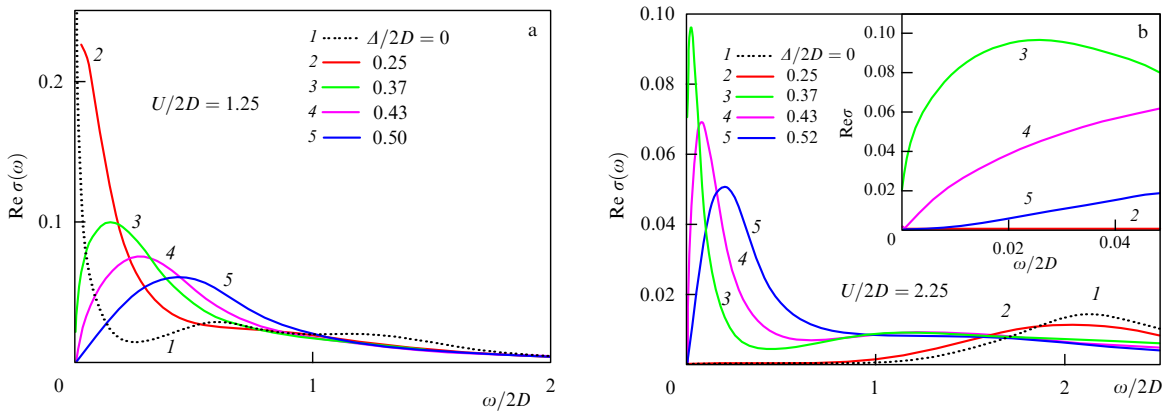

Figure 11. Real part of optical conductivity in the Anderson–Hubbard model at half-filling for different disorder levels Δ [39]. (a) Typical correlated metal with $U = 2.5D$. Curves *1*, *2* — metallic phase, curve *3* corresponds to the mobility edge (Anderson transition), and curves *4*, *5* — correlated Anderson insulator. (b) Typical Mott insulator with $U = 4.5D$. Curves *1*, *2* correspond to the Mott insulator, curve *3* — mobility edge (Anderson transition), and curves *4*, *5* — correlated Anderson insulator. Inset to figure b displays magnified low-frequency region.

bands at energies $\omega \sim U$ are almost unobservable. However, it is clearly visible that the metallic Drude peak typically centered at zero frequency is broadened and suppressed by disorder, gradually transforming into a peak at a finite frequency because of Anderson localization effects. The Anderson transition takes place at $\Delta_c \approx 0.74D = 0.37W$ (corresponding to curve *3* in all figures here and also in Fig. 10 for the DOS). Notice that this value depends on the cutoff (34) which is defined up to the coefficient of the order of unity [42, 86]. Naive expectations can bring us to the conclusion that the narrow quasiparticle band at the Fermi level, being formed in a strongly correlated metal, may be localized much more easily than the normal conduction band. However, we see that these expectations are wrong and the band localizes only at rather large disorder, $\Delta_c \sim D$, similar to that for the conduction band with a width of $\sim W$. The latter agrees with the known analysis of localization in the two-band model [94].

In the DMFT + Σ approach, critical disorder Δ_c does not depend on U, as interaction effects enter Eqn (32) only through $\Delta\Sigma^{RA}(\omega) \to 0$ as $\omega \to 0$ (for $T = 0$, $\varepsilon = 0$), and the influence of interaction at $\omega = 0$ disappears. In fact, this is the main shortcoming of the DMFT + Σ approach originating from the neglect of the interference effects between interaction and impurity scattering. Significant role of these interference effects has been known for a long time [71, 72, 75, 76]. On the other hand, the neglect of these effects allows performing the reasonable physical interpolation between two main limits — that of the Anderson transition because of disorder, and Mott–Hubbard transition because of strong correlations. Thus, one can consider this approximation as a reasonable first step to a future complete theory of metal–insulator transitions in strongly correlated disordered systems.

In Fig. 11b, we show the real part of optical conductivity of a Mott–Hubbard insulator with $U = 4.5D$ at different disorder levels Δ. In the inset to this figure we show low-frequency data demonstrating different types of conductivity behavior, especially close to the Anderson transition and within the Mott insulating phase. In the main part of the figure, the contribution to conductivity from transitions to the upper Hubbard band at about $\omega \sim U$ is distinctly seen. Disorder growth results in an origin of finite conductivity for the frequency range inside the Mott–Hubbard gap, which correlates with the restoration of the quasiparticle band in the DOS within the gap, as shown in Fig. 10b. This conductivity for $\Delta < \Delta_c$ is metallic (finite in the static limit $\omega = 0$), and for $\Delta > \Delta_c$ at low frequencies we get $\mathrm{Re}\,\sigma(\omega) \sim \omega^2$, which is typical for an Anderson insulator [40–42, 56, 85–87].

The appearance of a peak in $\mathrm{Re}\,\sigma(\omega)$ at low finite frequencies even in the metallic phase is a bit unusual. This happens because of the importance of localization effects. In the ladder approximation for $\Phi_\varepsilon^{0RA}(\omega, \mathbf{q})$, which neglects all localization corrections, we obtain the usual Drude peak at $\omega = 0$ [39], while the inclusion of localization effects shifts the peak in $\mathrm{Re}\,\sigma(\omega)$ to low (but finite) frequencies. As is well known [1], the metallic state is defined by finite static ($\omega = 0$) conductivity at zero temperature.

Above, we only presented conductivity data obtained when there is an increase in U from values typical to metallic phase to those for Mott insulating phase. As U decreases from values common to the Mott insulating phase, we observe the hysteresis of conductivity in the phase coexistence region defined (in the absence of disorder) by inequality $U_{c1} < U < U_{c2}$. A hysteresis of conductivity also shows itself in the coexistence region in the presence of disorder. Details of this behavior of optical conductivity can be found in Ref. [39].

Phase diagram of Anderson–Hubbard model at half-filling. The phase diagram of the Anderson–Hubbard model at half-filling was studied in Ref. [79], using direct DMFT calculations for the lattice with a finite number of sites with random realizations of energies ϵ_i in Hamiltonian (26) and subsequent averaging over these realizations to get an averaged DOS and geometrically mean local DOS which allows one to define critical disorder for transition into the Anderson insulator phase. Below, we present our results on the Anderson–Hubbard paramagnetic phase diagram with half-filling, obtained from the DOS and optical conductivity calculations within the DMFT + Σ approach. It should be emphasized that conductivity analysis is the most direct way to distinguish metallic and insulating phases [1].

A (Δ, U) phase diagram calculated at zero temperature in the disorder–correlation plane is shown in Fig. 12a. Anderson transition line $\Delta_c \approx 0.37W = 0.74D$ is defined as a disorder strength for which static conductivity becomes zero at $T = 0$.

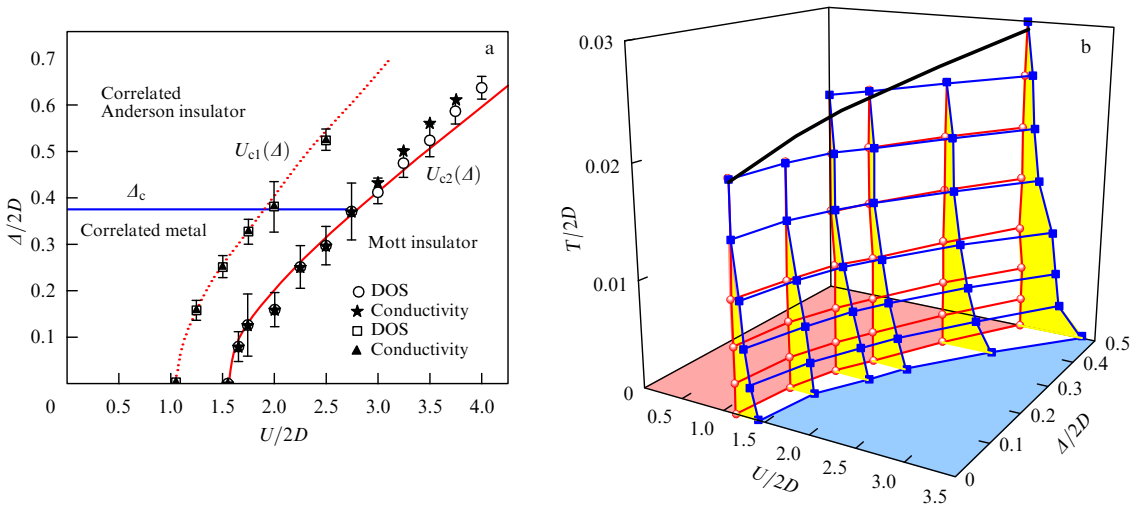

Figure 12. Phase diagram of the paramagnetic Anderson–Hubbard model. (a) Zero-temperature case [39]. Continuous curves $U_{c1,c2}(\Delta)$ are Mott insulating phase boundaries obtained from analytical estimate of Eqn (41); different symbols represent results for these boundaries obtained from calculations from the DOS and optical conductivity. Line of Anderson transition is given by $\Delta_c = 0.37$. (b) Boundaries of Mott insulating phase and phase coexistence region at various temperatures. Points are obtained from DOS calculations. Solid black curve is a linear fit $[T_c/2D = 0.02(1 + \Delta/2D)]$ to the T_c points, where the coexistence region disappears.

The Mott–Hubbard transition can be detected from the central (quasiparticle) peak disappearance in the DOS or from optical conductivity behavior based on observations of gap closing in the insulating phase or from static conductivity disappearance in the metallic phase.

We have already noticed that the DMFT + Σ approximation gives a universal (U-independent) strength of critical disorder Δ_c because of the neglect of interference between disorder scattering and Hubbard interaction. This leads to differences between the phase diagram of Fig. 12 and the one obtained in Ref. [79]. At the same time, the influence of disorder scattering on the Mott–Hubbard transition turns out to be highly nontrivial and qualitatively coincides overall with the results of Ref. [79]. The main distinction lies in the conservation of Hubbard bands in our results, even in the limit of high enough disorder, while in Ref. [79] they just disappear. Moreover, the phase coexistence region in Fig. 12 slowly widens with a disorder growth, instead of vanishing at some 'critical' point, as in the phase diagram of Ref. [79]. Coexistence region boundaries, which are defined by Mott insulating phase boundaries, obtained with an increase or decrease in U and represented by curves $U_{c1}(\Delta)$ and $U_{c2}(\Delta)$ in Fig. 12, can be obtained from the simple equation

$$\frac{U_{c1,c2}(\Delta)}{W_{\text{eff}}} = \frac{U_{c1,c2}}{W}\,, \tag{39}$$

where the effective bandwidth in the presence of disorder was calculated at $U = 0$ within the self-consistent Born approximation (28):

$$W_{\text{eff}} = W\sqrt{1 + 16\,\frac{\Delta^2}{W^2}}\,. \tag{40}$$

Thus, the boundaries of the phase coexistence region, which also define the Mott insulating phase boundaries, are given by

$$U_{c1,c2}(\Delta) = U_{c1,c2}\sqrt{1 + 16\,\frac{\Delta^2}{W^2}}\,. \tag{41}$$

Appropriate curves are plotted in Fig. 12 with dotted and solid lines. Phase transition points detected from the disappearance of a quasiparticle peak, as well as points following from qualitative changes in conductivity behavior, are shown in Fig. 12a by different symbols. These symbols demonstrate very good agreement with analytical results, supporting the choice of ratio (39) as a control parameter of Mott transition in the presence of disorder.

In Fig. 12b, we display the temperature dependence of Mott insulating phase boundaries $U_{c2}(\Delta)$ (squares) and the phase coexistence region $U_{c1}(\Delta)$ (circles).[5] It is well known that in 'pure' DMFT without disorder, the coexistence region narrows with temperature growth and vanishes at some critical temperature T_c. In the DMFT + Σ approach, the disorder strengthening at zero temperature widens the coexistence region, and this behavior remains for finite temperatures. It is also seen that disorder growth leads to a practically linear growth (solid black line) in this critical temperature. Noteworthy also is the very weak temperature dependence of the coexistence region boundary $U_{c1}(\Delta)$.

3.2.2 Two-dimensional systems. According to the scaling theory of localization [95], the metallic state in two-dimensional (2D) systems does not exists: electrons are localized already at any infinitely weak disorder. Despite the fact that this prediction for 2D systems was made for noninteracting particles, later it was found that the weak interaction among electrons in the simplest case also favors localization [96]. In the early 1980s, experiments done on different 2D systems [97–99] mostly confirmed these predictions. Later on, however, some theoretical studies [75, 76] pointed out that in general this point of view is incorrect, since in the limits of weak disorder and large enough interaction 2D systems can have finite conductivity at zero temperature. The experimental discovery of metal–insulator transition in 2D weakly disordered systems at low carrier concentration, absent in the single-particle theory, stimulated a new field of theoretical

[5] These results for different temperatures were calculated by N A Kuleeva.

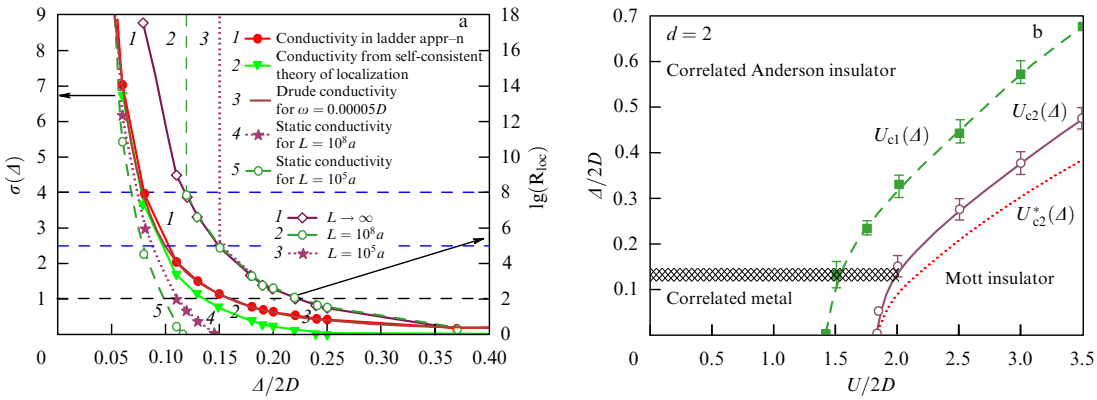

Figure 13. (a) Low finite frequency ($\omega = 0.00005D$) conductivity dependence on disorder strength Δ at $U/2D = 1$. Circles (curve *1*) show the results of ladder approximation, triangles (curve *2*) match the self-consistent theory of localization. Curve *3* (practically coinciding with the ladder approximation) is obtained from Drude formula (43). Curves *4* and *5* are the static conductivity of finite samples with sizes $L = 10^8 a$ and $L = 10^5 a$, respectively. On the right scale, localization radius logarithm is plotted versus disorder strength Δ: infinite-sized sample — curve *1*, samples with finite sizes $L = 10^8 a$ and $L = 10^5 a$ — curves *2* and *3*, respectively. (b) Phase diagram of the 2D paramagnetic Anderson–Hubbard model at zero temperature. Mott insulator region boundary $U_{c2}(\Delta)$ and phase coexistence region boundary $U_{c1}(\Delta)$ were obtained from density of states behavior. Hatched part exhibits the region of an effective Anderson metal–insulator transition in finite-sized systems. (Taken from Ref. [90].)

studies (see the introduction to this field in review papers [100, 101]).

In the DMFT + Σ approximation, as we shall see, the localization radius defined by Eqn (37) for infinite 2D system ($L \to \infty$) remains finite (even if exponentially large) for any infinitely weak disorder, signalling the absence of Anderson transition in such a system, similarly to the case of the conventional single-particle theory. However, as we shall demonstrate below, the localization radius in finite-sized systems diverges at some critical disorder which is defined by the characteristic size L of the system. Qualitatively, this critical disorder is determined by the condition that the localization radius of infinitely large system become comparable to characteristic sample size: $R_{\rm loc}^{L\to\infty} \sim L$. Thus, Anderson transition in finite two-dimensional systems in fact exists, as does the metallic phase for a disorder strength below some critical value. In the following, by 'correlated metal' phase we imply precisely such a phase for finite 2D systems.

Below, we discuss the most relevant results of the DMFT + Σ computations for the 2D Anderson–Hubbard model at half-filling on a square lattice with model rectangular bare density of states with the bandwidth $W = 2D$:

$$N_0(\varepsilon) = \begin{cases} \dfrac{1}{2D}\,, & |\varepsilon| \leqslant D, \\ 0\,, & |\varepsilon| > D, \end{cases} \tag{42}$$

which qualitatively corresponds precisely to a 2D case.

Density of states and optical conductivity. Calculations demonstrated that the qualitative behavior of the density of states in 2D systems is completely analogous to that discussed above in the three-dimensional case. Some quantitative distinctions are due to the different model of the bare density of states (42), leading in particular to a larger (than in the three-dimensional case) critical Hubbard interaction $U_{c2} \approx 1.83W$, corresponding to Mott metal–insulator transition in the absence of disorder, and $U_{c1} \approx 1.42W$, bounding from below the region of coexistence of metallic and insulating phases. Similar to the three-dimensional model for $U > U_{c2}$ (i.e. for a Mott insulator without disorder), an increase in disorder strength leads to restoration of the quasiparticle peak in the density of states. However, in this case such a behavior does not signal in general the transition to a correlated metal state — at least for infinitely large systems, we are dealing here with the correlated Anderson insulator.

Optical conductivity behavior in a wide frequency range is also qualitatively quite similar to that in the three-dimensional model. But for the infinite 2D model, zero-frequency conductivity always disappears (in the zero-temperature limit) and, in contrast to the $d = 3$ case [39], even at very weak disorder the peak in optical conductivity lies at a finite frequency. In the ladder approximation which does not contain localization corrections, the usual Drude peak is observed at zero frequency, and conductivity at $\omega = 0$ is finite.

More details concerning the results for the DOS and optical conductivity in the 2D model can be found in Ref. [90].

Localization radius and phase diagram of the 2D Anderson–Hubbard model at half-filling. In Fig. 13a, we illustrate the dependence of conductivity on disorder Δ at a finite but quite low frequency $\omega = 0.00005D$. Circles mark the results of ladder approximation, and triangles match the self-consistent theory of localization. Curve *3*, qualitatively coinciding with the ladder approximation, was obtained from the classical Drude expression

$$\sigma(\omega) = \sigma(0)\,\frac{\gamma^2}{\gamma^2 + \omega^2}\,, \tag{43}$$

where static conductivity $\sigma(0) = e^2 N(0) D_0 \approx (e^2/\hbar)\,\varepsilon_{\rm F}/(2\pi\gamma)$, $N(0)$ is the density of states at the Fermi level, and D_0 is the Drude diffusion coefficient. The impurity scattering rate was taken as $\gamma = \pi N(0)\,\Delta^2 \approx (\pi/2D)\,\Delta^2$. A significant contribution from localization corrections to conductivity at a finite frequency (a noticeable distinction of curve *2* from *1* and *3* curves) appears only when the conductivity reaches values on the order of minimal metallic conductivity $\sigma_0 = e^2/\hbar$ (whereon the conductivity is normalized in the figures). One should note that exactly in this range of disorder, as we shall see below, Anderson metal–insulator transition takes place (the localization radius diverges) in 2D systems of reasonable finite sizes.

Also in Fig. 13a, we demonstrate the dependences of the localization radius logarithm following from expression (37) (right scale) as a function of disorder strength: curve *1* is for an infinite sample, curves *2* and *3* are for finite-sized samples with $L = 10^8 a$ and $L = 10^5 a$, respectively. It is seen that the localization radius grows exponentially as disorder diminishes and remains finite in the infinite 2D system, where Anderson transition is absent. On the contrary, the localization radius for finite systems *diverges* at critical disorder determined by system size, demonstrating the existence of an effective Anderson transition. As can be seen from Fig. 13, the critical disorder is qualitatively defined by the condition that the localization radius of infinite system become comparable to the characteristic sample size $R_{\rm loc}^{L\to\infty} \sim L$. It should be noted that the localization radius barely depends on U within our approach (in contrast, for example, to paper [81]), which leads to the independence of critical disorder of correlation strength U in 2D finite-sized systems. An analogous situation is also realized in three-dimensional systems [39]. In general, it is, of course, a drawback to our approximations.

Also in Fig. 13a, we plot the dependence of static conductivity on disorder strength in finite samples with sizes $L = 10^8 a$ and $L = 10^5 a$ (curves *4* and *5*, respectively). In finite-sized systems with weak disorder, static conductivity is not zero (metal) and gradually falls with an increase in disorder strength. It becomes zero at critical disorder, where the localization radius also diverges in the sample of corresponding size. The static conductivity of finite-sized samples within our approximation barely depends on correlation strength U. A significant difference between static conductivity and conductivity at low finite frequency, observed in Fig. 13, is related to the above-mentioned exponential smallness of the frequency range with the localization behavior of conductivity.

Let us consider now the phase diagram of the 2D paramagnetic Anderson–Hubbard model at half-filling, obtained from DMFT + Σ calculated densities of states and from the analysis of localization radius behavior in finite-sized 2D systems. Such a phase diagram drawn in coordinates disorder (Δ) — correlation strength (U) is shown in the right part of Fig. 16.

The hatched stripe corresponds to the region of effective 'metal'–Anderson insulator transition. The boundaries of this region are determined by divergence of localization radius in finite samples with characteristic sizes $L = 10^5 a$ (upper boundary) and $L = 10^8 a$ (lower boundary) (see Fig. 13a). It should be emphasized that a further increase in the system size, e.g. tenfold, up to $L = 10^9 a$, leads only to a quite insignificant drop in critical disorder. In other words, it slightly shifts down the lower boundary of the hatched stripe (Fig. 13b) — characteristic region of an effective Anderson transition in finite-sized systems.

Curve $U_{\rm c2}(\Delta)$ computed from the density of states behavior defines the boundary of the Mott transition. The transition criteria are the disappearance of the central quasiparticle peak in the density of states $N(\varepsilon)$ together with gap opening on the Fermi level. Similarly to the three-dimensional model, a decrease in U starting from the insulating phase leads to the Mott transition at $U = U_{\rm c1}(\Delta) < U_{\rm c2}(\Delta)$ and a phase coexistence (hysteresis) region is observed in the phase diagram between curves $U_{\rm c1}(\Delta)$ and $U_{\rm c2}(\Delta)$ (Fig. 13b). In analogy with the three-dimensional case, we can guess that the ratio $U_{\rm c1,c2}(\Delta)/W_{\rm eff}(\Delta)$ between Hubbard interaction and effective bandwidth controls the Mott metal–insulator transition and is a universal constant which does not depend on disorder, and obtain qualitative dependence $U_{\rm c2}^*(\Delta)$ for the 2D model, which is fitted by the dotted curve in Fig. 13b. It is seen that, in contrast to the $d = 3$ case [39], the $U_{\rm c2}(\Delta)$ dependence obtained from straightforward calculations of densities of states significantly differs from the qualitative $U_{\rm c2}^*(\Delta)$ dependence. Apparently, it is related to the important change in the density-of-states lineshape (at $U = 0$) as disorder Δ grows, which is absent for the semielliptic band in the $d = 3$ case.

3.3 Singularities of electron dispersion in strongly correlated systems in DMFT and DMFT + Σ approaches

3.3.1 Cusps ('kinks') in electronic spectra. The electronic properties of crystalline solids are determined by single-particle and collective excitations of electron subsystem and their interactions with each other. These excitations are characterized by energy E and quasimomentum $\mathbf{k}$, which are related to each other via *dispersion* (spectrum) $E_{\mathbf{k}}$. Interaction between single-particle and collective modes can result in noticeable bends (cusps) of dispersion $E_{\mathbf{k}}$ — so-called 'kinks'. The lineshape and energy position of these features characterize interactions in the many-body system. For example, kinks in the electronic dispersions experimentally found by ARPES in copper oxides, with energies 40–70 meV below the Fermi level, are evidence of electron–phonon [102–108] or electron–magnon (spin-fluctuation) interactions [109, 110].

At the same time, ARPES experiments detect kinks in electron dispersion for a number of different systems at essentially higher energies (up to 800 meV) [111–113]. The physical nature of these kinks remains unknown. Among other attempts to find an explanation for these electronic spectra anomalies, a novel purely electronic mechanism of kink formation was proposed by Byczuk et al. [114]. This mechanism is applicable to strongly correlated metals, where the spectral function contains well-developed Hubbard subbands, together with a central quasiparticle peak as, for example, in transition metal oxides. The energy location of these kinks apparently determines the range of applicability of the conventional Landau Fermi-liquid theory.

As is well known [115], interaction generally results in a finite lifetime of excitations in the system, so that $E_{\mathbf{k}}$ becomes a complex function. For electron systems with Coulomb interaction, the Landau Fermi-liquid theory proves the existence of weakly damped fermionic quasiparticles for low enough temperatures and in the narrow energy interval around the Fermi surface [115]. Beyond the Fermi-liquid mode, the concept of quasiparticles with well-defined dispersion is not, strictly speaking, applicable, since the quasiparticle lifetime is too short. However, ARPES experiments in recent years have convincingly shown the existence of essentially $\mathbf{k}$-dependent (though with rather broad maxima) single-particle spectral function quite far from the Fermi level, despite the fact that one cannot speak about well-defined quasiparticles at these energies. In this case, we understand as particle dispersion precisely this $\mathbf{k}$-dependence of spectral function maxima, which replaces the usual notion of a quasiparticle spectrum.

3.3.2 Kinks of purely electronic nature. Let us consider in more detail a new mechanism of kink formation in the electronic dispersion of strongly correlated systems, which does not assume an interaction of electrons with phonons or other excitations [114]. In order to understand the nature of this

mechanism, we shall examine at the beginning a weakly correlated system described by standard Fermi-liquid theory. Because of the large enough quasiparticle lifetime close to the Fermi level and the weakness of correlations, in the first approximation interaction leads to a simple renormalization of initial dispersion of (noninteracting) quasiparticles $\epsilon_{\mathbf{k}}$, which is replaced by $E_{\mathbf{k}} = Z_{\mathrm{FL}}\epsilon_{\mathbf{k}}$, where Z_{FL} is the Fermi-liquid electron mass renormalization coefficient. This changes the slope of dispersion in the vicinity of the Fermi level, in contrast to a bare one. However, if we consider an electron with energy far away from the Fermi level, for weak interaction one can expect that its dispersion barely changes: $E_{\mathbf{k}} \approx \epsilon_{\mathbf{k}}$, though the damping here can already be pretty large. In this sense, one can say that electron–electron interaction by itself can result in the formation of bends (kinks) in the generalized dispersion (of the spectral function), and the position of such a kink on the energy scale is defined namely as energy, where a simple Fermi-liquid picture becomes inapplicable. However, in weakly correlated metals $Z_{\mathrm{FL}} \lesssim 1$, so that the slope of $E_{\mathbf{k}}$ will change insignificantly, making such kinks hard to observe.

This picture may be distinctly different from that in strongly correlated systems where Z_{FL} can be much less than unity, thus making kinks more pronounced. Strong correlation interactions give rise to strong spectral weight redistribution within the single-particle spectral function due to the formation of Hubbard subbands. Moreover, as is well known, in strongly correlated metals there is also a quasiparticle peak which appears in proximity to the Fermi level, between Hubbard subbands. Below, it will be shown that 'usual' Fermi-liquid quasiparticles exist in such systems only in a very narrow vicinity of the Fermi level, while beyond the Fermi-liquid mode (but still 'inside' the quasiparticle peak) there exists some intermediate mode with dispersion $E_{\mathbf{k}} \approx Z_{\mathrm{CP}}\epsilon_{\mathbf{k}}$, where renormalization factor Z_{CP} is determined by the central peak spectral weight and its value essentially differs from Z_{FL}. At these intermediate energies, which are much smaller than the interaction energy, electrons or holes strongly interact, and their dispersion differs from both the Fermi-liquid one and the one for noninteracting quasiparticles. In this energy range, we can speak about an 'intermediately' correlated situation, where $Z_{\mathrm{FL}} < Z_{\mathrm{CP}} < 1$. Consequently, at some energies $\pm\omega_\star$ inside the quasiparticle peak, a transition from renormalization coefficient Z_{FL} to Z_{CP} takes place. That leads to an emergence of kinks in electronic dispersion, and the energy positions of these kinks are directly related to energy boundaries of the domain of applicability of the usual Fermi-liquid theory. Let us emphasize that this mechanism gives rise to kink formation without any additional interactions with phonons or other collective modes. The only necessary condition for such kink formation is the presence of strong electron–electron correlations in the system.

For a microscopic description of electronic kinks, let us consider the Hubbard model which will be analyzed in the framework of standard DMFT, using the numerical renormalization group (NRG) to solve the effective Anderson single-impurity problem. For simplicity, we consider the single-band Hubbard model at half-filling. The strongly correlated mode in the Hubbard model occurs when the interaction strength becomes on the order of bare bandwidth: $U \approx W$. Consider as an example the computed results given in Fig. 14. It is clearly visible that dispersion moves from the Fermi-liquid mode (line *1* in Fig. 14) to intermediate mode

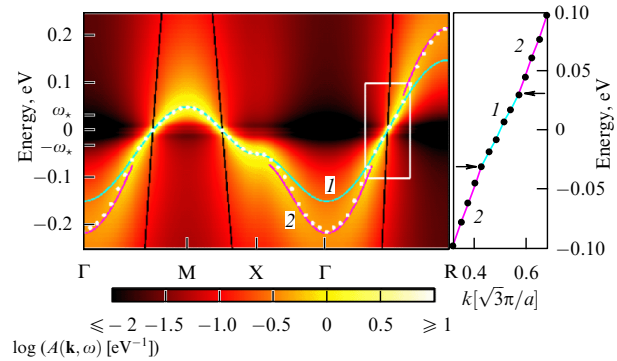

Figure 14. Cusps (kinks) in electronic dispersion $E_{\mathbf{k}}$ for strongly correlated systems. The logarithm of the DMFT spectral function $A(\mathbf{k},\omega)$ is indicated in color gradations on the contour plot for the Hubbard model on a cubic lattice. The Hubbard interaction is $U = 3.5$ eV, bandwidth $W \approx 3.64$ eV, band filling $n = 1$, calculated value of Fermi-liquid renormalization $Z_{\mathrm{FL}} = 0.086$, and temperature $T = 5$ K. Close to the Fermi level, the maxima of $A(\mathbf{k},\omega)$ (white dots) correspond to renormalized dispersion $E_{\mathbf{k}} = Z_{\mathrm{FL}}\epsilon_{\mathbf{k}}$ (line *1*). For energies $|\omega| > \omega_\star$ spectral function $A(\mathbf{k},\omega)$ keeps its shape but with different renormalization $E_{\mathbf{k}} = Z_{\mathrm{CP}}\epsilon_{\mathbf{k}} - c\,\mathrm{sgn}(E_{\mathbf{k}})$ (line *2*). Values of $\omega_\star = 0.03$ eV, $Z_{\mathrm{CP}} = 0.135$, and $c = 0.01$ eV are calculated in Ref. [114] from the values of Z_{FL} and $\epsilon_{\mathbf{k}}$ corresponding to the black line. The inset on the right shows in detail part of dispersion in the Γ-R direction, marked out with a white rectangle; kinks (cusps in dispersion) at energies $\pm\omega_\star$ are pointed by arrows. Black lines display bare (noninteracting) quasiparticle spectra.

described above (line *2* in Fig. 14) with the formation of well-defined cusps in dispersion (kinks) at energies $\pm\omega_\star = \pm 0.03$ eV. In some of the high-symmetry directions (e.g. around the X-point; see Fig. 14), the dispersion has quite a small slope in proximity to the Fermi level, making the kinks less pronounced.

Let us have a look at this situation from the point of view of single-particle Green function behavior. From general considerations it is clear that any cusps of dispersion caused by interaction appear because of the corresponding behavior of the self-energy or, more precisely, that of $\mathrm{Re}\,\Sigma_{\mathbf{k}}(\omega)$. In the majority of real physical systems, $\mathbf{k}$-dependence of self-energy, apparently, is less important than ω-dependence and, thus, omitting $\mathbf{k}$-dependence of self-energy, $\Sigma_{\mathbf{k}}(\omega) = \Sigma(\omega)$, is, more or less, a good approximation. In the framework of DMFT, this statement is exact. The self-consistent expression for the self-energy of the Hubbard model within DMFT can be written out as

$$\Sigma(\omega) = \omega + \mu - \frac{1}{G(\omega)} - \Delta\big(G(\omega)\big)\,, \tag{44}$$

where $G(\omega) = (1/N)\sum_{\mathbf{k}} G(\mathbf{k},\omega)$ is the local (averaged over $\mathbf{k}$) Green function, and $\Delta(G)$ is the frequency-dependent hybridization function expressed via $G(\omega)$.[6] The hybridization function describes quantum-mechanical coupling between an electron at a given site and other sites of the system.

In Fig. 15a, we plotted the frequency dependence of the spectral function (DOS) $A(\omega) = -\mathrm{Im}\,G(\omega)/\pi$ calculated for the same model parameters as in Fig. 14 and demonstrating a typical three-peak structure. Corresponding real parts of the

[6] In DMFT, $\Delta(G)$ is defined by $G(\omega) = G_0(\omega + \mu - \Sigma(\omega))$, i.e. $G_0(\Delta(G) + 1/G) = G$, where $G_0(\omega)$ is a noninteracting local Green function.

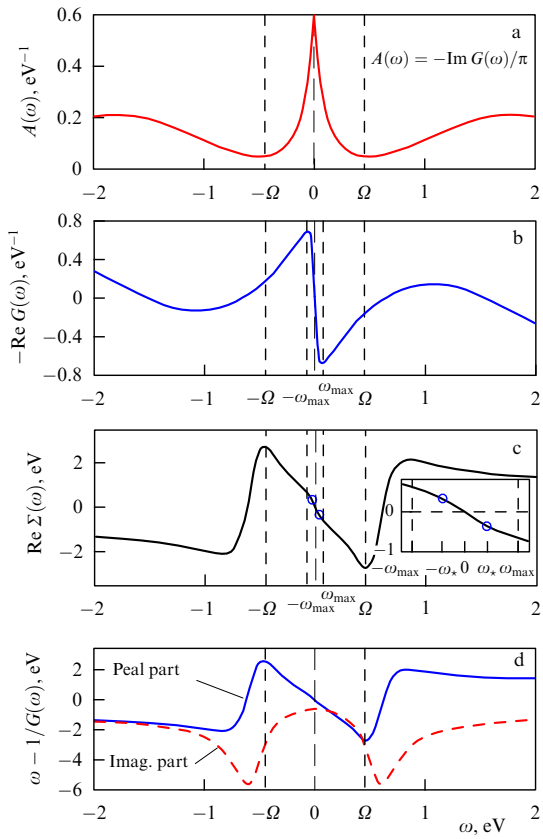

Figure 15. Green function characteristics for strongly correlated systems with parameters given in the caption to Fig. 14. (a) Three-peak structure of spectral function $A(\omega) = -\mathrm{Im}\, G(\omega)/\pi$ with minima at energies $\pm\Omega = 0.45$ eV. (b) Real part of Green function with relative minima and maxima at energies $\pm\omega_{\max}$ located 'inside' the quasiparticle peak. (c) Real part of self-energy with cusps at energies $\pm\omega_\star$ (circles) situated at the points of maximal curvature of $\mathrm{Re}\, G(\omega)$ ($\omega_\star = 0.4\omega_{\max} = 0.03$ eV). (d) Real part of $\omega - 1/G(\omega)$ (solid line) contributing to self-energy, which is linear, in general, in the energy interval $|\omega| < \Omega$. Change in energy dependence of $-\mathrm{Re}\, G(\omega)$ at energies $\pm\omega_\star$ defines the location of kinks (cusps) in electronic dispersion.

local Green function $G(\omega)$ and self-energy $\Sigma(\omega)$ are shown in Fig. 15b and Fig. 15c, respectively.

Kinks in $\mathrm{Re}\, \Sigma(\omega)$ are directly related to the three-peak structure of integrated spectral function (DOS) $A(\omega)$ (its minima are located at energies $\pm\Omega$) and define some new, quite small energy scale. To this end, $\mathrm{Re}\,[G(\omega)]$ should have maxima and minima on the energy interval $\pm\omega_{\max}$, i.e. inside the central peak (Fig. 15b). In turn, this directly leads to kink formation in $\mathrm{Re}\, \Sigma(\omega)$. Self-energy $\Sigma(\omega)$ comprises two contributions: $\omega + \mu - 1/G(\omega)$, and $-\Delta(G(\omega))$. Expression $\mathrm{Re}\,[\omega + \mu - 1/G(\omega)]$ is linear within a quite large energy range $|\omega| < \Omega$ (Fig. 15d), while the quantity $-\mathrm{Re}\,[\Delta(G(\omega))]$ is proportional to $-\mathrm{Re}\,[G(\omega)]$, at least in the first order of corresponding momenta expansion, only on the small energy interval $|\omega| < \omega_{\max}$. The sum of these two contributions gives rise to cusps in the real part of self-energy at energies $\pm\omega_\star$, where $\omega_\star = (\sqrt{2} - 1)\,\omega_{\max}$. At these energies, $\mathrm{Re}\,[G(\omega)]$ has maximal curvature (these points are marked by circles in Fig. 15c). Thus, the Fermi-liquid mode, where the slope of the real part of self-energy at the Fermi level is described by $\partial\, \mathrm{Re}\, \Sigma(\omega)/\partial\omega = 1 - 1/Z_{\mathrm{FL}}$, exists only within a narrow part of the central peak, namely on the energy interval $|\omega| < \omega_\star$. At higher (intermediate) energies, the slope of $\mathrm{Re}\, \Sigma(\omega)$ will be given by the expression $\partial\, \mathrm{Re}\, \Sigma(\omega)/\partial\omega = 1 - 1/Z_{\mathrm{CP}}$. As a result, effective dispersion $E_{\mathbf{k}}$ will demonstrate kinks at energies $\pm\omega_\star$.

This analysis also helps to understand why outside Fermi-liquid region $E_{\mathbf{k}}$ exhibits another value of renormalization of noninteracting electronic dispersion, given by Z_{CP} with small offset c. This behavior is determined by the magnitude of the main contribution $\omega + \mu - 1/G(\omega)$ to self-energy for energies $\omega_\star < |\omega| < \Omega$, i.e. within the central peak of the DOS. Quantities $\omega_\star$, Z_{CP}, and c can be expressed via Z_{FL} and characteristics of the noninteracting electron density of states. One can derive the expression for $\omega_\star = Z_{\mathrm{FL}}(\sqrt{2} - 1)\, D$, where D is the half-width of the bare band (see details in paper [114]). If correlations are weak so that $Z_{\mathrm{FL}} \lesssim 1$, the kink positions in $E_{\mathbf{k}}$ practically coincide with the edges of the bare electron band, which makes them almost unobservable. On the other hand, kink energy $\omega_\star/D \propto Z_{\mathrm{FL}}$ in the strongly correlated mode ($Z_{\mathrm{FL}} \ll 1$) approaches the Fermi level inside the central peak whose width diminishes as $\Omega/D \propto \sqrt{Z_{\mathrm{FL}}}$ with an increase in correlation strength [118].

These purely electronic kinks were first revealed in LDA + DMFT calculations for the $SrVO_3$ system [116]. The definition of energy scale $\omega_\star$ contains only parameters of the initial band structure, which can be obtained (for realistic systems) via band structure calculations, together with Fermi-liquid mass renormalization $Z_{\mathrm{FL}} = 1/(1 - \partial\, \mathrm{Re}\, \Sigma(0)/\partial\omega) \equiv m/m^*$, which can be experimentally determined from specific heat or spin susceptibility measurements. Notably, in Ref. [117] it was shown that kinks of an electronic nature can cause corresponding cusps in the linear (in temperature) term of electronic specific heat of strongly correlated metals, which was, apparently, observed in the LiV_2O_4 heavy-fermion system.

3.3.3 Role of electron–phonon interaction. The material in the previous section inevitably brings us to the question about the relationship and mutual influence of kinks of an electronic nature and the 'usual' kinks in the electronic dispersion, induced by electron–phonon interaction. This is related to a more general problem of interference between strong electronic correlations and electron–phonon interactions. In fact, the history of such investigations is relatively long, and one of the most popular models of electron–phonon interaction in strongly correlated systems is the Hubbard–Holstein model. The Hubbard model describes local Coulomb interaction on a lattice [8–13]. On the other hand, the Holstein model describes the linear interaction of conduction electrons with *local* (Einstein) phonon modes [119]. Studies of the Hubbard–Holstein model were performed in the framework of conventional DMFT [5], in particular with the use of the numerical renormalization group (NRG) [24] as an 'impurity solver'. Reducing the Hubbard–Holstein model to the Anderson–Holstein impurity problem was first performed by Hewson and Mayer [120]. These authors showed that by using NRG one can calculate the total electron–phonon contribution to self-energy, thus achieving a nonperturbative solution to the Hubbard–Holstein model, not only with respect to Hubbard interaction, but also with respect to electron–phonon interaction. It is worthy of note that the general structure of self-consistent DMFT equations in this approach is preserved.

Until recently, however, there had been no studies of strongly correlated electrons interacting with Debye pho-

nons, which is quite surprising in view of the rather wide discussion of the physics of kinks in electronic dispersion observed in ARPES experiments in high-T_c superconducting oxides [104]. The origin of these kinks is typically attributed to electron–phonon interaction [105]. The problem of kink formation in electronic dispersion caused by electron–phonon interaction in strongly correlated systems was briefly discussed in the framework of the Hubbard–Holstein model in papers [121, 122]. In this section, we overview DMFT + Σ results for the Hubbard model, adding interaction with Debye phonons under the assumption of the validity of the Migdal theorem (adiabatic approximation). This approximation is reasonable for electron–phonon coupling constant $\lambda < E_F/\omega_D \sim 10$, where E_F is the Fermi energy, and ω_D is the Debye frequency.

To consider electron–phonon interaction in a strongly correlated system, we introduce self-energy $\Sigma_{\mathbf{k}}(\varepsilon) = \Sigma_{ph}(\varepsilon, \mathbf{k})$ appearing in the usual Fröhlich model. According to the Migdal theorem, we can restrict ourselves in the adiabatic approximation to the simplest first-order contribution to $\Sigma_{ph}(\varepsilon, \mathbf{k})$. The main advantage of the adiabatic approximation is the possibility of neglecting any vertex corrections from electron–phonon interaction, which are small in regard to adiabatic parameter $\omega_D/E_F \ll 1$ [123].

In fact, $\Sigma_{ph}(\varepsilon, \mathbf{k})$ in this approximation exhibits only weak momentum dependence, which can be neglected, and we have to account only for the essential frequency dependence. Direct calculations (see, e.g., monograph [42]) in the case of the Debye phonon spectra $\omega_0(\mathbf{k}) = u|\mathbf{k}|$ for $|\mathbf{k}| < \omega_D/u$, where u is the speed of sound, give

$$\Sigma_{ph}(\varepsilon) = \frac{-ig^2}{4\omega_c^2} \int_{-\infty}^{+\infty} \frac{d\omega}{2\pi} \times \left\{ \omega_D^2 + \omega^2 \ln\left| \frac{\omega_D^2 - \omega^2}{\omega^2} \right| + i\pi\omega^2 \theta(\omega_D^2 - \omega^2) \right\} I(\varepsilon + \omega), \quad (45)$$

where g is the usual electron–phonon interaction constant, and

$$I(\epsilon) = \int_{-D}^{+D} d\xi \, \frac{N_0(\xi)}{E_\varepsilon - \xi} ,$$

$E_\varepsilon = \varepsilon - \Sigma(\varepsilon) - \Sigma_{ph}(\varepsilon)$, and $\omega_c = p_F u$ is the characteristic frequency of order the Debye one. In the case of semielliptic bare DOS $N_0(\varepsilon)$ with half-width D, one obtains $I(\epsilon) = (2/D^2)\,(E_\varepsilon - \sqrt{E_\varepsilon^2 - D^2})$. It is convenient to introduce a dimensionless electron–phonon coupling constant which for this model can be written as [42]

$$\lambda = g^2 N_0(\varepsilon_F) \, \frac{\omega_D^2}{4\omega_c^2} . \quad (46)$$

To simplify calculations, we neglect renormalization of phonons because of electron–phonon interaction [42], assuming from here on that the phonon spectrum is fixed by experiment.

3.3.4 Electronic and phonon kinks within the DMFT + Σ approach. Let us focus on the most interesting DMFT + Σ results obtained in this model, referring the reader for details to Refs [124, 125]. Here, we present results addressing the interaction of electrons with Debye phonons (the results for Einstein phonons are analogous [125]).

A comparison of DMFT and DMFT + Σ_{ph} densities of states, with the latters involving electron–phonon interaction, for strong ($U/2D = 1.25$) and weak ($U/2D = 0.625$) Hubbard interactions is drawn in the upper and lower panels on the left side of Fig. 16. The dimensionless constant λ (46) exploited in these calculations was chosen to be $\lambda = 0.8$, and the Debye frequency $\omega_D = 0.125D$. In both cases, we observe some spectral weight transfer caused by electron–phonon interaction. At $U/2D = 1.25$ (Fig. 16a), we see a well-developed three-peak structure typical for strongly correlated metals. On the energy interval $\pm\omega_D$ around the Fermi level (which is measured up to zero energy in all figures) there is practically no difference in the shape of the quasiparticle peaks in the DOS obtained within DMFT and DMFT + Σ_{ph} approaches. But beyond this interval, the DMFT + Σ_{ph} quasiparticle peak becomes significantly wider because of the partial transfer of spectral weight from Hubbard bands. This broadening of the quasiparticle peak in DMFT + Σ_{ph} leads to a delay in the metal–insulator transition, as we shall see later.

In the case of $U/2D = 0.625$ (see Fig. 16b), no clearly distinguishable Hubbard bands are formed, and we observe

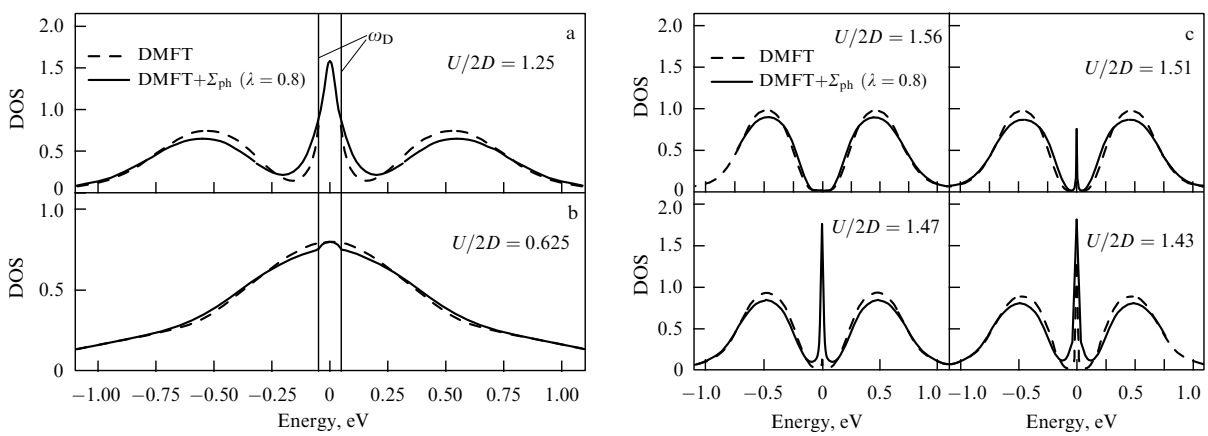

Figure 16. Comparison of conventional DMFT (dashed lines) and DMFT + Σ_{ph} (solid lines) densities of states. On the left side – for strong (upper panel, $U/2D = 1.25$) and weak (lower panel, $U/2D = 0.625$) Hubbard interactions. On the right side — evolution of densities of states in proximity to the metal–insulator transition. Dimensionless electron–phonon coupling constant is $\lambda = 0.8$ [124, 125].

only some side wings in the DOS. Redistribution of spectral weight in Fig. 16b is not very dramatic, despite a qualitative difference with the $U/2D = 1.25$ case (see Fig. 16a). The main distinction between DMFT and DMFT + $\Sigma_{\rm ph}$ results occurs here on the interval $\pm\omega_{\rm D}$, where the formation of a 'cap' in the DOS is evidenced, due to electron–phonon interaction. The corresponding spectral weight 'goes' over to the energies around $\pm U$, where Hubbard bands start to form.

In Fig. 16c, we compare the behavior of densities of states in DMFT without phonons and in DMFT + $\Sigma_{\rm ph}$ for different values of the $U/2D$ parameter near the Mott–Hubbard metal–insulator transition. At $U/2D = 1.56$, both standard DMFT and DMFT + $\Sigma_{\rm ph}$ yield an insulating solution. However, there are some distinctions between these solutions. In DMFT + $\Sigma_{\rm ph}$, the Hubbard bands are lower and wider than in DMFT, since additional (electron–phonon) interaction is included. With a decrease in U at $U/2D = 1.51$ and 1.47, we reveal that DMFT + $\Sigma_{\rm ph}$ results correspond to the metallic state (with a narrow quasiparticle peak at the Fermi level), while DMFT without phonons still furnishes the insulating solution. Only in proximity to $U/2D = 1.43$ do both DMFT and DMFT + $\Sigma_{\rm ph}$ results for DOS correspond to the metallic state. Thus, with an increase in U the finite strength of electron–phonon interaction slightly delays the Mott–Hubbard transition from the metallic to the insulating phase. This result is analogous to the one obtained in the Hubbard–Holstein model for weak electron–phonon coupling [126–128].

Therefore, moderate electron–phonon interaction brings to rather insignificant changes in the electron density of states both in correlated metal and in the Mott insulating state, only slightly delaying transition from metal to insulator with a growth in U.

Now we turn to the source of sharp slope changes of electron dispersion (kinks). It is well known that, in general, kinks are formed because of the interaction of electrons with bosonic modes. In electron–phonon interaction, the typical energy of the kink is around the Debye (or Einstein) frequency. We have shown in Section 3.3.1 that in strongly correlated metal, kinks of a purely electronic nature can arise [114]. The energy of such a kink for a semielliptical bare DOS is $\omega^* = Z_{\rm FL}(\sqrt{2}-1)\,D$, where D is the half-width of the bare band, and $Z_{\rm FL} = (1 - \partial\,{\rm Re}\,\Sigma/\partial\varepsilon|_{\varepsilon=E_{\rm F}})^{-1}$ is the Fermi-liquid renormalization factor. Roughly speaking, ω^* is defined by the half-width of the quasiparticle peak in the DOS.

A kink of an electronic nature is quite smooth, and its observation is rather difficult. DMFT + $\Sigma_{\rm ph}$ calculations give evidence that electronic kinks are hardly detectable against the background of phonon kinks, and the fine tuning of model parameters is necessary to pick them out. First of all, it is necessary to guarantee that $\omega_{\rm D} \ll \omega^*$ (in other cases, smooth electronic kinks will be practically indiscernible against kinks from electron–phonon interaction). For $U/2D = 1$ and $U = 3.5$ eV, we have $\omega^* \sim 0.1$D, while the Debye frequency can be taken to be quite small, e.g. $\omega_D \sim 0.01$D. In order to make the phonon kink pronounced enough at such a relatively low Debye frequency, one needs to increase the electron–phonon coupling constant to $\lambda = 2.0$.

To demonstrate the possibility of the coexistence of both types of kinks in the spectra, let us consider the energy dispersion for a simple cubic lattice with nearest neighbors hopping only. It is most convenient to discuss the high-symmetry direction $\Gamma - (\pi, \pi, \pi)$ of the Brillouin zone [114]. In Fig. 17a, we show electronic dispersion along this direction close to the Fermi level. The line with the diamonds is the electronic spectrum of standard DMFT without phonons. Lines with circles present DMFT + $\Sigma_{\rm ph}$ results. Electronic and phonon kinks are marked by arrows. Generally, kinks in electronic dispersion due to electron–phonon interaction dominate for most typical model parameters, making purely electronic kink observation predicted in paper [114] quite difficult.

In conclusion, we give the picture of phonon kink evolution in the electronic spectrum depending on the strength of Hubbard interaction U. With an increase in the $U/2D$ ratio, Fermi velocity goes down and the kink position on the momentum axis shifts farther away from $p_{\rm F}$, while the kink energy remains about $\omega_{\rm D}$. This behavior follows from direct DMFT + $\Sigma_{\rm ph}$ calculations [124, 125] and is shown in the right panel of Fig. 17. In the case of interaction with Einstein phonons, the results are quite analogous [125].

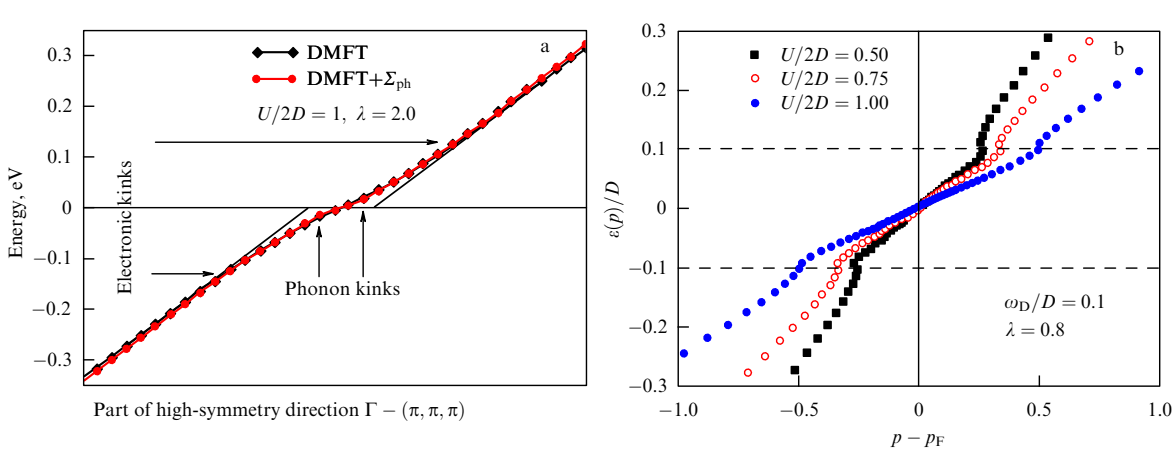

Figure 17. (a) Quasiparticle dispersion with kinks around the Fermi level, studied along $\Gamma - (\pi, \pi, \pi)$ high-symmetry direction in the Brillouin zone and obtained from 'bare' energy dispersion for the case of a simple cubic lattice with nearest neighbors hopping only: DMFT (curve with diamonds), and DMFT + $\Sigma_{\rm ph}$ (curve with circles) ($\lambda = 2$, $\omega_{\rm D} = 0.01D$). (b) DMFT + $\Sigma_{\rm ph}$ phonon kink evolution for different strengths of Hubbard interaction $U/2D = 0.5, 0.75, 1.0$; $\lambda = 0.8$, and $\omega_{\rm D} = 0.1D$ [124].

4. Electronic structure of real strongly correlated systems: LDA + DMFT and LDA + DMFT + Σ

At present, the most advanced *ab initio* (i.e. ideally without any fitting parameters) computational framework of electronic spectra of *realistic* strongly correlated systems is the LDA + DMFT method [2, 25]. The LDA band structure calculated by this method is used to obtain a 'noninteracting' starting Hamiltonian, while strong electron correlations are accounted afterwards within DMFT. In fact, the LDA + DMFT computational scheme combines two scientific areas: 'realistic' band structure calculations and traditional model approaches, which were essentially separated from each other before. Without DMFT, in just LDA there is no way to describe strongly correlated systems, while without LDA calculations, many-body methods cannot be material-specific. Below, we briefly discuss the basics of LDA + DMFT approach and its subsequent generalization to LDA + DMFT + Σ methods.

4.1 Density functional theory (DFT). Local density approximation (LDA)

In the Born–Oppenheimer adiabatic approximation [129], neglecting relativistic effects, electronic properties in solid-state physics are described by the Hamiltonian

$$\hat{H} = \sum_{\sigma} \int \mathrm{d}^3 r\, \hat{\Psi}^+(\mathbf{r},\sigma) \left[-\frac{\hbar^2}{2m_\mathrm{e}} \Delta + V_\mathrm{ion}(\mathbf{r}) \right] \hat{\Psi}(\mathbf{r},\sigma) + \frac{1}{2} \sum_{\sigma\sigma'} \int \mathrm{d}^3 r\, \mathrm{d}^3 r'\, \hat{\Psi}^+(\mathbf{r},\sigma)\, \hat{\Psi}^+(\mathbf{r}',\sigma')\, V_\mathrm{ee}(\mathbf{r}-\mathbf{r}') \times \hat{\Psi}(\mathbf{r}',\sigma')\, \hat{\Psi}(\mathbf{r},\sigma)\,. \tag{47}$$

Here, $\hat{\Psi}^+(\mathbf{r},\sigma)$ and $\hat{\Psi}(\mathbf{r},\sigma)$ are the respective creation and annihilation operators of an electron with coordinate $\mathbf{r}$ and spin σ, Δ is the Laplace operator, m_e is the electron mass, e is the electron charge, and

$$V_\mathrm{ion}(\mathbf{r}) = -e^2 \sum_i \frac{Z_i}{|\mathbf{r}-\mathbf{R}_i|}\,, \quad V_\mathrm{ee}(\mathbf{r}-\mathbf{r}') = \frac{e^2}{2} \sum_{\mathbf{r}\neq\mathbf{r}'} \frac{1}{|\mathbf{r}-\mathbf{r}'|} \tag{48}$$

denote a single-particle potential created by all ions i with charge eZ_i located at given positions $\mathbf{R}_i$, and electron–electron interaction.

Although the 'first principle' Hamiltonian (47) is easy to write down, it is impossible to solve the corresponding quantum-mechanical problem exactly. This is the reason to make substantial physical approximations. In particular, density functional theory (DFT) is based on the Hohenberg–Kohn theorem [130] (see also the review [131]), which asserts that ground-state energy is the unique functional of electron charge density, which is minimum for the equilibrium electron density in the ground state:

$$E[\rho] = E_\mathrm{kin}[\rho] + E_\mathrm{ion}[\rho] + E_\mathrm{Hartree}[\rho] + E_\mathrm{xc}[\rho]\,, \tag{49}$$

where the Hartree energy $E_\mathrm{Hartree}[\rho] = (1/2) \int \mathrm{d}^3 r' \mathrm{d}^3 r \times V_\mathrm{ee}(\mathbf{r}-\mathbf{r}')\, \rho(\mathbf{r}')\, \rho(\mathbf{r})$ and the potential energy of ions $E_\mathrm{ion}[\rho] = \int \mathrm{d}^3 r\, V_\mathrm{ion}(\mathbf{r})\, \rho(\mathbf{r})$ can be directly expressed via electron charge density. The term $E_\mathrm{kin}[\rho]$ denotes the kinetic energy of electrons, and $E_\mathrm{xc}[\rho]$ is an unknown, in general, exchange-correlation term containing electron–electron interaction energy unaccounted for in the Hartree term. In fact, all complexities of the many-body problem are transferred into the computation of $E_\mathrm{xc}[\rho]$.

In practice, instead of minimization of $E[\rho]$ over ρ, minimization is usually performed over some set of orthonormal basis functions φ_i related to ρ through the expression

$$\rho(\mathbf{r}) = \sum_{i=1}^{N} |\varphi_i(\mathbf{r})|^2. \tag{50}$$

Introducing arbitrary Lagrange parameters ε_i and requiring the fulfillment of the equality

$$\frac{\delta}{\delta\varphi_i(\mathbf{r})} \left\{ E[\rho] + \varepsilon_i \left[1 - \int \mathrm{d}^3 r |\varphi_i(\mathbf{r})|^2 \right] \right\} = 0\,, \tag{51}$$

one gets Kohn–Shem equations [132, 133]

$$\left[-\frac{\hbar^2}{2m_\mathrm{e}} \Delta + V_\mathrm{ion}(\mathbf{r}) + \int \mathrm{d}^3 r' V_\mathrm{ee}(\mathbf{r}-\mathbf{r}')\, \rho(\mathbf{r}') + \frac{\delta E_\mathrm{xc}[\rho]}{\delta\rho(\mathbf{r})} \right] \times \varphi_i(\mathbf{r}) = \varepsilon_i \varphi_i(\mathbf{r})\,. \tag{52}$$

Formally, this equation coincides with the stationary single-particle Schrödinger equation. Electron kinetic energy corresponding to charge density of the ground state is now given by the expression

$$E_\mathrm{kin}[\rho_\mathrm{min}] = -\sum_{i=1}^{N} \left\langle \varphi_i \left| \frac{\hbar^2 \Delta}{2m_\mathrm{e}} \right| \varphi_i \right\rangle, \tag{53}$$

where φ_i are the self-consistent (spin-degenerate) solutions of equations (50) and (52), corresponding to the smallest single-particle energy ϵ_i [134].

The most common way to calculate $E_\mathrm{xc}[\rho]$ is to use the *local density approximation* (LDA). It approximates the functional $E_\mathrm{xc}[\rho]$ by the local charge density functional

$$E_\mathrm{xc}[\rho] \to \int \mathrm{d}^3 r\, \rho(\mathbf{r})\, \epsilon_\mathrm{xc}^\mathrm{LDA}\big(\rho(\mathbf{r})\big)\,. \tag{54}$$

The explicit expression for $\epsilon_\mathrm{xc}^\mathrm{LDA}(\rho(\mathbf{r}))$ can be found in the framework of different models, e.g. from a numerical analysis of the 'jellium' model (electron gas against a positive ionic homogeneous background) [135].

In fact, LDA approximation corresponds to the replacement of the Hamiltonian (47) by the expression

$$\hat{H}_\mathrm{LDA} = \sum_{\sigma} \int \mathrm{d}^3 r\, \hat{\Psi}^+(\mathbf{r},\sigma) \left[-\frac{\hbar^2}{2m_\mathrm{e}} \Delta + V_\mathrm{ion}(\mathbf{r}) + \int \mathrm{d}^3 r'\, \rho(\mathbf{r}')\, V_\mathrm{ee}(\mathbf{r}-\mathbf{r}') + \frac{\delta E_\mathrm{xc}^\mathrm{LDA}[\rho]}{\delta\rho(\mathbf{r})} \right] \hat{\Psi}(\mathbf{r},\sigma)\,. \tag{55}$$

In practical calculations, electron field operators are expanded in terms of a some set of atomic-like functions (basis set) Φ_{ilm} (i denotes lattice site, l is the orbital quantum number, and m is the magnetic quantum number). In this representation, one has

$$\hat{\Psi}^+(\mathbf{r},\sigma) = \sum_{ilm} \hat{c}_{ilm}^{\sigma\dagger} \Phi_{ilm}(\mathbf{r})\,, \tag{56}$$

and the Hamiltonian (55) is rewritten as

$$\hat{H}_{\mathrm{LDA}} = \sum_{ilm,\,jl'm',\,\sigma} (\delta_{ilm,\,jl'm'}\varepsilon_{ilm}\,\hat{n}^{\sigma}_{ilm} + t_{ilm,\,jl'm'}\hat{c}^{\sigma\dagger}_{ilm}\hat{c}^{\sigma}_{jl'm'}). \quad (57)$$

Here $\hat{n}^{\sigma}_{ilm} = \hat{c}^{\sigma\dagger}_{ilm}\hat{c}^{\sigma}_{ilm}$ is the electron density operator on a given orbital, while matrix elements

$$t_{ilm,\,jl'm'} = \left\langle \Phi_{ilm} \middle| -\frac{\hbar^2\Delta}{2m_{\mathrm{e}}} + V_{\mathrm{ion}}(\mathbf{r}) + \int \mathrm{d}^3r'\rho(\mathbf{r}')\,V_{\mathrm{ee}}(\mathbf{r}-\mathbf{r}') + \frac{\delta E^{\mathrm{LDA}}_{\mathrm{xc}}[\rho]}{\delta\rho(\mathbf{r})} \middle| \Phi_{jl'm'} \right\rangle \quad (58)$$

in case of $ilm \neq jl'm'$ define effective hopping integrals, and single-particle eigenenergies ε_{ilm} are given by corresponding diagonal expressions in case of identical indices. At this point purely analytical work ends and numerical calculations follow within the chosen basis set, e.g. linearized muffin-tin orbitals (LMTO). Specific expressions for matrix elements (58) within the LMTO basis are presented in Refs [136, 137].

4.2 LDA + DMFT computational scheme

For strongly correlated materials, the onsite Coulomb interaction between d- and f-electrons is of primary importance, since this contribution to interaction energy is the largest one. The largest nonlocal contribution follows from the density–density type interaction involving nearest neighbors, where the main contribution comes from the Hartree term (see Refs [138, 139] and [140]), which was already taken into account in the LDA. Moreover, some part of the exchange-correlation interactions are taken into account in the LDA via effective single-electron potential $\delta E^{\mathrm{LDA}}_{\mathrm{xc}}[\rho]/\delta\rho(\mathbf{r})$.

In order to take into consideration strong local Coulomb interaction, one should supplement Hamiltonian (57) with approximate local Coulomb matrix comprising the most important parameters only [25]: onsite intraband Coulomb repulsion U, exchange interaction J, and interorbital Coulomb repulsion U' acting on different electronic orbitals of the same site i_{d}, where an atom with a partially filled d-shell resides (l — orbital quantum number, m — magnetic quantum number, and σ — spin index):

$$\hat{H} = \hat{H}_{\mathrm{LDA}} + U\sum_{m}\sum_{i=i_{\mathrm{d}},\,l=l_{\mathrm{d}}} \hat{n}_{ilm\uparrow}\hat{n}_{ilm\downarrow} + \sum_{i=i_{\mathrm{d}},\,l=l_{\mathrm{d}}}\sum_{m\neq m'}\sum_{\sigma\sigma'} (U' - \delta_{\sigma\sigma'}J)\,\hat{n}_{ilm\sigma}\hat{n}_{ilm'\sigma'} - \sum_{i=i_{\mathrm{d}},\,l=l_{\mathrm{d}}}\sum_{m\sigma} \Delta\epsilon_{\mathrm{d}}\hat{n}_{ilm\sigma}\,. \quad (59)$$

Here, for simplicity, only density–density type interactions are left, and so-called Kanamori parametrization is applied, when for the same orbitals ($m = m'$) the direct Coulomb interaction is taken as U, while for different orbitals ($m \neq m'$) this interaction is replaced by U'. Because of the rotational invariance of the single-atom problem, one has $U' = U - 2J$, and the exchange interaction parameter does not depend on the orbital index and is equal to J.

Moreover, the last term involving the quantity $\Delta\epsilon_{\mathrm{d}}$ was added to formula (59) (the so-called double-counting correction), which should correct for double counting of interaction contributions, as some part of local Coulomb interaction has already been included in $\hat{H}_{\mathrm{LDA}}$. The general microscopic expression for $\Delta\epsilon_{\mathrm{d}}$ via U and ρ is unknown. However, there are several qualitative recipes to determine the value of $\Delta\epsilon_{\mathrm{d}}$, which are employed in different modern LDA + DMFT calculations (a detailed discussion can be found in Refs [141, 142]). The simplest physical assumption lies in the fact that the Coulomb interaction energy can be written down within the DFT as

$$E_{\mathrm{DFT}} = \frac{1}{2}\,\bar{U}n_{\mathrm{d}}(n_{\mathrm{d}} - 1)\,, \quad (60)$$

where n_{d} is the total number of electrons in the d-shell, and $\bar{U}$ is the average Coulomb interaction (here, we assume averaging over all orbital pairs $m\sigma$, $m'\sigma'$ at a given site). Thus, $\Delta\epsilon_{\mathrm{d}}$ is taken as

$$\Delta\epsilon_{\mathrm{d}} = \frac{\partial E_{\mathrm{DFT}}}{\partial n_{\mathrm{d}}} = \bar{U}\left(n_{\mathrm{d}} - \frac{1}{2}\right). \quad (61)$$

The interaction parameters U, J, and U' can be obtained from the averaged Coulomb interaction $\bar{U}$ and Hund exchange parameter J. The averaged interaction $\bar{U}$ is related to the U and U' Coulomb parameters via the following relation:

$$\bar{U} = \frac{U + (N_{\mathrm{orb}} - 1)\,U' + (N_{\mathrm{orb}} - 1)(U' - J)}{2N_{\mathrm{orb}} - 1}\,, \quad (62)$$

where N_{orb} is the number of interacting orbitals. Since U and U' are not independent parameters, $\bar{U}$ and J are sufficient for determining U [29 – 31, 143].

Different methods have been developed for microscopic calculations of averaged Coulomb interaction, such as constrained LDA (CLDA) [144] or constrained RPA (CRPA) [145, 146]. Generalizations to calculating the Hund exchange parameter also exist. Unfortunately, there are rather large discrepancies between the values of parameters obtained with these methods. Particularly, the quantity $\bar{U}$ appears to be strongly dependent on the basis set used (e.g. in the problem of screening the long-range part of the Coulomb interaction). It is clear that the introduction of all these essentially model parameters takes us quite far away from the 'first principle' ideal, though it is the best one can do at the moment to calculate the electronic band structure of solids comprising transition metal atoms, where electron–electron interactions play the crucial role. In that sense, it is probably more correct to speak about 'modeling' of the electronic structure of such systems.

Matrix elements of the 'noninteracting' Hamiltonian $H^0_{\mathrm{LDA}}(\mathbf{k})$ in the reciprocal space can be calculated numerically at every point of the Brillouin zone, then the integrals over the Brillouin zone are usually calculated with the tetrahedron method [147]. In relatively simple band dispersions, where the analytical expression for $H^0_{\mathrm{LDA}}(\mathbf{k})$ dependence on $\mathbf{k}$ can be written explicitly, the hopping integrals can be found from LDA by projecting on corresponding Wannier functions [148 – 151]. Matrix elements of this Hamiltonian, i.e. single-particle LDA energies without local Coulomb interaction, can be written in the following way:

$$\left(H^0_{\mathrm{LDA}}(\mathbf{k})\right)_{qlm,\,q'l'm'} = \left(H_{\mathrm{LDA}}(\mathbf{k})\right)_{qlm,\,q'l'm'} - \delta_{qlm,\,q'l'm'}\delta_{ql,\,q_{\mathrm{d}}l_{\mathrm{d}}}\Delta\epsilon_{\mathrm{d}}n_{\mathrm{d}}\,, \quad (63)$$

where q is the atomic index in the unit cell.

The essence of the next step is to use in the DMFT or DMFT + Σ loop (see Section 2.1) the local lattice Green function (5) determined by the momentum-integrated Dyson's equation of the form

$$G_{qlm,q'l'm'}(\omega) = \frac{1}{V_{\mathrm{B}}}\int \mathrm{d}\mathbf{k}\left[\omega\delta_{qlm,q'l'm'} - \left(H^0_{\mathrm{LDA}}(\mathbf{k})\right)_{qlm,q'l'm'} + \delta_{ql,q_{\mathrm{d}}l_{\mathrm{d}}}\Sigma_{qlm,q'l'm'}(\omega)\right]^{-1}, \quad (64)$$

where $[\ldots]^{-1}$ denotes the inverse matrix with indices $n(=qlm)$, $n'(=q'l'm')$, while the integration is performed over the Brillouin zone of the volume V_{B}.

A significant simplification of computations can be achieved for the case of cubic lattice symmetry, where the crystal field strongly splits d-orbitals into threefold degenerate t_{2g} states and twofold degenerate e_g states nonmixed with the former. In this special case, both the Green function and the self-energy become diagonal with respect to orbital and spin indices, thus reducing the problem, in fact, to single-band. Then, the calculation of the local Green function of the lattice problem can be performed as energy integration with the use of unperturbed densities of states, which allows avoiding tedious integration over the Brillouin zone in expression (64) and writing

$$G(\omega) = G^0\big(\omega - \Sigma(\omega)\big) = \int \mathrm{d}\epsilon\, \frac{N^0(\epsilon)}{\omega - \Sigma(\omega) - \epsilon}\,. \quad (65)$$

In this case, double-counting correction $\Delta\epsilon_{\mathrm{d}}$ reduces to an immaterial shift of the chemical potential, and its particular mathematical form is irrelevant altogether.

4.3 Examples of LDA + DMFT calculations

4.3.1 Cubic perovskites $CaVO_3$ and $SrVO_3$. In this section, we consider examples of some LDA + DMFT calculations of electronic band structure of realistic compounds with strong enough electronic correlations. Transition metal oxides are an ideal testing area to study electronic correlations in solids. Among these materials, cubic perovskites have the simplest crystal structure and, therefore, can be viewed as a starting point for understanding the electronic properties of more complex systems. Usually, 3d states in such materials form comparatively narrow bands with the width $W \sim 2-3$ eV, leading to strong electron–electron Coulomb correlations.

The modern stage of experimental investigations of spectral and transport properties of strongly correlated $3d^1$ transition metal oxides started from the work of Fujimori et al. [152]. The authors, apparently for the first time, discovered a strongly pronounced lower Hubbard band in photoemission spectra, which could not be explained by standard methods of band structure calculations. In many earlier studies [153–156] devoted to the properties of the series of $Sr_{1-x}Ca_xVO_3$ compounds with different values of x, rather controversial results were reported. Whereas the thermodynamic characteristics (the Sommerfeld coefficient, electrical resistance, and magnetic susceptibility) appeared to be more or less x-independent, spectroscopic measurement data changed rather strongly as a system transformed from $x=0$ ($SrVO_3$) to $x=1$ ($CaVO_3$). These data indicated a transition from a strongly correlated metal ($SrVO_3$) to a practically ideal insulator ($CaVO_3$), with the concentration range $x \to 1$ in $Sr_{1-x}Ca_xVO_3$ being the boundary of the Mott–Hubbard transition.

An analysis of this problem was performed using high penetration depth photoemission experiments by Maiti et al. [157], and similar experiments with high-resolution photoemission by Sekiyama et al. [158]. In particular, it was shown in the last study that: (1) the surface preparation technique is very important (the cleavage method is preferable), and (2) the energy of an X-ray incident beam should be high enough to provide the penetration depth of several unit cells. At the same time, high instrumental resolution should be guaranteed (about 100 meV in the work [158]). Such an improvement in photoemission spectroscopy methods led to the observation of almost identical spectra for $Sr(Ca)VO_3$ [157, 158], demonstrating agreement of spectroscopic and thermodynamic measurements. The results of these experiments also agree with earlier 1s X-ray absorption spectra (XAS) obtained by Inoue et al. [159], which differ only for energies slightly above the Fermi level, in contrast, say, to bremsstrahlung isochromat spectroscopy (BIS) data [156]. In the framework of a single-band Hubbard model with a neglect of orbital structure of vanadium 3d shell, Rozenberg et al. [160] modelled $Sr_{1-x}Ca_xVO_3$ spectra obtained by high penetration depth photoemission spectroscopy [157] using adjustable parameters. Later on, it was demonstrated [158] that the data from Ref. [157] contained quite a significant surface contribution.

Below, we present results of LDA + DMFT(QMC) calculations performed without any adjustable parameters, both for the spectral function and density of electronic states in cubic $SrVO_3$ and in orthorhombic $CaVO_3$ perovskites. According to these, both systems in their ground states are strongly correlated metals, which are quite far away from the metal–insulator transition boundary. Despite the significantly smaller V–O–V bond angle in $CaVO_3$, the photoemission spectra of both systems are very similar and their quasiparticle peaks are almost identical. The results obtained agreed very well with modern high-resolution bulk sensitive photoemission data mentioned above. In the spectral function of $SrVO_3$, obtained from LDA + DMFT(QMC) calculations, kinks of a purely electronic nature at about 200 meV were observed, and later these kinks were found experimentally.

Results of LDA + DMFT calculations. First of all, from the LDA-calculated band structure we extract single-electron Hamiltonian $\hat{H}^0_{\mathrm{LDA}}$ with the subtracted averaged Coulomb interaction (to avoid its double counting) [25]. Supplementing $\hat{H}^0_{\mathrm{LDA}}$ with local Coulomb interaction between electrons, we obtain Hamiltonian (59) for the material of interest. Since the $CaVO_3$ symmetry is close to cubic, it is possible to simplify the calculations and use integration over band with the LDA density of states $N^0(\epsilon)$, instead of integration over the Brillouin zone. In Hamiltonian (59), local intraorbital and interorbital repulsions and exchange interactions are taken into account explicitly as U, U', and J. The strengths of these interactions for $SrVO_3$ were calculated by the constrained LDA method [144] with e_g states included in the screening [161]. The obtained strength of average Coulomb interaction is $\bar{U} = 3.55$ eV ($\bar{U} = U'$ for t_{2g} orbitals [26, 143]) and $J = 1.0$ eV. Intraorbital Coulomb repulsion U is fixed by rotational invariance: $U = U' + 2J = 5.55$ eV. $\bar{U}$ was not calculated for $CaVO_3$, since the standard procedure of calculating Coulomb interaction parameters between two t_{2g} electrons screened by e_g states is not applicable to the distorted crystal structure, where the e_g and t_{2g} orbitals are not separated by symmetry. On the other hand, it is known

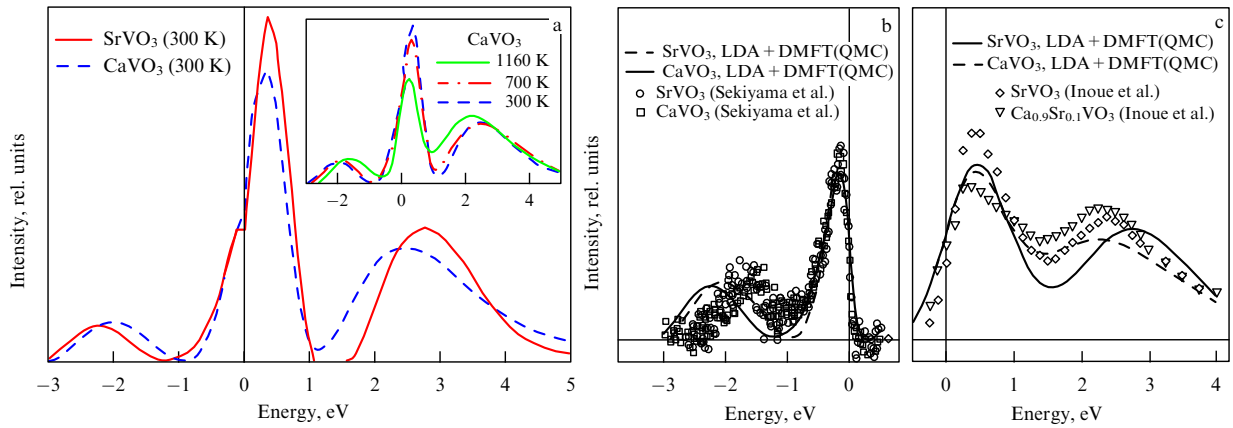

Figure 18. (a) LDA + DMFT(QMC) spectra for $SrVO_3$ (solid line) and $CaVO_3$ (dashed line) at $T = 300$ K (inset: temperature influence on $CaVO_3$ spectrum lineshape). (b, c) Comparison of calculated (without adjustable parameters) LDA + DMFT(QMC) spectra for $SrVO_3$ (solid line) and $CaVO_3$ (dashed line) with high-resolution bulk sensitive photoemission data ($SrVO_3$ — circles, and $CaVO_3$ — squares) [158] (b) and 1s-XAS spectra: ($SrVO_3$ — diamonds, and $Ca_{0.9}Sr_{0.1}VO_3$ — triangles) [159] (c). Horizontal line indicates experimental background.

that changes in *local* Coulomb interaction are usually much smaller than changes in density of states, which, as shown above, are weakly dependent on V–O–V bond angle. This means that $\bar{U}$ for $CaVO_3$ should be practically the same as for $SrVO_3$. Correspondingly, the values of $\bar{U} = 3.55$ eV and $J = 1.0$ eV were used for both $SrVO_3$ and $CaVO_3$. These values agree with other band structure calculations for vanadium compounds [161] and with the experimental data [162].

Further computations with Hamiltonian (59) were performed in the framework of DMFT by the quantum Monte Carlo (QMC) method [18–22] as an impurity solver. In QMC, the Green function was obtained for the imaginary time (or at Matsubara frequencies) and then continued to the real time (frequency) by the maximum entropy method [163]. In LDA + DMFT(QMC) spectra calculated for $SrVO_3$ and $CaVO_3$ and shown in Fig. 18a, we observe manifestations of correlation effects, such as formation of lower Hubbard bands near -2.0 eV and upper Hubbard bands at about 2.5 eV with well-developed quasiparticle peaks on the Fermi level. Thus, both $SrVO_3$ and $CaVO_3$ constitute strongly correlated metals. The difference in bare bandwidths (about 4%) is only responsible for a small additional spectral weight transfer from the quasiparticle peak to Hubbard bands and for slight changes in Hubbard band positions. Obviously, both systems are not close to the Mott–Hubbard metal–insulator transition. Many-body densities of states for both systems (see Fig. 18) are rather alike but not identical. Indeed, $SrVO_3$ is a bit less correlated than $CaVO_3$, in agreement with the difference between their LDA bandwidths. The inset to Fig. 18a gives evidence that temperature influence on the spectrum is small for $T \lesssim 700$ K.

In Fig. 18b, LDA + DMFT(QMC) spectra (calculated at $T = 300$ K, then multiplied by the Fermi function at an experimental temperature of 20 K and broadened with a Gaussian 0.1 eV wide to mimic experimental resolution [158]) are compared with experimental photoemission data after subtraction of oxygen and surface contributions. Notably, the height and the width of these spectra are almost the same in $SrVO_3$ and $CaVO_3$ (with a bit of difference above the Fermi level). On the other hand, the positions of lower Hubbard bands differ quite markedly. This variance might occur because of subtraction of the (estimated) oxygen contribution which can delete part of the 3d spectral weight below -2 eV, or due to uncertainties in $\bar{U}$ calculations.

In Fig. 18c we draw a comparison of calculated results with XAS data. Finite lifetime effects for holes are taken into account by broadening the theoretical spectra with a Lorentzian 0.2 eV wide [164], then multiplication by the inverse Fermi function (at $T = 80$ K), and further broadening with a Gaussian exhibiting an experimental resolution of 0.36 eV. The general agreement of weights and positions of the quasiparticle band and upper Hubbard t_{2g} band is good, including tendencies associated with the transition from $SrVO_3$ to $CaVO_3$ ($Ca_{0.9}Sr_{0.1}VO_3$ in the experiment). For $CaVO_3$, the quasiparticle spectral peak weight is a bit less than in the experiment. In contrast to single-band Hubbard model calculations, LDA + DMFT approach accounts for peculiarities of the concrete systems and reproduces the strong asymmetry of the spectra close to the Fermi energy, including relative weights and bandwidths. These results (see Fig. 18) allow a different interpretation of XAS data than in Ref. [159], where the maximum at 2.5 eV was associated with the e_g band and not with the upper Hubbard t_{2g} band. Small differences between quasiparticle peaks (see Fig. 18) lead to various values of effective masses: $m^*/m_0 = 2.1$ for $SrVO_3$, and $m^*/m_0 = 2.4$ for $CaVO_3$. These theoretical predictions agree with $m^*/m_0 = 2-3$ for $SrVO_3$ and $CaVO_3$ obtained from de Haas–van Alphen experiments and available thermodynamic data [153–155, 165]. Notice that the effective mass for $CaVO_3$, determined from optical experiments, is slightly larger: $m^*/m_0 = 3.9$ [162].

4.3.2 Kinks in the $SrVO_3$ spectral function. Let us consider in more details LDA + DMFT(QMC) results obtained for spectral function $A(\mathbf{k}, \omega)$ of $SrVO_3$ in Ref. [116]. Owing to ideal cubic lattice symmetry, the matrix of self-energy $\Sigma(\omega)$ is diagonal, and all diagonal elements are the same for all t_{2g} orbitals. The spectral function is defined by the imaginary part of Green function $\mathrm{Im}\, G(\mathbf{k}, \omega)$, i.e. in fact by self-energy $\Sigma(\omega)$ on the real axis. This self-energy was calculated by numerical solution of Dyson's equation for the known interacting and bare Green functions, as described in the Appendix to Ref. [151].

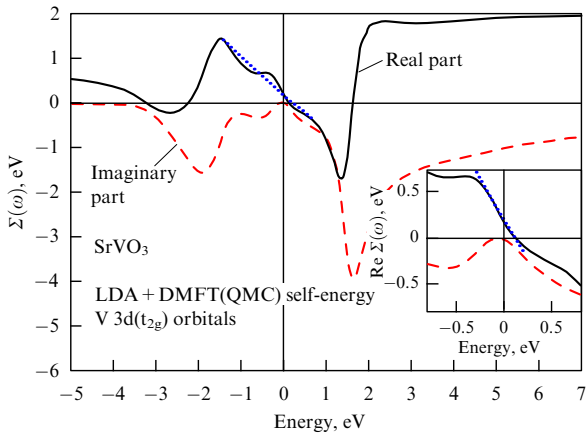

Figure 19. Real (black solid line) and imaginary (grey dashed line) parts of self-energy $\Sigma(\omega)$ obtained from the LDA + DMFT(QMC) calculations for V 3d (t_{2g}) orbitals in $SrVO_3$ [116]. In the inset to the figure, the self-energy in the vicinity of the Fermi level is shown in more detail. Dotted straight lines give the slope of $\mathrm{Re}\,\Sigma(\omega)$ far away and close to the Fermi level.

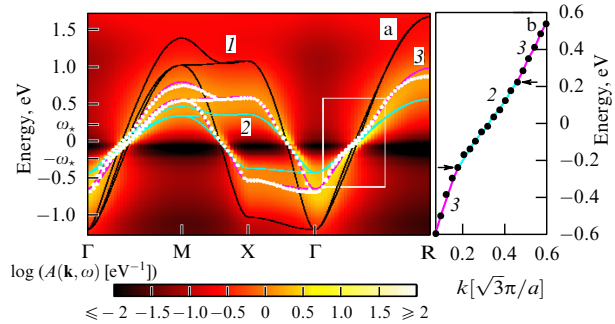

Figure 20. (a) Kinks in the dispersion relation $E_{n\mathbf{k}}$ (white dots) for $SrVO_3$ obtained from LDA + DMFT calculations. Lines *1* — LDA band structure $\epsilon_{n\mathbf{k}}$; lines *2* — LDA bands renormalized with the Fermi-liquid mass renormalization factor; lines *3* — band structure within the intermediate mode. (b) Kinks are marked with arrows, which correspond to the area within the white rectangle in figure a.

In Fig. 19, this self-energy $\Sigma(\omega)$ is plotted as a function of real frequencies. It is essentially asymmetric with respect to the Fermi level, as could be assumed from the asymmetry of the LDA density of states and band filling equal to 1/6. At energies $\omega \sim \pm 1.5$ eV, the real part of self-energy has extrema, corresponding to the transition region from the quasiparticle peak to the lower and upper Hubbard bands. Two extrema in the imaginary part of the self-energy, coinciding with $\mathrm{Re}\,\Sigma(\omega)$ zeros,[7] determine the energy positions of the lower and upper Hubbard bands (see Fig. 18a).

The asymmetric quasiparticle peak in the density of states is situated in the energy range from -0.8 to 1.4 eV (Fig. 18a). It is evident that imaginary part of self-energy, $\mathrm{Im}\,\Sigma(\omega)$, is sufficiently low at these energies, while its real part can be roughly approximated with the dashed straight line drawn in Fig. 19. The slope of this line determines quasiparticle mass renormalization $Z = m^*/m = 1 - \partial\,\mathrm{Re}\,\Sigma(\omega)/\partial\omega|_{\omega=0} = 1.9$. Such a Z value agrees with that obtained from primary QMC data at Matsubara frequencies: $m^*/m = 1 - \mathrm{Im}\,\Sigma(\omega_0)/\omega_0 \approx 2$, where ω_0 is the 'zeroth' Matsubara frequency. This value of renormalization is in agreement with the value of $m^*/m = 2.2$ from the studies [166, 167], as well as with the experimental estimate from ARPES data [168].

In the inset to Fig. 19 it is seen that Fermi-liquid behavior of self-energy [$\mathrm{Im}\,\Sigma(\omega) \sim -\omega^2$, together with $\mathrm{Re}\,\Sigma(\omega) \sim -\omega$] is evidenced only on the interval from -0.2 to 0.15 eV. The slope of $\mathrm{Re}\,\Sigma(\omega)$ in immediate proximity to the Fermi level is steeper than in the wider energy interval (see dashed straight line in Fig. 19). Thus, the Fermi-liquid mass renormalization value is larger than $m^*/m = 1.9$ and is equal to $m^*_{\mathrm{low}\,E}/m = 3$ (dotted straight line in the inset to Fig. 19). At the edges of the Fermi-liquid mode, sharp bends in $\mathrm{Re}\,\Sigma(\omega)$ at energies $\omega = \pm 0.25$ eV are seen. As the border of the Fermi-liquid mode we can consider energies whereat the imaginary part of self-energy starts to differ from the square-law dependence $\mathrm{Im}\,\Sigma(\omega) \sim -\omega^2$, which, in turn, leads to real part of self-energy deviating from the linear dependence $\mathrm{Re}\,\Sigma(\omega) \sim -\omega$ following from the Kramers–Kronig relation. Deviation from the square behavior of $\mathrm{Im}\,\Sigma$ at energies on the order of $\omega = \pm 0.25$ eV immediately gives rise to appearing cusps in $\mathrm{Re}\,\Sigma(\omega)$.

If the self-energy on the real axis is known, one can compute the spectral function $A(\mathbf{k}, \omega)$ and the quasiparticle dispersion determined by the momentum dependence of its maxima. In Fig. 20, we display the map of the spectral density obtained for $SrVO_3$ in Ref. [116]. In this multiband system (with degenerate bands), further analysis is similar to that for the single-band case of Section 3.3.2. White dots denote $E_{n\mathbf{k}}$ dispersion curves obtained from LDA + DMFT calculations for $SrVO_3$. In the narrow vicinity of the Fermi level, they coincide with the LDA band structure $\epsilon_{n\mathbf{k}}$ (lines *1*) renormalized with Fermi-liquid factor $Z_{\mathrm{FL}} = 0.35$, so that $E_{n\mathbf{k}} = Z_{\mathrm{FL}}\epsilon_{n\mathbf{k}}$ (lines *2*). Outside the Fermi-liquid region, dispersion curves correspond to the LDA band structure with a different renormalization factor: $E_{n\mathbf{k}} = Z_{\mathrm{CP}}\epsilon_{n\mathbf{k}} + c_{\pm}$ (lines *3*), where $Z_{\mathrm{CP}} = 0.64$, $c_+ = 0.086$ eV, and $c_- = 0.13$ eV. Along high-symmetry Γ–M and Γ–R directions in the Brillouin zone, the transition between these two modes leads to the formation of kinks in the effective dispersions at energies $\omega_\star = 0.22$ eV and $-\omega_\star = -0.24$ eV. These kinks are marked with arrows in Fig. 20b, which corresponds to the area surrounded by the white rectangle in the main part of the figure. On the contour plot of spectral function $A(\mathbf{k}, \omega)$, it is seen that the spectral function in the energy region sufficiently far away from the Fermi level keeps an explicit **k**-dependence, despite a pretty large damping value, replacing the traditional band structure picture for systems with strong electron–electron correlations.

Kinks of an electronic nature were discovered in this system in ARPES experiments [168] in the Γ–M direction at energies on the order of 0.25 eV, which agrees quite well with the above-given results of LDA + DMFT(QMC) calculations.

4.4 Electronic structure of copper oxides in the pseudogap state: LDA + DMFT + Σ

The pseudogap state — as already pointed out above — is one of the main anomalies in the normal (nonsuperconducting) state of high-T_c cuprates, and it is thought that

[7] Here, we recall that the real part of Green function is connected with the imaginary part of self-energy via the Kramers–Kronig relation [115].

clarification of its physical nature is the key point to understanding the high-temperature superconductivity mechanism [55, 56, 169]. The most powerful tool to investigate this state in recent years has been angular-resolved photoemission spectroscopy (ARPES). During the last ten years there has been remarkable progress in this area related to significant growth of ARPES resolution, both in energy and in momentum spaces [170 – 173]. The Fermi surface shape, quasiparticle dispersion and damping, and even self-energy profile can be directly restored from ARPES data [170 – 173]. These allowed studying in detail formation of the pseudogap, shadow bands, quite unusual phenomena of Fermi arc formation, and interlayer hybridization effects (bilayer splitting) in double-layer systems [170 – 173], as well as determining qualitative distinctions between electron- and hole-doped cuprates [170 – 173]. The purpose of the theory is to explain all these peculiarities, and this problem is much more complicated by the presence of rather strong electronic correlations, typical for these systems and making doubtful the standard band theory and Fermi-liquid approach.

In this section, we shall demonstrate that an account of AFM short-range order fluctuations is, in principle, enough for describing a number of ARPES experiments on real systems. To this end, we make use of the LDA + DMFT + Σ hybrid computational scheme [174 – 179]. On the one hand, this scheme inherits all the advantages of LDA + DMFT approach [25 – 31], i.e. the combination of single-electron first-principle density functional theory in the local density approximation (DFT/LDA) [132, 133, 180, 181] with dynamical mean-field theory for strongly correlated electrons [3 – 5, 7, 14]. On the other hand, such a hybrid scheme allows considering nonlocal correlations by the introduction of momentum-dependent self-energy, while the usual self-consistent set of DMFT equations is preserved [35 – 37]. To solve effectively the single-impurity problem of DMFT in the works described below, we employed the numerical renormalization group (NRG) method [23, 24].

Such a computational scheme works very well in describing the electronic properties of high-T_c cuprates in the normal (underdoped) state. First, all material-specific model parameters of a physically relevant Cu-3d$_{x^2-y^2}$ orbital can be obtained from LDA calculations. Second, stoichiometric (nondoped) cuprates are antiferromagnetic Mott insulators with $U \gg W$ (U is the local Coulomb interaction, and W is the conduction bandwidth), so that correlation effects in them are very important. At finite doping level (at least up to optimal doping), cuprates are typical strongly correlated metals, and the DMFT stage of the computational scheme allows one to account for strong electronic correlations. Finally, to study the 'antiferromagnetic scenario' of pseudogap formation, we introduce into the standard LDA + DMFT scenario the **k**-dependent self-energy $\Sigma_{\mathbf{k}}$ describing nonlocal correlations induced by (quasi)static Heisenberg spin fluctuations of AFM short-range order [58 – 60].

In the framework of the LDA + DMFT + Σ approach, we performed calculations for a series of high-temperature superconductors: hole-doped $Bi_2Sr_2CaCu_2O_{8-\delta}$ (Bi2212) [174] and $La_{2-x}Sr_xCuO_4$ (LSCO) [175], and also electron-doped $Nd_{2-x}Ce_xCuO_4$ (NCCO) [176, 177] and $Pr_{2-x}Ce_xCuO_4$ (PCCO) [178]. LDA + DMFT + Σ calculated results for Fermi surfaces and spectral functions can be compared with ARPES data for quasiparticle bands and experimental Fermi surface maps.

The crystal structures of Bi2212 [174], NCCO [176, 177], and PCCO [178] have tetragonal symmetry with the space group $I4/mmm$, while LSCO has a distorted orthorhombic structure *Bmab* [175]. Crystallographic data employed in LDA + DMFT + Σ calculations are presented in more detail in Refs [174 – 179].

It is well known that the physical properties of cuprates are determined in many respects by the quasi-two-dimensionality of their electronic properties. From this point of view, the main interest is focused on electronic states in the CuO_2 plane, where we are dealing with partially filled antibonding Cu-3d$_{x^2-y^2}$ orbitals with dispersion crossing the Fermi level. In the tight-binding approximation, this dispersion has the following form

$$\begin{aligned}\varepsilon(\mathbf{k}) = &-2t(\cos k_x a + \cos k_y a) - 4t' \cos k_x a \cos k_y a \\ &- 2t''(\cos 2k_x a + \cos 2k_y a) \\ &- 2t'''(\cos k_x a \cos 2k_y a + \cos 2k_x a \cos k_y a)\,. \qquad (66)\end{aligned}$$

Here, t, t', t'', t''' are Cu–Cu transfer integrals in the first four coordination spheres in the CuO_2 plane, and a is the lattice constant. The values of these effective transfer integrals calculated in the framework of the linearized muffin-tin orbitals (LMTO) method [136, 137] and subsequent use of Wannier functions obtained within the N-th-order LMTO (NMTO) method of Refs [148–150] are listed in Table 1. In what follows, we shall exploit the LDA-calculated effective antibonding Cu-3d$_{x^2-y^2}$ band as a 'bare' one in LDA + DMFT + Σ computations.

In double-layer systems, e.g. in Bi2212, hopping between two neighboring planes is also important. In the tight-binding approximation, an expression for the corresponding interlayer dispersion derived in Ref. [182] has the form

$$t_\perp(\mathbf{k}) = \frac{t_\perp}{4}\,(\cos k_x a - \cos k_y a)^2\,. \qquad (67)$$

The values of $t_\perp$ are given in Table 1. Consideration of interlayer hopping and 'bilayer splitting' effects requires a certain generalization of LDA + DMFT + Σ computational scheme [174].

To perform DMFT calculations, one should also calculate the strength of onsite Coulomb interaction. The values of this interaction U for the effective Cu-3d$_{x^2-y^2}$ orbital, obtained within the constrained LDA method [144], are also given in Table 1.

To account for AFM spin fluctuations, we employed the two-dimensional model of the pseudogap state [58 – 60], generalized for DMFT + Σ calculations [35, 37]. Additional external **k**-dependent self-energy $\Sigma_{\mathbf{k}}$ [35, 37] describes non-

Table 1. Calculated model energy parameters (in eV) and experimental correlation length ξ.

Compound	t	t'	t''	t'''	$t_\perp$	U	Δ	ξ
Bi2212	−0.627	0.133	0.061	−0.015	0.083	1.51	0.21	10a
NCCO	−0.44	0.153	0.063	−0.010	—	1.10	0.36	50a
PCCO	−0.438	0.156	0.098	—	—	1.10	0.275	50a
LSCO	−0.476	0.077	−0.025	−0.015	—	1.10	0.21	10a

Note. First four Cu–Cu transfer integrals in the CuO_2 plane are t, t', t'', and t'''; effective interlayer transfer integral is $t_\perp$; local Coulomb interaction is U, and pseudogap amplitude is Δ.

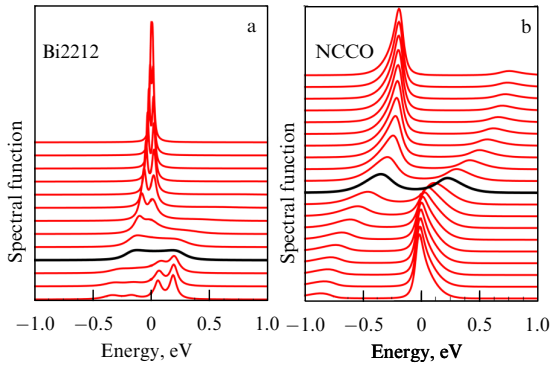

Figure 21. LDA + DMFT + Σ spectral functions for Bi2212 (a) and NCCO (b) along the bare Fermi surface in 1/8 of the Brillouin zone. The dark lines correspond to the hot spots [176, 177].

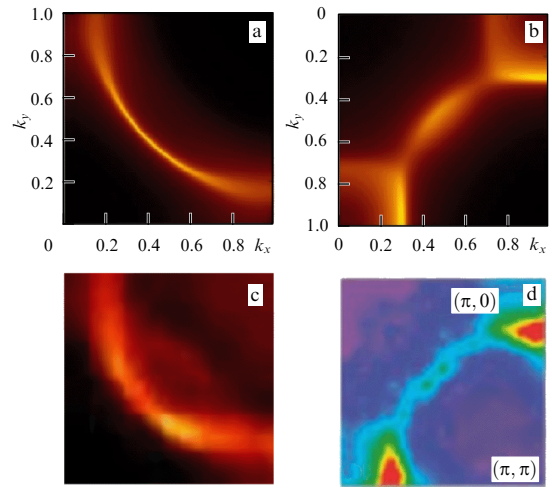

Figure 22. LDA + DMFT + Σ Fermi surface maps obtained in Refs [176, 177] for Bi2212 (a) and NCCO (b) compounds in a fourth of the Brillouin zone (k_x, k_y are given in units of π/a). Experimental Fermi surfaces for Bi2212 (c) [188] and NCCO (d) [186].

local correlations caused by (quasi)static [8] AFM spin fluctuations.

To specify $\Sigma_{\mathbf{k}}$, it is necessary to know two important parameters: the pseudogap amplitude Δ giving the energy scale of fluctuating SDW, and the correlation length ξ. The values of Δ were calculated as described in Refs [35, 37, 174]. The values of the correlation length were taken in accordance with those produced in neutron scattering experiments for NCCO [183, 184] and LSCO [185]. The values of Δ and ξ used for all systems under consideration are also listed in Table 1. To solve effectively the Anderson single-impurity problem in DMFT, we applied the numerical renormalization group method ([23, 24]). The temperature in DMFT(NRG) calculations was chosen equal to 0.011 eV, and electron or hole concentration (doping level) amounted to 15%.

LDA + DMFT + Σ calculations produced a clear picture of hot spots behavior in the spectral function and on maps of the Fermi surfaces for electron-doped systems [176–178], while for hole-doped systems only Fermi arcs arose [174, 175].

Figure 21 gives LDA + DMFT + Σ results for spectral functions calculated along 1/8 of the bare Fermi surface, from the nodal point on the diagonal of the Brillouin zone (upper curve) to the antinodal point at the boundary of the zone (lower curve). Results for Bi2212 are shown in the left panel of the figure, and for NCCO in the right panel. For both systems, quasiparticles are well defined in the nodal direction — a sharp peak of the spectral function situated practically on the Fermi level is clearly seen. As one moves to the antinodal point, quasiparticle damping grows, reaching a maximum at the hot spot (dark curve), and the peak of spectral density moves away from the Fermi level. This behavior is in complete agreement with the results of Refs [186, 187] (for a comparison with experiment, see Refs [176, 177]). From the LDA + DMFT + Σ results given in Fig. 21, it is directly seen that antinodal states in Bi2212 are formed by the low-energy edge of the pseudogap,[9] while in NCCO by the high-energy edge. For Bi2212, we also observe bilayer splitting of the quasiparticle peak, which is related to the presence of two CuO_2 planes in the unit cell.

The hot spots for NCCO are located closer to the Brillouin zone diagonal [176, 177]. This can be seen from the dark lines in Fig. 21, which correspond to the hot spots. Moreover, the correlation length in NCCO is much larger than in Bi2212. Thus, quasiparticles again are rather well defined for NCCO (in contrast to Bi2212) in the antinodal direction. For Bi2212, on the contrary, scattering near the Brillouin zone boundaries is strong everywhere, and instead of hot spots we observe quite strong 'destruction' of the Fermi surface close to these boundaries. Qualitatively the same picture is also observed in LSCO.

LDA + DMFT + Σ Fermi surface maps in the quarter of the Brillouin zone for Bi2212 are presented in Fig. 22a, and for NCCO in Fig. 22b. In Bi2212, we observe strong destruction of the Fermi surface by scattering on pseudogap fluctuations in proximity to the Brillouin zone boundaries.[10] In NCCO, in contrast, the Fermi surface is almost completely restored close to the Brillouin zone boundaries. On the other hand, the Fermi arc around the nodal direction in Bi2212 is pronounced rather clearly, while in NCCO it is noticeably smeared. This is another consequence of the fact that hot spots in NCCO are located closer to the Brillouin zone diagonal. A bit larger value of the pseudogap amplitude Δ also favors the stronger smearing of Fermi arcs in NCCO. Noteworthy also is the appearance of the shadow Fermi surface which is much more intensive in NCCO.

Qualitatively the same Fermi surfaces were discovered experimentally in real Bi [188] and Nd [186] systems (see Fig. 22c, d). Thus, the distinction of Fermi surface maps for these systems is related mainly to the distinction of the band structure parameters for these materials. In particular, LDA Fermi surfaces of NCCO are more bent, and hot spots appear to be rather far from the Brillouin zone boundaries; consequently, the Fermi surface in the vicinity of these

[8] The quasistatic approximation for AFM fluctuations necessarily restricts this approach to rather high temperatures (and energies not very close to the Fermi level) [58–60]. Thus, we cannot in fact judge, for instance, the nature of low-temperature (low-energy) damping, which is determined entirely by dynamical (inelastic) scattering processes.

[9] It is especially distinctly visible for the case of smaller correlation length $\xi = 5a$ considered in Ref. [174].

[10] Analogous behavior in entire accordance with ARPES results is also realized in another hole-doped system — LSCO. The LDA + DMFT + Σ calculations for this system were performed in Ref. [175].

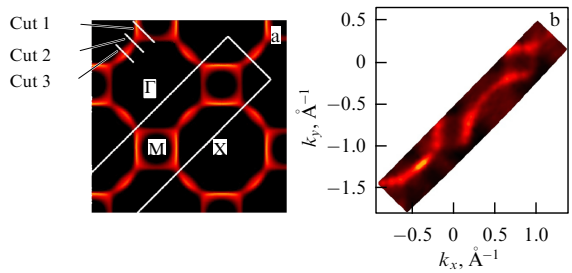

Figure 23. Fermi surface map for PCCO. (a) Results of LDA + DMFT + Σ calculations. The white rectangle in panel (a) shows the part of reciprocal space where ARPES measurements (panel b) were done. The lower left corner coincides with the X-point $(\pi/a, 0)$ of the Brillouin zone [178].

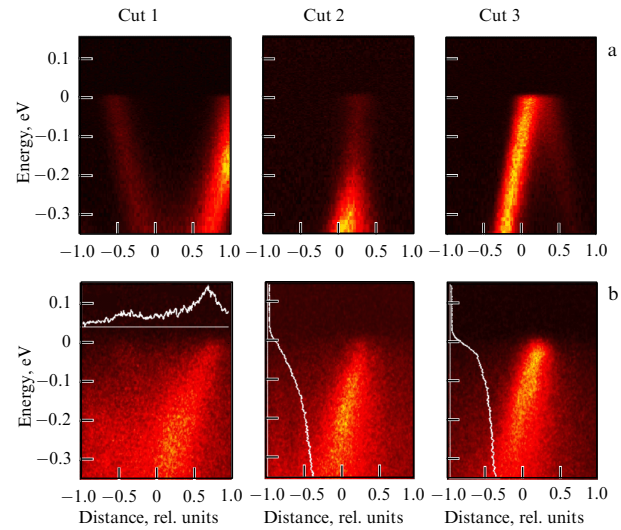

Figure 24. Momentum–energy distributions of intensity for characteristic cuts of the Brillouin zone plotted in Fig. 23 (upper panels — theoretical data, lower panels — experimental photoemission intensities). For cut 1, we show the momentum distribution curve (MDC) integrated over the energy window 60 meV in width around the Fermi level. Analogous MDC for cut 2 (through the hot spot) shows ARPES intensity suppression compared with MDC for cut 3 which is located quite far away from the hot spot [176, 177].

boundaries barely feels scattering by AFM fluctuations. In Bi2212, the LDA Fermi surface comes in rather close to the Brillouin zone boundaries in proximity to the $(\pi/a, 0)$ point, so that hot spots are also close to this point. Thus, they are more 'smeared' in Bi2212 by strong pseudogap scattering near the $(\pi/a, 0)$ point and are almost not observed. Hot spots in NCCO are more vivid also because of the much larger correlation length of fluctuations.

No less clear results were obtained in LDA + DMFT + Σ calculations and ARPES experiments for PCCO in Ref. [178]. Figure 23 displays a PCCO Fermi surface map (panel (a) — LDA + DMFT + Σ results, and panel (b) — experimental ARPES data). The Fermi surface is clearly distinguishable here only near first Brillouin zone boundaries and around the $(\pi/a/2, \pi/a/2)$ point (Fermi arc). Again, as in NCCO, we observe destruction of the Fermi surface in hot spots located at the intersection of the Fermi surface and its AFM shadow 'replica'. This destruction of the Fermi surface is due to the strong electron scattering by AFM spin (pseudogap) fluctuations. The shadow Fermi surface becomes observable, as happens in the case of AFM doubling of the lattice period. However, since there is no long-range order in the underdoped region in which we are interested, this shadow Fermi surface is strongly eroded. The PCCO Fermi surface is very similar to that observed in $Nd_{2-x}Ce_xCuO_4$ (NCCO) compound, which belongs to the same family of superconductors [176, 177, 186].

Let us compare (see Fig. 24) theoretical (upper panel) and experimental (lower panel) quasiparticle dispersions along the most characteristic cuts of the Fermi surface shown in Fig. 23. Theoretical data are multiplied by the Fermi function at a temperature of 30 K and convoluted (in energy) with a Gaussian distribution to simulate the experimental resolution.

Cut 1 crosses the quasiparticle and shadow Fermi surfaces near the Brillouin zone boundary. Correspondingly, it is possible to detect here a fork-like structure formed by a suppressed shadow band and much better defined by a quasiparticle band. This structure corresponds to the origin of formation of the Fermi surface cylinder around the $(\pi/a, 0)$ point. Cut 2 passes exactly through the hot spot. Here, we see a strong suppression of the quasiparticle band near the Fermi level. Finally, cut 3 crosses the Fermi arc and we can see a fairly well-defined quasiparticle band. However, the low-intensity shadow band is also present. In the case of the presence of long-range AFM order and a full doubling of the period, the Fermi surface and its shadow form a closed 'pocket' of the Fermi surface around the $(\pi/2a, \pi/2a)$ point, while in the present case a part of the pocket formed by the shadow band is strongly smeared. One can see a good agreement between calculated and experimental data. As already noted, two-particle properties within the LDA + DMFT + Σ framework can also be calculated [38], which allowed investigating the optical conductivity of Bi and Nd cuprates [176, 177], and also demonstrating significant differences in the effects of pseudogap fluctuations. In particular, we observe in the optical conductivity of NCCO, in qualitative agreement with experiment [189], a characteristic pseudogap dip and a smooth maximum due to absorption through the pseudogap at frequencies $\sim 2\Delta$. However, the characteristic pseudogap structure in optical conductivity of Bi2212 hardly occurs, either in theory or in experiment [190], which is related to sufficiently small values of Δ and the fluctuation correlation length in this system.

Let us summarize some of our conclusions. For all the systems studied, LDA + DMFT + Σ calculations give evidence that Fermi-liquid behavior persists only rather far away from hot spots (nodal direction), and destruction of the Fermi surface is observed near the hot spots. This destruction is due to strong scattering of correlated electrons on short-range order AFM (pseudogap) fluctuations. A comparison of ARPES data and LDA + DMFT + Σ calculated results points to the existence of quite distinct hot spots in the behavior of both the spectral density and maps of the Fermi surface in electron-doped systems, in contrast to hole-doped systems, where we only observe a strong destruction of the Fermi surface near the Brillouin zone boundaries and Fermi arcs around its diagonals.

There are several reasons for this distinction: (1) hot spots in electron-doped systems are located closer to the center of the Brillouin zone; (2) the correlation length of AFM fluctuations in electron-doped systems is longer, and (3) the width of the pseudogap in electron-doped systems is also

larger than in hole-doped ones. The experimental and theoretical results discussed above clearly confirm the AFM scenario of the formation of a pseudogap in both hole-doped [174, 175] and electron-doped [176 – 178] cuprates.

5. Conclusions

In this review, we discussed the DMFT + Σ generalization of the standard dynamical mean-field theory (DMFT), which allows us to include nonlocal correlations or additional (relative to the Hubbard one) interactions (theoretically of any type), while remaining within the single-impurity picture of DMFT and retaining the same set of self-consistent DMFT equations. The basic approximation of this method relies on the neglect of interference contributions from DMFT diagrams and additional interactions included in the analysis. Precisely this (strictly speaking not completely controllable) approximation allows preserving the overall structure of DMFT equations, which permits solving DMFT + Σ equations with the well-developed methods used in the standard DMFT. It should be emphasized that the self-consistent account of additional interactions at every step of the DMFT loop leads to a rather complicated procedure equivalent to the summation of infinite classes of diagrams.

The proposed approach proved to be versatile enough to be applied to a number of problems in systems with strong electron correlations — from a semiphenomenological account of nonlocal short-range order pseudogap fluctuations to the self-consistent framework for the metal–insulator transition in the disordered Anderson–Hubbard model and account of the electron–phonon interaction effects in the electronic spectra of strongly correlated systems. A salient feature of the DMFT + Σ approach is the possibility of studying, along with one-particle characteristics, the two-particle properties, i.e., in principle, any kind of response functions (optical conductivity, magnetic susceptibility, charge screening, etc.). The universality of the method allows one to hope for its successful application to solving a number of future problems.

Discussing all the problems of interest, one should keep in mind that similar in many respects physical results can also be obtained with more sophisticated approaches, using these or other methods of direct numerical simulation. For example, similar results for the formation of the pseudogap in the single-particle characteristics of the two-dimensional Hubbard model were obtained in the cluster generalizations of DMFT [32, 33]. However, these methods exhibit specific limitations (e.g. on cluster size) and are still not widely used to calculate the two-particle properties, such as the general response functions, notably, the optical conductivity. The DMFT + Σ approach has obvious advantages here, associated with saving computational resources: it requires a significantly lower cost of computational time, and its advantage in calculating the two-particle response functions is quite obvious. This opens up additional opportunities for the systematic comparison of various types of nonlocal fluctuations or additional interactions and their influence on the electronic properties of strongly correlated systems, providing an intuitively clear path to the analysis of experimental and theoretical results obtained via more complicated methods.

The rather simple generalization of our computational scheme enabled us also to formulate the generalized LDA + DMFT + Σ approach allowing us to perform calculations of all the effects discussed above for real compounds of transition metal elements with strong electronic correlations. One can expect that these calculations will be useful in analyzing and explaining new experimental findings.

Acknowledgments. The authors thank Th Pruschke for his significant contribution to the development of the DMFT + Σ approach in its initial stages, as well as for providing us with the very efficient NRG code that was used in most computations. We are also grateful to S V Borisenko and other members of the Dresden ARPES group with whom ARPES studies of PCCO were performed. Studies of $Sr(Ca)VO_3$, LSCO, and NCCO compounds were performed in the framework of a joint project with Osaka University (group leaded by Prof. S Suga and Prof. A Sekiyama).

This work was partially supported by RFBR grant No. 11-02-00147 and performed within the framework of the Programs 'Quantum Physics of Condensed Matter' (UB RAS 09-P-2-1009) of the Presidium of RAS, and 'Strongly Correlated Electrons in Solids' of the Physical Sciences Division of RAS (UB RAS 09-T-2-1011).

References

1. Mott N F *Metal-Insulator Transitions* 2nd ed. (London: Taylor & Francis, 1990) [Translated into Russian (Moscow: Nauka, 1979)]
2. Izyumov Yu A, Anisimov V I *Elektronnaya Struktura Soedinenii s Sil'nymi Korrelyatsiyami* (Electronic Structure of Strongly Correlated Materials) (Moscow – Izhevsk: RKhD, 2008) [Translated into English: Anisimov V, Izyumov Yu *Electronic Structure of Strongly Correlated Materials* (Heidelberg: Springer, 2010)]
3. Vollhardt D, in *Correlated Electron Systems* (Ed. V J Emery) (Singapore: World Scientific, 1993) p. 57
4. Pruschke Th, Jarrell M, Freericks J K *Adv. Phys.* **44** 187 (1995)
5. Georges A et al. *Rev. Mod. Phys.* **68** 13 (1996)
6. Vollhardt D *AIP Conf. Proc.* **1297** 339 (2010)
7. Kotliar G, Vollhardt D *Phys. Today* **57** (3) 53 (2004)
8. Hubbard J *Proc. R. Soc. London A* **276** 238 (1963)
9. Hubbard J *Proc. R. Soc. London A* **277** 237 (1964)
10. Hubbard J *Proc. R. Soc. London A* **281** 401 (1964)
11. Hubbard J *Proc. R. Soc. London A* **285** 542 (1965)
12. Hubbard J *Proc. R. Soc. London A* **296** 82 (1967)
13. Hubbard J *Proc. R. Soc. London A* **296** 100 (1967)
14. Metzner W, Vollhardt D *Phys. Rev. Lett.* **62** 324 (1989)
15. Anderson P W *Phys. Rev.* **124** 41 (1961)
16. Pruschke Th, Grewe N *Z. Phys. B* **74** 439 (1989)
17. Pruschke Th, Cox D L, Jarrell M *Phys. Rev. B* **47** 3553 (1993)
18. Hirsch J E, Fye R M *Phys. Rev. Lett.* **56** 2521 (1986)
19. Jarrell M *Phys. Rev. Lett.* **69** 168 (1992)
20. Rozenberg M J, Zhang X Y, Kotliar G *Phys. Rev. Lett.* **69** 1236 (1992)
21. Georges A, Krauth W *Phys. Rev. Lett.* **69** 1240 (1992)
22. Jarrell M, in *Numerical Methods for Lattice Quantum Many-Body Problems* (Ed. D J Scalapino) (Reading, Mass.: Addison-Wesley, 1997)
23. Wilson K G *Rev. Mod. Phys.* **47** 773 (1975)
24. Bulla R, Costi T A, Pruschke Th *Rev. Mod. Phys.* **80** 395 (2008)
25. Anisimov V I et al. *J. Phys. Condens. Matter* **9** 7359 (1997)
26. Lichtenstein A I, Katsnelson M I *Phys. Rev. B* **57** 6884 (1998)
27. Nekrasov I A et al. *Eur. Phys. J. B* **18** 55 (2000)
28. Held K et al. Ψ_k *Newsletter* (56) 65 (2003)
29. Held K et al. *Int. J. Mod. Phys. B* **15** 2611 (2001)
30. Held K et al., in *Quantum Simulations of Complex Many-Body Systems: From Theory to Algorithms* (Eds J Grotendorst, D Marx, A Muramatsu) (Julich: John von Neumann Institute for Computing, 2002) p. 175
31. Lichtenstein A I, Katsnelson M I, Kotliar G, in *Electron Correlations and Materials Properties 2* Vol. 2 (Eds A Gonis, N Kioussis, M Ciftan) (New York: Kluwer Acad./Plenum Publ., 2003) p. 428
32. Maier Th et al. *Rev. Mod. Phys.* **77** 1027 (2005)

33. Kotliar G et al. *Phys. Rev. Lett.* **87** 186401 (2001)
34. Capone M et al. *Phys. Rev. B* **69** 195105 (2004)
35. Sadovskii M V et al. *Phys. Rev. B* **72** 155105 (2005)
36. Kuchinskii E Z, Nekrasov I A, Sadovskii M V *Pis'ma Zh. Eksp. Teor. Fiz.* **82** 217 (2005) [*JETP Lett.* **82** 198 (2005)]
37. Kuchinskii E Z, Nekrasov I A, Sadovskii M V *Fiz. Nizkikh Temp.* **32** 528 (2006) [*Low Temp. Phys.* **32** 398 (2006)]
38. Kuchinskii E Z, Nekrasov I A, Sadovskii M V *Phys. Rev. B* **75** 115102 (2007)
39. Kuchinskii E Z, Nekrasov I A, Sadovskii M V *Zh. Eksp. Teor. Fiz.* **133** 670 (2008) [*JETP* **106** 581 (2008)]
40. Vollhardt D, Wölfle P *Phys. Rev. B* **22** 4666 (1980)
41. Vollhardt D, Wölfle P *Phys. Rev. Lett.* **48** 699 (1982)
42. Sadovskii M V *Diagrammatika* (Diagrammatics) 2nd ed. (Moscow – Izhevsk: Inst. Komp'yut. Issled., 2010); *Diagrammatics* (Singapore: World Scientific, 2006)
43. Kotliar G et al. *Phys. Rev. Lett.* **87** 186401 (2001)
44. Biroli G, Kotliar G *Phys. Rev. B* **65** 155112 (2002)
45. Lichtenstein A I, Katsnelson M I *Phys. Rev. B* **62** R9283 (2000)
46. Hettler M H et al. *Phys. Rev. B* **58** R7475 (1998)
47. Hettler M H et al. *Phys. Rev. B* **61** 12739 (2000)
48. Maier Th et al. *Phys. Rev. Lett.* **85** 1524 (2000)
49. Maier Th et al. *Eur. Phys. J. B* **13** 613 (2000)
50. Huscroft C et al. *Phys. Rev. Lett.* **86** 139 (2001)
51. Kusunose H *J. Phys. Soc. Jpn.* **75** 054713 (2006)
52. Toschi A, Katanin A A, Held K *Phys. Rev. B* **75** 045118 (2007)
53. Rubtsov A N, Katsnelson M I, Lichtenstein A I *Phys. Rev. B* **77** 033101 (2008)
54. Rubtsov A N, Katsnelson M I, Lichtenstein A I, Georges A *Phys. Rev. B* **79** 045133 (2009)
55. Timusk T, Statt B *Rep. Prog. Phys.* **62** 61 (1999)
56. Sadovskii M V *Usp. Fiz. Nauk* **171** 539 (2001) [*Phys. Usp.* **44** 515 (2001)]
57. Pines D, cond-mat/0404151
58. Schmalian J, Pines D, Stojković B *Phys. Rev. Lett.* **80** 3839 (1998)
59. Schmalian J, Pines D, Stojković B *Phys. Rev. B* **60** 667 (1999)
60. Kuchinskii E Z, Sadovskii M V *Zh. Eksp. Teor. Fiz.* **115** 1765 (1999) [*JETP* **88** 968 (1999)]
61. Sadovskii M V *Zh. Eksp. Teor. Fiz.* **77** 2070 (1979) [*Sov. Phys. JETP* **50** 989 (1979)]
62. Sadovskii M V *Zh. Eksp. Teor. Fiz.* **66** 1720 (1974) [*Sov. Phys. JETP* **39** 845 (1974)]
63. Sadovskii M V, Timofeev A A *J. Moscow Phys. Soc.* **1** 391 (1991)
64. Sadovskii M V, Strigina N A *Zh. Eksp. Teor. Fiz.* **122** 610 (2002) [*JETP* **95** 526 (2002)]
65. Vilk Y M, Tremblay A-M S *J. Physique I* **7** 1309 (1997)
66. Ding H et al. *Nature* **382** 51 (1996)
67. Kuchinskii E Z, Sadovskii M V *Zh. Eksp. Teor. Fiz.* **130** 477 (2006) [*JETP* **103** 415 (2006)]
68. Armitage N P et al. *Phys. Rev. Lett.* **87** 147003 (2001)
69. Basov D N, Timusk T *Rev. Mod. Phys.* **77** 721 (2005)
70. Hwang J, Timusk T, Gu G D *J. Phys. Condens. Matter* **19** 125208 (2007)
71. Lee P A, Ramakrishnan T V *Rev. Mod. Phys.* **57** 287 (1985)
72. Belitz D, Kirkpatrick T R *Rev. Mod. Phys.* **66** 261 (1994)
73. Mott N F *Proc. Phys. Soc. A* **62** 416 (1949)
74. Anderson P W *Phys. Rev.* **109** 1492 (1958)
75. Finkel'shtein A M *Zh. Eksp. Teor. Fiz.* **84** 168 (1983) [*Sov. Phys. JETP* **57** 97 (1983)]
76. Castellani C P et al. *Phys. Rev. B* **30** 527 (1984)
77. Dobrosavljević V, Kotliar G *Phys. Rev. Lett.* **78** 3943 (1997)
78. Dobrosavljević V, Pastor A A, Nikolić B K *Europhys. Lett.* **62** 76 (2003)
79. Byczuk K, Hofstetter W, Vollhardt D *Phys. Rev. Lett.* **94** 056404 (2005)
80. Henseler P, Kroha J, Shapiro B *Phys. Rev. B* **77** 075101 (2008)
81. Henseler P, Kroha J, Shapiro B *Phys. Rev. B* **78** 235116 (2008)
82. Pezzoli M E, Becca F *Phys. Rev. B* **81** 075106 (2010)
83. Ulmke M, Janiš V, Vollhardt D *Phys. Rev. B* **51** 10411 (1995)
84. Vlaming R, Vollhardt D *Phys. Rev. B* **45** 4637 (1992)
85. Wölfle P, Vollhardt D, in *Anderson Localization* (Springer Series in Solid State Sciences, Vol. 39, Eds Y Nagaoka, H Fukuyama) (Berlin: Springer, 1982) p. 26
86. Sadovskii M V, in *Soviet Scientific Reviews – Physics Reviews* Vol. 7 (Ed I M Khalatnikov) (New York: Harwood Acad. Publ., 1986) p. 1
87. Wölfle P, Vollhardt D, in *Electronic Phase Transitions* (Modern Problems in Condensed Matter Sciences, Vol. 32, Eds W Hanke, Yu V Kopaev) (Amsterdam: North-Holland, 1992) p. 1
88. Kuchinskii E Z et al. *Zh. Eksp. Teor. Fiz.* **107** 2027 (1995) [*JETP* **80** 1122 (1995)]
89. Kuchinskii É Z, Érkabaev M A *Fiz. Tverd. Tela* **39** 412 (1997) [*Phys. Solid State* **39** 357 (1997)]
90. Kuchinskii E Z et al. *Zh. Eksp. Teor. Fiz.* **137** 368 (2010) [*JETP* **110** 325 (2010)]
91. Bulla R *Phys. Rev. Lett.* **83** 136 (1999)
92. Bulla R, Costi T A, Vollhardt D *Phys. Rev. B* **64** 045103 (2001)
93. Blümer N "Mott – Hubbard metal – insulator transition and optical conductivity", Thesis (München: Univ. Augsburg, 2002)
94. Erkabaev M A, Sadovskii M V *J. Moscow Phys. Soc.* **2** 233 (1992)
95. Abrahams E et al. *Phys. Rev. Lett.* **42** 673 (1979)
96. Altshuler B L, Aronov A G, Lee P A *Phys. Rev. Lett.* **44** 1288 (1980)
97. Dolan G J, Osheroff D D *Phys. Rev. Lett.* **43** 721 (1979)
98. Bishop D J, Tsui D C, Dynes R C *Phys. Rev. Lett.* **44** 1153 (1980)
99. Uren M J, Davies R A, Pepper M *J. Phys. C* **13** L985 (1980)
100. Kravchenko S V, Sarachik M P *Rep. Prog. Phys.* **67** 1 (2004)
101. Abrahams E, Kravchenko S V, Sarachik M P *Rev. Mod. Phys.* **73** 251 (2001)
102. Valla T et al. *Phys. Rev. Lett.* **83** 2085 (1999)
103. Hengsberger M et al. *Phys. Rev. Lett.* **83** 592 (1999)
104. Lanzara A et al. *Nature* **412** 510 (2001)
105. Shen Z-X et al. *Philos. Mag. B* **82** 1349 (2002)
106. Rotenberg E, Schaefer J, Kevan S D *Phys. Rev. Lett.* **84** 2925 (2000)
107. Higashiguchi M et al. *J. Electron Spectrosc. Relat. Phenom.* **144–147** 639 (2005)
108. Sun Z et al. *Phys. Rev. Lett.* **97** 056401 (2006)
109. He H et al. *Phys. Rev. Lett.* **86** 1610 (2001)
110. Hwang J, Timusk T, Gu G D *Nature* **427** 714 (2004)
111. Ronning F et al. *Phys. Rev. B* **67** 165101 (2003)
112. Yoshida T et al. *Phys. Rev. Lett.* **95** 146404 (2005)
113. Graf J et al. *Phys. Rev. Lett.* **98** 067004 (2007)
114. Byczuk K et al. *Nature Phys.* **3** 168 (2007)
115. Abrikosov A A, Gorkov L P, Dzyaloshinski I E *Metody Kvantovoi Teorii Polya v Statisticheskoi Fizike* (Methods of Quantum Field Theory in Statistical Physics) (Moscow: Fizmatgiz, 1963) [Translation into English (New York: Dover Publ., 1975)]
116. Nekrasov I A et al. *Phys. Rev. B* **73** 155112 (2006)
117. Toshi A et al. *Phys. Rev. Lett.* **102** 076402 (2009)
118. Bulla R, Pruschke Th, Hewson A C *Physica B* **259–261** 721 (1999)
119. Holstein T *Ann. Physics* **8** 325 (1959)
120. Hewson A C, Mayer D *J. Phys. Condens. Matter* **17** 5413 (2002)
121. Koller W, Hewson A C, Edwards D M *Phys. Rev. Lett.* **95** 256401 (2006)
122. Hague J P *J. Phys. Condens. Matter* **15** 2535 (2003)
123. Migdal A B *Zh. Eksp. Teor. Fiz.* **34** 1438 (1958) [*Sov. Phys. JETP* **7** 999 (1958)]
124. Kuchinskii E Z, Nekrasov I A, Sadovskii M V *Phys. Rev. B* **80** 115124 (2009)
125. Sadovskii M V, Kuchinskii E Z, Nekrasov I A *J. Phys. Chem. Solids* **72** 366 (2011)
126. Koller W, Meyer D, Hewson A C *Phys. Rev. B* **70** 155103 (2004)
127. Jeon G S et al. *Phys. Rev. B* **70** 125114 (2004)
128. Koller W et al. *Europhys. Lett.* **66** 559 (2004)
129. Born M, Oppenheimer R *Ann. Physik* **389** 457 (1927)
130. Hohenberg P, Kohn W *Phys. Rev.* **136** B864 (1964)
131. Jones R O, Gunnarsson O *Rev. Mod. Phys.* **61** 689 (1989)
132. Kohn W, Sham L J *Phys. Rev.* **140** A1133 (1965)
133. Sham L J, Kohn W *Phys. Rev.* **145** 561 (1966)
134. Janak J F *Phys. Rev. B* **18** 7165 (1978)
135. Ceperley D M, Alder B J *Phys. Rev. Lett.* **45** 566 (1980)
136. Andersen O K *Phys. Rev. B* **12** 3060 (1975)
137. Andersen O K, Jepsen O *Phys. Rev. Lett.* **53** 2571 (1984)
138. Müller-Hartmann E *Z. Phys. B* **74** 507 (1989)
139. Müller-Hartmann E *Z. Phys. B* **76** 211 (1989)
140. Wahle J et al. *Phys. Rev. B* **58** 12749 (1998)
141. Held K *Adv. Phys.* **56** 829 (2007)
142. Karolak M et al. *J. Electron Spectrosc. Relat. Phenom.* **181** 11 (2010)

143. Zölfl M B et al. *Phys. Rev. B* **61** 12810 (2000)
144. Gunnarsson O et al. *Phys. Rev. B* **39** 1708 (1989)
145. Aryasetiawan F et al. *Phys. Rev. B* **70** 195104 (2004)
146. Miyake T, Aryasetiawan F *Phys. Rev. B* **77** 085122 (2008)
147. Lambin Ph, Vigneron J P *Phys. Rev. B* **29** 3430 (1984)
148. Andersen O K, Saha-Dasgupta T *Phys. Rev. B* **62** R16219 (2000)
149. Andersen O K et al. Ψ_k *Newsletter* (45) 86 (2001)
150. Andersen O K, Saha-Dasgupta T, Ezhov S *Bull. Mater. Sci.* **26** 19 (2003)
151. Anisimov V I et al. *Phys. Rev. B* **71** 125119 (2005)
152. Fujimori A et al. *Phys. Rev. Lett.* **69** 1796 (1992)
153. Aiura Y et al. *Phys. Rev. B* **47** 6732 (1993)
154. Inoue I H et al. *Phys. Rev. Lett.* **74** 2539 (1995)
155. Inoue I H et al. *Phys. Rev. B* **58** 4372 (1998)
156. Morikawa K et al. *Phys. Rev. B* **52** 13711 (1995)
157. Maiti K et al. *Europhys. Lett.* **55** 246 (2001)
158. Sekiyama A et al. *Phys. Rev. Lett.* **93** 156402 (2004)
159. Inoue I H et al. *Physica C* **235–240** 1007 (1994)
160. Rozenberg M J et al. *Phys. Rev. Lett.* **76** 4781 (1996)
161. Solovyev I, Hamada N, Terakura K *Phys. Rev. B* **53** 7158 (1996)
162. Makino H et al. *Phys. Rev. B* **58** 4384 (1998)
163. Jarrell M, Gubernatis J E *Phys. Rep.* **269** 133 (1996)
164. Krause M O, Oliver J H *J. Phys. Chem. Ref. Data* **8** 329 (1979)
165. Inoue I H et al. *Phys. Rev. Lett.* **88** 236403 (2002)
166. Pavarini E et al. *Phys. Rev. Lett.* **92** 176403 (2004)
167. Pavarini E et al. *New J. Phys.* **7** 188 (2005)
168. Yoshida T et al. *Phys. Rev. Lett.* **95** 146404 (2005)
169. Sadovskii M V, in *Strings, Branes, Lattices, Networks, Pseudogaps and Dust* (Moscow: Scientific World, 2007) p. 357 [Translated into English, cond-mat/0408489]
170. Damascelli A, Hussain Z, Shen Z-X *Rev. Mod. Phys.* **75** 473 (2003)
171. Campuzano J C, Norman M R, Randeria M, in *Physics of Superconductors* Vol. 2 (Eds K H Bennemann, J B Ketterson) (Berlin: Springer, 2004) p. 167
172. Fink J et al. *Lecture Notes Phys.* **715** 295 (2007)
173. Zhou X J et al., in *Handbook of High-Temperature Superconductivity: Theory and Experiment* (Ed. J R Schrieffer) (Berlin: Springer, 2007) p. 87
174. Kuchinskii E Z et al. *Zh. Eksp. Teor. Fiz.* **131** 908 (2007) [*JETP* **104** 792 (2007)]
175. Nekrasov I A et al. *Zh. Eksp. Teor. Fiz.* **137** 1133 (2010) [*JETP* **110** 989 (2010)]
176. Nekrasov I A et al. *J. Phys. Chem. Solids* **69** 3269 (2008)
177. Kokorina E E et al. *Zh. Eksp. Teor. Fiz.* **134** 968 (2008) [*JETP* **107** 828 (2008)]
178. Nekrasov I A et al. *Phys. Rev. B* **80** 140510(R) (2009)
179. Nekrasov I A, Kuchinskii E Z, Sadovskii M V *J. Phys. Chem. Solids* **72** 371 (2011)
180. Hedin L, Lundqvist B I *J. Phys. C* **4** 2064 (1971)
181. von Barth U, Hedin L *J. Phys. C* **5** 1629 (1972)
182. Andersen O K et al. *J. Phys. Chem. Solids* **56** 1573 (1995)
183. Zobkalo I A et al. *Solid State Commun.* **80** 921 (1991)
184. Motoyama E M et al. *Nature* **445** 186 (2007)
185. Hücker M et al. *Phys. Rev. B* **71** 094510 (2005)
186. Armitage N P et al. *Phys. Rev. Lett.* **88** 257001 (2002)
187. Kaminski A et al. *Phys. Rev. B* **71** 014517 (2005)
188. Borisenko S V et al. *Phys. Rev. Lett.* **84** 4453 (2000)
189. Onose Y et al. *Phys. Rev. Lett.* **87** 217001 (2001)
190. Quijada M A et al. *Phys. Rev. B* **60** 14917 (1999)

ISSN 0021-3640, JETP Letters, 2014, Vol. 99, No. 10, pp. 598–612. © Pleiades Publishing, Inc., 2014.
Original Russian Text © I.A. Nekrasov, M.V. Sadovskii, 2014, published in Pis'ma v Zhurnal Eksperimental'noi i Teoreticheskoi Fiziki, 2014, Vol. 99, No. 10, pp. 687–703.

Electronic Structure of New Iron-Based Superconductors: From Pnictides to Chalcogenides and Other Similar Systems

I. A. Nekrasov[a] and M. V. Sadovskii[a, b]

[a] *Institute for Electrophysics, Ural Branch, Russian Academy of Sciences, Yekaterinburg, 620016 Russia*

[b] *Institute for Metal Physics, Ural Branch, Russian Academy of Sciences, Yekaterinburg, 620990 Russia*

e-mail: nekrasov@iep.uran.ru, sadovski@iep.uran.ru

Received April 21, 2014

The electronic spectra of new iron-based high-temperature superconductors and a number of other chemically similar compounds have been discussed and compared with the focus on iron chalcogenide $K_{1-x}Fe_{2-y}Se_2$ and isostructural pnictide $BaFe_2As_2$ (122). It has been shown that the Fermi surfaces in $K_{1-x}Fe_{2-y}Se_2$ are significantly different from those in pnictides. The LDA + DMFT and LDA' + DMFT calculations have demonstrated that the effect of electron correlations in $K_{1-x}Fe_{2-y}Se_2$ on the electronic structure is much stronger than that in the most studied 122 system. The electronic structure of several multiband superconductors similar in chemical composition to iron-based high-temperature superconductors, but having a relatively low T_c value (such as $SrPt_2As_2$, APt_3P (A = Sr, Ca, La), and (Sr, Ca)Pd_2As_2), and the nonsuperconducting compound $BaFe_2Se_3$ has also been discussed. It has been shown that the electronic structure of these systems is significantly different from previously studied iron pnictides and chalcogenides. The T_c value in these systems can be understood within the simple Bardeen–Cooper–Schrieffer model.

DOI: 10.1134/S0021364014100075

1. INTRODUCTION

Discovery of a new class of iron-based superconductors [1] attracted great attention and initiated numerous experimental and theoretical studies (see reviews [2–4]). The known iron-based superconductors are classified among two classes: pnictides and chalcogenides. The main currently studied representatives of these classes are as follows (detailed references to experimental works can be found in [5]):

(i) doped RE1111 systems (RE = La, Ce, Pr, Nd, Sm, Tb, Dy) with the chemical formula $REO_{1-x}F_xFeAs$ and superconducting transition temperature T_c about 25–55 K,

(ii) doped A122 systems (A = Ba, Sr) such as $Ba_{1-x}K_xFe_2As_2$ and T_c near 38 K,

(iii) so-called 111 systems $Li_{1-x}FeAs$ with $T_c \sim 18$ K,

(iv) (Sr, Ca, Eu)FFeAs with $T_c \sim 36$ K,

(v) $FeSe_x$, $FeSe_{1-x}Te_x$ with T_c up to 14 K,

(vi) $(K, Cs)_{1-x}Fe_{2-y}Se_2$ with T_c up to 31 K.

Intensive search after the discovery of high-temperature superconductivity in iron arsenides made it possible to obtain several new superconducting systems that can be considered as chemical analogs of iron pnictides and iron chalcogenides (e.g., $BaNi_2As_2$ [6], $SrNi_2As_2$ [7], $SrPt_2As_2$ [8], and SrPtAs [9]). However, new systems have a quite low superconducting transition temperature T_c. Several platinum-based systems APt_3P (A = Sr, Ca, La) with $T_c = 8.4$, 6.6, and 1.5 K, respectively, were recently obtained [10]. The $BaFe_2Se_3$ (Ba123) system [11] was considered in [11] as a possible superconductor similar to (K, Cs)Fe_2Se_2 (superconductivity with $T_c \sim 11$ K was observed in it according to preliminary data). However, it was shown later that superconductivity in Ba123 does not appear down to 1.8 K [12]. This system appears to be an antiferromagnetic "spin ladder" with nontrivial ordering [11, 12]. Superconductivity was also discovered in palladium-based compounds (Sr, Ca)Pd_2As_2 with T_c = 0.92 and 1.27 K, respectively [13].

Here, we review our cycle of studies of the electronic structure of all the above systems within the density functional theory and modern methods of inclusion of strong correlations such as LDA + DMFT [14] and LDA' + DMFT [15, 16] for iron chalcogenides [17, 18] and using LDA calculations for the above attendant systems [19–22].

These works were preceded by a series of our works on iron pnictides and chalcogenides [23–27], which were reviewed in [2, 5].

All LDA calculations of the band structure reported in this work were performed with the linearized muffin-tin orbital (LMTO) basis [28] with default settings.

As will be shown below, all systems under consideration are typical multiband superconductors and are, thereby, interesting as candidates for high-temperature superconductors [29, 30].

2. ELECTRONIC STRUCTURE AND CORRELATIONS IN IRON CHALCOGENIDES

2.1. KFe_2Se_2 System

Compounds $K_{1-x}Fe_{2-y}Se_2$ [31], $Cs_{1-x}Fe_{2-y}Se_2$ [11], and (Tl, K)$Fe_{1-x}Se_{2-y}$ [32] are among the most interesting systems based on iron chalcogenides studied in recent years. It was shown experimentally that a nontrivial antiferromagnetic order with a quite high Néel temperature of 550 K was observed in $K_{0.8}Fe_{1.6}Se_2$. Ordering of vacancies in the iron sublattice occurs simultaneously in almost the same temperature range [33]. Numerous different phases are observed in the $K_{1-x}Fe_{2-y}Se_2$ system. For this reason, a phase that is the precursor of the superconducting phase is strictly speaking unknown. In a number of works [5, 34, 35], it was proposed to consider the stoichiometric compound KFe_2Se_2 as the initial phase for superconductivity. However, there are other points of view [36]. It is remarkable that the stoichiometric crystal KFe_2Se_2 has not yet been synthesized.

An important stage in study of this selenide was the measurement of the angular resolved photoemission spectrum for $K_{0.76}Fe_{1.72}Se_2$ [37]. According to these experiments, quasiparticle dispersions are noticeably renormalized owing to renormalization. For example, the experimentally determined renormalizations of the quasiparticle mass for Fe $3d_{xz,\,yz}$ and Fe $3d_{xy}$ orbitals are 3 and 10, respectively. These facts clearly indicate the necessity of theoretical study of the effect of electron–electron interactions on the properties of this system.

The electronic spectrum of $K_{1-x}Fe_2Se_2$ in the LDA approximation was first obtained in [27, 38].

Crystal structure. As was mentioned above, the $K_{1-x}Fe_2Se_2$ and $Cs_{1-x}Fe_2Se_2$ compounds are structural analogues of Ba122 (see [24]). The parameters of the crystal structure are $a = 3.9136$ Å, $c = 14.0367$ Å, and $z_{Se} = 0.3539$ for $K_{1-x}Fe_2Se_2$ [31] and $a = 3.9601$ Å, $c = 15.2846$ Å, and $z_{Se} = 0.3439$ for $Cs_{1-x}Fe_2Se_2$ [11].

Electronic structure. Figure 1 shows the band structure and densities of states for (left panels) Ba122 [24] in comparison with (right panels) the corresponding calculation data for (black lines) $K_{1-x}Fe_2Se_2$ and (gray lines) $Cs_{1-x}Fe_2Se_2$ of the stoichiometric compositions with $x = 0$ [27]. The $K_{1-x}Fe_2Se_2$ and $Cs_{1-x}Fe_2Se_2$ compounds have almost the same electronic structure. In contrast to Ba122, the Fe $3d$ and Se $4p$ states in these compounds are separated in energy. Furthermore, the Se $4p$ states in AFe_2Se_2 are 0.7 eV below the As $4p$ states.

Similar to Ba122, only the Fe $3d$ states reach the Fermi level in the chalcogenides under study. As in Ba122 [24] and other iron pnictides, the main contribution to the density of states at the Fermi level comes from t_{2g} states (xy, xz, and yz). States with the e_g symmetry ($3z^2 - r^2$ and $x^2 - y^2$) hardly contribute at the Fermi level. The main difference between Ba122 and new systems is observed near the Γ point. The antibonding part of the Se $4p_z$ orbital in the Z–Γ direction for (K, Cs)Fe_2Se_2 forms an electron pocket. The corresponding band in Ba122 is located higher by 0.4 eV and is much steeper. Thus, this band is quite far from the Γ point. Nevertheless, the band structure near the Fermi level for the hole-doped (K, Cs)Fe_2Se_2 compounds (at a hole doping level of 60%) would be similar to bands in Ba122 (three hole cylinders). The stoichiometric system KFe_2Se_2 has one small electron pocket and a larger hole pocket. The $CsFe_2Se_2$ compound has only one electron pocket near the Γ point.

Figure 2 shows the Fermi surface obtained in LDA calculations for (upper panels) $K_{1-x}Fe_2Se_2$ and (lower panels) $Cs_{1-x}Fe_2Se_2$ at doping levels $x =$ (left panels) 0, (middle panels) 0.2, and (right panels) 0.6. In all cases, there are almost two-dimensional electron sheets in the corners of the Brillouin zone at any doping level. The largest differences of the (K, Cs)Fe_2Se_2 compounds from the Ba122 pnictide are observed near the Γ point, particularly for $x = 0$ and 0.2. The Fermi surfaces in both selenides with K and Cs for the doping level $x = 0.6$ are similar to those in Ba122 (see Fig. 2 and [24]) with typical hole cylinders at the center of the Brillouin zone.

Thus, the topology of the Fermi surfaces for doping levels corresponding to superconducting compounds is strongly different from that for Ba122. In particular, there is no "nesting" of electron and hole Fermi surfaces (which is considered in many works as an important property for explanation of their magnetic properties and high-temperature superconductivity).

It was shown in [11] that the superconducting transition temperature T_c in K- and Cs-based materials depends on the height of Se above the Fe ion plane [39]. This problem was studied in detail in [40]. We obtain simple estimates with the standard expression $T_c = 1.14\omega_D e^{-2/gN(E_F)}$ in the Bardeen–Cooper–Schrieffer theory. The total density of states at the Fermi level $N(E_F)$ is 3.94 and 3.6 states/(eV electron cell) for KFe_2Se_2 and $CsFe_2Se_2$, respectively. Taking the Debye frequency $\omega_D = 350$ K and coupling constant $g =$ 0.21 eV for Ba122 (see [40]), we obtain $T_c = 34$ and 28.6 K for K- and Cs-based selenides, respectively (the ratio of the T_c values of these compounds is 1.18). These estimates are in good agreement with the experimental data (31 [31] and 27 K and a ratio of 1.15)

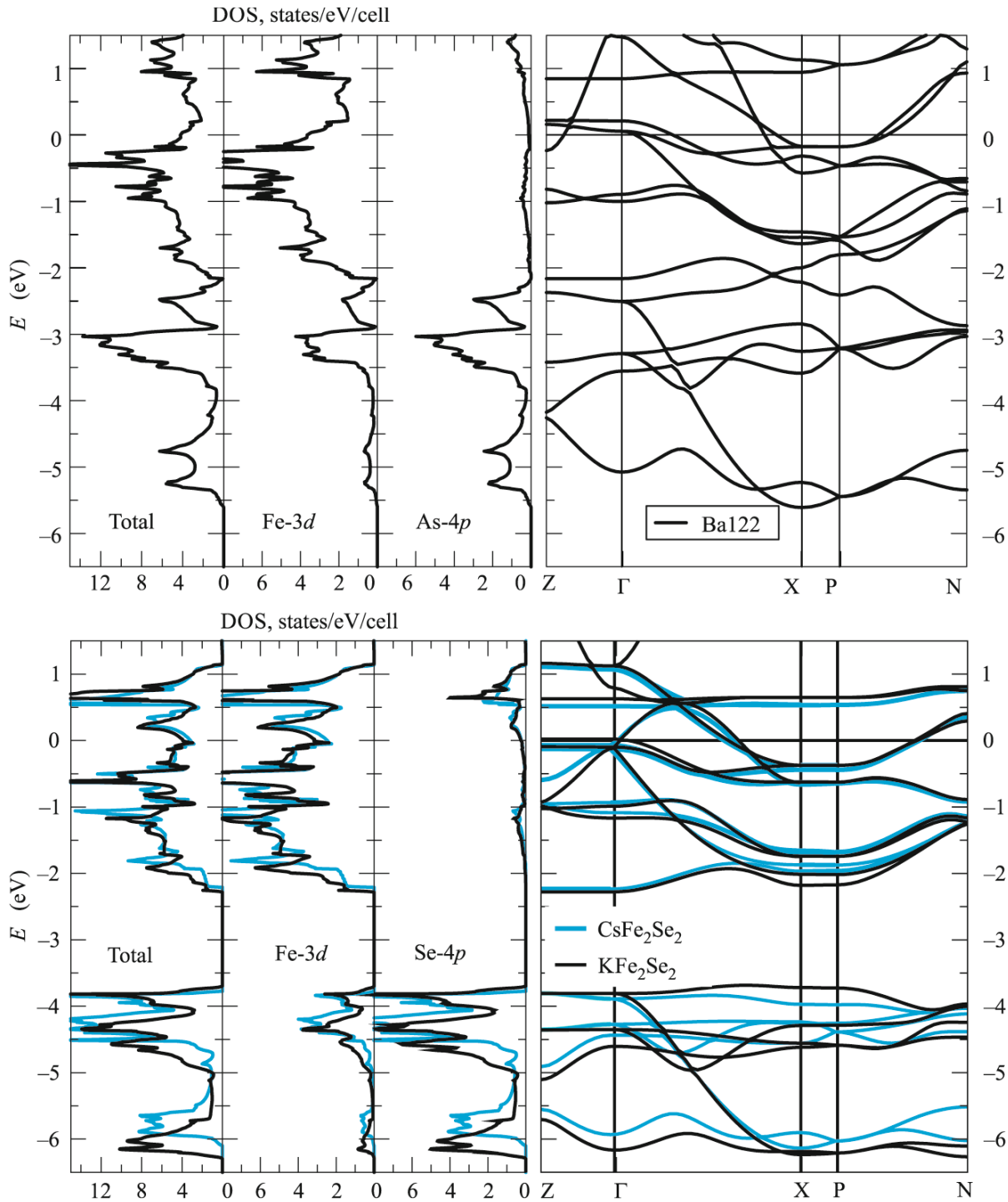

Fig. 1. (Color online) Band dispersion and densities of states obtained in LDA calculations for (left panels) Ba122, (right panel, black lines) KFe_2Se_2, and (right panel, gray lines) $CsFe_2Se_2$; energies are measured from the Fermi level.

[11]. Lower T_c values in $CsFe_2Se_2$ can be explained by the isotopic effect. According to the calculations, the $N(E_F)$ value at a hole doping level of 60% increases to 4.9 and 4.7 states/(eV electron cell) for K- and Cs-based selenides, respectively. Correspondingly, it can be expected that the corresponding superconducting transition temperatures in such doped compounds will be 57 and 52 K, respectively.

It is noteworthy that the above consideration does not imply the electron–phonon mechanism of superconductivity and the ω_D value can refer to any bosonic excitation responsible for pairing (e.g., spin fluctuations).

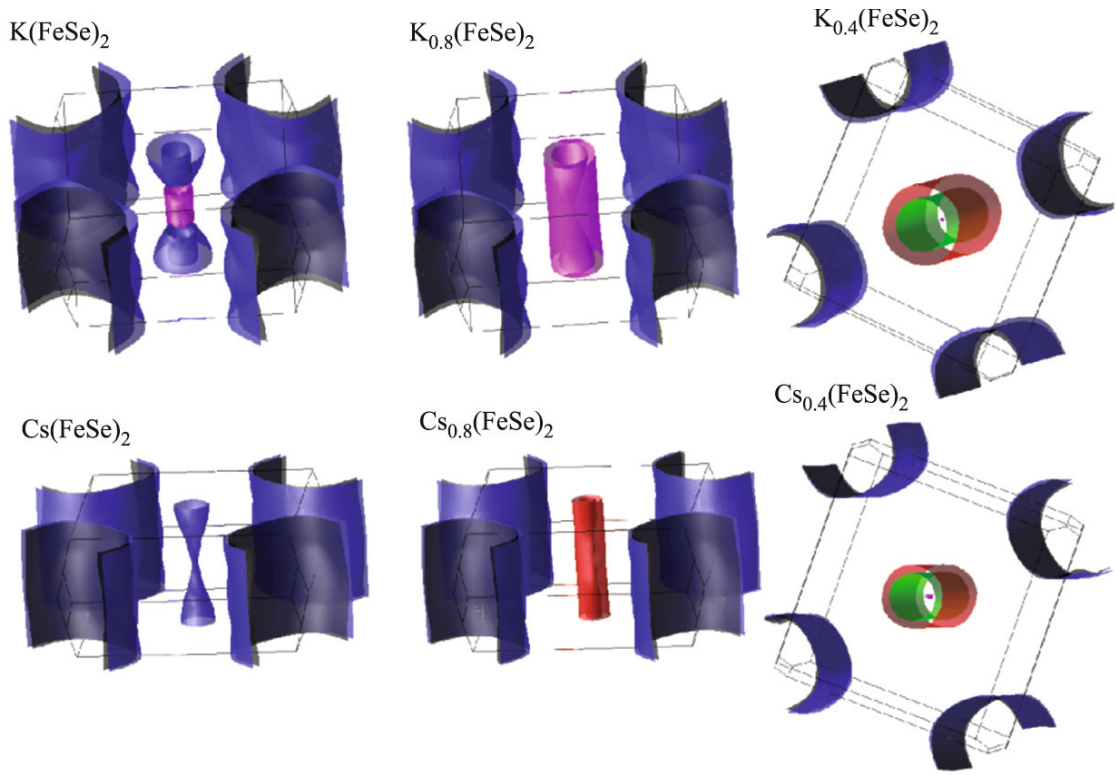

Fig. 2. (Color online) Fermi surfaces obtained in LDA calculations for (upper panels) $K_{1-x}Fe_2Se_2$ and (lower panels) $Cs_{1-x}Fe_2Se_2$ at doping levels x = (left panels) 0, (middle panels) 0.2, and (right panels) 0.6.

2.2. $K_{0.76}Fe_{1.72}Se_2$ Compound

To study correlation effects in the compounds $K_{0.76}Fe_{1.72}Se_2$ [17] and $K_{1-x}Fe_{2-y}Se_2$ with various hole doping levels [18], we used the standard LDA + MDFT approach [14] and our modification LDA' + DMFT [15, 16], which makes it possible to more consistently solve the problem of "double inclusion" of the Coulomb interaction [41].

We first discuss the band structures of the stoichiometric compound KFe_2Se_2 obtained in LDA and LDA' calculations. Similar to oxides of transition metals (see [15, 16]), energy dispersions at the Fermi level obtained in LDA' calculations for KFe_2Se_2 are similar in shape to those obtained in LDA calculations. However, there are small discrepancies near the Γ point. The energy shift of the Se 4*p* band in LDA' calculations toward lower energies with respect to LDA calculations is about 0.5 eV (see [18]).

The Coulomb and exchange interactions of electrons on the Fe 3*d* shell for DMFT calculations were taken to be $U = 3.75$ eV and $J = 0.56$ eV, respectively [37]. The DMFT (QMC) calculations were performed with the following parameters: inverse temperature $\beta = 40$ eV^{-1} (290 K), the number of intervals in imaginary time $L = 180$, and the number of flips of pseudospins at self-consistency ~10^6. The total number of electrons in DMFT calculations for the $K_{0.76}Fe_{1.72}Se_2$ system was $n_e = 26.52$.

The inclusion of the Coulomb interaction at this doping level near the Fermi level results in the following [17]. The results for the Fe $3d_{x^2-y^2}$ orbital do not change. The peak of the Hubbard band appears above the Fermi level for Fe $3d_{3z^2-r^2}$ states. Strong change in the density of states similar to a pseudogap behavior occurs for Fe $3d_{xz,yz}$ and Fe $3d_{xy}$ orbitals. Thus, even analysis of densities of states indicates that correlation effects in the $K_{0.76}Fe_{1.72}Se_2$ compound are rather strong, play different roles for different orbital states, and are particularly strong for the Fe $3d_{xz,yz}$ and Fe $3d_{xy}$ orbitals.

For the $K_{0.76}Fe_{1.72}Se_2$ compound, the spectral functions calculated in the (lower left panel) LDA + DMFT and (lower right panel) LDA' + DMFT approaches are shown in Fig. 3 in comparison with the ARPES spectra for (upper left panel) the polarization of light along the plane of iron atoms and (upper right panel) the sum of polarizations along and across this plane [37]. The lower panels show the spectral functions obtained in the LDA + DMFT and LDA' + DMFT calculations along the experimentally studied Γ–X direction in the same energy range.

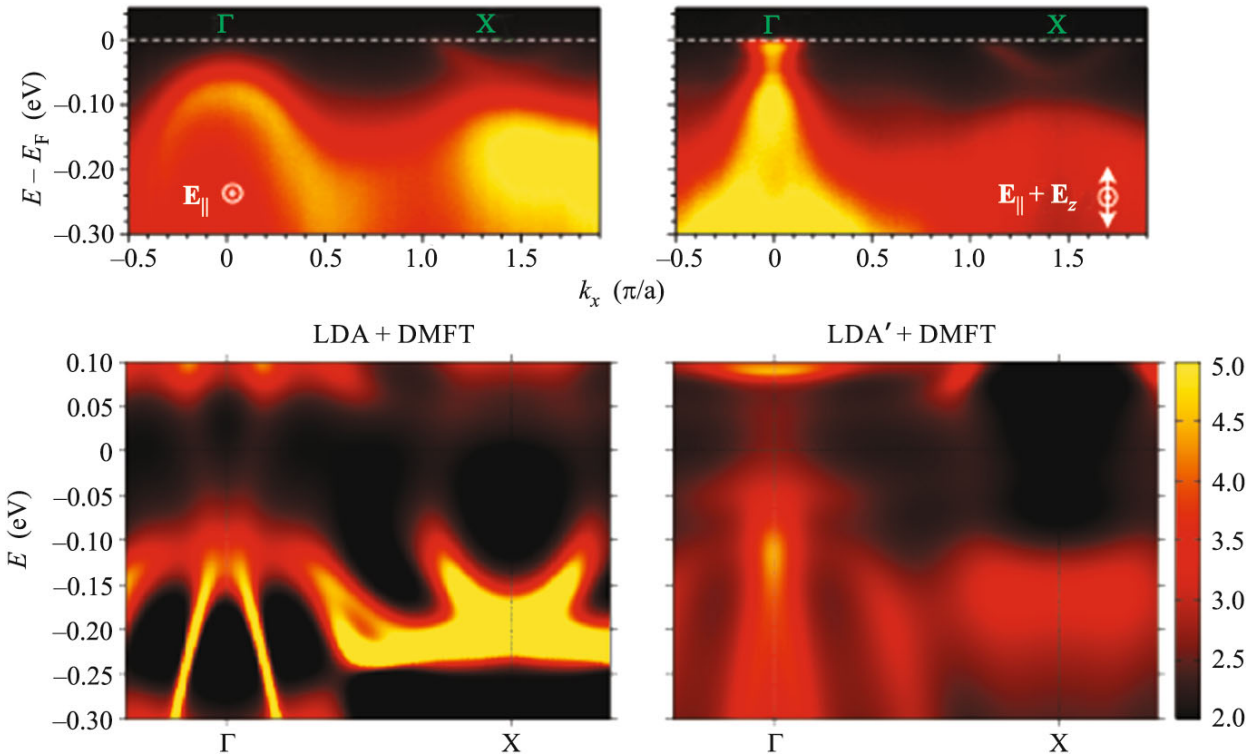

Fig. 3. (Color online) Spectral functions calculated in the (lower left panel) LDA + DMFT and (lower right panel) LDA' + DMFT approaches and (upper panels) the ARPES spectra for the $K_{0.76}Fe_{1.72}Se_2$ compound. Color indicates the intensity of the spectral function. Energies are measured from the Fermi level.

The spectral functions and ARPES spectra exhibit no pronounced maxima of the intensity near the Fermi level (±0.05 eV) except for the vicinity of the Γ point in the experiment with complete polarization. This means that the $K_{0.76}Fe_{1.72}Se_2$ compound is a poor metal and demonstrates a pseudogap behavior manifested in the densities of states [17]. The region of high intensity near the X point in ARPES spectra is in the energy range from –0.25 to –0.1 eV. This range includes also quasiparticle bands in the LDA + DMFT and LDA' + DMFT spectral functions. Energy dispersion with a wide maximum is observed near the Γ point in one of the ARPES spectra and energy dispersion with a narrower maximum, which reaches the Fermi level, is observed in the other ARPES spectrum. Two quasiparticle bands are present in this energy range in the calculated spectral functions. The shape of the quasiparticle band with the wide maximum is approximately the same in the LDA + DMFT and LDA' + DMFT spectral functions. The shape of the quasiparticle band with the narrow maximum in the LDA' + DMFT spectral function is closer to the corresponding energy dispersion in the ARPES spectrum (see Fig. 3).

Thus, correlation effects are important in iron selenide $K_{0.76}Fe_{1.72}Se_2$. They noticeably change the LDA energy dispersions. In contrast to iron arsenides, where quasiparticle bands near the Fermi level are pronounced [42–45], these bands at the Fermi level in the $K_{0.76}Fe_{1.72}Se_2$ compound are strongly suppressed. This also confirms that correlation effects in iron selenide $K_{0.76}Fe_{1.72}Se_2$ are stronger than those in iron arsenides. The quasiparticle renormalization value (correlation contraction) of bands at the Fermi level is 4–5, whereas this factor in iron arsenides is 2–3 [45] at the same interaction parameters.

Since correlation effects strongly affect the electronic properties of the $K_{0.76}Fe_{1.72}Se_2$ compound near the Fermi level, there is the question: How do correlation effects change at various doping levels of the $K_{1-x}Fe_{2-y}Se_2$ compound? To answer this question, three additional doping levels were chosen in [18]: one corresponds to the stoichiometric compound (n_e = 29.00) and the other two correspond to intermediate compounds with the total number of electrons n_e = 28.00 and 27.20. Since the LDA' + DMFT results for the $K_{0.76}Fe_{1.72}Se_2$ compound are in better agreement with the ARPES spectrum, only LDA' + DMFT calculations were performed for additional doping levels. It was shown that the shape and position of identical quasiparticle bands are noticeably transformed with variation of the doping level. The relative positions of quasiparticle bands also change. Consequently, the role of correlation effects for individual quasiparticle bands changes. To determine the effect of the local Coulomb interaction on each of the bands in the Fe 3*d*

Correlation renormalization coefficients of individual LDA' bands shown in Fig. 4. The energy shifts of LDA' bands are given in parentheses in electronvolts

Orbital character	$n_e = 26.52$	$n_e = 27.20$	$n_e = 28.00$	$n_e = 29.00$
xy, LHB *xy*, UHB	1.5 (–0.23) No	3.9 (–0.73) ~4.0 (+0.60)	2.65 (–0.61) 1.7 (+0.25) Part (upper)	1.7 (–0.35) ~4.0 (+0.75)
xz, *yz* (1) LHB *xz*, *yz* (1) UHB	4.2 (–0.78) 1.6 (+0.19)	3.0 (–0.75) ~2.5 (+0.48)	2.6 (–0.69) 3.0 (+0.56)	1.7 (–0.38) 4.0 (+0.77)
xz, *yz* (2)	2.3 (–0.48)	~2.5 (–0.60)	2.6 (–0.69)	1.7 (–0.38)
xz, *yz*, *xy*	1.2 (–0.1)	1.3 (–0.09)	1.3 (–0.10)	1.4 (–0.17)
$3z^2–r^2$ (1) $3z^2–r^2$ (2)	4.7 (–0.85) 1.1 (+0.25)	2.0 (–0.30) 1.3 (0.00)	1.3 (–0.03) 1.3 (–0.03)	1.25 (0.00) 1.25 (0.00)
xz, *yz* (3) *xz*, *yz* (4)	1.1 (+0.10) 1.1 (+0.10)	1.1 (+0.17) 1.1 (+0.15)	1.0 (+0.40) 1.0 (+0.35)	1.4 (–0.10) 1.4 (–0.17)
$x^2–y^2$	1.1 (+0.20)	1.0 (+0.32)	1.3 (–0.07)	1.3 (–0.07)
Fe3*d*-band as a whole	1.3	1.3	1.25	1.25

band at four doping levels under consideration, we found the correlation renormalization coefficients and shifts of the LDA' bands for coincidence with the maxima in the LDA' + DMFT spectral functions. The resulting renormalization coefficients and shifts (in electronvolts in parentheses) of the LDA' bands are summarized in the table.

Black dotted lines in Fig. 4 are the energy dispersions obtained in the LDA calculation. They are similar in shape and position to those obtained in the LDA' calculation. Consequently, the correlation renormalization coefficients in LDA + DMFT calculations will be approximately the same as LDA' + DMFT calculations (see table). This conclusion is confirmed by the data for the $K_{0.76}Fe_{1.72}Se_2$ compound ($n_e = 26.52$). The energy dispersions obtained in the LDA' calculation in the range from –1.0 to 0.4 eV are renormalized by the interaction more strongly than those below –1.0 eV.

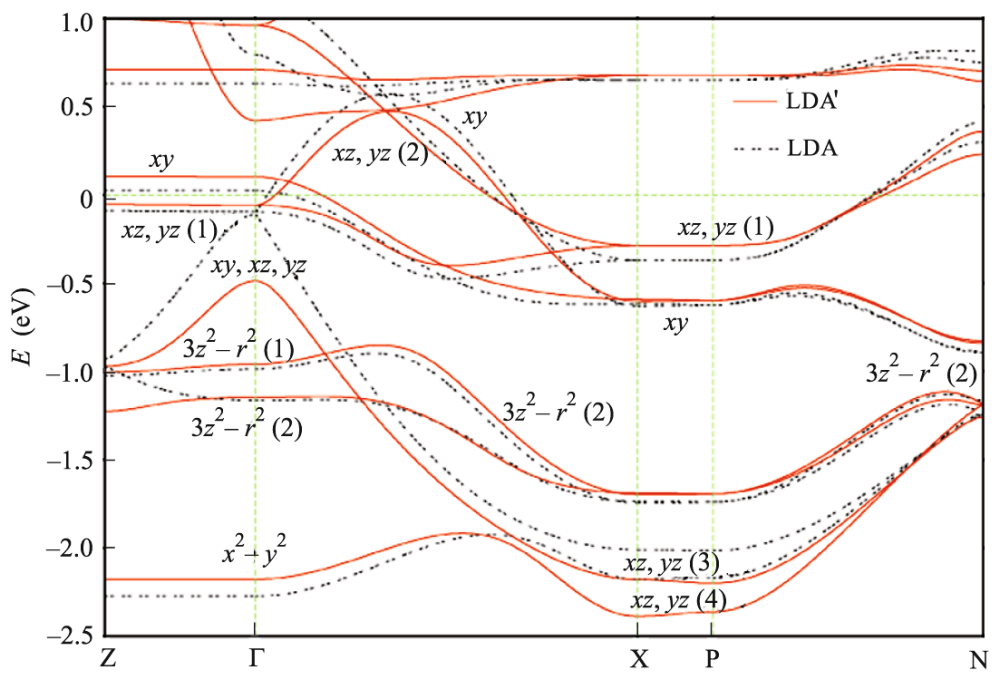

Fig. 4. (Color online) Energy dispersions from (red lines) the LDA' calculation for KFe_2Se_2 along the symmetric directions of the Brillouin zone with the indication of the bands for which the coefficients of correlation normalization were chosen. Black dotted lines are the energy dispersions of the LDA calculation. Energies are measured from the Fermi level.

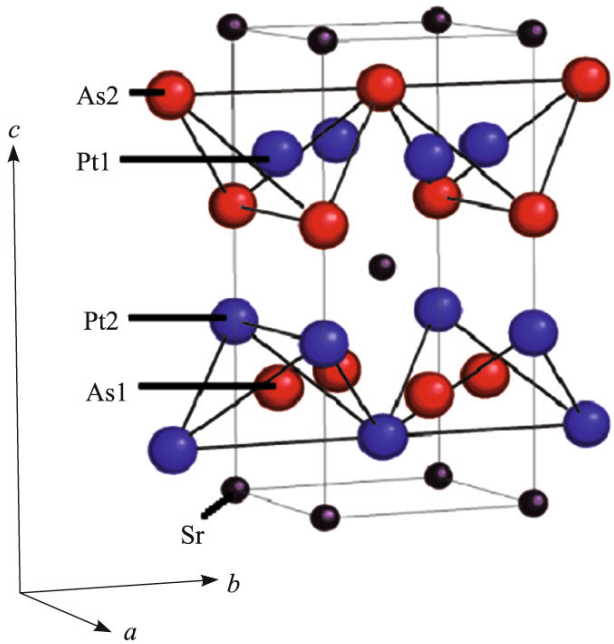

Fig. 5. (Color online) Idealized tetragonal crystal structure of $SrPt_2As_2$.

The correlation renormalization coefficients of the $3z^2 - r^2$ (2), xz, yz (3), xz, yz (4), and $x^2 - y^2$ bands (see Fig. 4 and table) that are below −1.0 eV in the LDA' calculation are close to the correlation renormalization coefficient of the Fe 3d band as a whole. The xz, yz, xy band located in the interval from −1.0 to −0.5 eV is weakly renormalized as the entire Fe 3d band and its correlation renormalization coefficient hardly depends on the doping level. The correlation renormalization coefficient of the xz, yz (2) band depends weakly on the doping level and is near 2.5, although this band is near the Fermi level. The correlation renormalization coefficient of the $3z^2 - r^2$ (1) band increases sharply to 4.7 at the filling factor $n_e = 26.62$.

The correlation renormalization coefficients in the lower and upper Hubbard bands for the xz, yz (1) band increase and decrease monotonically with an increase in the doping level, respectively. The dependence on the doping level for the xy band is nonmonotonic. The correlation effects in its lower Hubbard band increase with the hole doping level, reach a maximum at $n_e = 27.20$, and then decrease. The correlation renormalization coefficient in the upper Hubbard band at filling factors $n_e = 29.00$ and 27.20 is quite large (about 4.0). It is smaller (1.7) at complete filling ($n_e = 28.00$) and the upper xy Hubbard band is absent at $n_e = 26.52$.

Thus, hole doping of the $K_{1-x}Fe_{2-y}Se_2$ compound from the stoichiometric composition KFe_2Se_2 to the composition $K_{0.76}Fe_{1.72}Se_2$ results in an increase in correlation effects at unchanged direct (Hubbard U) and exchange (Hund J) Coulomb interactions. These effects are different for different quasiparticle bands and for different parts of the Brillouin zone.

The absence of pronounced quasiparticle bands in the close vicinity of the Fermi level is possibly the main qualitative manifestation of stronger correlation effects in the system under consideration as compared to all previously studied iron-based superconductors.

3. NEW SUPERCONDUCTORS, CHEMICAL ANALOGS OF IRON PNICTIDES

3.1. $SrPt_2As_2$ Compound

Crystal structure. In [46], it was shown that $SrPt_2As_2$ has an orthorhombic structure with the space symmetry group *Pmmn*. This system is in a certain sense similar to a tetragonal crystal structure $CaBe_2Ge_2$ with the space symmetry group *P*4/*nmm*. This structure is shown in Fig. 5 and has two layers of tetrahedra, $PtAs_4$ and $AsPt_4$, in a unit cell. A square lattice in one layer is formed by platinum ions, whereas this lattice in the other layer is formed by arsenic ions. The corresponding tetrahedra are shown by lines in Fig. 5. The high-temperature superconducting compound $BaFe_2As_2$ has the closest chemical formula to $SrPt_2As_2$ [47]. However, the unit cell in the former compound contains two layers of $FeAs_4$ tetrahedra specularly turned with respect to each other [24]. Most iron pnictides also have the *P*4/*nmm* structure [40]. We used the idealized tetrahedral structure with the symmetry group *P*4/*nmm* in the calculations (details can be found in [19]). The parameters of the tetrahedral crystal structure can be obtained by averaging $a = 4.482$ Å and $b = 4.525$ Å for the orthorhombic phase and leaving unchanged $c = 9.869$ Å.

Electronic structure. Figure 6 shows electron bands obtained in the LDA calculations and constructed along the highly symmetric directions in the first Brillouin zone for $SrPt_2As_2$. The bands in $SrPt_2As_2$ have a remote resemblance to, e.g., the 1111 FeAs system [23, 26] near the M point. However, near the Fermi level, they are strongly different from those in the 1111 and 122 systems. Since the Fermi level in $SrPtAs_2$ crosses several bands, the nature of superconductivity in this system is significantly multiband (four bands cross the Fermi level in the Γ–X direction and six bands cross it in the M–Γ direction).

As was shown in [19], the dominant contribution at the Fermi level comes from the Pt1 5d states. Nevertheless, the joint contribution from Pt2 5d, As1 4p, and As2 4p states to the density of states at the Fermi level E_F is quite significant. This circumstance distinguishes $SrPt_2As_2$ from high-temperature superconducting pnictides, where the As 4p states hardly reach the Fermi level [23–26]. The main part of the spectral weight of the Pt 5d states is far below the Fermi level because the number of valence electrons in Pt is larger

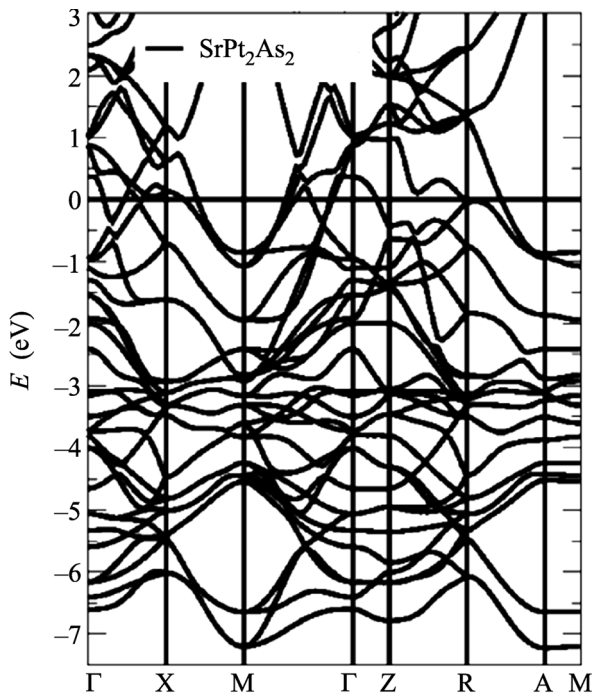

Fig. 6. Energy dispersions obtained in the LDA calculations for $SrPt_2As_2$. Energies are measured from the Fermi level.

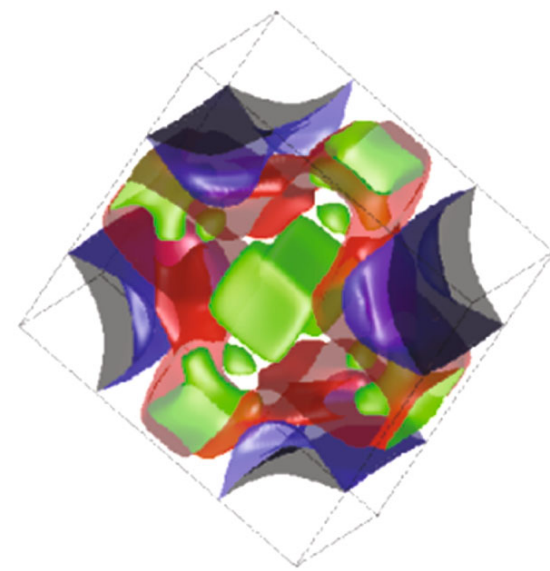

Fig. 7. (Color online) Fermi surface calculated for $SrPt_2As_2$ in the LDA approximation.

than that in Fe. Furthermore, the Pt 5*d* states are obviously more extended and wider than the Fe 3*d* states.

Figure 7 shows the complex Fermi surface obtained in the LDA approximation for the system under consideration. Most of the sheets of this Fermi surface are significantly three-dimensional; this property strongly distinguishes $SrPt_2As_2$ from 1111 and 122 pnictides.

According to the above consideration, $SrPt_2As_2$ has a complex band structure near the Fermi level and complex multisheet topology of the Fermi surface, which is strongly different from that observed in iron pnictides. The multiband system can generally also have a very complex type of Cooper pairing with superconducting gaps with different widths on different sheets of the Fermi surface as in, e.g., FeAs [29, 30]. According to the general symmetry analysis [48, 49], isotropic or anisotropic *s* pairing or several types of *d* pairing are possible in the case of tetragonal symmetry and singlet Cooper pairs. However, symmetry consideration cannot provide any information on the $s^{\pm}$ pairing with isotropic gaps of different signs on different sheets of the Fermi surface, which is considered as the most probable for iron pnictides [2, 30].

We obtain the simplest estimates of T_c within the Bardeen–Cooper–Schrieffer theory. The density of states at the Fermi level $N(E_F)$ obtained in our calculations is 5.6 states/(eV cell). Then, the coefficient of the contribution linear in temperature to the specific heat obtained in the LDA calculations is $\gamma_b = \frac{\pi^2}{3}N(E_F) = 13.1$ mJ/(mol K^2), which is in satisfactory agreement with an experimental estimate of 9.7 mJ/(mol K^2) [8]. The pairing coupling constant λ can be estimated from the Bardeen–Cooper–Schrieffer expression $T_c = 1.14\omega_D\exp(-1/\lambda)$ with the use of the experimental Debye frequency ω_D. For ω_D = 200 K and T_c = 5.2 K [8], we obtain λ = 0.26 for $SrPt_2As_2$. We now obtain estimates for isovalent superconductivity systems $BaNi_2As_2$ (T_c = 0.7 K) [6] and $SrNi_2As_2$ (T_c = 0.62 K) [7]. These estimates require the total LDA densities of states for the BaNi and SrNi systems. The calculations give $N(E_F)$ = 3.86 and 2.81 states/(eV cell) for BaNi and SrNi, respectively, which are in good agreement with the results obtained in [50, 51]. Changing the λ value proportionally to change in $N(E_F)$, we obtain T_c = 0.97 and 0.13 K for the respective systems in good agreement with the experimental data [6, 7].

3.2. APt_3P System

A new platinum-based system, APt_3P (A = Sr, Ca, La), was discovered and described in [10], where T_c = 8.4, 6.6, and 1.5 K, respectively, were obtained. Here, we consider the electronic structure of the $SrPt_3P$ system, which was first found in [21].

Crystal structure. Crystals $SrPt_3P$ have the tetragonal symmetry group *P*4/*nmm* with *a* = 5.8094 Å and *c* = 5.3833 Å [10] (see Fig. 8). An "antiperovskite" octahedron Pt_6P is sandwiched between strontium ion layers; planar Pt1 ions occupy positions 4*e* (1/4, 1/4, 1/2) and apex Pt2 ions occupy positions 2*c* (0, 1/2, 0.1409). Phosphorus inside the octahedron also occu-

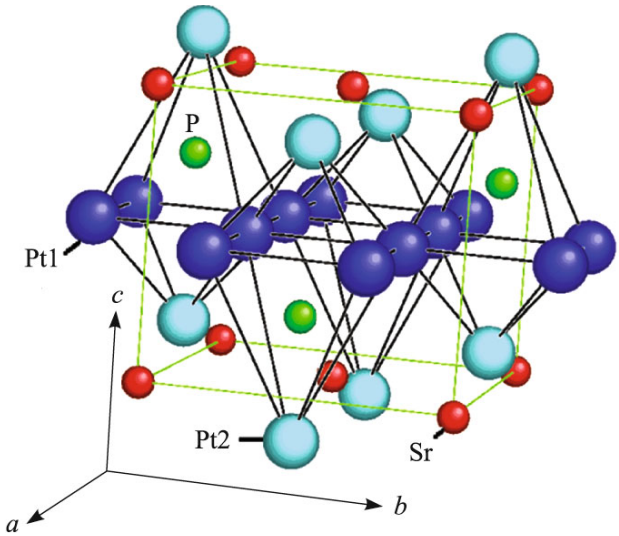

Fig. 8. (Color online) Crystal structure of $SrPt_3P$; Pt_6P octahedra are indicated by Pt–Pt bonds.

pies positions $2c$ with $z = 0.7226$. It is noteworthy that Pt_6P octahedra are not ideal. The distances from the PPt_2 layer to different Pt2 apex ions are different, whereas planar Pt1 ions form a square. It can be clearly seen in Fig. 8 that Pt_6P octahedra having a common face form a plane with a square lattice. Below, we assume that $LaPt_3P$ has the crystal structure identical to $SrPt_3P$.

Electronic structure. The density of states at the Fermi level is mainly determined by the Pt1 $5d$ states. We recall that Pt1 ions form a two-dimensional square lattice (see Fig. 8). Furthermore, there is a small addition of the Pt2 $5d$ and P $3p$ states at the Fermi level.

The densities of states at the Fermi level $N(E_F)$ in the Sr- and La-based compounds are 4.69 and 3.77 states/(eV cell), respectively. These values are comparable to similar values for the high-temperature superconducting pnictides with relatively high T_c values (see [40]). Then, the coefficient γ_b of the linear term in the specific heat is 11 and 8.9 mJ/(mol K^2) for $SrPt_3P$ and $LaPt_3P$, respectively. The former value is in quite good agreement with an experimental estimate $\gamma^{exp} = 12.7$ mJ/(mol K^2) for $SrPt_3P$ [10]. Strictly speaking, γ^{exp} should be slightly larger than the value in the model of free electrons because of the renormalization of the density of states by the electron–phonon interaction: $\gamma = (1 + \lambda)\gamma_b$, where λ is the dimensionless coupling constant. The comparison of the experimental data and calculations gives the estimate $\lambda = 0.15$. It corresponds to the case of weak coupling and is insufficient for obtaining the experimental T_c value. According to the experimental estimates obtained in [10], the so-called Wilson relation is $R_W \sim 1$, which emphasizes the absence of strong correlation interactions in $SrPt_3P$.

Figure 9 shows the band dispersions of (dark lines) $SrPt_3P$ and (gray lines) $LaPt_3P$ near the Fermi level obtained in the LDA calculations. These dispersions strongly differ from dispersions of $SrPt_2As_2$ (see Fig. 6) [19] and high-temperature superconducting pnictides and chalcogenides (see Fig. 1) [5]. Both APt_3P systems are significantly three-dimensional, which follows from the presence of dispersion along the Γ–Z direction. In terms of the chemical composition (disregarding lattice relaxation effects), the $LaPt_3P$ compound looks like the electron-doped $SrPt_3P$ system.

Figure 10 shows the Fermi surfaces obtained in our LDA calculations for (left panel) $SrPt_3P$ and (right panel) $LaPt_3P$. The shape of the Fermi surface of APt_3P systems strongly differs as a whole from iron pnictides and chalcogenides [24, 27]. In particular, these Fermi surfaces are three-dimensional and do not contain pronounced cylinders.

The above information on the electronic structure indicates that the APt_3P family is a new class of systems with multiband superconductivity, as was assumed in [10] on the basis of the measurements of

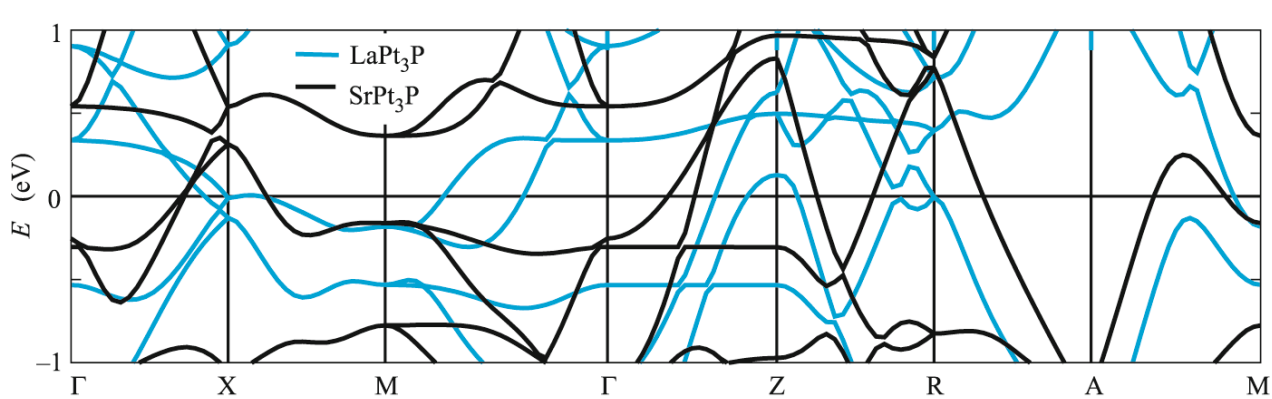

Fig. 9. (Color online) Energy dispersions near the Fermi level for (black lines) $SrPt_3P$ and (gray lines) $LaPt_3P$ calculated in the LDA approximation. Energies are measured from the Fermi level.

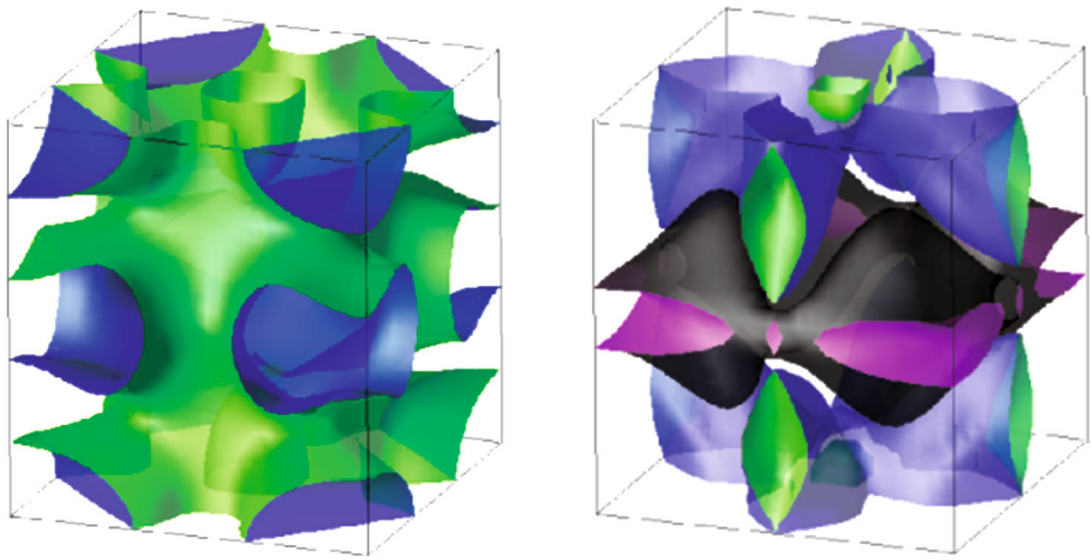

Fig. 10. (Color online) Fermi surfaces obtained from the LDA calculations for (left panel) $SrPt_3P$ and (right panel) $LaPt_3$.

the Hall coefficient. The $SrPt_3P$ compound is a significantly two-band superconductor, whereas $LaPt_3$ has a quite complex band structure near the Fermi surface. The Fermi surfaces of both compounds are characterized by a large number of sheets with a large number of "pockets" in the first Brillouin zone. Their topology easily and noticeably changes at doping.

In this case, general symmetry analysis [48, 49] again indicates that usual isotropic or anisotropic *s* pairing or several types of *d* pairing are in principle possible for singlet pairs. As was assumed in [10], *s* pairing is certainly most probable. Furthermore, additional difficulties appear in view of the multiband nature of APt_3P compounds. The three-dimensional structure of the multisheet Fermi surface can be responsible for a complex structure of a superconducting gap and different widths of superconducting gaps on different sheets of the Fermi surface (see discussion in [29, 30]). Nevertheless, the simple Bardeen–Cooper–Schrieffer expression $T_c = 1.14\omega_D\exp(-1/\lambda)$ allows estimates of the dimensionless coupling constant λ in terms of the experimental T_c values and Debye frequency $\omega_D = 190$ K [10]. The estimate for $T_c = 8.4$ K is $\lambda = 0.31$. Reducing λ proportionally to the density of states at the Fermi level from 4.69 states/(eV cell) in the $SrPt_3P$ compound to 3.77 states/(eV cell) in the $LaPt_3P$ compound, we obtain $T_c = 4$ K for $LaPt_3P$ in good agreement with an experimental value of 1.5 K.

The simplest expression of the Bardeen–Cooper–Schrieffer theory gives only a rather rough estimate for T_c. For this reason, it is better to use the McMillan formula [52]. A quite close estimate is also given by the Allen–Dynes expression [53], which is the best interpolation formula for T_c in superconductors with strong coupling. At the "optimistic" Coulomb pseudopotential $\mu^* = 0$, the Allen–Dynes expression gives $\lambda = 0.61$ for $SrPt_3P$ and $T_c = 5.6$ K for $LaPt_3P$. At a more typical value $\mu^* = 0.1$, we obtain $\lambda = 0.85$ for $SrPt_3P$ and $T_c = 5.4$ K for $LaPt_3P$.

In summary, the T_c values in $SrPt_3P$ and $LaPt_3P$ quite closely correlate with the total density of states at the Fermi level similar to high-temperature superconducting pnictides and chalcogenides [5, 40]. At the same time, the estimates obtained for T_c correspond to superconductivity with weak or intermediate pairing in APt_3P. This does not explain (see [53]) the unusually large ratio $2\Delta/T_c$ obtained from the measurement of the specific heat in [10] and indicates the necessity of the additional experimental refinement of the indicated ratio in other compounds.

3.3. $BaFe_2Se_3$ Compound

The $BaFe_2Se_3$ compound (Ba123) was synthesized in [11] as a possible superconductor similar to (K, Cs)Fe_2Se_2 ($T_c \sim 11$ K according to the preliminary data). However, superconductivity in this system was not observed more recently in [12] down to 1.8 K. Antiferromagnetic "spin ladders" with a Néel temperature of about 250 K were discovered by means of neutron diffraction in both cited works, but the form of the magnetic structure was established ambiguously. Here, we described the electronic and magnetic structures of Ba123 obtained in the LDA and LSDA calculations in [20].

Crystal structure. As usual, we begin with the discussion of the crystal structure of Ba123. The Ba123

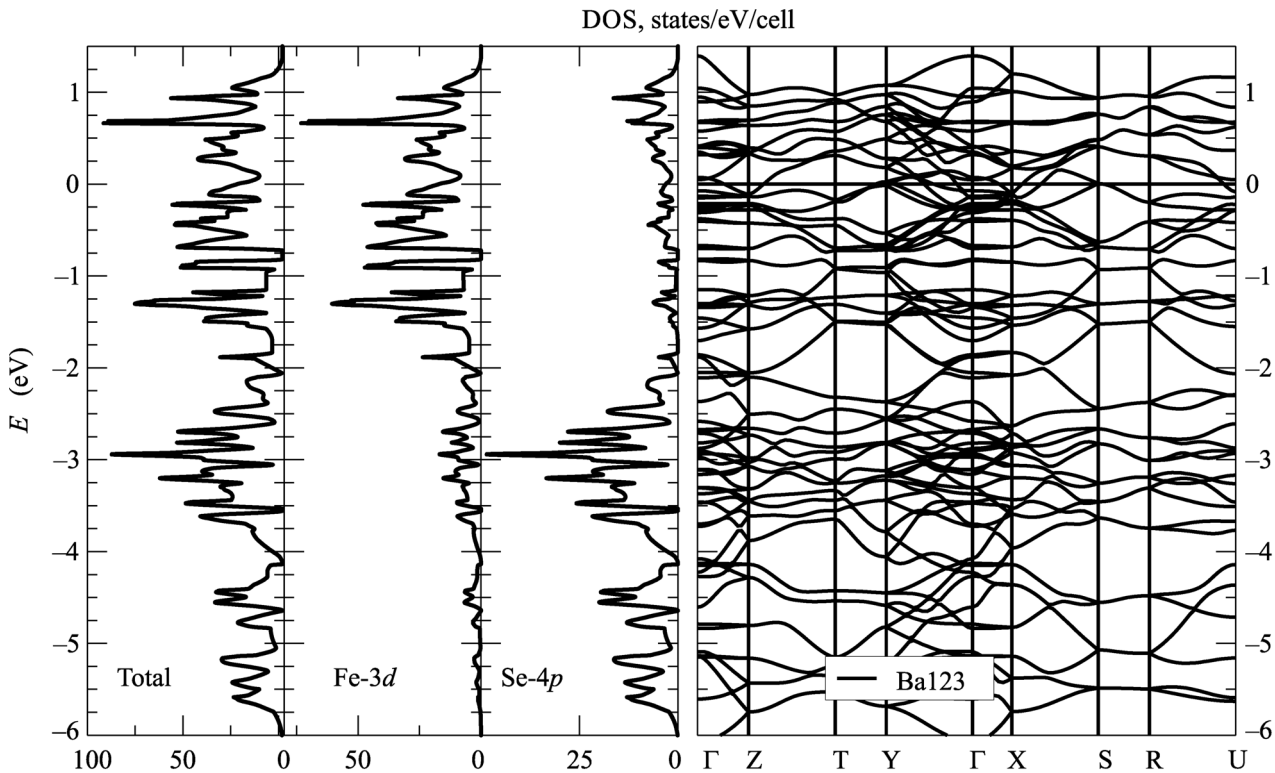

Fig. 11. (Right panel) Band dispersions and (left panel) densities of states obtained in the LDA calculation for the Ba123 system. Energies are measured from the Fermi level.

system has the orthorhombic symmetry group *Pnma* [11]. The so-called "two-leg" ladders directed along the *b* axis constitute the main structure element in this compound. These ladders are formed by iron ions surrounded by tetrahedra of Se ions. In the direction perpendicular to the *b* axis, ladders are arranged in checkerboard order (see [20]). This crystal structure is obviously strongly different from the crystal structure of iron-based high-temperature superconducting systems (see Section 2 and [5, 24, 27]), which have primitive or body-centered tetragonal symmetry group.

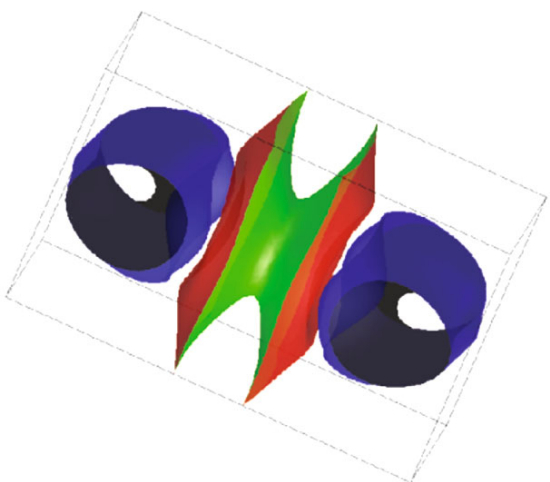

Fig. 12. (Color online) Fermi surface of the Ba123 compound obtained in the LDA calculations.

Electronic structure. Figure 11 shows (right panel) band dispersions and (left panel) densities of states for the Ba123 system. Similar to systems Ba122 [24] and AFe_2Se_2 [27], the electronic states at the Fermi level are formed mainly by Fe 3*d* orbitals. Bands below −2 eV belong to Se 4*p* orbitals. The hybridization of Fe 3*d* and Se 4*p* states is quite moderate.

The electron bands of the Ba123 system in the close vicinity of the Fermi level strongly differ from those in iron pnictides and iron chalcogenides [24, 27]. There are two electron pockets around the Γ point and three hole pockets are located at the edges of the Brillouin zone (Y point) (see Fig. 12). Several van Hove singularities are near the Fermi level; in this respect, this system is similar to AFe_2Se_2 (see Section 2) [27] and the topology of the surface can be quite simply changed by doping.

The Fermi surface obtained in the LDA calculation for Ba123 is shown in Fig. 12. The general shape of the Fermi surface is strongly different from that in iron pnictides and iron chalcogenides [24, 27]. In Ba123, it is significantly three-dimensional and does not have pronounced cylinders.

Magnetic structure. Neutron scattering experiments [11, 12] made it possible to determine the Néel

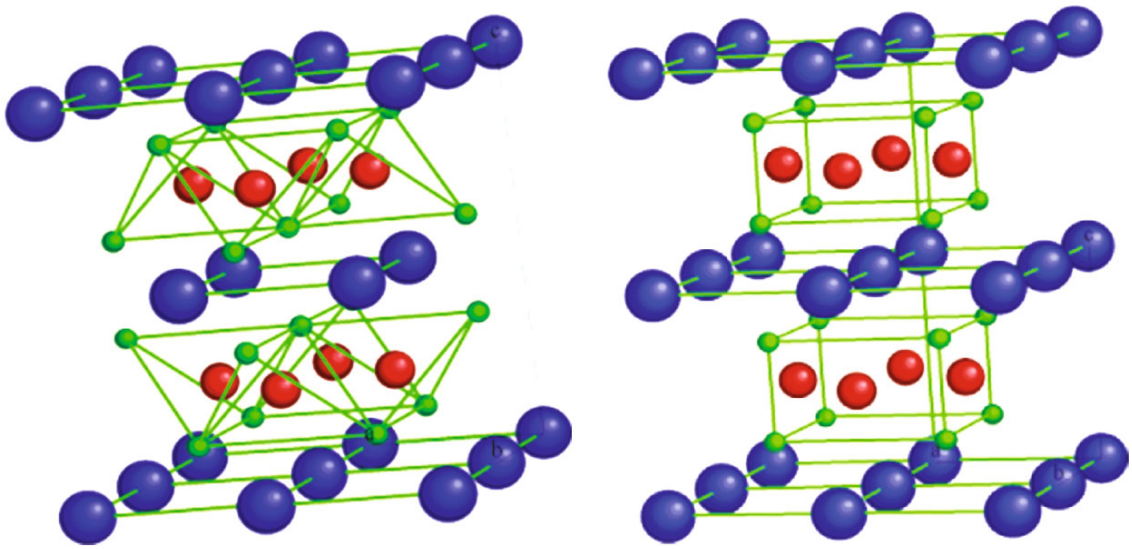

Fig. 13. (Color online) Crystal structure of (left) (Sr, Ca)Pd_2As_2 and (right) $BaPd_2As_2$. Blue spheres mark Sr and Ba ions, green spheres indicate As ions, and red spheres show Pd ions.

temperature for Ba123 ($T \ll T_N^{\rm exp} \sim 250$ K), as well as two possible spin configurations corresponding to the irreducible representations τ_1 and τ_2 of the spatial symmetry group *Pnma*, which give almost identical diffraction patterns. In [20], the type of magnetic structure was determined by the direct calculation of the Néel temperature for various spin configurations in the mean-field approximation for the Heisenberg model. The parameters of the Heisenberg model were obtained in LSDA calculations [54]. Our calculations show that the spin ladder configuration τ_1 ("plaquettes") has the Néel temperature $T_N(\tau_1) = 217$ K and the configuration τ_2 ("zigzags") has the Néel temperature $T_N(\tau_2) = 186$ K. Therefore, the configuration τ_2 is more energetically preferable in agreement with experimental work [12] and LSDA calculations of the total energy [55].

To summarize, in spite of the chemical formula similar to iron-based high-temperature superconducting systems, the Ba123 system has significantly different crystal and electronic structures. From the magnetic point of view, it is a "spin ladder." The problem of superconductivity in this system is unsolved.

3.4. APd_2As_2 System

Here, we consider the electronic structure [22] of (Sr, Ca)Pd_2As_2 and $BaPd_2As_2$ systems in which superconductivity with $T_c = 0.92$ and 1.27 K, respectively, was detected [13]. In addition, these systems are compared to the isovalent system (Sr, Ba)Ni_2As_2 [56–58].

Crystal structure. The crystal structure of $SrPd_2As_2$ and $CaPd_2As_2$ has the tetragonal symmetry group *I*/4*mmm* similar to the $BaFe_2As_2$ compound [47]. The shape of this structure is shown in the left panel in Fig. 13. It can be seen that it is similar to the Ba122 system [24].

Although the $BaPd_2As_2$ system is similar in chemical formula to the Ba122 pnictide, it has a strongly different crystal structure [13]. The $BaPd_2As_2$ system has the spatial symmetry group *P*/4*mmm* (right panel in Fig. 13). Similar to pnictides and chalcogenides, the $BaPd_2As_2$ system has a layered crystal structure, but Pd atoms have no tetrahedral environment of arsenic atoms.

Electronic structure. Energy dispersions along the highly symmetric directions, as well as densities of states, obtained in the LDA calculations for $SrPd_2As_2$ and $BaPd_2As_2$ are shown in the upper and lower panels in Fig. 14, respectively. It can be seen that Pd 4*d* and As 4*p* states give the main spectral weight in the $SrPd_2As_2$ system. The Pd 4*d* states are located between −4 and −0.5 eV (see the upper panels in Fig. 14) and the As 4*p* states are between −6 and −4 eV. As compared to Ba122, the Pd 4*d* states are certainly more extended in energy than the Fe 3*d* states. Significant hybridization between Pd 4*d* and As 4*p* states exists in $SrPd_2As_2$. The density of states at the Fermi level in $SrNi_2As_2$ is $N(E_F) = 1.93$ states/(eV cell), which is half the value in the Ba122 system, because the number of electrons in Pd is larger than that in Fe; as a result, the Fermi level is shifted toward smaller densities of states.

The electron dispersion and densities of states obtained in the LDA calculation for $BaPd_2As_2$ are shown in the lower panels in Fig. 14. Since the crystal structure of $BaPd_2As_2$ is completely different from the structure of $SrNi_2As_2$, it is reasonable that the resulting bands also have a different shape. The Fermi level in both systems with Sr and Ba crosses numerous bands

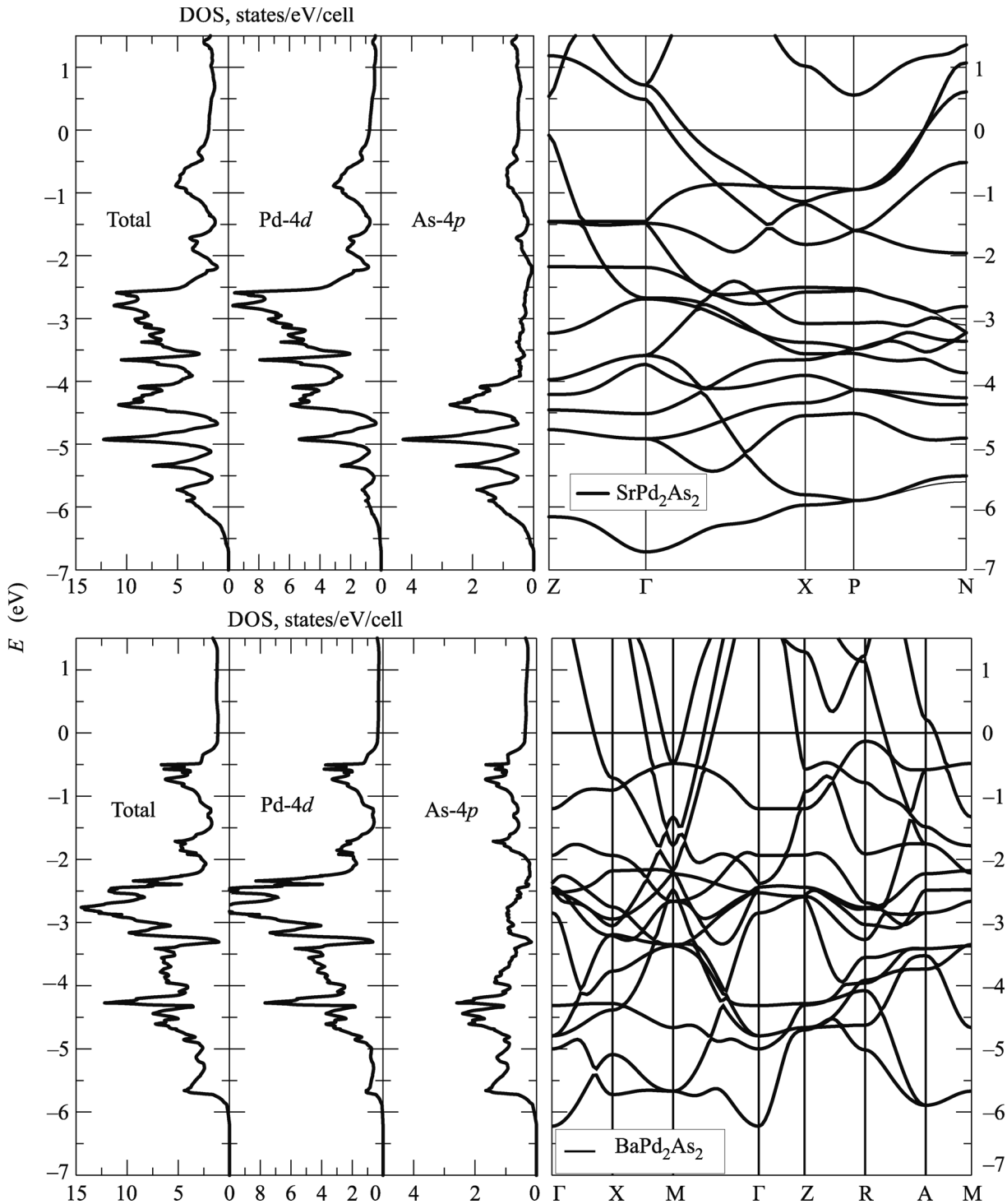

Fig. 14. (Left panels) Electron dispersions and (right panel) densities of states obtained in the LDA calculation for the (upper panels) $SrPd_2As_2$ and (lower panels) $BaPd_2As_2$ systems. Energies are measured from the Fermi level.

without any pronounced contributions from different valence shells. The total density of states at the Fermi level obtained in the LDA calculation for $BaPd_2As_2$ is 2.29 states/(eV cell).

Figure 15 shows the Fermi surfaces obtained in our band calculations for the (left) $SrPd_2As_2$ and (right) $BaPd_2As_2$ systems. In contrast to the Ba122 system [24], the Fermi surface for the system with Sr is significantly three-dimensional and complex and includes three sheets. As compared to $SrPd_2As_2$, the Fermi surface of $BaPd_2As_2$ has a quite simple shape, but is also significantly three-dimensional with the hole sheet

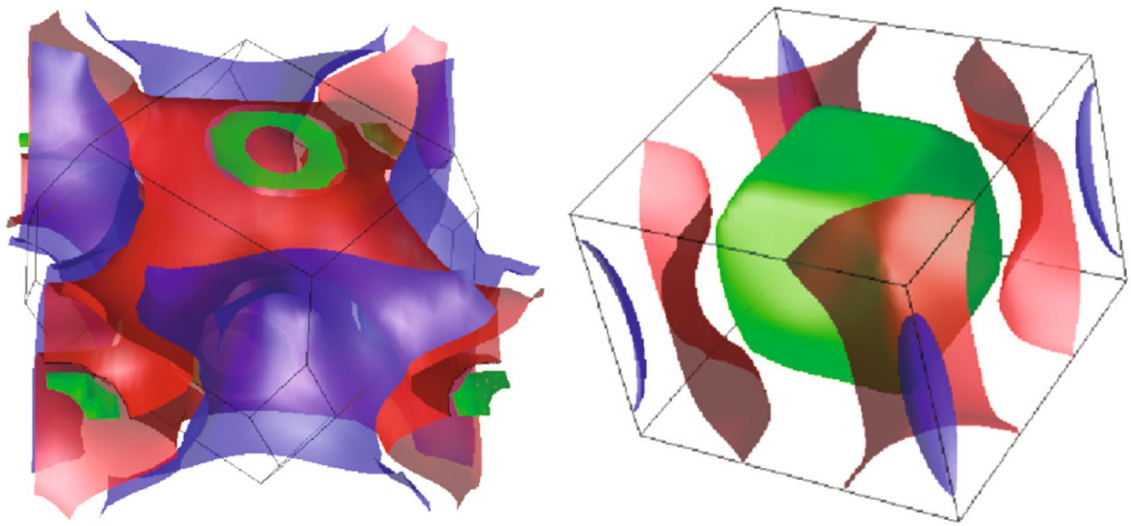

Fig. 15. (Color online) LDA Fermi surface for the (left) (Sr, Ca)Pd_2As_2 and (right) $BaPd_2As_2$ systems.

around the Γ point and electron sheets at the corners of the Brillouin zone.

4. CONCLUSIONS

We have reviewed the electronic structures of a number of new superconductors discovered in the experimental searches for new candidates for high-temperature superconductivity after the observation of high-temperature superconductivity in iron arsenides [1–4]. All these systems appear to be multiband superconductors with a rather complex topology of the Fermi surfaces. General theoretical reasons [30] indicate that the multiband electronic spectrum near the Fermi level should promote an increase in the superconductivity transition temperature T_c. However, the experimental picture is rather contradictory. Indeed, superconductivity is observed in the $K_{1-x}Fe_{2-y}Se_2$ system at a quite high temperature despite the absence of "nesting" of electron and hole Fermi surfaces, as well as the absence of pronounced quasiparticles near the Fermi level (in view of a sufficiently noticeable role of correlations in this system). At the same time, most of the other systems considered above exhibit superconductivity only at relatively low temperatures, although the electronic spectrum is pronouncedly multiband.

In view of this contradictory picture, there is the general question of the existence (or absence) of the electronic structure "optimal" for the observation of high-temperature superconductivity. At present, we cannot substantively answer this question, although our calculations indicate that the electronic spectra of most of the new systems with low T_c values are strongly different from the spectra of high-temperature superconductors based on iron pnictides and chalcogenides. The answer to this question seems to be an interesting aim for further studies.

This work was supported in part by the Russian Foundation for Basic Research (project nos. 11-02-00147 and 14-02-00065) and by the Ural Branch, Russian Academy of Sciences (project nos. 12-P-2-1002 and 12-T-2-1001, basic research program "Quantum Macrophysics and Nonlinear Dynamics").

REFERENCES

1. Y. Kamihara, T. Watanabe, M. Hirano, and H. Hosono, J. Am. Chem. Soc. **130**, 3296 (2008).
2. M. V. Sadovskii, Phys. Usp. **51**, 1201 (2008).
3. K. Ishida, Y. Nakai, and H. Hosono, J. Phys. Soc. Jpn. **78**, 062001 (2009).
4. P. J. Hirshfeld, M. M. Korshunov, and I. I. Mazin, Rep. Prog. Phys. **74**, 124508 (2011).
5. M. V. Sadovskii, E. Z. Kuchinskii, and I. A. Nekrasov, J. Magn. Magn. Mater. **324**, 3481 (2012).
6. E. D. Bauer, F. Ronning, B. L. Scott, and J. D. Thompson, Phys. Rev. B **78**, 172504 (2008).
7. F. Ronning, N. Kurita, E. D. Bauer, B. L. Scott, T. Park, T. Klimczuk, R. Movshovich, and J. D. Thompson, J. Phys.: Condens. Matter **20**, 342203 (2008).
8. K. Kudo, Y. Nishikubo, and M. Nohara, J. Phys. Soc. Jpn. **79**, 123710 (2010).
9. S. Elgazzar, A. M. Strydom, and S.-L. Drechsler, J. Supercond. Nov. Magn. **25**, 1795 (2012).
10. T. Takayama, K. Kuwano, D. Hirai, Y. Katsura, A. Yamamoto, and H. Takagi, Phys. Rev. Lett. **108**, 237001 (2012).
11. A. Krzton-Maziopa, E. Pomjakushina, V. Pomjakushin, V. Pomjakushin, D. Sheptyakov, D. Chernyshov, and V. Svitlyk, J. Phys.: Condens. Matter **23**, 402201 (2011).

12. J. M. Caron, J. R. Neilson, D. C. Miller, A. Llobet, and T. M. McQueen, Phys. Rev. B **84**, R180409 (2011).
13. V. K. Anand, H. Kim, M. A. Tanatar, R. Prozorov, and D. C. Johnston, Phys. Rev. B **87**, 224510 (2013).
14. K. Held, I. A. Nekrasov, N. Blümer, V. I. Anisimov, and D. Vollhardt, Int. J. Mod. Phys. B **15**, 2611 (2001); G. Kotliar, S. Y. Savrasov, K. Haule, V. S. Oudovenko, O. Parcollet, and C. A. Marianetti, Rev. Mod. Phys. **78**, 865 (2006).
15. I. A. Nekrasov, N. S. Pavlov, and M. V. Sadovskii, JETP Lett. **95**, 581 (2012).
16. I. A. Nekrasov, N. S. Pavlov, and M. V. Sadovskii, J. Exp. Theor. Phys. **116**, 620 (2013).
17. I. A. Nekrasov, N. S. Pavlov, and M. V. Sadovskii, JETP Lett. **97**, 15 (2013).
18. I. A. Nekrasov, N. S. Pavlov, and M. V. Sadovskii, J. Exp. Theor. Phys. **117**, 926 (2013).
19. I. A. Nekrasov and M. V. Sadovskii, JETP Lett. **92**, 751 (2010).
20. M. V. Medvedev, I. A. Nekrasov, and M. V. Sadovskii, JETP Lett. **95**, 33 (2012).
21. I. A. Nekrasov and M. V. Sadovskii, JETP Lett. **96**, 227 (2012).
22. I. A. Nekrasov and M. V. Sadovskii, JETP Lett. **98**, 24 (2013).
23. I. A. Nekrasov, Z. V. Pchelkina, and M. V. Sadovskii, JETP Lett. **87**, 560 (2008).
24. I. A. Nekrasov, Z. V. Pchelkina, and M. V. Sadovskii, JETP Lett. **88**, 144 (2008).
25. I. A. Nekrasov, Z. V. Pchelkina, and M. V. Sadovskii, JETP Lett. **88**, 543 (2008).
26. I. A. Nekrasov, Z. V. Pchelkina, and M. V. Sadovskii, JETP Lett. **88**, 679 (2008).
27. I. A. Nekrasov and M. V. Sadovskii, JETP Lett. **93**, 166 (2011).
28. O. K. Andersen, Phys. Rev. B **12**, 3060 (1975); O. Gunnarsson, O. Jepsen, and O. K. Andersen, Phys. Rev. B **27**, 7144 (1983); O. K. Andersen and O. Jepsen, Phys. Rev. Lett. **53**, 2571 (1984).
29. V. Barzykin and L. P. Gorkov, JETP Lett. **88**, 131 (2008).
30. E. Z. Kuchinskii and M. V. Sadovskii, JETP Lett. **89**, 543 (2009).
31. J. Guo, S. Jin, G. Wang, S. Wang, K. Zhu, T. Zhou, M. He, and X. Chen, Phys. Rev. B **82**, 180520(R) (2010).
32. M. Fang, H. Wang, C. Dong, Z. Li, C. Feng, J. Chen, and H. Q. Yuan, Phys. Rev. B **84**, 224506 (2011).
33. W. Bao, Q. Huang, G. F. Chen, M. A. Green, D. M. Wang, J. B. He, X. Q. Wang, and Y. Qiu, Chin. Phys. Lett. **28**, 086104 (2011).
34. A. A. Kordyuk, Low Temp. Phys. **38**, 888 (2012).
35. H.-H. Wen, Rep. Prog. Phys. **75**, 112501 (2012).
36. W. Li, H. Ding, Z. Li, P. Deng, K. Chang, K. He, S. Ji, L. Wang, X. Ma, J.-P. Hu, X. Chen, and Q.-K. Xue, Phys. Rev. Lett. **109**, 057003 (2012).
37. M. Yi, D. H. Lu, R. Yu, S. C. Riggs, J.-H. Chu, B. Lv, Z. K. Liu, M. Lu, Y.-T. Cui, M. Hashimoto, S.-K. Mo, Z. Hussain, C. W. Chu, I. R. Fisher, Q. Si, and Z.-X. Shen, Phys. Rev. Lett. **110**, 067003 (2013).
38. I. R. Shein and A. L. Ivanovskii, Phys. Lett. A **375**, 1028 (2011).
39. Y. Mizuguhci, Y. Hara, K. Deguchi, S. Tsuda, T. Yamaguchi, K. Takeda, H. Kotegawa, H. Tou, and Y. Takano, Supercond. Sci. Technol. **23**, 054013 (2010).
40. E. Z. Kuchinskii, I. A. Nekrasov, and M. V. Sadovskii, JETP Lett. **91**, 518 (2010).
41. E. Z. Kuchinskii, I. A. Nekrasov, and N. S. Pavlov, J. Exp. Theor. Phys. **117**, 327 (2013).
42. K. Haule, J. H. Shim, and G. Kotliar, Phys. Rev. Lett. **100**, 226402 (2008).
43. L. Craco, M. S. Laad, S. Leoni, and H. Rosner, Phys. Rev. B **78**, 134511 (2008).
44. A. O. Shorikov, M. A. Korotin, S. V. Streltsov, D. M. Korotin, and V. I. Anisimov, J. Exp. Theor. Phys. **108**, 121 (2008); arXiv: 0804.3283.
45. S. L. Skornyakov, A. V. Efremov, N. A. Skorikov, M. A. Korotin, Yu. A. Izyumov, V. I. Anisimov, A. V. Kozhevnikov, and D. Vollhardt, Phys. Rev. B **80**, 092501 (2009).
46. A. Imre, A. Hellmann, G. Wenski, J. Graf, D. Johrendt, and A. Mewisa, Z. Anorg. Allg. Chem. **633**, 2037 (2007).
47. M. Rotter, M. Tegel, and D. Johrendt, Phys. Rev. Lett. **101**, 107006 (2008).
48. G. E. Volovik and L. P. Gor'kov, Sov. Phys. JETP **61**, 843 (1985); Physica C **470**, S418 (2010).
49. M. Siegrist and K. Ueda, Rev. Mod. Phys. **63**, 239 (1991).
50. A. Subedi and D. J. Singh, Phys. Rev. B **78**, 132511 (2008).
51. Z. G. Chen, G. Xu, W. Z. Hu, X. D. Zhang, P. Zheng, G. F. Chen, J. L. Luo, Z. Fang, and N. L. Wang, Phys. Rev. B **80**, 094506 (2009).
52. W. L. McMillan, Phys. Rev. **167**, 331 (1968).
53. P. B. Allen and R. C. Dynes, Phys. Rev. B **12**, 905 (1975).
54. A. I. Liechtenstein, M. I. Katsnelson, V. P. Antropov, and V. A. Gubanov, J. Magn. Magn. Mater. **67**, 65 (1987); V. I. Anisimov, F. Aryasetiawan, and A. I. Lichtenstein, J. Phys.: Condens. Matter **9**, 767 (1997).
55. B. Saparov, S. Calder, B. Sipos, H. Cao, S. Chi, D. J. Singh, A. D. Christianson, M. D. Lumsden, and A. S. Sefat, Phys. Rev. B **84**, 245132 (2011).
56. N. Kurita, F. Ronning, Y. Tokiwa, E. D. Bauer, A. Subedi, D. J. Singh, J. D. Thompson, and R. Movshovich, Phys. Rev. Lett. **102**, 147004 (2009).
57. B. Zhou, M. Xu, Y. Zhang, G. Xu, Ch. He, L. X. Yang, F. Chen, B. P. Xie, X.-Y. Cui, M. Arita, K. Shimada, H. Namatame, M. Taniguchi, X. Dai, and D. L. Feng, Phys. Rev. B **83**, 035110 (2011).
58. I. R. Shein and A. L. Ivanovskii, Physica B **405**, 3213 (2010).

Translated by R. Tyapaev

ISSN 1063-7761, Journal of Experimental and Theoretical Physics, 2016, Vol. 122, No. 3, pp. 509–524. © Pleiades Publishing, Inc., 2016.

Contribution for the JETP special issue in honor of L.V. Keldysh's 85th birthday

DMFT+Σ Approach to Disordered Hubbard Model[1]

E. Z. Kuchinskii* and M. V. Sadovskii**

Institute for Electrophysics, Ural Branch, Russian Academy of Sciences, Yekaterinburg, 620016 Russia
Mikheev Institute for Metal Physics, Ural Branch, Russian Academy of Sciences, Yekaterinburg, 620990 Russia
**e-mail: Kuchinsk@iep.uran.ru*
*** e-mail: Sadovski@iep.uran.ru*

Received July 6, 2015

Abstract—We briefly review the generalized dynamic mean-field theory DMFT+Σ applied to both repulsive and attractive disordered Hubbard models. We examine the general problem of metal–insulator transition and the phase diagram in the repulsive case, as well as the BCS–BEC crossover region of the attractive model, demonstrating a certain universality of single-electron properties under disordering in both models. We also discuss and compare the results for the density of states and dynamic conductivity in the repulsive and attractive cases and the generalized Anderson theorem behavior of the superconducting critical temperature in the disordered attractive case. A brief discussion of the behavior of Ginzburg–Landau coefficients under disordering in the BCS–BEC crossover region is also presented.

DOI: 10.1134/S106377611603016X

1. INTRODUCTION

Strongly correlated electronic systems, which are mainly realized in a range of compounds containing transition or rare-earth elements with partially filled 3*d*, 4*f*, or 5*f* shells, attract attention of scientists because of their unusual physical properties and are notorious for major difficulties in theoretical description. Perhaps the most significant development in this area has been the discovery of high-temperature superconductivity in copper oxides, which are considered a typical example of strongly correlated systems.

Early qualitative ideas formulated mainly by Mott [1] as well as the introduction of the seminal model by Hubbard [2] inspired hundreds of theoretical papers, which now constitute a separate branch of condensed matter theory. Probably the most impressive achievement if this field in recent years was the development of dynamical mean-field theory (DMFT), which provides an asymptotically exact solution of the Hubbard model in the limit of infinitely large number of dimensions [3–8].

Most of the studies of strongly correlated systems within the Hubbard model are devoted to the case of repulsive interactions among electrons, which are directly related to many topical problems, with most attention payed to the physics of high-T_c superconductivity in cuprates and the general problem of the metal–insulator transition in cuprates and other similar oxides of transition metals.

Another direction of research is the studies of the Hubbard model with attractive interaction, which is related mainly to a rather old problem of strong-coupling superconductivity, especially to the theoretical description of the notorious BCS-to-BEC (Bardeen–Cooper–Schrieffer to Bose–Einstein condensation) crossover, which is also directly related to the problem of high-T_c superconductivity in copper oxides. Starting with pioneering papers by Eagles and Leggett [9, 10] at $T = 0$ and the important progress achieved by Nozières and Schmitt-Rink [11], who suggested an effective method to study the transition temperature crossover region, this field has produced a large number of theoretical papers published during the recent years, including successful applications of the DMFT approach.

This last area of research is also directly connected with recent progress in experimental studies of quantum gases in magnetic and optical dipole traps, as well as in optical lattices, with controllable parameters, such as the density and interaction strength (cf. reviews [12, 13]), which has increased the interest in superconductivity (superfluidity of fermions) with a strong pairing interaction, including the BCS–BEC crossover region.

In recent years we have developed the so-called generalized DMFT+Σ approach [14–17], which is

[1]The article is published in the original.

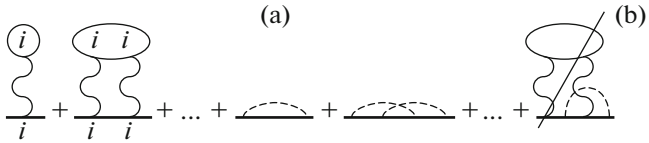

Fig. 1. Typical "skeleton" self-energy diagrams in the DMFT+Σ approximation.

very convenient for the studies of different additional interactions in the repulsive Hubbard model, such as pseudogap fluctuations [14–17], disorder [18, 19], electron–phonon interaction [20], and so on. This approach is also well suited to the analysis of two-particle properties, such as the optical (dynamic) conductivity [18, 21]. In [22], we used this approximation to calculate single-particle properties of the normal phase and optical conductivity in the attractive Hubbard model. Recently, we used the DMFT+Σ approach to study disorder influence on the superconducting transition temperature in this model [23, 24].

Below, we concentrate on a discussion the of disorder effects in both repulsive and attractive Hubbard models. There are not so many works devoted to the studies of disorder effects in Hubbard models, because of many theoretical complications related to the problem of the interplay of disorder scattering and Hubbard interaction. We concentrate exclusively on our DMFT+Σ approach, which is actually very convenient here and provides a good interpolation scheme between different limit cases. We discuss the results obtained in our previous work, and similarities and dissimilarities of disorder effects in repulsive and attractive Hubbard models, in some cases demonstrating universal dependences on disorder.

2. BASICS OF THE DMFT+Σ APPROACH TO DISORDERED SYSTEMS

The Hamiltonian of a disordered Hubbard model can be written as

$$H = -t\sum_{\langle ij\rangle\sigma} a_{i\sigma}^{\dagger}a_{j\sigma} + \sum_{i\sigma}\epsilon_i n_{i\sigma} + U\sum_i n_{i\uparrow}n_{i\uparrow}, \qquad (1)$$

where $t > 0$ is the transfer integral between nearest sites of the lattice, U is the onsite interaction ($U > 0$ in the case of repulsive interaction, and $U < 0$ in the case of attraction), $n_{i\sigma} = a_{i\sigma}^{\dagger}a_{i\sigma}$ is the operator of the number of electrons on lattice site i, $a_{i\sigma}$ ($a_{i\sigma}^{\dagger}$) is the annihilation (creation) operator for the electron with spin σ on site i. The local energy levels ϵ_i are assumed to be independent random variables at different lattice sites (Anderson disorder) [15]. To simplify the diagram technique in what follows, we assume the Gaussian distribution of these energy levels:

$$\mathcal{P}(\epsilon_i) = \frac{1}{\sqrt{2\pi}\Delta}\exp\left(-\frac{\epsilon_i^2}{2\Delta^2}\right). \qquad (2)$$

The parameter Δ represents the measure of disorder and this Gaussian random field (with "white noise" correlation on different lattice sites) generates "impurity" scattering and leads to the standard diagram technique for calculating the ensemble-averaged Green's functions [26].

The generalized DMFT+Σ approach [14–17] extends the standard DMFT [5–7] by introducing an additional self-energy $\Sigma_{\mathbf{p}}(\varepsilon)$ (in the general case, momentum dependent), which is due to some interaction mechanism outside the DMFT. It gives an effective procedure to calculate both single- and two-particle properties [18, 21]. The single-particle Green's function is then written in the form

$$G(\varepsilon, \mathbf{p}) = \frac{1}{\varepsilon + \mu - \varepsilon(\mathbf{p}) - \Sigma(\varepsilon) - \Sigma_{\mathbf{p}}(\varepsilon)}, \qquad (3)$$

where $\varepsilon(\mathbf{p})$ is the "bare" electronic dispersion, while the total self-energy completely neglects the interference between the Hubbard and additional interaction and is given by the additive sum of the local self-energy $\Sigma(\varepsilon)$ of DMFT and the "external" self-energy $\Sigma_{\mathbf{p}}(\varepsilon)$. This preserves the standard structure of DMFT equations [5–7]. However, there are two important differences for the standard DMFT. At each iteration of the DMFT loop, we recalculate the "external" self-energy $\Sigma_{\mathbf{p}}(\varepsilon)$ using some approximate scheme for the description of the "external" interaction, and the local Green's function is "dressed" by $\Sigma_{\mathbf{p}}(\varepsilon)$ at each step of the standard DMFT procedure.

In Fig. 1, we show the typical "skeleton" diagrams for self-energy in DMFT+Σ. Here, the first two terms are local DFMT self-energy diagrams due to the Hubbard interaction, while two diagrams in the middle show contributions to self-energy from the additional interaction (dashed interaction lines), and the last diagram b is a typical example of the interference process, which is neglected. Indeed, once we neglect such an interference, the total self-energy is defined as a simple sum of two contributions shown in Fig. 1a.

As an effective Anderson impurity solver in our DMFT calculations, we have always used the numerical renormalization group [27], which allows performing calculations at rather low temperatures.

For the self-energy due to disorder scattering produced by Hamiltonian (1), we use the simplest approximation neglecting the diagrams with "intersecting" interaction lines (like those in the fourth diagram in Fig. 1a), i.e., the so-called self-consistent Born approximation, represented by the third diagram in Fig. 1a. For the Gaussian distribution of site energies, it is momentum independent and is given by

$$\Sigma_{\mathbf{p}}(\varepsilon) \to \Delta^2\sum_{\mathbf{p}} G(\varepsilon, \mathbf{p}), \qquad (4)$$

where $G(\varepsilon, \mathbf{p})$ is the single-particle Green's function (3), and Δ is the strength of site energy disorder.

In what follows, we mainly consider the three-dimensional system with a "bare" semi-elliptic density of states (per unit cell and one spin projection), with the total bandwidth $2D$, which is given by

$$N_0(\varepsilon) = \frac{2}{\pi D^2}\sqrt{D^2 - \varepsilon^2}. \quad (5)$$

In this case, we can directly demonstrate, that the disorder influence on single-particle properties of the disordered Hubbard model (both repulsive and attractive) is completely described in the DMFT+Σ approximation by effects of general band widening by disorder scattering. Actually, in the system of self-consistent DMFT+S equations [15, 17, 18], both the "bare" band spectrum and disorder scattering enter only at the stage of calculations of the local Green's function:

$$G_{ii} = \sum_{\mathbf{p}} G(\varepsilon, \mathbf{p}), \quad (6)$$

where the full Green's function $G(\varepsilon, \mathbf{p})$ is determined by Eq. (3), while the self-energy due to disorder, in the self-consistent Born approximation, is given by Eq. (4). Then the local Green's function takes the form

$$\begin{aligned} G_{ii} &= \int_{-D}^{D} d\varepsilon' \frac{N_0(\varepsilon')}{\varepsilon + \mu - \varepsilon' - \Sigma(\varepsilon) - \Delta^2 G_{ii}} \\ &= \int_{-D}^{D} d\varepsilon' \frac{N_0(\varepsilon')}{E_t - \varepsilon'}, \end{aligned} \quad (7)$$

where we introduce

$$E_t = \varepsilon + \mu - \Sigma(\varepsilon) - \Sigma^2 G_{ii}.$$

In the case of a semi-elliptic density of states (5), this integral can be calculated in analytic form, and the local Green's function then becomes

$$G_{ii} = 2\frac{E_t - \sqrt{E_t^2 - D^2}}{D^2}. \quad (8)$$

It can be easily seen that Eq. (8) represents one of the roots of the quadratic equation

$$G_{ii}^{-1} = E_t - \frac{D^2}{4} G_{ii}, \quad (9)$$

reproducing the correct limit $G_{ii} \to E_t^{-1}$ for an infinitely narrow ($D \to 0$) band. Then we can write

$$\begin{aligned} G_{ii}^{-1} &= \varepsilon + \mu - \Sigma(\varepsilon) - \Delta^2 G_{ii} - \frac{D^2}{4} G_{ii} \\ &= \varepsilon + \mu - \Sigma(\varepsilon) - \frac{D_{\text{eff}}^2}{4} G_{ii}, \end{aligned} \quad (10)$$

where we introduce the effective half-width of the band (in the absence of electronic correlations, i.e., for $U = 0$) widened by disorder scattering:

$$D_{\text{eff}} = D\sqrt{1 + 4\frac{\Delta^2}{D^2}}. \quad (11)$$

Comparing (7), (9), and (10), we immediately see that the local Green's function can be written as

$$G_{ii} = \int_{-D_{\text{eff}}}^{D_{\text{eff}}} d\varepsilon' \frac{\tilde{N}_0(\varepsilon')}{\varepsilon + \mu - \varepsilon' - \Sigma(\varepsilon)}, \quad (12)$$

where

$$\tilde{N}_0(\varepsilon) = \frac{2}{\pi D_{\text{eff}}^2}\sqrt{D_{\text{eff}}^2 - \varepsilon^2} \quad (13)$$

represents the density of states in the absence of the interaction U widened by disorder. The density of states in the presence of disorder remains semi-elliptic, and therefore all effects of disorder scattering on single-particle properties of the disordered Hubbard model in the DMFT+Σ approximation reduce to only disorder widening of the conduction band, i.e., to the replacement $D \to D_{\text{eff}}$.

Within the DMFT+Σ approach, we can also investigate the two-particle properties [18, 21]. After the general analysis based on the Ward identity derived in [21], we can show that the real part of the dynamical (optical) conductivity in the DMFT+Σ approximation is given by [18, 21]

$$\begin{aligned} \operatorname{Re}\sigma(\omega) &= \frac{e^2\omega}{2\pi}\int_{-\infty}^{\infty} d\varepsilon [f(\varepsilon_-) - f(\varepsilon_+)] \\ &\operatorname{Re}\left\{\phi_\varepsilon^{0RA}(\omega)\left[1 - \frac{\Sigma^R(\varepsilon_+) - \Sigma^A(\varepsilon_-)}{\omega}\right]^2\right. \\ &\left. - \phi_\varepsilon^{0RR}(\omega)\left[1 - \frac{\Sigma^R(\varepsilon_+) - \Sigma^A(\varepsilon_-)}{\omega}\right]^2\right\}, \end{aligned} \quad (14)$$

where e is the electron charge, $f(\varepsilon_\pm)$ is the Fermi distribution with $\varepsilon_\pm = \varepsilon \pm \omega/2$, and

$$\begin{aligned} &\phi_\varepsilon^{0RR(RA)}(\omega) \\ &= \lim_{q\to 0} q^{-2}(\Phi_\varepsilon^{0RR(RA)}(\omega, \mathbf{q}) - \Phi_\varepsilon^{0RR(RA)}(\omega, 0)), \end{aligned} \quad (15)$$

where the two-particle loops $\Phi_\varepsilon^{0RR(RA)}(\omega, \mathbf{q})$ contain all vertex corrections from disorder scattering, but do not include any vertex corrections from Hubbard interaction (see the details in [8]). This considerably simplifies calculations of optical conductivity within the DMFT+Σ approximation, because we only have to solve the single-particle problem for the local self-energy $\Sigma(\varepsilon_\pm)$ via the DMFT+Σ procedure, while nontrivial contributions from disorder scattering enter only via $\Phi_\varepsilon^{0RR(RA)}(\omega, \mathbf{q})$, which can be calculated in an

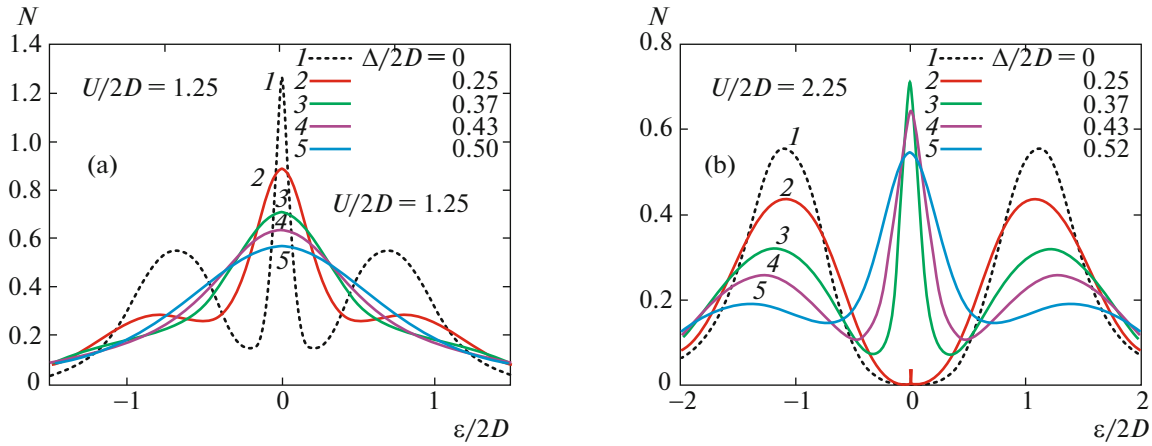

Fig. 2. (Color online) Density of states of the Hubbard model at half-filling for different disorder levels Δ [18]. (a) Correlated metal with $U = 2.5D$. (b) Mott insulator with $U = 4.5D$. Temperature $T/2D = 0.0005$.

appropriate approximation, neglecting vertex corrections from Hubbard interaction. To be more specific, to obtain the loop contributions $\Phi_{\varepsilon}^{0RR(RA)}(\omega, \mathbf{q})$ determined by disorder scattering, we can either use the standard "ladder" approximation for weak disorder or, following [18], use a direct generalization of the self-consistent theory of localization [28–30], which allows treating the case of strong enough disorder. In this approach, conductivity is mainly determined by the generalized diffusion coefficient obtained from a simple extension of the self-consistency equation [28–30] of this theory, which is to be solved in combination with the DMFT+Σ procedure [18].

3. MOTT–ANDERSON TRANSITION IN DISORDERED SYSTEMS

Below, we present some of the most interesting results for the repulsive Hubbard model at half-filling with semi-elliptic bare density of states (5) with the bandwidth $2D$ [18], which is qualitatively well suited to describe the three-dimensional case. The density of states is given below in units of the number of states in the energy interval for a cubic unit cell of the volume a^3 (where a is the lattice constant) and for one spin projection. The conductivity values are always given in natural units of $e^2/\hbar a$.

3.1. Evolution of the Density of States

In the standard DMFT approximation, the density of states of the repulsive Hubbard model at half-filling has a typical three-peak structure [5, 6, 32] with quite a narrow quasiparticle (central) peak at the Fermi level and rather wide upper and lower Hubbard bands located at energies $\varepsilon \sim \pm U/2$. As the Hubbard repulsive interaction U grows, the quasiparticle band narrows within the metallic phase and disappears at the Mott–Hubbard metal-insulator transition at the critical interaction value $U_{c2}/2D \approx 1.5$. At larger values of U, we observe an insulating gap at the Fermi level.

In Fig. 2, we present our results [18] for DMFT+Σ densities of states for a typical strongly correlated metal with $U = 2.5D$, both in the absence of disorder and for different values of disorder scattering Δ, including strong enough disorder, which transforms the correlated metal to a correlated Anderson insulator. In the metallic phase, disorder scattering leads to a typical broadening and suppression of the density of states.

Much more unusual is the result obtained for $U = 4.5D$, typical for the Mott insulator phase and shown in Fig. 2b. Here, we observe the recovery of the central peak (quasiparticle band) in the density of states with an increase in disorder, transforming the Mott insulator to correlated metal or to a correlated Anderson insulator. A similar behavior of the density of states for the disordered Hubbard model was also reported in [31], using direct numerical DMFT calculations in finite lattices.

The physical origin of this quite unexpected central peak restoration is evident. The control parameter of the metal–insulator transition in DMFT is the ratio of the Hubbard interaction U to the bare bandwidth $2D$. Introduction of disorder (in the absence of Hubbard interaction) leads to a new effective bandwidth $2D_{\text{eff}}$ (cf. (11)), which increases with disorder. This leads to diminishing values of the ratio $U/2D_{\text{eff}}$, which in its turn causes the restoration of the quasiparticle band.

Furthermore, in complete accordance with analytic arguments presented above, the behavior of the density of states in the disordered Hubbard model with semi-elliptic density of states actually demonstrates a universal dependence on disorder. This is clearly seen from Fig. 3, where we show properly normalized typical densities of states $2D_{\text{eff}}N(\varepsilon)$ in the metallic phase (with the normalized interaction value $U/2D_{\text{eff}} = 1.0$)

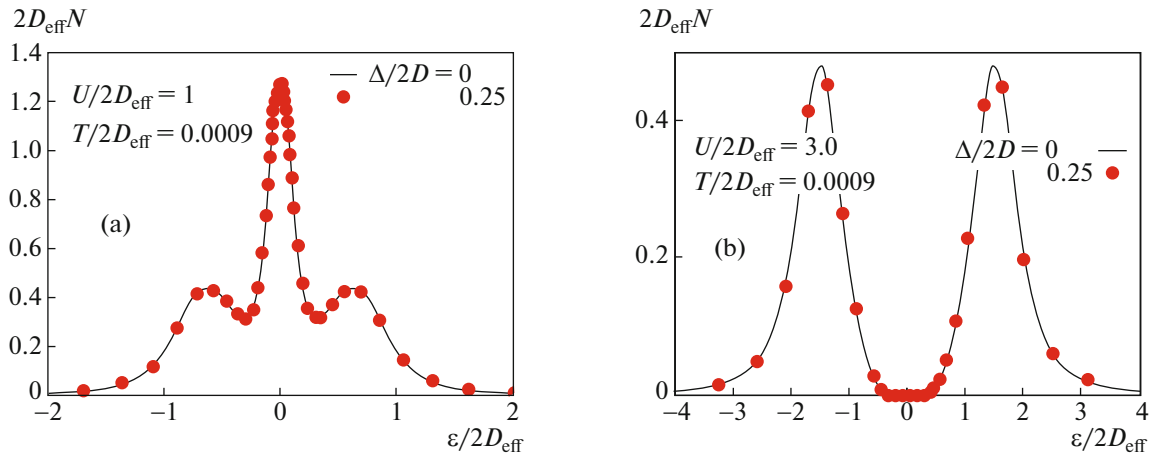

Fig. 3. (Color online) Universal dependence of the properly normalized density of states on the normalized energy $\varepsilon/2D_{\rm eff}$ in the Hubbard model for different disorder levels Δ. (a) Correlated metal ($U/2D_{\rm eff} = 1.0$) with no disorder and for $\Delta/2D = 0.25$. (b) Mott insulator ($U/2D_{\rm eff} = 3.0$) without disorder and for $\Delta/2D = 0.25$. Temperature $T/2D_{\rm eff} = 0.0009$.

and the insulating phase (corresponding to $U/2D_{\rm eff} = 3.0$) without disorder and for the typical value of disorder scattering $\Delta/2D = 0.25$. The densities of states in the absence and in the presence of disorder are actually described by the same (universal) dependences if expressed via properly normalized parameters.

In the absence of disorder, one of the characteristic features of the Mott–Hubbard metal-insulator transition is the hysteresis behavior of the density of states, occurring as U decreases starting from the insulating phase [6, 32]. The Mott insulator phase remains (meta)stable down to rather small values of U deep within the correlated metal phase, and the metallic phase is restored only at about $U_{c1}/2D \approx 1$.The corresponding interval of the interaction parameter $U_{c1} < U < U_{c2}$ represents a coexistence region of the metallic and Mott insulating phases, where, from a thermodynamic standpoint, the metallic phase is more stable [6, 32, 33]. Such a hysteresis in the behavior of the density of states is also observed in the presence of disorder [18, 19].

3.2. Optical Conductivity: Mott–Hubbard and Anderson Transitions

In the absence of disorder, our calculations reproduce the conventional DMFT results [5, 6], with the optical conductivity characterized by a typical Drude peak at low frequencies and a wide maximum at $\omega \sim U$, which corresponds to optical transitions to the upper Hubbard band. As U increases, the Drude peak is suppressed and disappears completely at the Mott transition. Introducing disorder leads to qualitative changes in the frequency dependence of the optical conductivity.

Figure 4a shows the real part of the optical conductivity of the Hubbard model at half-filling for different disorder levels Δ and $U = 2.5D$ typical for a correlated metal. Transitions to the upper Hubbard bands at energies $\omega \sim U$ are almost unobservable. However, it is clearly visible that the metallic Drude peak typically centered at the zero frequency is broadened and suppressed by disorder, gradually transforming into a peak at a finite frequency because of the Anderson localization effects. The Anderson transition takes place at $\Delta_c \approx 0.74D$ (corresponding to curve *3* on all figures here). We note that this value explicitly depends on the value of the cutoff in the equation for the generalized diffusion coefficient, which is defined up to a coefficient of the order of unity [26, 29]. Naive expectations can lead to the conclusion that a narrow quasiparticle band at the Fermi level (formed in a strongly correlated metal) can be localized much more easily than the usual conduction band. However, these expectations are wrong and the band localizes only at rather large disorder $\Delta_c \sim D$ of the order of the conduction band width ~$2D$. This is in qualitative agreement with the results for localization transition in the two-band model [36].

In the DMFT+Σ approach, the critical disorder value Δ_c does not depend on U because the interaction effects enter here only through $\Delta\Sigma^{RA}(\omega) \to 0$ as $\omega \to 0$ (for $T = 0$, $\varepsilon = 0$), and therefore the influence of interaction just disappears at $\omega = 0$. In fact, this is the main shortcoming of the DMFT+Σ approach, originating from the neglect of the interference effect between interaction and impurity scattering. A significant role of these interference effects is actually well known for a long time [34, 35]. However, the neglect of these effects allows us to perform a reasonable physical interpolation between two main limits: that of the

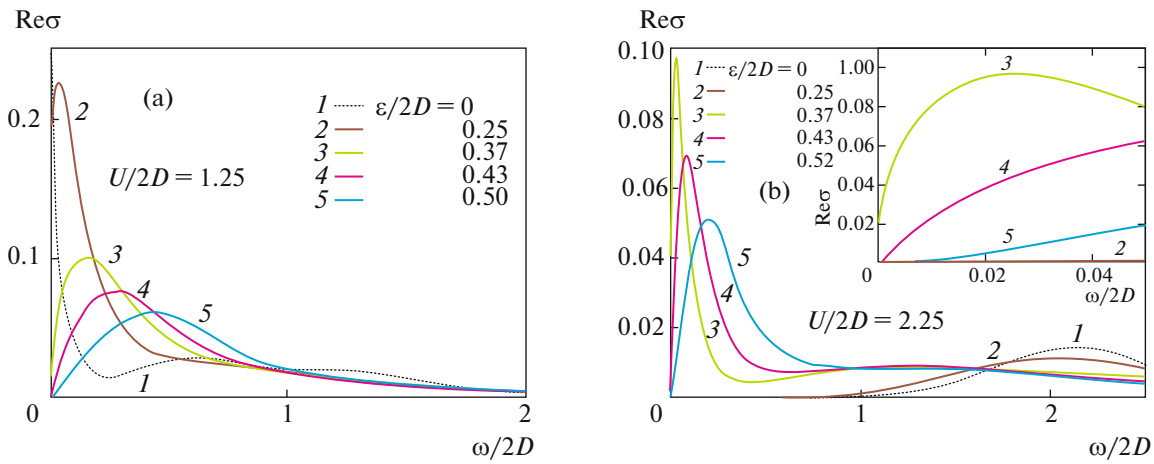

Fig. 4. (Color online) Real part of the optical conductivity of the Hubbard model at half-filling for different disorder levels Δ [18]. (a) Typical correlated metal with $U = 2.5D$. Curves *1*, *2* describe the metallic phase, curve *3* corresponds to the mobility edge (Anderson transition), curves *4*, *5* correspond to a correlated Anderson insulator. (b) Typical Mott insulator with $U = 4.5D$. Curves *1*, *2* correspond to a Mott insulator, curve *3* to the mobility edge (Anderson transition), curves *4*, *5* to a correlated Anderson insulator. The inset shows the low-frequency region magnified. Temperature $T/2D = 0.0005$.

Anderson transition due to disorder and the Mott–Hubbard transition due to strong correlations.

In Fig. 4b, we show the real part of the optical conductivity of the Mott–Hubbard insulator with $U = 4.5D$ for different disorder levels Δ. In the inset, we show low-frequency data, demonstrating different types of conductivity behavior, especially close to the Anderson transition and within the Mott insulator phase. On the main part of the figure, the contribution to conductivity from transitions to the upper Hubbard band at $\omega \sim U$ is clearly seen. Disorder growth results in the appearance of finite conductivity for the frequencies inside the Mott–Hubbard gap, correlating with the restoration of the quasiparticle band in the density of states within the gap as shown in Fig. 2b. This conductivity for $\Delta < \Delta_c$ is metallic (finite in the static limit $\omega = 0$), and for $\Delta > \Delta_c$ at low frequencies, we obtain $\mathrm{Re}\sigma(\omega) \sim \omega^2$, which is typical for an Anderson insulator [26, 28–30].

Somewhat unusual is the appearance in $\mathrm{Re}\sigma(\omega)$ of a peak at finite frequencies even in the metallic phase. This happens because of the importance of localization effects. In the "ladder" approximation for $\Phi_\varepsilon^{0RA}(\omega, \mathbf{q})$, with all localization effects neglected, we obtain the usual Drude peak at $\omega = 0$ [18], while taking localization effects into account shifts the peak in $\mathrm{Re}\sigma(\omega)$ to finite frequencies.

Above, we presented the data for conductivity obtained in the case of increasing U from the metallic to the Mott insulator phase. As U decreases from the Mott insulator phase, we observe a hysteresis of conductivity in the coexistence region defined (in the absence of disorder) by the inequality $U_{c1} < U < U_{c2}$. A hysteresis of conductivity is also observed in the coexistence region in the presence of disorder. More details can be found in [18, 19].

In general, the picture of the conductivity behavior obtained in the DMFT+Σ approximation is rather rich, demonstrating both the Mott–Hubbard transition due to strong correlations and the disorder-induced Anderson (localization) transition. The complicated behavior under disordering is essentially determined by the two-particle Green's function behavior and does not show a kind of universality demonstrated above for the single-particle density of states.

3.3. Phase Diagram of the Disordered Hubbard Model at Half-Filling

The phase diagram of the repulsive disordered Hubbard model at half-filling was studied in [31], using direct DMFT numerics for lattices with a finite number of sites with random realizations of energies ϵ_i in (1), with subsequent averaging over many lattice realizations to obtain the averaged density of states and the geometric mean local density of states, which allows determining the critical disorder for the Anderson transition. Below, we present our results on the disordered Hubbard-model phase diagram obtained from the density of states and optical conductivity calculations in the DMFT+Σ approach [8].

The calculated disorder-correlation strength (Δ, U) phase diagram at zero temperature is shown in Fig. 5 (actual calculations were performed at a very low value $T/2D = 0.0005$). The Anderson transition line $\Delta_c \approx 0.37D$ is defined as the disorder strength for which static conductivity vanishes at $T = 0$. The Mott–Hubbard transition can be detected either from the central peak disappearance in the density of states or from the

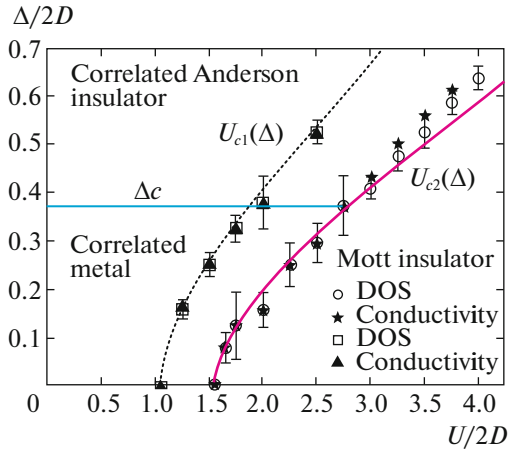

Fig. 5. (Color online) Phase diagram of the disordered Hubbard model [18]. Continuous curves are Mott insulator phase boundaries $U_{c1,c2}(\Delta)$ obtained from the analytic estimate in Eq. (17). Different symbols represent results for these boundaries obtained from calculations from the density of states and optical conductivity. The Anderson transition line is given by $\Delta_c = 0.37$.

optical conductivity by observation of gap closing in the insulating phase or from the static conductivity disappearance in the metallic phase.

We have already noted that the DMFT+Σ approximation gives a universal (U-independent) value of the critical disorder Δ_c because of the neglect of interference between disorder scattering and Hubbard interaction. This leads to a difference between the phase diagram in Fig. 5 and the one obtained by numerical simulations in [31]. At the same time, the qualitative form of our phase diagram is highly nontrivial and qualitatively coincides with the results in [31]. The main difference is the conservation of Hubbard bands in our results even in the limit of high enough disorder, while they just disappear in [31]. The phase coexistence region in Fig. 5 slowly widens as disorder increases instead of vanishing at some "critical" point as on the phase diagram in [31]. The coexistence boundaries (Mott insulator phase boundaries) obtained with a decrease or increase in U, represented by curves $U_{c1}(\Delta)$ and $U_{c2}(\Delta)$ in Fig. 5, can actually be obtained from the simple equation

$$\frac{U_{c1,c2}(\Delta)}{D_{\text{eff}}} = \frac{U_{c1,c2}}{D}, \tag{16}$$

where the effective bandwidth in the presence of disorder is calculated for $U = 0$ within self-consistent Born approximation (4), (11). Hence, the boundaries of the coexistence region (which also define the boundaries of the Mott insulator phase) are given by

$$U_{c1,c2}(\Delta) = U_{c1,c2}\sqrt{1 + 4\frac{\Delta^2}{D^2}}. \tag{17}$$

They are shown in Fig. 5 by dotted and solid lines. Phase transition points detected from the disappearance of a quasiparticle peak as well as points following from qualitative changes of conductivity behavior are shown in Fig. 5 by different symbols. These symbols demonstrate very good agreement with analytic results, confirming the choice of ratio (16) as a control parameter of the Mott transition in the presence of disorder. This transition is essentially controlled by simple band-widening effects due to disorder scattering, similarly to the behavior of the density of states discussed above.

We note that the values of the normalized density of states $2D_{\text{eff}}N(\varepsilon)$ are universal along each of these boundaries, as well as along any curve in the (Δ, U) plane determined by the equation

$$U(\Delta) = U(0)\sqrt{1 + 4\frac{\Delta^2}{D^2}} \tag{18}$$

in accordance with our discussion of the universal dependence of the densities of states on disorder presented above.

Essentially similar results were obtained for the behavior of the density of states, dynamic conductivity, and the phase diagram [19] in the case of the conduction band with a "flat" density of states in the absence of disorder and interactions, which qualitatively corresponds to the two-dimensional case. This is not surprising because large enough disorder and interactions both transform the "flat" band into a kind of smeared semi-elliptic band. Some explicit examples of this kind of behavior are presented below in the case of the attractive Hubbard model.

4. ATTRACTIVE HUBBARD MODEL WITH DISORDER

The studies of superconductivity in the BCS–BEC crossover region attracts theorists for a rather long time [10] and most important progress here was achieved by Nozieres and Schmitt-Rink [11], who proposed an effective approach to describe the T_c crossover. The attractive Hubbard model is probably the simplest model allowing theoretical studies of the BCS–BEC crossover [11]. This model was studied within DMFT in a number of recent papers [37–40]. But only a few results were obtained for the normal (nonsuperconducting) phase of this model, especially in the disordered case. Similarly, there were practically no studies of two-particle properties, such as optical conductivity. Below, we present a summary of our results obtained within the DMFT+Σ approach and compare then with similar results for the repulsive Hubbard model.

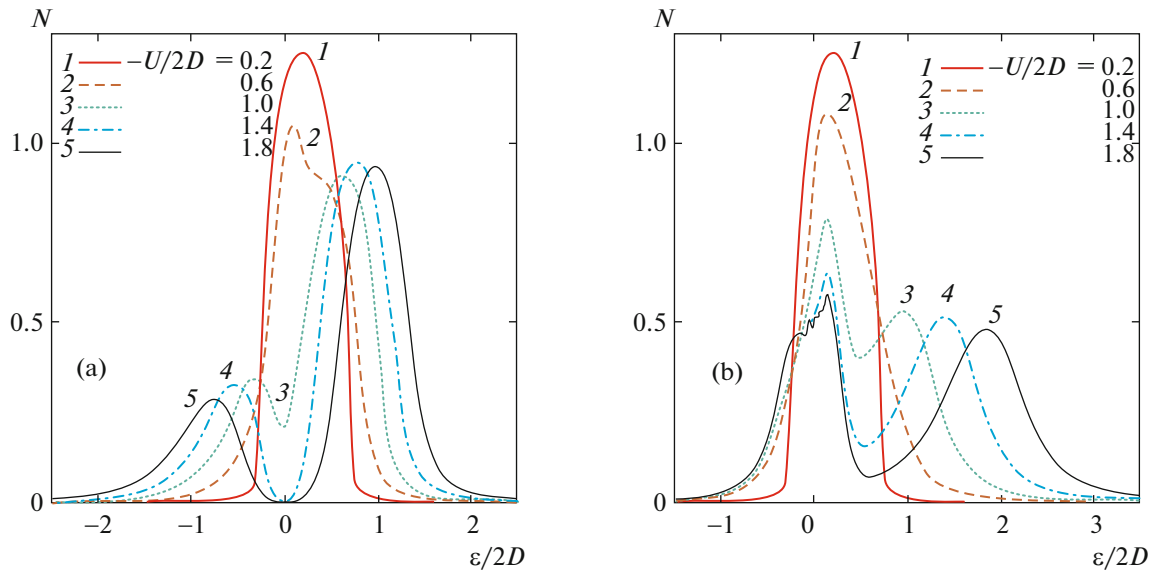

Fig. 6. (Color online) Densities of states for different values of Hubbard (a) attraction and (b) repulsion. Temperature $T/2D = 0.05$.

4.1. Density of States and Optical Conductivity

In the special case of a half-filled band ($n = 1$), the densities of states of attractive and repulsive Hub-bard models just coincide (due to an exact mapping of these models onto each other). Below, we discuss the more typical case of a quarter-filled band ($n = 0.5$). In Fig. 6, we show the densities of states obtained for $T/2D = 0.05$ for different values of attractive interaction ($U < 0$). Figure 6a is to be compared with Fig. 6b, where we present similar results for the repulsive ($U > 0$) case. We can see that the densities of states close to the Fermi level decrease with an increase in U, both for attraction (Fig. 6a) and repulsion (Fig. 6b), but a significant increase in $|U|$ in the repulsive case leads only to the vanishing of the quasiparticle peak, such that the density of states at the Fermi level becomes practically independent of U, while in the attractive case, the increase in $|U|$ leads to the superconducting pseudogap opening at the Fermi level (curve *3* in Fig. 6a); for $|U|/2D > 1.2$, we observe the full gap opening at the Fermi level (curves *4*, *5* in Fig. 7). This gap is not directly related to the emergence of a superconducting state, but is due to the appearance of preformed Cooper pairs at the temperatures larger than the superconducting transition temperature (which is lower than the temperature $T/2D = 0.05$ used in our calculations). Here, we actually observe the important difference between attractive and repulsive cases: in case of repulsion, a deviation from half-filling leads to a metallic state for arbitrary values of U and the insulating gap opens at large U not at the Fermi level.

This picture of the evolution of the density of states as $|U|$ increases is also supported by the behavior of optical conductivity shown in Fig. 7. We see that the increase in $|U|$ leads to the replacement of the Drude peak at zero frequency (curves *1–3* in Fig. 7) by a pseudogap dip (curves *5* and *6* in Fig. 7) and a wide maximum of the conductivity at a finite frequency, related with transitions across the pseudogap. A further increase in $|U|$ leads to the opening of the full gap in the optical conductivity due to the formation of Cooper pairs (curves *7–9* in Fig. 7).

In Fig. 8, we present the evolution of the density of states and optical conductivity with changing disorder. At weak enough attraction ($|U|/2D = 0.8$, Figs. 8a, 8b), the growth of disorder just widens the density of states. Disorder effectively masks peculiarities of the density of states due to correlation effects. In particular, the quasiparticle peak and the "wings" due to the upper

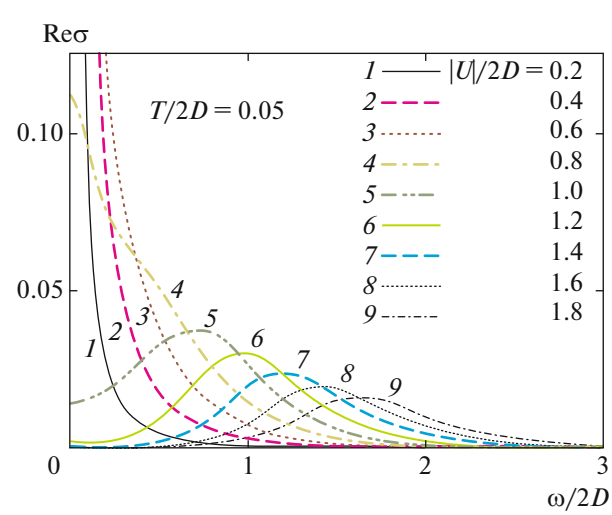

Fig. 7. (Color online) Optical conductivity for different values of attractive Hubbard model. Temperature $T/2D = 0.05$.

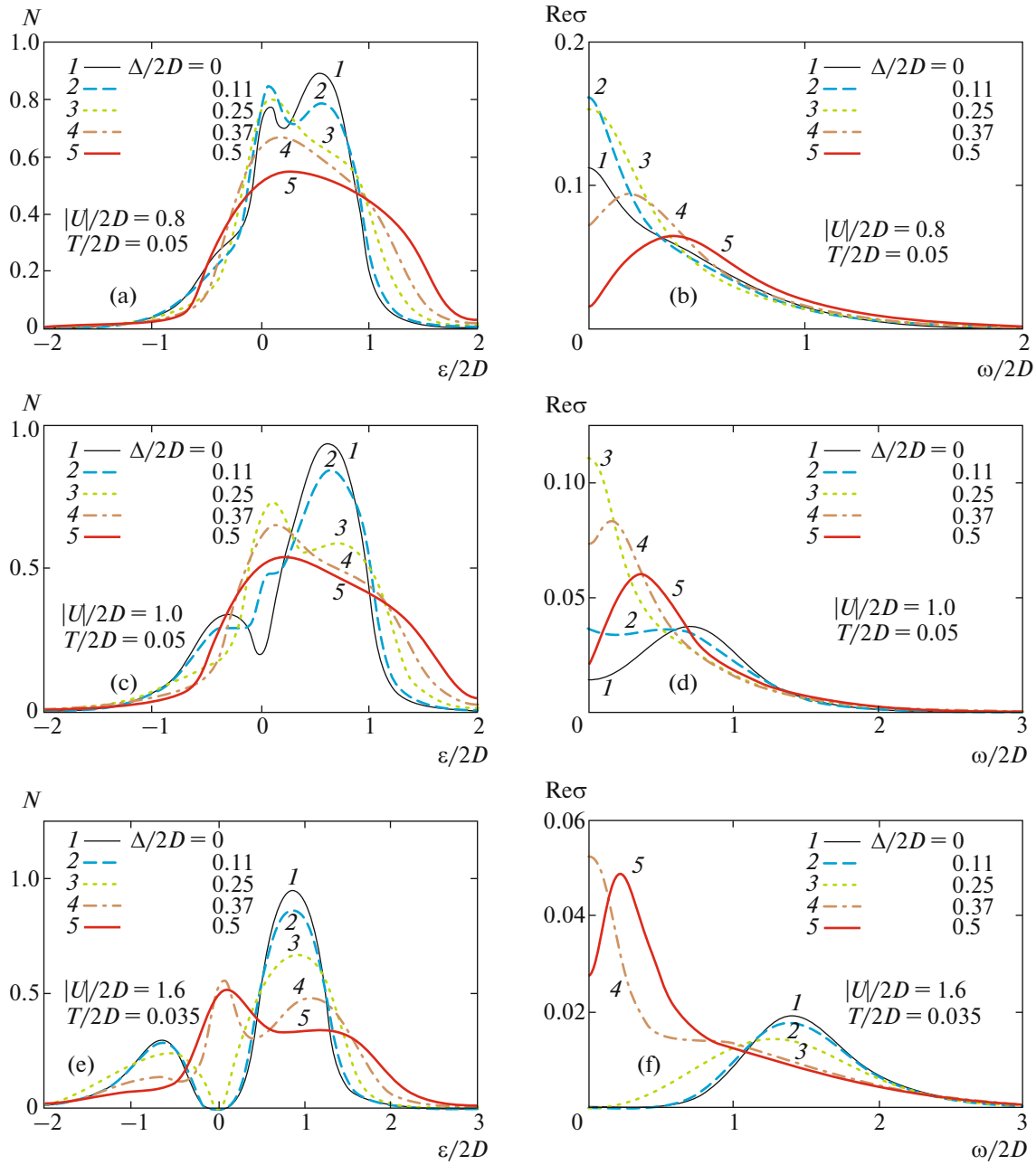

Fig. 8. (Color online) Evolution of the density of states (left panels) and optical conductivity (right panels) with disorder for different values of U: (a, b) $|U|/2D = 0.8$, (c, d) $|U|/2D = 1$, (e, f) $|U|/2D = 1.6$.

and lower Hubbard bands presented in Fig. 8a in the absence of disorder completely vanish at strong enough disorder. Evolution of the optical conductivity with the growth of disorder Δ, shown in Fig. 8b, generally agrees with the evolution of the density of states. Weak enough disorder (curve *2* in Fig. 8b) leads to some increase in the static conductivity, which is related with suppression of correlation effects at the Fermi level (curve *2* in Fig. 8a). Further increasing disorder leads to significant widening of the band and a decrease in the density of states (curve *3* in Figs. 8a, 8b), which leads to a decrease in static conductivity. Finally, the growth of disorder leads to Anderson localization, which occurs at $\Delta/2D = 0.37$ for $T = 0$ [18]. However, we here consider the case of a sufficiently high temperature $T/2D = 0.05$, such that the static conductivity (see curve *5* in Fig. 8b) always remains finite, although the localization behavior is also clearly seen and $\sigma(\omega) \sim \omega^2$. At larger values of the attractive interaction $|U|/2D = 1$, the evolution of the density of states and optical conductivity are largely similar (Figs. 8c, 8d). But in the absence of disorder,

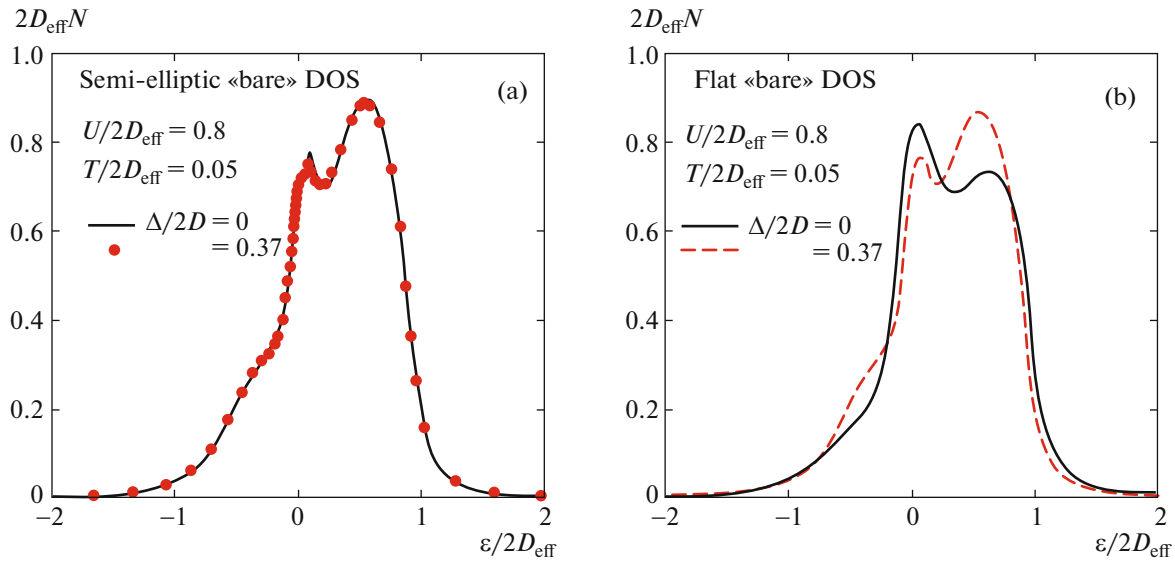

Fig. 9. (Color online) Universal dependence of the density of states on disorder in the attractive Hubbard model: (a) the model of a semi-elliptic "bare" density of states, (b) the model of a flat "bare" density of states.

we then observe a Cooper pairing pseudogap in the density of states, while disorder leads to its suppression, leading both to the growth of the density of states at the Fermi level and the related growth of static conductivity. Finally, at a still larger attraction $|U|/2D = 1.6$ (Figs. 8e, 8f) in the absence of disorder, there is a real Cooper pairing gap in the density of states. This gap is also evident in the optical conductivity. With an increase in disorder, the Cooper pairing gap in both the density of states and conductivity becomes narrower (curves *2*, *3*). A further increase in disorder leads to the complete suppression of this gap and restoration of a metallic state with a finite density of states at the Fermi level and finite static conductivity. This closure of the Cooper gap is obviously related to the effective growth of the conduction bandwidth $2D_{\rm eff}$, which leads to the decrease in the $|U|/2D_{\rm eff}$ ratio, which actually controls the formation of the Cooper gap. The situation here is similar to the closure of the Mott gap by disorder in the repulsive Hubbard model discussed above [8]. However, at large disorder (curve *5* in Fig. 8f), we clearly observe the localization behavior, such that the growth of disorder at $T = 0$ first leads to a metallic state (the closure of the Cooper pairing gap), while the further growth induces the Anderson metal-insulator transition. A similar picture is observed for large positive U at half-filling ($n = 1$) [18], where the growth of disorder leads to the Mott-insulator–correlated-metal–Anderson-insulator transition.

We now demonstrate the universality of the disorder dependence of the density of states as an example of the most important single-particle property. We concentrate on the most typical case of the evolution of the density of states shown in Fig. 8a. We can easily convince ourselves that this evolution is only due to the general widening of the band due to disorder (cf. (11)), because all the data for the density of states fit the same universal curve replotted in appropriate new variables, with all energies (and temperature) normalized by the effective bandwidth by replacing $D \to D_{\rm eff}$, as shown in Fig. 9a, in complete accordance with results obtained above in the repulsive Hubbard model for a semi-elliptic band.

In the case of the initial ("bare") conduction band with a flat density of states, there is no complete universality, as is seen from Fig. 9b for sufficiently low values of disorder. However, for large disorder, the dashed curve in Fig. 9b practically coincides with universal curve for the density of states shown in Fig. 9a. This reflects the simple fact that at enough disorder, the flat density of states is effectively transformed into a semi-elliptic one [24].

4.2. Generalized Anderson Theorem

The superconducting transition temperature T_c is not a single-particle characteristic of the system in general. The Cooper instability determining T_c is related to a divergence of the two-particle loop in the Cooper channel. In the weak-coupling limit, when superconductivity is due to the appearance of Cooper pairs at T_c, disorder only slightly influences superconductivity with *s*-wave pairing [41, 42]. This is the essence of the so-called Anderson theorem, and changes of T_c are only due to the relatively small changes of the density of states at the Fermi level induced by disorder.

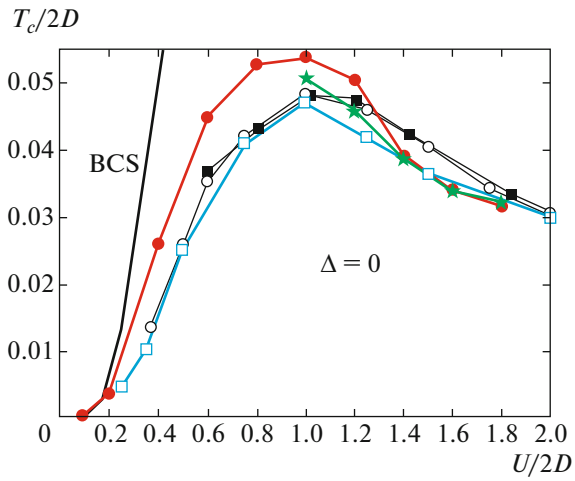

Fig. 10. (Color online) Dependence of the superconducting critical temperature on the attractive interaction strength. Black squares, white circles, and white squares respectively show the results in [37, 38, 40] for a quarter-filled band with $n = 0.5$. Stars represent the results obtained numerically from the instability criterion for the normal phase in [22]. Filled circles show T_c in the Nozieres–Schmitt-Rink approximations, combined with DMFT [22]. The continuous black curve represents the BCS theory result.

In the BCS–BEC crossover region and in the strong-coupling region, the Nozieres–Schmitt-Rink approach [11] assumes that corrections due to strong pairing attraction significantly change the chemical potential of the system, while possible corrections due to this interaction to the Cooper instability condition can be neglected, and we can hence always use the weak-coupling (ladder) approximation. Then the condition of a Cooper instability in the disordered Hubbard model takes the form

$$1 = -|U|\chi_0(q = 0, \omega_m = 0), \tag{19}$$

where

$$\chi_0(q = 0, \omega_m = 0) = -T\sum_n \sum_{\mathbf{pp}'} \Phi_{\mathbf{pp}'}(\varepsilon_n) \tag{20}$$

represents the two-particle loop (susceptibility) in the Cooper channel "dressed" only by disorder scattering, and $\Phi_{\mathbf{pp}'}(\varepsilon_n)$ is the averaged two-particle Green's function in the Cooper channel ($\omega_m = 2\pi mT$ and $\varepsilon_n = \pi T(2n + 1)$ are the usual boson and fermion Matsubara frequencies).

Using the exact Ward identity derived in [21],

$$G(\varepsilon_n, \mathbf{p}) - G(-\varepsilon_n, -\mathbf{p}) = -\sum_{\mathbf{p}'} \Phi_{\mathbf{pp}'}(\varepsilon_n) \tag{21}$$
$$(G_0^{-1}(\varepsilon_n, \mathbf{p}') - G_0^{-1}(-\varepsilon_n, \mathbf{p}')),$$

where $G(\varepsilon_n, \mathbf{p})$ is the impurity-averaged single-particle Green's function (not containing Hubbard interaction corrections!), we can show [24] that Cooper susceptibility (20) is given by

$$\chi_0(q = 0, \omega_m = 0)$$
$$= T\sum_n \frac{1}{2i\varepsilon_n}\left(\sum_{\mathbf{p}} G(\varepsilon_n, \mathbf{p}) - \sum_{\mathbf{p}} G(-\varepsilon_n, \mathbf{p})\right) \tag{22}$$
$$= T\sum_n \frac{1}{i\varepsilon_n}\sum_{\mathbf{p}} G(\varepsilon_n, \mathbf{p}).$$

After the standard summation over Matsubara frequencies [26], we obtain

$$\chi_0(q = 0, \omega_m = 0)$$
$$= \frac{1}{4\pi i}\int_{-\infty}^{\infty} \frac{d\varepsilon}{\varepsilon}\left(\sum_{\mathbf{p}} G^R(\varepsilon, \mathbf{p}) - \sum_{\mathbf{p}} G^A(\varepsilon, \mathbf{p})\right)\tanh\frac{\varepsilon}{2T} \tag{23}$$
$$= -\int_{-\infty}^{\infty} \frac{d\varepsilon}{2\varepsilon}\tilde{N}_0(\varepsilon)\tanh\frac{\varepsilon}{2T},$$

where $\tilde{N}_0(\varepsilon)$ is the density of states ($U = 0$) renormalized by disorder scattering. In Eq. (23), the energy ε origin is at the chemical potential. If the origin of energy is shifted to the middle of the conduction band, we have to replace $\varepsilon \to \varepsilon - \mu$, and the condition of Cooper instability (19) leads to the following equation for T_c:

$$1 = \frac{|U|}{2}\int_{-\infty}^{\infty} d\varepsilon\tilde{N}_0(\varepsilon)(\varepsilon - \mu)^{-1}\tanh\frac{\varepsilon - \mu}{2T_c}. \tag{24}$$

The chemical potential of the system at different values of U and Δ should now be determined from DMFT+Σ calculations, i.e., from the standard equation for the number of electrons (band-filling), determined by the Green's function given by Eq. (3), which allows finding T_c for a wide range of model parameters, including the BCS–BEC crossover and strong coupling regions, as well as for different levels of disorder. This is the gist of the Nozieres–Schmitt-Rink approximation: in the weak coupling region, the superconducting transition temperature is controlled by the equation for Cooper instability (24), while in the strong-coupling limit, it is determined by the temperature of Bose–Einstein condensation, which is controlled by the chemical potential. Then the joint solution of Eq. (24) and the equation for the chemical potential guarantees the correct interpolation for T_c through the BCS–BEC crossover region. In the absence of disorder, this combination of the Nozieres–Schmitt-Rink approximation with DMFT produces the results for the critical temperature, which, as shown in Fig. 10, are almost quantitatively close to the exact results obtained by direct numerical DMFT calculations [22, 37, 38, 40], but demand much less numerical efforts.

Equation (24) demonstrates that the Cooper instability depends on disorder only through the disorder

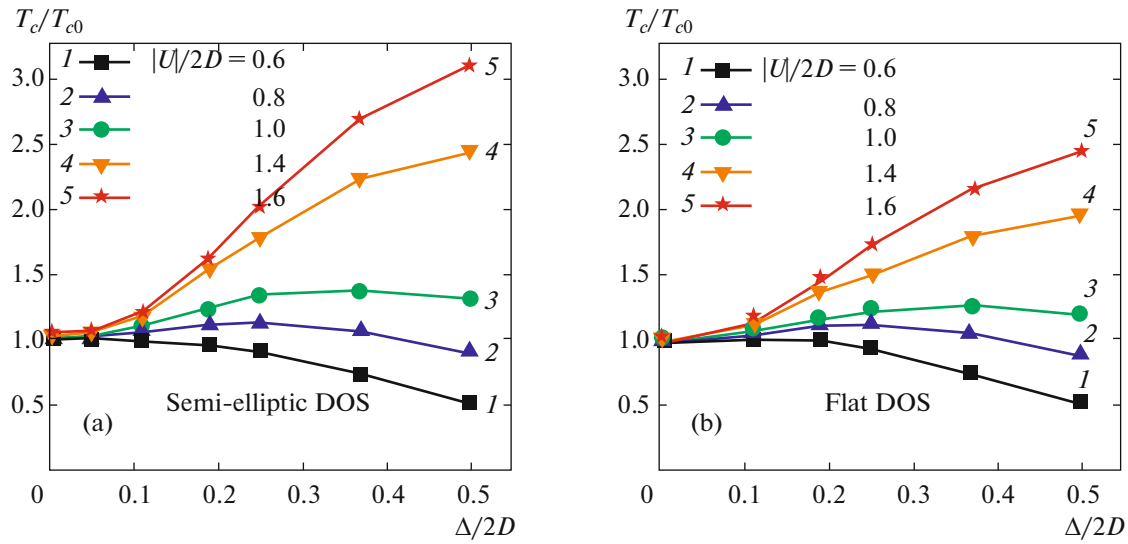

Fig. 11. (Color online) Dependence of superconducting transition temperature on disorder for different values of Hubbard attraction U: (a) semi-elliptic band, (b) flat band.

dependence of the density of states $\tilde{N}_0(\varepsilon)$, which is the main statement of the Anderson theorem. Within the Nozieres–Schmitt-Rink approach, Eq. (24) is also preserved in the strong-coupling region, where the critical temperature is determined by the BEC condition for compact Cooper pairs. However, the chemical potential μ entering Eq. (24) may significantly depend on disorder. In the DMFT+Σ approximation, this dependence of the chemical potential (as well as any other single-particle characteristics) in the model with a semi-elliptic density of states is only due to the disorder widening of the conduction band. In this sense, both in the BCS–BEC crossover region and in the strong-coupling limit, a kind of generalized Anderson theorem actually holds and Eq. (24) leads to a universal dependence of T_c on disorder, due to the change $D \to D_{\text{eff}}$. Such a universality is fully confirmed by direct numerical calculations of T_c in this model, performed in [23].

In Fig. 11, we present the dependence of T_c (normalized by the critical temperature in the absence of disorder $T_{c0} = T_c(\Delta = 0)$) on disorder for different values of the pairing interaction U for both models of the initial semi-elliptic density of states (Fig. 11a) and for a flat density of states (Fig. 11b). Qualitatively, the evolution of T_c with disorder is the same for both models. In the weak-coupling limit ($U/2D \ll 1$), disorder slightly suppresses T_c (curves *1*). At intermediate couplings ($U/2D \sim 1$), weak disorder increases T_c, while a further increase in disorder suppresses the critical temperature (curves *3*). In the strong-coupling region ($U/2D \gg 1$), the growth of disorder leads to a significant increase in the critical temperature (curves *4*, *5*). But this rather complicated dependence of T_c on disorder is actually completely determined simply by disorder widening of the initial ($U = 0$) conduction band, demonstrating the validity of the generalized Anderson theorem for all values of U. In Fig. 12, the curve with octagons shows the dependence of the critical temperature $T_c/2D$ on the coupling strength $U/2D$ in the absence of disorder ($\Delta = 0$) for both models of the initial conduction bands (semi-elliptic in Fig. 12a and flat in Fig. 12b). In both models, the superconducting transition temperature is well described by the BCS model in the weak-coupling region (in Fig. 12a, the dashed curve represents a solution of the BCS model, with T_c determined by Eq. (24), with the chemical potential independent of U and determined by the quarter-filling of the "bare" band), while in the strong-coupling region, the critical temperature is determined by Bose–Einstein condensation of Cooper pairs and decreases as t^2/U with an increase in U (inversely proportional to the effective mass of the pair), passing through a maximum at $U/2D_{\text{eff}} \sim 1$. The other symbols in Fig. 12a show the results for T_c obtained by a combination of the DMFT+Σ and Nozieres–Schmitt-Rink approximations for a semi-elliptic band. We can see that all data (expressed in normalized units of $U/2D_{\text{eff}}$ and $T_c/2D_{\text{eff}}$) ideally fit the universal curve obtained in the absence of disorder. For a flat band, the results of our calculations are shown in Fig. 12b and we do not observe the complete universality: data points corresponding to different degrees of disorder slightly deviate from the curve obtained in the absence of disorder. However, with an increase in disorder, the flat density of states gradually transforms to a semi-elliptic one and our data points move toward the universal curve obtained in the semi-elliptic case and shown by the dashed curve in

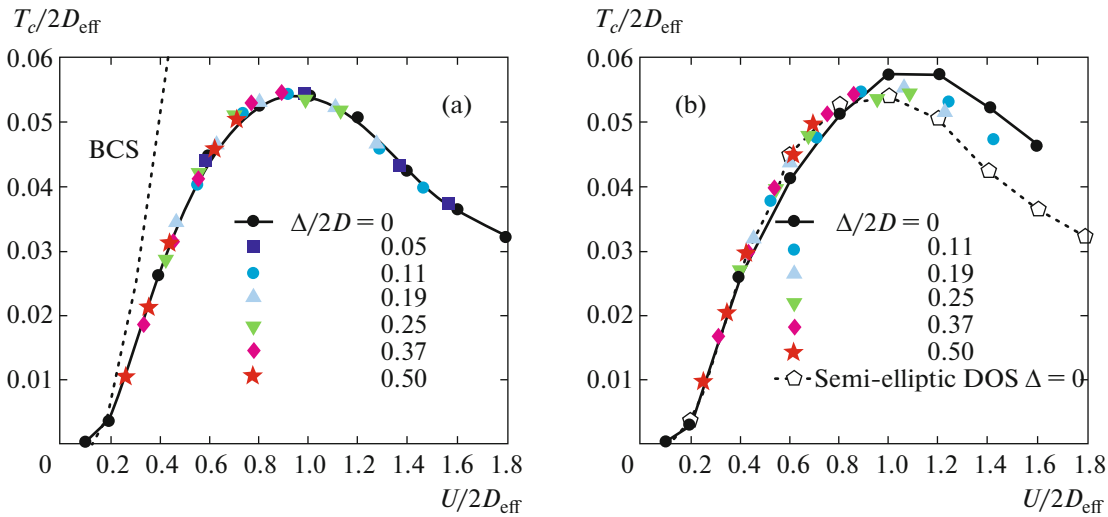

Fig. 12. (Color online) Universal dependence of the superconducting critical temperature on the Hubbard attraction U for different disorder levels: (a) semi-elliptic band. The dashed curve represents the BCS dependence in the absence of disorder, (b) flat band. The dashed line represents a similar dependence for a semi-elliptic band at $\Delta = 0$.

Fig. 12b, confirming the validity of the generalized Anderson theorem also in this case.

4.3. Ginzburg–Landau Coefficients

The universal dependence on disorder is also observed for the Ginzburg–Landau expansion coefficients A (the homogeneous quadratic term of the expansion) and B (the fourth-order term), related to Cooper-channel vertices with the zero sum of incoming (outgoing) momenta, $q = 0$. The coefficient A is given by [16]

$$A(T) = \chi_0(q = 0, T) - \chi_0(q = 0, T_c), \tag{25}$$

where χ_0 ($q = 0$, T) is Cooper susceptibility (20), and subtraction of χ_0 ($q = 0$, T_c) guarantees the zero value of A ($T = T_c$). Using (19) to determine χ_0 ($q = 0$, T_c) and (23) for χ_0 ($q = 0$, T), we obtain

$$A(T) = \frac{1}{|U|} - \int_{-\infty}^{\infty} d\varepsilon \tilde{N}_0(\varepsilon)(2(\varepsilon - \mu))^{-1} \tanh\frac{\varepsilon - \mu}{2T}, \tag{26}$$

whence the coefficient $A(T)$ vanishes as $T \to T_c$, and can be written as

$$A(T) = a(T - T_c). \tag{27}$$

For a "bare" band with a semi-elliptic density of states, the dependence of a on disorder is related only to the general widening of the band by disorder, i.e., is completely described by the replacement $D \to D_{\text{eff}}$. Thus, in the presence of disorder, we obtain the universal dependence of a on U (normalized by D_{eff}), shown in Fig. 13a.

The Ginzburg–Landau coefficient B is determined by the "loop" diagram with four Cooper vertices [26]. After a rather complicated analysis, to be presented elsewhere, based on some generalizations of Ward identity (21), it can be shown exactly that B is given by

$$B = \int_{-\infty}^{\infty} \frac{d\varepsilon}{4(\varepsilon - \mu)^3} \left(\tanh\frac{\varepsilon - \mu}{2T} - \frac{(\varepsilon - \mu)/2T}{\cosh^2(\varepsilon - \mu)/2T}\right)\tilde{N}_0(\varepsilon). \tag{28}$$

Hence, the dependence of the coefficient B on disorder, similarly to A, is determined only by the density of states $\tilde{N}_0(\varepsilon)$ renormalized (widened) by disorder and the chemical potential μ. Then, in the case of a semi-elliptic density of states, the dependence of B on disorder is reduced to the simple replacement $D \to D_{\text{eff}}$, and the presence of disorder we again obtain the universal dependence of B on U, shown in Fig. 13b.

We note that Eqs. (26) and (28) for the coefficients A and B were obtained using the exact Ward identities and also remain valid in the limit of strong disorder (the Anderson localized phase), where both A and B depend on disorder also only via the effective bandwidth D_{eff}.

This universal dependence on disorder (due to only the replacement $D \to D_{\text{eff}}$) is also reflected in the specific heat discontinuity at the transition temperature, which is determined by the coefficients a and B:

$$C_s(T_c) - C_n(T_c) = T_c \frac{a^2}{B}. \tag{29}$$

To determine the coefficient C in the gradient term of the Ginzburg–Landau expansion, we need the knowledge of the nontrivial of q-dependence of the Cooper vertex [26], which is essentially changed by disorder scattering. In particular, the behavior of the

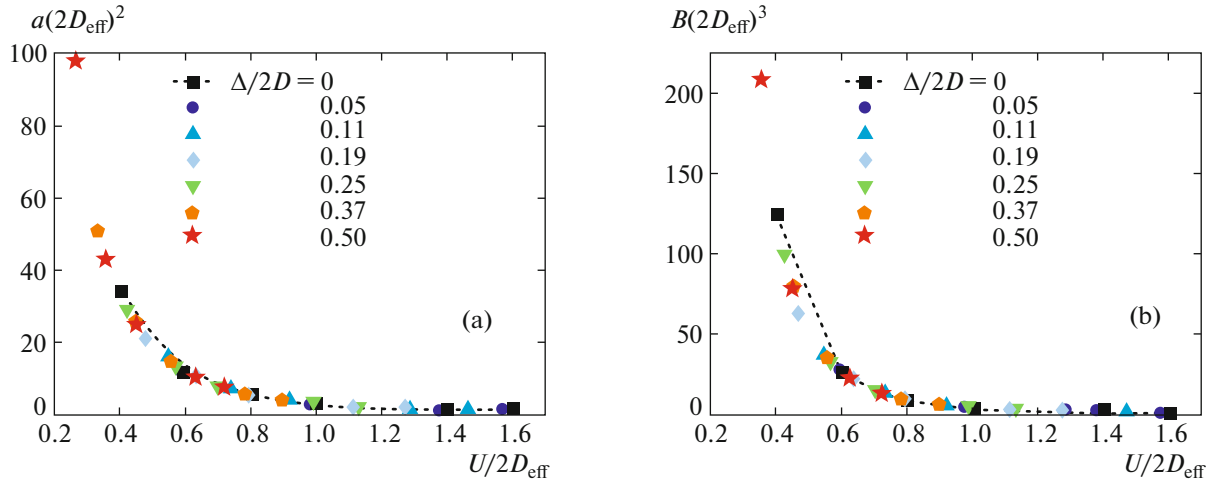

Fig. 13. (Color online) Universal dependence of the Ginzburg–Landau coefficients (a) a and (b) B on the Hubbard attraction for different disorder levels. The dotted line with black squares shows the case $\Delta = 0$.

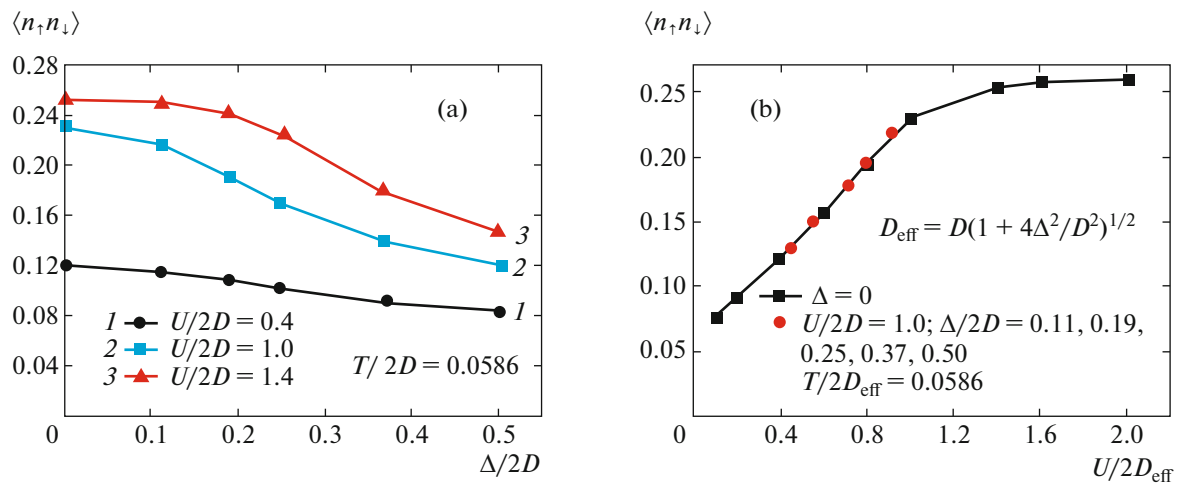

Fig. 14. (Color online) (a) Dependence of the number of local pairs on disorder for different values of the Hubbard attraction and (b) the universal dependence on disorder expressed via normalized variables at the fixed value $U/2D = 1$.

coefficient C qualitatively changes at the Anderson localization transition [41]. Thus, the coefficient C is basically determined by two-particle characteristics of the system and does not demonstrate a universal dependence on disorder due to only changes of the effective bandwidth.

4.4. Number of Local Pairs

Disorder in the attractive Hubbard model also leads to the suppression of the number of local pairs (doubly occupied sites). The average number of local pairs is determined by the local (single site) pair correlation function $\langle n_\uparrow n_\downarrow \rangle$, which in the absence of disorder increases with the increase in the Hubbard attraction U from $\langle n_\uparrow n_\downarrow \rangle = \langle n_\uparrow \rangle \langle n_\uparrow \rangle = n^2/4$ for $U/2D_{\rm eff} \ll 1$ to $\langle n_\uparrow n_\downarrow \rangle = n/2$ for $U/2D_{\rm eff} \gg 1$, when all electrons become paired. In our calculations, $n = 0.5$ (a quarter-filled band), whence $n/2 = 0.25$ and $n^2/4 = 0.0625$. The increase in $D_{\rm eff}$ with disorder leads to an effective suppression of the parameter $U/2D_{\rm eff}$ and the corresponding suppression of the number of doubly occupied sites. In Fig. 14a, we show the disorder dependence of the number of doubly occupied sites for three different values of the Hubbard attraction. In all cases, the growth of disorder suppresses the number of doubly occupied sites (local pairs). Similarly to T_c, the change of the number of local pairs with disorder can be attributed only to the change of the effective bandwidth (11) with the increase in disorder. In Fig. 14b, the curve with black squares shows the dependence of

the number of doubly occupied sites on attractive interaction in the absence of disorder at the temperature $T/2D = 0.0586$. This curve is actually universal: the dependence of the number of local pairs $\langle n_\uparrow n_\downarrow \rangle$ on the scaled parameter $U/2D_{\text{eff}}$ with an appropriately scaled temperature $T/2D_{\text{eff}} = 0.0586$ in the presence of disorder is given by the same curve that is shown by circles representing data obtained for five different disorder levels shown in Fig. 14b for $U/2D = 1$.

5. CONCLUSIONS

In this paper, in the framework of the DMFT+Σ generalization of dynamic mean field theory [17], we have studied and compared disorder effects in both repulsive and attractive Hubbard models. We examined the problems of both Mott–Hubbard and Anderson-metal-insulator transitions in repulsive case, and the BCS–BEC crossover region of the attractive Hubbard model. We also performed extensive calculations of the densities of states and dynamic (optical) conductivity for a wide range of interactions U and at different disorder levels Δ, demonstrating similarities and dissimilarities between repulsive and attractive cases.

We have shown analytically for case conduction band with a semi-elliptic density of states (which is a good approximation for the three-dimensional case) that in the DMFT+Σ approximation, disorder influences all single-particle properties (e.g., density of states) in a universal way: all changes of these properties are due to only the disorder widening of the conduction band. In the model of a conduction band with a flat density of states (which is more appropriate for two-dimensional systems), there is no such a universality in the region of weak disorder. But the main effects are again due to the general widening of the band and the complete universality is restored for high enough disorder, when the density of states effectively becomes semi-elliptic. Similar universal dependences on disorder are also reflected in the phase diagram of the repulsive Hubbard model and in the superconducting critical temperature of the attractive Hubbard model, where the combination of DMFT+Σ and Nozieres–Schmitt-Rink approximations demonstrates the validity of the generalized Anderson theorem in both the BCS–BEC crossover and strong-coupling regions.

Naturally, no universal dependences on disorder were obtained for the two-particle properties like optical conductivity, where vertex corrections due to disorder scattering become very important, leading to new physics, like that of Anderson transition.

Overall, using the DMFT+Σ approximation to analyze the disorder effects in the Hubbard model was shown to produce reasonable results for the phase diagram in the repulsive case, as compared to exact numerical simulations of disorder in DMFT, the behavior of the density of states and optical conductivity in both repulsive and attractive cases. However, the role of approximations made in DMFT+Σ, such as the neglect of the interference of disorder scattering and correlation effects, deserves further studies.

It is a pleasure and honor to dedicate this short review to Professor Leonid Keldysh' 85th birthday. This work is supported by the RSF grant no. 14-12-00502.

REFERENCES

1. N. F. Mott, *Metal–Insulator Transitions,* 2nd ed. (Taylor and Francis, London, 1990).
2. J. Hubbard, Proc. R. Soc. London, Ser. A **276**, 238 (1963); Proc. R. Soc. London, Ser. A **277**, 237 (1964); Proc. R. Soc. London, Ser. A **281**, 401 (1964); Proc. R. Soc. London, Ser. A **285**, 542 (1965); Proc. R. Soc. London, Ser. A **296**, 829 (1967); Proc. R. Soc. London, Ser. A **296**, 100 (1967).
3. W. Metzner and D. Vollhardt, Phys. Rev. Lett. **62**, 324 (1989).
4. D. Vollhardt, in *Correlated Electron Systems,* Ed. by V. J. Emery (World Scientific, Singapore, 1993), p. 57.
5. Th. Pruschke, M. Jarrell, and J. K. Freericks, Adv. Phys. **44**, 210 (1995).
6. A. Georges, G. Kotliar, W. Krauth, and M. J. Rozenberg, Rev. Mod. Phys. **68**, 13 (1996).
7. D. Vollhardt, AIP Conf. Proc. 1297, 339 (2010), arXiv:1004.5069.
8. G. Kotliar and D. Vollhardt, Phys. Today **57**, 53 (2004).
9. D. M. Eagles, Phys. Rev. **186**, 456 (1969).
10. A. J. Leggett, in *Modern Trends in the Theory of Condensed Matter,* Ed. by A. Pekalski and J. Przystawa (Springer, Berlin, 1980).
11. P. Nozieres and S. Schmitt-Rink, J. Low Temp. Phys. **59**, 195 (1985).
12. I. Bloch, J. Dalibard, and W. Zwerger, Rev. Mod. Phys. **80**, 885 (2008).
13. L. P. Pitaevskii, Phys. Usp. **44**, 333 (2006).
14. E. Z. Kuchinskii, I. A. Nekrasov, and M. V. Sadovskii, JETP Lett. **82**, 198 (2005) .
15. M. V. Sadovskii, I. A. Nekrasov, E. Z. Kuchinskii, Th. Prushke, and V. I. Anisimov, Phys. Rev. B **72**, 155105 (2005).
16. E. Z. Kuchinskii, I. A. Nekrasov, and M. V. Sadovskii, Low Temp. Phys. **32**, 398 (2006).
17. E. Z. Kuchinskii, I. A. Nekrasov, and M. V. Sadovskii, Phys. Usp. **55**, 325 (2012).
18. E. Z. Kuchinskii, I. A. Nekrasov, and M. V. Sadovskii, J. Exp. Theor. Phys. **106**, 581 (2008).
19. E. Z. Kuchinskii, N. A. Kuleeva, I. A. Nekrasov, and M. V. Sadovskii, J. Exp. Theor. Phys. **110**, 325 (2010).
20. E. Z. Kuchinskii, I. A. Nekrasov, and M. V. Sadovskii, Phys. Rev. B **80**, 115124 (2009).
21. E. Z. Kuchinskii, I. A. Nekrasov, and M. V. Sadovskii, Phys. Rev. B **75**, 115102 (2007).
22. N. A. Kuleeva, E. Z. Kuchinskii, and M. V. Sadovskii, J. Exp. Theor. Phys. **119**, 264 (2014).

23. E. Z. Kuchinskii, N. A. Kuleeva, and M. V. Sadovskii, JETP Lett. **100**, 192 (2014).
24. E. Z. Kuchinskii, N. A. Kuleeva, and M. V. Sadovskii, J. Exp. Theor. Phys. **120**, 1055 (2015); arXiv:1411.1547.
25. P. W. Anderson, Phys. Rev. **109**, 1492 (1958).
26. M. V. Sadovskii, *Diagrammatics* (World Scientific, Singapore, 2006).
27. R. Bulla, T. A. Costi, and T. Pruschke, Rev. Mod. Phys. **60**, 395 (2008).
28. D. Vollhardt and P. Wölfle, Phys. Rev. B **22**, 4666 (1980); Phys. Rev. Lett. **48**, 699 (1982); Springer Ser. Solid State Sci. **39**, 26 (1982).
29. M. V. Sadovskii, *The Theory of Electron Localizationin Disordered Systems*, Soviet Scientific Reviews—Physics Reviews, Vol. 7, Ed. by I. M. Khalatnikov (Harwood Academic, New York, 1986), p. 1; A. V. Myasnikov and M. V. Sadovskii, Sov. Phys. Solid State **24**, 2033 (1982); E. A. Kotov and M. V. Sadovskii, Zs. Phys. B **51**, 17 (1983).
30. P. Wölfle and D. Vollhardt, in *Electronic Phase Transitions,* Ed. by W. Hanke and Yu. V. Kopaev (North—Holland, Amsterdam, 1992), p. 1.
31. K. Byczuk, W. Hofstetter, and D. Vollhardt, Phys. Rev. Lett. **94**, 056404 (2005).
32. R. Bulla, Phys. Rev. Lett. 83, 136 (1999); R. Bulla, T. A. Costi, and D. Vollhardt, Phys. Rev. B **64**, 045103 (2001).
33. N. Blümer, PhD Thesis (München, 2002).
34. P. A. Lee and T. V. Ramakrishnan, Rev. Mod. Phys. **57**, 287 (1985); D. Belitz and T. R. Kirkpatrick, Rev. Mod. Phys. **66**, 261 (1994).
35. A. M. Finkelshtein, Sov. Phys. JETP **57**, 97 (1983); C. Castellani et al., Phys. Rev. B **30**, 527 (1984).
36. M. A. Erkabaev and M. V. Sadovskii, J. Moscow Phys. Soc. **2**, 233 (1992).
37. M. Keller, W. Metzner, and U. Schollwock, Phys. Rev. Lett. **86**, 4612 (2001).
38. A. Toschi, P. Barone, M. Capone, and C. Castellani, New J. Phys. **7**, 7 (2005).
39. J. Bauer, A. C. Hewson, and N. Dupis, Phys. Rev. B **79**, 214518 (2009).
40. A. Koga and P. Werner, Phys. Rev. A **84**, 023638 (2011).
41. M. V. Sadovskii, *Superconductivity and Localization* (World Scientific, Singapore, 2000).
42. P. G. de Gennes, *Superconductivity of Metals and Alloys* (W. A. Benjamin, New York, 1966).

 ©2016 Uspekhi Fizicheskikh Nauk, Russian Academy of Sciences

REVIEWS OF TOPICAL PROBLEMS PACS numbers: **74.20.–z**, 74.20.Fg, 74.20.Mn, 74.20.Rp, 74.25.Jb, **74.62.–c**, **74.70.–b**

100th ANNIVERSARY OF THE BIRTH OF V L GINZBURG

High-temperature superconductivity in FeSe monolayers

M V Sadovskii

DOI: https://doi.org/10.3367/UFNe.2016.06.037825

Contents

1. Introduction **947**
2. Main systems and experiments **948**
2.1 Intercalated FeSe-based systems; 2.2 Superconductivity in the FeSe monolayer on $SrTiO_3$
3. Electronic structure of iron–selenium systems **950**
3.1 $A_xFe_{2-y}Se_2$ system; 3.2 $[Li_{1-x}Fe_xOH]FeSe$ system; 3.3 FeSe monolayer
4. Possible mechanisms of T_c enhancement in iron–selenium monolayers **955**
4.1 Correlation between T_c and the density of states; 4.2 Multiple bands picture of superconductivity; 4.3 Models of T_c enhancement in FeSe monolayer due to interaction with elementary excitations in the substrate; 4.4 Excitonic mechanism by Allender, Bray, and Bardeen; 4.5 Interaction with optical phonons in STO; 4.6 Cooper pairing in the model with a dominant forward scattering; 4.7 Nonadiabatic superconductivity and other problems
5. Conclusions **965**
References **966**

Abstract. This paper reviews the basic experimental and theoretical aspects of high-temperature superconductivity in intercalated FeSe compounds and FeSe monolayer films on $SrTiO_3$ and similar substrates. The paper examines in detail the electronic structure of these systems, how it is calculated, and how the calculated results compare with ARPES experiments. It is emphasized that the reviewed systems have qualitatively different electronic spectra from the typical pattern of well-studied FeAs superconductors and explores the implications of these differences for a theoretical description of how these spectra form. Possible mechanisms of Cooper pairing in FeSe monolayers are discussed and the associated problems are examined. Because FeSe monolayer films on $SrTiO_3$ are typical Ginzburg 'sandwiches', the possibility of increasing their T_c via 'excitonic' superconductivity mechanisms is considered. It is shown that, while the classical version of this mechanism (as proposed for such systems by Allender, Bray, and Bardeen) fails to explain the observed values of T_c, the situation changes when optical phonons in $SrTiO_3$ (with energy of about 100 meV) are considered to be 'excitons'. Both the simplest possible model of T_c enhancement due to interaction with such phonons and more complex ones with dominant 'forward' scattering that explain successfully the increase in T_c compared to bulk FeSe and intercalated FeSe systems are verified. Problems related to the antiadiabatic nature of this superconductivity mechanism are also discussed.

Keywords: high-temperature superconductivity, iron chalcogenides, electronic spectrum, excitonic mechanism, electron–phonon mechanism

M V Sadovskii Institute for Electrophysics,
Ural Branch of the Russian Academy of Sciences,
ul. Amundsena 106, 620016 Ekaterinburg, Russian Federation
E-mail: sadovski@iep.uran.ru
M N Mikheev Institute for Metal Physics,
Ural Branch of the Russian Academy of Sciences,
ul. S. Kovalevskoi 18, 620290 Ekaterinburg, Russian Federation

Received 14 April 2016, revised 8 June 2016
Uspekhi Fizicheskikh Nauk **186** (10) 1035 – 1057 (2016)
DOI: 10.3367/UFNr.2016.06.037825
Translated by M V Sadovskii; edited by A Radzig

1. Introduction

The discovery of a new class of superconductors based upon iron pnictides has opened new perspectives in studies of high-temperature superconductivity. While possessing main superconducting characteristics somehow inferior to those of copper oxides (cuprates), these systems have attracted much attention from researchers, as the nature of superconductivity and other physical properties here are in many respects different from those of cuprates, while preserving many common features, which leads to hopes of a deeper understanding of the problem of high-temperature superconductivity as a whole. And this problem, which was put onto the agenda mainly due to the enthusiasm of V L Ginzburg [1–4], still remains among the central issues of the modern physics of condensed matter.

To date, the properties of iron pnictide superconductors have been rather well studied experimentally; there is also an almost overwhelmingly accepted theoretical conception of superconductivity in these systems, which is based on the idea of the leading role of pairing interactions due to exchange of (antiferro)magnetic fluctuations, which in most cases lead to $s^{\pm}$-pairing on different sheets of the Fermi surface, which appear in these *multiple band* systems. There are a number of review papers with detailed presentations of the modern experimental situation and basic theoretical concepts used in describing these systems [5–10].

The discovery of superconductivity in iron pnictides was soon followed by the discovery of similar phenomenon in iron *chalcogenide* FeSe, which even if attracted wide attention to itself it happened probably only due to the unusual simplicity of this compound, inasmuch as its superconducting characteristics (under normal conditions) were rather modest ($T_c \sim 8$ K), and its electronic structure was quite similar to that of iron pnictides. Nonetheless, this system was also thoroughly studied (cf. review [11]).

The situation with iron chalcogenides underwent a major change with the appearance of *intercalated* FeSe-based systems, where values of T_c ranging $\sim 30-40$ K were obtained and which attracted much attention because of their unusual electronic structures [12, 13]. At present, a number of such compounds are known with properties significantly different from those in traditional iron pnictides and which obviously require the elaboration of a new theoretical approach to the mechanisms of superconductivity, as the traditional picture of $s^{\pm}$-pairing for pnictides apparently does not work here.

All these problems became more acute after the experimental observation of superconductivity with $T_c \sim 80-100$ K in monolayers of FeSe (epitaxial films) grown on an $SrTiO_3$ substrate (and a number of similar compounds). At present, we can speak of a 'new frontier' in studies of high-temperature superconductivity [14].

This short review is devoted to describing the main experimental results on superconductivity in intercalated FeSe monolayers and single-layer FeSe films on substrates like $SrTiO_3$, and to discussing a number of related theoretical problems, including possible current-carrier pairing mechanisms leading to a significant enhancement of T_c. It should be said that we remain here with more questions than answers, but this is what attracts most researchers to studies of the systems discussed in this review. This field is developing very fast, and we cannot engage in a comprehensive discussion of all the available literature. Our presentation will intentionally focus on a rather elementary (general physics) level, with an intention to make it understandable to nonspecialists. The references to many important studies can be found in papers quoted below; many papers are not mentioned simply because of the limited space for the review. However, the author hopes that this review will be of interest to a wide community of *Physics Uspekhi* readers as a kind of introduction to this new field of research, especially in connection with centenary of the great physicist V L Ginzburg, whose ideas and views on the problem of high-temperature superconductivity had so much influence on everybody who is involved in this field.

2. Main systems and experiments

2.1 Intercalated FeSe-based systems

In Fig. 1a, we demonstrate schematically the simplest crystal structures of iron-based superconductors [5–11]. The common feature here is the presence of an FeAs or FeSe plane (layer), where the Fe ions form a simple square lattice, while ions of pnictogens (Pn–As) or chalcogens (Ch–Se) are placed in the centers of these squares, above and below the Fe plane in chess-board order. In Fig. 1b, the structure of this layer is shown in more detail. Actually, the electronic states of Fe ions in the FePn(Ch) plane play a decisive role in the formation of the electronic properties of these systems, including superconductivity. In this sense, these layers are quite similar to CuO_2 planes in cuprates (copper oxides), and these systems can be considered, in the first approximation, to be quasi-two-dimensional, though the anisotropy in most of them may be not so strong. Below, we shall frequently limit ourselves to such an oversimplified picture and speak about the physics of FeSe planes (monolayers).

In Fig. 1b, arrows show the direction of the spins on Fe in the antiferromagnetic structure typically realized in the stoichiometric state of FeAs-based systems [5–10], which are antiferromagnetic metals (in their ground state). Antiferromagnetic ordering is destroyed under electron or hole doping, when the superconducting phase just appears. In this sense, the phase diagrams of the systems under consideration are quite similar to those of cuprates [5–10]. These phase diagrams at present are rather well studied. In FeSe-based systems, which will be analyzed below, the character of magnetic ordering is not known so well. Because of this, as well as due to the lack of space, we shall not discuss the magnetic properties of FeSe systems much.

Notice that all the FeAs-based structures displayed in Fig. 1a constitute simple ionic–covalent crystals. The chemical formula, say, for a typical 122-system can be written out, for example, as $Ba^{+2}(Fe^{+2})_2(As^{-3})_2$. The charged FeAs layers are held together by Coulomb forces acting from surrounding ions. In bulk FeSe, the electroneutral FeSe layers are held by much weaker van der Waals interactions. This makes such a system convenient for intercalation by different atoms or molecules, which can easily enough penetrate between the FeSe layers. The chemistry of intercalation in iron selenide superconductors is discussed in detail in recent review [15].

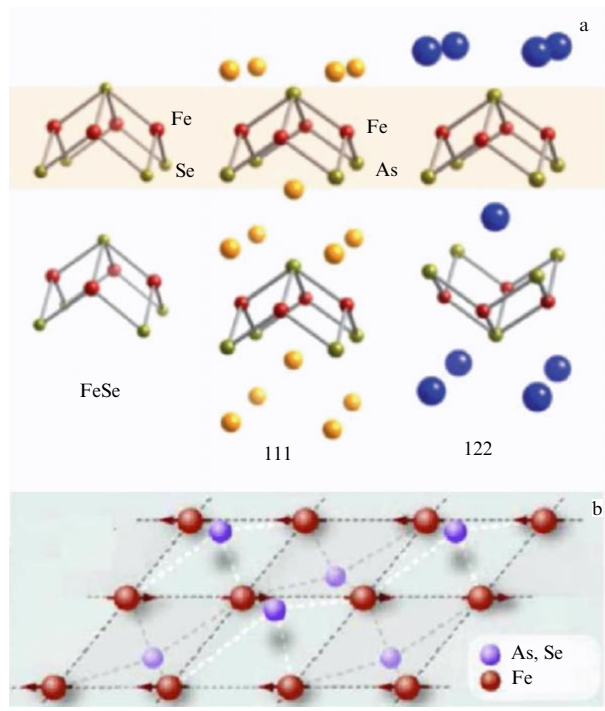

Figure 1. (Color online.) (a) Crystal structure of simplest iron-based superconductors. (b) Structure of highly conducting plane (layer) of iron ions and pnictogens (chalcogens). Arrows show directions of spins for typical ordering in the antiferromagnetic phase.

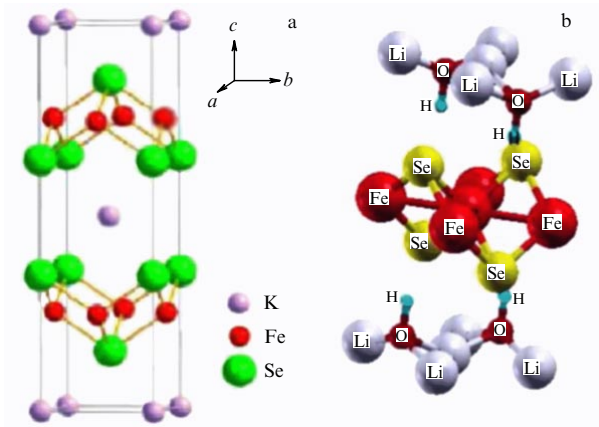

Figure 2. (Color online.) (a) Ideal ($x = 1$) crystal structure (122-type) of $K_xFe_2Se_2$ compound. (b) Ideal ($x = 0$) crystal structure of $[Li_{1-x}Fe_xOH]FeSe$ compound.

As we already noted, superconductivity in bulk FeSe, discovered immediately after high-temperature superconductivity was observed in iron pnictides, has been studied more or less in detail [11], but initially had not attracted much interest because of its similarity to superconductivity in iron pnictides and fairly low superconducting characteristics. This situation changed drastically after the discovery of high-temperature superconductivity in intercalated FeSe-based compounds and especially after the achievement of record-breaking values of T_c in single-layer FeSe films on $SrTiO_3$.

The first systems of this kind were $A_xFe_{2-y}Se_2$ (A = K, Rb, Cs) compounds, with T_c values of ~ 30 K [16, 17]. It is commonly assumed that superconductivity here is realized in a 122-like structure, shown in Fig. 2a, while real samples, studied up to now, have always been multiphased, consisting of a mesoscopic mixture of superconducting and insulating (antiferromagnetic) structures like $K_2Fe_4Se_5$, which naturally complicates the general picture. A significant further increase in T_c to values on the order of 45 K was achieved by intercalating the FeSe layers by large enough molecules in compounds like $Li_x(C_2H_8N_2)Fe_{2-y}Se_2$ [18] and $Li_x(NH_2)_y(NH_3)_{1-y}Fe_2Se_2$ [19]. The increase in T_c in these systems can be supposedly attributed to the rise of spacing between FeSe layers from 5.5 Å in bulk FeSe to ~ 7 Å in $A_xFe_{2-y}Se_2$, and to 8–11 Å in systems intercalated by large molecules, i.e., with the growth of their two-dimensional nature.

Recently, active studies have begun on the $[Li_{1-x}Fe_xOH]FeSe$ system, where T_c values of ~ 43 K were reached [20, 21] and it was possible to prepare rather good single-phase samples and single crystals. The crystal structure of this system is depicted in Fig. 2b.

An interesting discussion has developed on the nature of possible magnetic ordering on Fe ions replacing Li in intercalating LiOH layers. In Ref. [20], it was claimed that this ordering corresponds to a canted antiferromagnet. However, magnetic measurements of Ref. [21] has led to an unexpected conclusion about the *ferromagnetic* character of this ordering with the Curie temperature $T_C \sim 10$ K, i.e., much lower than the superconducting transition temperature. This conclusion was indirectly confirmed in Ref. [22] by the observation of neutron scattering on the lattice of Abrikosov vortices, supposedly induced in FeSe layers by ferromagnetic ordering of Fe spins in $Li_{1-x}Fe_xOH$ layers. At the same time, it was claimed in Ref. [23] that Mössbauer measurements on this system indicate the absence of any kind of magnetic ordering on Fe ions.

2.2 Superconductivity in the FeSe monolayer on $SrTiO_3$

A major breakthrough in studies of superconductivity in FeSe systems, as already noted above, is connected with the observation of record-breaking values of T_c in epitaxial films of the FeSe monolayer on an $SrTiO_3$ (STO) substrate [24]. These films were grown in Ref. [24] and, in most of the papers to follow, on the 001 plane of STO. The structure of these films is demonstrated in Fig. 3, where we can see, in particular, that the FeSe layer is adjacent to the TiO_2 layer on the STO surface. Notice that the lattice constant in the FeSe layer of bulk samples is 3.77 Å, while in STO it is significantly larger, being equal to 3.905 Å, so that the single-layer FeSe films are noticeably stretched, as compared to bulk FeSe, and are in a stressed state which disappears fast with the addition of the next layers. Tunneling measurements of Ref. [24] have demonstrated record values of the energy gap, while in resistance measurements the temperature of the onset superconducting transition substantially exceeded 50 K.

It should be stressed that the films under study were quite unstable in the air, so that in most of the studies resistive transitions were usually studied on films covered by amorphous Si or a number of FeTe layers, which significantly reduced the observed values of T_c. The unique *in situ* measurements of FeSe films on STO made in Ref. [25] have given record-breaking values of $T_c > 100$ K, which can be seen from the data shown in Fig. 4. So far, these results have not been confirmed by other authors, but ARPES measurements of the temperature-mediated behavior of the energy gap in such films *in situ* at present routinely demonstrate values of T_c in the interval of 65–75 K.

In films consisting of several layers of FeSe, the observed values of T_c are significantly lower than record values obtained in single-layer films [26]. Recently, single-layer FeSe films were also grown on the 110 plane of STO [27], covered up by several FeTe layers. Resistive measurements on these films (including measurements of the upper critical magnetic field H_{c2}) have given T_c values of ~ 30 K. At the same time, FeSe films grown on $BaTiO_3$ (BTO) doped with Nb (with even larger values of the lattice constant ~ 3.99 Å) have shown (in ARPES measurements) T_c values of ~ 70 K [28]. Recent paper [29] has reported the observation of record

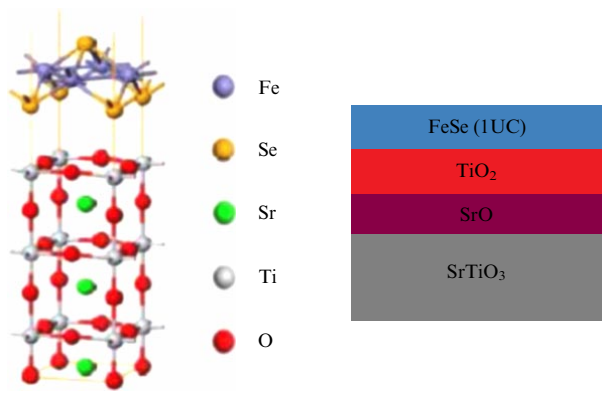

Figure 3. (Color online.) Structure of the FeSe monolayer on the $SrTiO_3$ substrate (001).

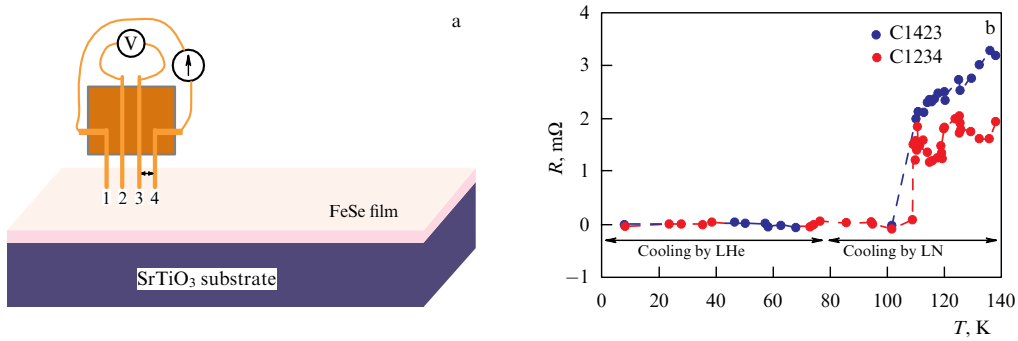

Figure 4. (Color online.) Experimental setup to measure resistance of a single-layer FeSe film on an $SrTiO_3$ substrate, and (b) temperature dependence of resistivity obtained in two samples [25].

(for FeSe systems) values of the superconducting gap (from tunneling) in FeSe monolayers on the (001) plane of TiO_2 (anatase), grown on the 001 plane of $SrTiO_3$. It was noted that the lattice constants of anatase are quite close to those of bulk FeSe, so that a FeSe film is not really stretched.

Single-layer FeSe films were also grown on a graphene substrate [30], but the T_c values of these films have not exceeded 8–10 K, characteristic of bulk FeSe, which stresses the role of substrates like $Sr(Ba)TiO_3$ possessing unique properties which may be determining in the significant enhancement of T_c.

We shall limit ourselves in this short review of the experimental situation to observations of superconductivity in FeSe monolayers in order to concentrate below on the discussion of the electronic structure and possible mechanisms explaining the record (for iron-based superconductors) values of T_c. More detailed information about experiments on this system can be found in recent review [31].

3. Electronic structure of iron–selenium systems

The electronic spectrum of iron pnictides has now been well studied both from numerical simulations based on modern energy band theory and experimentally, where the decisive role was played by angle-resolved photoemission spectroscopy (ARPES) [5–10]. As we already noted above, almost all effects of interest to us are produced by electronic states of the FeAs plane (layer), shown in Fig. 1b. The spectrum of carriers in the vicinity of the Fermi level (with a width of ~ 0.5 eV, where everything concerning the formation of a superconductive state obviously takes place) is practically determined only by d-states of Fe. Hybridization of Fe and As states according to all band structure calculations is very small. Accordingly, up to five bands (two or three hole-like and two electron-like) cross the Fermi level, forming the spectrum typical for a semimetal. A schematic diagram of Brillouin zones and Fermi surfaces is plotted in Fig. 5, and it is essentially rather simple.

In the first approximation, assuming that all As ions belong to the same plane as Fe ions, we have an elementary cell with one Fe and (square) lattice constant a (Fig. 5a). The corresponding Brillouin zone is shown in Fig. 5b. If we take into account that As ions are in fact placed above and below the Fe plane, as illustrated in Fig. 1b, the elementary cell will contain two Fe ions and the Brillouin zone is reduced by a factor of two, as shown in Fig. 5c. Two-dimensional Fermi surfaces for the case of four bands (two hole-like in the center and two electron-like at the edges or in the corners of appropriate Brillouin zones) are also schematically depicted in Fig. 5b, c.

In the narrow energy interval around the Fermi level, which is of interest to us, energy bands can be considered parabolic, so that the Hamiltonian of free carriers can be written out as [8]

$$H = \sum_{\mathbf{k},\sigma,i=\alpha_1,\alpha_2,\beta_1,\beta_2} \varepsilon^i_{\mathbf{k}} c^\dagger_{i\mathbf{k}\sigma} c_{i\mathbf{k}\sigma}\,, \tag{1}$$

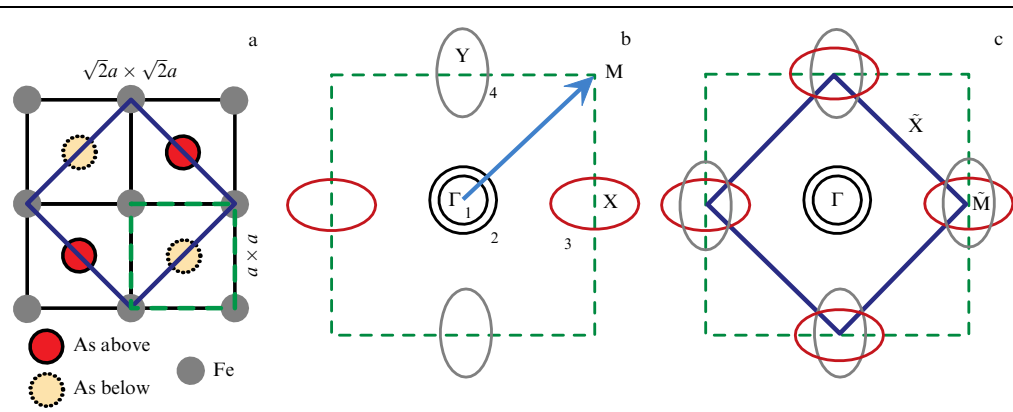

Figure 5. (Color online.) (a) Different choices of an elementary cell in the FeAs(Se) plane. (b) Brillouin zone and Fermi surfaces for the case of one Fe ion in the elementary cell. (c) Folded Brillouin zone and Fermi surfaces for the case of two Fe ions in the elementary cell.

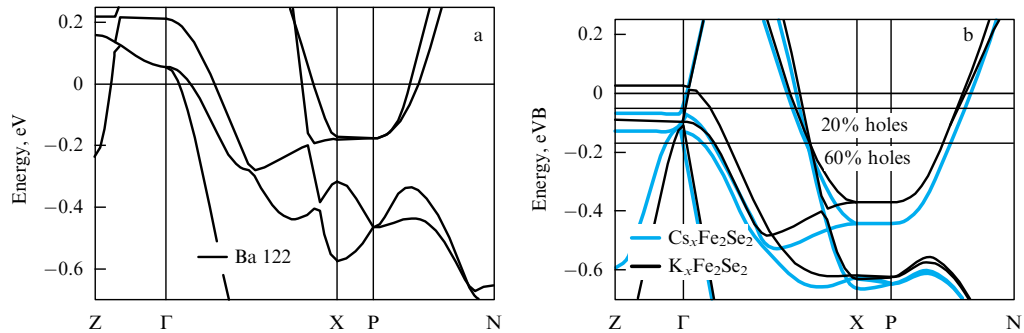

Figure 6. (a) LDA bands of Ba122 close to the Fermi level ($E = 0$) [37]. (b) LDA bands of $K_xFe_2Se_2$ (black lines) and $Cs_xFe_2Se_2$ (gray lines). Additional horizontal straight lines correspond to Fermi level positions at 20% and 60% hole doping [35].

where $c_{i\mathbf{k}\sigma}$ is the annihilation operator of an electron with momentum $\mathbf{k}$, spin σ, and band index i, while the hole α_i-band dispersions take the form

$$\varepsilon_{\mathbf{k}}^{\alpha_{1,2}} = -\frac{k^2}{2m_{1,2}} + \mu\,, \tag{2}$$

and the electron β_i-band dispersions are written out (in the coordinates of the Brillouin zone in Fig. 5b) as

$$\varepsilon_{\mathbf{k}}^{\beta_1} = \frac{(k_x - \pi/a)^2}{2m_x} + \frac{k_y^2}{2m_y} - \mu\,,$$
$$\varepsilon_{\mathbf{k}}^{\beta_2} = \frac{k_x^2}{2m_y} + \frac{(k_y - \pi/a)^2}{2m_x} - \mu\,. \tag{3}$$

More complicated band structure models valid in the vicinity of the Fermi level and in direct correspondence with the local density approximation (LDA) calculations can also be proposed (see, e.g., paper [32]), but the general, rather simple, picture of this 'standard model' of the iron pnictide spectrum remains the same. LDA + DMFT (dynamical mean-field theory) calculations [33, 34] taking into account the contribution from electron correlations show that in iron pnictides, in contrast to cuprates, their role is rather irrelevant and reduced to (actually noticeable) renormalization of the effective masses of electron and hole dispersions, as well as to the general 'compression' (reduced width) of the bands.

The presence of electron and hole Fermi surfaces with close sizes satisfying (approximately!) the 'nesting' conditions is very significant for the theories of superconducting pairing in iron pnictides, based on the decisive role of antiferromagnetic spin fluctuations [8]. Below, we shall see that the electronic spectrum and Fermi surfaces in Fe chalcogenides are significantly different from the qualitative pattern presented above, which poses new (and far from solved) problems for explaining the microscopic mechanism of superconductivity in these systems.

3.1 $A_xFe_{2-y}Se_2$ system

LDA calculations of the electronic spectrum of the $A_xFe_{2-y}Se_2$ (A = K, Cs) system were performed immediately after its discovery in experiment [35, 36]. Rather unexpectedly, this spectrum was found to be qualitatively different from the spectrum of bulk FeSe and the spectra of all the known FeAs systems. In Fig. 6, we compare the spectrum of $BaFe_2As_2$ (Ba122) [37], which is typical for all FeSe-based systems, and the $A_xFe_{2-y}Se_2$ (A = K, Cs) spectrum obtained in Ref. [5]. We can see the clear difference between these spectra in the vicinity of the Fermi level.

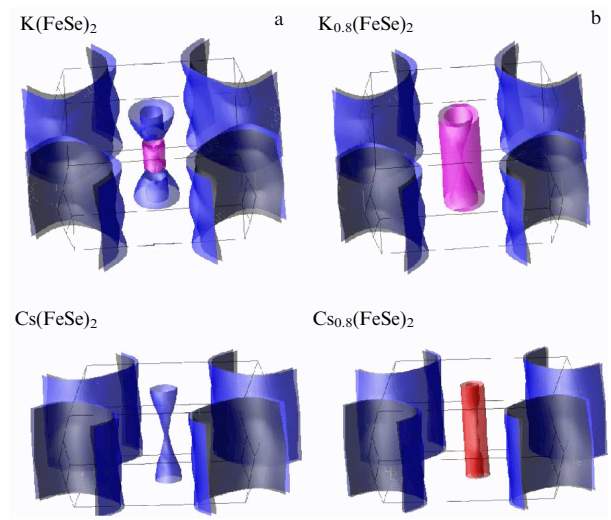

Figure 7. Fermi surfaces of $A_xFe_2Se_2$ (A = K, Cs) for the stoichiometric composition (a) and for the case of 20% hole doping (b) [35].

In Fig. 7, we exhibit the Fermi surfaces calculated in Ref. [35] for two typical compositions of $A_xFe_{2-y}Se_2$ (A = K, Cs). It can be seen that these are quite distinct from the Fermi surfaces of FeAs systems — in the center of the Brillouin zone there are only small (electron-like!) Fermi surfaces, while electron-like cylinders at the corners of the Brillouin zone are much larger. The shape of Fermi surfaces typical for bulk FeSe- and FeAs-based systems is reproduced only for much larger (unreachable) hole doping levels [38].

This shape of the Fermi surfaces in $A_xFe_{2-y}Se_2$ compounds was soon confirmed by ARPES experiments. As an example, we show in Fig. 8 ARPES data from Ref. [38], which are in obvious qualitative correspondence with LDA calculated results [35, 36].

It is seen that in this system we cannot speak of any, even approximate, 'nesting' properties of electron-like and hole-like Fermi surfaces, while it is precisely these properties that form the basis of most theoretical approaches to a microscopic description of FeAs-based systems [8], where the 'nesting' of electron-like and hole-like Fermi surfaces leads to a picture of well-developed spin fluctuations which make up the main mechanism of pairing interaction.

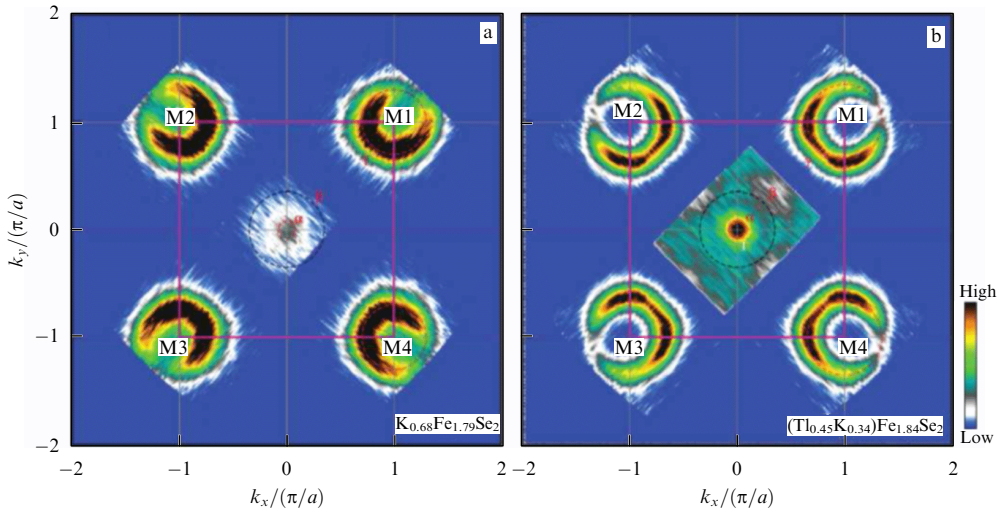

Figure 8. (Color online.) ARPES Fermi surfaces of (a) $K_{0.68}Fe_{1.79}Se_2$ ($T_c = 32$ K) and (b) $Tl_{0.45}K_{0.34}Fe_{1.84}Se_2$ ($T_c = 28$ K) [38].

LDA + DMFT calculations of $K_{1-x}Fe_{2-y}Se_2$ for different doping levels were performed in Refs [39, 40]. In this regard, besides the standard LDA + DMFT procedure, we also used the modified LDA′ + DMFT approach developed by us in Refs [41, 42], which allows, in our opinion, a more consistent solution to the 'double-counting' problem of Coulomb interactions in LDA + DMFT. For DMFT calculations, we chose $U = 3.75$ eV and $J = 0.56$ eV as the values of the Coulomb and exchange electron interactions in the 3d shell of Fe. As *impurity solver*, we have used the Quantum Monte Carlo (QMC) method. The results of these calculations were directly compared with the ARPES data from Refs [43, 44].

It can be seen that the correlation effects for a $K_{1-x}Fe_{2-y}Se_2$ system play a rather significant role. They lead to a noticeable change in LDA dispersions. In contrast to iron arsenides, where the quasiparticle bands close to the Fermi level remain well-defined, in $K_{1-x}Fe_{2-y}Se_2$ compounds in the vicinity of the Fermi level we observe rather strong suppression of quasiparticle bands. This reflects the fact that correlation effects in this system are stronger than in iron arsenides. The value of correlation renormalization (correlation narrowing) of the bands close to the Fermi level is given by the factor of 4 to 5, while in iron arsenides this factor is usually on the order of 2 to 3 for the same values of interaction parameters.

Results of these calculations are in general qualitative agreement with the ARPES data of Refs [43, 44], which also demonstrate the strong damping of quasiparticles in the immediate vicinity of the Fermi level and stronger renormalization of effective masses than in FeAs systems. At the same time, our calculations do not reveal the formation of an unusually 'shallow' (~ 0.05 eV below the Fermi level) electron-like band at the X point in the Brillouin zone, which was observed in ARPES experiments.

3.2 $[Li_{1-x}Fe_xOH]FeSe$ system

In Ref. [45], we performed LDA calculations of the stoichiometric LiOHFeSe compound; the appropriate results for energy dispersions are given in Fig. 9a. On first sight, the energy spectrum of this system is quite analogous to the spectra of the majority of FeAs systems and that of bulk FeSe. In particular, the main contribution to the density of states in a rather wide energy region around the Fermi level comes from d-states of Fe, while the Fermi surfaces qualitatively have the same shape as in the majority of Fe-based superconductors. However, this impression is wrong — in the real $[Li_{0.8}Fe_{0.2}OH]FeSe$ superconductor, the partial substitution of Fe for Li in intercalating LiOH layers leads to significant *electron* doping, so that the Fermi level goes upward in energy (as opposed to the stoichiometric case) by 0.15–0.2 eV. Whereas, as is clear from Fig. 9a, hole-like bands in the vicinity of point Γ move below the Fermi level, so that hole-like cylinders of the Fermi surface just vanish. The general shape of the Fermi surfaces for such an electron doping level, following from LDA calculations, is illustrated in Fig. 9b, and it has much in common with similar results for the $A_xFe_{2-y}Se_2$ system (cf. Fig. 7). This conclusion is confirmed by direct ARPES experiments [46], the results of which are displayed in Fig. 9c.

In particular, it can be seen from Fig. 9b that Fermi surfaces consist mainly of electron-like cylinders around points M, while the Fermi surface in the vicinity of point Γ is either absent or quite small. In any case, for this system there are no 'nesting' properties between electron and hole surfaces in any sense. Electronic dispersions determined from ARPES are quite similar to corresponding dispersions measured in Refs [43, 44] for the $K_{1-x}Fe_{2-y}Se_2$ system. These are qualitatively similar to dispersions obtained in LDA calculations taking into account the strong enough correlation narrowing of bands (the compression factor is actually different for various bands, as was shown by LDA + DMFT calculations in Refs [39, 40]). At the same time, the origin of an unusually 'shallow' electronic band ~ 0.05 eV deep close to point M remains unclear. To explain this peculiarity we need invoking of unusually strong correlation narrowing (while conserving the diameter of electron-like cylinders around the M point, which practically coincides with the results of LDA calculations), which is difficult to obtain from LDA + DMFT calculations.

In Ref. [45], local spin-density approximation (LSDA) calculations of exchange integrals were performed for typical configurations of Fe ions, replacing Li in LiOH layers. For the most probable configuration, leading to magnetic order-

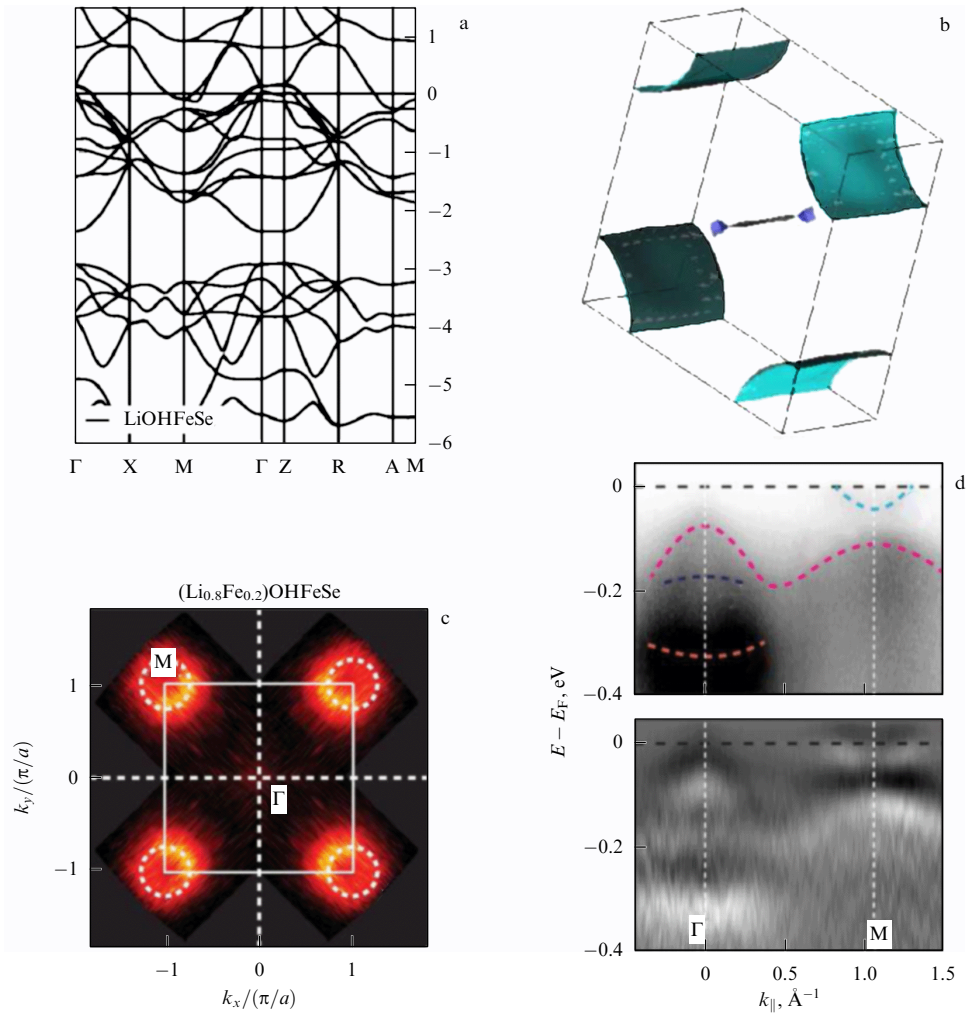

Figure 9. (Color online.) (a) LDA bands of LiOHFeSe (Fermi level at $E = 0$) [45]. (b) Fermi surface of LiOHFeSe corresponding to a doping level of 0.3 electrons per unit cell. (c) ARPES Fermi surfaces of $[Li_{0.8}Fe_{0.2}OH]FeSe$ [46]. (d) ARPES bands close to the Fermi level in $[Li_{0.8}Fe_{0.2}OH]$ FeSe [46]. Dashed lines in figure (d) indicate the positions of spectral density maxima defining electron dispersions.

ing, the positive (ferromagnetic) sign of exchange interaction was obtained and the simplest estimate of the Curie temperature has given the value of $T_C \approx 10$ K, in excellent agreement with the experimental data of Refs [21, 22], which reported the observation of ferromagnetic ordering on Fe in LiOH layers. At the same time, as we mentioned in Section 2.1, the other experiments had cast some doubts on this conclusion.

3.3 FeSe monolayer

LDA calculations of spectra of a single-layer FeSe can be done in the standard way [47]. The results of such calculations are represented in Fig. 10a. It is seen that the spectrum looks typical for FeAs systems and bulk FeSe, which was discussed in detail above. However, the ARPES experiments [48–50] showed convincingly that this is not so. In a monolayer of FeSe on STO, only electron-like Fermi surfaces are observed around M points in the Brillouin zone, while hole-like sheets around point Γ (at the zone center) are just absent. An example of this type of data is exhibited in Fig. 11a [48]. Thus, similarly to the case of intercalated FeSe systems, any kind of 'nesting' properties are lacking here. The apparent contradiction with the results of LDA calculations has a simple qualitative explanation — the observed Fermi surfaces can be easily obtained assuming that the system is electron-doped, so that the Fermi level moves upward in energy by $\sim 0.2-0.25$ eV, as shown by the red horizontal line in Fig. 10a. This corresponds to the doping level on the order of 0.15–0.20 electrons per Fe ion.

Strictly speaking, the origin of this doping remains unclear, but there is a general consensus that it is related to the formation of oxygen vacancies in $SrTiO_3$ substrate (in TiO_2 layer), appearing during different technological operations (annealing, etching, etc.) used during the growth of the films under study. It should be noted that the formation of electron gas at the interface with $SrTiO_3$ is well known and has been studied for a rather long time [51]. However, for the FeSe/STO system of interest to us, this problem has not been studied in any detail (cf., though, with Refs [52, 53]).

The influence of electron correlations on the spectrum of a single-layer FeSe is relatively weak. In Fig. 10b, we show the results of LDA + DMFT calculations for the case of a properly shifted (by electron doping) Fermi level [47]. DMFT calculations were performed for the values of the Coulomb and

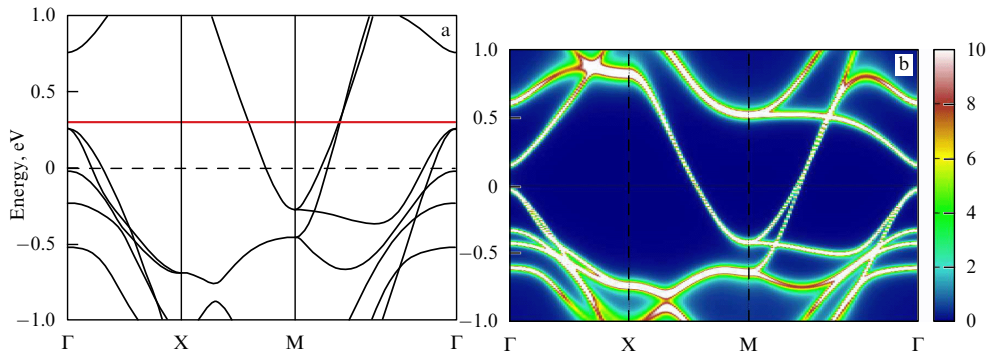

Figure 10. (Color online.) (a) LDA bands of a single-layer FeSe close to the Fermi level ($E = 0$). Horizontal red line denotes the approximate position of the Fermi level, corresponding to an electron doping level bringing about the Fermi surfaces observed in ARPES experiments [47]. (b) LDA + DMFT-calculated bands of a single-layer FeSe close to the Fermi level shifted by electron doping [47].

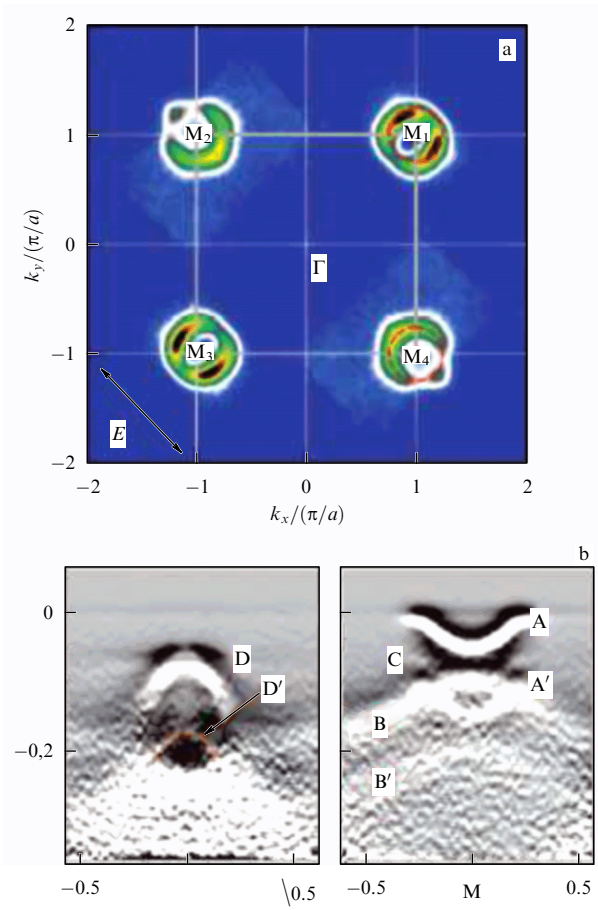

Figure 11. (Color online.) (a) ARPES Fermi surface of a single-layer FeSe [48]. (b) ARPES bands of an FeSe single layer close to the Fermi level [49].

exchange (Hund-like) interaction energies of electrons in the 3d shell of Fe, taken as $U = 3.5$ eV and $J = 0.85$ eV. As the *impurity solver*, we have used here the continuous–time quantum Monte Carlo (CT–QMC) method, and the dimensionless inverse temperature was taken to be $\beta = 40$. We can see that the spectrum is only weakly renormalized by correlations and conserves its LDA-like shape with a rather low bandwidth compression factor of ~ 1.3.

Electronic dispersions in FeSe monolayer films were measured by ARPES in a number of studies, e.g., in Refs [28, 49]. The results of Ref. [49] are presented in Fig. 11b. They are in agreement with data obtained in other papers and are, in general, analogous to the similar results obtained for intercalated FeSe systems (cf., e.g., Fig. 9c). By and large, these data are also qualitatively similar to the LDA + DMFT results, but the quantitative agreement is absent. In particular, ARPES experiments clearly demonstrate the presence of an unusually 'shallow' electron-like band at the point M with a Fermi energy of ~ 0.05 eV, while in theoretical calculations this band is almost an order of magnitude 'deeper'.

It should also be noted that the authors of Ref. [49] observed for the first time that a 'shadow' electron-like band exists at the point M, which lies about 100 meV below the main band and is a kind of a 'replica' of such a band. This band is clearly seen in Fig. 11b. Such a shadow band is absent in band structure calculations. The nature of this band and its possible significance for high-temperature superconductivity in FeSe monolayers on STO will be discussed in some detail below, in connection with possible mechanisms for increasing T_c.

As we noted above, the electron doping level of FeSe monolayers on STO is a rather poorly controlled parameter. However, in a number of papers, using different procedures of film annealing *in situ*, the authors successfully conducted ARPES experiments on samples with different doping levels [54, 55]. These experiments allowed some kind of phase diagrams for the FeSe/STO system to be obtained. In particular, a series of samples was demonstrated in Ref. [54] with consequent transitions from the topology of the Fermi surface typical of FeAs systems and bulk FeSe (with Fermi surface sheets around the point Γ in the center of the Brillouin zone) to the topology of Fermi surface sheets around point M. It was shown that high-T_c superconductivity appears only in samples without central Fermi surface sheets, whereas samples with the typical Fermi surface topology remain in the normal (N) phase. These results are given schematically in Fig. 12a. The presence of superconductivity was evidenced from ARPES measurements of the energy gap at the Fermi level, and T_c was derived from the temperature dependence of the gap.

In Ref. [55], similar measurements were done with electron concentration controlled by measurements of the area of electron pockets of the Fermi surface around the M points. The phase diagram obtained is plotted in Fig. 12b, where we see an insulating (antiferromagnetic?) phase at low doping levels, and a superconducting phase appearing at dopings exceeding the critical value of ~ 0.09, corresponding to the quantum critical point. These conclusions are also

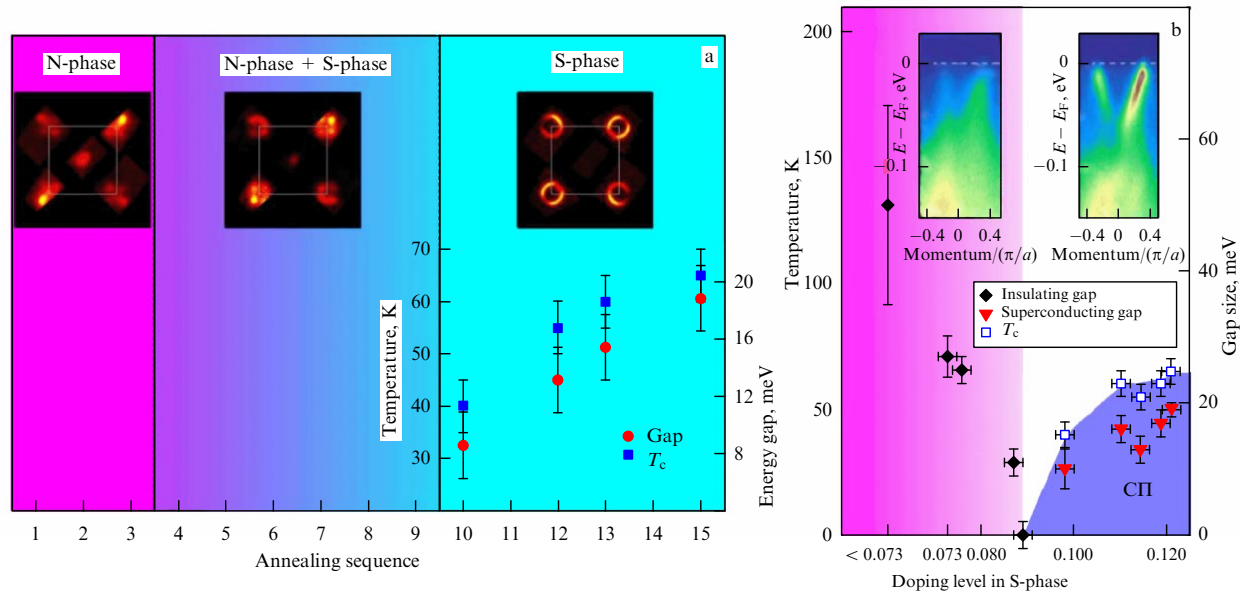

Figure 12. (Color online.) Phase diagram of an FeSe single layer on $SrTiO_3$. (a) Schematic phase diagram obtained in Ref. [54] on a series of samples with different electron dopings. Also shown are corresponding ARPES Fermi surfaces and, in the superconducting (S) phase, ARPES-measured values of the superconducting gap and T_c. (b) Phase diagram obtained from ARPES measurements in Ref. [55] and demonstrating the existence of insulating and superconducting phases. The values of superconducting and insulating gaps were also obtained from ARPES measurements.

based on ARPES measurements of superconducting and insulating energy gaps in the spectrum and their temperature dependences.

It is obvious that the results of Refs [54, 55] somewhat contradict each other, notably, the nature of the insulating phase observed in paper [55] remains unclear.

4. Possible mechanisms of T_c enhancement in iron–selenium monolayers

4.1 Correlation between T_c and the density of states

Let us now start discussing the mechanisms of high-temperature superconductivity in the systems under consideration. Concerning FeAs-based superconductors, there is a general consensus in the literature. The electron–phonon mechanism of Cooper pairing is considered to be insufficient in explaining the high values of T_c in these systems [5], and the preferable mechanism is assumed to be pairing due to the exchange of antiferromagnetic fluctuations. The repulsive nature of this interaction leads to a picture of $s^{\pm}$-pairing with different signs of superconducting order parameter (gap) Δ on hole-like (around the point Γ in the center of the Brillouin zone) and electron-like (around points M in the corners of the zone) sheets of the Fermi surface [8]. However, when we consider systems based on FeSe monolayers, this picture obviously becomes inconsistent — the observed topology of Fermi surfaces with a complete absence of any 'nesting' electron-like and hole-like sheets or even with a total absence of hole-like Fermi surfaces clearly contradicts this picture. There is simply no obvious way to produce well-developed spin (antiferromagnetic) fluctuations. Thus, we shall start with an elementary analysis based on the simple Bardeen–Cooper–Schrieffer (BCS) model.

In Ref. [56], an interesting empirical dependence was discovered between the superconducting transition temperature T_c in FeAs and FeSe systems and the height of anion (As or Se) position Δz_a above the Fe plane (layer) (cf. Fig. 1). A sharp maximum of T_c was observed for systems with $\Delta z_a \sim 1.37$ Å. In Refs [12, 57], we presented the results of systematic LDA calculations of the total density of states at the Fermi level, $N(E_F)$, for a wide choice of (stoichiometric) FeAs- and FeSe-based systems with different values of Δz_a (cf. Table 1). The obtained nonmonotone dependence of the density of states on Δz_a, shown in Fig. 13 (dots), which is determined by hybridization effects is, in principle, sufficient for explaining the corresponding dependence of T_c.

The appropriate dependence of T_c on Δz_a can be easily estimated along the lines of the elementary BCS model, applying the usual expression $T_c = 1.14\omega_D \times \exp(-1/\lambda)$ and taking into account that $N(E_F)$ directly enters dimensionless pairing interaction constant $\lambda = gN(E_F)$ (where g is the corresponding dimensional coupling constant). Taking the

Table 1. Total LDA-calculated density of states $N(E_F)$ and the values of T_c for iron-based superconductors.

System	Δz_a, Å	$N(E_F)$/cell/eV	T_c^{BCS}, K	T_c^{exp}, K
LaOFeP	1.130	2.28	3.2	6.6
$Sr_4Sc_2O_6Fe_2P_2$	1.200	3.24	19	17
LaOFeAs	1.320	4.13	36	28
SmOFeAs	1.354	4.96	54	54
CeOFeAs	1.351	4.66	48	41
NdOFeAs	1.367	4.78	50	53
TbOFeAs	1.373	4.85	52	54
SrFFeAs	1.370	4.26	38	36
$BaFe_2As_2$	1.371	4.22	38	38
CaFFeAs	1.420	4.04	34	36
$CsFe_2Se_2$	1.435	3.6	29	27
KFe_2Se_2	1.45	3.94	34	31
LiOHFeSe	1.485	4.14	36	43
LiFeAs	1.505	3.86	31	18
FeSe	1.650	2.02	3	8

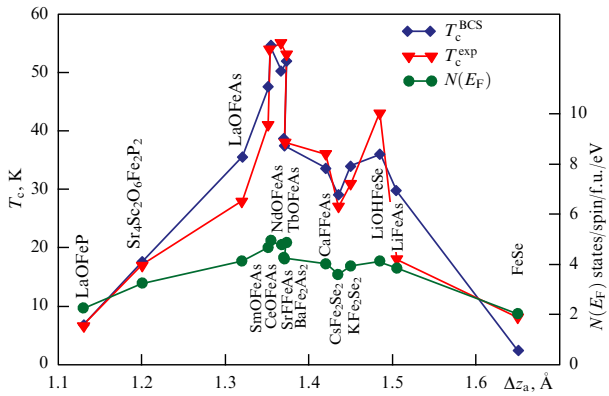

Figure 13. LDA-calculated values of the density of states $N(E_F)$ (dots, right axis) at the Fermi level and superconductor critical temperature T_c (left axis) obtained from elementary BCS type estimates, T_c^{BCS} (stars), and experimental values of T_c — T_c^{exp} (triangles) as functions of anion height Δz_a over the Fe layer for different iron-based superconductors.

rather arbitrary value of $\omega_D = 350$ K (which may be related to the characteristic value of phonon frequencies in FeAs systems [5]), we can determine the value of g fitting the experimental value of T_c, e.g., for the Ba122 system (~ 38 K), which gives $\lambda = 0.43$. Fixing this value of g, we can easily recalculate the values of T_c for all other systems just taking appropriate values of the density of states from LDA calculations (cf. Fig. 13). The relevant values of T_c given in Table 1 and plotted in Fig. 13 (stars) are in very reasonable agreement with the experimental values marked in the same figure (triangles), which are also compiled in Table 1.

FeSe-based systems just fit, in general, this dependence. This can be seen from the data of Table 1 and Fig. 13. For example, for the $[Li_{1-x}Fe_xOH]FeSe$ system, the calculated value of the density of states for stoichiometric composition LiOHFeSe is $N(E_F) = 4.14$ states/cell/eV, and the elementary estimate of T_c yields $T_c = 36$ K, which is somehow lower than the experimental value of $T_c^{exp} = 43$ K. However, introducing Fe into LiOH layers shifts the Fermi level, so that it moves to a higher value of $N(E_F)$ (4.55 states/cell/eV), leading to the relevant growth of T_c up to 45 K, which is very close to the experimental value [45].

It should be stressed that the above-given rough estimates do not necessarily mean that we assign an electron–phonon Cooper pairing mechanism to these systems, and ω_D in the BCS expression can just be considered a characteristic frequency of any kind of boson excitations responsible for pairing (e.g., magnetic fluctuations). These results simply show that there is an obvious correlation between experimental values of T_c and the value of the total density of states at the Fermi level obtained via band structure calculations for stoichiometric (!) compositions of FeAs- and FeSe-based compounds. Similar findings can be arrived at using more complicated expressions for T_c like the McMillan or Allen–Dynes formulas [57].

At the same time, for a single-layer FeSe, LDA calculations produce the value of $N(E_F) \approx 2$ states/cell/eV, which is practically the same as for bulk FeSe and changes weakly with electron doping (Fermi level shift) [47]. The corresponding elementary estimate of T_c does not produce values higher than 8 K, so the appearance of high T_c values in this case cannot be explained from analogous simple considerations.

However, there are a number of experimental papers where a significant increase in T_c was reported up to values on the order of 40 K in bulk crystals and multilayer films of FeSe under their electron doping achieved by covering the surface of FeSe with alkali metal (sodium) atoms [58–60]. It is possible that this treatment has led to the intercalation of FeSe layers by an alkali metal, so that these systems were transformed into an analogue of intercalated FeSe-based systems, similar to those discussed above, and the growth of T_c was related to an increase in $N(E_F)$. This point of view is confirmed by calculations presented in Ref. [61]. However, the growth of T_c to values > 40 K was also achieved in a number of papers by doping FeSe induced by a strong external electric field (at the gate) in field-effects transistor structures [62–64], where a similar explanation seems less probable.

4.2 Multiple bands picture of superconductivity

A basic feature of the electronic spectrum of iron pnictide and chalcogenide superconductors is its multiple band character: in general, the Fermi level is crossed by several bands formed with d-states of Fe, so that several sheets (pockets) appear on the Fermi surface (electron- and hole-like) [5, 8, 10]. In the superconducting state, an energy gap can open on each of these sheets and the values of these gaps can be quite different from each other [5, 10]. Thus, an elementary description of superconductivity based on the single-band BCS model used in the previous section is in fact oversimplified. Below, following mainly Refs [65, 66], we shall briefly describe the multiple-band formulation of the BCS model as applied to Fe-based superconductors.

Let us consider a simplified version of the electronic structure (Fermi surfaces) of the Fe square lattice, shown in Fig. 5b, with two hole-like pockets around point Γ and two electron-like pockets around points X and Y (in the Brillouin zone for the square lattice with one Fe ion per unit cell). Let Δ_i denote the superconducting order parameter (energy gap) on the ith sheet (pocket) of the Fermi surface ($i = 1, 2, 3, 4$ in Fig. 5b). The value of Δ_i is determined by the self-consistency equation for the corresponding anomalous Green's function in Gorkov's system of equations [65].

Pairing interaction in the multiple-band BCS model can be written out in the matrix form

$$\hat{V} = \begin{pmatrix} u & w & t & t \\ w & u' & t' & t' \\ t & t' & \lambda & \mu \\ t & t' & \mu & \lambda \end{pmatrix}, \tag{4}$$

where matrix elements $V^{i,j}$ define intraband and interband coupling constants. For example, $\lambda = V^{eX,eX} = V^{eY,eY}$ determines the pairing interaction on the same electron-like pocket at the point X or Y, while $\mu = V^{eX,eY}$ connects electrons on different pockets at points X and Y. Constants $u = V^{h1,h1}$, $u' = V^{h2,h2}$, and $w = V^{h1,h2}$ characterize BCS interaction on hole-like pockets — the smaller one (h1) and larger one (h2) — and between them, while $t = V^{h,eX} = V^{h,eY}$ pairs electrons at points X and Γ.

For the superconducting transition temperature, the standard BCS type expression appears:

$$T_c = \frac{2\gamma\omega_c}{\pi} \exp\left(-\frac{1}{g_{eff}}\right), \quad \gamma \approx 1.78\,, \tag{5}$$

where ω_c is the usual cut-off parameter in the Cooper channel (for simplicity, we assume that this parameter is the same for

all pairing interactions, while the generalization for, say, two characteristic cut-off frequencies is rather direct [67]), and $g_{\rm eff}$ stands for an *effective* pairing constant determined from the solvability condition for a system of linearized gap equations:

$$g_{\rm eff}\Delta_i = \sum_j g_{ij}\Delta_j\,, \tag{6}$$

where

$$g_{ij} \equiv -V^{i,j}\nu_j\,, \quad g_{\rm eff}^{-1} = \ln\frac{2\gamma}{\pi}\frac{\omega_{\rm c}}{T_{\rm c}} \tag{7}$$

is the matrix of dimensionless pairing constants g_{ij} determined by the products of matrix elements (4) and *partial* densities of states on different Fermi surface pockets, and ν_j denotes the density of states per spin projection on the jth pocket (cylinder).

From the symmetry arguments it is clear that $\nu_3 = \nu_4$, so that the system of equations (6) can produce two types of solutions [65]:

(1) corresponding to $d_{x^2-y^2}$-pairing, when the gaps on different sheets at points X and Y differ by sign, while gaps on hole-pockets are equal to zero:

$$\Delta_1 = \Delta_2 = 0\,, \qquad \Delta_3 = -\Delta_4 = \Delta\,, \tag{8}$$

or, as a special case, when relevant pockets are just absent;

(2) corresponding to so-called $s^{\pm}$-pairing, when gaps at points X and Y are equal: $\Delta_3 = \Delta_4$, while gaps on Fermi surface pockets surrounding point Γ have different signs in the presence of *repulsive* interaction between electron and hole pockets — $t > 0$, and usual s-wave pairing, when gaps on electron and hole pockets have the same sign in the presence of attraction — $t < 0$.

All these variants are qualitatively demonstrated in Fig. 14.

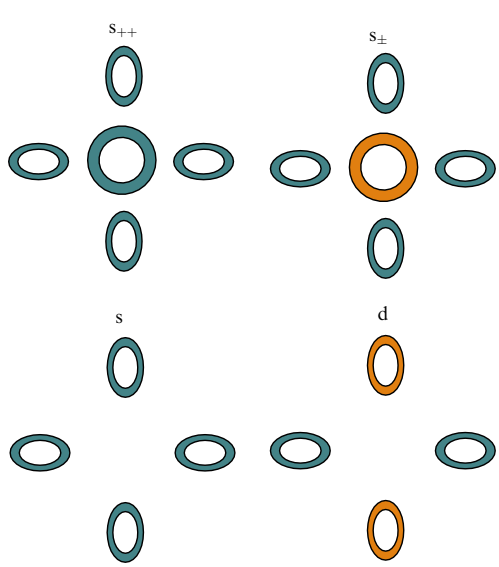

Figure 14. Main types of pairing in multiple-band scheme for superconductivity in FeAs- and FeS-based systems. Different colors mark different signs of superconducting gaps.

In the first case, we obtain the following expression for the effective pairing constant

$$g_{\rm eff} = (\mu - \lambda)\,\nu_3\,. \tag{9}$$

In the second case, we have $\Delta_3 = \Delta_4$ and $\nu_3 = \nu_4$, so that the two equations in set (6) just coincide and instead of expressions (4), (7) the coupling matrix 3×3 of the following form appears:

$$-\hat{g} = \begin{pmatrix} u\nu_1 & w\nu_2 & 2t\nu_3 \\ w\nu_1 & u'\nu_2 & 2t'\nu_3 \\ t\nu_1 & t'\nu_2 & 2\bar{\lambda}\nu_3 \end{pmatrix}, \tag{10}$$

where $\bar{\lambda} = (\lambda + \mu)/2$, and the solution to a set of equations (6) reduces to the standard procedure of finding the eigenvalues (and eigenvectors) for a matrix of dimensionless coupling constants g_{ij} (10), which are defined by the cubic secular equation

$$\mathrm{Det}\,(g_{ij} - g_{\rm eff}\delta_{ij}) = 0\,. \tag{11}$$

The physical solution is determined by the maximum positive value of $g_{\rm eff}$, which gives, in turn, the maximum value of $T_{\rm c}$. Eigenvectors of the problem determine here the ratios of the gaps Δ_i on different sheets of the Fermi surface for $T \to T_{\rm c}$. Temperature dependences of energy gaps for $T < T_{\rm c}$ can be found by solving the set of generalized BCS equations:

$$\Delta_i = \sum_j g_{ij}\Delta_j \int_0^{\omega_{\rm c}} {\rm d}\xi\, \frac{\tanh\left[\sqrt{\xi^2 + \Delta_j^2}/(2T)\right]}{\sqrt{\xi^2 + \Delta_j^2}}\,. \tag{12}$$

As $T \to 0$, these equations reduce to

$$\Delta_i = \sum_j g_{ij}\Delta_j F\left(\frac{\Delta_j}{\omega_{\rm c}}\right), \; F(x) = \ln\left(\frac{1 + \sqrt{1 + x^2}}{|x|}\right). \tag{13}$$

This analysis makes it clear that the value of $T_{\rm c}$ (effective pairing constant) in multiple-band system is determined, in general, not only by the value of the total density of states at the Fermi level (multiplied by the single dimensional coupling constant), but also by a rather complicated combination of several coupling constants, multiplied by partial densities of states for different bands. It is now becoming obvious that the multiple-band structure of the spectrum can lead to the growth of $T_{\rm c}$ by itself, reasonably enhancing the effective pairing constant in formula (5) [66]. To understand the essence of this effect, it is useful to analyze simple limiting cases.

Let a matrix of dimensionless coupling constants be diagonal (i.e., there are only intraband pairing interactions):

$$\hat{g} = \begin{pmatrix} g_1 & 0 & 0 & 0 \\ 0 & g_2 & 0 & 0 \\ 0 & 0 & g_3 & 0 \\ 0 & 0 & 0 & g_3 \end{pmatrix}. \tag{14}$$

Then, obviously, $g_{\rm eff} = \max\{g_i\}$, while $T_{\rm c}$ is determined by the density of states and pairing interaction on the single (and in this sense dominating) pocket of the Fermi surface.

Let us consider, in some sense, the opposite case, when all intraband and interband interactions in matrix (4) are the same and also all partial densities of states are just equal.

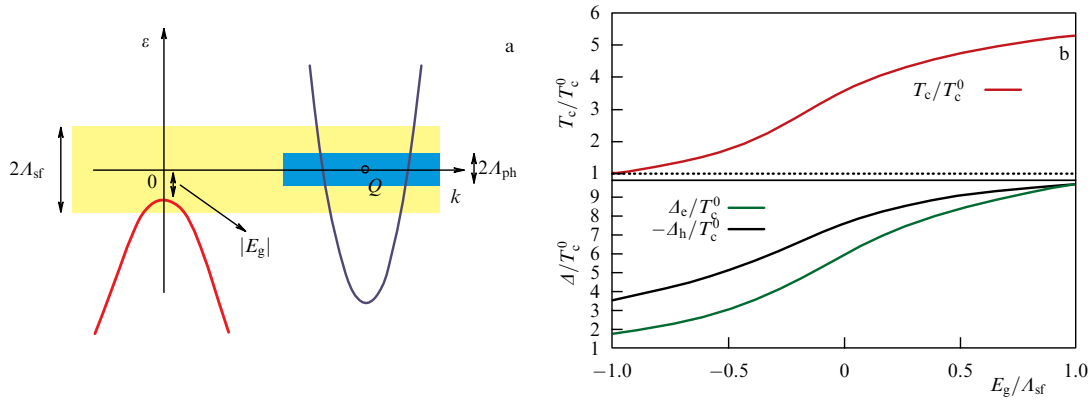

Figure 15. (Color online.) (a) Typical band structure of FeAs- and FeSe-based superconductors with a hole-like band approaching the Fermi level from below; shaded crossed areas denote the energy regions around the Fermi level, where two pairing interactions operate, e.g., electron–phonon (Λ_{ph}) and spin–fluctuation (Λ_{sf}). (b) T_c and energy gap (at $T = 0$ and on different sheets of the Fermi surface) behavior during the crossing of the Fermi level by a hole-like band (the Lifshits transition). T_{c0} is the temperature of the superconducting transition in the absence of the hole-like band. All energies are given in units of Λ_{sf} [67].

Then, we can introduce $g_0 = -uv$ and the matrix of dimensionless pairing constants takes the following form:

$$\hat{g} = g_0 \begin{pmatrix} 1 & 1 & 1 & 1 \\ 1 & 1 & 1 & 1 \\ 1 & 1 & 1 & 1 \\ 1 & 1 & 1 & 1 \end{pmatrix}. \tag{15}$$

In this case, we obtain $g_{\text{eff}} = 4g_0$, i.e., the real quadrupling of the effective pairing coupling constant, compared to the single-band model (or the model without interband pairing couplings). The generalization to the case of $n \times n$ matrices is obvious.

In Refs [66, 68], it was revealed that a certain choice of coupling constants in this model (with account for the LDA-calculated values of the partial densities of states) allows, in principle, a rather easy explanation of the observed (by ARPES) values of energy gap ratios on different pockets of the Fermi surface for a number of FeAs-based superconductors.

In Ref. [67], a similar analysis was done for a number of typical situations of electronic spectrum evolution, which can be realized in FeAs- and FeSe-based systems. It was explicitly shown that, for example, in a hole-like band approaching from below in energy (at the point Γ) and crossing the Fermi level (Lifshits transition), T_c and the values of the energy gaps on hole-like and electron-like pockets of the Fermi surface actually *grow*. In Fig. 15, we show the results of calculations [67] for a typical case which may be realized in the systems under consideration. We can see that as the distance of the hole-like band from the Fermi level E_g diminishes and changes its sign (upon the Lifshits transition) there is a significant growth of T_c and the gap values Δ_i (at $T = 0$). Specific values of parameters used in this calculations can be found in Ref. [67].

The basic conclusion from this elementary analysis is that the multiple-band structure, in general, facilitates the growth of the effective pairing coupling constant and the growth of T_c. It is also clear that the opening of new pockets on the Fermi surface (during the Lifshits transition) also leads to the growth of T_c, while closing such pockets leads to a drop in T_c. A number of experiments on FeAs systems under strong enough electron or hole doping evidently confirm these conclusions [69, 70].

At the same time, the general picture of electronic spectrum evolution during the transition from typical FeAs-based systems to intercalated FeSe systems, as well as all the data obtained for a single-layer FeSe/STO, drastically contradicts this conclusion — the high values of T_c are achieved in these systems after the disappearance of hole-like pockets around the point Γ, and only electron-like pockets remain around M points. The energy gaps appearing on these pockets are reliably measured in ARPES experiments and are practically isotropic [28, 50]. The relevant experimental data are exemplified in Fig. 16.

These data give rather convincing evidence of either d-wave pairing (case 1 above) or the usual s-wave pairing in

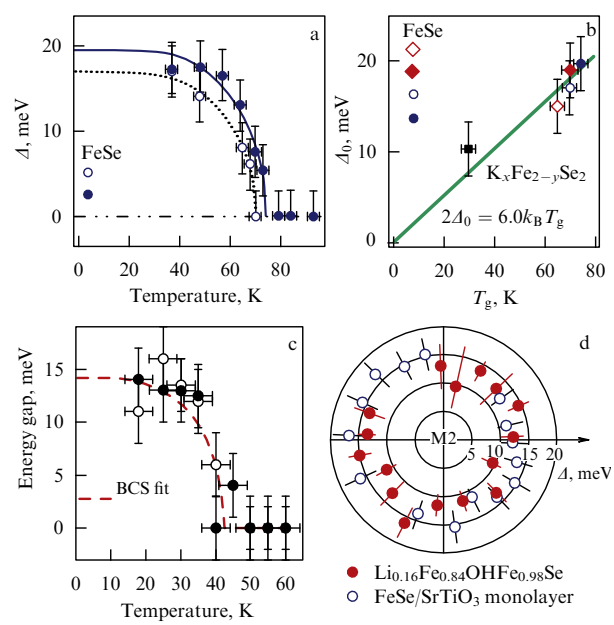

Figure 16. (a) Temperature dependence of the energy gap for two FeSe/BTO films [28]. (b) The values of the gaps for $K_xFe_{2-y}Se_2$ and FeSe monolayers [28]. (c) Temperature dependence of the energy gap in $Li_{0.16}Fe_{0.84}OHFe_{0.98}Se$ [50]. (d) Angular dependence of the energy gap in $Li_{0.16}Fe_{0.84}OHFe_{0.98}Se$ and an FeSe/STO monolayer [50].

the systems under discussion. The $s^{\pm}$ type pairing cannot be realized in these systems due to the absence (or smallness) of Fermi surface pockets around the point Γ. The absence of 'nesting' of electron-like and hole-like pockets on the Fermi surface also indicates the lacking of well-developed spin fluctuations, which can be responsible for repulsive interaction leading to a picture of $s^{\pm}$-pairing.

Apparently, the most probable scenario for these systems is s-wave pairing, when the usual isotropic gap opens on electron pockets. The variant of d-wave pairing (as in case 1) seems highly improbable. First of all, no microscopic mechanism (like spin fluctuations) has ever been proposed for realization of repulsive interaction on characteristic inverse lattice vectors connecting electron pockets at points M (or points X and Y in the Brillouin zone in Fig. 5b). This picture also contradicts direct experiments on the influence of magnetic and nonmagnetic adatoms on superconductivity in single-layer FeSe/STO films. It was reported in Ref. [71] that magnetic adatoms suppress superconductivity, while nonmagnetic adatoms barely influence it at all. This obviously corresponds to the picture of s-wave pairing.

4.3 Models of T_c enhancement in FeSe monolayer due to interaction with elementary excitations in the substrate

It is clear from the previous discussion that values of $T_c \sim 40$ K in intercalated FeSe layers can be achieved, in principle, by increasing the density of states at the Fermi level, in contrast to its value for bulk FeSe, which may be connected with the evolution of the band structure and doping effects. At the same time, it is also clear that an increase in T_c to values exceeding 65 K, observed in FeSe monolayers on STO (BTO), cannot be explained along these lines. It is natural to assume that such increase is somehow related to the nature of the STO (BTO) substrate, e.g., with additional pairing interaction of carriers in the FeSe layer appearing due to their interaction with some kind of elementary excitations in the substrate, in the spirit of the 'excitonic' mechanism, as was initially proposed by Ginzburg [1–4].

It is well known that $SrTiO_3$ is a semiconductor with an indirect energy gap of width 3.25 eV [72]. At room temperature, this compound is paraelectric with a very high dielectric constant reaching values of $\sim 10^4$ at low temperatures, remaining in the paraelectric state [73]. It is interesting to note that under electron doping in a concentration interval from 6.9×10^{18} cm^{-3} to 5.5×10^{20} cm^{-3}, $SrTiO_3$ becomes a superconductor with a maximum value of $T_c \sim 0.25$ K at an electron concentration on the order of 9×10^{19} cm^{-3} [74, 75]. The origin of superconductivity at such low concentrations (and the general shape of corresponding phase diagram) is by itself an interesting separate issue.

4.4 Excitonic mechanism by Allender, Bray, and Bardeen

The structure of FeSe films on $SrTiO_3$, shown in Fig. 3, represents the typical Ginzburg 'sandwich' [1–3], which indicates the possibility of realizing the excitonic mechanism of superconductivity. Let us consider the widely known version of this mechanism, as proposed for such a system long ago by Allender, Bray, and Bardeen (ABB) [76]. This mechanism is illustrated schematically in Fig. 17. An electron from a metal with momentum $\mathbf{k}_{1\uparrow}$ (arrow denotes spin direction) is transferred to the $\mathbf{k}_{2\uparrow}$ state due to excitation of the interband transition in a semiconductor from valence band state $\mathbf{k}_v$ to the $\mathbf{k}_c$ state in the conduction band, creating a virtual exciton. The second electron of the Cooper pair, which

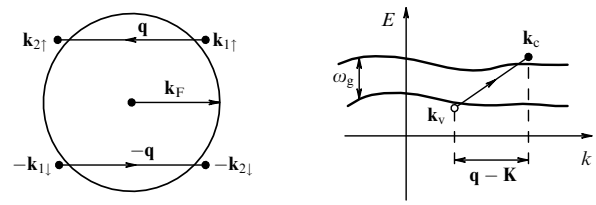

Figure 17. ABB excitonic mechanism.

resides initially in the $-\mathbf{k}_{1\downarrow}$ state, absorbs this exciton and goes into the $-\mathbf{k}_{2\downarrow}$ state. The momentum conservation law holds true: $\mathbf{q} = \mathbf{k}_2 - \mathbf{k}_1 = \mathbf{k}_v - \mathbf{k}_c + \mathbf{K}$, where $\mathbf{K}$ is an arbitrary inverse lattice vector. As a result, we obtain electron attraction within the pair, which is conceptually identical to that appearing due to phonon exchange.

In Ref. [76], a rough estimate of the corresponding attraction coupling constant was obtained as follows:

$$\lambda_{ex} = ba\mu\,\frac{\omega_p^2}{\omega_g^2}\,, \tag{16}$$

where μ is the dimensionless Coulomb potential, ω_p is the plasma frequency in a semiconductor, while ω_g is the width of the energy gap in a semiconductor, which plays the role of exciton energy. Dimensionless constant $b \sim 0.2$ defines the fraction of time the metallic electron spends inside the semiconductor, and the constant $a \sim 0.2-0.3$ is related to the screening of the Coulomb interaction within a metal. This estimate was criticized in Refs [77, 78] as an overestimate; additional arguments in favor of it were given in Ref. [79]. Without returning to this discussion, we further use the estimate given by formula (16) as obviously too optimistic.

To estimate T_c in the presence of two mechanisms of attraction (phonon and exciton), Ref. [76] proposed using the following simple expression which gives (as was shown in Ref. [76]) a better approximation to the numerical solution of the Eliashberg equations:

$$T_c = \frac{\omega_D}{1.45}\exp\left(-\frac{1}{g_{eff}}\right), \tag{17}$$

where

$$g_{eff} = \lambda^{\star}_{ph} + \frac{\lambda^{\star}_{ex} - \mu^{\star}}{1 - (\lambda^{\star}_{ex} - \mu^{\star})\,\ln(\omega_g/\omega_D)}\,, \tag{18}$$

$$\mu^{\star} = \frac{1}{1 + \mu\,\ln(E_F/\omega_g)}\,, \tag{19}$$

and the constants of electron–phonon and exciton exchange attractions are taken here in the renormalized form:

$$\lambda^{\star}_{ph} = \frac{\lambda_{ph}}{1+\lambda_{ph}}\,, \quad \lambda^{\star}_{ex} = \frac{\lambda_{ex}}{1+\lambda_{ex}}\,, \tag{20}$$

which takes into account qualitatively the effects of strong coupling, and E_F is the Fermi energy of a metallic film.

If we consider λ_{ex} a free parameter, we can easily estimate the possible extent of a T_c enhancement via the excitonic mechanism. Corresponding dependences calculated from Eqns (17)–(20) for typical values of Coulomb potential μ are

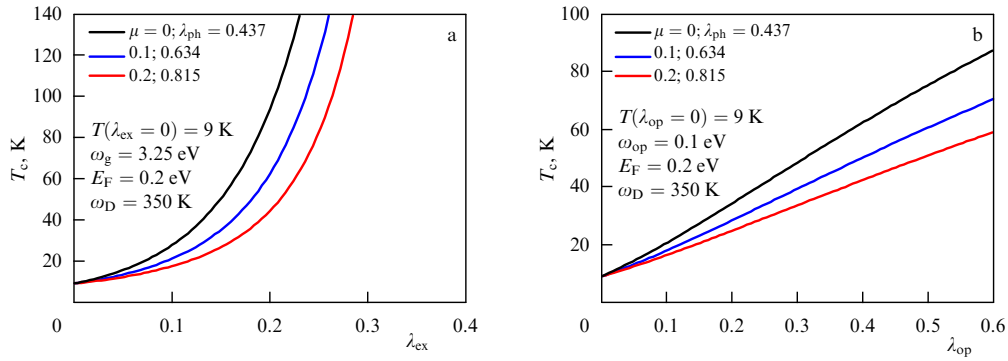

Figure 18. Dependence of T_c for FeSe/STO on the coupling constant with an ABB exciton (a) and optical phonon in STO (b).

shown in Fig. 18a. The value of ω_D was taken to be 350 K, while $\lambda_{ph} = 0.437$, as to reproduce the value of $T_c = 9$ K typical for bulk FeSe, while $E_F = 0.2$ eV was taken to be in agreement with LDA calculations of the FeSe monolayer. From Fig. 18a, we can see that for large enough values of λ_{ex} very high values of T_c can easily be obtained (as was theoretically predicted in Ref. [76]). The problem, however, is that even using the very optimistic estimate of λ_{ex} in Eqn (16), taking characteristic values of $\omega_p = 10$ eV, $\omega_g = 3.25$ eV, and for typical $\mu \sim 0.1-0.2$, we arrive at λ_{ex} values of $\sim 0.04-0.13$. Correspondingly, as we can see from Fig. 18a, even for these overoptimistic estimates, we obtain a quite modest increase in T_c and it is very far from the desirable values of $\sim 65-75$ K. These estimates convincingly demonstrate the ineffectiveness of the ABB excitonic mechanism as applied to FeSe/STO monolayers.

4.5 Interaction with optical phonons in STO

Ginzburg's initial notion to enhance T_c in 'sandwich' type structures [1–3] was based on the idea of electron interaction in metallic film with more or less high-energy excitations of an electronic nature ('excitons') within a semiconducting substrate. However, this idea can be understood in a wider context: the interaction of electrons of a metallic film with some arbitrary boson excitations in the substrate (e.g., with phonons) can lead to an increase in T_c. As we shall see, precisely this scenario is probably realized in FeSe monolayers on STO (BTO).

In $SrTiO_3$ or $BaTiO_3$ systems, almost dispersionless optical phonons exist with an unusually high excitation energy on the order of ~ 100 meV [80]. Examples of phonon dispersions and densities of states in these systems (both calculated and measured by neutron scattering method) are illustrated in Fig. 19. To estimate the prospects of T_c enhancement via interaction with such phonons, we can again utilize expressions (17)–(20) with simple replacements of $\omega_g \to \omega_{op}$ and $\lambda_{ex} \to \lambda_{op}$, where ω_{op} is the characteristic frequency of an optical phonon, and λ_{op} is the dimensionless coupling constant for such a phonon with electrons in a metallic film. Results of such calculations of T_c versus λ_{op} (similar to those shown in Fig. 18a for the ABB excitonic mechanism) with the choice of $\omega_{op} = 0.1$ eV are represented

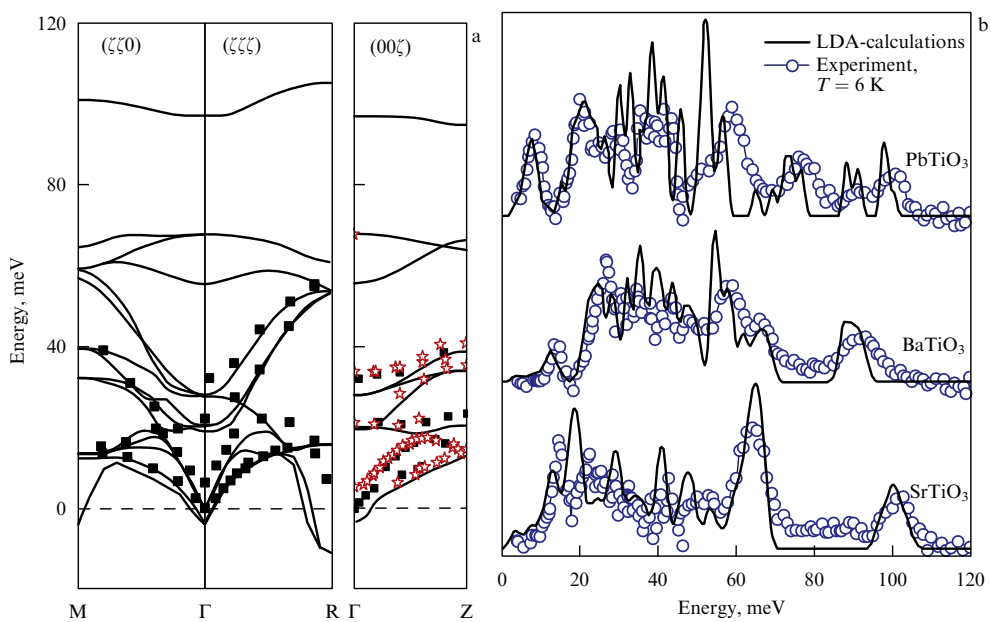

Figure 19. Phonons in $SrTiO_3$ and similar compounds: (a) phonon dispersions in $SrTiO_3$, both calculated and measured by inelastic neutron scattering, and (b) phonon density of states in $PbTiO_3$, $BaTiO_3$, and $SrTiO_3$ from neutron scattering and calculations [80].

in Fig. 18b. It can be seen that for large enough values of $\lambda_{\rm op} \sim 0.5-0.6$ and not very large μ we can easily achieve values of $T_{\rm c} \sim 60-80$ K, corresponding to experiments on FeSe/STO (BTO), even if we start from a relatively low initial $T_{\rm c}$ of about 9 K for FeSe in the absence of additional pairing interaction. Corresponding values of $\lambda_{\rm op}$ seem to be realistic enough, and below we shall present concrete evidence that interaction with optical phonons in these structures can be strong enough.

The idea that interactions with optical phonons from STO can play a significant role in the physics of FeSe/STO monolayers was first proposed by Lee et al. [49] in connection with ARPES measurements done in this work, which demonstrated the formation of a 'shadow' band at point M in the Brillouin zone, as shown in Fig. 11b. This band is situated approximately 100 meV below the main conduction electron band and practically replicates its dispersion. The formation of such a band can be linked to the interaction of FeSe electrons with an optical phonon of the corresponding energy from STO. To understand this situation, we have to consider a realistic enough picture of FeSe monolayer electrons interacting with optical phonons of STO, which was proposed in Ref. [49] and will be briefly described below (cf. also Ref. [81]).

Since STO resides in an almost ferroelectric state, it is natural to expect that charge transfer at the interface can induce the appearance of a layer of ordered dipoles. Free carriers in STO, appearing, for example, due to oxygen vacancies (or Nb doping), will screen the electric field far from the interface. Then, the dipole layer will be localized close to the interface. The appearance of dipoles is connected with the displacement of Ti cations relative to oxygen anions, so that oscillations of these anions will lead to modulation of the dipole potential along the FeSe layer. This situation is shown schematically in Fig. 20a.

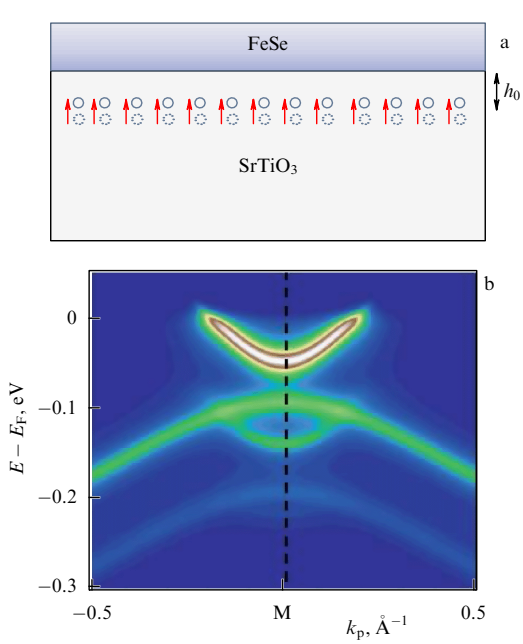

Figure 20. (Color online.) (a) Diagrams of dipole excitations close to an FeSe/STO interface. (b) Calculated electron spectral density in FeSe/STO in the model with a dominant forward scattering [49].

Let δP_z denote the change in dipole moment due to displacement of oxygen anions in the direction perpendicular to the interface:

$$\delta P_z(x, y, -h_0) = q_{\rm eff}\, \delta h(x, y, -h_0)\,. \tag{21}$$

Here, x, y are coordinates in the plane parallel to the interface, the origin of the z-axis is chosen in the Fe plane, and $q_{\rm eff}$ is the dipole charge. With respect to the Fe plane, the dipole layer is at $z = -h_0$. The induced change in the dipole potential in the Fe plane, connected with the 'frozen' displacement of oxygens, is given by the following expression:

$$\Phi(x, y, 0) = \frac{\epsilon_{\parallel}^{1/2} q_{\rm eff} h_0 n_{\rm d}}{\epsilon_{\perp}^{3/2}} \int {\rm d}x'\, {\rm d}y' \times \frac{\delta h(x', y', -h_0)}{\left[(\epsilon_{\parallel}/\epsilon_{\perp})\, h_0^2 + (x - x')^2 + (y - y')^2\right]^{3/2}}\,. \tag{22}$$

Performing the Fourier transform over x, y, we get

$$\Phi(\mathbf{q}_{\parallel}, 0) = \frac{2\pi q_{\rm eff} n_{\rm d}}{\epsilon_{\perp}} \exp\left(-|\mathbf{q}_{\parallel}| h_0 \sqrt{\frac{\epsilon_{\parallel}}{\epsilon_{\perp}}}\right) \delta h(\mathbf{q}_{\parallel}, -h_0)\,. \tag{23}$$

Here, $\mathbf{q}_{\parallel}$ is the wave vector parallel to the interface, $\epsilon_{\parallel}$, $\epsilon_{\perp}$ are dielectric constants parallel and perpendicular to the interface, and $n_{\rm d}$ is the density of the dipoles per unit area of the interface. Because electrons in FeSe move parallel to the interface, they contribute only to $\epsilon_{\parallel}$. As to carriers in STO, besides their role in screening, which we have mentioned above, they make approximately equal contributions (STO possesses a cubic structure) to both $\epsilon_{\parallel}$ and $\epsilon_{\perp}$. Thus, we can expect that the total dielectric constant $\epsilon_{\parallel}$ is much greater than $\epsilon_{\perp}$.

From Eqn (23), it becomes clear that the value of the matrix element of electron–phonon interaction has an important dependence on $\mathbf{q}_{\parallel}$, so that it can be written out as

$$\Gamma(p_{\parallel}, \mathbf{q}_{\parallel}) = \frac{2\pi q_{\rm eff} n_{\rm d}}{\epsilon_{\perp}} \exp\left(-\frac{|\mathbf{q}_{\parallel}|}{q_0}\right), \tag{24}$$

$$q_0^{-1} = h_0 \sqrt{\frac{\epsilon_{\parallel}}{\epsilon_{\perp}}}\,. \tag{25}$$

The fact that $\epsilon_{\parallel} \gg \epsilon_{\perp}$ leads to q_0 suppression by a factor of $1/\sqrt{\epsilon_{\parallel}/\epsilon_{\perp}}$ which, in turn, leads to a fairly sharp peak in electron–phonon interaction at $\mathbf{q}_{\parallel} = 0$.

Such a dominating role of forward scattering explains the appearance of the 'shadow' band in the electronic spectrum, which replicates the dispersion of the main band. In the case of electron–phonon interaction acting in the wide range of transferred momenta, it will lead to a superposition of many bands, each being moved by its own scattering vector, which will lead to a general smearing of the 'shadow' band.

The standard numerical calculation of second–order electron self-energy due to electron–phonon interaction was performed in Ref. [49] with the coupling constant written as $g(\mathbf{q}) = g_0 \exp(-|\mathbf{q}|/q_0)$, with $g_0 = 0.04$ eV, $q_0 = 0.3/a$ ($a = 3.9$ Å), optical phonon frequency $\Omega_0 = 80$ meV, and the bare spectrum of electrons and holes (one-dimensional — along the $\Gamma-$M direction) written as $\epsilon_{\rm e,h}(k) = -2t_{\rm e,h}\cos(k/a) - \mu_{\rm e,h}$ (close to the point M) with $t_{\rm e} = 125$ meV, $t_h = 30$ meV, $\mu_{\rm e} = -185$ meV, and $\mu_{\rm h} = 175$ meV, where all numerical parameters were taken from fitting the ARPES experiment data. Results of such a calculation for electron spectral density (imaginary part of Green's function)

are plotted in Fig. 20b. We can see that these calculations are in excellent agreement with the ARPES data in Fig. 11b. The standard dimensionless electron–phonon coupling constant can be estimated numerically using the same values of all the parameters, yielding [49]

$$\lambda = \frac{2}{N\Omega_0} \frac{\sum_{\mathbf{k},\mathbf{q}} |g(\mathbf{q})|^2 \delta(\epsilon_e(\mathbf{k}))\, \delta(\epsilon_e(\mathbf{k}-\mathbf{q}))}{\sum_{\mathbf{k}} \delta(\epsilon_e(\mathbf{k}))} = 0.5\,, \qquad (26)$$

(N is the number of lattice sites), which is (as noted above) quite sufficient for a significant increase in T_c in the FeSe/STO monolayer. As we shall see below, the peculiarities of the model of electron–phonon interaction with a dominant forward scattering also lead to some other, even more important, effects favorable to the enhancement of T_c.

4.6 Cooper pairing in the model with a dominant forward scattering

Dominant forward scattering in electron–phonon interactions was for a long time considered a special cause of T_c enhancement due to the specific dependences differing from the standard BCS, which appear in this model [82, 83]. These papers analyzed the possible role of such interactions in cuprates. An application of these ideas to FeSe/STO was considered recently in Refs [84, 85].

In the weak coupling approximation for the case of s-wave pairing, the gap equation in Eliashberg theory reduces to the following

$$\Delta(\mathrm{i}\varepsilon_n) = -\frac{T}{N} \sum_{\mathbf{q},m} |g(\mathbf{q})|^2 D(\mathbf{q}, \mathrm{i}\varepsilon_n - \mathrm{i}\varepsilon_m) \times \frac{\Delta(\mathrm{i}\varepsilon_m)}{(\varepsilon_m)^2 + \xi^2_{\mathbf{k}+\mathbf{q}} + \Delta^2(\mathrm{i}\varepsilon_m)}\,, \qquad (27)$$

where $D(\mathbf{q}, \mathrm{i}\varepsilon_n - \mathrm{i}\varepsilon_m) = -2\Omega_{\mathbf{q}}/[(\varepsilon_n - \varepsilon_m)^2 + \Omega^2_{\mathbf{q}}]$ is the Matsubara Green's function of an optical phonon with frequency $\Omega_{\mathbf{q}}$, $\xi_{\mathbf{k}} = v_F(|\mathbf{k}| - p_F)$ is the electronic spectrum close to the Fermi level (v_F, p_F are Fermi velocity and momentum), and $\varepsilon_n = (2n+1)\pi T$ is the fermion Matsubara frequency.

Before going to the results of the numerical solution to equation (27), let us consider the elementary model of exactly forward scattering by phonons, when all calculations can be done analytically. For this purpose, we introduce $|g(\mathbf{q})|^2 = g_0^2 N \delta_{\mathbf{q}} = (2\pi)^2 \delta(\mathbf{q})$. Then, gap equation (27) on the Fermi surface is easily transformed to

$$\Delta(\mathrm{i}\varepsilon_n) = \lambda_m \Omega_0^2 T_c \sum_m \frac{\Delta(\mathrm{i}\varepsilon_m)}{\varepsilon_m^2 + \Delta^2(\mathrm{i}\varepsilon_m)} \frac{2\Omega_0}{\Omega_0^2 + (\varepsilon_n - \varepsilon_m)^2}\,, \qquad (28)$$

where we have introduced the dimensionless coupling constant

$$\lambda_m = \frac{g_0^2}{\Omega_0^2}\,. \qquad (29)$$

Notice that this definition is somehow different from the standard definition of the electron–phonon coupling constant (26).

To find the critical temperature T_c, the authors of Ref. [84] used the following *Ansatz* for the energy gap function:

$$\Delta(\mathrm{i}\varepsilon_n) = \frac{\Delta_0}{1 + (\varepsilon_n/\Omega_0)^2}\,. \qquad (30)$$

Then, linearizing the gap equation, we arrive at the following equation for T_c [84]:

$$1 = \lambda_m \Omega_0^2 T_c \sum_m \frac{2\Omega_0}{\varepsilon_m^2 (1 + \varepsilon_m^2/\Omega_0^2)(\Omega_0^2 + \varepsilon_m^2)}\,. \qquad (31)$$

The sum over Matsubara frequencies is calculated directly, and we obtain

$$1 = \frac{\lambda_m}{2T_c} \frac{2\Omega_0 + \Omega_0 \cosh(\Omega_0/T_c) - 3T_c \sinh(\Omega_0/T_c)}{1 + \cosh(\Omega_0/T_c)}\,. \qquad (32)$$

Since for FeSe/STO one has $T_c \ll \Omega_0$, we can use here the asymptotic form of hyperbolic functions, and in the leading approximation the critical temperature becomes the quasilinear function of the coupling constant (for its small values):

$$T_c = \frac{\lambda_m}{2 + 3\lambda_m}\, \Omega_0\,. \qquad (33)$$

A similar result was previously obtained in the context of cuprate physics [82, 83]. For $\lambda_m = 0.16$ and $\Omega_0 = 100$ meV, we get $T_c = 75$ K, which is rather unexpected for such a small value of λ_m.

This value of T_c can be compared with the standard expression of BCS theory, where the linearized equation for T_c takes the following form:

$$1 = \pi T_c \lambda_m \sum_{|\varepsilon_m| < \omega_D} \frac{1}{|\varepsilon_m|} = \lambda_m \left[\ln\left(\frac{\omega_D}{2\pi T_c}\right) - \psi\left(\frac{1}{2}\right) \right], \qquad (34)$$

where we have used the asymptotic form at large ω_D/T_c. This leads to the usual BCS expression: $T_c = 1.13\omega_D \exp(-1/\lambda_m)$, so that for $\lambda_m = 0.16$ and $\omega_D = 100$ meV we obtain $T_c = 2.5$ K.

Comparing these results for T_c, we can conclude that the significant T_c enhancement obtained above appears due to the effective exclusion of momentum integration in the Eliashberg equation, which is related to the strong interaction peak at $\mathbf{q} = 0$. In the BCS model, we integrate over the whole Fermi surface and all momenta enter with the same weight, which leads to the appearance of the $\sum_m 1/|\varepsilon_m|$ term in the equation for T_c and to the corresponding logarithmic behavior. In the case of forward scattering, integration over momenta is lifted, so that only the ε_m^{-2} term remains in the sum over frequencies, which leads to a $1/T_c$ type behavior. Due to this, the model with strong forward scattering leads to the effective mechanism of T_c enhancement [82, 83].

Let us now discuss the numerical results for the general case [84]. In a realistic situation, the forward scattering dominates in the finite region of momentum space, with the size determined by the parameter q_0. The numerical solution of the Eliashberg equations with the coupling constant of the form $g(\mathbf{q}) = g_0 \exp(-|\mathbf{q}|/q_0)$ gives the temperature behavior of the superconducting gap (at the lowest Matsubara frequency) $\Delta(\mathrm{i}\pi T)$ shown in Fig. 21 (for several values of λ_m and $q_0 = 0.1/a$). We can see that T_c is already high enough for modest enough values of λ_m and grows approximately linearly in λ_m, as long as we remain in the weak coupling region. The finiteness of q_0 leads to some suppression of T_c, unlike the case of exact forward scattering (cf. the insert to Fig. 21), but in general the quasilinear dependence of T_c on λ_m can guarantee the values of T_c observed in FeSe/STO films.

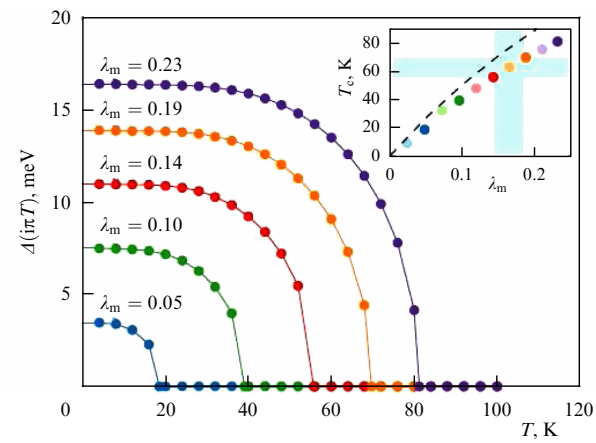

Figure 21. Temperature dependence of the energy gap $\Delta(i\pi T)$ (at the smallest Matsubara frequency) in the model with a dominant forward scattering ($q_0 = 0.1/a$) for different values of the coupling constant. In the inset, the dashed line shows the T_c-dependence of the coupling constant in the case of exactly forward scattering (33), while the dots represent the results of numerical calculations [84]. The shaded region covers the interval of λ_m values appropriate for FeSe/STO.

In the framework of this model, it is rather easy to explain the formation of the 'shadow' band in the vicinity of the M point [84, 85].

4.7 Nonadiabatic superconductivity and other problems

We have already noted above that the characteristic feature of the electronic spectrum of superconductors containing FeSe monolayers is the formation of an unusually 'shallow' electronic band in the vicinity of point M in the Brillouin zone (cf. Figs 9d, 11b). The value of Fermi energy $E_F \sim 0.05$ eV in these systems is almost an order of magnitude less than the values obtained in LDA and LDA + DMFT calculations. Such a small value of E_F creates additional difficulties for a consistent theory of superconductivity in the FeSe/STO system. Gor'kov [86] was the first to note that we are dealing here with an unusual situation, when the energy ~ 100 meV of an optical phonon in STO is significantly higher than the Fermi energy equal to ~ 50 meV.

Let us recall that in the great majority of superconductors we have the opposite inequality, $\omega_D \ll E_F$, which allows us to use the adiabatic approximation in describing the effects of electron–phonon interaction, which is based on the inequality $\omega_D/E_F \sim (m/M)^{1/2} \ll 1$ (m is the electron mass, and M is an ion mass). Then (as in the normal state), we can apply the Migdal theorem and ignore all vertex corrections to electron–phonon interactions, limiting ourselves to second-order diagrams for electron self-energy. In particular, the standard derivation of Eliashberg equations is entirely based on the adiabatic approximation, so that the common term is the Migdal–Eliashberg theory.

Breaking the relevant inequality in the FeSe/STO system means that the theory explaining T_c enhancement is to be developed, from the very beginning, but in the *antiadiabatic* approximation. An attempt to build such a theory was undertaken in recent papers by Gor'kov [86–88]. In particular, Refs [86, 87] were devoted to the FeSe/STO system and the general aspects of the problem, while a new theory was proposed in Ref. [88] for describing superconductivity in doped $SrTiO_3$, which, as was noted above, is by itself quite an unusual superconductor [74, 75].

Obviously, the frame of our review does not allow us to delve deeply into the discussion of rather complicated theoretical problems, so that we shall limit ourselves only to a qualitative presentation of the results obtained in Refs [86, 87], which are directly relevant to superconductivity in FeSe/STO. The only approximation which can apparently be used here is a *weak coupling* approximation, when the smallness of the electron–phonon coupling constant by itself allows neglecting of vertex corrections and the usual (ladder) series of Feynman diagrams in the Cooper channel to be summed. It is natural that in antiadiabatic approximation the cut-off of logarithmic divergence in the Cooper channel takes place not at phonon frequencies, but at energies on the order of the Fermi energy E_F (or the bandwidth) [87], so we can expect that $T_c \sim E_F \exp(-1/\lambda)$, where λ is determined by the details of the pairing interaction.

The interaction of FeSe electrons with longitudinal surface phonons at the STO interface can be introduced [86] via interactions with the polarization induced by these phonons:

$$\mathbf{P} = F_C \mathbf{u}\,, \tag{35}$$

where $\mathbf{u}$ is the atomic displacement, and coefficient F_C is defined by the model of electron interaction with surface longitudinal optical (SLO) phonons on the surface of an insulator [89]:

$$F_{C,i} = \left[4\pi e^2 \frac{\omega^i_{SLO}}{2}\left(\frac{1}{\epsilon_\infty + 1} - \frac{1}{\epsilon_0}\right)\right]^{1/2}, \tag{36}$$

where the subscript or superscript i enumerates phonon branches, ϵ_0 and ϵ_∞ are static and optical dielectric constants of the bulk insulator, and ω^i_{SLO} is the frequency of the ith SLO phonon.

The matrix element for two-electron scattering due to the exchange of a surface phonon then takes the form

$$M_i(\mathbf{q}, \varepsilon_n - \varepsilon_m) = -\frac{4\pi e^2}{|\mathbf{q}|}\left(\frac{1}{\epsilon_\infty + 1} - \frac{1}{\epsilon_0}\right) D^i_{SLO}(\mathbf{q}, \varepsilon_n - \varepsilon_m)\,, \tag{37}$$

where $D^i_{SLO}(\mathbf{q})$ is Green's function of the STO phonon, namely

$$D^i_{SLO}(\mathbf{q}, \varepsilon_n - \varepsilon_m) = \frac{(\omega^i_{SLO})^2}{(\omega^i_{SLO})^2 + (\varepsilon_n - \varepsilon_m)^2}\,, \tag{38}$$

where $\mathbf{q} = \mathbf{p} - \mathbf{k}$ and $\varepsilon_n - \varepsilon_m$ are the momentum and (Matsubara) frequency exchanged between electrons.

In a bulk insulator, the well-known Lyddane–Sachs–Teller relation holds between the frequencies of longitudinal (LO) and transverse (TO) optical phonons: $\omega^2_{LO}/\omega^2_{TO} = \epsilon_0/\epsilon_\infty$. According to Ref. [89], the frequency of the longitudinal surface phonon is given by the following expression: $\omega^2_{SLO}/\omega^2_{TO} = \epsilon_0 + 1/\epsilon_\infty + 1$. It should be stressed that the values of ϵ_0 and ϵ_∞ are considered here as model parameters depending on the details of STO surface preparation in the process of creating the FeSe/STO structures (e.g., $SrTiO_3$ doping by Nb) [86].

Finally, for the matrix element of two-electron scattering due to the exchange of surface LO phonons and (two-dimensional) Coulomb repulsion, dropping some factors

that are irrelevant at the moment [86], we obtain the following expression

$$M_{\rm tot}(\mathbf{p},\varepsilon_n|\mathbf{k},\varepsilon_m) = \frac{4\pi e^2}{(\epsilon_\infty+1)\,q} - \sum_i \frac{4\pi e^2}{(\epsilon_\infty+1)\,q}\, D^i_{\rm SLO}(\varepsilon_n-\varepsilon_m)\,. \qquad (39)$$

Here, the summation is performed over three IR-active phonons at point Γ of the bulk $SrTiO_3$, whose frequencies satisfy the inequality $\omega^i_{\rm LO} > T_{\rm c}$ [80]. In fact, in $SrTiO_3$ we have a single LO mode which has a very large gap compared to the frequencies of all TO phonons, and which is of fundamental importance here compensating for the Coulomb repulsion in Eqn (39) for $|\varepsilon_n-\varepsilon_m| \ll \omega_{\rm LO}$. The remaining LO phonons, as usual, make an additional contribution to attraction. Since the inequality $\epsilon_0 \gg \epsilon_\infty$ holds in $SrTiO_3$, we have left in Eqn (39) only the contributions from terms with $\epsilon_\infty+1$.

In the extreme antiadiabatic limit, when $\omega_{\rm SLO} \gg E_{\rm F}$, we can ignore $(\varepsilon_n-\varepsilon_m)^2$ terms in the denominator of the phonon Green's function, so that the matrix element of two-electron interaction can be written out as

$$M_{\rm tot}(\mathbf{p},\varepsilon_n|\mathbf{k},\varepsilon_m) = M(\mathbf{p}-\mathbf{k}) \approx -2\alpha^2\,\frac{4\pi e^2}{|\mathbf{p}-\mathbf{k}|(\epsilon_\infty+1)} < 0\,. \qquad (40)$$

Here, $\alpha^2 < 1$ represents some numerical correction factor [86].

Now, we also have to take into account the screening of Coulomb interaction by the two-dimensional electron gas of FeSe. Then, in the random phase approximation (RPA) we get [86]

$$M_{\rm scr}(\mathbf{p}-\mathbf{k}) \approx -2\alpha^2\,\frac{4\pi e^2}{\epsilon_\infty}\,\frac{1}{|\mathbf{p}-\mathbf{k}| + 4e^2m/(\epsilon_\infty+1)}\,. \qquad (41)$$

In an experimental situation typical for FeSe/STO, the inverse screening length q_0 is small compared with Fermi momentum $p_{\rm F}$, so that the following inequality always holds:

$$\frac{p_{\rm F}}{q_0} = \frac{p_{\rm F}(\epsilon_\infty+1)}{e^2m} \gg 1\,. \qquad (42)$$

Introducing the effective Bohr radius $a_{\rm B} = (\epsilon_\infty+1)/(e^2m)$, this inequality can be rewritten as $p_{\rm F}a_{\rm B} \gg 1$.

In the weak coupling approximation, the linearized gap equation can be written out as [86]

$$\Delta(\mathbf{p}) = -T\sum_m \int \frac{{\rm d}^2k}{(2\pi)^2}\, M_{\rm scr}(\mathbf{p}-\mathbf{k})\, G(-\mathbf{k})\, G(\mathbf{k})\, \Delta(\mathbf{k})\,, \qquad (43)$$

where the product of two Green's functions is $G(-\mathbf{k})\,G(\mathbf{k}) = [\varepsilon_m^2 + \xi_{\mathbf{k}}^2]^{-1}$.

Then, after somewhat cumbersome, though direct, analysis, we can obtain the following result for the critical temperature $T_{\rm c}$:

$$T_{\rm c}(x) \sim \frac{p_{\rm F}^2}{2m}\exp\left(-\frac{1}{\alpha^2\lambda(x)}\right) = \frac{2}{ma_{\rm B}^2}\,x^2\exp\left(-\frac{1}{\alpha^2\lambda(x)}\right), \qquad (44)$$

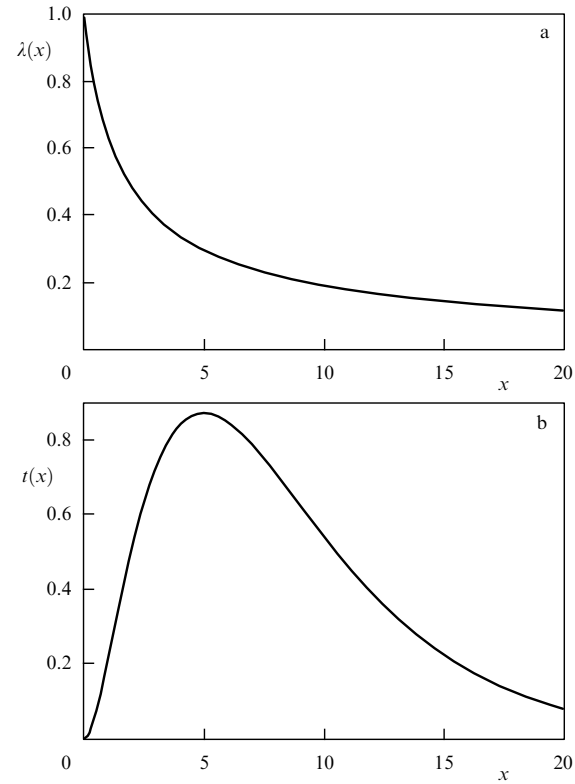

Figure 22. Dimensionless functions determining $T_{\rm c}$ in Gor'kov's model: (a) $\lambda(x)$ function, (b) $t(x) = x^2\exp(-1/\lambda(x))$ function.

where we have introduced the dimensionless parameter $x = (p_{\rm F}a_{\rm B})/2$, and

$$\lambda(x) = \frac{2}{\pi}\int_0^{\pi/2} \frac{{\rm d}u}{x\sin u + 1}\,. \qquad (45)$$

For our estimates, we can just put $\alpha^2 = 1$. Two dimensionless functions $\lambda(x)$ and $t(x) = x^2\exp(-1/\lambda(x))$ are plotted in Fig. 22. The maximum in $t(x)$ appears due to two competing factors: at a given value of $a_{\rm B}$, the critical temperature first grows with increasing electron concentration and then the increased screening suppresses the effective coupling constant.

Direct calculations [86] show that this model also reproduces the 'shadow' band in the electronic spectrum in the vicinity of point M. This is essentially due to the fact that from the form of pairing interaction (41) it becomes clear that Gor'kov's model also produces significant growth of interaction at small transferred momenta. The effective interaction is concentrated in the momentum region inside the inverse screening length q_0 satisfying inequality (42), so that $q_0 \ll 1/a$, in accordance with the estimates given above for the model with a dominant forward scattering.

Let us make the simplest estimate of the maximum value of $T_{\rm c}$ which can be achieved in this model. We put $E_{\rm F} = 60$ meV, which approximately corresponds to ARPES experiments. The maximum of $t(x)$, as can be seen from Fig. 22b, is close to $x = 5$, which corresponds to $\lambda(5) = 0.3$ (cf. Fig. 22a). Then it follows that $T_{\rm c} \approx 0.03 \times 60$ meV ≈ 20 K. Thus, this mechanism by itself cannot explain the values of $T_{\rm c} > 60$ K, observed in experiments on FeSe/STO.

However, in combination with some additional pairing interaction mechanism responsible for the initial value of $T_c \sim 8$ K in bulk FeSe (either due to the usual electron–phonon pairing mechanism or pairing due to exchange of antiferromagnetic fluctuations), we can obtain significantly higher values of T_c [86]. For example, if for the spin-fluctuation mechanism we make use of the estimate $T_c \sim E_F \exp(-1/\lambda_{sf})$, then at $E_F = 60$ meV the initial value of T_c is obtained for $\lambda_{sf} = 0.23$. Then, the combined pairing constant $\lambda = \lambda_{sf} + \lambda(5) = 0.48$ (assuming the same cut-off in the Cooper channel, the coupling constants are simply summed), leading to $T_c \approx 0.15 \times 60$ meV ≈ 90 K. In the case of combination with the conventional electron–phonon mechanism, we can estimate T_c using the upper curve (corresponding to $\mu = 0$) in Fig. 18b. Then, taking $\lambda_{op} = \lambda(5) = 0.3$, we immediately arrive at $T_c \approx 50$ K.

The situation with nonadiabatic effects in the model with a dominant forward scattering has recently been analyzed in Ref. [86] by direct calculations of vertex corrections to the electron–phonon interaction with the coupling constant $|g(\mathbf{q})|^2 = g_0^2 N \delta_{\mathbf{q}}$. It turned out that in this model the Migdal theorem breaks down for any values of the ratio Ω_0/E_F, which does not appear at all in vertex corrections. However, vertex corrections remain small for small values of the parameter $\lambda_m = g_0^2/\Omega_0^2$, and we have seen above that to explain the current experiments on FeSe/STO it is sufficient to keep the values of $\lambda_m \sim 0.15-0.20$.

The small values of Fermi energy E_F in the electron band at point M observed in intercalated FeSe systems and FeSe/STO (BTO) lead to one more important consequence. Typical values of the superconducting gap at low temperatures, observed in ARPES measurements on these systems, are $\Delta \sim 15-20$ meV (cf. Fig. 16). Correspondingly, here we have unusually large ratios $\Delta/E_F \sim 0.25-0.3$, which unambiguously points to the fact that these systems belong to the region of BCS–Bose crossover [90, 91], when the size of Cooper pairs, determined by coherence length ξ, becomes small and approaches the interelectron spacing, when $p_F\xi \sim \xi/a \sim 1$. The picture of superconducting transition and all estimates for physical characteristics like T_c in this region are different from those for the weak-coupling BCS theory and are closer to the picture of Bose–Einstein condensation of compact Cooper pairs [90, 91].

The emergence of such a situation was earlier noted in connection with some experiments on the $FeSe_xTe_{1-x}$ system [92], and also for bulk FeSe in an external magnetic field [93].

From the theoretical standpoint, we need here a special treatment [90, 91]. Unfortunately, a theoretical description of the BCS–Bose crossover for multiple-band systems like FeSe has remained, up to now, almost undeveloped. We can quote only the recent paper [94], but detailed discussion of different possibilities appearing here is outside the scope of the current review.

5. Conclusions

Basic conclusions from our discussion can be formulated as follows. A number of aspects of the physics of the systems under investigation are more or less clear:

• The electronic spectrum of intercalated FeSe systems and FeSe/STO (BTO) is significantly different from the spectrum of FeAs-based systems and bulk FeSe. Here, we have only electron-like Fermi surfaces surrounding the M points in the Brillouin zone. Hole-like Fermi surfaces 'sink' under the Fermi level. There are no 'nesting' properties of Fermi surfaces at all;

• The values of superconducting critical temperature T_c in intercalated systems are well correlated with the value of the total density of states at the Fermi level, obtained by LDA calculations, independently of the microscopic nature of pairing;

• Cooper pairing most probably reduces to the usual s-wave pairing; there is no possibility of $s^{\pm}$-pairing because of the absence of hole-like Fermi surfaces, while d-wave pairing also seems highly improbable;

• The record values of T_c observed in FeSe monolayers on STO (BTO) are apparently related to the additional pairing mechanism emerging, due to interaction with high-energy optical phonons of STO (BTO) in the geometry of the Ginzburg 'sandwich'. In this case, we may speak here of the realization of a 'pseudoexcitonic' pairing mechanism.

At the same time, many questions remain to be resolved:

• To date, the observation of the values of $T_c \sim 100$ K, reported in Ref. [25], has remained unconfirmed;

• The origin of unusually 'shallow' electron bands with extremely small values of the Fermi energy in the vicinity of M points remains unclear. This is probably related to our poor understanding of the role of electron correlations;

• The data on possible magnetically ordered phases in intercalated FeSe-based systems remain rather indeterminate. Practically nothing is known about the possible types of magnetic ordering in FeSe/STO (BTO) films;

• From the theoretical point of view, it remains obscure why the disappearance of some Fermi surfaces in FeSe systems is followed by a significant *increase* in T_c, contradicting general expectations based on the multiple-band BCS model;

• Practically no serious theoretical developments are known concerning possible manifestations of BCS–Bose crossover effects in these systems, their experimental consequences, or the role of these effects in the formation of high values of T_c.

Finally, let us discuss several proposals for possible ways to further increase T_c in FeSe monolayers on STO (or BTO). If we accept the concept of the decisive role of interactions with elementary excitations in the substrate (most probably with optical phonons), the natural idea appears of creating multiple-layer films and superstructures, like those demonstrated in Fig. 23 [81]. In particular, the structure shown in Fig. 23a is the direct realization of the Ginzburg 'sandwich', precisely as was proposed in his original work [1–3]. It seems

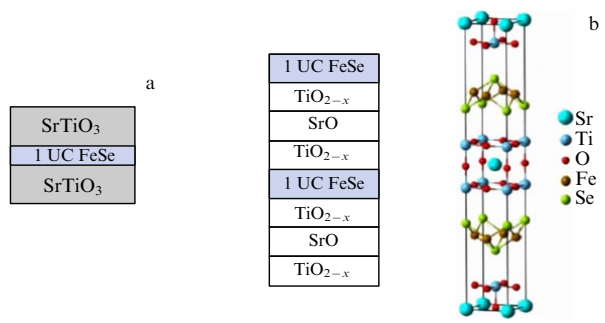

Figure 23. Possible FeSe/STO-based superstructures, where an increase in T_c can be expected [81]: (a) Ginzburg's 'sandwich' with two STO layers, and (b) multiple-layer superstructure.

obvious that the presence of the second $SrTiO_3$ layer (or the similar $BaTiO_3$ layer) will lead to the effective enhancement of the pairing constant due to interaction with optical phonons in the second STO layer. Obviously, the presence of the second STO layer will also serve as a good protection of the conductive FeSe layer from the external environment. Similarly, attempts to create bulk superstructures (compounds), like those shown in Fig. 23b, seem to be very promising. Despite all the technical problems appearing on the path to creating such structures (or their analogues), this way seems to have great potential. There is no doubt that the last word on studies of high-temperature superconductivity in FeSe-based monolayers and other similar systems is yet to be heard.

The author is grateful to E Z Kuchinskii and I A Nekrasov for discussions on a number of problems dealt with in this review, as well as for their help with some numerical computations.

This research was supported by the Russian Science Foundation grant No. 14-12-00502. Calculations of the electronic spectra of FeSe systems and the comparative analysis of mechanisms of Cooper pairing were performed under FASO State contract No. 0389-2014-0001 with a partial support from RFBR grant No. 14-02-00065.

Notes added in proof

During the time after the submission of this review, a number of new experimental and theoretical studies dealing with the systems under discussion have appeared in the literature. Below, we cite some of them with brief comments.

In Ref. [95], single-layer FeSe films on STO were studied at different doping levels, which were achieved by surface deposition of potassium *in situ*. A sharp growth of T_c from 60 K to 75 K was observed, accompanied by a Lifshits transition with the formation of a small *electron-like* pocket of the Fermi surface around point Γ, which was confirmed by ARPES measurements. Notice that such T_c behavior is in complete accordance with qualitative conclusions of the multiple-band superconductivity theory, discussed in our review.

Important results were achieved in Ref. [96], where high values of $T_c \sim 65$ K were obtained for FeSe monolayers on the (100) plane of rutile TiO_2. These results give evidence that the ferroelectric properties of $SrTiO_3$ (absent for TiO_2) are irrelevant for T_c growth in the systems under discussion and almost unambiguously confirm the important role of interactions with longitudinal optical phonons in the substrate, which in TiO_2 are practically the same as in STO. The electronic spectrum of FeSe films on TiO_2 measured by ARPES was observed to be practically the same as in FeSe/STO, with a 'replica' band clearly observed approximately 100 meV below the electron band at point M, similar to that observed in FeSe/STO [49].

Experiments carried out in Ref. [97] and taking advantage of high-resolution electron energy loss spectroscopy (HREELS) confirmed the presence of strong electron–phonon interaction at the FeSe/STO interface, giving an experimental estimate of the coupling constant with a 92-meV optical phonon in STO of ~ 1.

Theoretical results of Refs [49, 81, 84, 85] were critically reconsidered in Ref. [98]. However, the qualitative conclusion about the important role of a dominant forward scattering of electrons in the FeSe monolayer by the optical phonons of $SrTiO_3$ for an increase in T_c in FeSe/STO was essentially confirmed.

In Ref. [99], the '*first principles*' calculations of electron–phonon coupling in the FeSe/STO system were performed, confirming the significant enhancement of this interaction in the region of small transferred momenta. However, the numerical values of the corresponding coupling constant were too low to explain the experimentally observed high values of T_c. At the same time, it should be noted that calculations of the electronic spectrum for the FeSe/STO system done in this study were made neglecting the possible role of electron correlations, and spectra obtained were quite different from those observed in ARPES experiments (absence of the 'shallow' band). Thus, the conclusions about the value of the coupling constant made in this study may be rather approximate.

Gor'kov's approach to explaining superconductivity in $SrTiO_3$ [88] was criticized in Refs [100, 101]. In principle, this criticism can be extended to Refs [86, 87] dealing with superconductivity in FeSe/STO. At the same time, the use of phenomenological values of dielectric permeabilities at the FeSe/STO interface in [86, 87] makes the arguments reported in Refs [100, 101] only partly relevant for this case.

Finally, we can mention the recent rather detailed review of experiments on intercalated $A_xFe_2Se_2$ type systems [102].

References

1. Ginzburg V L *Contemp. Phys.* **9** 355 (1968); *Usp. Fiz. Nauk* **95** 91 (1968)
2. Ginzburg V L *Sov. Phys. Usp.* **13** 335 (1970); *Usp. Fiz. Nauk* **101** 185 (1970)
3. Ginzburg V L *Sov. Phys. Usp.* **19** 174 (1976); *Usp. Fiz. Nauk* **118** 315 (1976)
4. Ginzburg V L, Kirzhnits D A (Eds) *High-Temperature Superconductivity* (New York: Consultants Bureau, 1982); Translated from Russian: *Problema Vysokotemperaturnoi Sverkhprovodimosti* (Moscow: Nauka, 1977)
5. Sadovskii M V *Phys. Usp.* **51** 1201 (2008); *Usp. Fiz. Nauk* **178** 1243 (2008)
6. Ishida K, Nakai Y, Hosono H *J. Phys. Soc. Jpn.* **78** 062001 (2009)
7. Johnson D C *Adv. Phys.* **59** 83 (2010)
8. Hirschfeld P J, Korshunov M M, Mazin I I *Rep. Prog. Phys.* **74** 124508 (2011)
9. Stewart G R *Rev. Mod. Phys.* **83** 1589 (2011)
10. Kordyuk A A *Low Temp. Phys.* **38** 888 (2012); *Fiz. Nizk. Temp.* **38** 1119 (2012)
11. Mizuguchi Y, Takano Y *J. Phys. Soc. Jpn.* **79** 102001 (2010)
12. Sadovskii M V, Kuchinskii E Z, Nekrasov I A *J. Magn. Magn. Mater.* **324** 3481 (2012)
13. Nekrasov I A, Sadovskii M V *JETP Lett.* **99** 598 (2014); *Pis'ma Zh. Eksp. Teor. Fiz.* **99** 687 (2014)
14. Bozovic I, Ahn C *Nature Phys.* **10** 892 (2014)
15. Vivanco H K, Rodriguez E E *J. Solid State Chem.* **242** 3 (2016); arXiv:1603.02334
16. Guo J et al. *Phys. Rev. B* **82** 180520(R) (2010)
17. Yan Y J et al. *Chin. Sci. Rep.* **2** 212 (2012)
18. Hatakeda T et al. *J. Phys. Soc. Jpn.* **82** 123705 (2013)
19. Burrard-Lucas M et al. *Nature Mater.* **12** 15 (2013)
20. Lu X F et al. *Nature Mater.* **14** 325 (2015)
21. Pachmayr U et al. *Angew. Chem. Int. Ed.* **54** 293 (2015)
22. Lynn J W et al. *Phys. Rev. B* **92** 060510(R) (2015)
23. Nejadsattari F, Stadnik Z M *J. Alloys Comp.* **652** 470 (2015)
24. Wang Q-Y et al. *Chin. Phys. Lett.* **29** 037402 (2012)
25. Ge J-F et al. *Nature Mater.* **14** 285 (2015)
26. Miyata Y et al. *Nature Mater.* **14** 775 (2015)
27. Zhou G et al. *Appl. Phys. Lett.* **108** 202603 (2016); arXiv:1512.01948
28. Peng R et al. *Nature Commun.* **5** 5044 (2014)
29. Ding H et al. *Phys. Rev. Lett.* **117** 067001 (2016); arXiv:1603.00999
30. Song C-L et al. *Phys. Rev. B* **84** 020503(R) (2011)
31. Liu X et al. *J. Phys. Condens. Matter* **27** 183201 (2015)

32. Kuchinskii E Z, Sadovskii M V *JETP Lett*. **91** 660 (2010); *Pis'ma Zh. Eksp. Teor. Fiz*. **91** 729 (2010)
33. Skornyakov S L et al. *Phys. Rev. B* **80** 092501 (2009)
34. Nekrasov I A, Pavlov N S, Sadovskii M V *JETP Lett*. **102** 26 (2015); *Pis'ma Zh. Eksp. Teor. Fiz*. **102** 30 (2015)
35. Nekrasov I A, Sadovskii M V *JETP Lett*. **93** 166 (2011); *Pis'ma Zh. Eksp. Teor. Fiz*. **93** 182 (2011)
36. Shein I R, Ivanovskii A L *Phys. Lett. A* **375** 1028 (2011)
37. Nekrasov I A, Pchelkina Z V, Sadovskii M V *JETP Lett*. **88** 144 (2008); *Pis'ma Zh. Eksp. Teor. Fiz*. **88** 155 (2008)
38. Zhao L et al. *Phys. Rev. B* **83** 140508(R) (2011)
39. Nekrasov I A, Pavlov N S, Sadovskii M V *JETP Lett*. **97** 15 (2013); *Pis'ma Zh. Eksp. Teor. Fiz*. **97** 18 (2013)
40. Nekrasov I A, Pavlov N S, Sadovskii M V *JETP* **117** 926 (2013); *Zh. Eksp. Teor. Fiz*. **144** 1061 (2013)
41. Nekrasov I A, Pavlov N S, Sadovskii M V *JETP Lett*. **95** 581 (2012); *Pis'ma Zh. Eksp. Teor. Fiz*. **95** 659 (2012)
42. Nekrasov I A, Pavlov N S, Sadovskii M V *JETP* **116** 620 (2013); *Zh. Eksp. Teor. Fiz*. **143** 713 (2013)
43. Yi M et al. *Phys. Rev. Lett*. **110** 067003 (2013)
44. Niu X H et al. *Phys. Rev. B* **93** 054516 (2016)
45. Nekrasov I A, Sadovskii M V *JETP Lett*. **101** 47 (2015); *Pis'ma Zh. Eksp. Teor. Fiz*. **101** 50 (2015)
46. Niu X H et al. *Phys. Rev. B* **92** 060504(R) (2015)
47. Nekrasov I A, Pavlov N S, Sadovskii M V, Slobodchikov A A *Low Temp. Phys*. **42** 891 (2016); *Fiz. Nizk. Temp*. **42** 1137 (2016); arXiv:1605.02404
48. Liu D et al. *Nature Commun*. **3** 931 (2012)
49. Lee J J et al. *Nature* **515** 245 (2014)
50. Zhao L et al. *Nature Commun*. **7** 10608 (2016)
51. Fu H, Reich K V, Shklovskii B I *JETP* **122** 456 (2016); *Zh. Eksp. Teor. Fiz*. **149** 530 (2016)
52. Zhou Y, Mills A J *Phys. Rev. B* **93** 224506 (2016); arXiv:1603.02728
53. Chen M X, Agterberg D F, Weinert M, arXiv:1603.03841
54. Shaolong H et al. *Nature Mater*. **12** 605 (2013)
55. He J et al. *Proc. Natl. Acad. Sci. USA* **111** 18501 (2014)
56. Mizuguhci Y et al. *Supercond. Sci. Technol*. **23** 054013 (2010)
57. Kuchinskii E Z, Nekrasov I A, Sadovskii M V *JETP Lett*. **91** 518 (2010); *Pis'ma Zh. Eksp. Teor. Fiz*. **91** 567 (2010)
58. Miyata Y et al. *Nature Mater*. **14** 775 (2015)
59. Wen C H P et al. *Nature Commun*. **7** 10840 (2016)
60. Ye Z R et al., arXiv:1512.02526
61. Zheng F et al. *Phys. Rev. B* **93** 075428 (2016)
62. Shiogai J et al. *Nature Phys*. **12** 42 (2016)
63. Hanzawa K et al. *Proc. Natl. Acad. Sci. USA* **113** 3986 (2016); arXiv:1508.07689
64. Lei B et al. *Phys. Rev. Lett*. **116** 077002 (2016)
65. Barzykin V, Gor'kov L P *JETP Lett*. **88** 131 (2008); *Pis'ma Zh. Eksp. Teor. Fiz*. **88** 142 (2008)
66. Kuchinskii E Z, Sadovskii M V *JETP Lett*. **89** 156 (2009); *Pis'ma Zh. Eksp. Teor. Fiz*. **89** 176 (2009)
67. Chen X et al. *Phys. Rev. B* **92** 224514 (2015)
68. Kuchinskii E Z, Sadovskii M V *Physica C* **470** S418 (2010)
69. Sato T et al. *Phys. Rev. Lett*. **103** 047002 (2009)
70. Sekiba Y et al. *New J. Phys*. **11** 025020 (2009)
71. Fan Q et al. *Nature Phys*. **11** 946 (2015)
72. van Benthem K, Elsässer C, French R H *J. Appl. Phys*. **90** 6156 (2001)
73. Müller K A, Burkard H *Phys. Rev. B* **19** 3593 (1979)
74. Koonce C S et al. *Phys. Rev*. **163** 380 (1967)
75. Lin X et al. *Phys. Rev. X* **3** 021002 (2013)
76. Allender D, Bray J, Bardeen J *Phys. Rev. B* **7** 1020 (1973)
77. Inkson J C, Anderson P W *Phys. Rev. B* **8** 4429 (1973)
78. Uspenskii Yu A, Zharkov G F *Sov. Phys. JETP* **38** 1254 (1974); *Zh. Eksp. Teor. Fiz*. **65** 2511 (1974)
79. Allender D, Bray J, Bardeen J *Phys. Rev. B* **8** 4433 (1973)
80. Choudhury N et al. *Phys. Rev. B* **77** 134111 (2008)
81. Lee D-H, arXiv:1508.02461
82. Danylenko O V et al. *Eur. Phys. J. B* **9** 201 (1999)
83. Kulić M L *AIP Conf. Proc*. **715** 75 (2004)
84. Rademaker L et al. *New J. Phys*. **18** 022001 (2016)
85. Wang Y et al. *Supercond. Sci. Technol*. **29** 054009 (2016); arXiv: 1602.00656
86. Gor'kov L P *Phys. Rev. B* **93** 060507(R) (2016)
87. Gor'kov L P *Phys. Rev. B* **93** 054517 (2016)
88. Gor'kov L P *Proc. Natl. Acad. Sci. USA* **113** 4646 (2016); arXiv: 1508.00529
89. Wang S Q, Mahan G D *Phys. Rev. B* **6** 4517 (1972)
90. Nozières P, Schmitt-Rink S *J. Low. Temp. Phys*. **59** 195 (1985)
91. Randeria M, in *Bose–Einstein Condensation* (Eds A Griffin, D W Snoke, S Stringari) (Cambridge: Cambridge Univ. Press, 1995) p. 355
92. Lubashevsky Y et al. *Nature Phys*. **8** 309 (2012)
93. Kasahara S et al. *Proc. Natl. Acad. Sci. USA* **111** 16309 (2014)
94. Chubukov A V, Eremin I, Efremov D V *Phys. Rev. B* **93** 174516 (2016); arXiv:1601.01678
95. Shi X et al., arXiv:1606.01470
96. Rebec S N et al., arXiv:1606.09358
97. Zhang S et al. *Phys. Rev. B* **94** 081116(R) (2016); arXiv:1605.06941
98. Kulić M L, Dolgov O V, arXiv:1607.00843
99. Wang Y et al. *Phys. Rev. B* **93** 134513 (2016); arXiv:1602.03288
100. Ruhman J, Lee P A, arXiv:1605.01737
101. Klimin S N et al., arXiv:1606.00644
102. Krzton-Maziopa A et al. *J. Phys. Condens. Matter* **28** 293002 (2016)

 © 2021 Uspekhi Fizicheskikh Nauk, Russian Academy of Sciences

PHYSICS OF OUR DAYS PACS numbers: 72.10.Di, 72.15.Cz, 72.15.Lh

Planckian relaxation delusion in metals

M V Sadovskii

DOI: https://doi.org/10.3367/UFNe.2020.08.038821

Contents

1. **Introduction** **175**
2. **Experiments** **176**
3. **Quantum estimates for resistivity of metals** **179**
   3.1 Ioffe–Regel limit; 3.2 Planckian relaxation; 3.3 Electron–phonon interaction
4. **Elementary model of scattering by quantum fluctuations in metals** **181**
   4.1 Scattering by quantum fluctuations; 4.2 Phonons; 4.3 More general model; 4.4 Vicinity of the quantum critical point
5. **General relations for the Green's function and conductivity** **184**
   5.1 Green's function for a system of interacting particles; 5.2 General expressions for conductivity; 5.3 Self-consistent calculation; 5.4 Planckian relaxation delusion; 5.5 Once again on the uncertainty principle
6. **Conclusions** **188**

Appendix. Momentum distribution in the case of Planckian relaxation **189**

References **190**

Abstract. We present a critical review of recent attempts to introduce a new quantum ('Planckian') limit for the temperature dependence of the inelastic scattering rate of electrons in metals. We briefly discuss the main experimental facts and some simple theoretical models explaining the linear-in-temperature growth of resistivity (starting from very low temperatures) in superconducting cuprates and some similar systems. There is no commonly accepted theoretical explanation for such behavior up to now. We also discuss the known quantum limits for electrical conductivity (resistance). It is shown that the universal Planckian limit for the inelastic relaxation rate proposed in some papers is a kind of delusion related to a certain procedure to represent the experimental data.

Keywords: resistivity of metals, relaxation time, effective mass, quantum fluctuations, high-temperature superconductors

1. Introduction

Linear in temperature (T-linear) growth of electrical resistivity of cuprates and some other correlated systems in the wide temperature region from pretty low to rather high temperatures has remained among the most challenging problems of the physics of high-temperature superconductors (HTSCs) for many years. Observed in cuprates since the early experiments [1, 2], it became one of the marked properties of these compounds in the normal phase in optimally doped systems, starting with the temperature of the superconducting transition T_c and continuing up to the highest temperatures achievable before the samples are destroyed. Later, a similar behavior of resistivity was also observed in some other systems.

By itself, the T-linear growth of resistivity in metals is not at all surprising: it is practically always observed, though at fairly high temperatures $T > \Theta_D/5$, where Θ_D is the Debye temperature, which is usually several hundred degrees. What is surprising is the fact that the T-linear growth in cuprates takes place starting at significantly lower temperatures. The commonly accepted explanation for such behavior is still lacking, though over the years a number of theoretical models with a purported explanation were proposed. But this is not the aim of the current paper.

The fact of the matter is that recently a number of interesting papers have appeared [3, 4] in which, after rather detailed analyses of a wide range of experimental material on many compounds, it was shown that, in the T-linear region of resistivity, the scattering rate of electrons (inverse relaxation time) is pretty accurately described by the dependence $\Gamma(T) = 1/\tau = \alpha k_B T/\hbar$, where $\alpha \sim 1$, and k_B is the Boltzmann constant, which weakly varies from one material to another. In particular, for systems in the vicinity of quantum critical points (on the phase diagram of cuprates and some similar systems), the value of α is in the interval of 0.7–1.1 and is seemingly universal and independent of the strength of interaction, leading to relaxation of the electronic current. Furthermore, it was discovered that a similar dependence gives a rather good description of the data for a number of usual metals (Cu, Au, Al, Ag, Pb, Nb, etc.) in the T-linear region of their resistivity. In this case, the values of α belong to a noticeably wider interval from 0.7 to 2.8 [3, 4]. In connection with these (and similar) results, the concept of the universal (independent of interaction strength) 'Planckian' *upper* limit of the scattering rate $1/\tau_P = \Gamma_P \sim k_B T/\hbar$ was introduced in Ref. [5].

M V Sadovskii Institute of Electrophysics,
Ural Branch of the Russian Academy of Sciences,
ul. Amundsena 106, 620016 Ekaterinburg, Russian Federation
E-mail: sadovski@iep.uran.ru

Received 5 August 2020
Uspekhi Fizicheskikh Nauk **191** (2) 182 – 198 (2021)
Translated by M V Sadovskii

Below, we shall present a short review of the relevant experimental data and discuss some theoretical models, imposing quantum limitations on the resistivity of metals, with the aim of understanding the degree of validity of the concept of 'Planckian' relaxation in metals.

2. Experiments

The temperature dependence of resistivity at quite low temperatures ($T < 0.2\Theta_D \ll E_F$, Θ_D — Debye temperature, E_F — Fermi energy) is described by the following expression:

$$\rho(T) = \rho_0 + \rho_T(T) = \rho_0 + a_{ee}\left(\frac{k_B T}{E_F}\right)^2 + a_{ep}\left(\frac{T}{\Theta_D}\right)^5, \quad (1)$$

where ρ_0 is residual resistivity at zero temperature due to impurity scattering, the second term is the contribution of electron–electron scattering, while the third term is the low temperature contribution from electron–phonon scattering, described by the Bloch–Grüneisen theory [6]. For fairly high temperatures $T > 0.2\Theta_D$, this theory gives

$$\rho(T) - \rho_0 = AT. \quad (2)$$

This behavior of resistivity is clearly seen in experiments, as shown in Fig. 1, where we show the data for a number of simple metals [7]. These results show that the temperature dependence of resistivity (conductivity) is almost totally related to the processes of inelastic scattering by phonons. In the case of a significant contribution of scattering by other collective excitations, e.g., spin fluctuations, we can write down in fact very similar expressions.

From these data, it is seen that for temperatures $T > \Theta_D/5$ the resistivity of a metal grows linearly with temperature. In most metals, $\Theta_D \sim 200-600$ K. At the same time, the critical temperature of the superconducting transition in cuprates is commonly several dozen degrees, so that $T_c \sim \Theta_D/5$. Thus, for a rather long time there was a hope [8] that T-linear growth of resistivity in cuprates could be explained by the usual electron–phonon scattering, taking into account that it takes place outside the region of low temperature power — like growth, which is masked by a superconducting transition. There were some cases of a few exceptional samples with low values of T_c, where T-linear growth of resistivity was observed starting from anomalously low temperatures $T < 10$ K [9], but these were rather rare. There were no experiments in the normal phase at low enough temperatures simply because the destruction of the superconducting state in typical cuprates required extremely strong magnetic fields.

This situation changed in recent years after such experiments were successfully performed [3, 4]. These studies presented data on resistivity in a number of high-temperature cuprate superconductors as well as in some analogous systems in very high magnetic fields, suppressing superconductivity. A detailed analysis of these experiments and data obtained by other authors has shown that T-linear behavior of resistivity is conserved in the normal phase, in many cases, up to the lowest temperatures.

Typical examples of experimental data from Refs [3, 4] are shown in Figs 2–4. In these papers, characterized by the very detailed analysis of the experimental situation, many additional data can be found. These results further complicated the question of the nature of T-linear resistivity in the systems under consideration. It should be stressed from the very beginning that this problem remains unsolved to date, but its analysis is not the aim of the present work.

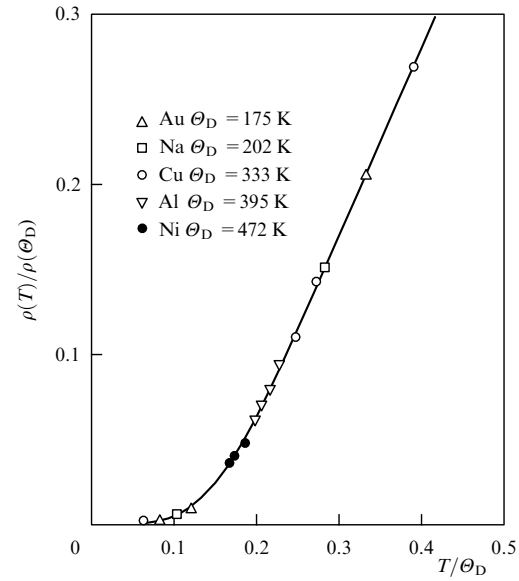

Figure 1. Temperature dependence of resistivity for typical metals [7].

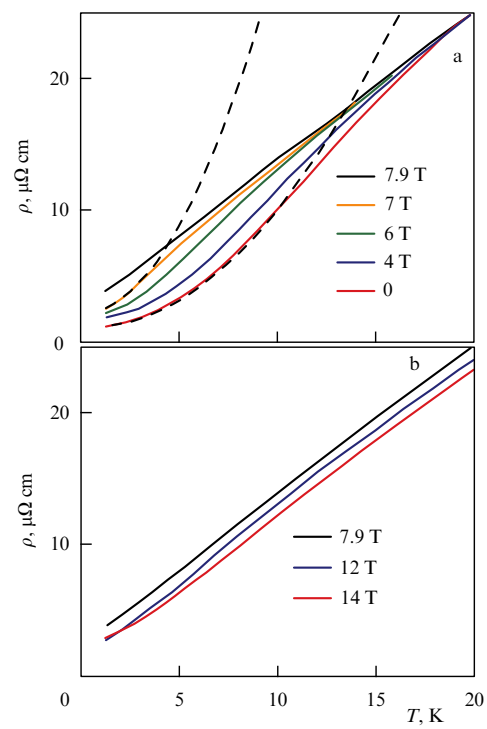

Figure 2. (Color online.) (a) Resistivity ρ as a function of temperature T of a very pure single crystal of $Sr_3Ru_2O_7$ in a zero magnetic field (red line), 4 T (blue), 6 T (green), 7 T (orange) magnetic fields and in critical field $H_c = 7.9$ T (black), corresponding to the quantum critical point (H_c, $T = 0$). Dashed lines — a fit to $\rho_0 + AT^2$ dependence at low temperatures, which demonstrates the narrowing of the region of quadratic dependence on temperature and crossover to linear dependence [3]. (b) Temperature dependence of resistivity ρ in fields H_c (black), 12 T (blue), and 14 T (red) [3].

For us, the main focus now is the analysis of experimental data presented in Refs [3, 4], which allowed the authors to determine the temperature dependence of relaxation time τ

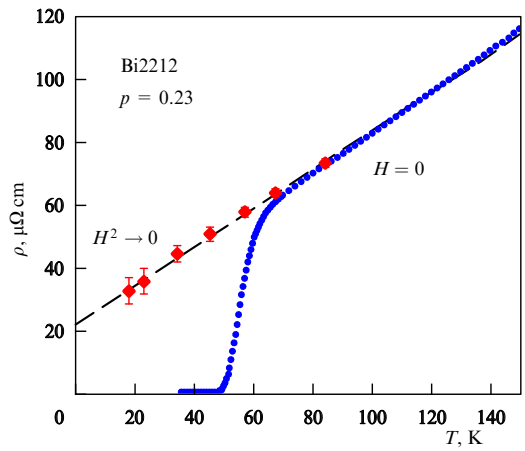

Figure 3. (Color online.) Resistivity of a Bi2212 thin film as a function of temperature for $H = 0$ (blue curve). Red diamonds (and dashed line) show resistivity in the normal phase for $T < T_c$, obtained by suppressing superconductivity by an external magnetic field and extrapolation from the $\rho = a + bH^2$ dependence [4].

from the values of resistivity and to attain rather unexpected results and reach unanticipated conclusions.

The main idea of the analysis performed in Refs [3, 4] was as follows. Let us write the Drude expression for conductivity as

$$\sigma = \frac{ne^2\tau}{m^\star} = \frac{ne^2 v_F \tau}{\hbar k_F}\,, \tag{3}$$

where v_F is the electron velocity on the Fermi surface, $m^\star$ is the effective mass, and $p_F = m^\star v_F = \hbar k_F$ is the Fermi momentum. Correspondingly, for resistivity we have[1]

$$\rho = \frac{m^\star}{ne^2\tau} = \frac{\hbar k_F}{ne^2 v_F \tau}\,. \tag{4}$$

The effective mass $m^\star$ or the value of $\hbar k_F/v_F$ in Refs [3, 4] were determined from the electron contribution to the specific heat, which can be measured at low temperatures, or from measurements of the de Haas–van Alphen effect, which are

[1] For shortness, we write here all expressions for the one-band model. In the multiple band case, we have to take into account contributions from all pockets of the Fermi surface. Appropriate expressions can be found in Refs [3, 4].

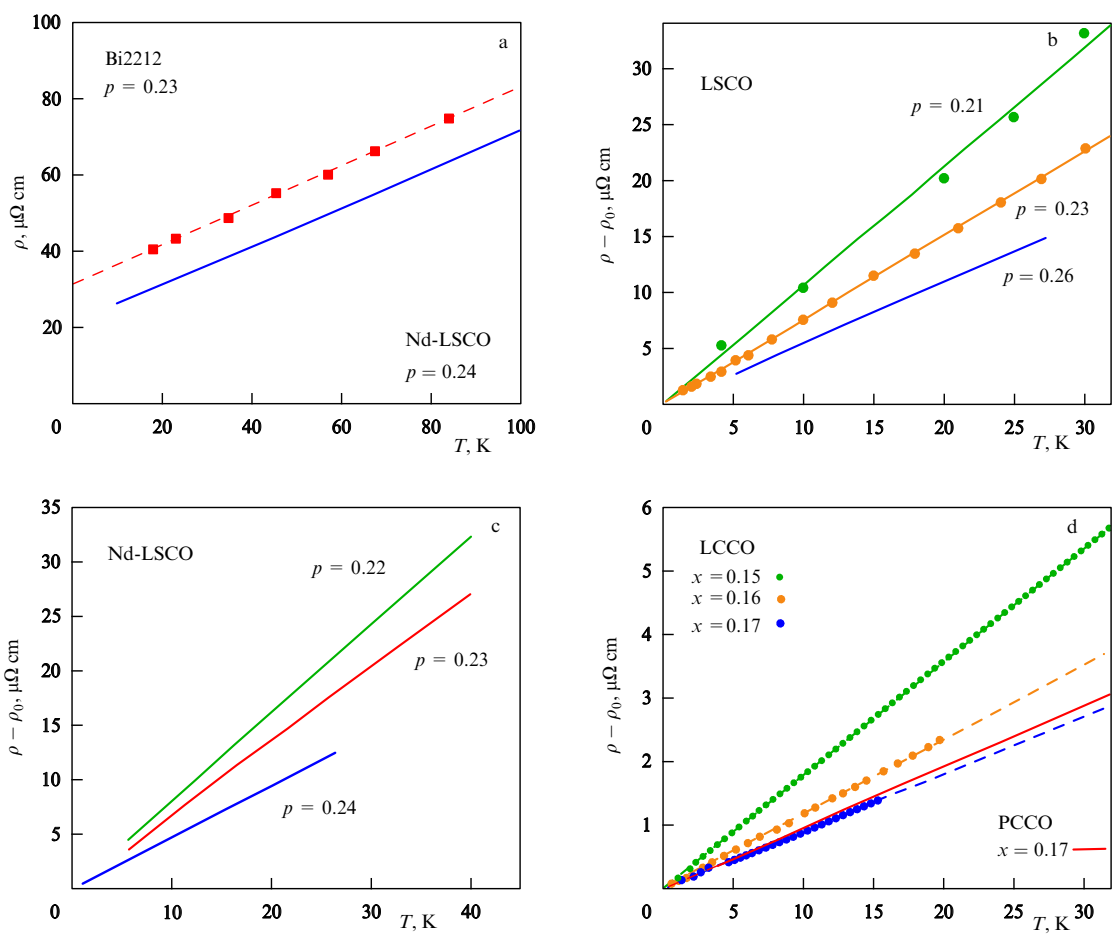

Figure 4. (Color online.) Linear in temperature dependence of resistivity in overdoped cuprates showing the behavior of ρ in highly-conducting plane (i.e., ρ_{ab}) in (a) Nd-LSCO for $p = 0.24$ (blue line, $H = 16$ T) and Bi2212 for $p = 0.23$ (red symbols, $H = 55$ T); (b) $\rho(T) - \rho_0$ in LSCO for $p = 0.21$ (green symbols, $H = 48$ T) and $p = 0.23$ (orange, $H = 48$ T), $p = 0.26$ (blue, $H = 18$ T); (c) $\rho(T) - \rho_0$ in Nd-LSCO at $H = 33$ T for $p = 0.22$ (green), $p = 0.23$ (orange), and $p = 0.24$ (blue); (d) $\rho(T) - \rho_0$ in LCCO for $x = 0.16$ (orange, $H = 6.5$ T) and $x = 0.17$ (blue, $H = 4$ T), and PCCO for $x = 0.17$ (red, $H = 16$ T) [4].

Table 1. Experimental values of some parameters for a number of quasi-two-dimensional systems.

Compound	Doping	n, 10^{27} m^{-3}	$m^\star/m_0$	A/d, Ω K^{-1}	α
$Bi_2Sr_2CaCu_2O_{8-\delta}$ (Bi2212)	$p = 0.23$	6.8	8.4 ± 1.6	8.0 ± 0.9	1.1 ± 0.3
$Bi_2Sr_2CuO_{6+\delta}$ (Bi2201)	$p = 0.40$	3.5	7 ± 1.5	8 ± 2	1.0 ± 0.4
$La_{2-x}Sr_xCuO_4$ (LSCO)	$p = 0.26$	7.8	9.8 ± 1.7	8.2 ± 1.0	0.9 ± 0.3
$La_{1.6-x}Nd_{0.4}Sr_xCuO_4$ (Nd-LSCO)	$p = 0.24$	7.9	12 ± 4	7.4 ± 0.8	0.7 ± 0.4
$Pr_{2-x}Ce_xCuO_{4\pm\delta}$ (PCCO)	$x = 0.17$	8.8	2.4 ± 0.1	1.7 ± 0.3	0.8 ± 0.2
$La_{2-x}Ce_xCu_4$ (LCCO)	$x = 0.15$	9.0	3.0 ± 0.3	3.0 ± 0.45	1.2 ± 0.3
$(TMTSF)_2PF_6$ (TMTSF)	$P = 11$ kbar	1.4	1.15 ± 0.2	2.8 ± 0.45	1.0 ± 0.3

also made at fairly low temperatures. These measurements in fact determine the value of the effective mass $m^\star$ and Fermi wave vector k_F as some average values for each of the pockets of the Fermi surface.

Electron density n, entering expressions (3) and (4), can be calculated (for systems of different dimensionality) as

$$n = \frac{2k_F}{\pi d_b d_c} \quad \text{(quasi-one-dimensional case)}\,, \tag{5}$$

$$n = \frac{k_F^2}{2\pi d} \quad \text{(quasi-two-dimensional case)}\,, \tag{6}$$

$$n = \frac{k_F^3}{3\pi^2} \quad \text{(three-dimensional case)}\,, \tag{7}$$

where d_b and d_c are the distances between adjacent conducting chains (oriented along the a axis) in the directions of the b and c axes in a quasi-one-dimensional system, while d is the distance between adjacent conducting planes in the quasi-two-dimensional case.

If we express the temperature-dependent part of resistivity as in (2) and introduce the T-linear (Planckian) relaxation rate as

$$\Gamma = \frac{1}{\tau} = \alpha\,\frac{k_B T}{\hbar}\,, \quad \alpha \sim \text{const}\,, \tag{8}$$

we immediately obtain

$$A = \frac{d\rho}{dT} = \alpha\,\frac{k_B}{\hbar}\,\frac{m^\star}{ne^2} \quad \text{or} \tag{9}$$

$$\frac{ne^2}{k_B k_F}\,\frac{d\rho}{dT} = \alpha\,\frac{m^\star}{\hbar k_F} = \frac{\alpha}{v_F}\,, \tag{10}$$

which gives working formulae to represent experimental data in the T-linear region of resistivity [3, 4].

In Refs [3, 4], a very detailed analysis of experimental data was performed for a rather wide set of systems (compounds) with very different electronic structures, from high-temperature superconducting copper oxides and iron-based superconductors to organic metals like $(TMTSF)_2PF_6$, to compounds like $Sr_3Ru_2O_7$, $CeCoIn_5$, UPt_3, $CeRu_2Si_2$, where a T-linear growth of resistivity is observed.

It was discovered that, for all these quite different systems, the experimental data for the thus defined relaxation rate are well described by a dependence like (8), and the value of α for the majority of these systems falls in the interval 0.7–1.1 and seems to be universal (independent of the peculiarities of the electronic spectrum or the strength of interaction, leading to the scattering of electrons). Moreover, it was also shown that a similar dependence appropriately describes the data for a number of usual metals as well (Cu, Au, Al, Ag, Pb, Nb), though the values of α for them are in a wider interval from 0.7–2.8 [3, 4].

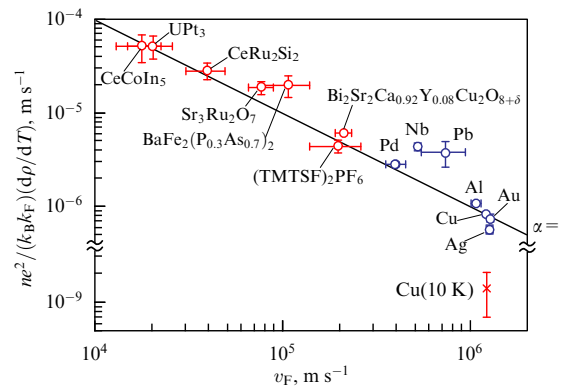

Figure 5. (Color online.) General picture for different metals (different Fermi velocities v_F), demonstrating the T-linear growth of resistivity. These metals include heavy-fermion systems, oxides, pnictides, and organic metals, where the T-linear growth of resistivity at low temperatures appears after the application of a magnetic field or change in the chemical composition or external hydrostatic pressure. Analogous data represent the situation in common metals with T-linear behavior of resistivity at fairly high temperatures (blue symbols), while for lower temperatures their resistivity is orders of magnitude smaller (appropriate value for Cu at $T = 10$ K is shown in the lower-right corner). The straight line, denoted by $\alpha = 1$, corresponds to $(\tau T)^{-1} = k_B/\hbar$ [4].

In Table 1, we show, as an example, the experimental values of some parameters under discussion, determined in Ref. [4], for a number of quasi-two-dimensional systems (hole doped and electron doped cuprates, organics).

In Refs [3, 4], further details can be found on similar data for all the systems mentioned above.

All this is nicely illustrated by the consolidated graph shown in Fig. 5, where data are shown on a logarithmic scale representing Eqn (10). These results seem to be quite nontrivial and apparently confirm the concept of the universal 'Planckian' mechanism of electronic relaxation in metals, which was introduced earlier [5] and applied to cuprate physics. Furthermore, the value of $\alpha \sim 1$, which is observed for such a wide set of materials with very different electronic spectra and quite different Fermi surfaces, suggests the idea that (8) is actually the universal quantum *upper* limit for the inelastic (temperature-dependent) relaxation rate for electrons in metals.

To explain such temperature behavior of resistivity for such different systems from the lowest temperatures, a number of complicated theoretical models were recently proposed [10–13], including some very exotic ones taken from the physics of black holes, cosmology, and superstring theory (see, e.g., [14–17]). Below, we shall limit ourselves to a simple analysis based on the traditional approaches of the quantum theory of solids.

3. Quantum estimates for resistivity of metals

Let us recall some elementary theoretical estimates with respect to the conductivity (resistivity) of metals. Drude expressions for elastic and inelastic scattering are written as

$$\sigma_0 = \frac{ne^2}{m}\,\tau_0\,, \qquad \rho_0 = \frac{m}{ne^2}\,\frac{1}{\tau_0}\,, \tag{11}$$

$$\sigma_{\rm i}(T) = \frac{ne^2}{m}\,\tau(T)\,, \qquad \rho_{\rm i}(T) = \frac{m}{ne^2}\,\frac{1}{\tau(T)}\,, \tag{12}$$

where τ_0 is the mean free time due to elastic impurity scattering, determining the residual resistivity, and $\tau(T)$ is relaxation time due to inelastic scattering by phonons (or some other collective excitations), or due to electron–electron scatterings. Mass m here is always understood as free electron mass (band structure mass in a solid!), which *does not include* corrections due to electron-electron or electron-phonon interactions (see more details below). Then, assuming the additive contributions of different scattering mechanisms (Matissen rule), the total resistivity is written as

$$\rho(T) = \frac{m}{ne^2}\left(\frac{1}{\tau_0} + \frac{1}{\tau(T)}\right) \equiv \frac{m}{ne^2}\left(\Gamma_0 + \Gamma(T)\right), \tag{13}$$

where we have introduced the appropriate scattering rates:

$$\Gamma_0 = \frac{1}{\tau_0}\,, \tag{14}$$

$$\Gamma(T) = \frac{1}{\tau(T)}\,. \tag{15}$$

In the general theory of interacting fermions (electrons), by order of magnitude we have $\Gamma \sim \operatorname{Im}\Sigma$, where Σ is the electron self-energy, taking into account all the relevant interactions. A consistent approach to calculating conductivity (resistivity) requires, of course, the treatment of a full two-particle Green's function [18].

3.1 Ioffe–Regel limit

The most prominent quantum limitation for the conductivity (resistivity) of metals is the Ioffe–Regel limit [19], which is relevant to strongly disordered systems. For $T = 0$, we have

$$\sigma_0 = \frac{ne^2}{m}\,\tau_0 = \frac{ne^2}{p_{\rm F}}\,l\,, \tag{16}$$

where $l = v_{\rm F}\tau_0$ is the mean free path. The usual kinetic theory is valid for $p_{\rm F}l/\hbar \gg 1$ or $E_{\rm F}\tau_0/\hbar \gg 1$. Taking into account $n = p_{\rm F}^3/(3\pi^2\hbar^3)$, we get the estimate for conductivity in the Ioffe–Regel limit as $p_{\rm F}l_{\rm el}/\hbar \sim 1$ or $E_{\rm F}\tau_0/\hbar \sim 1$:

$$\sigma_{\rm IR} = \frac{e^2 p_{\rm F}}{3\pi^2\hbar^2} \sim \frac{e^2}{3\pi^2\hbar a}\,, \tag{17}$$

where $a \sim n^{-3}$ is the average distance between electrons. For typical metallic densities, a is of the order of the interatomic distance (lattice constant). In this case (for $n \sim 10^{23}$ cm^{-3}), corresponding resistivity $\rho_{\rm IR} = \sigma_{\rm IR}^{-1} \sim 150-300$ μΩ cm. For the majority of usual ('good') metals, e.g., for Cu, $\rho(T = 300\ {\rm K}) \sim 1$ μΩ cm, so that this limit remains unachievable even at the highest temperatures, not exceeding the melting temperature. However, this is not so in strongly disordered (highly-resistive) alloys, where the resistivity can approach the Ioffe–Regel limit.

An estimate quite close to (17) was also proposed by Mott for the so-called 'minimal metallic conductivity' $\sigma_{\rm c}$, at which a discontinuous metal–insulator transition takes place at $T = 0$ (Anderson localization) (achieved as disorder grows, e.g., the mean free path is reduced) [20]. In fact, as shown in the scaling theory of localization [21, 22], this transition is continuous, and $\sigma_{\rm c}$ plays the role of the characteristic conductivity scale in the vicinity of the Anderson transition:

$$\sigma \sim \sigma_{\rm c}\left(\frac{l - l_{\rm c}}{l_{\rm c}}\right)^{(d-2)\nu}\,, \tag{18}$$

where $\sigma_{\rm c} \sim e^2/(\hbar a^{d-2})$, $2 < d < 4$ is a dimension of space, and the critical value of the mean free path can be estimated from $p_{\rm F}l_{\rm c}/\hbar \sim 1$, i.e., $l_{\rm c} \sim a$. Here, we introduced the critical exponent of localization length, which in the self-consistent theory of localization [18, 23] is given by

$$\nu = \frac{1}{d-2}\,, \tag{19}$$

so that $\nu = 1$ for $d = 3$. Current numerical calculations of the Anderson transition give values of ν in the interval 1.5–1.8 [24]. For us, it is not these details that are important, but the actuality of the continuous nature of this transition and the nonexistence of any critical level of conductivity (resistivity).

Strictly speaking, these estimates are valid only for $T = 0$, when the Anderson transition is a well-defined quantum phase transition in a system of noninteracting electrons. At finite temperatures and taking into account electron–electron interactions, the situation is much more complicated, and we shall not discuss it here.

In most cases, the growth of resistivity with temperature slows down and saturates as resistivity approaches the Ioffe–Regel limit [25]. In such strongly disordered metals (highly-resistive alloys), an *empirical* Mooij rule is at work: after reaching a resistivity level (at low temperatures) of the order of $\rho_{\rm IR}$, the temperature dependence of resistivity becomes very weak, and in a wide temperature interval from low to room temperatures, or even higher, it is often observed that the temperature coefficient of resistivity becomes *negative* [25, 26]. This fact does not to date have a commonly accepted explanation.

There is a common belief that this is not so in 'strange' metals like high-temperature superconducting copper oxides [27, 28] (in the region of optimal doping) and in a number of other systems [29] where the T-linear growth of resistivity continues even after overpassing values of the order of $\rho_{\rm IR} = \sigma_{\rm IR}^{-1} \sim 100-300$ μΩ cm, up to the highest possible temperature $T \sim 1000$ K. However, here, we always face the problem of the correct estimate of resistivity in the Ioffe–Regel limit. From the estimates given above, it becomes clear that it depends significantly on the concentration of current carriers (which in cuprates is much lower than in usual metals), so that, for instance, for $n \sim 10^{21}$ cm^{-3}, we obtain $\rho_{\rm IR} \sim 1-10$ mΩ cm. In recent experiments involving weakly doped cuprates [30], it was clearly shown that their resistivity saturates at $\rho_{\rm IR} \sim 3-5$ mΩ cm, in complete accordance with the concentration of carriers obtained from measurements of the Hall effect (at $T \sim 300$ K). Thus, it is quite possible that in the experiments cited above on optimally doped cuprates, the correct value of the Ioffe–Regel limit was simply not achieved up to the highest possible temperatures (before the destruction of samples).

However, our main interest in the following will be related to resistivity of very 'pure' metals in the T-linear region.

3.2 Planckian relaxation

The idea of a Planckian relaxation mechanism in metal at high enough temperatures seems to be very attractive. Let us give some elementary arguments making it seemingly justified and based upon quite general quantum mechanical estimates using the uncertainty principle [15]. At finite temperatures $T > 0$, different processes of inelastic scattering (electron–phonon, interaction with spin fluctuations, etc.) are at work. Precisely these processes are responsible for establishing thermodynamic equilibrium in an electron system — the Fermi distribution. In a system of interacting particles at finite temperatures, the particle (electron) distribution function is qualitatively of the same form [18]. The conductivity of a metal (degenerate case) is determined by electron distribution in a layer $\sim k_B T$ around the Fermi level (chemical potential). Let us make an elementary estimate using the time–energy uncertainty relation:

$$\Delta E \tau > \hbar \,, \tag{20}$$

where τ is the lifetime of a quantum state, while ΔE is the uncertainty of its energy. In our case, $\tau = \tau(T)$, and it seems natural to take $\Delta E \sim k_B T$, so that we immediately obtain an estimate:

$$\Gamma(T) = \frac{1}{\tau(T)} < \alpha \frac{k_B T}{\hbar} \equiv \Gamma_P = \frac{1}{\tau_P} \,, \tag{21}$$

where $\alpha \sim 1$. It is now evident that, according to this elementary estimate, the Planckian relaxation defines an *upper* limit for resistivity due to inelastic scatterings:

$$\rho(T) - \rho_0 = \frac{m}{ne^2}\,\Gamma(T) < \frac{m}{ne^2}\,\alpha\,\frac{k_B T}{\hbar} \equiv \rho_P(T) \,. \tag{22}$$

Obviously, this estimate is of a rather speculative nature for a system of many, in general, strongly interacting particles, but it correlates well with the results of experiments described above.

If such a universal upper limit exists for the relaxation rate, the qualitative picture of the temperature dependence of resistivity of metals can be suggested as shown in Fig. 6 [31]. The idea here is that in 'usual' metals all the temperature dependence of resistivity develops below the Ioffe–Regel limit, while the 'Planckian' limit is reached in unusual systems like HTSC cuprates, which are near the quantum critical point and where the Ioffe–Regel limit may be surpassed with the growth of the temperature (however, see Ref. [30]).

From the estimates given above, it is easy to derive the ratio of 'Planckian' to Ioffe–Regel resistivity [15],

$$\frac{\rho_P(T)}{\rho_{IR}} \sim \frac{k_B T}{E_F} \,, \tag{23}$$

so that this limit may be exceeded for $k_B T > E_F$, which can be realized experimentally only in systems with low enough values of E_F (low carrier concentration), such as copper oxides or in multiple band systems (with several pockets of the Fermi surface). In any case, according to this picture, resistivity does not exceed the upper limit determined by the 'Planckian' relaxation rate, which is achieved in 'strange' metals. It is quite surprising that the experimental data quoted above seem to confirm the attainment of this limit for many (!) metals, including some quite 'usual' ones.

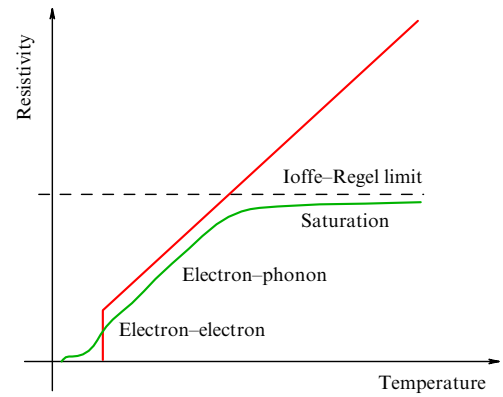

Figure 6. (Color online.) 'Planckian' limit of electrical resistivity [31]. Red line — the Planckian limit, green line — the usual temperature dependence of resistivity in metals.

3.3 Electron–phonon interaction

Consider the most important case for the theory of metals — electron–phonon interaction, which will be described within the Eliashberg–McMillan theory, as the modern generalization of the Bloch–Grüneisen theory [32]. Within this theory, the high-temperature ($T > \Theta_D/5$) phonon contribution to resistivity is given by [33, 34]

$$\rho_{ph}(T) = \frac{4\pi m T}{ne^2\hbar}\int_0^\infty \frac{d\omega}{\omega}\,\alpha_{tr}^2(\omega)F(\omega) = \frac{2\pi m T}{ne^2\hbar}\,\lambda_{tr} \,, \tag{24}$$

where $\alpha_{tr}^2(\omega)F(\omega)$ is the transport Eliashberg–McMillan function [33, 34] ($F(\omega)$ is the phonon density of states), determining the transport electron–phonon coupling constant as

$$\lambda_{tr} = 2\int_0^\infty \frac{d\omega}{\omega}\,\alpha_{tr}^2(\omega)F(\omega) \,. \tag{25}$$

For most metals, we have $\alpha^2 \approx \alpha_{tr}^2$, where [34]

$$\lambda = 2\int_0^\infty \frac{d\omega}{\omega}\,\alpha^2(\omega)F(\omega) \tag{26}$$

is the Eliashberg–McMillan coupling constant [32] determining the temperature of superconducting transition. Then, we get a simple estimate:

$$\rho_{ph}(T) \approx \frac{2\pi m T}{ne^2\hbar}\,\lambda \equiv 2\pi\lambda\rho_P(T) \,, \tag{27}$$

where in the last equality in the definition of $\rho_P(T)$ from (22) we put $\alpha = 1$. In fact, the values of $\lambda > 1$ are not very rare in metals [32], and it becomes clear that even the usual electron–phonon interaction can easily *break* the Planckian limit, so that $\rho_{ph}(T) > \rho_P(T)$ doses not seem exotic. This simple example immediately casts certain doubts on the universality of 'Planckian' relaxation, though it seems that our arguments, based on the uncertainty principle, must work for any system and interaction. However, this simple example contradicts it.

4. Elementary model of scattering by quantum fluctuations in metals

4.1 Scattering by quantum fluctuations

Here, following mainly Ref. [35], we shall consider an elementary, though realistic enough, model of electron scattering by quantum fluctuations, which will allow us to analyze our problem in a rather general form. Consider the usual Hamiltonian of electrons in a metal interacting with some Bose–like quantum fluctuations of some arbitrary nature (N is the total number of atoms in a crystal):[2]

$$H_{\text{int}} = \frac{1}{\sqrt{N}} \sum_{\mathbf{pq}} g_{\mathbf{q}} a^{+}_{\mathbf{p}+\mathbf{q}} a_{\mathbf{p}} \rho_{\mathbf{q}} \,, \tag{28}$$

where we have used the standard notations of creation and annihilation operators of electrons, and $\rho_{\mathbf{q}}$ is an operator of quantum fluctuation of 'any kind' (e.g., the density of ions in a solid or collective excitations of an electronic subsystem, including spin excitations, though spin indices are dropped for brevity). Let us introduce the appropriate (Matsubara time) Green's function as [40]

$$F(\mathbf{q}, \tau) = -\left\langle T_\tau \rho_{\mathbf{q}}(\tau) \rho^{+}_{\mathbf{q}}(0) \right\rangle . \tag{29}$$

We can then write the usual spectral representation for it as [37]

$$F(\mathbf{q}, \omega_m) = \int_{-\infty}^{\infty} \mathrm{d}\omega \, \frac{A(\mathbf{q}, \omega)}{\mathrm{i}\omega_m - \omega} \,, \tag{30}$$

where $\omega_m = 2\pi m T$, and the spectral density is defined as

$$A(\mathbf{q}, \omega) = Z^{-1} \sum_{mn} \exp\left(-\frac{E_n}{T}\right) \left|(\rho_{\mathbf{q}})_{nm}\right|^2 \times \left[1 - \exp\left(-\frac{\omega_{mn}}{T}\right)\right] \delta(\omega - \omega_{mn}) \,, \tag{31}$$

where $\omega_{mn} = E_m - E_n$, $(\rho_{\mathbf{q}})_{nm} = \langle n|\rho_{\mathbf{q}}|m\rangle = (\rho^{+}_{\mathbf{q}})_{mn}$, and m, n enumerate the exact many-particle states of the system.

The dynamic structure factor of fluctuations is defined as [36, 38]

$$S(\mathbf{q}, \omega) = Z^{-1} \sum_{mn} \exp\left(-\frac{E_n}{T}\right) \left|(\rho_{\mathbf{q}})_{nm}\right|^2 \delta(\omega - \omega_{mn}) \,. \tag{32}$$

Comparing (31) and (32), we obtain

$$A(\mathbf{q}, \omega) = S(\mathbf{q}, \omega) \left[1 - \exp\left(-\frac{\omega}{T}\right)\right] . \tag{33}$$

The electron Green's function in the Matsubara representation is written in a standard form:

$$G(\varepsilon_n, \mathbf{p}) = \frac{1}{\mathrm{i}\varepsilon_n - \xi_{\mathbf{p}} - \Sigma(\varepsilon_n, \mathbf{p})} \,, \tag{34}$$

where $\varepsilon_n = (2n+1)\pi T$, $\xi_{\mathbf{p}}$ is the free-electron spectrum counted from the Fermi level (chemical potential), and the self-energy part can be taken in the simplest approximation shown by the diagram in Fig. 7:

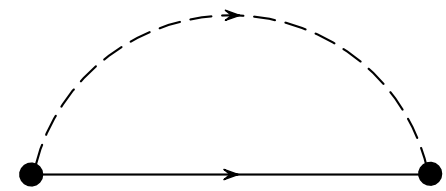

Figure 7. Second order diagram for electron self-energy. Dashed line represents the Green's function of a quantum fluctuation F, continuous line represents the electronic Green's function G.

$$\Sigma(\varepsilon_n, \mathbf{p}) = -\frac{T}{N} \sum_{\mathbf{q}} g^2_{\mathbf{q}} \sum_m F(\mathbf{q}, \mathrm{i}\omega_m) G(\varepsilon_n + \omega_m, \mathbf{p} + \mathbf{q})$$
$$= -\frac{T}{N} \sum_{\mathbf{q}} g^2_{\mathbf{q}} \sum_m \int_{-\infty}^{\infty} \mathrm{d}\omega \, \frac{S(\mathbf{q}, \omega)}{\mathrm{i}\omega_m - \omega} \left[1 - \exp\left(-\frac{\omega}{T}\right)\right] \times \frac{1}{\mathrm{i}\varepsilon_n + \mathrm{i}\omega_m - \xi_{\mathbf{p}+\mathbf{q}}} \,, \tag{35}$$

where $g_{\mathbf{q}}$ is the coupling constant (matrix element of the interaction potential).

Consider now the case where the average frequency of fluctuation $\langle \Omega \rangle$ is much lower than the temperature T, i.e., the classic limit for fluctuations. Then, in Eqn (35), it is sufficient to take into consideration only the term with $m = 0$, going actually to the picture of *quasi-elastic* scattering by fluctuations:

$$\Sigma(\varepsilon_n, \mathbf{p}) = \frac{1}{N} \sum_{\mathbf{q}} g^2_{\mathbf{q}} \int_{-\infty}^{\infty} \mathrm{d}\omega \, \frac{S(\mathbf{q}, \omega)}{\mathrm{i}\varepsilon_n - \xi_{\mathbf{p}+\mathbf{q}}}$$
$$= \sum_{\mathbf{q}} g^2_{\mathbf{q}} S(\mathbf{q}) \, \frac{1}{\mathrm{i}\varepsilon_n - \xi_{\mathbf{p}+\mathbf{q}}} \,, \tag{36}$$

where we have introduced the structure factor of fluctuations [38]

$$S(\mathbf{q}) = \frac{1}{N} \int_{-\infty}^{\infty} \mathrm{d}\omega \, S(\mathbf{q}, \omega) \,. \tag{37}$$

In fact, this is in direct analogy with the well-known Ziman–Edwards approximation in the theory of liquid metals [39–41]. The case of $S(\mathbf{q}) = \text{const}$ corresponds to a totally chaotic distribution of static scattering centers [18].

4.2 Phonons

In the case of scattering by phonons, fluctuation operator $\rho_{\mathbf{q}}$ can be expressed via (Bose) creation and annihilation operators of phonons as [38]

$$\rho_{\mathbf{q}} = \frac{1}{\sqrt{2}} \left(b^{+}_{\mathbf{q}} + b_{-\mathbf{q}}\right) . \tag{38}$$

Then,

$$S(\mathbf{q}, \omega) = Z^{-1} \sum_m \exp\left(-\frac{E_m}{T}\right) \left[\langle m|b_{\mathbf{q}} b^{+}_{\mathbf{q}}|m\rangle \delta(\omega - \omega_{\mathbf{q}}) + \langle m|b^{+}_{-\mathbf{q}} b_{-\mathbf{q}}|m\rangle \delta(\omega + \omega_{\mathbf{q}})\right] , \tag{39}$$

[2] Further on, we shall use the units $\hbar = k_{\mathrm{B}} = 1$.

where $\omega_{\mathbf{q}}$ is the phonon spectrum. Introducing the usual Bose distribution,

$$n_{\mathbf{q}} = Z^{-1} \sum_m \exp\left(-\frac{E_m}{T}\right) \langle m | b_{\mathbf{q}}^{+} b_{\mathbf{q}} | m \rangle = \frac{1}{\exp(\omega_{\mathbf{q}}/T) - 1}\,, \tag{40}$$

we get [38]

$$\begin{aligned} S(\mathbf{q}, \omega) &= \left[(n_{\mathbf{q}} + 1)\delta(\omega - \omega_{\mathbf{q}}) + n_{\mathbf{q}}\delta(\omega + \omega_{\mathbf{q}})\right] \\ &= \delta(\omega - \omega_{\mathbf{q}}) + n_{\mathbf{q}}\left[\delta(\omega - \omega_{\mathbf{q}}) + \delta(\omega + \omega_{\mathbf{q}})\right]. \end{aligned} \tag{41}$$

Under the conditions of $T \gg \omega_{\mathbf{q}}$, we go to the classical limit (equipartition theorem):

$$n_{\mathbf{q}} = \frac{T}{\omega_{\mathbf{q}}}\,, \tag{42}$$

and, accordingly,

$$S(\mathbf{q}) = \frac{2T}{\omega_{\mathbf{q}}}\,. \tag{43}$$

Thus, we obtain the structure factor linearly growing with temperature, while its momentum dependence is determined by the phonon spectrum. Then,

$$\Sigma(\varepsilon_n, \mathbf{p}) = T \sum_{\mathbf{q}} \frac{2g_{\mathbf{q}}^2}{\omega_{\mathbf{q}}} \frac{1}{\mathrm{i}\varepsilon_n - \xi_{\mathbf{p}+\mathbf{q}}}\,. \tag{44}$$

To simplify the model further, let us assume that the phonon spectrum is dispersionless (Einstein phonon or optical phonon with very weak dispersion), taking $\omega_{\mathbf{q}} = \Omega_0$. Then, performing all calculations as in the problem of an electron in a system of random impurities [18], we get

$$\Sigma(\varepsilon_n, \mathbf{p}) = -\mathrm{i}\pi \operatorname{sign} \varepsilon_n \frac{2g_0^2}{\Omega_0} N(0) T\,, \tag{45}$$

where $N(0)$ is the density of states on the Fermi level. Correspondingly, the damping is written as

$$\frac{\Gamma(T)}{2} = \pi \frac{2g_0^2}{\Omega_0} N(0) T = \pi\lambda_0 T\,, \tag{46}$$

where we have introduced the usual dimensionless coupling constant of electron–phonon interaction:

$$\lambda_0 = \frac{2g_0^2 N(0)}{\Omega_0}\,. \tag{47}$$

After standard calculations [18], we obtain the resistivity as

$$\rho(T) = \frac{m}{ne^2}\,\Gamma(T) = 2\pi\lambda_0 \rho_{\mathrm{P}}(T)\,, \tag{48}$$

which is essentially the high–temperature limit of the Eliashberg–McMillan theory (27). Now, the constant α used in the definition of 'Planckian' relaxation time (21) is expressed via the parameters of the theory as

$$\alpha = 2\pi\lambda_0\,. \tag{49}$$

Naturally, it is not universal and is just proportional to the coupling constant.

Practically the same result can be easily obtained in the Eliashberg–McMillan approximation [18], where the expression for Matsubara self-energy is written as

$$\begin{aligned} \Sigma(\varepsilon_n) &= \int \mathrm{d}\varepsilon' \int_0^\infty \mathrm{d}\omega\, \alpha^2(\omega) F(\omega) \\ &\quad \times \left(\frac{f(\varepsilon') + n(\omega)}{\mathrm{i}\varepsilon_n - \varepsilon' + \omega} + \frac{1 - f(\varepsilon') + n(\omega)}{\mathrm{i}\varepsilon_n - \varepsilon' - \omega}\right), \end{aligned} \tag{50}$$

where $f(\varepsilon)$ and $n(\omega)$ are standard Fermi and Bose distributions. In the high-temperature limit $T \gg \omega$, Eqn (50) reduces to

$$\begin{aligned} \Sigma(\varepsilon_n) &= \int \mathrm{d}\varepsilon' \int_0^\infty \mathrm{d}\omega\, \alpha^2(\omega) F(\omega) \\ &\quad \times \frac{T}{\omega}\left(\frac{1}{\mathrm{i}\varepsilon_n - \varepsilon' + \omega} + \frac{1}{\mathrm{i}\varepsilon_n - \varepsilon' - \omega}\right) \\ &= T \int_{-\infty}^{\infty} \mathrm{d}\varepsilon'\, 2 \int_0^\infty \frac{\mathrm{d}\omega}{\omega}\, \alpha^2(\omega) F(\omega)\, \frac{1}{\mathrm{i}\varepsilon_n - \varepsilon'} \\ &= -\mathrm{i}\pi\lambda T \operatorname{sign} \varepsilon_n\,, \end{aligned} \tag{51}$$

where we have introduced the standard definition of the coupling constant of the Eliashberg–McMillan theory (26), thus reproducing a result like (46). For resistivity, we again get Eqn (48) with an obvious replacement $\lambda_0 \to \lambda$, where λ is defined[3] in (26).

4.3 More general model

Now, let us try to avoid the explicit introduction of phonons (or any other quasiparticles related to fluctuations). From Eqn (33), for $\omega \ll T$ we get

$$A(\mathbf{q}, \omega) \approx \frac{\omega}{T}\, S(\mathbf{q}, \omega)\,, \tag{52}$$

or

$$S(\mathbf{q}, \omega) \approx \frac{T}{\omega}\, A(\mathbf{q}, \omega)\,. \tag{53}$$

Substituting this expression into Eqn (36), we obtain the following expression for self-energy:

$$\Sigma(\varepsilon_n, \mathbf{p}) = \frac{T}{N} \sum_{\mathbf{q}} g_{\mathbf{q}}^2 \int_{-\infty}^{\infty} \frac{\mathrm{d}\omega}{\omega} \frac{A(\mathbf{q}, \omega)}{\mathrm{i}\varepsilon_n - \xi_{\mathbf{p}+\mathbf{q}}}\,, \tag{54}$$

where everything is determined by the spectral density of fluctuations $A(\mathbf{q}, \omega)$, which is not necessarily of a quasiparticle form. Naturally, for the simplest model with $A(\mathbf{q}, \omega) = \delta(\omega - \Omega_0)$ (Einstein model for fluctuations), from (54) immediately follow the Eqns (45)–(47) derived above. In the case of no $\mathbf{q}$ dependence, from (54) we immediately obtain

$$\begin{aligned} \Sigma(\varepsilon_n, \mathbf{p}) &= \frac{T}{N} \sum_{\mathbf{q}} g_0^2 \int_{-\infty}^{\infty} \frac{\mathrm{d}\omega}{\omega} \frac{A(\omega)}{\mathrm{i}\varepsilon_n - \xi_{\mathbf{p}+\mathbf{q}}} \\ &= -\mathrm{i}\pi \operatorname{sign} \varepsilon_n\, N(0)\, \frac{T}{N}\, g_0^2 \int_{-\infty}^{\infty} \frac{\mathrm{d}\omega}{\omega}\, A(\omega) \\ &= -\mathrm{i}\pi \operatorname{sign} \varepsilon_n\, \frac{2g_0^2}{\langle\Omega\rangle}\, N(0) T\,, \end{aligned} \tag{55}$$

[3] Here and in what follows, we ignore for brevity the insignificant (for our aims) difference between λ and λ_{tr}.

where we have introduced an average frequency of fluctuations:

$$\langle\Omega\rangle^{-1} = 2\int_0^\infty \frac{\mathrm{d}\omega}{\omega}\, A(\omega)\,. \tag{56}$$

This result is actually equivalent to (45).

In the general case, when we can not ignore the momentum dependence of the spectral density of fluctuations, we can use the Eliashberg–McMillan approach, assuming that fluctuations scatter electrons in some narrow ($\sim T$) layer around the Fermi surface. Then, we can introduce the self-energy averaged over the momenta *on the Fermi surface*:

$$\Sigma(\varepsilon_n) = \frac{1}{N(0)}\sum_{\mathbf{p}} \delta(\xi_{\mathbf{p}})\Sigma(\varepsilon_n, \mathbf{p})\,, \tag{57}$$

and also an effective (averaged over initial and final momenta on the Fermi surface) interaction:

$$\begin{aligned} & g^2_{\mathbf{pp}'} A(\mathbf{p}-\mathbf{p}', \omega) \\ & \Longrightarrow \frac{1}{N(0)}\sum_{\mathbf{p}} \frac{1}{N(0)}\sum_{\mathbf{p}'} g^2_{\mathbf{pp}'} A(\mathbf{p}-\mathbf{p}', \omega)\delta(\xi_{\mathbf{p}})\delta(\xi_{\mathbf{p}'}) \\ & \equiv \frac{1}{N(0)}\,\alpha^2(\omega)F(\omega)\,, \end{aligned} \tag{58}$$

where

$$F(\omega) = \sum_{\mathbf{q}} A(\mathbf{q}, \omega) \tag{59}$$

is the density of states of fluctuations. Then, from (54), we obtain for (57) ,

$$\begin{aligned} \Sigma(\varepsilon_n) &= \frac{T}{N(0)}\int_{-\infty}^{\infty} \frac{\mathrm{d}\omega}{\omega}\,\alpha^2(\omega)F(\omega)N(0)\int_{-\infty}^{\infty} \mathrm{d}\xi\, \frac{1}{\mathrm{i}\varepsilon_n - \xi} \\ &= -\mathrm{i}\pi\,\mathrm{sign}\,\varepsilon_n T\int_{-\infty}^{\infty} \frac{\mathrm{d}\omega}{\omega}\,\alpha^2(\omega)F(\omega) \\ &= -\mathrm{i}\pi\,\mathrm{sign}\,\varepsilon_n \lambda T \equiv -\mathrm{i}\,\frac{\Gamma(T)}{2}\,\mathrm{sign}\,\varepsilon_n\,, \end{aligned} \tag{60}$$

where we again introduced the dimensionless coupling constant as in the Eliashberg–McMillan theory defined by Eqn (26), the value of which is in fact determined by the (averaged as in (58)) spectral density of fluctuations $A(\mathbf{q}, \omega)$, which does not necessarily describe any quasiparticles.

Finally, we obtain

$$\Gamma(T) = 2\pi\lambda T\,, \tag{61}$$

which is of the same form as Eqn (46) and leads immediately to (48). Strictly speaking, this is not necessarily so if we remember the possible temperature dependence of spectral density $A(\mathbf{q}, \omega)$. Planckian distribution is obtained only in the absence or weakness of this dependence. It is obvious that Eqn (46) immediately follows from (26) and (60) if $F(\omega) = \delta(\omega - \Omega_0)$, which corresponds to the Einstein spectrum of fluctuations.

4.4 Vicinity of the quantum critical point

The simplest model considered above certainly does not explain the T-linear behavior of resistivity in cuprates and similar systems in the normal state, starting from very low temperatures. It should be noted that this behavior is often related to the closeness of these systems to some quantum critical point.

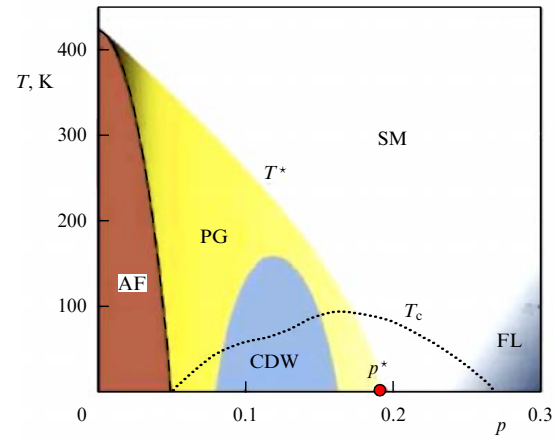

Figure 8. (Color online.) Typical phase diagram of hole-doped cuprates. Superconducting state is observed in the region of temperatures below T_c, shown by dashed line. Antiferromagnetic region (AF) is shown in brown. Pseudogap phase (PG) exists at temperatures below $T^\star$ (yellow) and ends at $T = 0$ at the critical point $p^\star$ (red dot). Inside the pseudogap phase exists the phase with a charge density wave (CDW) (blue). The region of a strange metal (SM) (white) continuously transforms into the Fermi-liquid region (FL) at higher dopings [42].

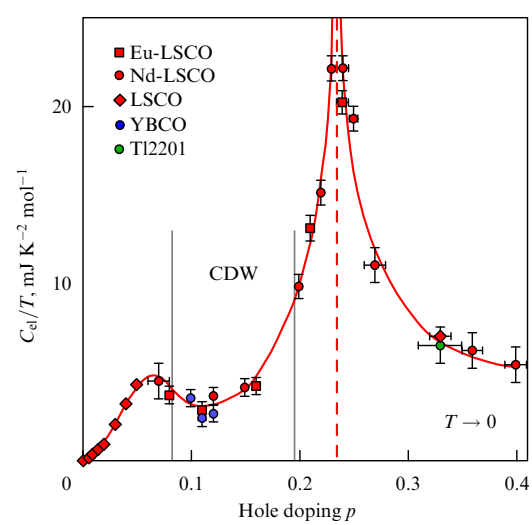

Figure 9. (Color online.) Electronic specific heat coefficient $\gamma = C_{\mathrm{el}}/T$ in normal state ($T = 5$ K) in the vicinity of the quantum critical point (superconductivity is suppressed by an external magnetic field) as a function of doping p for $La_{1.8-x}Eu_{0.2}Sr_xCuO_4$ (Eu-LSCO, red squares), $La_{1.6-x}Nd_{0.4}Sr_xCuO_4$ (Nd-LSCO, red dots), $La_{2-x}Sr_xCuO_4$ (LSCO, red diamonds), $YBa_2Cu_3O_y$ (YBCO, blue dots), and $Tl_2Ba_2CuO_{6-\delta}$ (Tl2201, green dot) [42].

Let us consider the schematic phase diagram of hole-doped cuprates shown in Fig. 8 [42].

This diagram has been well known for a long time, but what is important for us now is the possible existence here of a quantum critical point [43, 44] at carrier (hole) concentration $p = p^\star$, where the pseudogap region ends [45–47]. Experimental evidence in favor of the existence of such a critical point is quite extensive [42]. As an example, in Fig. 9, we show

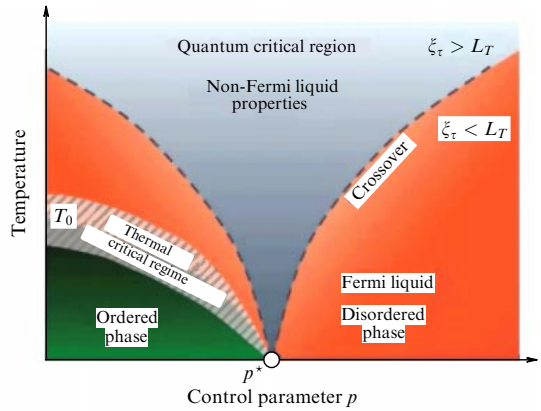

Figure 10. (Color online.) Phase diagram in the vicinity of the quantum critical point. A non-Fermi-liquid behavior of relaxation rate and resistivity can be observed in the quantum critical region, where $\xi_\tau > L_T = \hbar/(k_B T)$, which corresponds to $\hbar\Omega_0 < k_B T$.

just one of the most striking cases — the sharp singularity of the electronic specific heat coefficient $\gamma = C_{el}/T$ at $p = p^\star$ in the normal state of cuprates, obtained in a strong magnetic field suppressing superconductivity [42].

The nature of the pseudogap state in cuprates has not been completely clarified to date. In particular, it is not clear whether the PG region on the phase diagram of Fig. 8 is some new phase and the line $T^\star$ defines the critical temperature of a true phase transition, or it is the region of some crossover to antiferromagnetic phase AF, with well developed fluctuations of AF short-range order [45–47]. The antiferromagnetic scenario of pseudogap formation also has serious experimental support [42], though some authors believe that the transition to the pseudogap phase is a true phase transition with some still unknown order parameter. A number of specific models (see, e.g., [48]) of such a phase transition have been proposed, allowing us to consider $p = p^\star$ as a true quantum critical point. However, it is still unclear whether we can speak of the quantum critical point in the crossover scenario. In any case, the T-linear behavior of resistivity in cuprates is observed close to optimal doping, which nearly coincides with $p = p^\star$. To the left of this concentration resistivity is demonstrated some dielectric (localization) effects (a strong negative temperature coefficient of resistivity) [49, 50], while to the right we have a crossover to more or less usual Fermi-liquid-like behavior with a quadratic growth of resistivity with temperature.

The closeness of the system to the quantum critical point can, in principle, explain the T-linear growth of resistivity even within the elementary model considered above. To observe such growth at low temperatures, it is sufficient to satisfy the inequality $\Omega_0 \ll T$, where Ω_0 is the characteristic frequency of fluctuations scattering the electrons. In the vicinity of the quantum critical point (of any nature), we can expect a typical 'softening' of the appropriate fluctuation mode according to the relation [43, 44]

$$\Omega_0 \sim |p - p^\star|^{z\nu}, \tag{62}$$

where p is the concentration of carriers (holes or electrons). Here, ν and z are the standard critical exponents of the theory of quantum phase transitions, determining the critical behavior of characteristic lengths:

$$\xi \sim |p - p^\star|^{-\nu}, \quad \xi_\tau \sim |p - p^\star|^{-z\nu}. \tag{63}$$

Here, τ denotes the imaginary (Matsubara) time, and above we just put $\Omega_0 \sim \xi_\tau^{-1}$.

As shown in Fig. 10, the quantum critical region is defined by the inequality [43, 44]

$$\xi_\tau > \frac{1}{T} \quad \text{or} \quad \Omega_0 < T, \tag{64}$$

which may guarantee the T-linear behavior of resistivity in this region in cuprates or similar systems. However, the nature of quantum fluctuations of importance here, as well as the mechanism of their interaction with electrons, remains an open question.

5. General relations for the Green's function and conductivity

5.1 Green's function for a system of interacting particles

Let us recall some general expressions for an arbitrary system of interacting electrons. We have the following general expression for the Matsubara Green's function [37]:

$$G(\varepsilon_n, \mathbf{p}) = \frac{1}{\mathrm{i}\varepsilon_n - \xi_{\mathbf{p}} - \Sigma(\varepsilon_n, \mathbf{p})}. \tag{65}$$

Keeping in mind the electron–phonon coupling and its analogs (quantum fluctuations of a general nature), dropping the momentum dependence of self-energy, we can write the following expression in the standard notations of the Eliashberg–McMillan theory:

$$\Sigma(\varepsilon_n) = \left[1 - z(\varepsilon_n)\right] \mathrm{i}\varepsilon_n + \chi(\varepsilon_n). \tag{66}$$

Then,

$$G(\varepsilon_n, \mathbf{p}) = \frac{1}{z(\varepsilon_n)\,\mathrm{i}\varepsilon_n - \xi_{\mathbf{p}} - \chi(\varepsilon_n)} = \frac{Z(\varepsilon_n)}{\mathrm{i}\varepsilon_n - Z(\varepsilon_n)\xi_{\mathbf{p}} - Z(\varepsilon_n)\chi(\varepsilon_n)}, \tag{67}$$

where we have defined

$$Z(\varepsilon_n) = z^{-1}(\varepsilon_n). \tag{68}$$

Let us also define

$$\varepsilon(\mathbf{p}, \varepsilon_n) = Z(\varepsilon_n)\xi_{\mathbf{p}} + \mathrm{Re}\,\chi(\varepsilon_n), \tag{69}$$

$$\Gamma(T)\,\mathrm{sign}\,\varepsilon_n = -2Z(\varepsilon_n)\,\mathrm{Im}\,\chi(\varepsilon_n). \tag{70}$$

The Green's function can then be written in the following very general form:

$$G(\varepsilon_n, \mathbf{p}) = \frac{Z(\varepsilon_n)}{\mathrm{i}\varepsilon_n - \varepsilon(\mathbf{p}, \varepsilon_n) + (\mathrm{i}/2)\Gamma(T)\,\mathrm{sign}\,\varepsilon_n}. \tag{71}$$

If there is no dependence on ε_n in (69), we can write the Green's function in the usual form,

$$G(\varepsilon_n, \mathbf{p}) = \frac{Z}{\mathrm{i}\varepsilon_n - \varepsilon(\mathbf{p}) + (\mathrm{i}/2)\Gamma(T)\,\mathrm{sign}\,\varepsilon_n}, \tag{72}$$

which is sufficient for our aims.

These expressions more or less correspond to the usual picture of electron–phonon interaction, when $\lambda \ll 1$, though we can try to 'drag' them to the region of $\lambda > 1$, using the Migdal theorem [18], which allows us to disregard vertex corrections. In particular, in this approach, the renormalization factor is [18]

$$Z = \frac{1}{1+\lambda} \tag{73}$$

and does not depend explicitly on ε_n. Equation (73) is valid within an energy layer of the order of the double Debye frequency around the Fermi level (in the case of interaction with phonons) or the double average frequency of fluctuations $\langle\Omega\rangle$. Outside this layer, it is obvious that $Z = 1$ fluctuations are practically irrelevant for electrons of high enough energy.

5.2 General expressions for conductivity

The diagonal element of the conductivity tensor at $\mathbf{q} = 0$ can be written as [18, 51]

$$\sigma_{xx}(\omega) = \frac{1}{\mathrm{i}\omega}\left[\Phi_{xx}(\omega + \mathrm{i}\delta) - \Phi_{xx}(0 + \mathrm{i}\delta)\right], \tag{74}$$

where

$$\Phi_{xx}(\mathrm{i}\omega_m) = -2eT\sum_n\sum_{\mathbf{p}} \frac{p_x}{m} J_x(\mathbf{p}, \mathbf{p}, \varepsilon_n, \varepsilon_n + \omega_m) \times G(\varepsilon_n\mathbf{p})\, G(\varepsilon_n + \omega_m\mathbf{p}), \tag{75}$$

which corresponds to the usual loop diagram shown in Fig. 11, where the 'current' vertex can be written as

$$J_\mu(\mathbf{p}, \mathbf{p}, \varepsilon_n, \varepsilon_n + \omega_m) \equiv \frac{e}{m}\, p_\mu\, \Xi(\mathbf{p}, \varepsilon_n, \varepsilon_n + \omega_m), \tag{76}$$

and the 'bare' current vertex is $(e/m)\, p_\mu$.

Then, rewriting Eqn (75) as

$$\Phi_{xx}(\mathrm{i}\omega_m) = -2e^2T\sum_n\sum_{\mathbf{p}} \frac{p_x^2}{m^2}\, \Xi(\mathbf{p}, \varepsilon_n, \varepsilon_n + \omega_m) \times G(\varepsilon_n\mathbf{p})\, G(\varepsilon_n + \omega_m\mathbf{p}) \tag{77}$$

and performing the standard summation over n and analytic continuation $\mathrm{i}\omega_m \to \omega + \mathrm{i}\delta$ [51], we obtain the static conductivity at $(\omega \to 0)$:

$$\sigma_{xx} = \frac{e^2}{2\pi}\sum_{\mathbf{p}} \frac{p_x^2}{m^2}\, \Xi(\mathbf{p}) G^{\mathrm{R}}(\mathbf{p}, 0) G^{\mathrm{A}}(\mathbf{p}, 0), \tag{78}$$

where we have introduced the static limit $\Xi(\mathbf{p}) = \Xi(\mathbf{p}, 0 - \mathrm{i}\delta, 0 + \mathrm{i}\delta)$.

Obviously, the main difficulty here is related to the explicit calculation of the vertex part for the system of interacting particles. The simplest estimate can be obtained using in Eqn (75) the obvious Ward identity [51], which is valid for $\omega_m = 0$:

$$J_\mu(\mathbf{p}, \mathbf{p}, \varepsilon_n, \varepsilon_n) = -e\,\frac{\partial}{\partial p_\mu}\, G^{-1}(\varepsilon_n, \mathbf{p}) = -e\left[-v_{\mathbf{p}}^\mu - \frac{\partial\Sigma(\varepsilon_n, \mathbf{p})}{\partial p_\mu}\right], \tag{79}$$

where velocity $v_{\mathbf{p}}^\mu = \partial\xi_{\mathbf{p}}/\partial p_\mu$. If we assume here that the self-energy is momentum independent, i.e., $\Sigma(\varepsilon_n, \mathbf{p}) = \Sigma(\varepsilon_n)$, as usually takes place for electron–phonon interaction, vertex (79) is reduced to the 'bare' one:

$$J_\mu(\mathbf{p}, \mathbf{p}, \varepsilon_n, \varepsilon_n) = e v_{\mathbf{p}}^\mu = \frac{e}{m}\, p_\mu, \tag{80}$$

which corresponds to $\Xi(\mathbf{p}, \varepsilon_n, \varepsilon_n) = 1$. Using (79) in (75), we get

$$\begin{aligned}\Phi_{xx}(\mathrm{i}\omega_m) &= -2e^2T\sum_n\sum_{\mathbf{p}} \frac{p_x}{m}\left[\frac{\partial}{\partial p_\mu}\, G^{-1}(\varepsilon_n, \mathbf{p})\right] \\ &\quad\times G(\varepsilon_n\mathbf{p})\, G(\varepsilon_n + \omega_m\mathbf{p}) \\ &= -2e^2T\sum_n\sum_{\mathbf{p}} \frac{p_x^2}{m^2}\, G(\varepsilon_n\mathbf{p})\, G(\varepsilon_n + \omega_m\mathbf{p}),\end{aligned} \tag{81}$$

and then, making all transformations as in going from (75) to (78), we obtain the following approximate relation for static conductivity:

$$\sigma_{xx} = \frac{e^2}{2\pi}\sum_{\mathbf{p}} \frac{p_x^2}{m^2}\, G^{\mathrm{R}}(\mathbf{p}, 0) G^{\mathrm{A}}(\mathbf{p}, 0), \tag{82}$$

which simply corresponds to the choice of $\Xi(\mathbf{p}) = 1$ in (78). In contrast to (78), this is certainly a kind of approximation. It is used, for example, in Ref. [48]. What is lost here will become clear below.

Further calculations will be done for the general case of (78). Keeping in mind the typical metal, where all the physics of conductivity is determined in the vicinity of the Fermi surface (and scattering is rather weak), we can use the usual integration over the energy spectrum linearized close to the Fermi level and write (78) as ($\mathrm{Re}\,\Sigma(0)$ can be included in the renormalization of the chemical potential)

$$\begin{aligned}\sigma_{xx} &= \frac{e^2}{2\pi}\, N(0)\int_{-\infty}^{\infty} \mathrm{d}\xi_p\, \frac{1}{3}\,\frac{p_{\mathrm{F}}^2}{m^2}\, \Xi(p_{\mathrm{F}}) G^{\mathrm{R}}(\mathbf{p}, 0) G^{\mathrm{A}}(\mathbf{p}, 0) \\ &= \frac{e^2}{2\pi}\,\frac{1}{3}\, v_{\mathrm{F}}^2 \Xi(p_{\mathrm{F}}) N(0)\int_{-\infty}^{\infty} \mathrm{d}\xi_p\, \frac{1}{\xi_p^2 + \mathrm{Im}^2\Sigma(0)} \\ &= e^2\,\frac{1}{3}\, v_{\mathrm{F}}^2 N(0)\,\frac{\Xi(p_{\mathrm{F}})}{2\,\mathrm{Im}\,\Sigma(0)} \equiv \frac{ne^2}{m}\,\tau_{\mathrm{tr}}.\end{aligned} \tag{83}$$

From this expression, it is clear, by the way, that approximation $\Xi(p_{\mathrm{F}}) = 1$ corresponds to ignoring the difference between τ and τ_{tr}, which we used everywhere above. For the case of scattering by point-like impurities or Einstein phonons, this is simply always valid — from (83) we immediately get (48). Precisely the same expression for conductivity is used, for instance, in Ref. [48]. It now is clear that the mass renormalization, appearing, for example, in the expression for electronic specific heat, *does not enter* the expression for σ_{xx}, where everything is determined by the 'bare' (band) mass. This result has been well known, actually, for a long time [52–55].

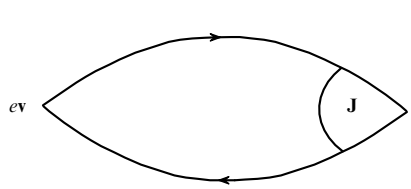

Figure 11. Loop diagram determining conductivity.

The contribution from the possible momentum dependence of $\Sigma(\varepsilon, \mathbf{p})$ to the static conductivity can also be obtained in a rather simple way [51]. Let us write

$$G^{\mathrm{R}}(\varepsilon, \mathbf{p}) = \left[Z^{-1}\varepsilon - b^{-1}\xi_p + \operatorname{Im}\Sigma(\varepsilon, p_{\mathrm{F}})\right]^{-1}, \tag{84}$$

where, as usual, we introduced

$$Z^{-1} = 1 - \frac{\partial}{\partial\varepsilon}\operatorname{Re}\Sigma(\varepsilon, p_{\mathrm{F}})\big|_{\varepsilon=0}, \tag{85}$$

$$b^{-1} = 1 + \frac{\partial}{\partial\xi_p}\operatorname{Re}\Sigma(0, \mathbf{p})\big|_{|\mathbf{p}|=p_{\mathrm{F}}}. \tag{86}$$

Then, using Eqn (84), we obtain the density of states renormalization on the Fermi level and get

$$\begin{aligned}\tilde{N}(0) &= -\frac{1}{\pi}\sum_{\mathbf{p}}\operatorname{Im}G^{\mathrm{R}}(0, \mathbf{p}) \\ &= \frac{1}{\pi}\int_{-\infty}^{\infty}\mathrm{d}\xi_p\,\frac{1}{b^{-2}\xi_p + \operatorname{Im}\Sigma(0, \mathbf{p})} = bN(0).\end{aligned} \tag{87}$$

Now, we may repeat all calculations for conductivity done above using (84) and obtain the final result for static conductivity as [51]

$$\sigma_{xx} = \frac{ne^2}{m}\,\frac{\Xi(p_{\mathrm{F}})}{2\operatorname{Im}\Sigma(0)}\,b = \frac{ne^2}{m}\,\tau_{\mathrm{tr}}\,\frac{\tilde{N}(0)}{N(0)}. \tag{88}$$

5.3 Self-consistent calculation

Let us return to the simplest model of electron–phonon interaction and make the self-consistent calculation, when the electron line in the diagram of Fig. 7 is 'dressed', i.e., takes into account all orders of nonintersecting interaction lines. Again, we assume the validity of Migdal's theorem [18]. Acting in the spirit of Eqns (66)–(72), we can write the expression for the Green's function as (simplified variant of Eqn (71))

$$G(\varepsilon_n, \mathbf{p}) = \frac{Z}{\mathrm{i}\varepsilon_n - Z\xi_{\mathbf{p}} + (\mathrm{i}/2)Z\Gamma(T)\operatorname{sign}\varepsilon_n}, \tag{89}$$

which corresponds to a choice of $Z(\varepsilon_n) = Z$, $\operatorname{Re}\chi(\varepsilon_n) = 0$, and $\operatorname{Im}\chi(\varepsilon_n) = -\Gamma(T)$ in Eqn (67). Renormalization factor $Z < 1$ is assumed to be a constant for simplicity. Then, it may seem that, taking $\Gamma(T) = 2\pi\lambda T$, we may introduce the renormalized damping as

$$\tilde{\Gamma}(T) = Z\Gamma(T) = 2\pi\lambda ZT = 2\pi\,\frac{\lambda}{1+\lambda}\,T, \tag{90}$$

where we have accounted for the known result due to electron–phonon interactions in the *low-temperature* limit [18]:

$$Z = \frac{1}{1+\lambda}. \tag{91}$$

Accordingly, for $\lambda \ll 1$ we have (46), and for $\lambda \gg 1$ we get

$$\tilde{\Gamma}(T) = 2\pi T, \tag{92}$$

i.e., the *universal* 'Planckian' behavior of relaxation rate (21) with $\alpha = 2\pi$ *independent* of the coupling constant of electrons with fluctuations (phonons). In the general case, for arbitrary values of λ we have $\alpha < 2\pi$, so that the upper limit for α appears in a natural way and is defined by (92).

However, substituting (89) into (44), which is obtained in the *high-temperature* limit, in the model with the Einstein spectrum of fluctuations (phonons), we immediately obtain

$$\begin{aligned}\Sigma(\varepsilon_n, \mathbf{p}) = \Sigma(\varepsilon_n) &= -\mathrm{i}\pi\,\frac{2g_0^2}{\Omega_0}\,N(0)T\operatorname{sign}\varepsilon_n \\ &= -\frac{\mathrm{i}}{2}\,\Gamma(T)\operatorname{sign}\varepsilon_n,\end{aligned} \tag{93}$$

so that the renormalization factor Z in damping is *canceled out*, and we just reproduce the usual result derived above without any renormalizations. This is not surprising at all — it is clear from the very beginning that $Z \approx 1$ for temperatures (energies) much higher than the characteristic phonon frequencies (or any other fluctuation quanta scattering the electrons). Similar results are valid not only in the Einstein model but also in the general case, described by the Eliashberg–McMillan approximation (51), (60) [35].

It may also seem that the limitations discussed above may be obtained from completely different considerations. Let us write the quite general expression for the Matsubara Green's function in the high-temperature limit as

$$G(\varepsilon_n, \mathbf{p}) = \frac{1}{\mathrm{i}\varepsilon_n - \varepsilon_{\mathbf{p}} + (\mathrm{i}/2)\Gamma(T)\operatorname{sign}\varepsilon_n}. \tag{94}$$

After substituting the limiting value of $\Gamma(T)$ from (21) to (94), we obtain

$$G(\varepsilon_n, \mathbf{p}) = \frac{1}{\mathrm{i}\varepsilon_n - \varepsilon_{\mathbf{p}} + (\mathrm{i}/2)\alpha T\operatorname{sign}\varepsilon_n}. \tag{95}$$

We then immediately see that the constant α, seemingly, can not reach the value of $\alpha = 2\pi$, as Matsubara frequencies in (95) become in this case *even*, i.e., the system of fermions 'turns' into bosons, which is just impossible because of the general spin-statistics theorem — no interaction (leading, for example, to temperature-dependent relaxation) can change the statistics of particles. Then, apparently, we have to introduce the same limitation again:

$$\Gamma(T) = \frac{1}{\tau(T)} < 2\pi T, \tag{96}$$

which means, notably, that in our model, according to Eqn (61), we always have an inequality $\lambda < 1$. Such a limitation on the coupling constant agrees with recent results of quantum Monte Carlo calculations of electron–phonon interactions [56] but contradicts many years of experience in studies of superconductivity within the Eliashberg–McMillan theory [33, 34]. A discussion of these contradictions and possible solutions can be found in the recent paper [57].

In fact, the arguments given above are incorrect, and the value of α can take any values, including integers, with no paradoxes like the change of statistics. These values are not special, and the system may continuously pass through them with the growth of α (i.e., the coupling strength). This can be easily understood by making, for instance, explicit calculations of the distribution function (see Appendix).

It should be noted, of course, that the T-linear behavior of damping in the Green's function in all cases breaks the

standard criteria for Fermi-liquid behavior [38], so that quasiparticles in the system are badly defined. This is also seen from the explicit form distribution function, which is rather far from the usual Fermi step-like function.

5.4 Planckian relaxation delusion

In Refs [3, 4], experimental data on resistivity were represented by Drude expression (13), where the effective mass $m^\star$ was determined from measurements of specific heat or the de Haas–van Alphen effect, which in the model with electron–phonon or a more general model of scattering by quantum fluctuations of an arbitrary nature, is obtained from the band structure effective mass by a simple substitution $m \to m^\star = m(1+\lambda)$, which takes into account mass renormalization by interactions (at low temperatures!). The inconsistency of this approach was already stressed in Ref. [48]. Let us show that precisely this representation of experimental data leads to the *delusion* of universal Planckian relaxation in metals. In fact, Eqn (48) for the *high-temperature* limit of resistivity can be identically rewritten as

$$\rho(T) = \frac{m(1+\lambda)}{ne^2}\,\frac{\Gamma(T)}{1+\lambda} = \frac{m^\star}{ne^2}\,\tilde{\Gamma}(T)\,, \tag{97}$$

where

$$\tilde{\Gamma}(T) = 2\pi\,\frac{\lambda}{1+\lambda}\,T\,, \tag{98}$$

which always leads to

$$\tilde{\Gamma}(T) < 2\pi T \tag{99}$$

just imitating the universal 'Planckian' behavior of relaxation rate (21) with $\alpha = 2\pi$ as an upper limit independent of the coupling constant of electrons with fluctuations (phonons). The substitution of $m \to m^\star = m(1+\lambda)$ in (97) by itself is correct, despite being used in an expression in the high-temperature limit. Also correct is the treatment of experimental data in Refs [3, 4], where they used the effective mass $m^\star$, obtained from *low-temperature* measurements. However, this approach clouds the crux of the matter, creating the delusion of universal Planckian behavior.

It is easy to estimate that the experimentally observed values [3, 4] of $\alpha \sim 1$ correspond to the rather typical $\lambda \sim 0.2$, while $\alpha \sim 2.8$ for lead [3] corresponds to $\lambda \sim 0.53$. Calculations within the Eliashberg–McMillan theory for Pb give $\lambda \sim 1.5$ [34]. For Nb, in Ref. [3] it was found that $\alpha \sim 2.3$, which, according to the expressions given above, corresponds to $\lambda \sim 0.43$, while the calculations in [34] give $\lambda \sim 1.26$. Suppression by a factor of ~ 3 of our values of λ may be possibly related to the fact that in expressions for resistivity we must use $\lambda_{\rm tr} < \lambda$. However, the calculated values of $\lambda_{\rm tr}$ [34] equal 1.19 for Pb and 1.17 for Nb, which does not improve much the agreement with experiments.

Much more important may be the account of mass renormalization due to electron–electron interactions, which also contribute to electron specific heat, which, in practice, is difficult to separate from the phonon contribution. Accordingly, Eqn (98) should be rewritten as

$$\tilde{\Gamma}(T) = 2\pi\,\frac{\lambda}{1+\lambda+\lambda_{\rm ee}}\,T\,, \tag{100}$$

where we have introduced $\lambda_{\rm ee}$ — a dimensionless parameter determining mass renormalization due to electron–electron interaction. In the Landau–Silin Fermi-liquid theory, $\lambda_{\rm ee} = F_1^{\rm s}/3$, where $F_1^{\rm s}$ is the appropriate coefficient in the expansion of the Landau function [38]. For typical metals, $\lambda_{\rm ee} \sim 1$. Then,

$$\alpha = \frac{2\pi\lambda}{1+\lambda+\lambda_{\rm ee}}\,, \tag{101}$$

so that, taking $\lambda \sim 0.4$ and $\lambda_{\rm ee} \sim 1$ as typical, we immediately obtain $\alpha \sim 1.04$, while for $\lambda \sim 0.5$ we have $\alpha \sim 1.25$, in good agreement with the majority of the data of Refs [3, 4]. For Pb, taking $\lambda = 1.68$ [34] and $\lambda_{\rm ee} = 1$, we get $\alpha \sim 2.86$, in reasonable agreement with the 'experimental' value of $\alpha_{\rm exp} = 2.8$ [3]. Similarly, for Nb we have $\lambda = 1.26$ [34], so that, again, using $\lambda_{\rm ee} \sim 1$, we obtain $\alpha \sim 2.42$, in good agreement with the 'experimental' value of $\alpha = 2.3$ [3]. The interval of the values of $\alpha = 0.7-2.8$ [3, 4] for $\lambda_{\rm ee} = 1$ corresponds to the interval of $\lambda = 0.25-1.5$, which seems quite reasonable.

More detailed results of such estimates (assuming $\lambda_{\rm ee} = 1$) are given in Table 2.

Table 2. Estimates of the coefficient α for a number of metals.

Metal	λ	$\frac{2\pi\lambda}{1+\lambda}$	$\frac{2\pi}{1+\lambda+\lambda_{\rm ee}}$	$\alpha_{\rm exp}$
Pb	1.68	3.93	2.86	2.8
Nb	1.26	3.50	2.42	2.3
Cu	0.14	0.77	0.41	1.0
Al	0.44	1.91	1.13	1.1
Pd	0.35	1.63	0.93	1.1

We can now see that, for all metals under consideration here, with the exception of Cu, experimental data on coefficient α are described rather satisfactorily, and full agreement can be achieved by minor variations in $\lambda_{\rm ee}$ around the value of $\lambda_{\rm ee} = 1$. This is not so only for Cu, where agreement can be reached by the introduction of $\lambda_{\rm ee} < 0$. Negative values of $\lambda_{\rm ee}$ are possible, taking into account that the general limitation here [38] is $F_1^{\rm s} > -3$, i.e., $\lambda_{\rm ee} > -1$.

Thus we come to the main conclusion: the 'experimentally' observed universal Planckian relaxation in metals, independent of the value of the coupling constant, is nothing more than a *delusion*, related to the procedure of representation of experimental data in Refs [3, 4] (determination of the effective mass in the expression for resistivity from low-temperature measurements). Similarly, the same applies to the results of a recent paper [58], where this procedure was used to represent experimental data on bilayer graphene near the 'magic' angle of (mis)orientation of the layers.

5.5 Once again on the uncertainty principle

Where is the problem with estimates of the relaxation time based on the energy–time uncertainty relation? This is rather simple — in Eqn (20), ΔE should be taken not as $k_{\rm B}T$, but as a real 'level width' (spectrum damping) in the system of many interacting (!) particles:

$$\Gamma(T) = 2\pi\lambda T\,. \tag{102}$$

Then, we immediately have

$$\frac{\hbar}{\tau} \leqslant 2\pi\lambda T\,, \tag{103}$$

so that the use of the uncertainty relation becomes a kind of tautology. Then, the 'upper limit' of the high-temperature relaxation rate is not universal and naturally proportional to the coupling constant.

At the same time, the result of Eqn (99) obtained above formally defines some universal upper limit for the relaxation rate of *quasiparticles*, so that the estimates based on the uncertainty relation can probably be applied here.

6. Conclusions

As we stressed above, our aims did not include an explanation of T-linear growth of resistivity, starting from the lowest temperatures, which is observed in copper oxide high-temperature superconductors and some similar systems. In the models of scattering by quantum fluctuations of an arbitrary nature (e.g., phonons), such a behavior appears at temperatures of the order of or higher than the characteristic frequency of these fluctuations, i.e., in the classical limit. At present, it is unclear whether such low-frequency fluctuations exist in the vicinity of the quantum critical point on the phase diagram of cuprates, which could have explained their anomalous behavior. But this is the simplest calculable model which clearly shows that the universal Planckian behavior of the relaxation rate is just absent, as is the universal upper limit for this relaxation rate. A dependence on the interaction parameters in the relaxation rate does not disappear, and it can, in principle, easily overcome the limit of $\alpha \sim 1$.

In the literature, quite a number of microscopic models have been proposed to explain the T-linear growth of resistivity (inelastic scattering rate) in metals. We have already mentioned Refs [10, 11, 13], where this behavior appeared in the model of 'fermion' condensation and was related, in particular, to the formation of 'flat' bands near the Fermi level and the appearance of low-frequency zero-sound excitations, so that scattering by these excitations leads to a T-linear growth of the scattering rate.

In Ref. [12], an interesting model was proposed with random interactions of electrons, where the 'flat' band also forms, and for a wide interval of parameters, the T-linear growth of resistivity is realized. It is unclear, however, what relation, if any at all, the model of interactions assumed in Ref. [12] has to real metals.

Note also that in all these approaches the universal 'Planckian' dependence on temperature does not appear, and the dependence on the coupling strength (though probably a weak one) is conserved. A similar situation is realized in a popular phenomenological model of a marginal Fermi liquid [48], which successfully explains many properties of cuprates.

An interesting model was proposed recently in Ref. [59] to explain the anomalous temperature dependence of resistivity in $Sr_3Ru_2O_3$ by electron–electron scattering processes, taking into account the rather complicated real electronic spectrum of this compound, leading to a many-sheet Fermi surface, with some special 'hot' pockets, where electrons are nondegenerate (classical limit). It is the scattering of electrons from 'cold' (degenerate) parts of the Fermi surface, with a transition of one of these electrons to the 'hot' pocket, which leads to the linear growth of resistivity with temperature. The analogy with the model with scattering by nondegenerate fluctuations (classical limit) considered above is pretty obvious. Of course, the dependence on the value of the appropriate coupling constant does not disappear, and the 'universal' Planckian behavior appears only for the renormalized (in the sense discussed above) scattering rate of the quasiparticles.

A special place is occupied by Refs [14–17], based on analogies taken from black hole physics, cosmology, and superstring theory, which pretend to explain the universal 'Planckian' behavior of the relaxation rate. Being very interesting from the theoretical point of view, these papers, in our opinion, have a weak relation to solid state physics.

In this paper, we have limited ourselves to an elementary analysis based on the standard approaches of the solid state theory and shown that the observed universal 'Planckian' behavior of the electron relaxation rate in many metals [3, 4] has a rather simple explanation not related to some special deep physics but simply to the method of representation of experimental data used in these papers. The use in the Drude expression for conductivity (resistivity) of the effective mass, determined from low-temperature measurements, which includes the renormalization due to many-particle effects (interactions), inevitably leads to appropriate renormalization of the relaxation rate (time), which is replaced by an effective rate $\tilde{\Gamma}$ (98) of relaxation for quasiparticles, which is relatively weakly dependent on the coupling strength and, in principle, produces the universal 'Planckian' behavior as an upper limit for this relaxation rate. However, this behavior is a pure *delusion* and does not reflect any kind of special physics. In microscopic theory, it is the unrenormalized (by interactions) band mass which enters the Drude expression for conductivity, and the relaxation rate is naturally proportional to the strength of interaction, as has been well known since the early days of quantum solid state theory.

The size of the effective relaxation rate $\hbar/\tau = k_B T$ (i.e., in fact, the 'Planckian' rate discussed above) in the standard theory, as is also well known, defines some characteristic scale which separates regions of different behavior of the resistivity of metals, as shown in Fig. 12, taken from textbook [25]. There, we also show characteristic temperature dependences of resistivity of metals. The 'Planckian' scattering rate determines the diagonal on this figure, but does not define any new quantum limit. In principle, all this has been known

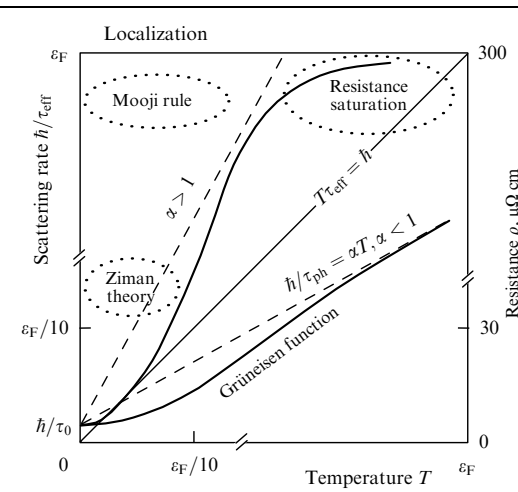

Figure 12. Temperature–disorder plane (T, $\hbar/\tau$), where regions of applicability of different models of electrical resistivity are shown. Also shown are the temperature dependences of resistivity. The 'Planckian' relaxation rate determines the diagonal on this plane.

for a long time and does not require any 'exotic' approaches to explain it.

The author is grateful to E Z Kuchinskii and D I Khomskii for their useful discussions. This study was partially supported by the Russian Foundation for Basic Research (grant no. 20-02-00011).

Appendix. Momentum distribution in the case of Planckian relaxation

Consider the momentum distribution corresponding to Green's function (95):

$$N(\mathbf{p}) = T\sum_n G(\mathrm{i}\varepsilon_n, \mathbf{p})\,. \tag{A.1}$$

Performing the standard summation over fermion Matsubara frequencies [18], we obtain[4]

$$\begin{aligned} N(\mathbf{p}) &= -\frac{1}{2\pi\mathrm{i}}\int_c \mathrm{d}\varepsilon\, f(\varepsilon) G(\varepsilon, \mathbf{p}) \\ &= -\frac{1}{2\pi\mathrm{i}}\int_{-\infty}^{\infty} \mathrm{d}\varepsilon\, f(\varepsilon)\big(G^{\mathrm{R}}(\varepsilon, \mathbf{p}) - G^{\mathrm{A}}(\varepsilon, \mathbf{p})\big) \\ &= \int_{-\infty}^{\infty} \mathrm{d}\varepsilon\, f(\varepsilon) A(\varepsilon, \mathbf{p})\,, \end{aligned} \tag{A.2}$$

where $f(\varepsilon) = 1/[\exp(\varepsilon/T) + 1]$ is the Fermi distribution, and the spectral density $A(\varepsilon, \mathbf{p}) = -(1/\pi)\,\mathrm{Im}\, G^{\mathrm{R}}(\varepsilon, \mathbf{p})$ for Green's function (95) is given by the Lorentzian

$$A(\varepsilon, \mathbf{p}) = \frac{1}{\pi}\,\frac{(\alpha/2)T}{(\varepsilon - \varepsilon_{\mathbf{p}})^2 + [(\alpha/2)T]^2}\,. \tag{A.3}$$

In Fig. 13, we show distribution functions $N(\mathbf{p})$, obtained numerically directly from (A.2) with spectral density (A.3) for different values of α. However, for special $\alpha = 2\pi n$, $n = 0, 1, \ldots$, distribution functions can be obtained analytically. For $\alpha = 0$, we obviously get the usual Fermi distribution $N(\mathbf{p}) = f(\varepsilon_{\mathbf{p}})$. For $\alpha = 2\pi$, we obtain

$$G(\mathrm{i}\varepsilon_n, \mathbf{p}) = \frac{1}{\mathrm{i}\varepsilon_n - \varepsilon_{\mathbf{p}} + \mathrm{i}\pi T\,\mathrm{sign}\,\varepsilon_n} = \frac{1}{\mathrm{i}2\pi T m - \varepsilon_{\mathbf{p}}}\,, \tag{A.4}$$

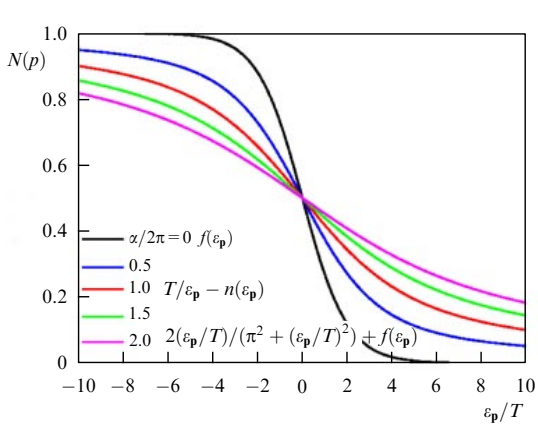

Figure 13. (Color online.) Distribution function for Planckian relaxation with different α.

[4] The calculations presented below were done by E Z Kuchinskii.

where m is an integer, but sign ε_n excludes the value of $m = 0$. Then, the distribution function of particles is

$$\begin{aligned} N(\mathbf{p}) &= T\sum_n G(\mathrm{i}\varepsilon_n, \mathbf{p}) = T\sum_{m\neq 0}\frac{1}{\mathrm{i}2\pi T m - \varepsilon_{\mathbf{p}}} \\ &= T\sum_m \frac{1}{\mathrm{i}2\pi T m - \varepsilon_{\mathbf{p}}} + \frac{T}{\varepsilon_{\mathbf{p}}}\,. \end{aligned} \tag{A.5}$$

Note that the sign before summation over seemingly even Matsubara frequencies remained the same (fermion-like), which is related to initial summing over odd frequencies. The second term in the last expression in (A.5) compensated the contribution of $m = 0$, which appeared in the sum over m in the first term. Making the standard summation over even frequencies $\varepsilon_m = 2\pi T m$, we get

$$\begin{aligned} T\sum_m \frac{1}{\mathrm{i}\varepsilon_m - \varepsilon_{\mathbf{p}}} &= \frac{1}{2\pi\mathrm{i}}\int_c \mathrm{d}\varepsilon\,\frac{1}{\varepsilon - \varepsilon_{\mathbf{p}} \pm \mathrm{i}\delta}\, n(\varepsilon) \\ &= \frac{1}{\pi}\int_{-\infty}^{\infty}\mathrm{d}\varepsilon\,\mathrm{Im}\,\frac{1}{\varepsilon - \varepsilon_{\mathbf{p}} + \mathrm{i}\delta}\, n(\varepsilon) \\ &= -\int_{-\infty}^{\infty}\mathrm{d}\varepsilon\,\delta(\varepsilon - \varepsilon_{\mathbf{p}}) n(\varepsilon) = -n(\varepsilon_{\mathbf{p}})\,, \end{aligned} \tag{A.6}$$

where $n(\varepsilon) = 1/[\exp(\varepsilon/T) - 1]$ is the Bose distribution.

Thus, for $\alpha = 2\pi$,

$$N(\mathbf{p}) = \frac{T}{\varepsilon_{\mathbf{p}}} - n(\varepsilon_{\mathbf{p}})\,. \tag{A.7}$$

Note once again that the minus sign before the Bose distribution in (A.7) is related to initial summation over fermion frequencies.

For $\alpha = 4\pi$, again we have summation over odd frequencies, but with the two fermion Matsubara frequencies closest to zero excluded:

$$\begin{aligned} N(\mathbf{p}) &= T\sum_n \frac{1}{\mathrm{i}\varepsilon_n - \varepsilon_{\mathbf{p}} + \mathrm{i}2\pi T\,\mathrm{sign}\,\varepsilon_n} \\ &= T\sum_{n\neq 0,-1}\frac{1}{\mathrm{i}2\pi T(n + 1/2) - \varepsilon_{\mathbf{p}}} \\ &= T\sum_n \frac{1}{\mathrm{i}\varepsilon_n - \varepsilon_{\mathbf{p}}} - T\left(\frac{1}{\mathrm{i}\pi T - \varepsilon_{\mathbf{p}}} + \frac{1}{-\mathrm{i}\pi T - \varepsilon_{\mathbf{p}}}\right) \\ &= f(\varepsilon_{\mathbf{p}}) + \frac{2T\varepsilon_{\mathbf{p}}}{\varepsilon_{\mathbf{p}}^2 + (\pi T)^2}\,. \end{aligned} \tag{A.8}$$

In Fig. 13, for $\alpha = 2\pi$ and $\alpha = 4\pi$ we show both distributions obtained numerically from (A.2) with spectral density (A.3) and obtained directly from (A.7) and (A.8) (obviously, these are identical).

In general, it can be seen that the distribution functions in our model are quite different from the usual step-function of the Fermi-liquid theory.

Note added in proof. After this work was accepted for publication we have learned on the paper [60], where the authors came to similar conclusions in the context of electron–phonon interaction.

References

1. Batlogg B *Phys. Today* **44** (6) 44 (1991)
2. Iye Y, in *Physical Properties of High Temperature Superconductors III* (Ed. D M Ginsberg) (Singapore: World Scientific, 1992) p. 285
3. Bruin J A N et al. *Science* **339** 804 (2013)
4. Legros A et al. *Nat. Phys.* **15** 142 (2019)
5. Zaanen J *Nature* **430** 512 (2004)
6. Ziman J M *Electrons and Phonons*; *the Theory of Transport Phenomena in Solid* (Oxford: Clarendon Press, 1960); Translated into Russian: *Elektrony i Fonony*: *Teoriya Yavlenii Perenosa v Tverdykh Telakh* (Moscow: IL, 1962)
7. Meißner W, in *Handbuch der Experimentalphysik* Vol. 11, Pt. 2 (Leipzig: Akad. Verlagsgesellschaft, 1935) p. 338
8. Maksimov E G *Phys. Usp.* **43** 965 (2000); *Usp. Fiz. Nauk* **170** 1033 (2000)
9. Martin S et al. *Phys. Rev. B* **41** 846(R) (1990)
10. Shaginyan V R, Popov K G, Khodel V A *Phys. Rev. B* **88** 115103 (2013)
11. Shaginyan V R et al. *JETP Lett.* **110** 290 (2019); *Pis'ma Zh. Eksp. Teor. Fiz.* **110** 266 (2019)
12. Patel A A, Sachdev S *Phys. Rev. Lett.* **123** 066601 (2019)
13. Volovik G E *JETP Lett.* **110** 352 (2019); *Pis'ma Zh. Eksp. Teor. Fiz.* **110** 335 (2019)
14. Zaanen J *Nature* **448** 1000 (2007)
15. Hartnoll S A *Nat. Phys.* **11** 54 (2015)
16. Herzog C P et al. *Phys. Rev. D* **75** 085020 (2007)
17. Hartnoll S A et al. *Phys. Rev. B* **76** 144502 (2007)
18. Sadovskii M V *Diagrammatics*: *Lectures on Selected Problems in Condensed Matter Theory* (Singapore: World Scientific, 2019); Translated from Russian: *Diagrammatika*: *Lektsii po Izbrannym Zadacham Teorii Kondensirovannogo Sostoyaniya* (Moscow – Izhevsk: Inst. Komp'yut. Issled. – RKhD, 2019)
19. Ioffe A F, Regel A R, in *Progress in Semiconductors* Vol. 4 (London: Heywood, 1960) p. 237
20. Mott N F *Metal – Insulator Transitions* (London: Taylor and Francis, 1974); Translated into Russian: *Perekhody Metall – Izolyator* (Moscow: Nauka, 1979)
21. Abrahams E et al. *Phys. Rev. Lett.* **42** 673 (1979)
22. Sadovskii M V *Sov. Phys. Usp.* **24** 96 (1981); *Usp. Fiz. Nauk* **133** 223 (1981)
23. Vollhardt D, Wölfle P, in *Electronic Phase Transitions* (Modern Problems in Condensed Matter Sciences, Vol. 32, Eds W Hanke, Yu V Kopaev) (Amsterdam: North-Holland, 1992) p. 1
24. Markoš P *Acta Phys. Slovaca* **56** 561 (2006)
25. Gantmakher V F *Electrons and Disorder in Solids* (Oxford: Clarendon Press, 2005); Translated from Russian: *Elektrony v Neuporyadochennykh Sredakh* (Moscow: Fizmatlit, 2013)
26. Mooij J H *Phys. Status Solidi A* **17** 521 (1973)
27. Gurvitch M, Fiory A T *Phys. Rev. Lett.* **59** 1337 (1987)
28. Takagi H et al. *Phys. Rev. Lett.* **69** 2975 (1992)
29. Hussey N E (II), Takenaka K, Takagi H *Philos. Mag.* **84** 2847 (2004)
30. Poniatowski N R et al. *Phys. Rev. B* **103** L020501 (2021); arXiv:2007.03685
31. Zaanen J, unpublished talks
32. Allen P B, Mitrović B, in *Solid State Physics* Vol. 37 (Eds H Ehrenreich, F Seitz, D Turnbull) (New York: Academic Press, 1983) p. 1
33. Allen P B *Phys. Rev. B* **3** 305 (1971)
34. Savrasov S Y, Savrasov D Y *Phys. Rev. B* **54** 16487 (1996)
35. Sadovskii M V *JETP Lett.* **111** 188 (2020); *Pis'ma Zh. Eksp. Teor. Fiz.* **111** 203 (2020)
36. Pines D *The Many–Body Problem* (New York: W.A. Benjamin, 1961); Translated into Russian: *Problema Mnogikh Tel* (Moscow: IL, 1963)
37. Abrikosov A A, Gorkov L P, Dzyaloshinski I E *Methods of Quantum Field Theory in Statistical Physics* (Englewood Cliffs, N.J.: Prentice-Hall, 1963); Translated from Russian: *Metody Kvantovoi Teorii Polya v Statisticheskoi Fizike* (Moscow: Fizmatgiz, 1962); *Metody Kvantovoi Teorii Polya v Statisticheskoi Fizike* (Moscow: Dobrosvet, 1998)
38. Pines D, Nozières P *The Theory of Quantum Liquids* Vol. 1 (New York: W.A. Benjamin, 1966); Translated into Russian: *Teoriya Kvantovykh Zhidkostei* (Moscow: Mir, 1967)
39. Ziman J M *Models of Disorder*: *the Theoretical Physics of Homogeneously Disordered Systems* (Cambridge: Cambridge Univ. Press, 1979); Translated into Russian: *Modeli Besporyadka*: *Teoreticheskaya Fizika Odnorodno Neuporyadochennykh Sistem* (Moscow: Mir, 1982)
40. Edwards S F *Philos. Mag.* **6** 617 (1961)
41. Edwards S F *Proc. R. Soc. Lond. A* **267** 518 (1962)
42. Proust C, Taillefer L *Annu. Rev. Condens. Matter Phys.* **10** 409 (2019)
43. Sachdev S *Quantum Phase Transitions* (Cambridge: Cambridge Univ. Press, 1999)
44. Stishov S M *Phys. Usp.* **47** 789 (2004); *Usp. Fiz. Nauk* **174** 853 (2004)
45. Sadovskii M V *Phys. Usp.* **44** 515 (2001); *Usp. Fiz. Nauk* **171** 539 (2001)
46. Sadovskii M V, in *Struny. Brany, Reshetki, Setki, Psevdoshcheli i Pylinki*: *Trudy Seminara im. I.E. Tamma* (Strings, Branes, Lattices, Pseudogap, and Dust: Proceedings of the I.E. Tamm Seminar) (Sci. Eds M A Vasiliev, L V Keldysh, A M Semikhatov) (Moscow: Nauchnyi Mir, 2007) p. 357; cond-mat/0408489
47. Kuchinskii E Z, Nekrasov I A, Sadovskii M V *Phys. Usp.* **55** 325 (2012); *Usp. Fiz. Nauk* **182** 345 (2012)
48. Varma C M *Rev. Mod. Phys.* **92** 031001 (2020)
49. Sadovskii M V *Phys. Rep.* **282** 225 (1997)
50. Sadovskii M V *Superconductivity and Localization* (Singapore: World Scientific, 2000)
51. Fukuyama H, Ebisawa H, Wada Y *Prog. Theor. Phys.* **42** 494 (1969)
52. Nakajima S, Watabe M *Prog. Theor. Phys.* **29** 341 (1963)
53. Prange R E, Kadanoff L P *Phys. Rev.* **134** A566 (1964)
54. Heine V, Nozières P, Wilkins J W *Philos. Mag.* **13** 741 (1966)
55. Grimvall G *Phys. Scripta* **14** 63 (1976)
56. Esterlis I et al. *Phys. Rev. B* **97** 140501(R) (2018)
57. Chubukov A V et al. *Ann. Physics* **417** 168190 (2020)
58. Cao Y et al. *Phys. Rev. Lett.* **124** 076801 (2020)
59. Mousatov C H, Berg E, Hartnoll S A *Proc. Natl. Acad. Sci. USA* **117** 2852 (2020)
60. Hwang E H, Das Sarma S *Phys. Rev. B* **99** 085105 (2019)

Limits of Eliashberg Theory and Bounds for Superconducting Transition Temperature

M.V. Sadovskii
Institute for Electrophysics, Russian Academy of Sciences,
Ural Branch, Ekaterinburg 620016, Russia
E-mail: sadovski@iep.uran.ru

The discovery of record – breaking values of superconducting transition temperature T_c in quite a number of hydrides under high pressure was an impressive demonstration of capabilities of electron – phonon mechanism of Cooper pairing. This lead to an increased interest to foundations and limitations of Eliashberg – McMillan theory as the main theory describing superconductivity in a system of electrons and phonons. Below we shall consider both elementary basics of this theory and a number of new results derived only recently. We shall discuss limitations on the value of the coupling constant related to lattice instability and a phase transition to another phase (CDW, bipolarons). Within the stable metallic phase the effective pairing constant may acquire arbitrary values. We consider extensions beyond the traditional adiabatic approximation. It is shown that Eliasberg – McMillan theory is also applicable in the strong antiadiabatic limit. The limit of very strong coupling, being most relevant for the physics of hydrides, is analyzed in details. We also discuss the bounds for T_c appearing in this limit.

Contents

I. Introduction 1

II. Eliashberg – McMillan approximation 2

III. Migdal theorem 4

IV. Strong coupling and lattice instability 6

V. McMillan expression for electron – phonon coupling constant 9

VI. Eliashberg equations 10
A. Weak and intermediate coupling 11
B. Lower bound for T_c in the limit of very strong coupling 12

VII. Maximal T_c? 14

VIII. Superhydrides and Eliashberg theory 16

IX. Conclusions 17

References 17

I. INTRODUCTION

The discovery [1] of superconductivity with critical temperature approaching $T_c = 203$ K under pressure in the interval of 100-250 GPa (in diamond anvils) in H_3S system lead to a stream of papers devoted to experimental studies of high – temperature superconductivity in hydrides in megabar region (cf. reviews [2, 4, 5]). Theoretical analysis immediately confirmed, that these record – breaking values of T_c are ensured by traditional electron – phonon interaction in the limit of strong enough electron – phonon coupling [3, 6]. More so, the detailed calculations for a number of rare earth hydrides under pressure [6] lead to the prediction of pretty large number of such systems with record values of T_c. In some cases these predictions were spectacularly confirmed. In particular experimentally the values of $T_c = 220$ - 260 K were obtained in systems like LaH_{10} [7, 8], YH_6 [9], $(La,Y)H_{6,10}$ [10], YH_9 [11]. At last, quite recently a psychological border was crossed, when in Ref. [12] superconductivity with $T_c = 287.7\pm1.2$ K (i.e. about +15 degrees Celsius) was obtained in C-H-S systems at pressures of 267±10 GPa.

The matter of principle here is that these works explicitly demonstrated the absence of any significant limitations for T_c within electron – phonon mechanism of Cooper pairing, where it was traditionally believed that T_c can not exceed 30-40 K. Correspondingly, the most pressing now became the question of the upper limit of T_c, which can be achieved due to this pairing mechanism.

Since the appearance of BCS theory it became obvious, that the increase of T_c in superconductors can be realized by increasing the frequency of phonons responsible for Cooper pairing, as well as by the increase of the effective interaction of these phonons with electrons. These questions were studied by numerous authors. The most developed approach for description of superconductivity in the system of electrons of phonons remains Eliashberg – McMillan theory [3, 13–16]. It is well known that this theory is entirely based upon the adiabatic approximation and Migdal theorem [17–20], which allows to neglect vertex corrections while calculating the effects of electron – phonon interaction in typical metals. The real small parameter of perturbation theory here is $\lambda\frac{\Omega_0}{E_F} \ll 1$, where λ is dimensionless constant of electron – phonon interaction, Ω_0 is characteristic phonon frequency and E_F is Fermi energy of electrons. In particular, this leads to the conclusion that vertex corrections in this theory can be neglected even in case of $\lambda > 1$, because of inequality $\frac{\Omega_0}{E_F} \ll 1$ being valid in typical metals. Recently, a number of papers appeared [21–23], where some doubts were expressed on these conclusions and some revisions pro-

posed, based on the results of quantum Monte – Carlo calculations for electron – phonon system.

In Refs. [24–26] we have shown that under conditions of strong nonadiabaticity, when $\Omega_0 \gg E_F$, the theory acquires new small parameter $\lambda_D \sim \lambda\frac{E_F}{\Omega_0} \sim \lambda\frac{D}{\Omega_0} \ll 1$ (D is the half – width of electron band), so that corrections to electronic spectrum becomes insignificant. Vertex corrections can also be neglected in this case, as was earlier shown in Ref. [27]. In general case the renormalization of electron spectrum (effective mass of an electron) is determined by the new dimensionless coupling constant $\tilde{\lambda}$, which tends to the usual λ in adiabatic limit, while in the strong antiadiabatic limit it tends to λ_D. At the same time, the temperature of superconducting transition T_c in antiadiabatic limit is determined by the usual pairing constant of Eliashberg – McMillan theory λ, generalized for the account of the finiteness of phonon frequency. Thus, the Eliashberg – McMillan approach remains valid also in the strong antiadiabatic limit.

In general, the interest towards the problem of superconductivity in the strong antiadiabatic limit is stimulated by the discovery of a number of other superconductors, where adiabatic approximation becomes invalid and characteristic phonon frequencies are of the order of or even higher than electron Fermi energy. Typical in this respect are intercalated systems with FeSe monolayers, as well as single – layer films of FeSe on $Sr(Ba)TiO_3$ (FeSe/STO) substrates [28]. The nonadiabatic nature of superconductivity in FeSe/STO system was first noted by Gor'kov [29, 30], while discussing the possible mechanism of superconducting T_c enhancement in FeSe/STO due to interaction with high – energy optical phonons of $SrTiO_3$ [28]. Similar situation in fact appears also in an old problem of superconductivity in doped $SrTiO_3$ [31], as well as in twisted bi(tri)layers of graphene [32]. In hydrides there are also possibility of existence of some small "pockets" of the Fermi surface with small values of Fermi energy [3].

This paper is devoted to the critical review of these problems on rather elementary level. Our presentation does not pretend to be exhaustive or giving the complete review of multiple papers devoted to to studies of Eliashberg equations in recent decades. However, the author hopes that such presentation can be useful both to young theorists and also to some experts in this field.

II. ELIASHBERG – MCMILLAN APPROXIMATION

Fröhlich Hamiltonian which is usually used to describe electron – phonon interaction can be written as [13, 19]:

$$H = \sum_{\mathbf{p}} \varepsilon_{\mathbf{p}} a^+_{\mathbf{p}} a_{\mathbf{p}} + \sum_{\mathbf{k}} \Omega_{0\mathbf{k}} b^+_{\mathbf{k}} b_{\mathbf{k}} + \\ + \frac{1}{\sqrt{N}} \sum_{\mathbf{pk}} g_{\mathbf{k}} a^+_{\mathbf{p+k}} a_{\mathbf{p}} (b_{\mathbf{k}} + b^+_{-\mathbf{k}}) \quad (1)$$

where $\varepsilon_{\mathbf{p}}$ is electron spectrum counted from the Fermi level, $\Omega_{0\mathbf{k}}$ is phonon spectrum[1] and we have introduced the standard notations for creation $a^+_{\mathbf{p}}$ and annihilation $a_{\mathbf{p}}$ operators of electrons and phonons – $b^+_{\mathbf{k}}$ and $b_{\mathbf{k}}$, N is the number of atoms in crystal.

The matrix element of electron – phonon interaction has the following form [13, 19]:

$$g_{\mathbf{k}} = -\frac{1}{\sqrt{2M\Omega_{0\mathbf{k}}}} \langle \mathbf{p}|\mathbf{e}(\mathbf{q})\nabla V_{ei}(\mathbf{r})|\mathbf{p}+\mathbf{q}\rangle \\ \equiv -\frac{1}{\sqrt{2M\Omega_{0\mathbf{k}}}} I(\mathbf{k}) \quad (2)$$

where V_{ei} is electron – ion interaction potential, M is ion mass, and $\mathbf{e}(\mathbf{q})$ is polarization vector of a phonon with frequency $\Omega_{0\mathbf{q}}$.

To describe the phonon spectrum we often use simplified Debye and Einstein models. In Debye model the phonon spectrum is assumed to be $\Omega_{0\mathbf{k}} = ck$ (c is the speed of sound) for all $k < k_D$, which gives an elementary model of acoustic phonons. In this case Debye frequency $\Omega_D = ck_D$ defines the upper limit of phonon frequencies. In Einstein model phonon frequency is assumed to be independent of the wave vector: $\Omega_{0\mathbf{k}} = \Omega_0$ for all k within Brillouin zone, which gives the simplified model of optical phonons.

To describe interaction of electrons with optical (Einstein) phonons often the so called Holstein model is also used. Its Hamiltonian is commonly written in coordinate (site) representation in the lattice and electron – phonon interaction is assumed to be local (single – site):

$$H = -t\sum_{ij\sigma}(t_{ij}a^+_{i\sigma}a_{j\sigma} + c.c.) + \Omega_0 \sum_i b^+_i b_i \; - \mu \sum_{i\sigma} n_{i\sigma} \\ + g\sum_i (b_i + b^+_i) \sum_\sigma n_{i\sigma} \quad (3)$$

where $a^+_{i\sigma}$ and $a_{i\sigma}$ are creation and annihilation operators of electron with spin σ on lattice site i, $n_i = a^+_{i\sigma}a_{i\sigma}$ is electron density operator on site, t_{ij} – transfer integrals of electrons between lattice sites, determining their spectrum (bandwidth) in tight – binding approximation, b^+_i and b_i corresponding operators for phonons with frequency Ω_0. The strength of electron – phonon interaction is determined by interaction constant g. Obviously this interaction describes the local interaction of Einstein phonon with electron density at a lattice site. The chemical potential μ is determined by conduction band filling and defines the origin of the energy scale for electrons.

Consider the simplest second – order diagram of electron – phonon interaction, shown in Fig. 1. Let us perform calculations in Matsubara technique (i.e at finite

[1] Note that here we have introduced the "bare" phonon spectrum *in the absence* of electron – phonon interaction, which has no obvious definition in a real metal.

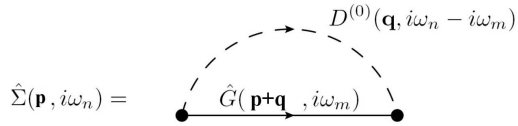

FIG. 1: Second – order diagram for electronic self – energy.

temperatures $T > 0$). Analytical expression corresponding to this diagram has the form:

$$\Sigma(i\omega_n, \mathbf{p}) = -T \sum_{n=-\infty}^{\infty} \sum_{\mathbf{p}'} |g_{\mathbf{pp}'}|^2 G_0(i\omega_{n'}, \mathbf{p}') \times \times D_0(i\omega_n - i\omega_{n'}, \mathbf{p} - \mathbf{p}') \quad (4)$$

Subscript 0 at Green's functions of electron $G_0(i\omega_{n'}, \mathbf{p}')$ and phonon $D_0(i\omega_n - i\omega_{n'}, \mathbf{p} - \mathbf{p}')$ (4) indicates that these are Green's functions of free particles.

Summation over Matsubara frequencies is performed in a standard way [19, 20], so that:

$$\Sigma(i\omega_n, \mathbf{p}) = \sum_{\mathbf{p}'} |g_{\mathbf{pp}'}|^2 \left\{ \frac{f_{\mathbf{p}'} + n_{\mathbf{p}-\mathbf{p}'}}{i\omega_n - \varepsilon_{\mathbf{p}'} + \Omega_{0\mathbf{p}-\mathbf{p}'}} + \frac{1 - f_{\mathbf{p}'} + n_{\mathbf{p}-\mathbf{p}'}}{i\omega_n - \varepsilon_{\mathbf{p}'} - \Omega_{0\mathbf{p}-\mathbf{p}'}} \right\} \quad (5)$$

where $f(\mathbf{p}) = \frac{1}{e^{\frac{\varepsilon_p}{T}}+1}$ is Fermi distribition of electrons, while $n_q = \frac{1}{e^{\frac{\Omega_{0q}}{T}}+1}$ is Planckian (Bose) distribition of phonons. For temperatures $T \to 0$ Fermi distribution of electrons transforms into step – function, while Planckian function of phonons tends to zero, so that the first term in figure brackets is different from zero only for $\varepsilon_{p'} < 0$, while the second one for $\varepsilon_{p'} > 0$. Correspondingly, in the limit of $T = 0$, after the substitution $i\omega_n \to \varepsilon + i\delta sign\varepsilon_{p'}$, the contribution of diagram of Fig. 1 can be written as [13]:

$$\Sigma(\varepsilon, \mathbf{p}) = \sum_{\mathbf{p}'} |g_{\mathbf{pp}'}|^2 \left\{ \frac{f_{\mathbf{p}'}}{\varepsilon - \varepsilon_{\mathbf{p}'} + \Omega_{0\mathbf{p}-\mathbf{p}'} - i\delta} + \frac{1 - f_{\mathbf{p}'}}{\varepsilon - \varepsilon_{\mathbf{p}'} - \Omega_{0\mathbf{p}-\mathbf{p}'} + i\delta} \right\} \quad (6)$$

Eq. (6) can be identically rewritten as:

$$\Sigma(\varepsilon, \mathbf{p}) = = \int d\omega \sum_{\mathbf{p}'} |g_{\mathbf{pp}'}|^2 \delta(\omega - \Omega_{0\mathbf{p}-\mathbf{p}'}) \left\{ \frac{f_{\mathbf{p}'}}{\varepsilon - \varepsilon_{\mathbf{p}'} + \omega - i\delta} + + \frac{1 - f_{\mathbf{p}'}}{\varepsilon - \varepsilon_{\mathbf{p}'} - \omega + i\delta} \right\} \quad (7)$$

Scattering of electrons by phonons in fact takes place in some narrow energy layer close to Fermi level with the width of the order of double Debye frequency $2\Omega_D$, and in typical metals we always have $\Omega_D \ll E_F$. In this situation with high accuracy we can assume that both initial and final momenta of electron $\mathbf{p}$ and $\mathbf{p}'$ are at the Fermi surface. The main idea of Eliashberg – McMillan approach is that we can avoid explicit dependence on momenta, performing the averaging of the matrix element of electron – phonon interaction over surfaces of constant energy, corresponding to initial and final momenta $\mathbf{p}$ and $\mathbf{p}'$, which is practically the same as the averaging over corresponding real Fermi surfaces of a metal, which are define by equations $\varepsilon(\mathbf{p}) = 0$ and $\varepsilon(\mathbf{p}') = 0$. This is achieved by the following substitution ($N(0)$ is the density of states at the Fermi level):

$$|g_{\mathbf{pp}'}|^2 \delta(\omega - \Omega_{0\mathbf{p}-\mathbf{p}'}) \Longrightarrow \frac{1}{N(0)} \sum_{\mathbf{p}} \frac{1}{N(0)} \sum_{\mathbf{p}'} |g_{\mathbf{pp}'}|^2 \delta(\omega - \Omega_{0\mathbf{p}-\mathbf{p}'}) \delta(\varepsilon_{\mathbf{p}}) \delta(\varepsilon_{\mathbf{p}'}) \equiv \frac{1}{N(0)} \alpha^2(\omega) F(\omega) \quad (8)$$

where in the final line we have introduced the standard *definition* of Eliashberg function $\alpha^2(\omega)$, which reflects the strength of electron – phonon interaction, while $F(\omega) = \sum_{\mathbf{q}} \delta(\omega - \Omega_{0\mathbf{q}})$ is the ohonon density of states, In principle, these functions can be directly determined from experiments.

In the case when phonon energy becomes comparable or even exceeds Fermi energy, electron scattering takes place not in a narrow layer close to Fermi surface, but in much wider energy interval. Then, for an initial $|\mathbf{p}| \sim p_F$ the averaging over $\mathbf{p}'$ in expression like (8) should be made over surface of constant energy, corresponding to $E_F + \Omega_{0\mathbf{p}-\mathbf{p}'}$ [24, 26]. Correspondingly, Eq. (8) is obviously generalized as:

$$|g_{\mathbf{pp}'}|^2 \delta(\omega - \Omega_{\mathbf{p}-\mathbf{p}'}) \Longrightarrow \frac{1}{N(0)} \sum_{\mathbf{p}} \frac{1}{N(0)} \sum_{\mathbf{p}'} |g_{\mathbf{pp}'}|^2 \delta(\omega - \Omega_{0\mathbf{p}-\mathbf{p}'}) \delta(\varepsilon_{\mathbf{p}}) \delta(\varepsilon_{\mathbf{p}'} - \Omega_{0\mathbf{p}-\mathbf{p}'}) \equiv \frac{1}{N(0)} \alpha^2(\omega) F(\omega) \quad (9)$$

which in the last δ-function simply corresponds to a transition from chemical potential μ to $\mu + \Omega_{\mathbf{p}-\mathbf{p}'}$. Remember, that we always put the origin of an energy scale at $\mu = 0$.

After the replacement (8) the explicit dependence on momenta in self – energy vanishes and in the following we are dealing with the average over the Fermi surface $\Sigma(\varepsilon) \equiv \frac{1}{N(0)} \sum_{\mathbf{p}} \delta(\varepsilon_{\mathbf{p}}) \Sigma(\varepsilon, \mathbf{p})$, which is written now as:

$$\Sigma(\varepsilon) = \int d\varepsilon' \int d\omega \alpha^2(\omega) F(\omega) \left\{ \frac{f(\varepsilon')}{\varepsilon - \varepsilon' + \omega - i\delta} + + \frac{1 - f(\varepsilon')}{\varepsilon - \varepsilon' - \omega + i\delta} \right\} \quad (10)$$

In case of the self – energy depending only on frequency (and not on momentum), we can use the usual expres-

sions for the (inverse) residue at the pole of Green's function and electron mass renormalization [20][2]

$$Z = 1 - \left.\frac{\partial \Sigma(\varepsilon)}{\partial \varepsilon}\right|_{\varepsilon=0} \tag{11}$$

$$m^\star = Zm = m\left(1 - \left.\frac{\partial \Sigma(\varepsilon)}{\partial \varepsilon}\right|_{\varepsilon=0}\right) \tag{12}$$

Defining the dimensionless electron – phonon coupling constant of Eliashberg – McMillan theory as:

$$\lambda = 2\int_0^\infty \frac{d\omega}{\omega}\alpha^2(\omega)F(\omega) \tag{13}$$

by direct calculations we immediately obtain from (10) the standard expression for electron mass renormalization due to interaction with phonons as:

$$m^\star = m(1+\lambda) \tag{14}$$

The function $\alpha^2(\omega)F(\omega)$ in the expression for Eliashberg constant of electron – phonon interaction (13) is to be calculated via (8) or is to be determined from experiments.

Using Eq. (8) we can rewrite (13) as:

$$\lambda = \frac{2}{N(0)}\int_0^\infty \frac{d\omega}{\omega}\sum_{\mathbf{p}}\sum_{\mathbf{p}'}|g_{\mathbf{p}\mathbf{p}'}|^2\delta(\omega-\Omega_{0\mathbf{p}-\mathbf{p}'})\delta(\varepsilon_{\mathbf{p}})\delta(\varepsilon_{\mathbf{p}'}) \tag{15}$$

which gives the standard way to calculate electron – phonon coupling constant λ, which determines, in particular, the Cooper pairing in Eliashberg – McMillan theory.

In the model of Einstein phonons $\Omega_{0k} \to \Omega_0$ and $g_k \to g_0$, so that dimensionless electron – phonon coupling constant (15) immediately reduces to the standard form [20]:

$$\lambda_0 = \frac{2g_0^2 N(0)}{\Omega_0} \tag{16}$$

However, we must remember, that in general case the function $\alpha^2(\omega)F(\omega)$ in the expression for Eliashberg electron – phonon coupling constant (13) is to be calculated either via (8) or from (9), depending on the ratio of Fermi energy E_F and characteristic phonon frequency Ω_0. Until $\Omega_0 \ll E_F$ we can use the standard expression (8), while in the case of $\Omega) \sim E_F$ we have to use (9). Using Eq. (9) we can rewrite (13) in the following form:

$$\lambda = \frac{2}{N(0)}\int_0^\infty \frac{d\omega}{\omega}\sum_{\mathbf{p}}\sum_{\mathbf{p}'}|g_{\mathbf{p}\mathbf{p}'}|^2 \times \\ \times\delta(\omega-\Omega_{0\mathbf{p}-\mathbf{p}'})\delta(\varepsilon_{\mathbf{p}})\delta(\varepsilon_{\mathbf{p}'}-\Omega_{0\mathbf{p}-\mathbf{p}'}) \tag{17}$$

[2] Here we use the notation inverse to that used in the theory of normal metals [20] to make it consistent with notations usually used in Eliashberg equations of superconductivity theory. Correspondingly we have $Z \geq 1$, so that the residue at the pole of Green's function is given by $Z^{-1} \leq 1$.

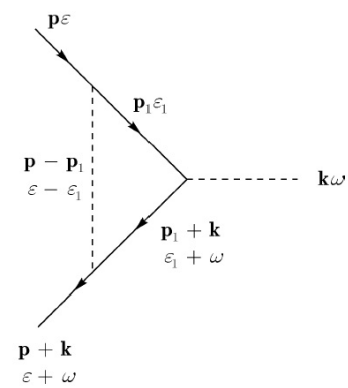

FIG. 2: Simplest vertex correction due to electron – phonon interaction.

which gives the most general way to calculate electron – phonon constant λ, determining the Cooper pairing in Eliashberg – McMillan theory.

III. MIGDAL THEOREM

Above, while calculating electron self – energy due to electron – phonon interaction we have limited ourselves to a simplest contribution shown in Fig. 1. It may seem that we must take into account also other graphs related to corrections to one of the vertices in this diagram. In fact this is unnecessary, as these corrections to vertex part are small over adiabatic parameter $\frac{\Omega_0}{E_F} \sim \sqrt{\frac{m}{M}} \ll 1$ (Migdal theorem) [17] (cf. also Refs. [13, 18–20]). Here Ω_0 is characteristic phonon frequency of the order of Debye frequency.

Let us show this by estimating the simplest vertex correction determined by graph shown in Fig. 2. We shall limit our analysis to a model with Einstein spectrum of phonons. The analytic expression corresponding to diagram of Fig. 2 is:

$$\Gamma^{(1)} = -g_0^3\int G_0(\mathbf{p}_1\varepsilon_1)G_0(\mathbf{p}_1+\mathbf{k},\varepsilon_1+\omega)\times \\ \times D_0(\varepsilon-\varepsilon_1,\mathbf{p}-\mathbf{p}_1)\frac{d^3p_1 d\varepsilon_1}{(2\pi)^4} \tag{18}$$

Let us make a rough estimate of this expression. Consider first the integral over ε_1. Assuming that the characteristic momentum transfer due to phonon exchange is of the order of $k_D \sim p_F$, and taking into account that $D_0(\varepsilon-\varepsilon_1)$ drops quadratically in the region of $|\varepsilon-\varepsilon_1| \gg \Omega_0$, we obtain the main contribution to this integral from the region of $|\varepsilon-\varepsilon_1| \sim \Omega_0$. Then the integral over ε_1 is of the order of 1, and we can write:

$$\Gamma^{(1)} \sim g_0^3\int d^3p_1$$

$$\frac{1}{(\varepsilon_1 - \varepsilon_{\mathbf{p_1}} + i\delta sign\varepsilon_{\mathbf{p_1}})(\varepsilon_1 + \omega - \varepsilon_{\mathbf{p+k}} + i\delta sign\varepsilon_{\mathbf{p_1+k}})} \tag{19}$$

Consider now the remaining integral over p_1. Characteristic momentum transfer here is of the order of $k_D \sim p_F$. Then we can estimate all denominators to be $\sim E_F$, and $\int d^3p_1 \sim N(0)E_F$. Then we obtain:

$$\Gamma^{(1)} \sim g_0^3 N(0)\frac{E_F}{E_F^2} \sim g_0^3 \frac{N(0)}{\Omega_0}\frac{\Omega_0}{E_F} \sim g_0\lambda_0\frac{\Omega_0}{E_F} \tag{20}$$

Thus the relative size of this correction is:

$$\frac{\Gamma^{(1)}}{g_0} \sim \lambda_0\frac{\Omega_0}{E_F} \sim \lambda_0\sqrt{\frac{m}{M}} \tag{21}$$

where we have used $\frac{\Omega_0}{E_F} \sim \frac{\omega_D}{E_F} \sim \sqrt{\frac{m}{M}}$, where m is electron mass, M is ion mass. Electrons are much lighter than ions (nuclei) and this correction to vertex part is negligible. More accurate analysis confirms this conclusion [13, 18], which is the essence of Migdal theorem.

Migdal's theorem allows us to neglect vertex corrections in calculations related to electron – phonon interaction in typical metals. The actual small parameter of perturbation theory is $\lambda_0\frac{\Omega_0}{E_F} \ll 1$, where λ_0 is the dimensionless constant of electron – phonon interaction, Ω_0 is characteristic phonon frequency, while E_F is Fermi energy of electrons, which in typical metals is of the order of conduction band width and determines the maximal energy scale. In particular this leads to a common belief, that vertex corrections in this theory can be neglected even in case of $\lambda_0 > 1$, until inequality $\frac{\Omega_0}{E_F} \ll 1$ is valid, which is characteristic for typical metals. In fact this means that taking into account the diagram of Fig. 1 only is sufficient even in the case of strong enough coupling between electrons and phonons.

Previous analysis implicitly assumed conduction band of infinite width. In case of sufficiently large characteristic frequency of phonons it may become comparable not only to Fermi energy, but also to conduction band width. Curiously enough in the limit of very strong nonadiabaticity, when $\Omega_0 \gg E_F \sim D$ (D is conduction band half – width), a new small parameter of perturbation theory $\lambda_D/\Omega_0 \sim \lambda E_F/\Omega_0$

appears [24, 26]. Naturally, λ in this case should be calculated using Eq. (17).

Consider the case of conduction band of finite width $2D$ with constant density of states (two – dimensional case). Fermi level as above is assumed to be at zero of energy scale and we assume the typical case of half – filled band, so that $E_F = D$. Then Eq. (10) reduces to:

$$\Sigma(\varepsilon) = \int_{-D}^{D} d\varepsilon' \int_0^\infty d\omega\alpha^2(\omega)F(\omega)\left\{\frac{f(\varepsilon')}{\varepsilon - \varepsilon' + \omega - i\delta} + \right.$$
$$\left. + \frac{1 - f(\varepsilon')}{\varepsilon - \varepsilon' - \omega + i\delta}\right\} =$$
$$= \int_0^\infty d\omega\alpha^2(\omega)F(\omega)\left\{\ln\frac{\varepsilon + D + \omega - i\delta}{\varepsilon - D - \omega + i\delta}\right.$$
$$\left. - \ln\frac{\varepsilon + \omega - i\delta}{\varepsilon - \omega + i\delta}\right\} \tag{22}$$

Correspondingly, from Eq. (22) we get:

$$-\left.\frac{\partial\Sigma(\varepsilon)}{\partial\varepsilon}\right|_{\varepsilon=0} = 2\int_0^D d\varepsilon' \int_0^\infty d\omega\alpha^2(\omega)F(\omega)\frac{1}{(\omega + \varepsilon')^2}$$
$$= 2\int_0^\infty d\omega\alpha^2(\omega)F(\omega)\frac{D}{\omega(\omega + D)} \tag{23}$$

so that we can define the generalized coupling constant as:

$$\tilde{\lambda} = 2\int_0^\infty \frac{d\omega}{\omega}\alpha^2(\omega)F(\omega)\frac{D}{\omega + D} \tag{24}$$

which for $D \to \infty$ reduces to the usual Eliashberg – McMillan constant (13), while for $D \to 0$ it gives the "antiadiabatic" coupling constant:

$$\lambda_D = 2D\int \frac{d\omega}{\omega^2}\alpha^2(\omega)F(\omega) \tag{25}$$

Eq. (24) describes a smooth crossover between the limits of wide and narrow conduction bands. Mass renormalization, in general, is determined by constant $\tilde{\lambda}$:

$$m^\star = m(1 + \tilde{\lambda}) \tag{26}$$

For the model of one Einstein phonon with frequency Ω_0 we have $F(\omega) = \delta(\omega - \Omega_0)$, so that:

$$\tilde{\lambda} = \frac{2}{\Omega_0}\alpha^2(\Omega_0)\frac{D}{\Omega_0 + D} = \lambda\frac{D}{\Omega_0 + D} = \lambda_D\frac{\Omega_0}{\Omega_0 + D} \tag{27}$$

where Eliashberg – McMillan coupling constant:

$$\lambda = 2\int_0^\infty \frac{d\omega}{\omega}\alpha^2(\omega)F(\omega) = \alpha^2(\Omega_0)\frac{2}{\Omega_0} \tag{28}$$

Comparison with Eq. (16) gives $\alpha^2(\Omega_0) = g_0^2N(0)$ and λ_D reduces to:

$$\lambda_D = 2\alpha^2(\Omega_0)\frac{D}{\Omega_0^2} = 2\alpha^2(\Omega_0)\frac{1}{\Omega_0}\frac{D}{\Omega_0} \tag{29}$$

where in the last term we have explicitly written the new small parameter $D/\Omega_0 \ll 1$, appearing in the strong antiadiabatic limit. Correspondingly, in this limit we always have:

$$\lambda_D = \lambda\frac{D}{\Omega_0} \sim \lambda\frac{E_F}{\Omega_0} \ll \lambda \tag{30}$$

so that for reasonable values of λ (up to the strong coupling region of $\lambda \sim 1$) the "antiadiabatic" coupling constant remains small.

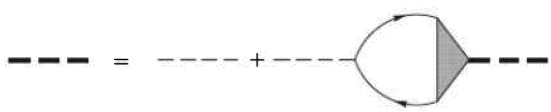

FIG. 3: Dyson equation for the full ("dressed") phonon Green's function.

It is obvious that vertex corrections also become small in this limit as was shown by direct calculations in Ref. [27]. Thus we came to an unexpected conclusion — in strong antiadiabatic limit electron – phonon coupling becomes weak again! In this sense we can again speak of validity of Migadl theorem also in antiadiabatic limit. The physics here is simple – in strong nonadiabatic limit ions move much faster than electrons, so that electrons can not "adjust" to rapidly changing ion configurations and, in this sense, only are only weakly reacting to ion movements.

IV. STRONG COUPLING AND LATTICE INSTABILITY

The general expression for phonon Green's function, taking into account the interaction with electrons, is given by Dyson equation shown in Fig. 3. In analytic form we have:

$$D^{-1}(\mathbf{k}, i\omega_m) = D_0^{-1}(\mathbf{k}, i\omega_m) - |g_{\mathbf{k}}|^2 \Pi(\mathbf{k}, i\omega_m) \quad (31)$$

Then we obtain:

$$D(\mathbf{k}, i\omega_m) = \frac{2\Omega_{0\mathbf{k}}}{(i\omega_m)^2 - \Omega_{0\mathbf{k}}^2 - 2\Omega_{0\mathbf{k}}|g_{\mathbf{k}}|^2 \Pi(\mathbf{k}, i\omega_m)} \quad (32)$$

After the usual transition to real frequencies the phonon spectrum (renormalized by interaction) is determined from the equation:

$$\Omega_{\mathbf{k}}^2 = \Omega_{0\mathbf{k}}^2 \left[1 + \frac{2|g_{\mathbf{k}}|^2}{\Omega_{0\mathbf{k}}} \Pi(\mathbf{k}, \Omega_{\mathbf{k}})\right] \quad (33)$$

In adiabatic approximation, taking into account Migdal theorem, polarization operator here can be taken as a simple loop. In the simplest case of free electrons we have [20]:

$$\Pi(\mathbf{k}, \omega_m) = -2N(0) \left\{1 + \frac{i\omega_m}{2v_F k} \ln \frac{i\omega_m - v_F k}{i\omega_m + v_F k}\right\} \quad (34)$$

or, after $i\omega_m \to \omega + i\delta$

$$\Pi(\mathbf{k}, \omega + i\delta) = -2N(0) \left\{1 + \frac{\omega}{2v_F k} \ln \frac{\omega - v_F k + i\delta}{\omega + v_F k + i\delta}\right\} \quad (35)$$

where v_F is electron velocity at Fermi surface, which much exceeds the sound velocity, so that the values of $v_F k$ are much higher than frequencies of acoustical phonons, and for typical $k \sim p_F$ also those of optical phonons. This again demonstrates the importance of adiabatic approximation in metals. Thus, in calculations of phonon spectrum using (33) we can, with high accuracy, immediately put $\omega = 0$ in polarization operator. In this case the imaginary part of polarization operator becomes zero and we simply have $\Pi(0,0) = -2N(0)$. Then the phonon spectrum, renormalized by interaction with electrons, is determined from:

$$\Omega_{\mathbf{k}}^2 = \Omega_{0\mathbf{k}}^2 \left[1 + \frac{2|g_{\mathbf{k}}|^2}{\Omega_{0\mathbf{k}}} \Pi(0,0)\right] = \Omega_{0\mathbf{k}}^2 \left[1 + \frac{\lambda_0^k}{N(0)} \Pi(0,0)\right] \quad (36)$$

and takes the form:

$$\Omega_{\mathbf{k}}^2 = \Omega_{0\mathbf{k}}^2 [1 - 2\lambda_0^k] \quad (37)$$

where we have introduced the usual definition of dimensionless coupling constant of electron – phonon interaction [20]:

$$\lambda_0^k = \frac{2|g_{\mathbf{k}}|^2 N(0)}{\Omega_{0\mathbf{k}}} \quad (38)$$

In this (rough enough) approximation the relatively small damping of phonons due to electron – phonon interaction just vanishes. It can be obtained with more accurate treatment of the imaginary part of polarization operator [20].

The "bare" Green' function of phonons at real frequencies ($T = 0$)

$$D_0(\mathbf{k}\omega) = \frac{1}{\omega - \Omega_{0\mathbf{k}} + i\delta} - \frac{1}{\omega + \Omega_{0\mathbf{k}} - i\delta} = \frac{2\Omega_{0\mathbf{k}}}{\omega^2 - \Omega_{0\mathbf{k}}^2 + i\delta} \quad (39)$$

after such "dressing" by interaction with electrons transforms into [20]:

$$D(\mathbf{k}\omega) = \frac{2\Omega_{0\mathbf{k}}}{\omega^2 - \Omega_{\mathbf{k}}^2 + i\delta} \quad (40)$$

where the renormalized phonon spectrum is given by (37).

The spectrum given by Eq. (37) signifies the lattice instability for $\lambda_0^k > 1/2$. This instability is often considered to be unphysical, as was noted already in an early paper by Fröhlich [33], where it was obtained for the first time. This point can be explained as follows. Let us rewrite the "dressed" Green's function (40) identically as:

$$D(\mathbf{k}\omega) = \frac{2\Omega_{\mathbf{k}}}{\omega^2 - \Omega_{\mathbf{k}}^2 + i\delta} \frac{\Omega_{0\mathbf{k}}}{\Omega_{\mathbf{k}}} \quad (41)$$

Then it becomes clear that during diagram calculations, and Fig. 1 in particular for electron self – energy, using from the very beginning this renormalized Green's function of phonons, the physical coupling constant of electron – phonon coupling takes the form (instead of (38)):

$$\lambda^k = \frac{2|g_{\mathbf{k}}|^2 N(0)}{\Omega_{\mathbf{k}}} \frac{\Omega_{0\mathbf{k}}}{\Omega_{\mathbf{k}}} = \frac{2|g_{\mathbf{k}}|^2 N(0)}{\Omega_{0\mathbf{k}}} \frac{\Omega_{0\mathbf{k}}^2}{\Omega_{\mathbf{k}}^2} = \lambda_0^k \frac{\Omega_{0\mathbf{k}}^2}{\Omega_{\mathbf{k}}^2} \quad (42)$$

or, using (37):

$$\lambda^k = \frac{\lambda_0^k}{1-2\lambda_0^k} \tag{43}$$

We see, that for $\lambda_0^k \to 1/2$ the *renormalized* coupling constant λ^k monotonously grows and finally diverges. It is this costant that determines the "true" value of electron – phonon interaction (with "dressed" phonons) and there is no limitations for its value at all. This physical picture was discussed in detail, e.g. in the famous book [34].

In a model with single Einstein phonon, which is a reasonable approximation for an optical phonon, we have $\Omega_{\mathbf{k}} = \Omega_0$ and we can forget about dependence of the coupling constant on phonon momentum, so that:

$$\lambda_0 = \frac{2g_0^2 N(0)}{\Omega_0} \tag{44}$$

$$\Omega^2 = \Omega_0^2[1-2\lambda_0] \tag{45}$$

$$\lambda = \frac{2g_0^2 N(0)}{\Omega_0}\left(\frac{\Omega_0}{\Omega}\right)^2 = \frac{\lambda_0}{1-2\lambda_0} \tag{46}$$

Eq. (43) can be reversed and we can write:

$$\lambda_0^k = \frac{\lambda^k}{1+2\lambda^k} \tag{47}$$

expressing nonphysical "bare" constant of electron – phonon coupling λ_0^k via the "true" physical coupling constant λ^k. Using this relation in the equation for renormalized phonon spectrum (37), we can write it as:

$$\Omega_{\mathbf{k}}^2 = \Omega_{0\mathbf{k}}^2\left[1-\frac{2\lambda^k}{1+2\lambda^k}\right] = \Omega_{0\mathbf{k}}^2\frac{1}{1+2\lambda^k} \tag{48}$$

so that in this representation there is no instability of spectrum (lattice), and the growth of λ^k just leads to continuous "softening" of spectrum due to the growth of electron – phonon coupling.

In a model of Einstein phonon all relations simplify and we get:

$$\lambda_0 = \frac{\lambda}{1+2\lambda} \tag{49}$$

$$\Omega = \frac{\Omega_0}{\sqrt{1+2\lambda}} \tag{50}$$

In Eliashberg – McMillan formalism, where we perform the averaging over the momenta of electrons on the (arbitrary) Fermi surface, McMillan function $\alpha^2(\omega)F(\omega)$, naturally should be determined bu the physical (renormalized) spectrum of phonons:

$$\alpha^2(\omega)F(\omega) = \frac{1}{N(0)}\sum_{\mathbf{pp'}}|g_{\mathbf{pp'}}|^2\delta(\omega-\Omega_{\mathbf{p-p'}})\delta(\varepsilon_{\mathbf{p}})\delta(\varepsilon_{\mathbf{p'}}) \tag{51}$$

In particular case of Einstein phonon it immediately reduces to (46) and there is no limitations on the value of λ.

In self – consistent derivation of Eliashberg equations we have to use the diagram of Fig. 1, where the the phonon Green's function is taken in "dressed" form (40) or (41) and describes the physical (renormalized) phonon spectrum. In this case we *do not have to* include corrections to this function due to electron – phonon interaction, as they are already taken into account in phonon spectrum (37).

It should be noted that the value of critical coupling constant obtained above, at which Fröhlich instability of phonon spectrum appears, is obviously directly related to the use of the simplest expression for polarization operator of the gas of free electrons (34), (35), which was calculated neglecting vertex corrections and self – consistent "dressing" of electron Green's functions entering the loop. Naturally, even in the simplest cases like the problem with Einstein spectrum accounting for these higher corrections, as well as more realistic structure of electron spectrum in a lattice, can somehow change the value of λ_0, corresponding to instability of the "bare" phonon spectrum, so that it will differ from 1/2. In this sense it is better to speak about instability at some "critical" value $\lambda_0^c \sim 1/2$.

In general case the inverse influence of electrons on phonons can be taken into account by generalizing Eq. (51) in the following way:

$$\begin{aligned}\alpha^2(\omega)F(\omega) &= \frac{1}{N(0)}\sum_{\mathbf{pp'}}|g_{\mathbf{pp'}}|^2\left(-\frac{1}{\pi}ImD^R(\omega,\mathbf{p}-\mathbf{p'})\right)\\ &\times\delta(\varepsilon_{\mathbf{p}})\delta(\varepsilon_{\mathbf{p'}}) =\\ &= \frac{1}{N(0)}\sum_{\mathbf{pp'}}|g_{\mathbf{pp'}}|^2 B(\mathbf{p}-\mathbf{p'},\omega)\delta(\varepsilon_{\mathbf{p}})\delta(\varepsilon_{\mathbf{p'}})\end{aligned} \tag{52}$$

where we have introduced phonon spectral density $B(\mathbf{q},\omega)$, which determines the phonon Green's function (in Matsubara representation) via the spectral relation:

$$D(\mathbf{q},i\omega_m) = \int_0^\infty B(\mathbf{q},\omega)\frac{2\omega}{(i\omega_m)^2-\omega^2}d\omega \tag{53}$$

In particular, from here we get:

$$D(\mathbf{q},0) = -2\int_0^\infty \frac{d\omega}{\omega}B(\mathbf{q},\omega) \tag{54}$$

Then we can write the following general relation for Eliashberg – McMillan constant λ:

$$\begin{aligned}\lambda &= 2\int_0^\infty \frac{d\omega}{\omega}\alpha^2(\omega)F(\omega) =\\ &= \frac{2}{N(0)}\int_0^\infty \frac{d\omega}{\omega}\sum_{\mathbf{pp'}}|g_{\mathbf{pp'}}|^2 B(\mathbf{p}-\mathbf{p'},\omega)\delta(\varepsilon_{\mathbf{p}})\delta(\varepsilon_{\mathbf{p'}}) =\\ &= -\frac{1}{N(0)}\sum_{\mathbf{pp'}}|g_{\mathbf{pp'}}|^2 D(\mathbf{p}-\mathbf{p'},0)\delta(\varepsilon_{\mathbf{p}})\delta(\varepsilon_{\mathbf{p'}})\end{aligned} \tag{55}$$

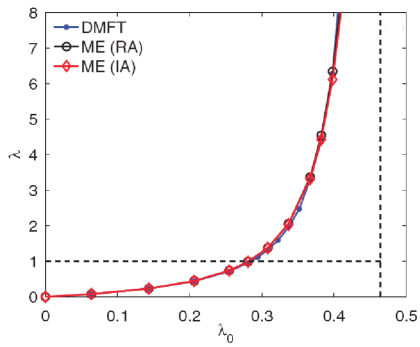

FIG. 4: Dependence of the renormalized coupling constant λ, calculated from (56), on the "bare" λ_0, obtained within self – consistent Eliashberg theory (ME(RA) – real frequency technique, ME(IA) – Matsubara technique) and in DMFT(QMC) [39]. Vertical dashed line corresponds to $\lambda_0^c \approx$0.464.

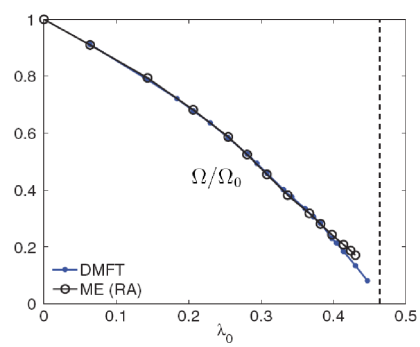

FIG. 5: Dependence of renormalized Einstein phonon frequency Ω on "bare" λ_0, obtained within self – consistent Eliashberg theory (ME(RA) – real frequency technique, ME(IA) – Matsubara technique) and in DMFT(QMC) [39]. Vertical dashed line corresponds to $\lambda_0^c \approx$0.464.

For the model of optical phonon with frequency Ω_0 this immediately reduces to:

$$\lambda = -g_0^2 N(0) \left\langle D(\mathbf{p}-\mathbf{p}',0)\right\rangle_{FS} = -\frac{\lambda_0 \Omega_0}{2} \left\langle D(\mathbf{p}-\mathbf{p}',0)\right\rangle_{FS} \tag{56}$$

where we have introduced the usual notation for momentum averaging over Fermi surface.

The previous analysis can be significantly improved within simplified Holstein model (3), where the local (single site) nature of interaction allows solving it using the dynamical mean field theory (DMFT) [35–38], which becomes (numerically) exact in the limit of lattice of infinite dimensions (infinite number of nearest neighbors). Such analysis was performed e.g. in Ref. [39], using as quantum Monte – Carlo (QMC) as impurity solver in DMFT. The main results are shown in Figs. 4, 5.

In particular in Fig. 4 we show the dependence of renormalized λ on "bare" λ_0. It can be seen, that the usual behavior of Fröhlich theory is nicely reproduced with slightly changed λ_0^c=0.464. Similar behavior is observed for renormalized phonon frequency Ω, as seen in Fig. 5. Rather insignificant deviations from predictions of Eliashberg theory are observed only in immediate vicinity of λ_0^c, especially for λ_0 >0.4.

The instability appearing at $\lambda_0 = \lambda_0^c$ in Holstein model (in DMFT approximation) with half – filled bare band, was convincingly interpreted in Ref. [40] as transition into the state of *bipolaron insulator*. Until this transition the system remains metallic and is nicely described by Eliashberg theory (with insignificant numerical corrections).

In a series of papers [21–23] direct calculations by dynamical quantum Monte – Carlo (DQMC) were performed for a number of characteristics of Holstein model on two – dimensional (square) lattice. The results obtained were in some respects similar to the conclusions of Refs. [39, 40] — up to the values of the "bare" constant λ_0=0.4 there is a good agreement with predictions of Eliashberg theory, but in the interval of λ_0 from 0.4 to 0.5 certain deviations are observed. This interval of λ_0 values, according to the same calculations, corresponds to the interval of renormalized λ from 1.7 to 4.6. For $\lambda_0 \approx 0.5$ system undergoes transition into the state of bipolaron insulator with commensurate charge density wave (CDW).

It is quite clear that the critical value of electron – phonon coupling constant obtained above, corresponding to Fröhlich instability of phonon spectrum at λ_0=1/2, was the direct result of our use of the simplest expression for polarization operator of free electron gas (34), (35), where there was no significant dependence on the wave vector $\mathbf{k}$. Naturally, this dependence is also absent in DMFT approximation. If we go to some more realistic model of electron spectrum, like tight – binding approximation in some definite crystal lattice (not in infinite dimensions!), we can obtain instability of phonon spectrum at some finite value of phonon wave vector $\mathbf{k}$ [21–23, 41]. The appearance of such instabilities, as is well known, usually corresponds to formation in the system of charge density waves (CDW) [20]. In the case of the "nesting" properties of Fermi surface, these instabilities appear (at $T = 0$) even for infinitesimal values of the coupling constant of electron – phonon interaction [20]. After that, metal acquires the new ground state (of dielectric nature) so that all theoretical analysis is to be performed in a new way. In general case, considered here, this instability appears at finite (large enough) values of the "bare" constant of electron – phonon interaction. Naturally, the usual Eliashberg – McMillan theory "works" only within usual metallic phase, which is of the main interest to theory of superconductivity. In this sense, we are in certain disagreement with terminology of Refs. [21–23], where it was claimed, that Eliashberg theory becomes invalid for the values of $\lambda_0 \sim \lambda_0^c$. In reality, in this rather narrow region we are observing corrections due to closeness of the system to instability — the phase transition into a new ground state (bipo-

larons, CDW), where become important fluctuations of corresponding order parameter. Eliashberg theory, considered as a mean – field theory, nicely describes almost all metallic region, except this "critical" neighborhood of λ_0^c, including large enough values of *physical* coupling constant λ (which simply diverges at this transition).

It should be stressed here, that all conclusions on instability of metallic phase were done above in the framework of purely *model* approaches (Fröhlich and Holstein models) and in terms of "bare" parameters of these models like λ_0 and Ω_0, which, as was often noted in the literature, are not so well defined physically. This is known for a long time and was discussed many times. The problem nere is that the phonon spectrum in a metal, considered as system of ions and electrons, is usually assumed to be calculated in adiabatic approximation [42]. This spectrum is relatively weakly renormalized due to nonadiabatic effects, which are small over the small parameter $\sqrt{\frac{m}{M}}$ [42, 43]. In this respect, it is drastically different from the "bare" spectra of Fröhlich or Holstein models, which, as we have seen above, is significantly renormalized by electron – phonon interaction. The physical meaning of the "bare" spectrum Ω_0 in these models remains not so clear, in contrast to phonon spectrum in metals, calculated in adiabatic approximation. In any case it can not be determined from any experiments, Similarly, the same can be said about the parameters of electron – phonon interaction. There were numerous attempts to build a consistent theory of electron – phonon interaction on the background of physical (adiabatic) phonon spectrum [43], but these were not so successful. Rather detailed discussion of the modern state of this problem can be found in Ref. [44]. The short recipe for practical calculations is to identify the renormalized ("dressed") spectrum of phonons Ω in Fröhlich or Holstein models with physical (adiabatic) phonon spectrum, which is not to be further renormalized, and should be taken from adiabatic calculations or from the experiment[3] Precisely this point of view is usually implicitly accepted in calculations within Eliashberg – McMillan theory. Until the system remains in metallic phase, this point of view remains quite consistent. Then there are practically no limitations on the value of physical (renormalized) coupling constant λ and Eliashberg – McMillan theory remains valid up to its large enough values (limited only by Migdal theorem).

[3] Ideologically, situation here is quite analogous to the standard approach in quantum electrodynamics, where the physical charge and mass of an electron are defined by infinite series of perturbation theory and are taken from the experiment.

V. MCMILLAN EXPRESSION FOR ELECTRON – PHONON COUPLING CONSTANT

McMillan has derived a simple expression for the dimensionless electron – phonon coupling in Eliashberg theory [16]. Let us write down Eliashberg – McMillan function (8) using (2) as:

$$\begin{aligned}&\alpha^2(\omega)F(\omega) = \\ &= \frac{1}{N(0)}\sum_{\mathbf{p}}\sum_{\mathbf{p}'}|g_{\mathbf{p}\mathbf{p}'}|^2\delta(\omega-\Omega_{\mathbf{p}-\mathbf{p}'})\delta(\varepsilon_{\mathbf{p}})\delta(\varepsilon_{\mathbf{p}'}) = \\ &= \frac{1}{N(0)}\sum_{\mathbf{p}}\sum_{\mathbf{p}'}\frac{1}{2M\Omega_{\mathbf{p}-\mathbf{p}'}}|I(\mathbf{p}-\mathbf{p}')|^2\delta(\omega-\Omega_{\mathbf{p}-\mathbf{p}'}) \\ &\times\delta(\varepsilon_{\mathbf{p}})\delta(\varepsilon_{\mathbf{p}'})\end{aligned} \tag{57}$$

where $\Omega_{\mathbf{p}-\mathbf{p}'}$ is assumed to be the physical frequency of phonons. Then we immediately get:

$$\int_0^\infty d\omega\alpha^2(\omega)F(\omega)\omega = \frac{N(0)\langle I^2\rangle}{2M} \tag{58}$$

Now rewrite (13)as:

$$\begin{aligned}\lambda &= 2\int_0^\infty\frac{d\omega}{\omega}\alpha^2(\omega)F(\omega) = \\ &= \frac{2}{\langle\Omega^2\rangle}\int_0^\infty d\omega\alpha^2(\omega)F(\omega)\omega\end{aligned} \tag{59}$$

where the mean square phonon frequency is defined as:

$$\begin{aligned}\langle\Omega^2\rangle &= \frac{\int_0^\infty d\omega\alpha^2(\omega)F(\omega)\omega}{\int_0^\infty\frac{d\omega}{\omega}\alpha^2(\omega)F(\omega)} = \\ &= \frac{2}{\lambda}\int_0^\infty d\omega\alpha^2(\omega)F(\omega)\omega\end{aligned} \tag{60}$$

From this expression we can immediately see that:

$$\lambda = \frac{N(0)\langle I^2\rangle}{M\langle\Omega^2\rangle} \tag{61}$$

where we have introduces the matrix element of the gradient of electron – ion potential averaged over Fermi surface:

$$\begin{aligned}\langle I^2\rangle &= \frac{1}{[N(0)]^2}\sum_{\mathbf{p}}\sum_{\mathbf{p}'}|I(\mathbf{p}-\mathbf{p}')|^2\delta(\varepsilon_{\mathbf{p}})\delta(\varepsilon_{\mathbf{p}'}) = \\ &= \frac{1}{[N(0)]^2}\sum_{\mathbf{p}}\sum_{\mathbf{p}'}|\langle\mathbf{p}|\nabla V_{ei}(\mathbf{r})|\mathbf{p}'\rangle|^2)\delta(\varepsilon_{\mathbf{p}})\delta(\varepsilon_{\mathbf{p}'}) = \\ &= \langle|\langle\mathbf{p}|\nabla V_{ei}(\mathbf{r})|\mathbf{p}'\rangle|^2\rangle_{FS}\end{aligned} \tag{62}$$

Eq. (61) gives very useful representation for λ, which is often used in the literature and in practical calculations.

VI. ELIASHBERG EQUATIONS

Eliashberg theory is based on a system of equations for normal and anomalous Green's functions of a superconductor [20]. Obviously, the solution of these *integral* equations, taking into account the real spectrum of phonons, represents rather difficult problem. However, a significant progress was achieved and the theory of traditional superconductors, based on the picture of pairing due to electron – phonon interaction, is an example of very successful application of Green's functions. Very good presentation of methods used and applications of Eliashberg equations can be found in Ref. [16].

Below we shall present somehow simplified derivation of Eliashberg equations, dropping some technical details. In particular, we shall not consider the role of direct Coulomb repulsion of electrons within Cooper pair, which is accounted for in the complete Eliashberg – McMillan theory [16], limiting ourselves only to electron – phonon interaction. The accounting for Coulomb contributions is not especially difficult [16] and reduces at the end to introduction of Coulomb pseudopotential $\mu^\star$ [16], which in typical metals is rather small and not so important in the limit of very strong coupling with phonons, which will be of the main interest for us in the following[4]

Taking into account Migdal theorem, in adiabatic approximation vertex corrections are irrelevant, so that Eliashberg equations can be derived by calculating the diagram of Fig. 1, where electron Green's function in superconducting state is taken in Nambu matrix representation [19]. Calculations are similar to derivation of (10) and can be performed in Matsubara technique ($T \neq 0$). In Nambu formalism electronic Green's function of superconductor is written in a standard way as ($\hat{\sigma}_i$ are Pauli matrices) [16]:

$$\hat{G}^{-1}(i\omega_n, \mathbf{p}) = i\omega_n \hat{1} - \varepsilon_{\mathbf{p}} \hat{\sigma}_z - \hat{\Sigma}(i\omega_n, \mathbf{p}) \tag{63}$$

where matrix self – energy is represented as[5]:

$$\hat{\Sigma}(i\omega_n, \mathbf{p}) = (1 - Z(i\omega_n))i\omega_n \hat{1} + Z(i\omega_n)\Delta(i\omega_n)\hat{\sigma}_x \tag{64}$$

Here we are introducing a number of simplifying assumptions like independence of renormalization factor $Z(i\omega_n)$ and gap function $\Delta(i\omega_n)$ on momentum [16]. Then we have:

$$\hat{G}(i\omega_n, \mathbf{p}) = \frac{Z(i\omega_n)i\omega_n \hat{1} + \varepsilon_{\mathbf{p}}\hat{\sigma}_z + Z(i\omega_n)\Delta(i\omega_n)\hat{\sigma}_x}{Z^2(i\omega_n)(i\omega_n)^2 - Z^2(i\omega_n)\Delta^2(i\omega_n) - \varepsilon_{\mathbf{p}}^2} \tag{65}$$

Self – energy part corresponding to diagram like Fig. 1 with matrix Green's function of electron (65) is written as:

$$\hat{\Sigma}(\omega_n, \mathbf{p}) = -T \sum_m \sum_{\mathbf{p}'} |g_{\mathbf{p}\mathbf{p}'}|^2 D(i\omega_n - i\omega_m, \mathbf{p} - \mathbf{p}') \times \times \hat{\sigma}_z \hat{G}(i\omega_m, \mathbf{p}')\hat{\sigma}_z \tag{66}$$

where phonon Green's function $D(i\omega_n - i\omega_m, \mathbf{p} - \mathbf{p}')$ can be taken as in Eq. (39), denoting the phonon frequency $\Omega_{\mathbf{p}-\mathbf{p}'}$ as in Eq. (6).

As we know, all physics of conventional superconductivity develops in a layer with the width of the order of $2\Omega_D \ll E_F$ close to Fermi surface. Thus we can make here the substitution (8) and obtain from (66) the expression for self – energy part averaged over momenta on Fermi surface (similar to (10)). As a result, we obtain the general system of equations for the gap $\Delta(\omega_n)$ and renormalization factor $Z(\omega_n)$ of the following form:

$$\Delta(\omega_n)Z(\omega_n) = T \sum_{n'} \int_{-\infty}^{\infty} d\xi \int_0^{\infty} d\omega \alpha^2(\omega) F(\omega) \times \times D(\omega_n - \omega_{n'}; \omega) \frac{\Delta(\omega'_n)}{\omega'^2_n + \xi^2 + \Delta^2(\omega_{n'})} \tag{67}$$

$$1 - Z(\omega_n) = \frac{\pi T}{\omega_n} \sum_{n'} \int_{-\infty}^{\infty} d\xi \int_0^{\infty} d\omega \alpha^2(\omega) F(\omega) \times \times D(\omega_n - \omega_{n'}; \omega) \frac{\omega'_n}{\omega'^2_n + \xi^2 + \Delta^2(\omega_{n'})} \tag{68}$$

where we have introduced

$$D(\omega_n - \omega_{n'}; \omega) = \frac{2\omega}{(\omega_n - \omega_{n'})^2 + \omega^2} \tag{69}$$

The integral over ξ here is easily calculated and gives:

$$\int_{-\infty}^{\infty} d\xi \frac{1}{\omega_{n'}^2 + \xi^2 + \Delta^2(\omega_{n'})} = \frac{\pi}{\sqrt{\omega_{n'}^2 + \Delta^2(\omega_{n'})}} \to \to \frac{\pi}{|\omega_{n'}|} \text{ for } \Delta(\omega_{n'}) \to 0 \tag{70}$$

Then the linearized gap equation (equation for T_c) has the form:

$$\Delta(\omega_n)Z(\omega_n) = \pi T \sum_{n'} \int_0^{\infty} \alpha^2(\omega) F(\omega) \times \times D(\omega_n - \omega_{n'}; \omega) \frac{\Delta(\omega_{n'})}{|\omega_{n'}|} \tag{71}$$

where

$$1 - Z(\omega_n) = \frac{\pi T}{\omega_n} \sum_{n'} \int_{-\infty}^{\infty} d\xi \int_0^{\infty} d\omega \alpha^2(\omega) F(\omega) \times \times D(\omega_n - \omega_{n'}; \omega) \frac{\omega_{n'}}{|\omega'_n|} \tag{72}$$

[4] Surely, accounting for $\mu^\star$ is very important for quantitative estimates of superconducting transition temperature in the weak and intermediate coupling region.

[5] Possible contribution proportional to $\hat{\sigma}_y$ is removed by the appropriate choice of the phase of superconducting order parameter, while the term proportional to $\hat{\sigma}_z$ reduces to renormalization of chemical potential [16].

The general gap equation is:

$$\Delta(\omega_n)Z(\omega_n) = \pi T \sum_{n'} \int_0^\infty \alpha^2(\omega)F(\omega) \times$$
$$\times D(\omega_n - \omega_{n'};\omega)\frac{\Delta(\omega_{n'})}{\sqrt{\omega_{n'}^2 + \Delta^2(\omega_{n'})}} \quad (73)$$

where factor $Z(\omega_n)$ is determined from the following equation:

$$1 - Z(\omega_n) = \frac{\pi T}{\omega_n} \sum_{n'} \int_0^\infty d\omega \alpha^2(\omega)F(\omega) \times$$
$$\times D(\omega_n - \omega_{n'};\omega)\frac{\omega_{n'}}{\sqrt{\omega_{n'}^2 + \Delta^2(\omega_{n'})}} \quad (74)$$

to be solved jointly with (73).

In a model with Einstein spectrum of phonons Eq. (73) reduces to:

$$\Delta(\omega_n)Z(\omega_n) = \pi T\lambda \sum_{n'} \frac{\Omega_0^2}{(\omega_n - \omega_{n'})^2 + \Omega_0^2} \times$$
$$\times \frac{\Delta(\omega_{n'})}{\sqrt{\omega_{n'}^2 + \Delta^2(\omega_{n'})}} \quad (75)$$

while Eq. (74) becomes:

$$Z(\omega_n) = 1 + \frac{\pi T\lambda}{\omega_n} \sum_{n'} \frac{\Omega_0^2}{(\omega_n - \omega_{n'})^2 + \Omega_0^2} \frac{\omega_{n'}}{\sqrt{\omega_{n'}^2 + \Delta^2(\omega_{n'})}} \quad (76)$$

where the coupling constant λ, determined by standard expressions (13) or (28), appears explicitly.

To determine T_c (in the limit of $\Delta(\omega_{n'}) \to 0$) in a system with Einstein spectrum of phonons we obtain the following system of linear homogeneous Eliashberg equations:

$$\Delta(\omega_n)Z(\omega_n) = \pi T\lambda \sum_{n'} \frac{\Omega_0^2}{(\omega_n - \omega_{n'})^2 + \Omega_0^2} \frac{\Delta(\omega_{n'})}{|\omega_{n'}|} \quad (77)$$

where

$$Z(\omega_n) = 1 + \frac{\pi T\lambda}{\omega_n} \sum_{n'} \frac{\Omega_0^2}{(\omega_n - \omega_{n'})^2 + \Omega_0^2} \frac{\omega_{n'}}{|\omega_{n'}|} \quad (78)$$

It is clear that the value of T_c is determined by zero determinant of this system of equations.

Note that in general equations (73), (74) the coupling constant λ does not appear explicitly. Usually this is achieved by reduction of these equations to "Einstein" form like (75), (76) by introduction of the average square of phonon frequency, defined as:

$$\langle \Omega^2 \rangle = \frac{2}{\lambda} \int_0^\infty d\omega \alpha^2(\omega)F(\omega)\omega \quad (79)$$

and the following replacement in (73), (74):

$$\frac{1}{(\omega_n - \omega_{n'})^2 + \omega^2} \Longrightarrow \frac{1}{(\omega_n - \omega_{n'})^2 + \langle \Omega^2 \rangle} \quad (80)$$

which gives (75), (76), and also the equations for T_c (77), (78) with simple replacement of Ω_0^2 by $\langle \Omega^2 \rangle$. In this sense the general structure "Einstein" Eliashberg equations conserves also for the case of general phonon spectrum. This approximation with identification of Ω_0^2 and $\langle \Omega^2 \rangle$ is always assumed in the following.

For the model of phonon spectrum consisting of discreet set of Einstein phonons:

$$\alpha^2(\omega)F(\omega) = \sum_i \alpha^2(\Omega_i)\delta(\omega - \Omega_i)$$
$$= \sum_i \frac{\lambda_i}{2}\Omega_i \delta(\omega - \Omega_i) \quad (81)$$

In this case from (79) we simply obtain:

$$\langle \Omega^2 \rangle = \frac{1}{\lambda} \sum_i \lambda_i \Omega_i^2 \quad (82)$$

where $\lambda = \sum_i \lambda_i$.

A. Weak and intermediate coupling

There is a vast literature on solving Eliashberg equations in the weak or intermediate coupling region $\lambda < 1$ [13, 14, 16]. Here we only present qualitative results for T_c, dropping unimportant (for our aims) numerical coefficients ~ 1. In a model with Einstein spectrum of phonons and Coulomb potential $\mu^\star = 0$ we have [20]:

$$T_c \sim \Omega_0 \exp\left(-\frac{1+\lambda}{\lambda}\right) \quad (83)$$

This expression is in fact close to the results of an exact numerical analysis performed at a time by McMillan [13, 14, 16][6]

Similar estimates of T_c can be obtained also in the strong antiadiabatic limit, considering Eliashberg equations for $\lambda < 1$ in the problem with a narrow electron band of half – width $D \sim E_F \ll \Omega_0$ [24–26]. Then the appropriately generalized Eliashberg equations give for the same model with Einstein spectrum:

$$T_c \sim \frac{D}{1 + D/\Omega_0} \exp\left(-\frac{1+\tilde{\lambda}}{\lambda}\right) \quad (84)$$

where the effective constant $\tilde{\lambda}$ was defined above in Eqs. (24), (27) and (30).

Eq. (84) interpolates between adiabatic and antiadiabatic limits. For $D \gg \Omega_0$ it gives (83), while for $D \ll \Omega_0$

[6] Here we drop some numerical coefficients ~ 1. If we remember a number of (not so well controlled) approximations made during the derivation of Eliashberg equations, it becomes clear that we are not loosing much in accuracy here.

it reduces to:

$$T_c \sim D \exp\left(-\frac{1}{\lambda}\right) \tag{85}$$

i.e. to BCS – like expression (weak coupling!), where preexponential factor is determined not by phonon frequency, but by the electron band half – width (Fermi energy), which now plays the role of cutoff parameter for divergence in Cooper channel. This fact was first noted by Gor'kov in Refs. [29–31].

For more general model of phonon spectrum consisting of discrete set of Einstein phonons (81) these relations are obviously generalized to [25, 26]:

$$\lambda = 2\sum_i \frac{\alpha^2(\Omega_i)}{\Omega_i} \equiv \sum_i \lambda_i \tag{86}$$

$$\tilde{\lambda} = 2\sum_i \frac{\alpha^2(\Omega_i)D}{\Omega_i(\Omega_i + D)} = \sum_i \lambda_i \frac{D}{\Omega_i + D} \equiv \sum_i \tilde{\lambda}_i \tag{87}$$

and instead of (84) we have:

$$T_c \sim \prod_i \left(\frac{D}{1+\frac{D}{\Omega_i}}\right)^{\frac{\lambda_i}{\lambda}} \exp\left(-\frac{1+\tilde{\lambda}}{\lambda}\right) \tag{88}$$

In the simplest case of two Einstein phonons with frequencies Ω_1 and Ω_2 this gives:

$$T_c \sim \left(\frac{D}{1+\frac{D}{\Omega_1}}\right)^{\frac{\lambda_1}{\lambda}} \left(\frac{D}{1+\frac{D}{\Omega_2}}\right)^{\frac{\lambda_2}{\lambda}} \exp\left(-\frac{1+\tilde{\lambda}}{\lambda}\right) \tag{89}$$

where $\tilde{\lambda} = \tilde{\lambda}_1 + \tilde{\lambda}_2$ and $\lambda = \lambda_1 + \lambda_2$. In case of $\Omega_1 \ll D$ (adiabatic phonon), and $\Omega_2 \gg D$ (antiadiabatic phonon) (89) reduces to:

$$T_c \sim (\Omega_1)^{\frac{\lambda_1}{\lambda}} (D)^{\frac{\lambda_2}{\lambda}} \exp\left(-\frac{1+\tilde{\lambda}}{\lambda}\right) \tag{90}$$

Eq. (88) is easily rewritten as:

$$T_c \sim \langle \Omega_{\ln} \rangle \exp\left(-\frac{1+\tilde{\lambda}}{\lambda}\right) \tag{91}$$

where we have introduced mean logarithmic frequency $\langle \Omega_{\ln} \rangle$:

$$\ln\langle \Omega_{\ln} \rangle = \ln \prod_i \left(\frac{D}{1+\frac{D}{\Omega_i}}\right)^{\frac{\lambda_i}{\lambda}} = \sum_i \frac{\lambda_i}{\lambda} \ln \frac{D}{1+\frac{D}{\Omega_i}} \tag{92}$$

In the limit of continuous distribution of phonon frequencies the last expression reduces to:

$$\ln\langle \Omega_{\ln} \rangle = \frac{2}{\lambda} \int \frac{d\omega}{\omega} \alpha^2(\omega) F(\omega) \ln \frac{D}{1+\frac{D}{\omega}} \tag{93}$$

where λ is given by the usual relation (13).

In general case, the preexponential factor in the expression for T_c in Eliashberg theory for weak or intermediate coupling is always given by mean logarithmic phonon frequency [16], and Eq. (93) gives the generalization of the standard expression for this frequency for the case of electron band of finite width. From Eq. (93) we can easily obtain the standard expression [16] (see also below) for adiabatic limit, when $D \to \infty$.

B. Lower bound for T_c in the limit of very strong coupling

To achieve really high values of T_c the region of strong and very strong coupling $\lambda > 1$ is of the main interest and will be discussed in the following. The general Eliashberg equations in Matsubara representation, determining superconducting gap $\Delta(\omega_n)$ at arbitrary temperatures, are given in (73), (74) [13, 14].

Limitations on the value of T_c in the limit of very strong coupling are easily derived analytically. We shall see shortly, that appropriate behavior follows form the estimate of the *lower* bound for T_c [45]. Consider the linearized gap equation (71), determining T_c:

$$\Delta(\omega_n) Z(\omega_n) = \pi T \sum_{n'} \int_0^\infty \alpha^2(\omega) F(\omega) \times \\ \times D(\omega_n - \omega_{n'}; \omega) \frac{\Delta(\omega_{n'})}{|\omega_{n'}|} \tag{94}$$

where phonon Green's function is defined in (69). Let us consider the term with $n = 0$. Then, leaving in the sum in Eq. (78) only the contribution from $n' = 0$, we obtain:

$$Z(0) = 1 + \lambda \tag{95}$$

which after the substitution into Eq. (94) for $n = 0$ just cancels the similar (corresponding to $n' = 0$) term in the r.h.s. of Eq. [15, 46], so that the equation for $\Delta(0) = \Delta(\pi T)$ takes the form:

$$\Delta(0) = \pi T \sum_{n' \neq 0} \int_0^\infty \alpha^2(\omega) F(\omega) \frac{2\omega}{(\pi T - \omega_{n'})^2 + \omega^2} \frac{\Delta(\omega_{n'})}{|\omega_{n'}|} \tag{96}$$

All terms in the r.h.s. here are positive. Let us leave only the contribution from $n' = -1$, so that taking into account $\Delta(-1) = \Delta(-\pi T) = \Delta(\pi T) = \Delta(0)$, and canceling $\Delta(0)$ in l.h.s and r.h.s. we immediately get the *inequality* [45]:

$$1 > \int_0^\infty d\omega \frac{2\alpha^2(\omega) F(\omega) \omega}{(2\pi T)^2 + \omega^2} \tag{97}$$

Actually here $T = T_c$, and this equation gives the *lower* estimate of T_c. In particular, in the model with Einstein spectrum of phonons $F(\omega) = \delta(\omega - \Omega_0)$ and this inequality is immediately rewritten as:

$$1 > 2\alpha^2(\Omega_0) \frac{\Omega_0}{(2\pi T)^2 + \Omega_0^2} = \lambda \frac{\Omega_0^2}{(2\pi T)^2 + \Omega_0^2} \tag{98}$$

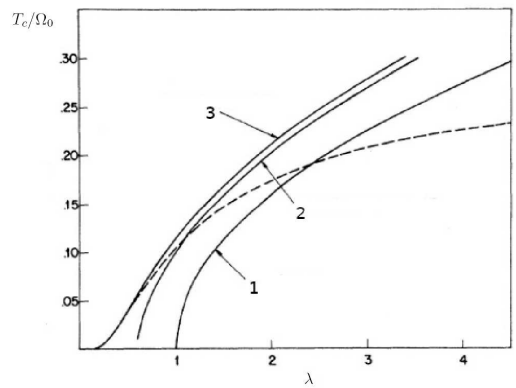

FIG. 6: Temperature of superconducting transition in Einstein model of phonon spectrum in units of T_c/Ω_0 as a function of pairing constant λ [45]: 1 – lower bound (99), 2 – solution of the system of two linear equations ($n = 0, \pm 1$), 3 – numerically exact solution of the full system of equations ($n \leq 63$) [45]. McMillan expression for T_c [16] is shown by dashed line (for the case of $\mu^\star$=0).

so that for T_c we get:

$$T_c > \frac{1}{2\pi}\sqrt{\lambda - 1}\Omega_0 \tag{99}$$

which for $\lambda \gg 1$ reduces to:

$$T_c > \frac{1}{2\pi}\sqrt{\lambda}\Omega_0 \approx 0.16\sqrt{\lambda}\Omega_0 \tag{100}$$

For discrete spectrum of phonons (81) inequality (97) reduces to:

$$1 > \sum_i \lambda_i \frac{\Omega_i^2}{(2\pi T)^2 + \Omega_i^2} \tag{101}$$

which in the limit of very strong coupling for $2\pi T \gg \Omega_i$ immediately gives the natural generalization of (100):

$$T_c > \frac{1}{2\pi}\sqrt{\lambda\langle\Omega^2\rangle} \tag{102}$$

where $\lambda = \sum_i \lambda_i$ and $\langle\Omega^2\rangle$ was defined above in Eq. (82).

If we solve 2×2 system of equations and appropriate quadratic equation for T_c, following from Eqs. (77), (78) for $n = 0; \pm 1$, the constant 0.16 in (100) is replaced by 0.18. The solution of system with $n \leq$63, performed in Ref. [45] lead to replacement of 0.18 by 0.182, which practically corresponds to numerically exact solution. It is obvious, that even the simplest solution (99) is quite sufficient for qualitative estimates of T_c in the limit of very strong coupling. The general situation is illustrated in Fig. 6. From this figure it can be seen, in particular, that asymptotic behavior of T_c for $\lambda \gg$1 (100) with coefficient 0.18, rather well approximates the values of critical temperature already starting from the values of $\lambda >$1.5-2.0 (cf. curve 2 in this figure).

Consider now the very strong coupling case in strong antiadiabatic limit, though realization of such coupling in this limit is rather doubtful, as pairing constant λ, defined according to (17), typically rapidly drops with the growth of phonon frequency, as it exceeds Fermi energy [24, 26].

Consider again the electron band of finite width $2D$ (constant density of states). Then in general Eliashberg equations considered above, instead of integral in infinite limits (70) we have:

$$\int_{-D}^{D} d\xi \frac{1}{\omega_{n'}^2 + \xi^2 + \Delta^2(\omega_{n'})} =$$
$$= \frac{2}{\sqrt{\omega_{n'}^2 + \Delta^2(\omega_{n'})}} arctg \frac{D}{\sqrt{\omega_{n'}^2 + \Delta^2(\omega_{n'})}} \rightarrow$$
$$\rightarrow \frac{2}{|\omega_{n'}|} arctg \frac{D}{|\omega_{n'}|} \text{ for } \Delta(\omega_{n'}) \rightarrow 0 \tag{103}$$

Then the linearized Eliashberg equations take the following general form:

$$\Delta(\omega_n) Z(\omega_n) =$$
$$= T \sum_{n'} \int_0^\infty d\omega \alpha^2(\omega) F(\omega) D(\omega_n - \omega_{n'}; \omega) \times$$
$$\times \frac{2\Delta(\omega_{n'})}{|\omega_{n'}|} arctg \frac{D}{|\omega_{n'}|} \tag{104}$$

where

$$Z(\omega_n) = 1 + \frac{T}{\omega_n} \sum_{n'} \int_0^\infty d\omega \alpha^2(\omega) F(\omega) \times$$
$$\times D(\omega_n - \omega_{n'}; \omega) \frac{\omega_{n'}}{|\omega_{n'}|} arctg \frac{D}{|\omega_{n'}|} \tag{105}$$

Now we directly obtain the equation for $\Delta(0)$:

$$\Delta(0) = T \sum_{n' \neq 0} \int_0^\infty d\omega \alpha^2(\omega) F(\omega) \frac{2\omega}{(\pi T - \omega_{n'})^2 + \omega^2} \times$$
$$\times \frac{2\Delta(\omega_{n'})}{|\omega_{n'}|} arctg \frac{D}{|\omega_{n'}|} \tag{106}$$

Again, taking into account only the contribution of $n' = -1$ in the r.h.s., we immediately obtain an inequality:

$$1 > \frac{2}{\pi} \int_0^\infty d\omega \alpha^2(\omega) F(\omega) \frac{2\omega}{(2\pi T)^2 + \omega^2} arctg \frac{D}{\pi T} \tag{107}$$

In Einstein model of phonon spectrum we have $F(\omega) = \delta(\omega - \Omega_0)$, so that Eq. (107) reduces to:

$$1 > \frac{2}{\pi} \lambda arctg \frac{D}{\pi T} \frac{\Omega_0^2}{(2\pi T)^2 + \Omega_0^2} \tag{108}$$

For $D \gg \pi T$ it immediately gives the result of Allen and Dynes:

$$T_c > \frac{1}{2\pi}\sqrt{\lambda - 1}\Omega_0 \rightarrow 0.16\sqrt{\lambda}\Omega_0 \text{ for } \lambda \gg 1 \tag{109}$$

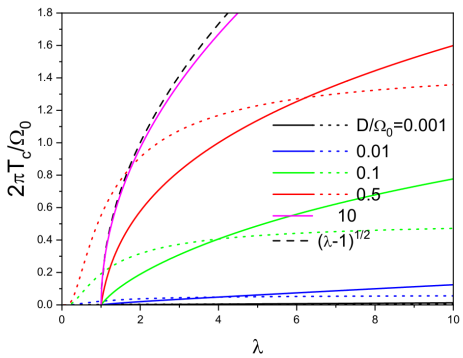

FIG. 7: Temperature of superconducting transition (lower bound) in Einstein model of phonon spectrum in units of $2\pi T_c/\Omega_0$, as a function of pairing constant λ for different values of inverse adiabaticity parameter D/Ω_0. Dashed lines show appropriate dependencies for $2\pi T_c/\Omega_0$ in the region of weak and intermediate coupling (84). Black dashed line — Allen – Dynes estimate (99), valid in adiabatic limit [45]

.

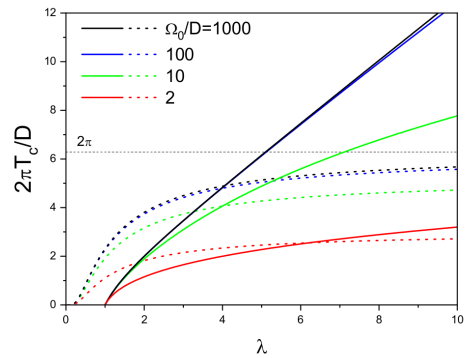

FIG. 8: Temperature of superconducting transition (lower bound) in Einstein model of phonon spectrum in units of $2\pi T_c/D$, as a function of pairing constant λ for different values of adiabaticity parameter Ω_0/D. Dashed lines show appropriate dependencies for $2\pi T_c/D$ in weak and intermediate coupling region (84).

For $D \ll \pi T$ Eq. (108) gives:

$$T > \frac{1}{2\pi}\sqrt{\lambda^*(T) - 1}\Omega_0 \tag{110}$$

where

$$\lambda^*(T) = \frac{2D}{\pi^2 T}\lambda \tag{111}$$

so that in strong antiadiabatic limit we have:

$$T_c > (2\pi^4)^{-1/3}(\lambda D\Omega_0^2)^{1/3} \approx 0.17(\lambda D\Omega_0^2)^{1/3} \tag{112}$$

From the obvious condition $\lambda^*(T) > 0$ we get:

$$T_c < \frac{2}{\pi^2}\lambda D \approx 0.202\lambda D \tag{113}$$

which bounds T_c from above.

Thus we have to satisfy an inequality:

$$(2\pi^4)^{-1/3}(\lambda D\Omega_0^2)^{1/3} < T_c < \frac{2}{\pi^2}\lambda D \tag{114}$$

which reduces to the condition:

$$\Omega_0 < \frac{4}{\pi}\lambda D \approx 1.27\lambda D \text{ or } \frac{D}{\Omega_0} > \frac{0.78}{\lambda} \tag{115}$$

so that for self – consistency of our analysis we have to satisfy the condition:

$$\lambda \gg \frac{\Omega_0}{D} \gg 1 \tag{116}$$

where the last equality corresponds to the limit of strong antiadiabaticity. Correspondingly, all the previous estimates become invalid for $\lambda \sim 1$ and can describe only the limit of very strong coupling.

In Fig. 7 and Fig. 8 we show the results of numerical calculations of T_c boundaries, following from the solution of (108), as compared to the values of T_c in the region of weak and intermediate coupling (84), for different values of adiabaticity parameter Ω_0/D. It is clear that in the vicinity of crossing dashed and continuous lines in graphs, shown in Fig. 7 and Fig. 8, we actually have a smooth crossover from T_c behavior in the region of weak and intermediate coupling to its asymptotic behavior in very strong coupling region of $\lambda \gg 1$. From Fig. 8 it is seen that the boundary (113) is practically achieved in the region of large values of λ and Ω_0/D. From these figures we can also see that simple rising of phonon frequency and transition to antiadiabatic limit do not lead, in general, to an increase of T_c as compared with adiabatic case.

VII. MAXIMAL T_c?

The problem of maximal possible temperature of superconducting transition has arisen immediately after the creation of BCS theory. It was studied in numerous papers with sometimes contradictory results. Among these papers was the notorious paper by Cohen and Anderson [47], where rather elegant arguments were given, seemingly quite convincing, that characteristic scale of T_c values due to electron – phonon, or any other similar mechanism, based on exchange of Bose – like excitations in metals, can be of the order of about 10–30 K only. This paper was immediately seriously criticized in Refs. [34, 48], with conclusion that in reality there are no such limitations. Even more, the analysis performed in these papers has shown that Ref. [47] is just erroneous. However, the point of view expressed in Cohen – Anderson paper be-

came popular in physics community (Anderson himself till the end of his life adhered to the view expressed in Ref. [47]), so that at the time of discovery of high – temperature superconductivity in cuprates (1986 – 1987), almost total belief was that the "usual" electron – phonon mechanism does not allow values of T_c higher, that 30-40 K. Because of this after the discovery of superconductivity in cuprates the "great race" has started for new theoretical models and mechanisms of superconductivity, which may explain the high values of T_c. The problems of superconductivity in cuprates are outside the scope of this work. Most probably, in cuprates really dominates some kind of non – phonon pairing mechanism (due to antiferromagnetic fluctuations). But most important result of discovery of record values of T_c in hydrides under high pressures, in our opinion, is the final (and experimental!) rebuttal of the point of view expressed in Ref. [47].

Thus, the problem of maximal value of T_c, which may be achieved due to electron – phonon mechanism of Cooper pairing is most important as ever. Below we try to discuss this problem once again within standard approach, based on Eliashberg equations, as most successful theory, describing superconductivity in the system of electrons and phonons in metals.

There is a vast literature on numerical solution of Eliashberg equations for different temperatures and different models of phonon spectrum [14, 16].

A number of analytic expressions for T_c were proposed by different authors, to approximate the results of numerical computations. As an example we quote here the popular interpolation formula for T_c due to Allen and Dynes [14], which is appropriate for rather wide interval of values of dimensionless coupling constant of electron – phonon interaction λ, including the strong coupling region of $\lambda > 1$:

$$T_c = \frac{f_1 f_2}{1.20}\langle\Omega_{\ln}\rangle \exp\left\{-\frac{1.04(1+\lambda)}{\lambda - \mu^\star(1+0.62\lambda)}\right\} \tag{117}$$

where

$$f_1 = [1+(\lambda/\Lambda_1)^{3/2}]^{1/3};\ f_2 = 1 + \frac{[\langle\Omega^2\rangle^{1/2}/\langle\Omega_{\ln}\rangle - 1]\lambda^2}{\lambda^2+\Lambda_2^2}$$
$$\Lambda_1 = 2.46(1+3.8\mu^\star);\ \Lambda_2 = 1.82(1+6.3\mu^\star)\frac{\langle\Omega^2\rangle^{1/2}}{\langle\Omega_{\ln}\rangle} \tag{118}$$

Here $\langle\Omega_{\ln}\rangle$ is the mean logarithmic frequency of phonons:

$$\ln\langle\Omega_{\ln}\rangle = \frac{2}{\lambda}\int_0^\infty \frac{d\omega}{\omega}\alpha^2(\omega)F(\omega)\ln\omega = \\ = \frac{\int_0^\infty \frac{d\omega}{\omega}\ln\omega\alpha^2(\omega)F(\omega)}{\int_0^\infty \frac{d\omega}{\omega}\alpha^2(\omega)F(\omega)} \tag{119}$$

$\langle\Omega^2\rangle$ is the average (over the phonon spectrum) square of frequency, defined in Eq. (79):

$$\langle\Omega^2\rangle = \frac{2}{\lambda}\int_0^\infty d\omega\alpha^2(\omega)F(\omega)\omega = \frac{\int_0^\infty d\omega\omega\alpha^2(\omega)F(\omega)}{\int_0^\infty \frac{d\omega}{\omega}\alpha^2(\omega)F(\omega)} \tag{120}$$

The Coulomb pseudopotential $\mu^\star$ determines repulsion between electrons within Cooper pair. According to most calculations [14, 16] its values are small and belong to the interval 0.1 – 0.15.

In the limit of very strong coupling $\lambda > 10$ this gives the expression for T_c, which was. in fact. obtained above from simple inequality (99):

$$T_c \approx 0.18\sqrt{\lambda\langle\Omega^2\rangle} \tag{121}$$

It may seem now, that limitations on the values of T_c are simply absent, so that in the limit of very strong coupling very high T_c can be obtained from electron – phonon mechanism. The only more or less obvious limit is related to the limits of adiabatic approximation, which is usually considered to be the cornerstone of Eliashberg theory. However, we have seen above. that similar results can be obtained also in the strong antiadiabatic limit (cf. estimated for T_c given in Eqs. (112), (113)).

In the model with Einstein spectrum of phonons we simply have: $\langle\Omega_{\ln}\rangle = \langle\Omega^2\rangle^{1/2} = \Omega$, where Ω is assumed to be the renormalized phonon frequency. Then (121) reduces to:

$$T_c = 0.18\sqrt{\lambda}\Omega \tag{122}$$

so that seemingly for $\lambda \gg 1$ we can, in principle, obtain even $T_c > \Omega$. However, if we remember the renormalization of phonon spectrum and take into account Eq. (50), we immediately obtain from Eq. (122):

$$T_c = 0.18\sqrt{\lambda}\Omega = 0.18\Omega_0\sqrt{\frac{\lambda}{1+2\lambda}} \tag{123}$$

which in the limit of $\lambda \gg 1$ tends to the value $T_c^{max} \approx 0.13\Omega_0$, because of significant softening of phonon spectrum. At the same time, as noted above, the physical meaning of "bare" frequency Ω_0 in a metal is poorly defined, and in particular it can not be determined from experiments. Correspondingly, the estimate of Eq. (123) somehow hangs in the air.

However, this analysis is valid only under the condition of rigid fixation of all relation between "bare" and "dressed" phonon spectra. If we "forget" about "bare" spectrum of phonons and consider parameters Ω and λ *independent*, we can obtain from Eq. (122) very high values of T_c. A certain , though rather artificial model, leading precisely to this kind of behavior was recently introduced in Ref. [49]. It considers the interaction of N–component electrons with $N \times N$–component system of Einstein phonons in the limit of $N \to \infty$. It was shown that in this model the renormalization of phonon spectrum due to interaction with conduction electrons is suppressed, so that in the limit of very strong coupling

with $1 \ll \lambda \ll N$ we always have Allen – Dynes estimate (122) with $\Omega = \Omega_0$.

However, the problem her is, that in real situation we never can consider Ω and λ as independent parameters simply because of the general relations (13) and (79), which express λ and $\langle\Omega^2\rangle$ via integrals of Eliashberg – McMillan function $\alpha^2(\omega)F(\omega)$. In fact, we may rewrite the expression for T_c in the region of very strong coupling as:

$$T_c = 0.18\sqrt{\lambda\langle\Omega^2\rangle} = 0.25\left[\int_0^\infty d\omega\alpha^2(\omega)F(\omega)\omega\right]^{1/2} \tag{124}$$

in adiabatic case and, correspondingly

$$T_c = (2\pi^4)^{-1/3}(\lambda D\langle\Omega^2\rangle)^{1/3} = \\ = (2\pi)^{-1/3}\left[2D\int_0^\infty d\omega\alpha^2(\omega)F(\omega)\omega\right]^{1/3} \tag{125}$$

in antiadiabatic limit. We see, that these expressions for T_c are completely determined by integrals of $\alpha^2(\omega)F(\omega)$.

In famous Ref. [50] a simple inequality for T_c was proposed, limiting its value by the square A under $\alpha^2(\omega)F(\omega)$:

$$T_c \leq 0.2309\int_0^\infty d\omega\alpha^2(\omega)F(\omega) \equiv 0.2309A \tag{126}$$

For the case of Einstein spectrum of phonons, taking into account Eq. (28), this inequality can be rewritten as:

$$T_c \leq 0.115\lambda\Omega_0 \tag{127}$$

This inequality is relatively often used in calculations.

The limitation given by Eq. (113) obtained above in antiadiabatic limit is essentially quite similar to Eq. (127), with replacement $\Omega_0 \to 2D$, which is quite natural in antiadiabatic limit.

Connection of λ and $\langle\Omega^2\rangle$ is markedly expressed in McMillan formula (61) for λ. If we use this expression in (121), we immediately obtain:

$$T_c = 0.18\sqrt{\frac{N(0)\langle I^2\rangle}{M}} \tag{128}$$

where

$$\langle I^2\rangle = \frac{1}{[N(0)]^2}\sum_{\mathbf{p}}\sum_{\mathbf{p}'}|I(\mathbf{p}-\mathbf{p}')|^2\,\delta(\varepsilon_{\mathbf{p}})\delta(\varepsilon_{\mathbf{p}'}) = \\ = \frac{1}{[N(0)]^2}\sum_{\mathbf{p}}\sum_{\mathbf{p}'}|\langle\mathbf{p}|\nabla V_{ei}(\mathbf{r})|\mathbf{p}'\rangle|^2)\delta(\varepsilon_{\mathbf{p}})\delta(\varepsilon_{\mathbf{p}'}) = \\ = \langle|\langle\mathbf{p}|\nabla V_{ei}(\mathbf{r})|\mathbf{p}'\rangle|^2\rangle_{FS} \tag{129}$$

so that both λ and $\langle\Omega^2\rangle$ just drop out from expression for T_c, which is expressed now simply via the averaged over Fermi surface matrix element of the gradient of electron – ion potential, ion mass and electron density of states at the Fermi level. This expression is convenient for "first principle" calculations, where it is often used, but it does not contain illustrative physical parameters in terms of which we usually treat T_c.

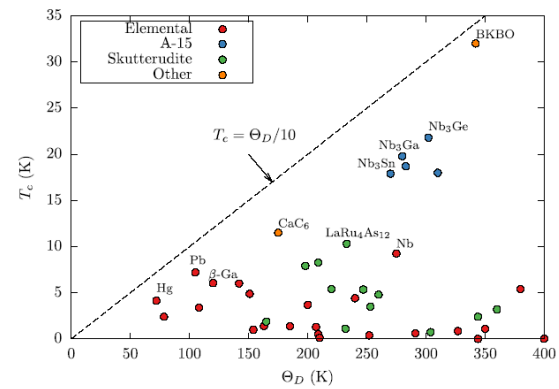

FIG. 9: Experimental values of the temperature of superconducting transition for conventional superconductors dependence on their Debye temperature Θ_D [51].

In Ref. [51] a new semiempirical limit for T_c was proposed for conventional (electron – phonon) semiconductors, which is written in a very simple form:

$$k_B T_c \leq A_{max}\Theta_D = A_{max}\hbar\Omega_D \tag{130}$$

where $A_{max} \approx 0.10$, and $\Theta_D = \hbar\Omega_D$ is Debye temperature, which may be determined e.g. from standard measurements of specific heat. This inequality obviously correlated with T_c^{max}, obtained above in the limit of $\lambda \to \infty$ in Eq. (123), if we identify Ω_0 with Ω_D. It is seen from Fig. 9 this limitation is satisfied for most of conventional superconductors [51]. Below we shall see, that is apparently not so in superhydrides.

VIII. SUPERHYDRIDES AND ELIASHBERG THEORY

In this Section we shall briefly discuss some results of application of Eliashberg theory to T_c calculations in hydrides under high pressures. Our presentation here will be very short, much more details may be found, for example, in reviews [3, 5, 6] and in original papers, some of these will be quoted below.

Eliashberg equations were widely used for calculations of T_c in hydrides. Actually, both crystal structure of H_3S under high pressures and high values of T_c ∼200K were *predicted* in Ref. [52]. For the structure $Im-3m$ under pressure of 200GPa, they obtained the value of pairing constant $\lambda \approx 2.2$ and mean logarithmic frequency of phonons $\Omega_{ln} \approx 1335$K, so that for T_c calculated from Allen – Dynes expression (117) with Coulomb pseudopotential values $\mu^\star$ =0.1–0.13 the values of T_c =191K–204K were obtained. These results were found to be in quite satisfactory agreement with experiment [1]. The achieve-

ment of room temperature values of T_c in C-S-H system [12] was reasonably explained in a recent paper [53], where it was shown that hole doping of $Im-3m$ structure of H_3S by introduction of carbon shifts Fermi level to a maximum of Van – Hove singularity in the density of states and certain softening of phonon spectrum. Combined, all these lead to the growth of λ up to the value of 2.4, which is sufficient, in principle, to explain the values of $T_c \approx$288K.

In Table I we show the calculated parameters of several hydrides of rare – earth elements from Ref. [6], for which the record values of T_c were predicted. In last two columns of the Table we give the boundaries for T_c, calculated from inequality (99) and from asymptotic expression of Allen and Dynes (122), under the simplest assumption of $\langle\Omega_{\ln}\rangle = \langle\Omega^2\rangle^{1/2} = \Omega$. We can see that these values are close enough to those obtained from more detailed calculations of Ref. [6] and determine in fact the lower and upper bounds for T_c. This clearly shows that the systems with highest values of T_c achieved are practically already in the very strong coupling region of Eliashberg theory.

In a recent paper [54] the extensive calculations of T_c were performed for practically all possible binary compounds of hydrogen with other elements of periodic system for the values of external pressure 100, 200 and 300 GPa (for which the stable crystal structures were also determined). As many as 36 new systems were discovered for which T_c may exceed 100K, and in 18 cases T_c exceeded 200K. In particular, for NaH_6 system the values of T_c =248-279K were obtained, and for CaH_6 — T_c =216-253K, already for pressured of 100 GPa. The results of this paper clearly show, that the highest possible values of T_c are achieved in the region of very strong coupling, up to the values of λ =5.81 in NaH_6 (under 100 GPa).

Summarizing we may say, that the record values of T_c in superhydrides are achieved for typical values of λ = 2–3.5 (or even more) and for characteristic phonon frequencies from 1000K to 2000K. We must also note, that the upper bound expressed by Eq. (130) is already quite surpassed in some of the known superhydrides.

IX. CONCLUSIONS

We consciously presented all problems related to derivation and use of Eliashberg equations on sufficiently elementary level, trying to stress all approximations and simplifications.

Eliashberg theory remains the main theory, which completely explains the values of the critical temperature in superconductors with electron – phonon mechanism of pairing. This theory is also applicable in the region of strong electron – phonon coupling, limited only by the applicability of adiabatic approximation, based on Migdal theorem, which is valid in the vast majority of metals, including the new superhydrides with record values of T_c. The values of (renormalized, physical) pairing coupling constant λ can surely exceed unity until the system possess the metallic ground state. This is not so in the vicinity of phase transition to a new ground state like charge density wave (CDW) or Bose – condensate of bipolarons.

More so, Eliashberg theory is qualitatively applicable also in strong antiadiabatic limit. Simple interpolation expressions for T_c can be constructed, connecting adiabatic and antiadiabatic regions, The strong antiadiabatic limit may be of importance in exotic enough systems with very narrow electronic bands and(or) anomalously small values of Fermi energy (like monolayers of FeSe, $SrTiO_3$ and, probably, some hydrides).

Unfortunately this theory does not produce a simple expression for maximal values of T_c in terms of experimentally measurable (or calculated) parameters like characteristic (average) values of phonon frequencies and pairing coupling constant. Formally, such limit is just absent, if we consider these parameters as independent. However, if take into account their interdependence, the maximal values of T_c are in fact determined by some "game" of atomic constants. However, all new data on superhydrides strongly indicate that all these systems are very close to the strong coupling region coupling of Eliashberg theory, which means that maximal values of T_c for "usual" metals are already achieved. The only hope probably remains only for metallic hydrogen [55].

This work was partially supported by RFBR grant No. 20-02-00011.

[1] A.P. Drozdov, M.I. Eremets, I.A. Troyan, V. Ksenofontov, S.I. Shylin. Nature **525**, 73 (2015)

[2] M.I. Eremets, A.P. Drozdov. Usp. Fiz. Nauk **186**, 1257 (2016)

[3] L.P. Gor'kov, V.Z. Kresin. Rev. Mod. Phys. **90**, 01001 (2018)

[4] C.J. Pickard, I. Errea, M.I. Eremets. Annual Reviews of Condensed Matter Physics **11**, 57 (2020)

[5] J.A. Flores-Livas, L. Boeri, A. Sanna, G. Pinofeta, R. Arita, M. Eremets. Physics Reports **856**, 1 (2020)

[6] H. Liu, I.I. Naumov, R. Hoffman, N.W. Ashcroft, R.J. Hemley. PNAS **114**, 6990 (2018)

[7] A.P. Drozdov, et al. Nature **569**, 528 (2019)

[8] M. Somayazulu, et al. Phys. Rev. Lett. **122**, 027001

TABLE I: Calculated values of T_c for La-H and Y-H compounds, obtained from numerical solution of Eliashberg equations [6] compared with its boundary values.

Compound	Pressure (GPa)	λ	$\Omega_{\ln}$(K)	$T_c(\mu^\star = 0.1)$(K)	$T_c(\mu^\star = 0.13)$(K)	$\frac{1}{2\pi}\sqrt{\lambda - 1}\Omega$	$0.18\sqrt{\lambda}\Omega$
LaH_{10}	210	3.41	848	286	274	209	282
LaH_{10}	250	2.29	1253	274	257	226	341
LaH_{10}	300	1.78	1488	254	241	209	357
YH_{10}	250	2.58	1282	326	305	256	370
YH_{10}	300	2.06	1511	308	286	247	390

(2019)

[9] I.A. Troyan et al. ArXiv:1908.01534; Advanced Materials (2021)

[10] D.V. Semenok et al. ArXiv:2012.04787; Nature Materials (2021)

[11] E.Snider, N. Dasenbrock-Gammon, R. McBride, X. Wang, N. Meyers, K.V. Lawler, E. Zurek, A. Salamat, R.P. Dias. Phys. Rev. Lett. **126**, 117003 (2021)

[12] E. Snider, N. Dasenbrock-Gammon, R. McBride, M. Debessai, H. Vindana, K. Vencatasamy, K.V. Lawler, A. Salamat, R.P. Dias. Nature **586**, 373 (2020)

[13] D.J. Scalapino. In "Superconductivity", p. 449, Ed. by R.D. Parks, Marcel Dekker, NY, 1969

[14] P.B. Allen, B. Mitrović. Solid State Physics, Vol. Vol. 37 (Eds. F. Seitz, D. Turnbull, H. Ehrenreich), Academic Press, NY, 1982, p. 1

[15] V.Z. Kresin, H. Morawitz, S.A. Wolf. Superconducting State. Mechanisms and Properties. Oxford University Press, 2014

[16] S.V. Vonsovsky, Yu. A. Izyumov, E.Z. Kurmaev. Superconductivity of Transition Metals, Their Alloys and Compounds, Springer, Berlin – Heidelberg, 1982

[17] A.B. Migdal. Zh. Eksp. Teor. Fiz. **34**, 1438 (1958) [Sov. Phys. JETP **7**, 996 (1958)]

[18] A.A. Abrikosov, L.P. Gor'kov, I.E. Dzyaloshinskii. Quantum Field Theoretical Methods in Statistical Physics. Pergamon Press, Oxford, 1965

[19] J.R. Schrieffer. Theory of Superconductivity, WA Benjamin, NY, 1964

[20] M.V. Sadovskii. Diagrammatics. World Scientific, Singapore, 2019

[21] I. Esterlis, B. Nosarzewski, E.W. Huang, B. Moritz, T.P. Devereaux, D.J. Scalapino, S.A. Kivelson. Phys. Rev. B**97**, 140501(R) (2018)

[22] I. Esterlis, S.A. Kivelson, D.J. Scalapino. Phys. Rev. B**99**, 174516 (2019)

[23] A.V. Chubukov, A. Abanov, I. Esterlis, S.A. Kivelson. Ann. Phys. **417**, 168190 (2020)

[24] M.V. Sadovskii. Zh. Eksp. Teor. Fiz. **155**, 527 (2019); [JETP **128**, 455 (2019)]

[25] M.V. Sadovskii. Pis'ma J. Esp. Teor. Fiz. **109**, 165 (2019) [JETP Letters **109**, 166 (2019)]

[26] M.V. Sadovskii. Journal of Superconductivity and Novel Magnetism **33**, 19 (2020)

[27] M.A. Ikeda, A. Ogasawara, M. Sugihara. Phys. Lett. A **170**. 319 (1992)

[28] M.V. Sadovskii. Usp. Fiz. Nauk **186**, 1035 (2016) [Physics Uspekhi **59**, 947 (2016)]

[29] L.P. Gor'kov. Phys. Rev. B**93**, 054517 (2016)

[30] L.P. Gor'kov. Phys. Rev. B**93**, 060507 (2016)

[31] L.P. Gor'kov. PNAS **113**, 4646 (2016)

[32] Young Woo Choi, Hyong Joon Choi. Phys. Rev. Lett. **127**, 167001 (2021)

[33] H. Fröhlich. Proc. Roy. Soc. **A215**, 291 (1952)

[34] High – Temperature Superconductivity. Ed. by V.L. Ginzburg and D.A. Kirzhnits, Consultants Bureau, NY, 1982, Ch. 3

[35] D. Vollhardt. Correlated Electron Systems (Ed. by V.J. Emery), World Scientific, Singapore, 1993, p. 57

[36] Th. Pruschke, M. Jarrell, J.K. Freericks. Adv. Phys. **44**, 210 (1995)

[37] A. Georges, G. Kotliar, W. Krauth, M.J. Rozenberg. Rev. Mod. Phys. **68**, 13 (1996)

[38] D. Vollhardt. AIP Conference Proceedings **1297**, 339 (2010)

[39] J. Bauer, J.E. Han, O. Gunnarsson. Phys. Rev. B**84**, 184531 (2011)

[40] D. Meyer, A.C. Hewson, R. Bulla. Phys. Rev. Lett. **89**, 196401 (2002).

[41] F. Schrodi, A. Aperis, P.M. Oppeneer. Phys. Rev. B**103**, 064511 (2021)

[42] E.G. Brovman, Yu.M. Kagan. Usp. Fiz. Nauk **112**, 369 (1974)

[43] B.T. Geilikman. Usp. Fiz. Nauk **115**, 403 (1975)

[44] E.G. Maksimov, A.E. Karakozov. Usp. Fiz. Nauk **178**, 561 (2008)

[45] P.B. Allen, R.C. Dynes. Phys. Rev. **12**, 905 (1975)

[46] V.Z. Kresin, H. Gutfreund, W.A. Little. Solid State Communications **51**, 339 (1984)

[47] M.L. Cohen, P.W. Anderson. AIP Conference Proceedings on d– and f – Band Superconductivity, Rochester, NY, 1972, p. 17

[48] O.V. Dolgov. E.G. Maksimov, D.A. Kirzhnits. Rev. Mod. Phys. **53**, 81 (1981)

[49] J.S. Hoffmann, D. Chowdhuri, S.A. Kivelson, E.Berg. ArXiv:2105.09322

[50] C.R. Leavens. Solid State Communications **17**, 1499 (1975)

[51] I. Esterlis, S.A. Kivelson, D.J. Scalapino. npj Quant. Mater. **3**, 59 (2018)

[52] D. Duan, Y. Liu, F. Tian, D. Li, X. Huang, Z. Zhao, H. Yu, B. Liu, W. Tian, T. Cui. Sci. Rep. **4**, 6968 (2014)

[53] Y. Ge, F. Zhang, R.P. Dias, R.J. Hemley, Y. Yao. Materials Today Physics **15**, 100330 (2020)

[54] A.M.Shipley, M.J. Hutcheon, R.J. Needs, C.J. Pickard. ArXiv:2105.02296

[55] E.G. Maksimov. Usp. Fiz. Nauk **178**, 175 (2008)

LIST OF SCIENTIFIC PUBLICATIONS BY M.V. SADOVSKII

Books and Reviews:

1. M.V. Sadovskii. Superconductivity and Localization. World Scientific, 2000
2. M.V. Sadovskii. Lectures on Statistical Physics. "ICS", Moscow-Izhevsk, 2003 (in Russian)
3. M.V. Sadovskii. Lectures on Quantum Field Theory. "ICS", Moscow-Izhevsk, 2003 (in Russian)
4. M.V. Sadovskii. Diagrammatics. "ICS", Moscow-Izhevsk, 2004 (in Russian)
5. M.V. Sadovskii. Diagrammatics. World Scientific, 2006
6. M.V. Sadovskii. Diagrammatics, 2 ed. "ICS", Moscow-Izhevsk, 2010 (in Russian)
7. M.V. Sadovskii. Statistical Physics. Walter de Gruyter, Berlin/Boston, 2012
8. M.V. Sadovskii. Quantum Field Theory. Walter de Gruyter, Berlin/Boston, 2013
9. M.V. Sadovskii. Diagrammatics, 3 ed. "ICS", Moscow-Izhevsk, 2019 (in Russian)
10. M.V. Sadovskii. Diagrammatics, 2nd Edition. World Scientific, 2019
11. M.V. Sadovskii. Statistical Physics, 2nd Edition. De Gruyter, 2019
12. M.V. Sadovskii. Quantum Field Theory, 2nd Edition. De Gruyter, 2019
13. V.A. Alekseev, A.A. Andreev, M.V. Sadovskii. Semiconductor–Metal Transition in Liquid Semiconductors. Sov. Phys. – Uspekhi, v. 23, No. 9, 551–575 (1980)
14. M.V. Sadovskii. Electron Localization in Disordered Systems: Critical Behavior and Macroscopic Manifestations. Sov. Phys. – Uspekhi, v. 24, No. 2, 96–115 (1981)
15. M.V. Sadovskii. Theory of Electron Localization in Disordered Systems. Sov. Sci. Rev. A. Physics Reviews, Ed. by I.M. Khalatnikov, v. 7, 1–130, Harwood Academic Publishers, NY, 1986
16. B.N. Goshchitskii, V.L. Kozhevnikov, M.V. Sadovskii. High-T_c Studies in Sverdlovsk. Int. J. Mod. Phys. B, v. 2, No. 6, 1331–1379 (1988)
17. M.V. Sadovskii. Superconductivity in Strongly Disordered Systems. In "Studies of High-Temperature Superconductors", Ed. by A.V. Narlikar, v. 11, 131–223, Nova Science Publishers, NY, 1993
18. M.V. Sadovskii. Superconductivity and Localization. Superconductivity, Physics, Chemistry, Technology, v. 8, No. 3, 337–442 (1995) (in Russian)
19. M.V. Sadovskii. Superconductivity and Localization. Physics Reports, v. 282, No. 5&6, 225–348 (1997)

20. M.V. Sadovskii. Pseudogap in High-Temperature Superconductors. Physics Uspekhi, v. 44, No. 5, 515–540 (2001)

21. M.V. Sadovskii. Models of the Pseudogap State in High-Temperature Superconductors. In "Strings, branes, lattices, networks, pseudogaps and dust" (Proceedings of I.E. Tamm Seminar), 357–441, "Scientific World", Moscow, 2007 (in Russian); ArXiv: cond-mat/0408489

22. E.Z. Kuchinskii, I.A. Nekrasov, M.V. Sadovskii. Pseudogaps: Introducing the Length Scale into DMFT. Low Temp. Phys. v. 32, No. 4/5, 398–405 (2006)

23. M.V. Sadovskii. High-Temperature Superconductivity in Iron Based Layered Compounds. Physics Uspekhi, v. 51, No. 12, 1201–1227 (2008)

24. E.Z. Kuchinskii, I.A. Nekrasov, M.V. Sadovskii. Generalized Dynamical Mean Field Theory in the Physics of Strongly Correlated Systems. Physics Uspekhi, v. 55, No. 4, 325–355 (2012)

25. I.A. Nekrasov, M.V. Sadovskii. Electronic Structure of New Iron-Based Superconductors: From Pnictides to Chalcogenides and Other Similar Systems. JETP Letters, v. 99, No. 10, 598–612 (2014)

26. E.Z. Kuchinskii, M.V. Sadovskii. DMFT+Σ Approach to Disordered Hubbard Model. JETP, v. 122, No. 3, 510–525 (2016)

27. M.V. Sadovskii. High-Temperature Superconductivity in FeSe Monolayers. Physics Uspekhi, v. 59, No. 10, 947–967 (2016)

28. N.A. Kuleeva, E.Z. Kuchinskii, M.V. Sadovskii. Ginzburg–Landau Expansion and the Upper Critical Field in Disordered Attractive Hubbard Model. JETP Letters, v. 112, No. 9, 555–567 (2020)

29. M.V. Sadovskii. Planckian Relaxation Delusion in Metals. Physics Uspekhi, v. 64, No. 2, 157–190 (2021)

30. M.V. Sadovskii. Limits of Eliashberg Theory and Bounds for Superconducting Transition Temperature. Physics Uspekhi, v. 65, No. 7 (2022)

Selected papers:

1. M.V. Sadovskii. On the Theory of Conductivity of Metals with Non-Magnetic Impurities in Quantizing Magnetic Field. Phys. Metals and Phys. Metallography, v. 29, No. 6, 1160–1168 (1970)

2. P.S. Zyryanov, M.V. Sadovskii. On the Influence of Electron Scattering on Damping of Quantum Waves in the Fermi–Liquid of Metals. Phys. Metals and Phys. Metallography, v. 30, No. 5, 1099–1102 (1970)

3. L.N. Bulaevskii, M.V. Sadovskii. On the Influence of Crystal Lattice Disordering on Peierls Transition. Sov. Phys. – Solid State, v. 16, No. 4, 743 (1974)

4. M.V. Sadovskii. A Model of a Disordered System (A Contribution to the Theory of "Liquid Semiconductors"). Sov. Phys. – JETP, v. 39, No. 5, 845–850 (1974)

5. M.V. Sadovskii. Theory of Quasi-one-dimensional Systems Undergoing Peierls Transition. Sov. Phys. – Solid State, v. 16, No. 9, 1632 (1974)

6. M.V. Sadovskii. Localization of Electrons in Disordered Systems. The Mobility Edge and Theory of Critical Phenomena. Sov. Phys. – JETP, v. 43, No. 5, 1008–1010 (1976)

7. V.A. Alekseev, V.G. Ovcharenko, Yu.F. Ryzhkov, M.V. Sadovskii. Experimental Evidence of Anderson Localization in Liquid Selenium. JETP Letters, v. 24, No. 4, 189 (1976)

8. M.V. Sadovskii. Collective Excitations of Charge Density Waves in Quasi-one-dimensional Structures. Sov. Phys. – Solid State, v. 19, No. 4, 607 (1977)

9. M.V. Sadovskii. Electron in a Random Field in a Space of $d = 4 - \varepsilon$ Dimensions. Sov. Phys. – Solid State, v. 19, No. 8, 1366–1368 (1977)

10. V.A. Alekseev, V.G. Ovcharenko, Ju.F. Ryzhkov, M.V. Sadovskii. Possibility of Anderson Transition in Liquid Se and As in the Region of High Temperatures and Pressures. Phys. Lett., v. 65A, No. 2, 173–174 (1978)

11. M.V. Sadovskii. Electron in a Random Field, Theory of Phase Transitions, and Finite-Action Nonlinear Solutions. Sov. Phys. – Solid State, v. 21, No. 3, 435–439 (1979)

12. M.V. Sadovskii, Yu.N. Skryabin. Superconductivity in Spin-Glasses. Phys. Stat. Sol. (b), v. 95, No. 1, 59–64 (1979)

13. M.V. Sadovskii. Exact Solution for the Density of Electronic States in a Model of a Disordered System. Sov. Phys. – JETP, v. 50, No. 5, 989–994 (1979)

14. M.V. Sadovskii. Electron Localization in the Random-Phase Model and in Magnetic Field. Sov. Phys. – JETP, v. 53, No. 3, 581–587 (1981)

15. M.V. Medvedev, M.V. Sadovskii. Localization of One-Particle Spin Excitations in a Ferromagnet with a Random Easy-Axis Anisotropy. Sov. Phys. – Solid State, v. 23, No. 7, 1135–1137 (1981)

16. M.V. Sadovskii. Localization of Electrons in Disordered Systems and Critical Behavior at the Mobility Edge. In "Electronic Structure and Properties of Solids", Sverdlovsk, 1982, 36–41 (in Russian)

17. M.V. Medvedev, M.V. Sadovskii. Random Bond Ising Model in Self-Avoiding Walk Approximation. Phys. Stat. Sol. (b), v. 109, 49–57 (1982)

18. M.V. Medvedev, M.V. Sadovskii. Random Site Ising Model in Self-Avoiding Walk Approximation. Phys. Stat. Sol. (b), v. 109, 449–456 (1982)

19. M.V. Sadovskii. Localization Criterion in the Field Theory of an Electron in a Random Field. Sov. Phys. – JETP, v. 56, No. 4, 816–822 (1982)

20. A.V. Myasnikov, M.V. Sadovskii. Self-Consistent Theory of Localization in Spaces with $2 < d < 4$ Dimensions. Sov. Phys. – Solid State, v. 24, No. 12, 2033 (1982)

21. E.A. Kotov, M.V. Sadovskii. Self-Consistent Theory of Localization for the Anderson Model. Zs. Phys., v. 51, No. 1, 17–23 (1983)

22. M.I. Katsnelson, M.V. Sadovskii. Electron Interaction in Self-Consistent Theory of Localization. Sov. Phys. – Solid State, v. 25, No. 11, 1942 (1983)

23. M.I. Katsnelson, M.V. Sadovskii. Density of States and Screening near the Mobility Edge. Sov. Phys. – JETP, v. 60, No. 2, 300–306 (1984)

24. L.N. Bulaevskii, M.V. Sadovskii. Localization and Superconductivity. JETP Letters, v. 39, No. 11, 640–643 (1984)

25. L.N. Bulaevskii, M.V. Sadovskii. Anderson Localization and Superconductivity. J. Low-Temp. Phys., v. 59, No. 1/2, 89–113 (1985)

26. E.A. Kotov, M.V. Sadovskii. Hall Effect in Self-Consistent Theory of Localization. Phys. Metals and Phys. Metallography, v. 60, No. 1, 22–30 (1985)

27. L.N. Bulaevskii, A.A. Varlamov, M.V. Sadovskii. Fluctuations of Conductivity and Diamagnetic Susceptibility in Dirty Superconductors Close to the Edge of Anderson Localization. Sov. Phys. – Solid State, v. 28, No. 6, 1799 (1986)

28. L.N. Bulaevskii, M.V. Sadovskii. Increase of Spatial Fluctuations in Superconductors near the Anderson Transition. JETP Letters, v. 43, No. 2, 99–103 (1986)

29. S.A. Davydov, V.E. Arkhipov, B.N. Goshchitskii, M.V. Sadovskii. Metal Insulator Transition and Superconductivity in Mo_6Se_8 under Disordering. Phys. Metals and Phys. Metallography, v. 62, No. 6, 1130–1135 (1986)

30. L.N. Bulaevskii, S.V. Panyukov, M.V. Sadovskii. Inhomogeneous Superconductivity in Disordered Metals. Sov. Phys. – JETP, v. 65, No. 2, 380–388 (1987)

31. V.R. Galakhov et al. Electron and Phonon Properties of $La_{2-x}Sr_xCuO_{4-y}$. Phys. Metals and Phys. Metallography, v. 63, No. 4, 829–830 (1987)

32. V.L. Kozhevnikov et al. Galvanomagnetic Phenomena in La-Sr-Cu-O. Phys. Metals and Phys. Metallography, v. 64, No. 1, 184–186 (1987)

33. I.F. Berger et al. Structure, Magnetic Properties and Specific Heat of Superconductors $RBa_2Cu_3O_7$(R = Er, Ho). Phys. Metals and Phys. Metallography, v. 64, No. 2, 394–396 (1987)

34. A.V. Zaborov, M.V. Sadovskii. Nearest Neigbour Pairing in Hubbard Model. Series of preprints: "Problems of High-Temperature Superconductivity", No. 5, Ural Branch of the USSR Academy of Sciences, Syktyvkar, 1988

35. L.N. Bulaevskii, S.V. Panyukov, M.V. Sadovskii. Superconductivity in Metals with Strong Disorder. In "Problems of Theoretical Physics and Astrophysics", Nauka, Moscow, 1989, 120–137 (in Russian)

36. S.A. Davydov, B.N. Goshchitskii et al. Effects of Localization in Atomic-Disordered High-T_c Superconductots. Int. J. Mod. Phys. B, v. 3, No. 1, 87–92 (1989)

37. S.A. Davydov, B.N. Goshchitskii et al. Effects of Localization in Atomic-Disordered High-T_c Superconductots. In "Advances in Superconductivity", Kitazawa, Ishiguro (Eds.), Springer-Verlag, Tokyo, 1989, 463–468

38. E.Z. Kuchinskii, N.A. Kuleeva, M.V. Sadovskii. Ginzburg–Landau Expansion in Strongly Disordered Attractive Hubbard Model. JETP, v. 125, No. 1, 111–122 (2017)

39. B.N. Goshchitskii, S.A. Davydov, A.E. Karkin, A.V. Mirmelstein, M.V. Sadovskii, V.I. Voronin. Localization Effects in Disordered High-T_c Superconductors. Physica C, v. 162–164, 1019–1020 (1989)

40. B.N. Goshchitskii, S.A. Davydov, A.E. Karkin, A.V. Mirmelstein, M.V. Sadovskii, V.I. Voronin. Localization Effects in Atomic-Disordered High-T_c Superconductors. In "Progress in High Temperature Superconductivity", v. 11, World Scientific Singapore, 270–280 (1989)

41. B.A. Aleksashin, V.P. Voronin, S.V. Verkhovskii, B.N. Goshchitskii, S.A. Davydov, Yu.I. Zhdanov, A.E. Karkin, V.L. Kozhevnikov, A.V. Mirmelshtein, K.N. Mikhalev, M.V. Sadovskii, V.V. Serikov, S.M. Cheshnitskii. Localization Effects in Atomically Disordered High-Temperature Superconductors. Sov. Phys. – JETP, v. 68, No. 2, 382–394 (1989)

42. B.N. Goshchitskii, S.A. Davydov, A.E. Karkin, A.V. Mirmelstein, M.V. Sadovskii, V.I. Voronin, S.V. Verkhovskii, V.V. Serikov, B.A. Aleksashin, Yu.I. Zhdanov. Radiation Effects in High-T_c Superconductors. In "Progress in High Temperature Superconductors", v. 21, World Scientific, Singapore, 1990, 104–115

43. B.N. Goshchitskii, S.A. Davydov, A.E. Karkin, A.V. Mirmelstein, M.V. Sadovskii. Localization Effects in Radiationally Disordered High-Temperature Superconductors: Theoretical Interpretation. In "Progress in High Temperature Superconductors", v. 22, World Scientific, Singapore, 1990, 474–476

44. M.V. Sadovskii. Localization Effects in High-Temperature Superconductors. AIP Conf. Proc., v. 213, 207–216 (1990); Ann. NY Ac. Sci., v. 581, 207–216 (1990)

45. E.Z. Kuchinskii, M.V. Sadovskii. Energy Level Fluctuations in Finite Systems near the Metal–Insulator Transition. Sov. Phys. – JETP, v. 71, No. 2, 354–359 (1990)

46. M.V. Sadovskii, A.A. Timofeev. Optical Conductivity of High-Temperature Superconductors in "Spin-Bag" Model: Exact Solution? Superconductivity: Physics, Chemistry, Technology, v. 4, No. 1, 11–23 (1991)

47. E.Z. Kuchinskii, M.V. Sadovskii. Upper Critical Field of a Superconductor near Anderson Metal–Insulator Transition. Superconductivity: Physics, Chemistry, Technology, v. 4, No. 12, 2278–2292 (1991)

48. M.V. Sadovskii, A.A. Timofeev. Optical Conductivity of High-Temperature Superconductors: Exact Solution for a "Spin-Bag" Model. Physica C, v. 185–189, 1431–1432 (1991)

49. E.Z. Kuchinskii, M.V. Sadovskii. Upper Critical Field of a Superconductor near Anderson Transition. Physica C, v. 185–189, 1477–1478 (1991)

50. M.V. Sadovskii, A.A. Timofeev. The Two-Particle Green Function in a Model of a One-Dimensional Disordered System: An Exact Solution? J. Moscow Phys. Soc., v. 1, 391–406 (1991)

51. M.V. Medvedev, D.R. Plotitsin, M.V. Sadovskii. Critical State of High-Temperature Superconductor with Paramagnetic Ions. Superconductivity: Physics, Chemistry, Technology, v. 5, No. 11, 1999–2011 (1992)

52. M.A. Erkabaev, M.V. Sadovskii. Self-Consistent Localization Theory in the Two-Band Model. J. Moscow Phys. Soc., v. 2, 233–241 (1992)

53. S.V. Verkhovskii, Yu.I. Zhdanov, A.M. Bogdanovitch, K.N. Mikhalyov, B.A. Aleksashin, V.V. Serikov, V.V. Lavrentjev, M.V. Sadovskii. NMR and Spin-Lattice Relaxation Rate of ^{89}Y, ^{63}Cu in Radiation Disordered $YBa_2Cu_3O_{6.9}$. Appl. Magn. Reson., v. 3, 649–663 (1992)

54. E.Z. Kuchinskii, M.V. Sadovskii. Upper Critical Field of Two-Dimensional and Quasi-Two-Dimensional Superconductors near Anderson Metal–Insulator Transition. Superconductivity: Physics, Chemistry, Technology, v. 6, No. 6, 1119–1137 (1993)

55. E.Z. Kuchinskii, M.V. Sadovskii. Normal Impurities in Superconductors with an "Odd" Pairing. JETP Letters, v. 57, No. 8, 515–518 (1993)

56. E.Z. Kuchinskii, M.V. Sadovskii. Temperature Dependence of the Upper Critical Field in High-Temperature Superconductors: Localization Effects. JETP Letters, v. 58, No. 11, 819–823 (1993)

57. Yu.I. Zhdanov, A.M. Bogdanovitch, B.A. Aleksashin, K.N. Mikhalyov, V.V. Lavrentjev, S.V. Verkhovskii, V.V. Serikov, M.V. Sadovskii. Changes in Electron Spectrum of $YBa_2Cu_3O_{6.9}$ under Radiation Disordering: the ^{89}Y, ^{63}Cu NMR Data. JETP, v. 76, No. 5, 868–879 (1993)

58. E.Z. Kuchinskii, M.V. Sadovskii, M.A. Erkabaev. On the Theory of Superconductors with "Odd" Pairing. JETP, v. 77, No. 4, 692–699 (1993)

59. M.V. Sadovskii, E.Z. Kuchinskii, M.A. Erkabaev. On the Theory of "Odd-Pairing" Superconductors. Superconductors. Physica C, v. 235–240, 2403–2404 (1994)

60. E.Z. Kuchinskii, M.V. Sadovskii. Temperature Dependence of the Upper Critical Field in High-Temperature Superconductors: Localization Effects. Physica C, v. 235–240, 2621–2622 (1994)

61. E.Z. Kuchinskii, A.I. Posazhennikova, M.V. Sadovskii. The Ginzburg–Landau Expansion and the Physical Properties of Superconductors with Odd Pairing. JETP, v. 80, No. 2, 324–333 (1995)

62. E.Z. Kuchinskii, M.V. Sadovskii, V.G. Suvorov, M.A. Erkabaev. Self-Consistent Theory of Metal–Insulator Transitions in Disordered Systems. JETP, v. 107, No. 6, 2027–2047 (1995)

63. M.V. Sadovskii. Josephson Effect in Superconductors with Odd-Gap Pairing. JETP Letters, v. 61, No. 2, 129–130 (1995)

64. A.I. Posazhennikova. M.V. Sadovskii. Ginzburg–Landau Expansion and the Slope of the Upper Critical Field in Disordered Superconductors with Anisotropic Pairing. JETP Letters, v. 63, No. 5, 358–364 (1996)

65. E.Z. Kuchinskii, M.V. Sadovskii. M.A. Erkabaev. Superconductivity Suppression Close to the Metal–Insulator Transition in Strongly Disordered Systems. JETP, v. 85, No. 1, 104–108 (1997)

66. A.I. Posazhennikova. M.V. Sadovskii. Disorder Effects in Superconductors with Anisotropic Pairing: From Cooper Pairs to Compact Bosons. JETP Letters, v. 65, No. 3, 270–275 (1997)

67. A.I. Posazhennikova. M.V. Sadovskii. Ginzburg–Landau Expansion and the Slope of the Upper Critical Field in Superconductors with Anisotropic Normal Impurity Scattering. JETP, v. 85, No. 6, 1162–1167 (1997)

68. A.I. Posazhennikova. M.V. Sadovskii. Ginzburg–Landau Expansion and the Slope of the Upper Critical Field in Disordered Superconductors with Anisotropic Pairing. Physica C, v. 282–287, 1847–1848 (1997)

69. A.I. Posazhennikova. M.V. Sadovskii. Disorder Effects in Superconductors with Anisotropic Pairing: From Cooper Pairs to Compact Bosons. Physica C, v. 282–287, 1849–1850 (1997)

70. E.Z. Kuchinskii, M.V. Sadovskii. Combinatorics of Feynman Diagrams for the Problems with Gaussian Random Field. JETP, v. 86, No. 2, 367–374 (1998)

71. A.I. Posazhennikova, M.V. Sadovskii. Ginzburg–Landau Expansion in a Toy Model of Superconductor with Pseudogap. JETP, v. 88, No. 2, 347–355 (1999)

72. E.Z. Kuchinskii, M.V. Sadovskii. Models of the Pseudogap State of Two-Dimensional Systems. JETP, v. 88, No. 5, 968–979 (1999)

73. M.V. Sadovskii. Optical Conductivity in a Simple Model of Pseudogap State in Two-Dimensional System. JETP Letters, v. 69, No. 6, 483–489 (1999)

74. E.Z. Kuchinskii, M.V. Sadovskii. Superconductivity in a Toy Model of the Pseudogap State. JETP, v. 90, No. 3, 613–623 (2000)

75. M.V. Sadovskii. Models of the Pseudogap State in Cuprates. Physica C, v. 341–348, 811–814 (2000)

76. E.Z. Kuchinskii, M.V. Sadovskii. Superconductivity in a Toy Model of the Pseudogap State. Physica C, v. 341–348, 879–882 (2000)

77. M.V. Sadovskii. Optical Conductivity in a Simple Model of the Pseudogap State. Physica C, v. 341–348, 939–940 (2000)

78. E.Z. Kuchinskii, M.V. Sadovskii. Superconductivity in the Pseudogap State due to Fluctuations of Short-Range Order. JETP, v. 92, No. 3, 480–492 (2001)

79. A.E. Karkin, V.I. Voronin, T.V. Dyachkova, N.I. Kadirova, A.P. Tyutyunik, V.G. Zubkov, Yu.G. Zainulin, M.V. Sadovskii, B.N. Goshchitskii. Superconducting Properties of the Atomically Disordered MgB_2 Compound. JETP Letters, v. 73, No. 10, 570–572 (2001)

80. E.Z. Kuchinskii, M.V. Sadovskii. Superconductivity in an Exactly Solvable Model of the Pseudogap State: Absence of Self-Averaging. JETP, v. 94, No. 3, 654–769 (2002)

81. N.A. Strigina, M.V. Sadovskii. Optical Conductivity in a Two-Dimensional Model of the Pseudogap State. JETP, v. 95, No. 3, 526–537 (2002)

82. E.Z. Kuchinskii, M.V. Sadovskii, N.A. Strigina. Superconductivity in the Pseudogap State in "Hot-Spots" Model: Ginzburg–Landau Expansion. JETP, v. 98, No. 4, 748–759 (2004)

83. N.A. Strigina, M.V. Sadovskii. Optical Conductivity in the "Hot Spots" Model of the Pseudogap State. Physica C, v. 408–410, 418–419 (2004)

84. N.A. Kuleeva, E.Z. Kuchinskii, M.V. Sadovskii. Superconductivity in the "Hot-Spots" Model of the Pseudogap State: Impurity Scattering and Phase Diagram. JETP, v. 99, No. 6, 1264–1278 (2004)

85. E.Z. Kuchinskii, I.A. Nekrasov, M.V. Sadovskii. "Destruction" of the Fermi Surface due to Pseudogap Fluctuations in Strongly Correlated Systems. JETP Letters, v. 82, No. 4, 198–203 (2005)

86. M.V. Sadovskii, I.A. Nekrasov, E.Z. Kuchinskii, Th. Pruschke, V.I. Anisimov. Pseudogaps in Strongly Correlated Metals: A Generalized Dynamical Mean-Field Theory Approach. Phys. Rev. B, v. 72, No. 15, 155105 (2005)

87. E.Z. Kuchinskii, M.V. Sadovskii. Non-Fermi Liquid Behavior in Fluctuating Gap Model: From Pole to Zero of the Green's Function. JETP, v. 103, No. 3, 415–427 (2006)

88. E.Z. Kuchinskii, I.A. Nekrasov, M.V. Sadovskii. Pseudogaps in Strongly Correlated Metals: Optical Conductivity within the Generalized Dynamical Mean-Field Theory Approach. Phys. Rev. B, v. 75, No. 11, 115102 (2007)

89. E.Z. Kuchinskii, I.A. Nekrasov, Z.I. Pchelkina, M.V. Sadovskii. Pseudogap Behavior in $Bi_2Ca_2SrCu_2O_8$: Results of the Generalized Dynamical Mean-Field Approach. JETP, v. 104, No. 5, 792–804 (2007)

90. I.A. Nekrasov, E.Z. Kuchinskii, Z.V. Pchelkina, M.V. Sadovskii. Pseudogap in Normal Underdoped Phase of $Bi_2Ca_2SrCu_2O_8$: LDA+DMFT+Σ_k. Physica C, v. 460–462, 997–999 (2007)

91. M.V. Sadovskii, E.Z. Kuchinskii, I.A. Nekrasov. Destruction of the Fermi Surface due to Pseudogap Fluctuations in Correlated Systems. Physica C, v. 460–462, 1084–1085 (2007)

92. E.Z. Kuchinskii, I.A. Nekrasov, M.V. Sadovskii. Mott–Hubbard Transition and Anderson Localization: Generalized Dynamical Mean-Field Theory Approach. JETP, v. 106, No. 3, 581–596 (2008)

93. E.Z. Kuchinskii, N.A. Kuleeva, I.A. Nekrasov, M.V. Sadovskii. Optical Sum Rule in Strongly Correlated Systems. JETP, v. 107, No. 2, 281–287 (2008)

94. I.A. Nekrasov, E.E. Kokorina, E.Z. Kuchinskii, Z.V. Pchelkina, M.V. Sadovskii. Comparative Study of Electron and Hole Doped High-T_c Compounds in Pseudogap Regime: LDA+DMFT+Σ_k Approach. J. Phys. Chem. Solids, v. 69, No. 12, 3269–3273 (2008)

95. E.E. Kokorina, E.Z. Kuchinskii, I.A. Nekrasov, Z.V. Pchelkina, M.V. Sadovskii, A. Sekiyama, S. Suga, M. Tsunekawa. Origin of "Hot-Spots" in the Pseudogap Regime of $Nd_{1.85}Ce_{0.15}CuO_4$: LDA+DMFT+Σ_k Study. JETP, v. 107, No. 5, 828–838 (2008)

96. I.A. Nekrasov, Z.V. Pchelkina, M.V. Sadovskii. High Temperature Superconductivity in Transition Metal Oxypnictides: a Rare-Earth Puzzle? JETP Letters, v. 87, No. 10, 560–564 (2008)

97. I.A. Nekrasov, Z.V. Pchelkina, M.V. Sadovskii. Electronic Structure of Prototype AFe_2As_2 and ReOFeAs High-Temperature Superconductors: a Comparison. JETP Letters, v. 88, No. 2, 144–149 (2008)

98. I.A. Nekrasov, Z.V. Pchelkina, M.V. Sadovskii. Electronic Structure of New LiFeAs High-T_c Superconductor. JETP Letters, v. 88, No. 8, 543–545 (2008)

99. I.A. Nekrasov, Z.V. Pchelkina, M.V. Sadovskii. Electronic Structure of New AFFeAs Prototype of Iron Arsenide Superconductors. JETP Letters, v. 88, No. 10, 679–682 (2008)

100. E.Z. Kuchinskii, M.V. Sadovskii. Reconstruction of the Fermi Surface in the Pseudogap State of Cuprates. JETP Letters, v. 88, No. 3, 192–196 (2008)

101. E.Z. Kuchinskii, M.V. Sadovskii. Multiple Bands – a Key to High-Temperature Superconductivity in Iron Arsenides. JETP Letters, v. 89, No. 3, 156–160 (2009)

102. E.Z. Kuchinskii, I.A. Nekrasov, M.V. Sadovskii. Interplay of Electron–Phonon Interaction and Strong Correlations: LDA+DMFT+Σ_k Study. Phys. Rev. B, v. 80, 115124 (2009)

103. I.A. Nekrasov, N.S. Pavlov, E.Z. Kuchinskii, M.V. Sadovskii, Z.V. Pchelkina, V.B. Zabolotnyy, J. Geck, B. Buchner, S.V. Borisenko, D.S. Inosov, A.A. Kordyuk, M. Lambacher, A. Erb. Electronic Structure of $Pr_{2-x}Ce_xCuO_4$ studied via ARPES and LDA+DMFT+Σ_k. Phys. Rev. B, v. 80, 140510 (2009)

104. E.Z. Kuchinskii, M.V. Sadovskii. Multiple Bands – a Key to High-Temperature Superconductivity in Iron Arsenides. Physica C, v. 470, S418–S419 (2009)

105. E.Z. Kuchinskii, N.A. Kuleeva, I.A. Nekrasov, M.V. Sadovskii. Two-Dimensional Anderson–Hubbard Model in DMFT+Σ_k Approximation. JETP, v. 110, No. 2, 325–335 (2010)

106. E.Z. Kuchinskii, I.A. Nekrasov, M.V. Sadovskii. Anion Height Dependence of T_c and Density of States in Iron Based Superconductors. JEPT Letters, v. 91, No. 10, 518–522 (2010)

107. E.Z. Kuchinskii, M.V. Sadovskii. Electronic Structure and Possible Pseudogap Behavior in Iron Based Superconductors. JETP Letters, v. 91, No. 12, 660–664 (2010)

108. I.A. Nekrasov, E.E. Kokorina, E.Z. Kuchinskii, M.V. Sadovskii, S. Kasai, A. Sekiyama, S. Suga. ARPES Spectral Functions and Fermi Surface for $La_{1.86}Sr_{0.14}CuO_4$ Compared with LDA+DMFT+Σ_k Calculations. JETP, v. 110, No. 6 (2010)

109. I.A. Nekrasov, M.V. Sadovskii. Electronic Structure of Novel Multiple-Band Superconductor $SrPt_2As_2$. JETP Letters, v. 92, No. 11, 751 (2010)

110. I.A. Nekrasov, M.V. Sadovskii. Electronic Structure, Topological Phase Transitions and Superconductivity in $(K,Cs)_xFe_2Se_2$. JETP Letters, v. 93, No. 3, 166–169 (2011)

111. M.V. Sadovskii, E.Z. Kuchinskii, I.A. Nekrasov. Interplay of Electron–Phonon Interaction and Strong Correlations: DMFT+Σ Approach. J. Phys. Chem. Solids, v. 72, 366–370 (2011)

112. I.A. Nekrasov, E.Z. Kuchinskii, M.V. Sadovskii. Pseudogap Phase of High-T_c Compounds Described within the LDA+DMFT+Σ_k Approach. J. Phys. Chem. Solids, v. 72, 371–375 (2011)

113. M.V. Medvedev, I.A. Nekrasov, M.V. Sadovskii. Electronic and Magnetic Structure of Possible Iron Based Superconductor $BaFe_2Se_3$. JETP Letters, v. 95, No. 1, 33–37 (2012)

114. E.Z. Kuchinskii, I.A. Nekrasov, M.V. Sadovskii. Electronic Structure of Two-Dimensional Hexagonal Diselenides: Charge Density Waves and Pseudogap Behavior. JETP, v. 114, No. 4, 671–680 (2012)

115. I.A. Nekrasov, N.S. Pavlov, M.V. Sadovskii. Consistent LDA'+DMFT – an unambiguous way to avoid double counting problem: NiO test. JETP Letters, v. 95, No. 11, 581–585 (2012)

116. I.A. Nekrasov, M.V. Sadovskii. Electronic Structure of New Multiple Band Pt-Pnictide Superconductor APt_3P. JETP Letters, v. 96, No. 4, 227–230 (2012)

117. M.V. Sadovskii, E.Z. Kuchinskii, I.A. Nekrasov. Iron Based Superconductors: Pnictides versus Chalcogenides. JMMM, v. 324, 3481–3486 (2012)

118. I.A. Nekrasov, N.S. Pavlov, M.V. Sadovskii. Consistent LDA'+DMFT Approach to Electronic Structure of Transition Metal Oxides: Charge Transfer Insulators and Correlated Metals. JETP, v. 116, No. 4, 620–634 (2013)

119. I.A. Nekrasov, N.S. Pavlov, M.V. Sadovskii. LDA'+DMFT Investigation of Electronic Structure of $K_{1-x}Fe_{2-y}Se_2$ Superconductor. JETP Letters, v. 97, No. 1, 15–19 (2013)

120. I.A. Nekrasov, N.S. Pavlov, M.V. Sadovskii. Doping Dependence of Correlation Effects in of $K_{1-x}Fe_{2-y}Se_2$ Superconductor: LDA'+DMFT Insvestigation. JETP, v. 117, No. 5, 926–932 (2013)

121. I.A. Nekrasov, M.V. Sadovskii. Comparative Study of Electronic Structure of New Superconductors (Sr, Ca)Pd_2As_2 and Related Compound $BaPd_2As_2$. JETP Letters, v. 98, No. 1, 24–27 (2013)

122. N.A. Kuleeva, E.Z. Kuchinskii, M.V. Sadovskii. Normal Phase and Superconducting Instability in Attractive Hubbard Model: the DMFT (NRG) Study. JETP, v. 119, No. 2, 264–271 (2014)

123. I.A. Nekrasov, M.V. Sadovskii. Electronic Structure of New Iron-Based Superconductors: From Pnictides to Chalcogenides and Other Similar Systems. JETP Letters, v. 99, No. 10, 598–612 (2014)

124. E.Z. Kuchinskii, N.A. Kuleeva, M.V. Sadovskii. Disorder Effects in BCS–BEC Crossover Region of Attractive Hubbard Model. JETP Letters, v. 100, No. 3, 192–196 (2014)

125. E.Z. Kuchinskii, N.A. Kuleeva, M.V. Sadovskii. Attractive Hubbard Model with Disorder and the Generalized Anderson Theorem. JETP, v. 120, No. 6, 1055–1063 (2015)

126. I.A. Nekrasov, M.V. Sadovskii. Electronic and Magnetic Properties of the New Iron-Based Superconductor $[Li_{1-x}Fe_xOH]FeSe$. JETP Letters, v. 101, No. 1, 47–50 (2015)

127. I.A. Nekrasov, N.S. Pavlov, M.V. Sadovskii. Electronic Structure of NaFeAs Superconductor: LDA+DMFT calculations compared with ARPES experiments. JETP Letters, v. 102, No. 1, 26–31 (2015)

128. E.Z. Kuchinskii, N.A. Kuleeva, M.V. Sadovskii. Attractive Hubbard Model: Homogeneous Ginzburg–Landau Expansion and Disorder. JETP, v. 122, No. 2, 375–383 (2016)

129. E.Z. Kuchinskii, M.V. Sadovskii. DMFT+Σ Approach to Disordered Hubbard Model. JETP, v. 122, No. 3, 510–525 (2016)

130. E.Z. Kuchinskii, N.A. Kuleeva, M.V. Sadovskii. Attractive Hubbard Model within the Generalized DMFT: Normal State Properties, Disorder Effects and Superconductivity. Journal of Superconductivity and Novel Magnetism, v. 29, 1097 (2016)

131. I.A. Nekrasov, N.S. Pavlov, M.V. Sadovskii. Electronic Structure of NaFeAs Superconductor: LDA+DMFT calculation compared with ARPES experiment. Journal of Superconductivity and Novel Magnetism, v. 29, 1117 (2016)

132. I.A. Nekrasov, N.S. Pavlov, M.V. Sadovskii. A.A. Slobodchikov. Electronic Structure of FeSe Monolayer Superconductors. Low Temperature Physics, v. 42, No. 10, 891–899 (2016)

133. E.Z. Kuchinskii, N.A. Kuleeva, M.V. Sadovskii. Ginzburg–Landau expansion in BCS–BEC crossover region of disordered attractive Hubbard model. Low Temperature Physics, v. 43, No. 1, 17–26 (2017)

134. I.A. Nekrasov, N.S. Pavlov, M.V. Sadovskii. On the origin of the shallow and "replica" bands in FeSe monolayer superconductors. JETP Letters, v. 105, No. 6, 370–374 (2017)

135. E.Z. Kuchinskii, N.A. Kuleeva, M.V. Sadovskii. Ginzburg–Landau Expansion in Strongly Disordered Attractive Hubbard Model. JETP, v. 125, No. 1, 111–122 (2017)

136. E.Z. Kuchinskii, N.A. Kuleeva, M.V. Sadovskii. Temperature Dependence of the Upper Critical Field in Disordered Hubbard Model with Attraction. JETP, v. 125, No. 6, 1127–1136 (2017)

137. I.A. Nekrasov, N.S. Pavlov, M.V. Sadovskii. Electronic Structure of FeSe Monolayer Superconductors: Shallow Bands and Correlations. JETP, v. 126, No. 4, 485–496 (2018)

138. E.Z. Kuchinskii, N.A. Kuleeva, M.V. Sadovskii. Temperature Dependence of Paramagnetic Critical Magnetic Field of Disordered Attarctive Hubbard Model. JETP, v. 127, No. 4, 753–760 (2018)

139. M.V. Sadovskii. Electron–Phonon Coupling in Eliashberg–McMillan Theory Beyond Adiabatic Approximation. JETP, v. 128, No. 3, 455–463 (2019)

140. M.V. Sadovskii. Antiadiabatic Phonons, Coulomb Pseudopotential and Superconductivity in Eliashberg–McMillan Theory. JETP Letters, v. 109, No. 3, 166–170 (2019)

141. M.V. Sadovskii. Antiadiabatic Phonons and Superconductivity in Eliashberg–McMillan Theory. J. Superconductivity and Novel Magnetism, v. 33, No. 1, 19–26 (2020)

142. M.V. Sadovskii. On Planckian Limit for Inelastic Relaxation in Metals. JETP Letters, v. 111, No. 3, 188–192 (2020)

143. M.V. Sadovskii. Superconducting Transition Temperature for Very Strong Coupling in the Antiadiabatic Limit of Eliashberg Equations. JETP Letters, v. 113, No. 9, 581–585 (2021)

144. E.Z. Kuchinskii, N.A. Kuleeva, D.I. Khomskii, M.V. Sadovskii. Hall Effect in Doped Mott Insulator: DMFT Approximation. JETP Letters, v. 115, No. 7, 444–447 (2022)

Michael V. SADOVSKII

Reviews on Condensed Matter Physics
(in Two Volumes)

САДОВСКИЙ Михаил Виссарионович

Обзоры по физике конденсированного состояния
(в двух томах)

ISBN 978-5-907502-81-9

9 785907 502819

Отпечатано в ООО Универсальная Типография «Альфа Принт»
620049, г. Екатеринбург, пер. Автоматики, 2ж
www.alfaprint24.ru

Michael V. Sadovskii graduated in 1971 the Physical Department of the Ural State University (Sverdlovsk).

Ph.D. – 1975, Dr.Sci. – 1986.

1971–1974 – Ph.D work – theoretical department of P.N. Lebedev Physical Institute, USSR Academy of Sicences, Moscow.

1974–1986 – researcher at the Institute for Metal Physics USSR Academy of Sciences, Ural Scientific Centre (Sverdlovsk).

In 1987–2017 head of theoretical physics laboratory of the Institute for Electrophysics, Russian Academy of Sciences, Ural Branch (Ekaterinburg), at present the chief researcher in this laboratory. During 1993–2002 – deputy director of the Institute. In 2011–2013 also headed the laboratory of quantum theory of condensed matter, Institute for Metal Physics, Russian Academy of Sciences, Ural Branch, in 2013–2018 chief researcher of this laboratory and scientific supervisor of the Department of Theoretical Physics of the Institute for Metal Physics.

Professor of the Ural State University (Theoretical Physics), 1991–2010.

Author of more than 150 papers on condensed matter theory. Main interests – electronic theory of disordered systems (Anderson localization, pseudogap), superconductivity (disordered superconductors, high-temperature superconductivity). Developed the field theory approach to Anderson localization, self-consistent theory of localization, theory of superconductors close to the Anderson transition. Formulated exactly solvable models of the pseudogap state, models of disorder effects in the theory of Peierls transition. Recent interests were connected with extensions of dynamical mean field theory approach to the theory of electrons in strongly correlated systems and theoretical studies of iron based superconductors.

Corresponding member of the Russian Academy of Sciences (1994), Full Member (2003), member of the Presidium of the Ural Branch of RAS, member of the Bureau of the Physics Division of RAS and the RAS Comission on pseudoscience, member of American Physical Society, Fellow of the Institute of Physics (UK) – 2002. Member of editorial boards of JETP and Physics Uspekhi. Member of the "July 1st Club" opposing 2013 governmental reform of the Russian Academy of Sciences.

9 785907 502819

A.G. Stoletov Prize in Physics of the Russian Academy of Sciences (2002)

V.L. Ginzburg Gold Medal of the Russian Academy of Sciences (2016)

M.N. Mikheev Silver Medal of the Institute for Metal Physics (2017)
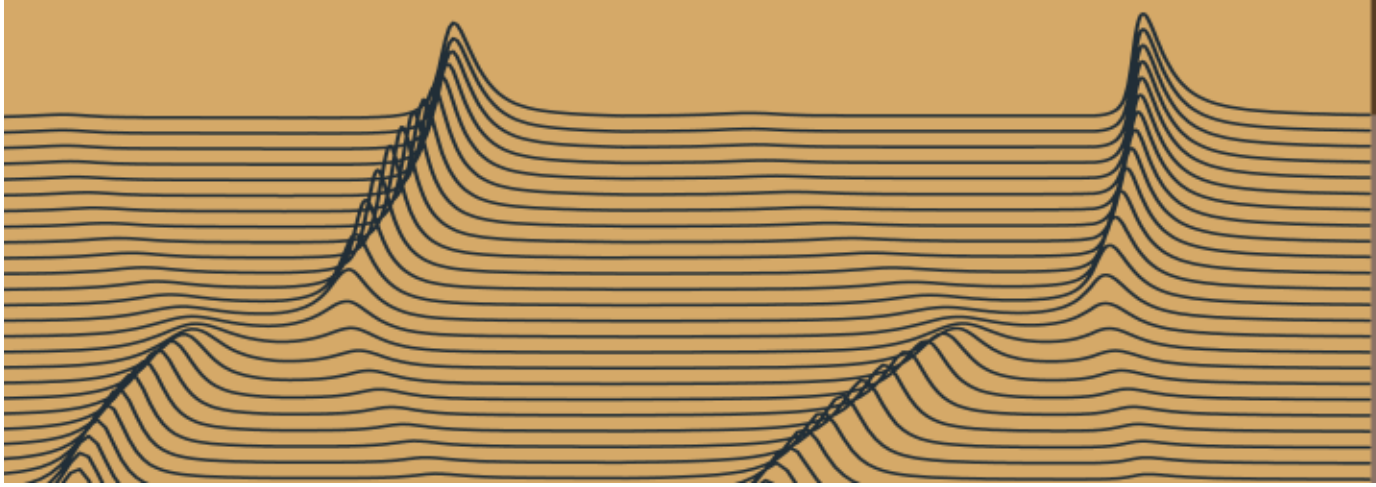
S.V. Vonsovsky Gold Medal of the Ural Branch of the Russian Academy of Sciences (2018)